Quantification of Landscape Evolution on Multiple Time-Scales: Applications of High-Resolution 3-D Laser Scanning and Erosion Measurements to Tectonic and Geomorphological Questions

Dissertation zur Erlangung des Doktorgrades
der Fakultät für Geowissenschaften der
Ludwig-Maximilians-Universität München

vorgelegt von

Ramona Baran

am 29. Februar 2012

1. Gutachter: Prof. Dr. Anke M. Friedrich

2. Gutachter: Prof. Dr. Fritz Schlunegger

Tag der mündlichen Prüfung: 14. Juni 2012

Für meine Oma.

Niemals wirst du umkehren,
Denn das Sein ist dir lieber als der Schein;
Auch im Leben wirst du immer erkennen
Wertvolle Erze im tauben Gestein.

Halte durch, Geolog!
Gib nicht auf, Geolog!
Des Windes und Sturmes Freund!

aus "Ich mache mir Sorgen, Mama", Wladimir Kaminer

Table of Contents

Short-Term Sediment Transport in Context of Post-Glacial Landscape Evolution: Insights from Field Mapping and High-Resolution LiDAR Measurements, Alp Valley, Switzerland

Acknowledgements

Silent gratitude isn't much use to anyone.

Gertude Stein (1874–1946)

To be honest, I didn't really know how to start with this, because many different people supported me in many different ways throughout the last years. A few days ago, I read the words of Gertrude Stein and thought that she was absolutely right. However, the way of communicating my gratitude to all of you is indeed silent when you read it, but it won't be 'silent' anymore when you have read it. So, thank you!!!

Abstract

Essential information about the activity or even the mechanics of tectonic and erosional processes can be extracted from their surface expression. For this purpose, it is necessary to appropriately constrain the temporal as well as the spatial framework, in which to consider a specific process. While recently developed dating techniques, such as thermochronology or radiocarbon dating, allow to assess the age of landforms and therefore rates of tectonic and erosional processes, detailed spatial information is also required to assess these rates correctly. Due to a lack of appropriate topographic data in the past it was sometimes challenging to reliably approximate the spatial framework, because the size of a particular landform can often cover a wide range of spatial scales. Recently available, conventional topographic data, such as those of the Shuttle Radar Topography Mission, substantially improved the definition of an appropriate spatial framework due to their spatial coverage and resolution of down to less than 1 m. However, to constrain this framework at a detail beyond the resolution of several decimeter terrestrial laser scanning provides a highly efficient approach. This technique permits the rapid acquisition (within minutes) of tremendous amounts of topographic data with both, a high resolution of a few centimeters and a high accuracy of a few millimeters. High-resolution topographic maps of a certain area of the surface of the Earth are derived from individual laser-scanner measurements, that in turn allow to characterize the in-situ geomorphic setting at great detail. Moreover, repeated measurements of this area allow to quantify morphological changes thereby supporting the survey of surface processes on short-term scales ranging from days up to several years. The former approach is best suited for tectono- and the latter one for fluvial-geomorphic studies, and we present results from two case studies that are either based on single or repeated laser-scanner measurements. In the first case, we combined field mapping and high-resolution digital elevation model (DEM) analysis to evaluate the detailed meter- to hundred meter-scale structure and surface expression of one flank of the Rex Hills pressure ridge in the western United States. Based on terrestrial laser scanning (Riegl *LMS-Z420i*®) we derived a DEM with cm-scale resolution and extracted high-resolution topographic cross-sections. This enabled us to identify fault scarps and determine their relative ages and geometry. In the second case, we carried out a detailed field mapping of erosion and sedimentation patterns in the Alp Valley, central Switzerland, to assess its Holocene evolution. Simultaneously, we conducted repeated high-resolution (less than 1 cm locally) laser-scanning surveys (Topcon *TLS-1000*®) along two tributaries, the Erlenbach and Vogelbach, to determine channel-morphology changes and the nature of shortest-term sediment transport by comparing the individual DEMs derived from these measurements, as well as to evaluate the context to the longer-term evolution of the Alp Valley. Both case studies, however, highlight the potential of medium-range laser scanners with measurement distances of up to hundreds of meters. Such scanners are most appropriate to efficiently analyze closely-spaced fault scarps across a broad range of spatial scales, and to document complex morphologic changes in small mountainous torrents due to sediment transport. Moreover, terrestrial laser scanning is a key tool to monitor surface processes, but the insights gained from this method are generally evaluated best in the context of further data sets including geochronological, structural, subsurface, or climate data.

Surface processes, in particular erosion, sediment transport, and deposition in sedimentary basins are intermittent in space and time challenging both, the appropriate definition of a spatiotemporal framework addressed above and a comprehensive process understanding. A major objective of this thesis is to contribute to a better understanding of scale linkage

concerning these processes. We therefore first carried out a comprehensive comparison of short- to long-term erosion measurements from the Alps based on an approach originally established to evaluate the significance of geologic and geodetic measurements along intra-continental faults on time scales of millions to tens of years. In a second step, we re-assessed the sediment budget of the Alps, a data set that is usually considered to be an appropriate measure of long-term erosion in the Alps. The two major results of both studies indicate that: short- and medium-term erosion in the Alps over years to ten thousands of years is dominantly influenced by climate and weather variability, e.g., due to seasonal differences in the amount of precipitation; whereas long-term erosion over millions of years is controlled by tectonic processes.

Zusammenfassung

Im Allgemeinen können aus der Gestalt der Erdoberfläche wesentliche Informationen über die Aktivität oder sogar Mechanik von Erosions- und tektonischen Prozessen gewonnen werden. Hierfür ist es unerlässlich den zeitlich-räumlichen Rahmen, innerhalb dessen ein bestimmter Prozess betrachtet werden soll, adäquat zu definieren. Während mit unlängst entwickelten Datierungsmethoden, wie der Thermochronologie oder der Radiokarbonaltersbestimmung, das Alter von Geländeformen und somit Raten von Erosions- und tektonischen Prozessen bestimmt werden können, sind dafür aber auch detaillierte räumliche Informationen erforderlich. Da geeignete topographische Daten in der Vergangenheit oft nicht vorhanden waren, war es nicht immer einfach den räumlichen Rahmen angemessen zu definieren, auch weil die Größe einer bestimmten Geländeform über mehrere Größenordnungen hinweg variieren kann. Gegenwärtig erleichtern konventionelle Topographiedaten, wie die der Shuttle Radar Topography Mission, die Definition des räumlichen Rahmens beträchtlich vor allen Dingen wegen ihrer räumlichen Abdeckung und Auflösung von bis zu weniger als 1 m. Um den räumlichen Rahmen nun aber in einem Detail definieren zu können, das jenseits einer Auflösung von mehreren Dezimetern liegt, bietet das terrestrische Laserscannen einen hoch effizienten Lösungsansatz. Mit dieser Technik können innerhalb von ein paar Minuten große Mengen topographischer Daten sowohl mit einer hohen Auflösung von wenigen Zentimetern als auch einer hohen Genauigkeit von wenigen Millimetern erhoben werden. Auf Grundlage einzelner Laserscannermessungen können hochaufgelöste, topographische Karten eines bestimmten Ausschnittes der Erdoberfläche generiert werden, die eine sehr detaillierte Charakterisierung der gegenwärtigen geomorphologischen Situation ermöglichen. Außerdem können durch wiederholte Vermessung desselben Ausschnittes Oberflächenänderungen quantifiziert werden, was wiederum das Monitoring von Oberflächenprozessen über Tage bis mehrere Jahre hinweg erlaubt. Der erste dieser beiden Ansätze ist für tektonische und der letztere für fluviatile geomorphologische Studien am besten geeignet. In dieser Dissertation werden nun die Ergebnisse zweier Fallstudien vorgestellt, die entweder auf der einmaligen oder wiederholten Anwendung eines terrestrischen Laserscanners beruhen. Für die erste Fallstudie haben wir eine geologische Geländekartierung mit der Analyse eines hochaufgelösten digitalen Höhenmodells (DHM) kombiniert, um die Struktur und Morphologie einer störungsbedingten Struktur, den Rex Hills in den westlichen USA, umfassend zu untersuchen. Mit Hilfe terrestrischer Laserscanner-Messungen (Riegl *LMS-Z420i*®) haben wir ein DHM mit einer Auflösung im cm-Bereich generiert, aus dem wir wiederum hochaufgelöste topographische Profile extrahiert haben. Anhand dieser Profile konnten wir Erdbeben bedingte Terrainstufen entlang einer Flanke der Rex Hills identifizieren sowie deren relative Alter und Geometrie erfassen. Für die zweite Fallstudie haben wir mittels einer detaillierten Kartierung von Erosions- und Sedimentationsmustern im Alptal in der zentralen Schweiz die Holozäne Entwicklung dieses Tales rekonstruiert. Gleichzeitig haben wir wiederholt hochauflösende (teilweise unter 1 cm) Laserscanner-Messungen (Topcon *TLS-1000*®) entlang der Nebenbäche Erlenbach und Vogelbach durchgeführt. Durch den Vergleich einzelner DHMs konnten wir morphologische Änderungen der Bachsohle und die Art des kurzfristigen Sedimenttransportes in beiden Bächen dokumentieren und einen Bezug zur längerfristigen Entwicklung des Alptales ableiten. Die Ergebnisse beider Studien verdeutlichen das Potenzial von Laserscannern mit Messdistanzen von mehreren Hundert Metern. Diese sind am besten für die effiziente Analyse eng beieinander liegender, Erdbeben bedingter Terrainstufen sowie die Charakterisierung komplexer, morphologischer Änderungen auf Grund von Materialtransport

in Wildbächen geeignet und das über mehrere räumliche Größenordnungen hinweg. Das terrestrische Laserscannen ist eine Schlüsseltechnologie, um Oberflächenprozesse zu überwachen, aber die Erkenntnisse, die mit dieser Methode gewonnen werden, sollten unter Einbeziehung weiterer Datensätze evaluiert werden. Dazu gehören u.a. geochronologische und strukturelle Daten oder auch Untergrund- und Klimadaten.

Oberflächenprozesse insbesondere Erosion, Sedimenttransport und Ablagerung in Sedimentbecken sind ihrer Natur nach episodische Prozesse und das in Raum und Zeit. Dies erschwert einerseits ein umfassendes Prozessverständnis und andererseits die adäquate Definition des räumlich-zeitlichen Rahmens wie eben diskutiert. Ein Hauptziel dieser Dissertation ist es, zu einem besseren Verständnis der räumlich-zeitlichen Verknüpfung von Skalen bezüglich dieser Prozesse beizutragen. Daher haben wir zunächst einen detaillierten Vergleich von kurz- bis langfristigen Erosionsmessungen in den Alpen durchgeführt. Dieser Vergleich beruht auf einem Ansatz, der ursprünglich dazu verwendet wurde, die Bedeutung geologischer und geodätischer Messungen entlang intrakontinentaler Störungen über Zeiträume von Millionen von Jahren bis zu zehn Jahren zu evaluieren. Des Weiteren haben wir das Sedimentbudget der Alpen neu untersucht. Dieser Datensatz wird gewöhnlich als eine geeignete Messung der langfristigen Erosion in den Alpen betrachtet. Die zwei wichtigsten Ergebnisse dieser beiden Studien zeigen, dass über kurz- und mittelfristige Zeiträume von mehreren Jahren bis zehn Tausend Jahren Erosion in den Alpen wohl primär durch klimatische Variabilität beeinflusst wird, z.B. durch jahreszeitliche Unterschiede der Niederschlagsmenge; wohingegen über langfristige Zeiträume von Millionen von Jahren hinweg Erosion durch tektonische Prozesse kontrolliert wird.

1. Introduction

1.1.   Introduction

Erosion and tectonics modify the surface of the Earth in a manner, that resulting changes often provide information about spatiotemporal process activity or process mechanics (e.g., Yeats et al., 1997). Fault scarps, for example, represent the most obvious surface expression of tectonic activity. Such scarps had been extensively studied to constrain fault kinematics as well as scarp-degradation processes (e.g., Wallace, 1977; Arrowsmith et al., 1998). Fault scarps are due to coseismic surface offset, and in postseismic times the initially relatively steep scarps tend to become less steep due to erosion of material at the top and deposition at the base of the scarp (Fig. 1.1).

Or, fluvial channel patterns change in response to changes in sediment load, grain size of transported sediment, stream flow-velocity, or stream gradient (Fig. 1.2A; e.g., Schumm and Khan, 1971). It is common along a river course that braided rivers favored by high sediment loads and flow velocities change downstream into meandering rivers when stream gradient and sediment load decline (Fig. 1.2A; e.g., Burbank and Anderson, 2001). This behavior bears potential information about tectonic uplift patterns as suggested by experimental results (e.g., Fig. 1.2B; Ouchi, 1985), although each of the factors influencing channel patterns can be independent of tectonic activity (Burbank and Anderson, 2001).

Conceptual landscape evolution models introduced in the past, such as the models of Davis (1899) and Penck (1953), hinge on assumptions about the timing of tectonic forcing. The former model assumes a short-lived, tectonically induced uplift in the beginning that results in the formation of topography during the 'youth' stage (Fig. 1.3A). Subsequently, erosion progressively lowers the topography during the stage of 'maturity' resulting in the formation of a peneplain during the 'old age' stage (Fig. 1.3A). The latter model assumes tectonically induced uplift increases from the beginning toward a maximum, and diminishes afterwards (Fig. 1.3B). This would result in the gradual growth of topography toward a maximum stage of relief. Erosion is presumed to affect the uplifting region during the building of topography, to exceed uplift when it diminishes, and to progressively lower topography at the end (Fig. 1.3B). However, in the absence of a chronological framework these models remained unconstrained and therefore speculative (Burbank and Anderson, 2001). New techniques developed during the last decades, including thermochronology, cosmogenic nuclide or radiocarbon dating, allow now to constrain the age of landforms, and hence to assess the rates of tectonic and erosional processes (e.g., Burbank and Anderson, 2001).

Apart from temporal constraints, however, detailed spatial information is also required to assess these process rates appropriately. This demand is exemplarily emphasized in chapter IV, in which we re-evaluated the sediment budget of the Alps (Kuhlemann et al., 2001, 2002). This is based on the assumption that material deposited in all circum-Alpine sedimentary basins is solely derived from the Alps, which allows to determine erosion rates in the Alps. However, we observed two phases in the spatiotemporal Alpine erosion-deposition pattern. Sediments were deposited in proximal basins during the first phase, whereas deposition occurred in distal basins during the second phase. Apparently, sediments have not been derived solely from the Alps during the latter phase, they had also been derived from the area of the proximal basins. This implies a drastic increase of the potential erosion area. Therefore, the basic assumption of the sediment budget is valid during the first phase when the spatial framework is appropriately defined by erosion of material occurring in the Alps and its deposition in the proximal basins. In contrast, this assumption is presumably invalid during the second phase due to the increase of the potential erosion area. Hence, the spatial framework needs to be re-defined to constrain erosion rates in the Alps correctly. Erosion of

Alpine material occurred in the Alps and proximal basins and was deposited in the distal basins.

The definition of a suitable spatial framework primarily depends on the size of a specific landform that can often cover a broad range of spatial scales. To proceed with the fault-scarp example mentioned above (Fig. 1.1), such scarps range in height from only a few cm – up to 25 cm high scarps formed near Lompoc in the NW Transverse Ranges, California, during a M_L 2.5 earthquake that occurred on 7 April 1981 (Yerkes et al., 1983); or coseismic radar interferograms yielded a displacement of 56 cm related to the 28 June 1992 M_W 7.3 Landers earthquake (Massonnet et al., 1994) – up to tens of metres – a more than 45 m high scarp had been reported along the NW flank of the Humboldt Range, Nevada, that is most likely due to the occurrence of repeated earthquakes along the fault (Wallace, 1977).

Recently available, topographic data facilitate the definition of an appropriate spatial framework because of their spatial coverage and resolution. On one hand, such data comprise, for example, satellite imagery or Shuttle Radar Topography Mission (SRTM) data with a global coverage of continental topography and a resolution ranging from tens of metres – e.g., 90 m for STRM data – down to less than 1 m for satellite imagery (e.g., Li, 1998). On the other hand, these data also comprise sets of limited spatial coverage such as airborne Light Detection And Ranging (LiDAR) data or aerial photography (Fig. 1.4A; e.g., Heritage and Hetherington, 2007). All these data are commonly based on either remote sensing or airborne data-acquisition techniques, and they can replace field-based labor-intensive techniques, such as plane-table measurements carried out by e.g., Hudnut and Sieh (1989), or GPS leveling utilized by e.g., Carretier et al. (2002) and Friedrich et al. (2004). Furthermore, they are particularly suited for detailed mapping purposes, e.g., to constrain fault patterns, drainage networks, or the distribution of landforms such as moraines.

To approximate the spatial framework at a detail beyond the resolution of several decimeter terrestrial laser scanning provides an efficient approach (Fig. 1.4A; e.g., Large and Heritage, 2009). This technique enables the detailed mapping of morphologic characteristics of individual landforms that cannot be derived when mapping is based on satellite imagery or similar data. For example, the latter allows to map drainage networks as mentioned above, and at most to map the outlines of gravel bars along a river bed. In contrast, the application of terrestrial laser scanning allowed to determine the grain-scale topography of such gravel bars (Entwistle and Fuller, 2009; Hodge et al., 2009).
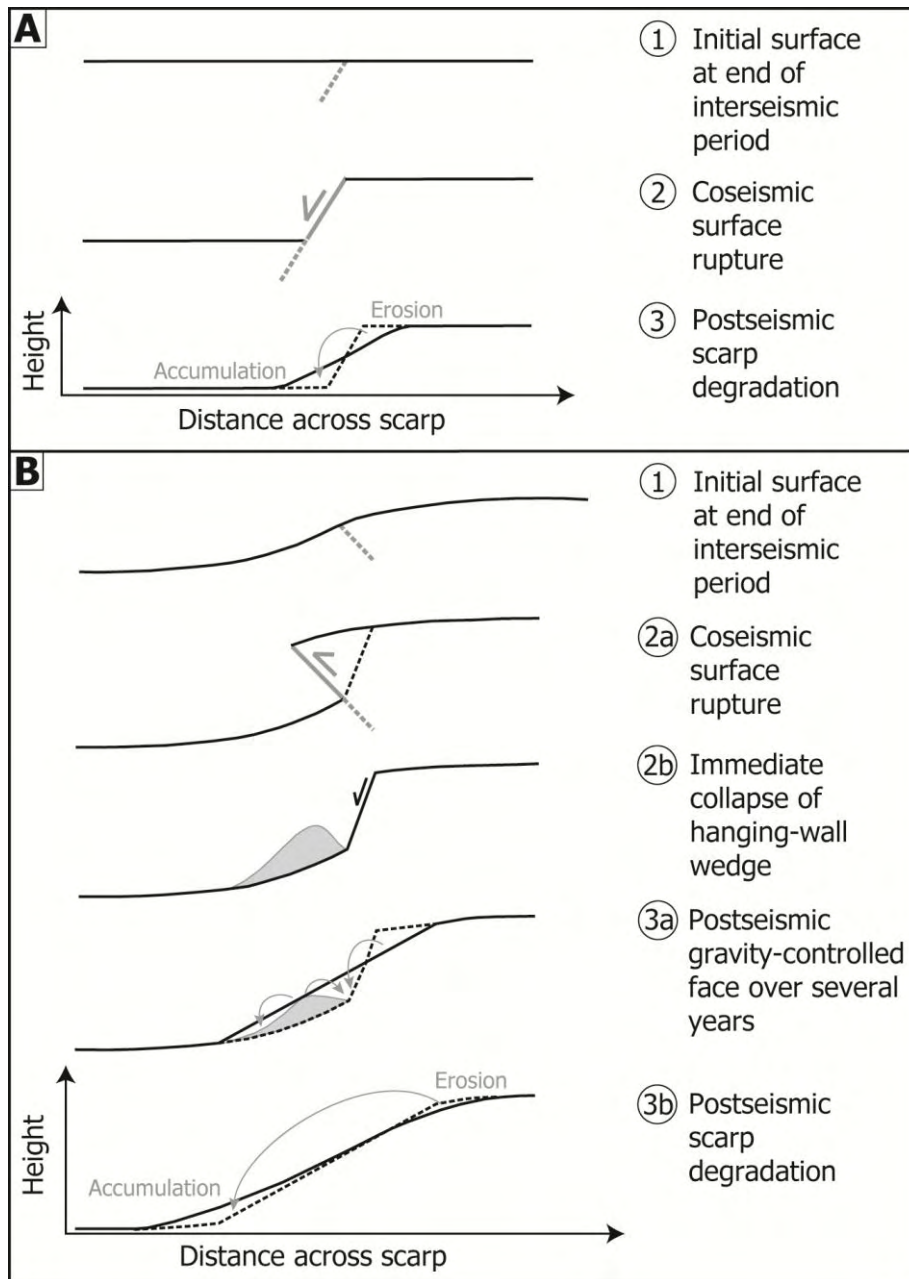
Fig. 1.1 (A) Simplified geomorphic development of a normal fault-scarp. **(B)** Conceptual geomorphic evolution of a reverse fault scarp (simplified after Carretier et al., 2002).
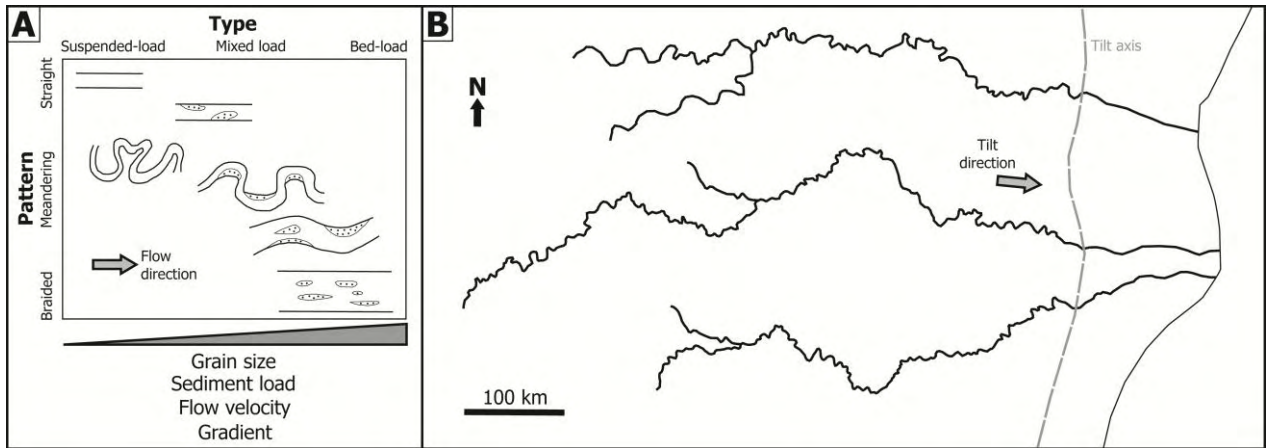
Fig. 1.2 (A) Changing fluvial channel patterns in response to variations in sediment load, grain size of transported material, stream flow-velocity, or stream gradient (simplified after Burbank and Anderson, 2001). **(B)** Map of an exemplary drainage network to demonstrate that river patterns provide potential information about regional tilting due to tectonic processes. Rivers meander due to a higher gradient west of the tilt axis, whereas they are straight east of it due to a lower gradient. Hence, this region appears to be tilted toward the east.
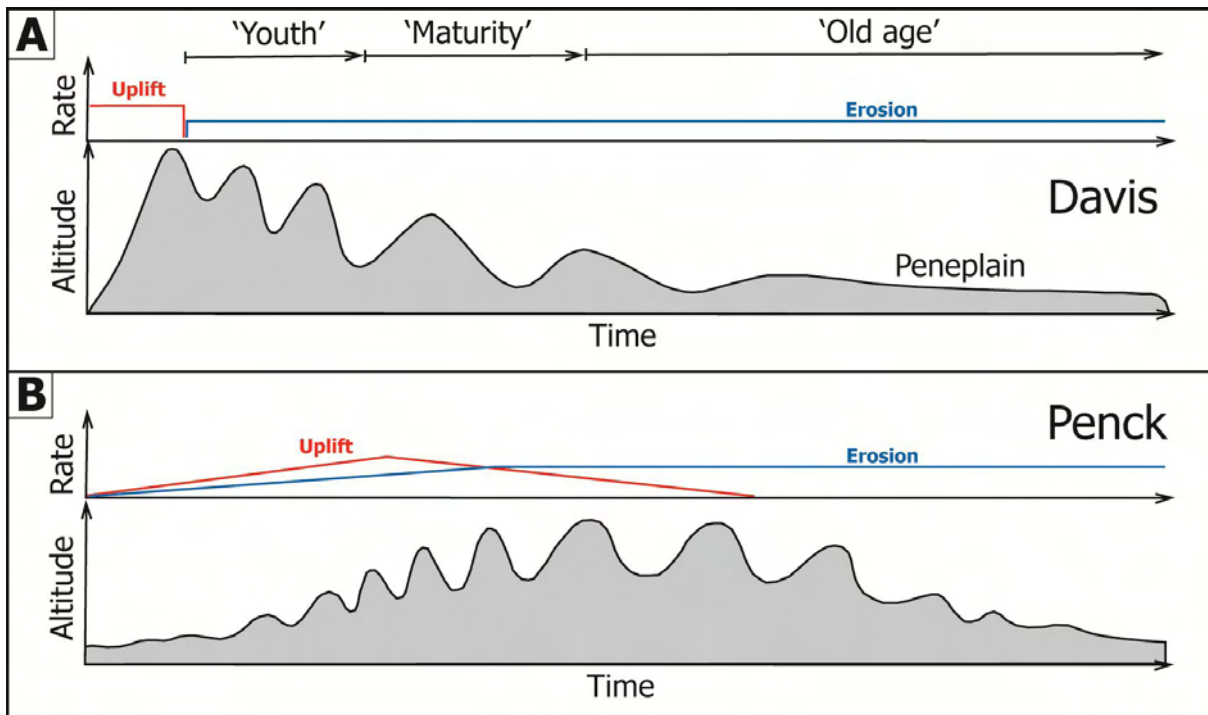
Fig. 1.3 Conceptual models of landscape evolution (simplified after Burbank and Anderson, 2001). **(A)** Model of Davis (1899): After short-lived uplift and building of topography, erosion results in the progressive reduction of relief through time. **(B)** The model of Penck (1953) is based on the relationship between erosion and uplift. The initial uplift is slow, followed by first accelerated, then decelerated uplift, and finally by quiescence. Erosion affects the uplifting region during building of topography, exceeds uplift when it diminishes, and progressively lowers topography at the end.
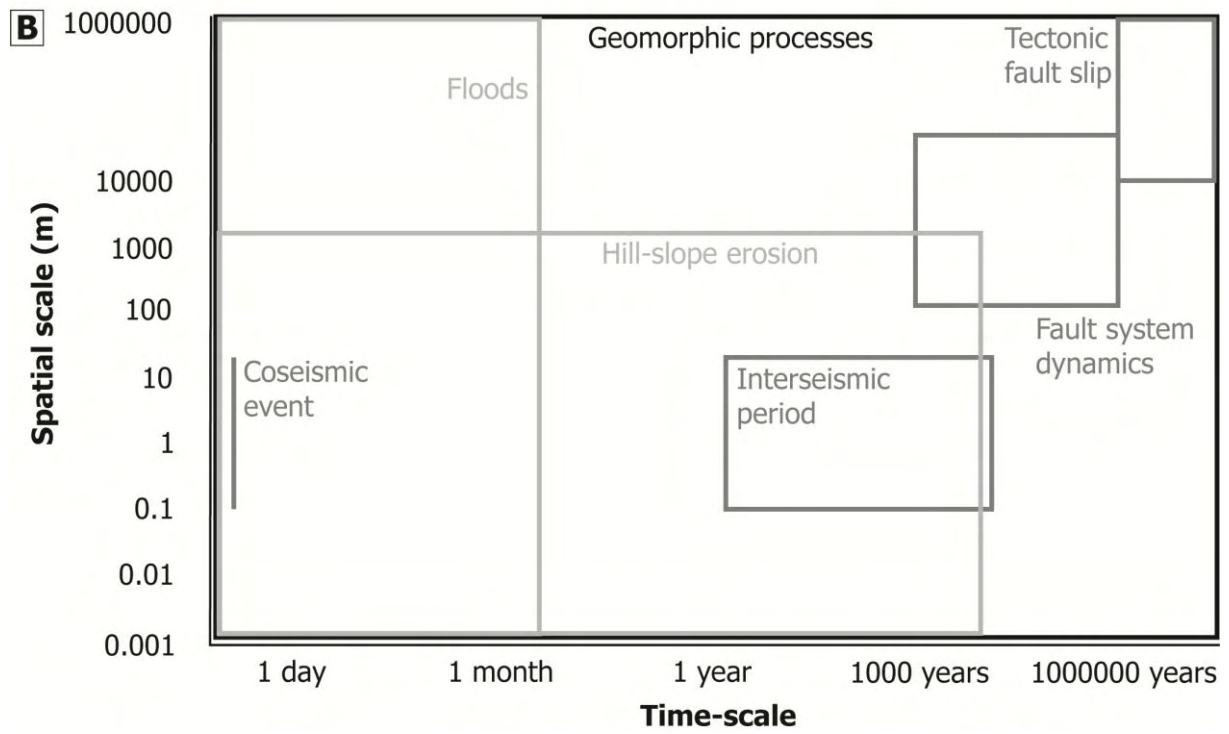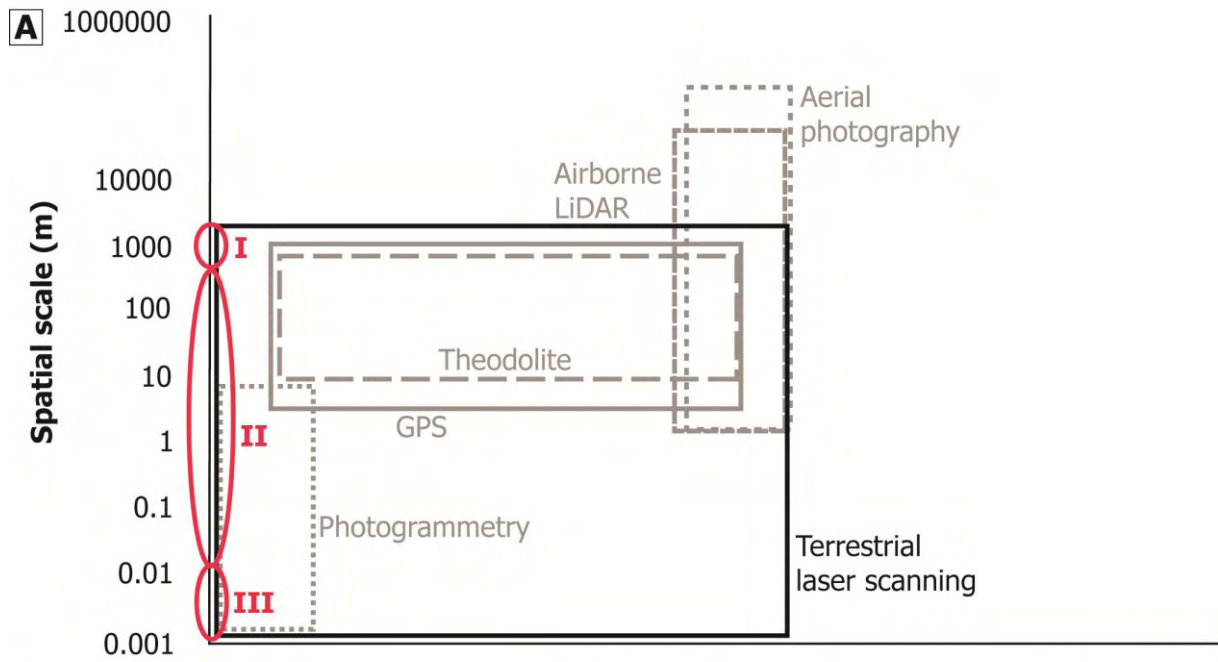
Fig. 1.4 (A) Spatial and short-term scale coverage of terrestrial laser scanning is shown in black (modified after Heritage and Hetherington, 2007). Various types of laser scanners (red ellipses: I – long range, II – medium range, III – short range) allow for observation of Earth surface processes across a broad range of spatial scales. Single measurements, the 'static' approach in the text, provide high-resolution topographic base maps, and allow to characterize the in-situ geomorphic situation of a certain area. Repeated measurements, the 'dynamic' approach in the text, allow to monitor surface processes on short-term scales of days to years. For comparison, gray colored items indicate spatial and temporal limitations of conventional geomorphic surveying techniques (modified after Heritage and Hetherington, 2007). However, terrestrial laser scanning covers spatial and temporal scales that cannot be considered by the common approaches. **(B)** Spatiotemporal scales of geomorphic process activity including both, erosional and tectonic processes, are outlined in black to be compared with the methodological scale coverage shown in Figure 1.4A. Spatiotemporal scales of selected erosional processes are highlighted in light gray. Large floods flush sediment to coastal areas that are often more than 1000 km away from the river head (e.g., Frostick and Jones, 2002), whereas even small streams can transport large amounts of material during a short time (e.g., Wolman and Miller, 1960). Hill-slope erosion comprises mass-wasting processes, such as sudden landslides and rock-fall, or slow soil creep, which can affect only certain areas of a hill-slope or entire mountain flanks (e.g., Trenhaile, 2007). Spatiotemporal scales of tectonic processes are shown in dark gray to illustrate the significance of different scales. Time-scale constraints of the latter approximated after Friedrich et al. (2003). In summary, modern airborne and terrestrial survey-technologies shown in Figure 1.4A have a temporal limit to monitor geomorphic processes, so that especially their short-term activity can be measured and evaluated using these techniques.

1.2.   High-Resolution Topography Data from Terrestrial Laser Scanning

1.2.1.   Evolution of the Discipline

Plane Table, Theodolite, and Remote Sensing Techniques

In past and modern times, the technical progress of field surveying disciplines supported scientific progress. Newly acquired data allowed new observations which in turn improved the understanding of Earth surface processes. In the 1970s, for example, while new developments in spaceborne remote-sensing technologies permitted a systematic observation of the Earth's surface at a global scale, scientists recognized the growing need to study the Earth as a complex system of processes that operate over a variety of spatiotemporal scales (Fig. 1.4; e.g., Salomonson et al., 2006). However, a brief review of a few surveying techniques including exemplary applications illustrates this evolution.

On one hand, conventional surveying comprise traditional, graphical methods with manual data acquisition such as the plane table. On the other hand, they comprise more recent terrestrial techniques such as the theodolite, and modern remote sensing technologies including satellite imagery etc. The latter type of survey technique also allows an automated data acquisition without field work. Hence, technical progress is generally time saving by reducing labor-intense field work, and it is economic by reducing financial efforts (e.g., Large and Heritage, 2009).

The plane table is a rotatable drawing board usually mounted horizontally on a tripod and set up above a certain point (e.g., Ritchie et al., 1988). A so-called alidade, often a rule with a telescopic sight, allows to sight objects of interests and to perform a graphical triangulation in the field. Thus, topographic information of a study site can be directly obtained. Prior to detailed mapping with a plane table it is recommended to define a set of control points, whose coordinates or relative positions are known in order to prevent the accumulation of errors associated with the graphical triangulation. However, plane tables had been traditionally used, for example, to survey beach profiles (Duncan Jr., 1964) or for geologic mapping purposes (e.g., Holmes and Page, 1956).

Theodolites were the most commonly used survey instrument prior to the establishment of laser-scanning sensors, and they are still one of the standard tools owing to their versatility, accuracy and ease of operation (Fig. 1.4A; Large and Heritage, 2009). Furthermore, a theodolite is an Electromagnetic Distance Measuring (EDM) device enabling two basic operations; it measures angles in horizontal and vertical planes (e.g., Ritchie et al., 1988). Surveys using this instrument were carried out in the field, for example, to determine fault-creep rates (Galehouse, 2002), to monitor the topographic growth of volcanoes (e.g., Nakada et al., 1995), or to measure the orientation of geological structures (e.g., Gross et al., 1997).

Remote sensing, an equivalent term for observing the Earth at some distance, developed rapidly (e.g., Liang, 2008). These techniques provide manifold data of the surface of the Earth that can be used to monitor surface processes with a high spatial coverage (Fig. 1.4). Prior to the 1970s, black and white aerial photographs had been used for terrain analysis over several decades (Fig. 1.4A; Townsend, 1981). In contrast, newer techniques became available starting in the 1970s. Sensors carried by satellites or airplanes generally record electromagnetic radiation that has been reflected or emitted by the Earth's surface, and that has been subject to modification by the atmosphere (e.g., Hardy, 1981). However, satellite based sensors comprise, for example, microwave (radar) and optical (lidar) devices (Salomonson et al., 2006), and airborne based sensors comprise photographic devices (Fig. 1.4A; e.g., Hardy, 1981).

Terrestrial Laser Scanning

Since the development of the first terrestrial laser scanner in 1999 (e.g., Large and Heritage, 2009), laser scanning has developed into an effective and widely utilized tool in geomorphology to provide high-resolution topographic maps, and to monitor surface processes (e.g., White and Jones, 2008; Large and Heritage, 2009). This technique is simply based on the emission of a laser beam and its reflection from the terrain surface to depict a certain area in 3-D. The method generally allows the rapid acquisition (within minutes) of large amounts of topographic data with both, a high resolution of up to a few cm and a high accuracy of a few mm (e.g., Buckley et al., 2008). This provided the great opportunity to derive high-density spatial information across landscapes that are unsuited for conventional surveying due to their inaccessibility and spatial extent (Large and Heritage, 2009).

Terrestrial laser-scanning applications cover a broad range of spatial and short-term scales that are otherwise not considered (Fig. 1.4A; e.g., Milan et al., 2007). Single laser-scanner measurements represent the base for high-resolution topographic maps, that allow to describe the in-situ geomorphic setting of a certain area at great detail (Fig. 1.4A). This herein called 'static' approach is most appropriate for tectono-geomorphic studies, e.g., to reconstruct the rupture pattern along a fault segment or to determine fault displacements (Fig. 1.4B; e.g., Oldow and Singleton, 2008; Wilkinson et al., 2010). In contrast, repeated measurements of a certain area allow to quantify changes, which facilitates the monitoring of surface processes on short-term scales ranging from days up to several years (Fig. 1.4A). This 'dynamic' approach is therefore most suitable for fluvial-geomorphic studies, e.g., to measure erosion and aggraddation of material along a river bed (Fig. 1.4B; e.g., Milan et al., 2007; Heritage and Hetherington, 2007).

The availability of various scanner types allow for measurements of variable resolution across a broad range of spatial scales (Fig. 1.4A). Short-range scanners, such as the *VIVID-910*[®] (Konica Minolta), measure across distances of only a few m with mm-scale resolution, and are therefore particularly suited to monitor surface processes at areas of several squaremeters or even less in size (e.g., Baran, 2005, unpublished diploma thesis). In contrast, long-range scanners, such as the *LMS-Z620*[®] (Riegl), with measurement distances of up to several km are well suited to monitor landslides (e.g., Dunning et al., 2009) and areas of rock-

fall (e.g., Abellán et al., 2010) that can cover entire mountain flanks. However, medium-range scanners, such as the *TLS-1000*[®] (Topcon) or *LMS-Z420i*[®] (Riegl), measure across distances ranging from 1 m up to hundreds of m with cm-scale resolution. Due to this flexibility, the latter type of scanner is best suited for applications in various geomorphic settings as demonstrated in this project.

1.2.2. Tectonic Geomorphology – 'Static' Studies

There are two fields of tectonic research, in which terrestrial laser scanning had been utilized (e.g., Wei et al., 2010; Pollyea and Fairley, 2011). The first one comprises the detailed analysis of fault and fracture surfaces. These surfaces often display irregularities, such as bumps, or long wavelength and low amplitude curvatures, which can have major effects on the mechanical behavior of a fault during coseismic slip (Sagy et al., 2007; Jones et al., 2009). Moreover, a better understanding of the interaction between this irregular geometry and fault kinematics is required to improve the knowledge of processes including reactivation of faults, and fluid flow in faulted reservoirs (e.g., Jones et al., 2009). However, the 3-D geometry of fault and fracture surfaces was rarely quantified in the past beyond a dm-scale resolution mainly due to the usage of labor-intense techniques, such as the plane table or theodolite, so that these features had often been examined in 1-D transects or 2-D maps (e.g., Olariu et al., 2008). So far, a few studies had been carried out to image and analyze fault and fracture surfaces in 3-D with a resolution of less than 10 cm based on measurements with terrestrial laser scanners (e.g., Renard et al., 2006; Sagy et al., 2007; Olariu et al., 2008; Jones et al., 2009).

The second field of research is the detailed reconstruction of spatial rupture and displacement patterns along fault systems. Laser-scanner measurements were conducted to supplement the reconstruction of fault-rupture histories covering longer time-scales of several earthquake cycles, and short-term scales of postseismic deformation. Wilkinson et al. (2010), the short-term scale example, monitored the postseismic deformation on and near the surface rupture of the L'Aquila earthquake (M_W 6.3) from 6th April 2009 in central Italy based on repeated laser-scanner surveys 8–124 days after the earthquake. Oldow and Singleton (2008), the long-term scale example, applied laser scanning in the Alvord basin along the northwestern margin of the Great Basin, USA, where ancient wave-cut terraces of the former Lake Alvord were crosscut by normal faults. They determined the late Pleistocene and Holocene fault displacement based on the terrace offset across these faults.

The latter example illustrates that the acquisition and interpretation of data in the field is generally facilitated where tectonically induced surface deformation, i.e., fault scarps, are exposed in areas of simple and uniform topography. In contrast, this is challenging when fault scarps are superimposed on complex and dissected topography. Such topography is commonly observed in flower structures, which are important to evaluate the evolution and linking of strike-slip fault systems (e.g., Sylvester, 1988; Cowgill et al., 2004a, 2004b). Here, we combined detailed field mapping and high-resolution digital elevation model (DEM) analysis to evaluate the structure and surface expression of one flank of the Rex Hills pressure ridge (Fig. 1.8). Based on terrestrial laser scanning using the scanner *LMS-Z420i*[®] (Riegl), we derived a detailed DEM with a cm-scale resolution and extracted high-resolution topographic cross-sections, that allowed us to study the complex high-resolution fault-scarp morphology across a flower structure despite the absence of subsurface data (chapter I).

1.2.3. Fluvial Geomorphology – 'Dynamic' Studies

Terrestrial laser-scanning in fluvial environments had been conducted to characterize the grain-scale topography of gravel-bed rivers (e.g., Entwistle and Fuller, 2009), and to monitor

morphologic changes along channel beds due to the erosion and deposition of material (e.g., Milan et al., 2007; Heritage and Hetherington, 2007). The actual surface morphology of gravel-bed channels is a key component of the fluvial system that also influences sediment transport (Hodge et al., 2009). In the past, it was difficult to quantify this effect appropriately by using methodologies, such as profilers or photogrammetry, due to an inadequate data density (Fig. 1.4A; Milan et al., 2007; Hodge et al., 2009). It requires grain-scale elevation data of in-situ fluvial gravel surfaces that are difficult to obtain (Hodge et al., 2009). So far, only a few detailed studies evaluate the suitability of terrestrial laser scanning in this context (e.g., Hodge et al., 2009; Entwistle and Fuller, 2009). These studies then focus on describing the in-situ setting captured by a scan, or they consider only short-term scales of a few days in length (e.g., Milan et al., 2007). However, the significance of such measurements is rarely evaluated in the context of longer geological time-scales. The case study presented here therefore focuses on the context between short-term sediment transport measured with laser scanners in small gravel-bed streams and mountainous landscape evolution since the last glacial maximum (LGM; chapter II).

In the Alps, landscape response to glacier retreat following the LGM had often been evaluated on a long-term scale of thousands of years (e.g., Hinderer, 2001). However, long-term erosion measurements often represent averaged values without considering its short-term event character (e.g., Wittmann et al., 2007). In contrast, even small streams can transport large amounts of material during a short time (e.g., Wolman and Miller, 1960), but the cumulative effect of such short-term erosion events for longer time-scales is rarely considered. To bridge this gap, we carried out detailed geomorphic-geologic mapping based on a LiDAR DEM to best constrain the post-glacial evolution of the Alp Valley located in the northern Swiss Prealps (Fig. 1.9B). We then compared it with results derived from repeated laser-scanner surveys (*TLS-1000*[®], Topcon, and *ScanStation*[®], Leica) in the Erlenbach and Vogelbach channel beds to monitor short-term sediment transport at a cm-scale resolution (Fig. 1.9B).

1.2.4. Measurements and Data Processing

The basic field work with the medium-range laser scanners used in this study − *LMS-Z420i*[®] (Riegl), *TLS-1000*[®] (Topcon), and *ScanStation*[®] (Leica) − follows a simple and established principle (e.g., Bonnaffe et al., 2007; Buckley et al., 2008). The particular scanner is mounted on a tripod at the first scan position (Fig. 1.5). The scanner power was taken either from an external battery (e.g., *LMS-Z420i*[®], Riegl; Fig. 1.5A) or an internal set of batteries (e.g., *TLS-1000*[®], Topcon). The scanning procedure was easily controlled with a laptop, and both, a wireless and a default wire-lead data transmission between scanner and laptop were possible. In case of the Topcon scanner *TLS-1000*[®], a control panel also allowed the manual operation of the scanner, and data were stored directly on a memory card. Furthermore, two of the laser scanners − the *LMS-Z420i*[®] (Riegl) and *TLS-1000*[®] (Topcon) − carried a digital camera allowing a later combination of scans and photographs (Fig. 1.5A). During scanning, each scanner can rotate 360° around a vertical axis (Fig. 1.5A). While a scanner was set up at its position, several reflectors were distributed as marker points in the region of interest to avoid distortions during subsequent DEM generation (Fig. 1.5B). Following a calibration process for scanner and camera (definition of scan resolution, scan window etc.), the first scan was performed at position P1 while the camera took pictures of the scanned area (Fig. 1.5B). The scanner was then moved to the next position (P2; Fig. 1.5B). At least three reflectors (black circles in Fig. 1.5B) need to be located in the overlapping region between scans P1 and P2 (marked by ellipse in Fig. 1.5B). Using the scanner software packages, it was possible to search for such overlapping marker points within individual scans and thereby link these

scans to form a merged data set covering a larger area. This procedure was repeated until the area of interest was completely covered.

The basic result of such laser-scanner measurements was a large point cloud with a cm-scale resolution and an accuracy of approximately ±5 cm or less (1 σ). Such a point cloud provides the basis for the subsequent data processing. The specific details on using the individual laser scanners and associated software packages during data processing are further outlined in chapters I and II. In this study, however, there are differences concerning the scanning procedure and subsequent data processing when applying a laser scanner in a tectonic or fluvial setting.

For the tectonic application (chapter I), the resulting point cloud with cm-scale resolution mentioned above represents the basis for a DEM. The surface of the generated DEM is defined by a triangulated irregular network (TIN), in which the points define the triangle corners (Fig. 1.6A). Clearly, the size and number of triangles depend on point density and terrain complexity (e.g., red circle in Fig. 1.6A). For the purpose to examine the surface expression of tectonic processes, geo-referencing of the DEM into global coordinates was not necessary. Furthermore, this DEM permitted the extraction of detailed sub-data sets, e.g., in the form of topographic cross-sections, and the identification and analysis of subtle features not obvious in the field.

In contrast to the tectonic application, several requirements need to be matched to monitor surface-morphology changes that are due to fluvial sediment transport (chapter II). These are: (i) repeated laser-scanning surveys of the same site allow to monitor such changes; (ii) geo-referencing of the point clouds derived from the repeated surveys into local or global coordinates in order to compare data of the same site but of different acquisition dates; and (iii) DEM generation based on the geo-referenced point clouds in the form of regular grids (Fig. 1.6B) in order to derive quantitative insight into surface-morphology changes by subtracting one grid from another. However, it has to be noted that regular grids should be of a smaller size to display the topography of a rugged terrain appropriately (Moore et al., 1991), but since the grid is regular, a smooth terrain is then represented by a large number of squares resulting in partial redundancy (e.g., red circle in Fig. 1.6B).
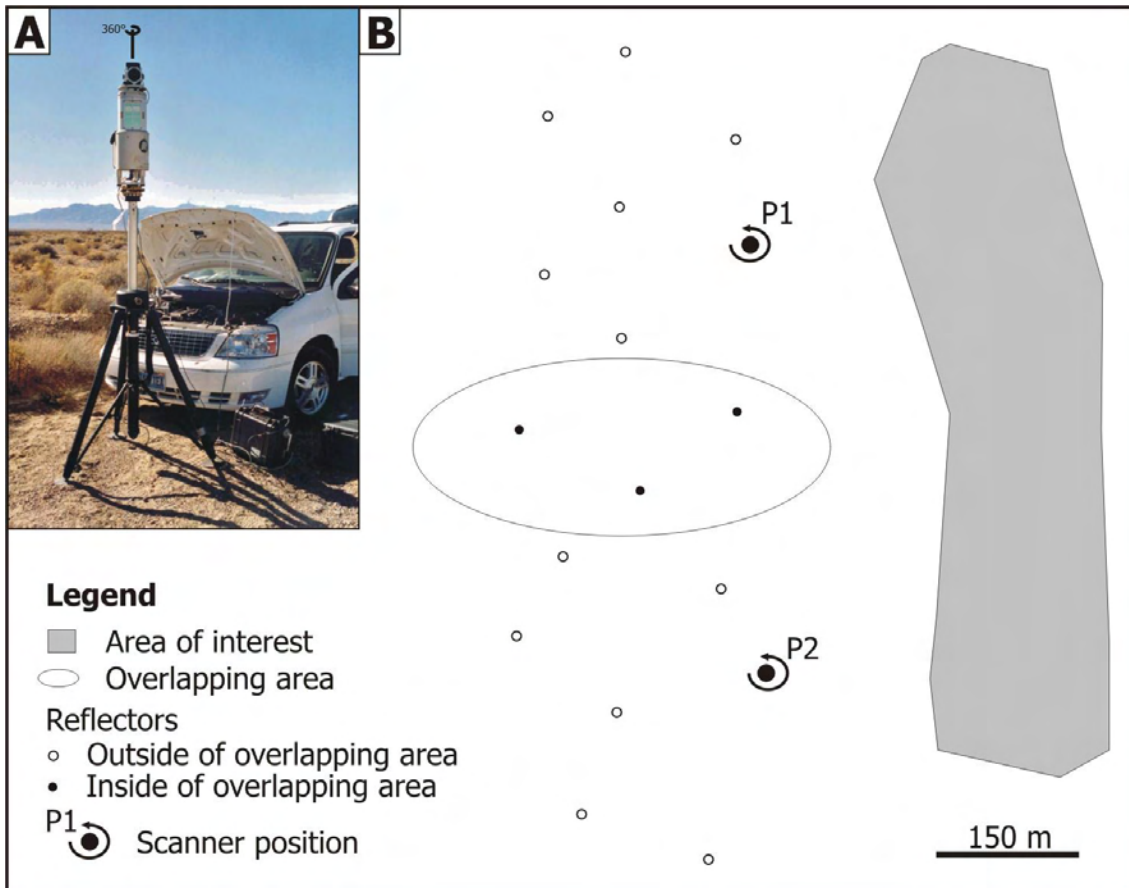
Fig. 1.5 (A) Photograph of the laser scanner *LMS-Z420i*® set-up for field work. The vertical rotation axis of the scanner is additionally shown. **(B)** The sketch emphasizes the scanning procedure. The scanner is shifted from position P1 to P2 after the first scan. The second scan is performed at P2. An overlap (white area) exists between both positions, where reflectors (black circles) are used to link the individual scans.
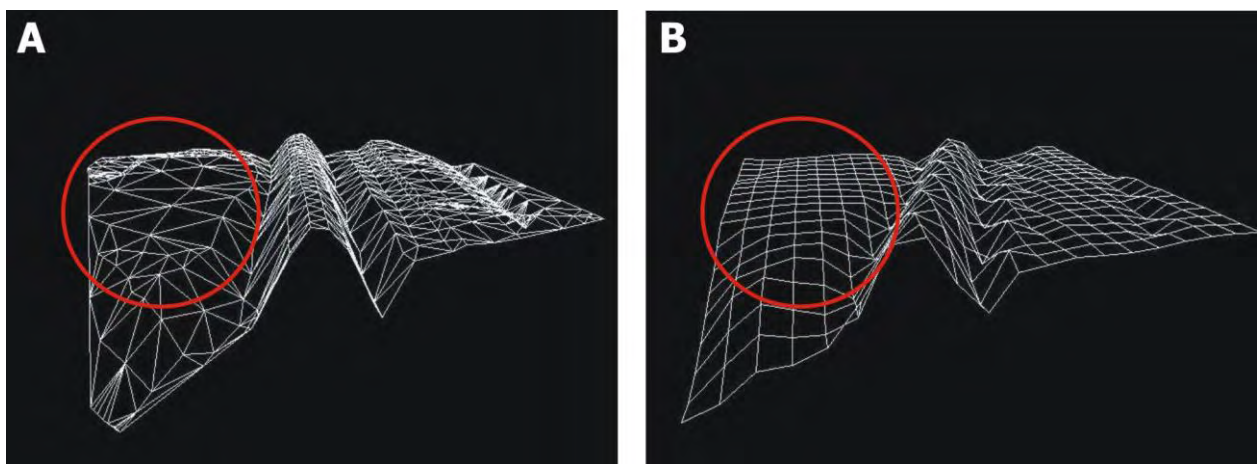
Fig. 1.6 Example of a DEM surface represented by both, **(A)** a triangulated irregular network (TIN), and **(B)** a regular square grid (modified after Brostuen and Cox, 2000). **(A)** Points define the triangle corners respectively nodes of the TIN. The size and number of triangles depend on point density as well as terrain complexity, e.g., area within red circle. **(B)** To display the topography of a rugged terrain appropriately requires regular grids of a smaller size, but a smooth terrain is then represented by a large number of squares resulting in redundancy (e.g., area within red circle).

1.3. Quantifying Erosion on Multiple Time-Scales

Erosion, sediment transport, and deposition in sedimentary basins are episodic across spatial and temporal scales (Fig. 1.4B; e.g., Frostick and Jones, 2002). This intermittency can be recognized in sedimentary deposits, because large floods, for example, that flush sediment into coastal areas are recorded in the form of perceptible layers in near-coastal deposits (Frostick and Jones, 2002). Furthermore, it is well known from the monitoring of river loads in mountainous areas that fluvial processes are episodic (e.g., Wolman and Miller, 1960; Keller and Weibel, 1991). The length of such records typically ranges from a few years up to tens of years (e.g., Kirchner et al., 2001). However, erosion rates derived from such short-term observations were reported as basin-averaged rates, and had also been extrapolated to longer time-scales implying continuity without temporal changes (Richards, 2002). Longer-term erosion measurements over thousands to millions of years were similarly given as average values without considering the event character of erosion, which also depends on the temporal resolution of these measurements.

The contrast between this implied continuity and actual episodicity as well as the consideration of individual spatiotemporal scales aggravates a comprehensive understanding of erosion (e.g., Frostick and Jones, 2002). Hence, an integrated view of erosion across all scales is needed (e.g., Jones and Frostick, 2002), but rarely discussed in the literature (e.g., Kirchner et al., 2001). To conduct such a comprehensive comparison, we selected an approach that has been originally established to evaluate the spectral character of tectonic deformation (Fig. 1.7A). Friedrich et al. (2003) utilized the cumulative displacement with time approach to investigate the significance of geologic and geodetic measurements along intra-continental faults on time-scales of millions of years to tens of years. This approach facilitated the direct comparison of displacement rates from different time-scales (Fig. 1.7A).

In chapter III, we adopted the approach of Friedrich et al. (2003) and considered cumulative erosion with time to evaluate directly the variability of erosion on the long- (millions of years), medium- (thousands to ten thousand years), and short-term (years to decades) scale, and to discuss the potential significance of erosion measurements (Fig. 1.7B). We compiled published data from the Alps to compare erosion rates quantitatively especially due to the availability of various data. Lastly, a continuous short-term data set on bed-load transport from the Erlenbach basin, located in the northern Swiss Prealps, enabled us to evaluate the short-term nature of mountainous erosion in detail (Fig. 1.7B).
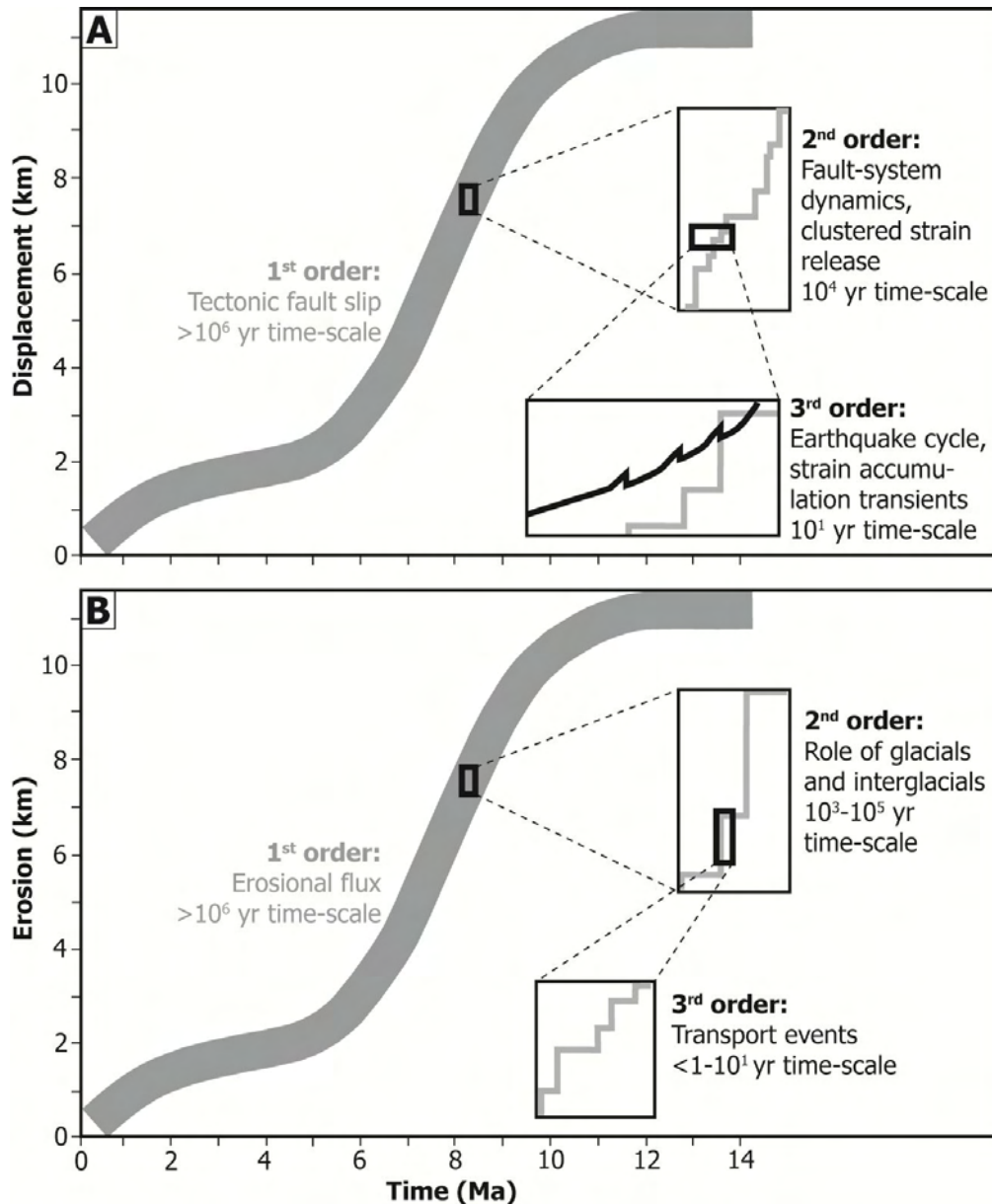
Fig. 1.7 (A) Schematic plot indicating the significance of tectonic, fault dynamic and transient processes on three different temporal scales (modified after Friedrich et al., 2003). **(B)** Plot shown in Figure 1.7A redrawn with the purpose to illustrate the adopted approach of cumulative erosion described in the text, and to indicate a potential significance of erosion measurements at three different time-scales.

1.4. Geological Setting of the Study Areas

1.4.1. Eastern California Shear Zone, USA

Deformation along the Pacific-North American plate boundary is spread across a broad zone of faulting in the western United States (Fig. 1.8A). The San Andreas fault that forms the actual plate boundary accommodates approximately 35 mm/a of the 48 mm/a of relative plate motion (e.g., Bennett et al., 2003). However, about 9–23% of the total relative motion is absorbed by the Eastern California Shear Zone, a diffuse array of northwest striking faults east and south of the Sierra Nevada-Great Valley microplate (Fig. 1.8A; Dokka and Travis, 1990). Between latitudes 35°N and 37°N, the dextral strike-slip Stateline fault system (SFS) represents the eastern limit of the Eastern California Shear Zone (Fig. 1.8A). Geodetic data

point to a surface velocity jump in the NW component across the northern Amargosa segment of the SFS (Fig. 1.8B) from ~0 mm/a east of the fault to 0.9–1.1 mm/a west of the fault with respect to a fixed North American reference frame (Wernicke et al., 2004). Furthermore, tectono-geomorphic observations suggest Holocene activity along portions of the SFS and Pleistocene activity along the entire fault system (Menges et al., 2003; Guest et al., 2007).

Offset estimates for the three segments of the SFS vary from ~25–45 km (e.g., Stevens, 1991; Schweickert and Lahren, 1997) in the north, to ~10 km in Stewart Valley, W of Pahrump (Burchfiel et al., 1983), and 3 km in the south (Walker et al., 1995). Those estimates are typically derived from the offset of pre-Cenozoic markers. The most recent offset estimate of ~30 km during the last ~13.1 Ma along the southern SFS was found by Guest et al. (2007), and is based on the dextral offset of ~13.1 Ma old proximal volcanic and associated rock-avalanche deposits (Fig. 1.8B). This estimate corresponds to a minimum long-term time-averaged geologic displacement rate of ~2.3 mm/a for the southern Pahrump and Mesquite segments of the SFS (Fig. 1.8B). The current geodetic surface velocity across the northern portion of the SFS alone is 0.7–1.2 mm/a with respect to a fixed North American reference frame (Wernicke et al., 2004; Hill and Blewitt, 2006).

On the earthquake-recurrence time-scale of ~10 ka, however, morphologic changes due to surface ruptures along the SFS and fault-scarp degradation processes are poorly constrained and have therefore not been associated with the evolution of fault structures and the SFS. Hence, we examined fault scarps and drainage offsets related to the Rex Hills flower structure based on high-resolution topographic data derived from terrestrial laser scanning (chapter I).
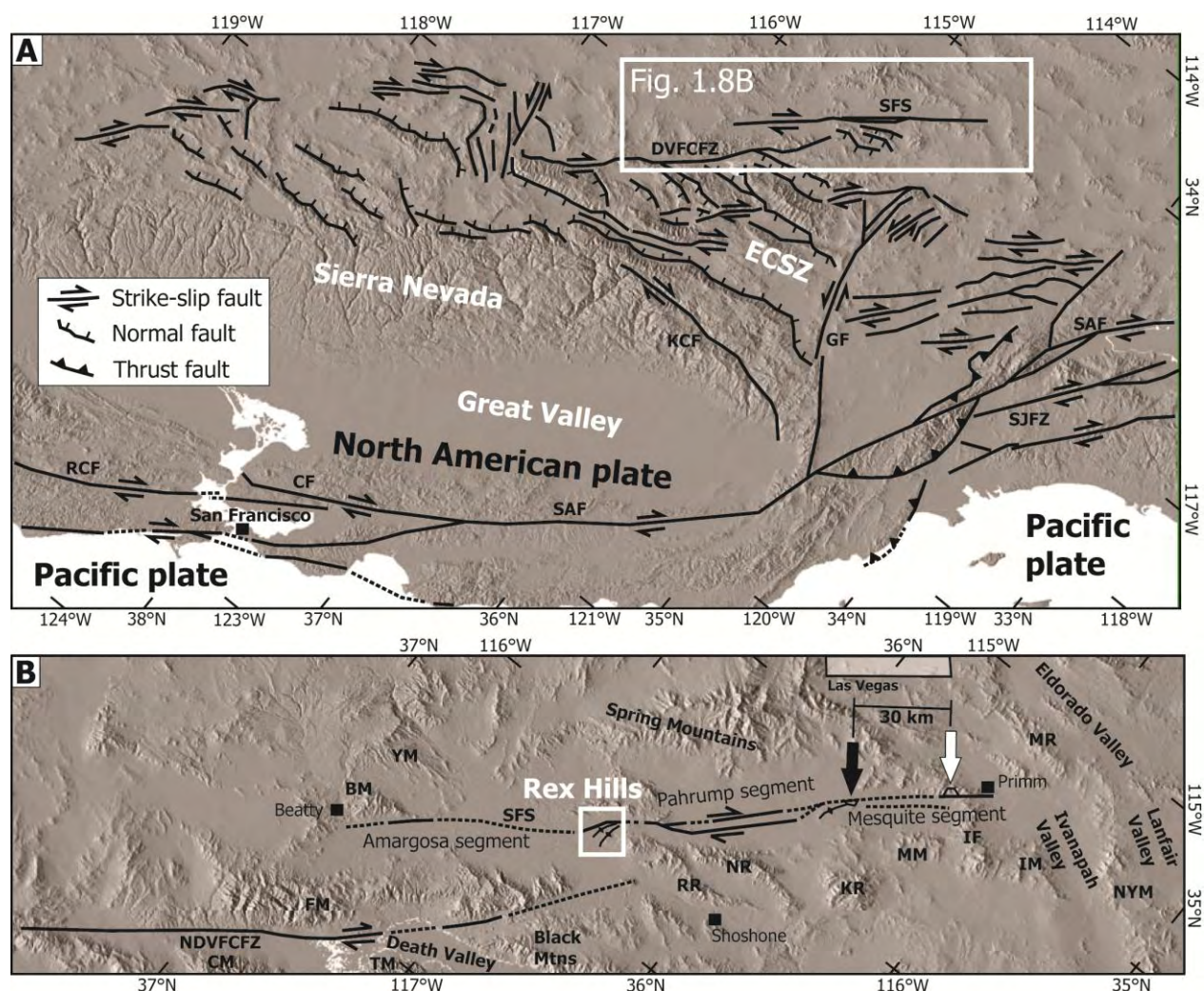
Fig. 1.8 (A) Shaded relief map indicating the location of the Stateline fault system with respect to other major fault zones involved in accommodating dextral motion along the Pacific-North American plate boundary (modified after Guest et al., 2007). Abbreviations: ECSZ – Eastern California Shear Zone, SFS – Stateline fault system, RCF – Rogers Creek fault, CF – Calaveras fault, SAF – San Andreas fault, SJFZ – San Jacinto fault zone, GF – Garlock fault, DVFCFZ – Death Valley Furnace Creek fault zone, and KCF – Kern Canyon fault. **(B)** Shaded relief map showing the Stateline fault system and nearby major active faults of the surrounding area (modified after Guest et al., 2007). The white arrow marks the position of the Devil Peak rhyolite intrusions, and the black arrow marks the offset volcanic and associated rock-avalanche deposits at Black Butte described by Guest et al. (2007). Abbreviations: IF – Ivanapah fault, NDVFCFZ – northern Death Valley Furnace Creek fault zone, SFS—Stateline fault system, BM – Bare Mountains, CM – Cottonwood Mountains, FM – Funeral Mountains, IM – Ivanapah Mountains, KR – Kingston Range, MM – Mesquite Mountains, MR – McCullough Range, NR – Nopah Range, NYM – New York Mountains, RR – Resting Spring Range, TM – Tucki Mountain, and YM – Yucca Mountain.

1.4.2. Alpine Orogeny

The Alpine orogeny is often described as a series of episodes of tectonic, metamorphic, and erosional activity from Cretaceous to Quaternary times (e.g., Schlunegger et al., 2007; Bernet et al., 2009; Handy et al., 2010). The convergence between the European and Adriatic plates started approximately in the late Cretaceous, and resulted in the collision of both plates during the late Eocene (Schmid et al., 1996). Slab break-off occurred presumably at about 34–29 Ma (von Blanckenburg and Davies, 1995), during which the dense oceanic part of the subducting European plate was detached from its upper buoyant part (Davies and von Blanckenburg, 1995; Regard et al., 2008). However, convergence continued after the collision obvious from thrusting along the Periadriatic fault and propagation of the Helvetic nappes from 32–19 Ma, as well as foreland propagation in the Southern Alps since 19 Ma (Fig. 1.9A; Schmid et al., 1996). Foreland basins formed north and south of the Alps due to continental collision and convergence since the Eocene that led to crustal thickening and loading of the subducting European plate (Fig. 1.9A; e.g., Schmid et al., 1996; Andeweg and Cloetingh, 1998).

Sedimentation in the north-Alpine foreland basin (Molasse basin) during the Oligocene was characterized by deep marine conditions with deposition of turbidites, locally referred to as Flysch deposits (e.g., Hesse, 1975; Sinclair, 1997). In contrast, the so-called Molasse sedimentation was characterized by shallow marine conditions during the early Miocene and more continental conditions during the late Miocene (e.g., Doppler, 1989; Schlunegger et al., 2001; Kuhlemann et al., 2001). Deposition of sediments in the Molasse basin ceased between 8.5 and 4.5 Ma (Fig. 1.9A; e.g., Lemcke, 1974; Bernet et al., 2009). Parts of the basin deposits were affected by the propagating thrust front and consequently exhumed to the surface, where they are reworked since the late Miocene (e.g., Kuhlemann et al., 2001). However, sedimentation in the south-Alpine foreland basin (Po basin) during the early Oligocene occurred under deep marine conditions due to turbidity currents, and from late Oligocene to middle Miocene under submarine conditions along submarine fans and canyons (Fig. 1.9A; e.g., Schlunegger, 1999). Following the desiccation of the Mediterranean from 5.6–5.5 Ma, renewed sedimentation occurred under fluvial-deltaic and lagoonal conditions obvious from the stratigraphic record of the Lago Mare deposits of the Messinian salinity crisis (Willett et al., 2006).

Exhumation in the Alps is due to normal faulting and erosion at the surface (e.g., Bernet et al., 2009), which is similar to other convergent orogens (Ring et al., 1999). Large extensional structures, such as the Tauern window in the Eastern Alps (Fig. 1.9A), are treated as indicators of tectonic exhumation (e.g., Schlunegger and Willett, 1999). Zircon fission track ages of exposed bedrock show clear differences in Alpine cooling ages between the Western

and Eastern Alps (Bernet et al., 2001). Cooling ages in large parts of the Western Alps are relatively young (less than 36 Ma), and older in most areas of the Eastern Alps (more than 50 Ma).

1.4.3. Alp Valley, Switzerland

The Alp Valley is located in the northern foothills of the Swiss Alps (Fig. 1.9A), south of the town of Einsiedeln (Fig. 1.9B). The Alp River drains the valley toward the north. The two sub-study sites of the fluvial case study are the small tributary basins of the Erlenbach (0.74 km²) and Vogelbach (1.56 km²). The former of these two is located on the eastern flank of the southern Alp Valley, and the latter on the western flank of the central valley (Fig. 1.9B).

The Alp Valley is cut into Alpine thrust sheets that are composed of sedimentary rocks (Fig. 1.9B). In the north, the Helvetic frontal thrust is the contact between the subalpine Molasse to the north and the Cretaceous Wägital Flysch to the south (Fig. 1.9B). The latter belongs to the Ultrahelvetic-Penninic Flysch series exposed in the central and southern Alp Valley, which further comprise the Habkern and Schlieren Flysch (Fig. 1.9B; Hantke, 1967). These Flysch series are distinguished by their tectonic position, where the Schlieren Flysch represents the eastern-most and the Wägital Flysch the western-most (Stammbach, 1988). The southern Alp Valley is marked by the prominent Penninic cliffs of the Grosser and Kleiner Mythen, that were thrust over Helvetic and Ultrahelvetic-Penninic Flysch units (Fig. 1.9B). The Helvetic units are part of the so-called Einsiedler Schuppenzone (e.g., Kuhn, 1972).

Wide areas of the Alp Valley flanks are subject to sliding processes of unconsolidated material (Hantke, 1967). Furthermore, the appearance of the Alp Valley floor in the north is dominated by a gravel terrace of Würmian age, whereas the valley floor in the south is shaped by alluvial fans. Late Würmian-aged lateral moraines are located at the base of the Mythen mountain peaks in the southern Alp Valley (Hantke, 1967 and 1970).

Previously derived geologic and geomorphic maps of the Alp Valley lack either structural and geomorphic detail (Fig. 1.9B; e.g., Hantke, 1967; Winkler et al., 1985), or cover only parts of the valley (e.g., Stammbach, 1988; Schuerch et al., 2006). The post-glacial landscape evolution of the Alp Valley has therefore not been constrained appropriately, and the context between short-term sediment transport and this evolution was also rarely considered in the past (e.g., Stammbach, 1988). Hence, we combined detailed geomorphic-geologic mapping in the Alp Valley with repeated terrestrial laser-scanner surveys in the Erlenbach and Vogelbach basins to better explore this context (chapter II).
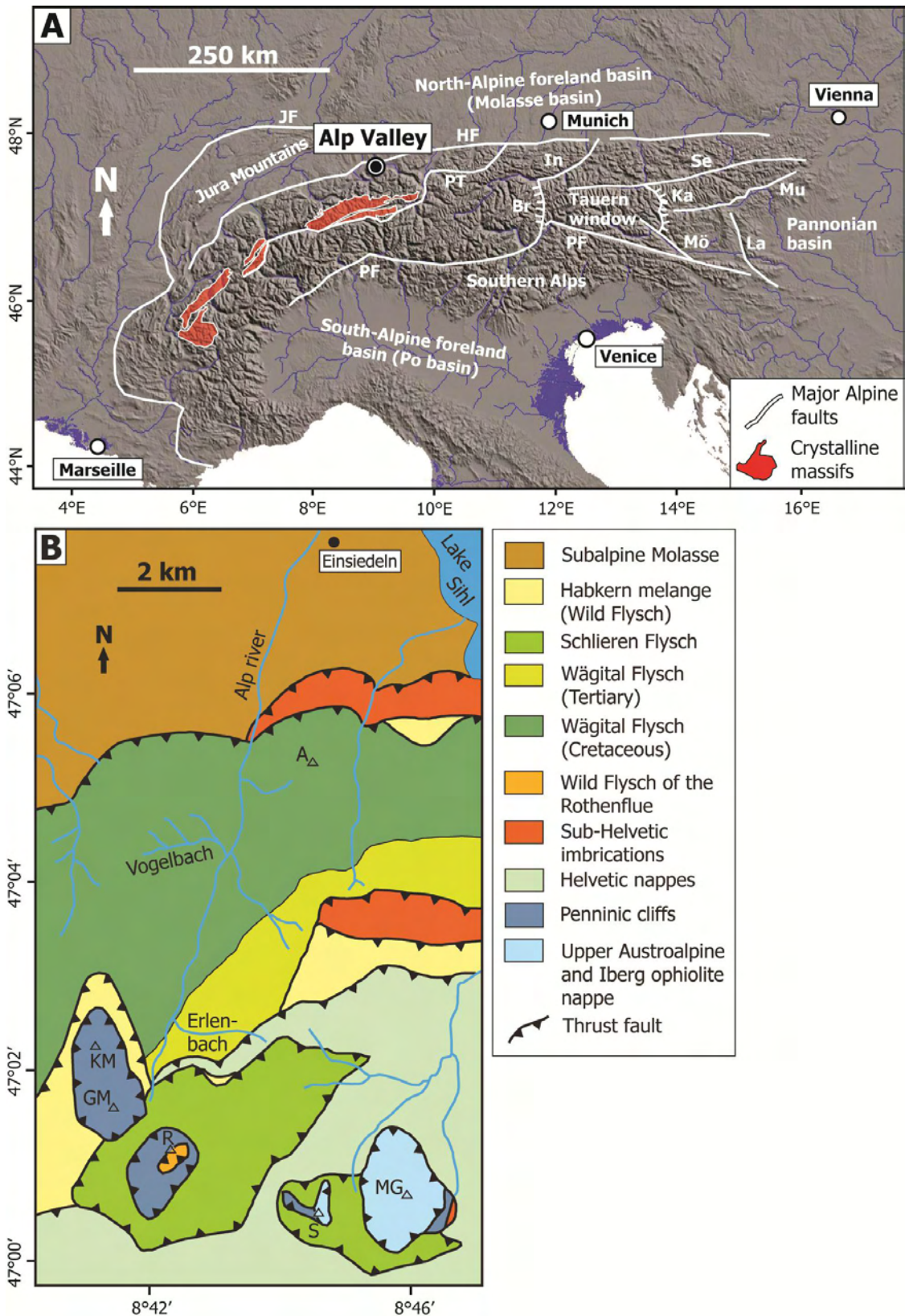
Fig. 1.9 (A) Shaded relief map of the Alps showing major units and fault systems, and the location of the Alp Valley (compiled from Willett et al.; 2006; Robl et al., 2008). Abbreviations: Br – Brenner fault, In – Inntal fault, Ka – Katschberg fault, La – Lavanttal fault, Mö – Mölltal fault, Mu – Mur-Mürz fault, PF – Periadriatic fault, Se – Salzachtal-Ennstal fault, JF – Jura front, HF – Helvetic front, and PT – Penninic thrust. **(B)** Geologic map of the Alp Valley area (modified after Winkler et al., 1985). Abbreviations: A – Amselspitz, GM – Grosser Mythen, KM – Kleiner Mythen, R – Rotenflue, MG – Mördergruebli, and S – Schijen.

30

1.5. General Remark

The major chapters of this thesis have been published in or will be submitted to peer-reviewed journals. The relevant articles are:

Baran, R., Guest, B., and Friedrich, A.M. (2010) High-resolution spatial rupture pattern of a multiphase flower structure, Rex Hills, Nevada: New insights on scarp evolution in complex topography based on 3-D laser scanning: Geological Society of America Bulletin, Volume 122, Number 5/6, p. 897-914, doi: 10.1130/B26536.1

Baran, R., McArdell, B.W., Schlunegger, F., Wunderlich, T.A., and Friedrich, A.M. (in preparation for submission to Geomorphology) Short-term sediment transport in context of post-glacial landscape evolution: Insights from field mapping and high-resolution LiDAR measurements, Alp Valley, Switzerland

Baran, R., McArdell, B.W., Schlunegger, F., and Friedrich, A.M. (in preparation for submission to International Journal of Earth Sciences) Sediment Transport and Erosion Rates in the Alps on Scales Ranging from Years to Millions of Years − Implications for the Variability of Mountainous Erosion

Baran, R., Schlunegger, F., and Friedrich, A.M. (in preparation for submission to Geology) Erosion of Dying Foreland Basins: Did the Sediment Discharge of the Alps Really Accelerate Five Million Years Ago?

For reasons of readability, although it causes some redundancies, and consistency of the formatting, the first article appears in a modified format in this thesis. The reprint version of this article and the related data repository are contained in the appendix of the thesis. Similarly, the latter three of the four articles will be submitted in a modified form to the relevant journals. Lastly, the envelope attached to the inside of the back-cover contains a CD with a PDF file of this thesis.

1.6. References

Abellán, A., Clavet, J., Vilaplana, J.M., and Blanchard, J.; 2010; Detection and spatial prediction of rockfalls by means of terrestrial laser scanner monitoring; Geomorphology; vol. 119; p. 162–171; doi: 10.1016/j.geomorph.2010.03.016.

Andeweg, B., and Cloetingh, S.; 1998; Flexure and 'unflexure' of the North Alpine German-Austrian Molasse Basin: constraints from forward tectonic modeling; *in:* Mascle, A., Puigdefàbregas, C., Luterbacher, H.P., and Fernandez, M. (eds.); Cenozoic Foreland Basins of Western Europe; Geological Society, London, Special Publications, vol. 134, p. 403–422.

Arrowsmith, J.R., Rhodes, D.D., and Pollard, D.D.; 1998; Morphologic dating of scarps formed by repeated slip events along the San Andreas Fault, Carrizo Plain, California; Journal of Geophysical Research; v. 103; p. 10141–10160; doi: 10.1029/98JB00505.

Baran, R.; 2005; Multitemporale Überwachung von Oberflächenveränderungen in einem von Degradation betroffenen Testgebiet; Institute of Earth Sciences, University Potsdam, Germany; unpublished diploma thesis; 72 pp.

Bennett, R.A., Wernicke, B.P., Niemi, N.A., Friedrich, A.M., and Davis, J.L.; 2003; Contemporary strain rates in the northern Basin and Range province from GPS data; Tectonics, vol. 22, pp. 31, doi: 10.1029/2001TC001355.

Bernet, M., Zattin, M., Garver, J.I., Brandon, M.T., and Vance, J.A.; 2001; Steady-state exhumation of the European Alps; Geology; vol. 29; p. 35–38.

Bernet, M., Brandon, M., Garver, J., Balestieri, M.L., Ventura, B., and Zattin, M.; 2009; Exhuming the Alps through time: clues from detrital zircon fission-track thermochronology; Basin Research; vol. 21; p. 781–798.

Bonnaffe, F., Jennette, D., and Andrews, J.; 2007; A method for acquiring and processing ground-based lidar data in difficult-to-access outcrops for use in three-dimensional, virtual-reality models; Geosphere; vol. 3; p. 501–510; doi: 10.1130/GES00104.1.

Brostuen, D., and Cox, S.; 2000; Minimizing Subjectivity in Digital Orthophoto Imagery; ESRI User Conference Proceedings; 20th Annual Esri International User Conference; 26-30 June 2000; San Diego, California, USA.

Buckley, S.J., Howell, J.A., Enge, H.D., and Kurz, T.H.; 2008; Terrestrial laser scanning in geology: Data acquisition, processing and accuracy considerations; Journal of the Geological Society; vol. 165; p. 625–638; doi: 10.1144/0016-76492007-100.

Burbank, D.W., and Anderson, R.S.; 2001; Tectonic Geomorphology; Blackwell Science; USA; 274 pp.

Burchfiel, B.C., Hamill, G.S., and Wilhelms, D.E.; 1983; Structural geology of the Montgomery Mountains and the northern half of the Nopah and Resting Spring ranges, Nevada and California; Geological Society of America Bulletin; vol. 94; p. 1359–1376; doi: 10.1130/0016-7606(1983)94<1359:SGOTMM>2.0.CO;2.

Carretier, S., Ritz, J.-F., Jackson, J., and Bayasgalan, A.; 2002; Morphological dating of cumulative reverse fault scarps: Examples from the Gurvan Bogd fault system, Mongolia; Geophysical Journal International; v. 148; p. 256–277; doi: 10.1046/j.1365-246X.2002.01599.x.

Cowgill, E., Yin, A., Arrowsmith, J.R., Feng, W.X., and Shuanhong, Z.; 2004a; The Akato Tagh bend along the Altyn Tagh fault, northwest Tibet 1: Smoothing by vertical-axis rotation and the effect of topographic stresses on bend-flanking faults; Geological Society of America Bulletin; vol. 116; p. 1423–1442; doi: 10.1130/B25359.1.

Cowgill, E., Arrowsmith, J.R., Yin, A., Feng, W.X., and Shuanhong, Z.; 2004b; The Akato Tagh bend along the Altyn Tagh fault, northwest Tibet 2: Active deformation and the importance of transpression and strain hardening within the Altyn Tagh system; Geological Society of America Bulletin; vol. 116; p. 1443–1464; doi: 10.1130/B25360.1.

Davis, W.M.; 1899; The geographical cycle; Geographical Journal, vol. 14, p. 481–504.

Davies, J.H., and von Blanckenburg, F.; 1995; Slab breakoff: A model of lithosphere detachment and its test in the magmatism and deformation of collisional orogens; Earth and Planetary Science Letters, vol. 129, p. 85–102.

Dokka, R.K., and Travis, C.J.; 1990; Role of the eastern California shear zone in accommodating Pacific-North American plate motion; Geophysical Research Letters; vol. 17; p. 1323–1326; doi: 10.1029/GL017i009p01323.

Doppler, G.; 1989; Zur Stratigraphie der nördlichen Vorlandmolasse in Bayrisch-Schwaben; Geologica Bavarica vol. 94, p. 83–133.

Duncan Jr., J.R.; 1964; The Effects of Water Table and Tide Cycle on Swash-Backwash Sediment Distribution and Beach Profile Development; Marine Geology, vol. 2, p. 186–197.

Dunning, S.A., Massey, C.I., and Rosser, N.J.; 2009; Structural and geomorphological features of landslides in the Bhutan Himalaya derived from terrestrial laser scanning; Geomorphology; vol. 103; p. 17–29; doi: 10.1016/j.geomorph.2008.04.013.

Entwistle, N.S., and Fuller, I.C.; 2009; Terrestrial laser scanning to derive the surface grain size facies character of gravel bars; in: Heritage, G., and Large, A.R.G. (eds.); Laser scanning for the environmental sciences; Wiley-Blackwell; United Kingdom; p. 102–114.

Friedrich, A.M., Wernicke, B.P., and Niemi, N.A.; 2003; Comparison of geodetic and geologic data from the Wasatch region, Utah, and implications for the spectral character of Earth deformation at periods of 10 to 10 million years; Journal of Geophysical Research; vol. 108; 23 pp.; doi: 10.1029/2001JB000682.

Friedrich, A.M., Lee, J., Wernicke, B.P., and Sieh, K.; 2004; Geologic context of geodetic data across a Basin and Range normal fault, Crescent Valley, Nevada; Tectonics, vol. 23, 24 pp., doi: 10.1029/2003TC001528.

Frostick, L.E., and Jones, S.J.; 2002; Impact of periodicity on sediment flux in alluvial systems: grain to basin scale; Geological Society; London; Special Publications; vol. 191; p. 81–95; doi: 10.1144/GSL.SP.2002.191.01.06.

Galehouse, J.S.; 2002; Data from Theodolite Measurements of Creep Rates on San Francisco Bay Region Faults, California: 1979–2001; U.S. Geological Survey, Open-File Report 02–225, 94 pp.

Gross, M.R., Bahat, D., and Becker, A.; 1997; Relations between jointing and faulting based on fracture-spacing ratios and fault-slip profiles: A new method to estimate strain in layered rocks; Geology, vol. 25, p. 887–890.

Guest, B., Niemi, N.A., and Wernicke, B.P.; 2007; Stateline fault system: A new component of the Miocene-Quaternary Eastern California shear zone; Geological Society of America Bulletin; vol. 119; p. 1337–1347; doi: 10.1130/0016-7606(2007)119[1337:SFSANC]2.0.CO;2.

Handy, M.R., Schmid, S.M., Bousquet, R., Kissling, E., and Bernoulli, D.; 2010; Reconciling plate-tectonic reconstructions of Alpine Tethys with the geological–geophysical record of spreading and subduction in the Alps; Earth Science Reviews, vol. 102, p. 102–158, doi: 10.1016/j.earscirev.2010.06.002.

Hantke, R.; 1967; Geologische Karte des Kantons Zürich und seiner Nachbargebiete; Kommissionsverlag Leemann, Zürich, Switzerland.

Hantke, R.; 1970; Die spätwürmeiszeitlichen Stadien auf der schweizerischen Alpennordseite; Eiszeitalter und Gegenwart, vol. 21, p. 71–80.

Hardy, J.R.; 1981; Data collection by remote sensing for land resources survey; in: Townsend, J.R.G. (ed.); Terrain Analysis and Remote Sensing; George Allen & Unwin Ltd., London, Great Britain, p.16–37.

Heritage, G., and Hetherington, D.; 2007; Towards a protocol for laser scanning in fluvial geomorphology; Earth Surface Processes and Landforms; vol. 32; p. 66–74.

Hesse, R.; 1975; Turbiditic and non-turbiditic mudstone of Cretaceous flysch sections of the East Alps and other basins; Sedimentology, vol. 22, p. 387-416.

Hill, E.M., and Blewitt, G.; 2006; Testing for fault activity at Yucca Mountain, Nevada, using independent GPS results from the BARGEN network; Geophysical Research Letters; vol. 33; p. L14302, doi: 10.1029/2006GL026140.

Hinderer, M.; 2001; Late Quaternary denudation of the Alps, valley and lake fillings and modern river loads; Geodinamica Acta; vol. 14; p. 231–263.

Hodge, R., Brasington, J., and Richards, K.; 2009; Analysing laser-scanned digital terrain models of gravel bed surfaces: linking morphology to sediment transport processes and hydraulics; Sedimentology; vol. 56; p. 2024–2043; doi: 10.1111/j.1365-3091.2009.01068.x.

Holmes, C.N., and Page, B.M.; 1956; Geology of the Bituminous Sandstone Deposits Near Sunnyside, Carbon County, Utah; *in:* Peterson, J.A. (ed.); Geologv Mid Economic Deposits of East Central Utah; 7th Annual Field Conference, Intermountain Association of Petroleum Geologists, p. 171–177.

Hudnut, K.W., and Sieh, K.E.; 1989; Behavior of the Superstition Hills fault during the past 330 years; Bulletin of the Seismological Society of America, vol. 79, p. 304–329.

Jones, S.J., and Frostick, L.E.; 2002; Introduction; Geological Society; London; Special Publications; vol. 191; p. 1–4; doi: 10.1144/GSL.SP.2002.191.01.01.

Jones, R.R., Kokkalas, S., and McCaffrey, K.J.W.; 2009; Quantitative analysis and visualization of nonplanar fault surfaces using terrestrial laser scanning (LIDAR) – The Arkitsa fault, central Greece, as a case study; Geosphere; vol. 5; p. 465–482; doi: 10.1130/GES00216.1.

Keller, H.M., and Weibel, P.; 1991; Suspended sediments in streamwater – indicators of erosion and bed load transport in mountainous basins; *in:* Sediment and Stream Water Quality in a Changing Environment: Trends and Explanation; Proceedings of the Vienna Symposium; August 1991; IAHS Publication no. 203; p. 53–61.

Kirchner, J.W., Finkel, R.C., Riebe, C.S., Granger, D.E., Clayton, J.L., King, J.G., and Megahan, W.F.; 2001; Mountain erosion over 10 yr, 10 k.y., and 10 m.y. time scales; Geology; vol. 29; p. 591–594.

Kuhlemann, J., Frisch, W., Dunkl, I., and Székely, B.; 2001; Quantifying tectonic versus erosive denudation by the sediment budget: the Miocene core complexes of the Alps; Tectonophysics; vol. 330; p. 1–23.

Kuhlemann, J., Frisch, W., Székely, B., I. Dunkl, I., and Kázmér, M.; 2002; Post-collisional sediment budget history of the Alps: tectonic versus climatic control; International Journal of Earth Sciences, vol. 91, p. 818–837, doi: 10.1007/s00531-002-0266-y.

Kuhn, J.A.; 1972; Stratigraphisch-mikropaläontologische Untersuchungen in der Äusseren Einsiedler Schuppenzone und im Wägital Flysch E und W des Sihlsees (Kt. Schwyz); Eclogae Geologicae Helvetiae, vol. 65, p. 485–553.

Large, A.R.G., and Heritage, G.L.; 2009; Laser Scanning – Evolution of the Discipline; *in:* Heritage, G., and Large, A.R.G. (eds.); Laser scanning for the environmental sciences; Wiley-Blackwell; United Kingdom; p. 1–20.

Lemcke, K.; 1974; Vertikalbewegungen des vormesozioschen Sockels im nördlichen Alpenvorland Perm bis zur Gegenwart?; Eclogae Geologicae Helvetiae, vol. 67, p. 121–133.

Li, R.; 1998; Potential of High-Resolution Satellite Imagery for National Mapping Products; Photogrammetric Engineering & Remote Sensing; v.64; p. 1165–1169.

Liang, S.; 2008; Recent Advances in Land Remote Sensing: An Overview; *in:* Liang, S. (ed.); Advances in Land Remote Sensing – System, Modeling, Inversion and Application; Springer-Verlag GmbH, Berlin Heidelberg, Germany, p. 1–6.

Massonnet, D., Feigl, K., Rossi, M., and Adragna, F.; 1994; Radar interferometric mapping of deformation in the year after the Landers earthquake; Nature, vol. 369, p. 227–230.

Menges, C.M., Fridrich, C., Blakely, R.J., and Thompson, R.; 2003; Late Quaternary surface rupture and associated transpressive uplift on a section of the State Line Fault in the south-central Amargosa Desert basin, southwestern Nevada; Eos (Transactions, American Geophysical Union); vol. 84; Fall Meeting Supplement; Abstract S11D-0327.

Milan, D.J., Heritage, G.L., and Hetherington, D.; 2007; Application of a 3D laser scanner in the assessment of erosion and deposition volumes and channel change in a proglacial river; Earth Surface Processes and Landforms; vol. 32; p. 1657–1674; doi: 10.1002/esp.1592.

Moore, I.D., Grayson, R.B., and Ladson, A.R.; 1991; Digital terrain modelling: A review of hydrological, geomorphological, and biological applications; Hydrological Processes; vol. 5; p. 3–30.

Nakada, S., Miyake, Y., Sato, H., Oshima, O., and Fujinawa, A.; 1995; Endogenous growth of dacite dome at Unzen volcano (Japan), 1993–1994; Geology, vol. 23, p. 157–160.

Olariu, M.I., Ferguson, J.F., Aiken, C.L.VOL., and, Xu, X.; 2008; Outcrop fracture characterization using terrestrial laser scanners: Deep-water Jackfork sandstone at Big Rock Quarry, Arkansas; Geosphere; vol. 4; p. 247–259; doi: 10.1130/GES00139.1.

Oldow, J.S., and Singleton, E.S.; 2008; Application of Terrestrial Laser Scanning in determining the pattern of late Pleistocene and Holocene fault displacement from the offset of pluvial lake shorelines in the Alvord extensional basin, northern Great Basin, USA; Geosphere; vol. 4; p. 536–563; doi: 10.1130/GES00101.1.

Ouchi, S.; 1985; Response of alluvial rivers to slow active tectonic movement; Geological Society of America Bulletin, vol. 96, p. 504–515.

Penck, W.; 1953; Morphological analysis of landforms; St. Martin's Press, New York, United States, 429 pp.

Pollyea, R.M., and Fairley, J.P.; 2011; Estimating surface roughness of terrestrial laser scan data using orthogonal distance regression; Geology, vol. 39, p. 623–626, doi: 10.1130/G32078.1.

Regard, V., Faccenna, C., Bellier, O., and Martinod, J.; 2008; Laboratory experiments of slab break-off and slab dip reversal: insight into the Alpine Oligocene reorganization; Terra Nova, vol. 20, p. 267–273, doi: 10.1111/j.1365-3121.2008.00815.x.

Renard, F., Voisin, C., Marsan, D., and Schmittbuhl, J.; 2006; High resolution 3D laser scanner measurements of a strikeslip fault quantify its morphological anisotropy at all scales; Geophysical Research Letters; vol. 33; doi: 10.1029-2005GL025038.

Richards, K.; 2002; Drainage basin structure, sediment delivery and the response to environmental change; Geological Society; London; Special Publications; vol. 191; p. 149–160; doi: 10.1144/GSL.SP.2002.191.01.10.

Ring, U., Brandon, M.T., Willett, S.D., and Lister, G.S.; 1999; Exhumation Processes; Geological Society; London; Special Publications; vol. 154; p. 1–27; doi: 10.1144/GSL.SP.1999.154.01.01.

Ritchie, W., Wood, M., Wright, R., and Tait, D.; 1988; Surveying and Mapping for Field Scientists; Longman Scientific & Technical, United States, 180 pp.

Robl, J., Hergarten, S., and Stüwe, K.; 2008; Morphological analysis of the drainage system in the Eastern Alps; Tectonophysics; vol. 460; p. 263–277.

Sagy, A. Brodsky, E.E., and Axen, G.J.; 2007; Evolution of fault-surface roughness with slip; Geology; vol. 35; p. 283–286; doi: 10.1130/G23235A.1.

Salomonson, V.V., Barnes, W., and Masuoka, E.J.; 2006; INtroduction to MODIS and an Overview of Associated Activities; *in:* Qu, J.J., Gao, W., Kafatos, M., Murphy, R.E., and Salomonson, V.V. (eds.); Earth Science Satellite Remote Sensing – Science and Instruments; Tsinghua University Press, Beijing, China, and Springer-Verlag GmbH, Berlin Heidelberg, Germany, p. 12–32.

Schlunegger, F.; 1999; Controls of surface erosion on the evolution of the Alps: constraints from the stratigraphies of the adjacent foreland basins; International Journal of Earth Sciences, vol. 88, p. 285–304.

Schlunegger, F., and Willett, S.; 1999; Spatial and temporal variations in exhumation of the central Swiss Alps and implications for exhumation mechanisms; Geological Society; London; Special Publications, vol. 154; p. 157–179.

Schlunegger, F., Melzer, J., and Tucker, G.E.; 2001; Climate, exposed source-rock lithologies, crustal uplift and surface erosion: a theoretical analysis calibrated with data from the Alps/North Alpine Foreland Basin system; International Journal of Earth Sciences; vol. 90; p. 484–499.

Schlunegger, F., Rieke-Zapp, D., and Ramseyer, K.; 2007; Possible environmental effects on the evolution of the Alps-Molasse Basin system; Swiss Journal of Geosciences, vol. 100, p. 383–405.

Schmid, S.M., Pfiffner, O.A., Froitzheim, N., Schönborn, G., and Kissling, E.; 1996; Geophysical-geological transect and tectonic evolution of the Swiss-Italian Alps; Tectonics; vol. 15; p. 1036–1064.

Schuerch, P., Densmore, A.L., McArdell, B.W., and Molnar, P.; 2006; The influence of landsliding on sediment supply and channel change in a steep mountain catchment; Geomorphology, vol. 78, p. 222–235.

Schumm, S.A., and Khan, H.R.; 1971; Experimental Study of Channel Patterns; Nature, vol. 233, p. 407–409.

Schweickert, R.A., and Lahren, M.M.; 1997; Strike-slip fault system in Amargosa Valley and Yucca Mountain, Nevada; Tectonophysics; vol. 272; p. 25–41; doi: 10.1016/S0040-1951(96)00274-0.

Sinclair, H.D.; 1997; Flysch to molasse transition in peripheral foreland basins: The role of the passive margin versus slab breakoff; Geology, vol. 25, p. 1123–1126.

Stammbach, M.; 1988; Rutschungen im hinteren Alptal (Kt. Schwyz); University Zurich, Switzerland, unpubl. diploma thesis, 96 pp.

Stevens, C.H.; 1991; Paleogeographic and structural significance of an upper Mississippian facies boundary in southern Nevada and east-central California; Geological Society of America Bulletin; vol. 103; p. 876–885; doi: 10.1130/0016-7606(1991)103<0876:PASSOA>2.3.CO;2.

Sylvester, A.G.; 1988; Strike-slip faults; Geological Society of America Bulletin; vol. 100; p. 1666–1703; doi: 10.1130/0016-7606(1988)100<1666:SSF>2.3.CO;2.

Townsend, J.R.G.; 1981; Terrain Analysis and Remote Sensing; George Allen & Unwin Ltd., London, Great Britain, 232 pp.

Trenhaile, A.S.; 2007; Geomorphology – A Canadian perspective; Oxford University Press, Canada, 498 pp.

von Blanckenburg, F., and Davies, J.H.; 1995; Slab breakoff: A model for syncollisional magmatism and tectonics in the Alps; Tectonics, vol. 14, p. 120–131.

Walker, J.D., Burchfiel, B.C., and Davis, G.A.; 1995; New age controls on initiation and timing of foreland belt thrusting in the Clark Mountains; Geological Society of America Bulletin; vol. 107; p. 742–750; doi: 10.1130/0016-7606(1995)107<0742:NACOIA>2.3.CO;2.

Wallace, R.E.; 1977; Profiles and ages of young fault scarps, north-central Nevada; Geological Society of America Bulletin; v. 88; p. 1267–1281; doi: 10.1130/0016-7606(1977)88<1267:PAAOYF>2.0.CO;2.

Wei, Z., He, H., Shi, F., Gao, X., and Xu, C.; 2010; Topographic Characteristics of Rupture Surface Associated with the 12 May 2008 Wenchuan Earthquake; Bulletin of the Seismological Society of America, vol. 100, p. 2669–2680, doi: 10.1785/0120090260.

Wernicke, B.P., Davis, J.L., Bennett, R.A., Normandeau, J.E., Friedrich, A.M., and Niemi, N.A.; 2004; Tectonic implications of a dense continuous GPS velocity field at Yucca Mountain, Nevada; Journal of Geophysical Research; vol. 109; p. B12404; doi: 10.1029/2003JB002832.

White, P.D., and Jones, R.R.; 2008; A cost-efficient solution to true color terrestrial laser scanning; Geosphere; vol. 4; p. 564–575; doi: 10.1130/GES00155.1.

Wilkinson, M., McCaffrey, K.J.W., Roberts, G., Cowie, P.A., Phillips, R.J., Michetti, A.M., Vittori, E., Guerrieri, L., Blumetti, A.M., Bubeck, A., Yates, A., and Sileo, G.; 2010; Partitioned postseismic deformation associated with the 2009 M_w 6.3 L'Aquila earthquake surface rupture measured using a terrestrial laser scanner; Geophysical Research Letters; vol. 37; p. L10309; doi: 10.1029/2010GL043099.

Willett, S.D., Schlunegger, F., and Picotti, VOL.; 2006; Messinian climate change and erosional destruction of the central European Alps; Geology; vol. 34; p. 613–616.

Winkler, P.W., Wildi, W., van Stuijvenberg, J., and Caron, C.; 1985; Wägital-Flysch et autres flyschs penniques en Suisse Centrale - Stratigraphie, sédimentlogie et comparaisons; Eclogae Geologicae Helvetiae, vol. 78; p. 1–22.

Wittmann, H., von Blanckenburg, F., Kruesmann, T., Norton, K.P., and Kubik, P.; 2007; The relation between rock uplift and denudation from cosmogenic nuclides in river sediment in the Central Alps of Switzerland; Journal of Geophysical Research–Earth Surface; vol. 112; doi:10.1029/2006JF000729.

Wolman, M.G., and Miller, J.P.; 1960; Magnitude and frequency of forces in geomorphic processes; Journal of Geology; vol. 68; p. 54–74.

Yeats, R.S., Sieh, K.E., and Allen, C.R.; 1997; The Geology of Earthquakes; Oxford University Press, USA; 576 pp.

Yerkes, R.F., Ellsworth, W.L., and Tinsley, T.C.; 1983; Triggered reverse fault and earthquake due to crustal unloading, northwest Transverse Ranges, California; Geology; v. 11; p. 287–291.

2. Chapter I

High-resolution Spatial Rupture Pattern of a Multiphase Flower Structure, Rex Hills, Nevada: New Insights on Scarp Evolution in Complex Topography Based on 3-D Laser Scanning

2.1. Abstract

Fault scarps represent the most obvious expression of tectonic activity at the Earth's surface. Studies on scarp morphology place constraints on fault kinematics and scarp-degradation processes, and were often based on geomorphic dating techniques. Fault scarps exposed in areas of simple topography facilitate data acquisition and interpretation, whereas little work had been done where fault scarps are superimposed on complex, dissected topography. Fault scarps developed in complex topography are commonly observed along flower structures and at tips of strike-slip faults. Such structures are important elements for evaluating the evolution and linking of strike-slip fault systems, and appear to be scale-independent from several meters to hundreds of kilometers. We examined the detailed meter- to hundred meter-scale structure and surface expression of a flank of one fault-scarp bounded pressure ridge (Rex Hills flower structure) by combining field mapping with high-resolution digital elevation model (DEM) analysis. Based on terrestrial laser scanning we generated a detailed DEM and extracted high-resolution topographic cross-sections, which enabled us to identify fault scarps and to determine their relative ages and geometry. Our study site is located on the transpressional left-bend between the Pahrump and Amargosa segments of the dextral Stateline fault system (SFS). The topography is characterized by alternating valleys and ridges (each ~100 m long, relief of ~4 m). We observed the following: the southern Rex Hills slope exhibits three fault scarps related to three reverse fault branches; the basal scarp (scarp 1) is most continuous, and exhibits five segments, the upper two scarps (scarps 2 and 3) are less continuous. Furthermore, fault scarps exposed on ridge crests are more numerous (up to four to five scarps) and smaller (~5 m high); valleys often exhibit single large (>10 m high), smoothed scarps. To easily detect differences between the scarps, we evaluated the height and slope angle of the scarps using topographic cross-sections. Our analysis indicates that scarp shape is influenced by fault dip, lithology, and degradation processes resulting in large scatter and broad overlap in scarp-height–slope-angle space. The analysis further indicates that scarp degradation is stronger in the valleys, and that the preservation potential of small, individual fault scarps is therefore greater on the ridge crests. We compared our fault-scarp data with published, calibrated data yielding an age of ~2 ka for the Rex Hills scarps consistent with an earlier finding. This suggests that the scarp shape mainly reflects progressive degradation since the most recent surface rupture. Our approach of analyzing high-resolution topographic data of closely-spaced fault scarps is promising especially when combined with subsurface data as well as geochronological and paleoseismic data, and it provides a basic scheme for analyzing scarp populations in a complex topographic region. Despite the absence of subsurface data, our approach allowed the study of complex high-resolution fault-scarp morphologies across a flower structure for the first time.

2.2. Introduction

Generally, fault scarps represent the best recognizable natural surface expression of seismic activity along active fault systems (e.g., Wallace, 1977; Yeats et al., 1997). Fault-scarp morphology studies had been conducted to constrain fault kinematics and especially scarp degradation often by using geomorphic dating techniques (Fig. 2.1; e.g., Bucknam and Anderson, 1979; Hanks et al., 1984; Avouac, 1993; Arrowsmith et al.; 1998 as examples along strike-slip and normal faults). Typically these studies are carried out where fault scarps are continuously exposed in areas of relatively simple and uniform topography, and where single isolated fault-scarp profiles can be easily acquired using labour-intensive techniques (e.g., Arrowsmith et al., 1998). These techniques are difficult to apply in areas where many small scarps are exposed, or where scarps are very subtle. Consequently, the patterns that result from fault scarps that are superimposed on a more complex and dissected topography have not been adequately explored at smaller spatial scales and compared with a larger spatial scale as considered by e.g., Landgraf et al. (2009).

A potentially efficient solution to close this gap in our knowledge is provided by recently developed terrestrial laser-scanning technologies, which are rapidly developing into effective research tools in tectonic geomorphology. A laser-scanner survey can rapidly (within minutes) acquire large amounts of topographic data with both a high resolution (up to a few cm) and high accuracy (of only a few mm; e.g., Buckley et al., 2008). These data can then be converted into high-resolution digital elevation models from which geomorphological data sets can be extracted. Furthermore, the high resolution of these data permits the extraction of large sub-data sets, and the identification and analysis of subtle features not obvious in the field.

Fault scarps that form in complex topography are commonly observed along flower structures occurring at fault bends and tips of strike-slip faults (e.g., Sylvester and Smith, 1976; Sylvester, 1988; van der Pluijim and Marshak, 2004; Cowgill et al., 2004a, 2004b). These structures are particularly important for the evolution and linkage of separate strike-slip fault segments (Cunningham and Mann, 2007; Landgraf et al., 2009).

As with faults in general, flower structures are scale-independent features ranging in size from the orogeny scale of hundreds of kilometres to more regional scales of tens of kilometers in extent, such as the Confidence Hills in southern Death Valley (Dooley and McClay, 1996), and down to the tens of meters scale of small sag ponds and pressure ridges (e.g., Crowell, 1974; Wakabayashi et al., 2004 for the latter two scales). As such, there have been many studies of these features where their internal geometry and evolution typically are inferred by interpreting geological mapping, seismic data, and analogue modelling (e.g., Wilcox et al., 1973; Harding, 1985; Naylor et al., 1986; McClay and Dooley, 1995; Dooley and McClay, 1996; McClay and Bonora, 2001). In contrast, however, few detailed studies of small-scale flower-structure surface morphology have been documented in the geologic literature. The likely reason is that these studies require time-consuming and occasionally expensive field work, and the complexity of the data returned requires acquisition of a very large data set. Therefore, a large amount of under-utilized information about the geometry and kinematics of flower structures is contained in their surface expression, especially in surfaces exhibiting fault scarps or sets of fault scarps. For example, fault-scarp analysis can provide information about how deformation is distributed in time and space on the thousand to hundred thousand year scales (e.g., Wallace, 1987; Arrowsmith et al., 1998; Carretier et al., 2002; Friedrich et al., 2003 and 2004; Wesnousky, 2005; Landgraf et al., 2009). To this end, high-resolution surface scans provide an efficient approach for extracting and analyzing the detailed surface characteristics of a given structure and quantifying its spatial and temporal evolution.

There are several small-scale transpressional flower structures within the eastern California shear zone; however, only a few exhibit surface fault-scarps. The Rex Hills (informal name)

flower structure is located near Pahrump, Nevada, on a left-bend of the Stateline fault system (Fig. 2.2), and it exhibits a set of subtle fault scarps on its flanks which are challenging to map in the field using traditional methods. Furthermore, due to their size and accessibility the Rex Hills are an excellent natural laboratory to study the surface expression of a positive flower structure in an arid environment using a terrestrial laser scanner.

In this chapter we present the results of a study aimed at characterizing the shape of fault scarps exposed along the kilometer-scale Rex Hills flower structure where we combined detailed field mapping with high-resolution digital elevation model (DEM) analysis. A new feature of our approach is the use of very high-resolution DEM data derived from a ground-based laser-scanning survey. This technique allows us to identify very subtle scarps not recognized otherwise, and facilitates efficient extraction of sub-data sets. It also provides a potentially powerful tool for evaluating scarp degradation (Fig. 2.1) superposed on larger scale erosion patterns of hillslopes, and for morphological relative dating within scarp populations. The latter may be the critical component required to evaluate ancient scarp populations.
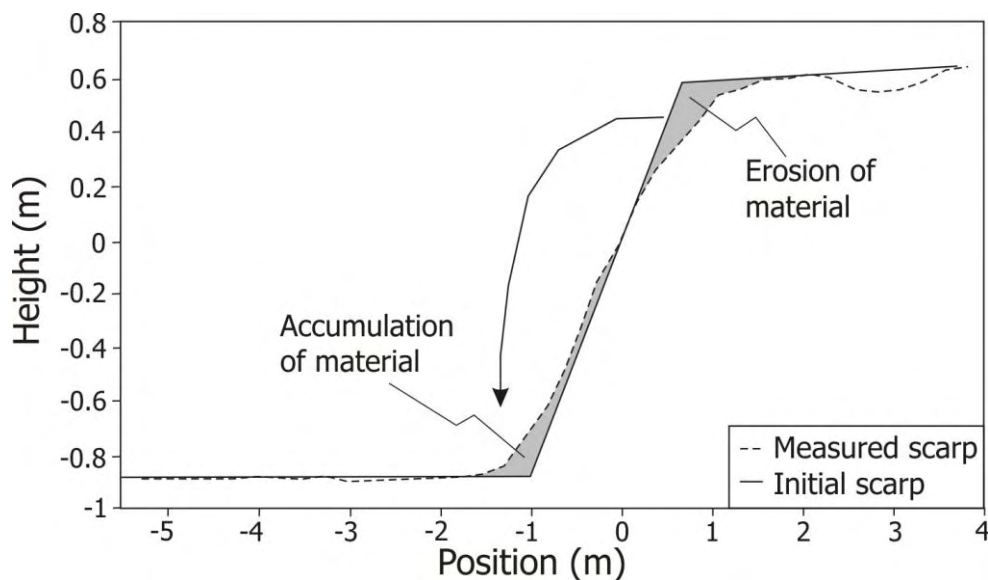
Fig. 2.1 Vertical exaggerated topographic profile of a 100-yr-old scarp where the dotted line indicates the measured profile and the black line is the form of the initial scarp derived by using an initial slope of 41° (modified after Nivière et al., 1998). The gray shaded areas mark the location of erosion and accumulation of material along the scarp profile explaining scarp degradation.

2.3. Stateline Fault System (SFS)

The Stateline fault system (SFS) is a dextral strike-slip fault that, between latitudes 35°N and 37°N, probably forms the eastern limit of the Eastern California Shear Zone–southern Walker Lane belt as defined by Dokka and Travis (1990) and Stewart (1980), (Guest et al., 2007; Fig. 2.2A). Geodetic data indicate an increase in the NW component of the surface velocity across the northernmost segment of the SFS (Fig. 2.2B) from ~0 mm/a east of the fault to 0.9–1.1 mm/a west of the fault with respect to a fixed North American reference frame (Wernicke et al., 2004). Holocene activity along portions of the SFS and Pleistocene activity along the entire fault is documented by tectono-geomorphic observations (Menges et al., 2003; Guest et al., 2007).

Offset estimates for different segments of the SFS range from ~25–45 km (Poole and Sandberg, 1977; Cooper et al., 1982; Stevens, 1991; Schweickert and Lahren, 1997) in the

north, to ~10 km in Stewart Valley, west of Pahrump (Burchfiel et al., 1983), and 3 km (Walker et al., 1995) in the south. These offset estimates are typically based on the offset of pre-Cenozoic markers. The most recent offset estimate of ~30 km during the last ~13.1 Ma along the southern SFS was determined by Guest et al. (2007), and is based on the dextral offset of ~13.1 Ma old proximal volcanic and associated rock-avalanche deposits (Fig. 2.2B). This provides a minimum long-term time-averaged geologic displacement rate of ~2.3 mm/a for the southern Pahrump and Mesquite segments of the SFS (Fig. 2.2B). The geodetic surface velocity across the northern part of the SFS alone is 0.7–1.2 mm/a with respect to a fixed North American reference frame (Wernicke et al., 2004; Hill and Blewitt, 2006).

On the earthquake-recurrence time-scale (~10 ka), however, fault-scarp degradation (Fig. 2.1) and morphologic changes due to ruptures along the SFS are poorly documented and have therefore not been related to the evolution of fault structures and the SFS. Hence, we evaluated fault scarps and drainage offsets related to the Rex Hills flower structure using high-resolution topographic data based on 3-D laser scanning.

2.4. Tectono-Geomorphic Setting of the Study Area

Following Guest et al. (2007), the SFS is divided into three segments which are separated by contractional left-bends: the Amargosa segment to the north, the central Pahrump segment, and the Mesquite segment to the south (Fig. 2.2B).

The Rex Hills study site lies along a transpressional left-bend between the Pahrump and Amargosa segments of the SFS where the central part of the SFS crosses from Stewart Valley into southern Amargosa Valley (Fig. 2.2B). Late Quaternary surface deformation along this portion of the SFS is associated with a large transpressive domal uplift centered on the northern piedmont of the Resting Spring Range (Menges et al., 2003). Linear pressure ridges in this area are typically bounded by a discontinuous, 8–10 km long set of aligned, en-echelon fault scarps. These scarps are up to ~3 m high with slope angles of 20–30°, and associated with dextral drainage offsets of 0.5 to ~5 m. Menges et al. (2003) determined vertical and lateral offsets yielding an average dextral-reverse net slip of ~3 m for the most recent faulting event. Furthermore, they inferred a latest Holocene age (<2 ka) for this event based on stratigraphic relationships and scarp morphology. This rupture event was a M_w 7.1–7.3 event whose rupture zone most likely continued ~35–40 km to the SE through Stewart Valley into northwestern Pahrump Valley (Menges et al., 2003). Lastly, this rupture-length estimate is based on the rupture length–displacement relationship of Wells and Coppersmith (1994) because the rupture length is poorly constrained in this area, and the displacement size indicates that the rupture length is greater than the exposed fault-scarp system.

The Rex Hills are two small connected hills: the NW hill is 40 m high and has a dome shape with a diameter of ~900 m; the SE hill is 45 m high, boat hull-shaped, and ~1500 m long by ~750 m wide (Fig. 2.3A). The hills consist of poorly consolidated Plio-Pleistocene conglomerate with rare bedding exposures that strike parallel to the trend of the hills (Fig. 2.3B). Unconsolidated and locally overturned (Fig. 2.4A) Plio-Pleistocene fluvio-lacustrine sediments are located at the base of the southern Rex Hills flank and on their northwestern slope (Fig. 2.3B). The sediments exposed at the Rex Hills site consist of quartzite and carbonate clasts, and are presumably derived from the Montgomery Mountains and Resting Spring Range, which consist of Precambrian and Paleozoic sedimentary rocks (Figs. 2.2B and 2.3B; Burchfiel et al., 1983). However, due to uncertainty about the amount of dextral offset in this region other source regions are possible.

The Rex Hills fault pattern exhibits a reverse and a dextral strike-slip component. The dextral component is expressed as drainage offsets with a magnitude of up to ~10 m (Fig. 2.4C), commonly associated with zones of highly fractured clasts within the Plio-Pleistocene

conglomerate that show dextral sense of shear (Fig. 2.4D). The thrust component is expressed as 0.3- to 2-m-high fault scarps (Fig. 2.4B).

The southern flank of the eastern Rex Hills is defined by a N-dipping reverse fault. The main evidence supporting this interpretation is the presence of steeply N-dipping, overturned, channelized fluvial sediments sticking out in the footwall of the fault defining the north limb of a footwall syncline (Figs. 2.4A and 2.3B). The surface expression of this fault is characterized by 1- to 2-m-high fault scarps (Fig. 2.4B) and dextral drainage offsets of 0.75–1.5 m.

The northern flank of the Rex Hills is also bounded by dextral oblique reverse faults. The eastern Rex Hills north flank exhibits clear dextral offsets of 2–3 m (Fig. 2.4C) as well as small poorly defined fault scarps (Fig. 2.3B). Faults exposed along the western Rex Hills north flank exhibit dextral drainage offsets of 2–3 m to ~10 m, dextrally fractured conglomerate, and 1- to 2-m-high fault scarps. Here, the fault is vertical to steeply S-dipping (Fig. 2.3B) based on fracture orientations in the conglomerate. The Plio-Pleistocene strata on the northern flank show no clear evidence of folding (e.g., overturned bedding) but bedding adjacent to the fault in the footwall dips steeply to the SW.

The fault pattern in the adjacent area SE of the Rex Hills is marked by a general NW-SE trend. The fault location is inferred from different characteristics: two springs are located in this area where several shrubs lie along a NW-SE trend, subparallel to the strike of the main fault trace (Fig. 2.3B). Small scarps observed on the surface of the Pleistocene terrace level P_{t2} are aligned in NW-SE direction and are probably fault related (Fig. 2.3B).

Fig. 2.2 (A) Simplified location map of the Stateline fault and major fault zones of the Eastern California Shear Zone. Abbreviations: GF – Garlock fault, SF – Stateline fault, FCF – Furnace Creek fault, DVF – Death Valley fault. **(B)** Shaded relief map showing the Stateline fault system (SFS) and nearby major active faults of the surrounding area (modified after Guest et al., 2007). The white arrow marks the position of the Devil Peak rhyolite intrusions, and the black arrow marks the offset volcanic and associated rock-avalanche deposits at Black Butte described by Guest et al. (2007). Abbreviations: IF – Ivanapah fault, NDVFCFZ – northern Death Valley Furnace Creek fault zone, SFS – Stateline fault system, BM – Bare Mountains, CM – Cottonwood Mountains, FM – Funeral Mountains, IM – Ivanapah Mountains, KR – Kingston Range, MM – Mesquite Mountains, MR – McCullough Range, NR – Nopah Range, NYM – New York Mountains, RR – Resting Spring Range, TM – Tucki Mountain, and YM – Yucca Mountain.

Fig. 2.3 (**A**) U.S. Geological Survey digital elevation model (DEM) of the Rex Hills with 10 m resolution derived from the National Elevation Data set (NED). The mapping (Fig. 2.3B) and laser-scanning area are indicated with a black frame and a blue frame, respectively. Labels in brackets and points with indicated view direction (yellow and black) emphasize the locations of pictures shown in Figure 2.4. (**B**) Detailed geologic map of the Rex Hills site. The scanning area is marked with a blue frame. The inset shows a general geologic cross-section.
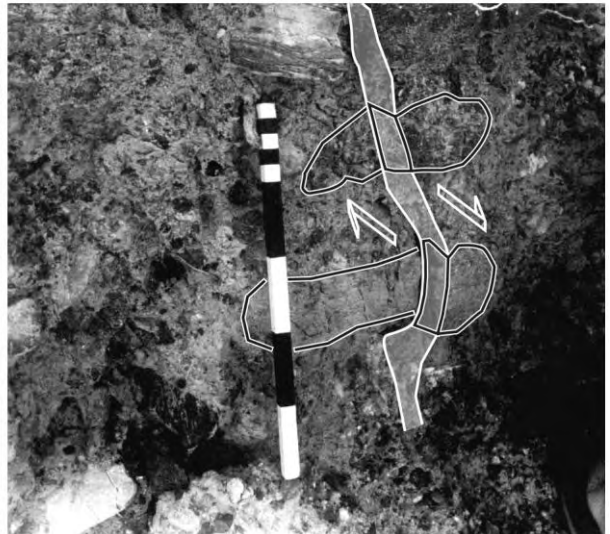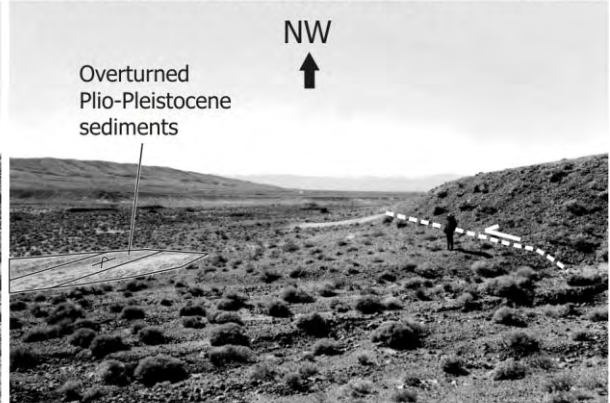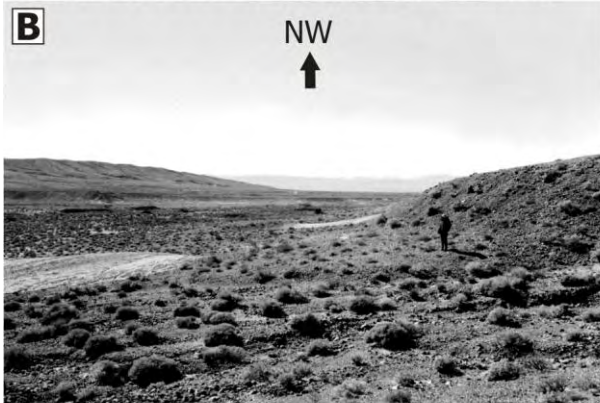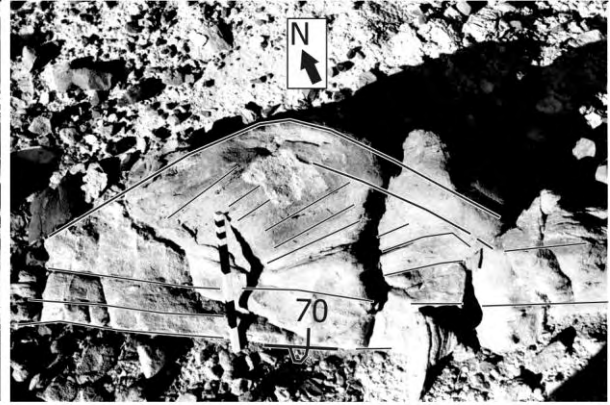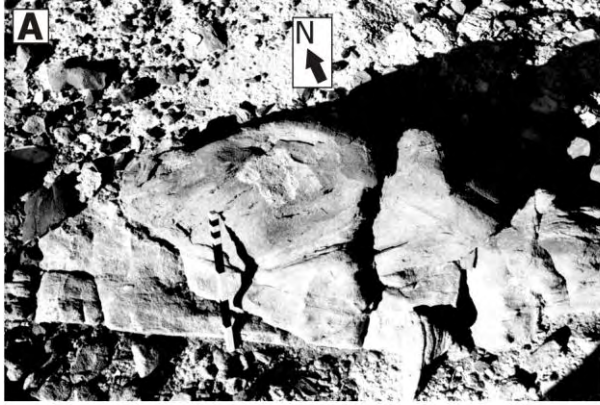
Fig. 2.4 Locations of pictures are shown in Figure 2.3A. The colored version of this figure is contained in Figure DR4 [see footnote 1]. **(A)** Photo looking down onto overturned Plio-Pleistocene lacustrine sedimentary rock sticking out at the southern Rex Hills base. The black lines emphasize bedding, outline of the trough, and crossbedding within this small trough. The strike and dip of the bed measured at the steeply dipping bedding-plane (upside down) is 110/70 NNE, and indicated by the appropriate symbol. The bedding plane appears as a line due to the map-view perspective of this photo. The arrow pointing to the north is rotated slightly relative to the strike and dip symbol in order to ensure the accuracy of the view. **(B)** Fault scarp exposed on the southern flank of the Rex Hills. **(C)** Dextral drainage offset exposed on the northern Rex Hills flank. The location of the offset channel and fault scarp are indicated by appropriate text labels. **(D)** Fault zone within the Plio-Pleistocene conglomerate. The vertical fault plane is indicated by transparent white, and is outlined with a solid white line. The offset clasts are outlined by a solid black line. The right-hand white arrow is supposed to indicate movement out of the rock along the fault, whereas the left-hand white arrow indicates movement into the rock.

2.5. Methods

To study the morphology of the Rex Hills scarps, we combined detailed geological mapping (Fig. 2.3B) with the interpretation of a high-resolution DEM (Fig. 2.5). We focused on mapping of individual faults, fault scarps, and offsets recorded in bedrock gullies. The DEM is based on measurements made with a terrestrial laser scanner (Riegl 3-D laser scanner *LMS-Z420i*®) in March and April 2006, and it covers the E-W trending southern flank of the eastern boat hull-shaped half of the Rex Hills indicated by a blue frame in Figure 2.3. This method is based on the emission of a laser beam and its reflection from the terrain surface. The resulting point data are used to generate a detailed DEM with cm-scale resolution. We summarized the field work and scanning procedure in the GSA Data Repository Item 2010050 accompanying the published paper respectively in Figure DR1 of this item, which can be found in the appendix of this thesis.

2.6. Results

2.6.1. Laser-Scanner Based DEM (LDEM)

Two surface features of the Rex Hills southern slope are identified in different display formats of the LDEM; different views of the LDEM (Figs. 2.5A and 2.5B) on one hand and a contour map of the LDEM (Fig. 2.5C) on the other. The first feature is the alternation of small valleys and ridges (each ~100 m long, relief of ~4 m) descending from the main ridge axis along the S-dipping slope of the Rex Hills (Fig. 2.5A and 2.5C). The second is a set of triangular facets at the base of the slope related to the oblique-reverse fault scarps (Fig. 2.5A), which we interpreted as gravity-controlled faces due to fluvial undercutting of their base resulting in scarp retreat. Hence, they will not be considered further.

The slope angle is a critical diagnostic feature of fault scarps (e.g., Bucknam and Anderson, 1979; Nash, 1980). Young scarps should have a steep slope angle, whereas the slope angle decreases with age assuming a constant diffusivity, and a homogenous material (e.g., Bucknam and Anderson, 1979). We used the slope map of the LDEM to identify fault scarps and to attempt a distinction between the different fault scarps (Fig. 2.6B). All scarps formed in the same material because the entire southern Rex Hills slope consists of Plio-Pleistocene conglomerate (Fig. 2.3B). Linear features with a steep angle are assumed to be fault scarps, if there is no alternative scarp-producing process available, e.g., fluvial drainage. These linear features are evident in the LDEM at the base of the southern Rex Hills slope (Fig. 2.6B) and correspond to the reverse segment identified in Figure 2.3B. In contrast, the eastern part of the southern slope is characterized by the alternation of small valleys and ridges with steep slopes (Fig. 2.6A), which makes fault-scarp mapping using the slope map in

this area more difficult. We marked the traces mapped along the eastern Rex Hills slope (Fig. 2.6B) in an oblique view of the LDEM for comparison (Fig. 2.5B). Furthermore, the set of gravity-controlled and fault-related triangular facets observed in Figure 2.5A are characterized by a steep angle, and marked with a dotted line as retreating scarp (Fig. 2.6B).

In order to detect fault scarps that cannot be identified in the LDEM at first sight, and to image especially their spatial distribution and continuation, 83 detailed topographic profiles mainly perpendicular to the E-W trend of the eastern half of the Rex Hills were extracted. These profiles are spaced unevenly based on the width of the valleys and ridges, and include profiles that traverse along small valleys and ridge crests (Fig. 2.5A). The profiles were used to extract the scarp height and slope angle for each identified scarp (Table DR1 [see footnote 1]; Fig. 2.7A). Frequently more than one scarp can be observed in a profile (Fig. DR2 [see footnote 1]). In these cases, the fault-scarp labeling listed in Table DR1 starts with the lowermost scarp.

The uncertainty associated with the scarp-height determinations amounts to ±20 cm (1 σ). Individual point locations have a measurement uncertainty of ±5 cm (1 σ) representing an error induced by the laser scanner. The scarp height, as indicated in Figure 2.7A, is defined by the difference in the z-coordinate between two points resulting in a total measurement uncertainty of ±10 cm (1 σ). The remaining uncertainty of ±10 cm (1 σ) is subjectively introduced by selecting the base and top points of each scarp profile manually (Fig. 2.7A). Due to the large point-cloud density, repeated selection of single top and base points yielded similar scarp-height values for each scarp differing by ~20 cm. Thus, the total uncertainty adds up to ±20 cm (Figs. 10–14).

To establish a fault-branch configuration that explains the observed fault-scarp pattern, we followed the assumptions first stated by Bucknam and Anderson (1979) that the slope angle of fault scarps decreases with time and therefore with age (Fig. 2.7B). Next, we isolated a set of fault-scarp profiles fitting this assumption (Fig. 2.7C), and based on this evaluation we assigned a possible configuration of reverse fault branches and segmentation patterns to the entire fault-scarp set (Fig. 2.8). The scarp lines 1–3 in Figure 2.8 are intended to give the general configuration of the scarps and associated fault branches. We used these lines to approximate fault locations based on scarp symmetry, although the exact fault locations cannot be determined without subsurface data.

Based on the topographic profile analysis, we identified three fault scarps (Fig. 2.8): scarp 1 is continuous, extends along the base of the slope, and exhibits five segments; scarps 2 and 3 are less distinct and extend along the upper part of the slope where scarp 2 exhibits four segments. In an oblique 3-D view of the LDEM, scarp 1 is most obvious due to its continuous surface expression in contrast to scarp 2 which is less clearly defined (Fig. 2.5B). Scarp 3 cannot be detected using such a perspective.

Generally, the steeper, smaller, individual fault scarps are better preserved along profiles that lie parallel to a ridge crest (e.g., profile numbers 20, 39, 46 and 61; Fig. 2.8A), whereas profiles located in valleys commonly exhibit a higher, single fault scarp (e.g., profile numbers 42, 53, 64 and 77; Fig. 2.8A). The scarp height for all scarps ranges from 0.3 m up to 13.2 m over two orders of magnitude. The slope angles generally increase from E to W (Fig. 2.8A).

To evaluate the influence of fault dip on scarp morphology along the Rex Hills slope, we approximated the local near-surface dip angle of the two fault branches related to the more continuous scarps 1 and 2 (Fig. 2.5C). Where possible we mapped the fault trace on a topographic map of the LDEM (1 m contour-line interval; Fig. 2.5C) by assuming that the base of scarps 1 and 2 are equivalent to the fault trace (Fig. 2.8). Based on the intersection of the local fault trace with topography, we inferred that the fault associated with scarp 1 exhibits a shallow near-surface dip of 10–15°. In contrast, the scarp 2 fault is characterized by a steeper dip of ~10–20° (Fig. 2.5C).

Dextral offsets in the drainage network were identified in the field as a common morphological feature of the Rex Hills structure (Fig. 2.4C). Within the LDEM, magnitudes for nine dextral offset features were measured along straight lines, taken from one termination of the offset feature to the other (Fig. 2.9; Fig. DR3 [see footnote 1]). All of these features were formed in poorly consolidated Plio-Pleistocene conglomerate (Fig. 2.3B). The offset magnitude ranges from 7.77 m to 56.5 m (Fig. 2.9; Table DR2 and Fig. DR3 [see footnote 1]). We estimated the uncertainty bound for each measurement to be 30% (equal to 3 σ) of the derived offset value given that some of the offset features are curvilinear and intersect the fault at low angles (Fig. 2.9B; Table DR2 [see footnote 1]). Moreover, erosion focused in the drainage valleys led to the deposition of younger sediments, which may have masked parts of the older offset channel-bed. The 30% bound further accounts for subjectively introduced uncertainties mainly due to the fact that some offset features are not as obvious as the examples shown in Figures 9B–9E. In some cases, the offset evaluation is further hampered by the LDEM resolution. Where the LDEM grid next to the offset feature is coarser, e.g., triangles increase in size, the low point-cloud density is due to shielding effects during the scanning induced by the Rex Hills valley-ridge morphology (e.g., Fig. DR3E [see footnote 1]).

Fig. 2.5 High-resolution topographic maps showing the results of the 3-D laser-scanner survey with cm-scale resolution. **(A)** 3-D view of the laser-scanner based digital elevation model (LDEM). Triangular facets described in the text and the alternation of ridges and valleys are clearly visible in this view. The location of the LDEM is marked in Figure 2.3 by a blue frame. The black arrow on the right side of the LDEM indicates the elevation difference of 40 m. The dashed white line at the bottom of the LDEM marks the location of the lowermost points of topographic profiles extracted from the LDEM. The profile numbering is also shown, and the topographic profiles are evenly spaced between the indicated profile location intervals traversing along the ridges and valleys. The white frame shows the outline of the LDEM contour map (Fig. 2.5C). **(B)** Both pictures show an oblique 3-D view of the LDEM looking east along the Rex Hills front. The location of the basal scarp is obvious in this view, and is indicated by a solid white line in the right-hand picture. In contrast, the mapped upper fault trace is more difficult to recognize, and indicated by a dashed white line. **(C)** Contour map of a LDEM section (Fig. 2.5A for location). The black lines indicate local fault traces.
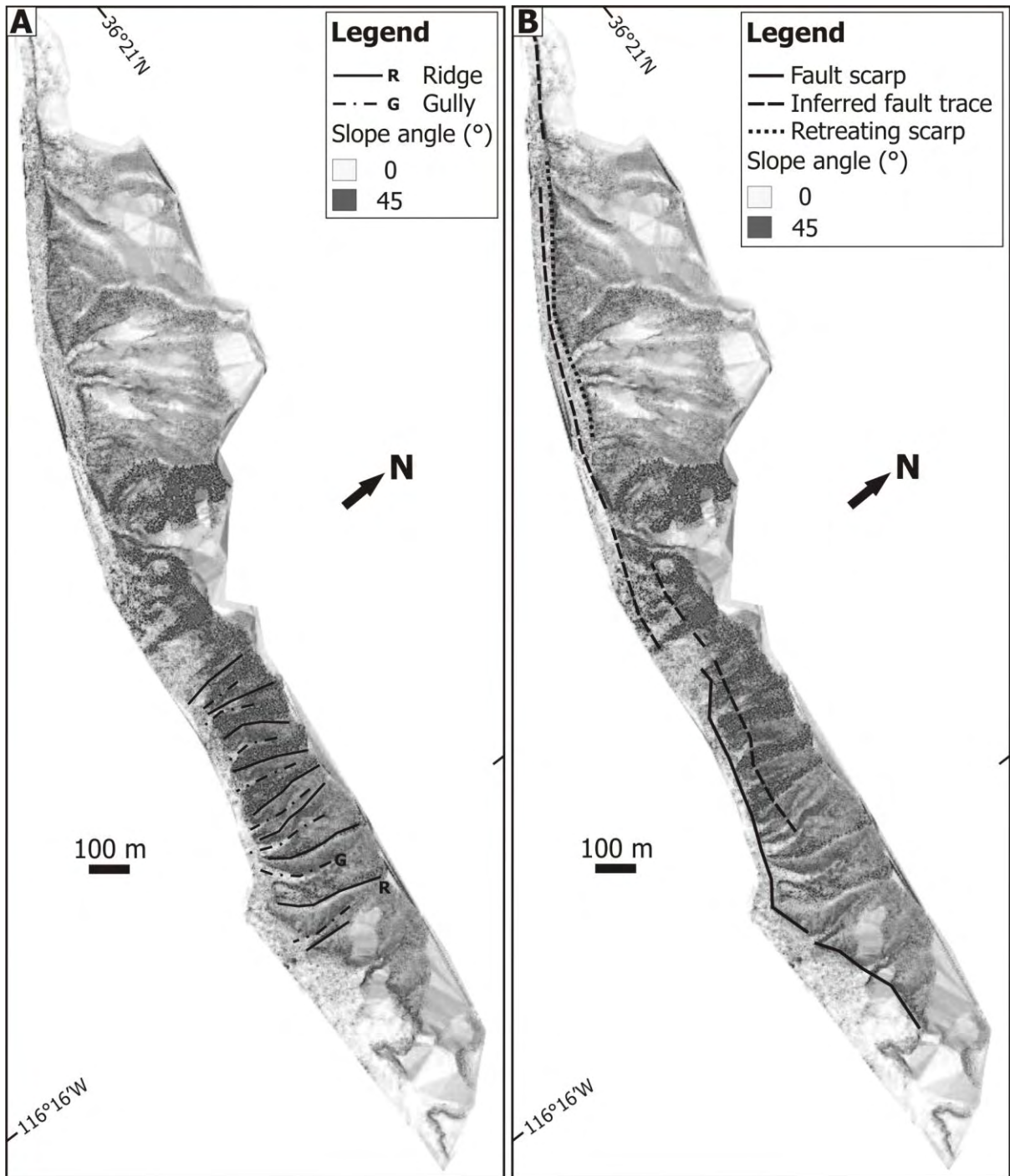
Fig. 2.6 Slope-angle map of the LDEM: the very light-gray color fits to a minimum slope-angle of 0°, and the dark-gray color correlates with slope angles of 45°. The colored version of this figure is further contained in Figure DR5 [see footnote 1]. **(A)** Slope map showing the alternation of gullies and ridges. **(B)** Slope map showing location of mapped fault scarps, inferred fault traces, and gravity-controlled scarps.
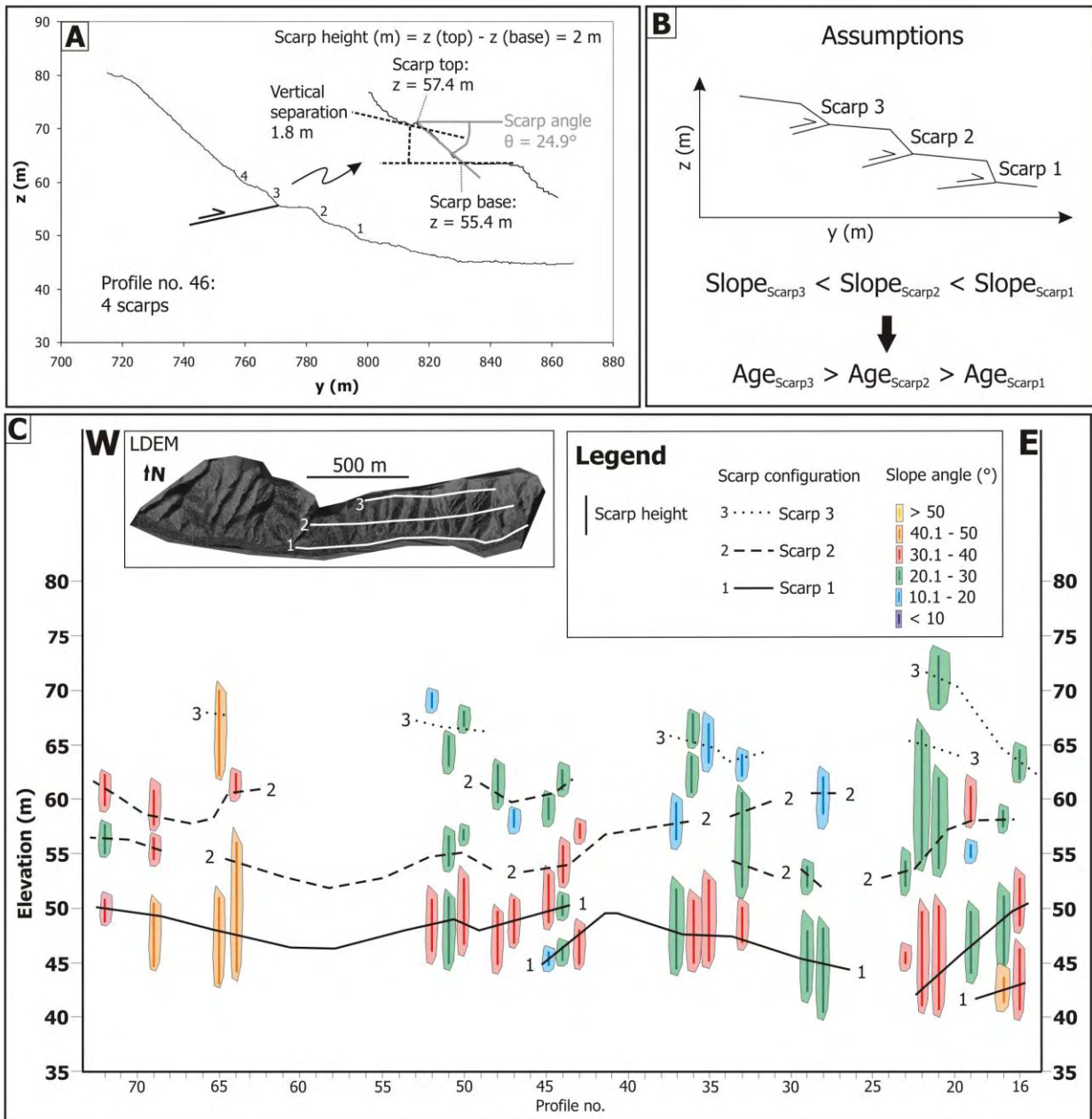
Fig. 2.7 (A) Topographic profile number 46 and definition of scarp height, slope angle θ, and vertical separation used for the profile analysis in Figure 2.8. The profile location is shown in Figure 2.5A. **(B)** The sketch shows the expected fault-scarp profile according to the assumption that the scarp-slope angle decreases with age (Bucknam and Anderson, 1979). **(C)** Scarp profiles extracted from the LDEM fitting the expected profile shape shown in Figure 2.7B. We inferred the scarp configuration based on these selected profiles and adopted this pattern in Figure 2.8. The location of the three fault scarps is also shown in the LDEM, and the profile locations can be obtained from Figure 2.5A.
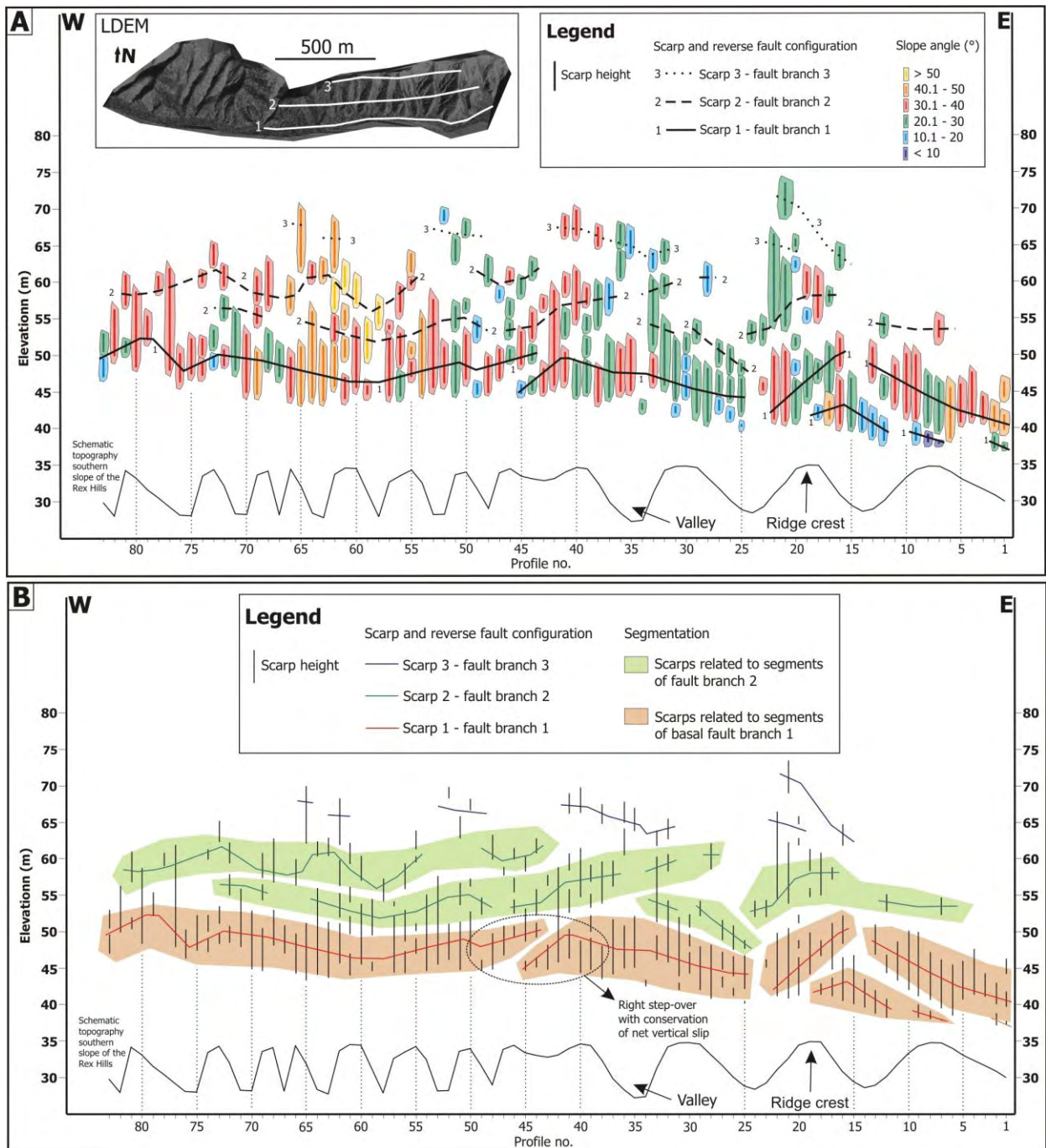
Fig. 2.8 Summary of the topographic profile analysis. **(A)** The scarp-slope map shows scarp heights and maximum slope-angles of the individual fault scarps identified in the 83 topographic profiles extracted from the LDEM. The location of the topographic profiles is sketched at the bottom of the plot, and can be alternatively inferred from Figure 2.5A. The location of the three fault scarps is shown in the LDEM. **(B)** This plot is similar to Figure 2.8A but without the scarp slope-angle. Instead, it shows only the scarp heights of the individual fault scarps. The possible configuration of reverse fault branches and their segmentation are colored in order to explain the observed fault-scarp pattern.
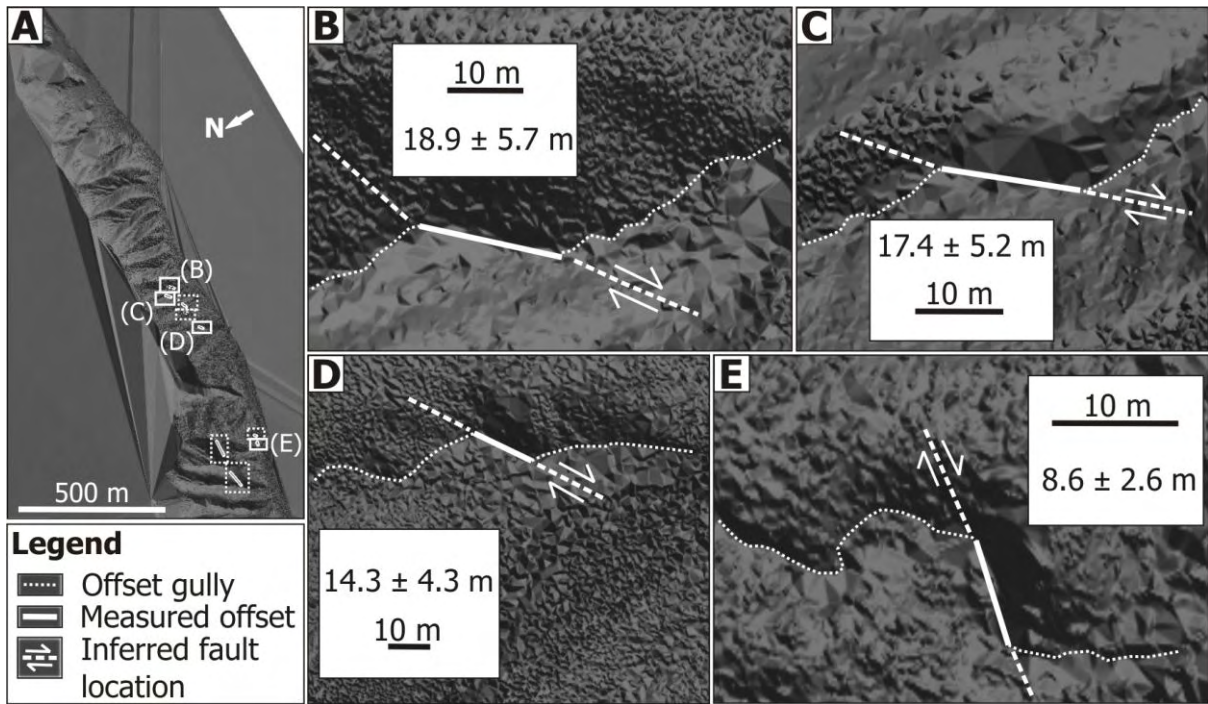
Fig. 2.9 (A) The location of nine measured dextral offsets is marked in the LDEM, and summarized in Table DR2 [see footnote 1]. The offsets marked with a continuous rectangle are shown in detail in Figures 2.9B–2.9E. In contrast, no detail is shown for offsets marked with a dashed rectangle. The legend is valid for the offsets shown in Figures 2.9B–2.9E. **(B)** Details of dextral offset number 1. **(C)** Details of offset number 2. **(D)** Details of offset number 5. **(E)** Details of offset number 9.
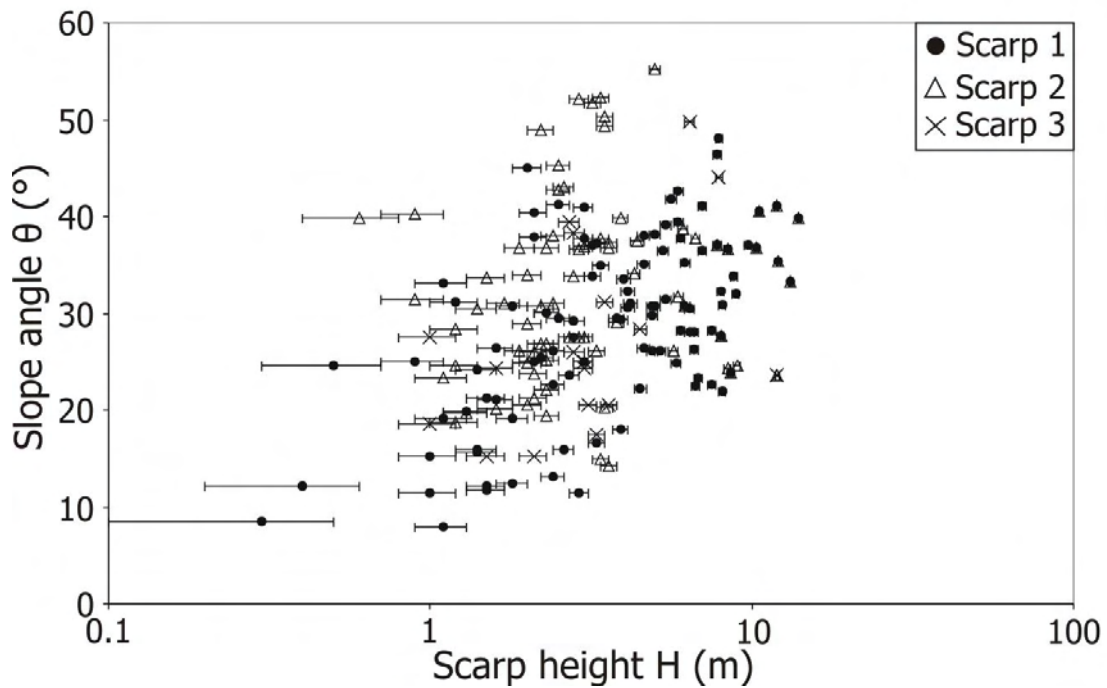
Fig. 2.10 Plot of scarp height H versus slope angle θ for the three identified fault scarps showing broad scatter. The thin error bars indicate scarp-height uncertainties.

2.6.2. Scarp-Height vs. Slope-Angle Plots

The height and slope angle of fault scarps are two diagnostic features required to characterize the evolution of normal fault scarps in cohesionless material (Bucknam and Anderson 1979; Nash, 1980; Hanks et al., 1984; Fig. 2.1 for comparison). Profile studies on late Quaternary normal fault scarps revealed that the slope angle is related to the logarithm of scarp height for a given age, and that for fault scarps of a given height the slope angle decreases with age (Bucknam and Anderson, 1979). Here, the approach described by Bucknam and Anderson (1979) is sufficient although more sophisticated models are available. We evaluated the relationship between scarp height and slope angle for the scarps identified in the 83 topographic profiles extracted along the southern slope of the Rex Hills (Fig. 2.8). Using this basic approach enabled us to easily detect differences between several fault scarps in detail without any modelling efforts.

Considering slope angle and scarp height of all scarps extracted from the 83 profiles yields a scatter plot with a near circular data distribution (Fig. 2.10) resulting in poor correlation for the three fault scarps. In an effort to reduce the scatter, we plotted the profile results from ridges (black dots) and valleys (white dots) separately for each scarp (Fig. 2.11). The resultant scatter plots show an improvement in the ridge-profile correlation coefficients for scarps 1 and 3, and minimal improvement for scarp 2 (black regression lines in Fig. 2.11). The valley-profile data (gray regression lines in Fig. 2.11) generally exhibit less correlation except for scarp 3 (Fig. 2.11C).

To further improve the correlations and obtain insights into the surface processes controlling the scarp geometries, we reduced the data in several steps until better correlation coefficients were obtained compared to Figure 2.11. This procedure is justified because we extracted the topographic profiles manually from the LDEM. First, we removed ambiguous scarp profiles from the fault-scarp data. These are possible compound fault scarps where the upper and lower portions may belong to separate scarps that have merged (e.g., profile numbers 22, 42, 53, 64, 77, and 80 in Fig. 2.8). Secondly, we eliminated scarp profiles located at the tips of fault-scarp segments (e.g., profile numbers 43, 44 and 45 for the basal fault scarp in Fig. 2.8B), which are characterized by smaller offsets than the central portion of the segments. After completing this operation, we were able to obtain a slight improvement in the overall correlation (Fig. 2.12), and noted that we obtained better correlation for the ridge-profile data (black regression lines) than for the valley-profile data (gray regression lines) except in the case of scarp 2 (Fig. 2.12B), which exhibits less correlation than scarps 1 and 3 (Figs. 2.12A and 2.12C). To further improve the correlation for scarp 2, we isolated profiles which are located solely on the ridge crests and neglected profiles from the entire valley walls and floors where erosion would affect scarp morphology. Some of the scarp profiles previously indicated as ridge profiles (Figs. 2.11B and 2.12B) are not located on ridge crests. They are actually located on the uppermost valley walls (e.g., profile number 21 in Fig. 2.8), where the slope is rather gentle compared to the middle part of a valley wall (also Fig. 2.6). Considering only ridge-crest profiles yields an improved correlation coefficient for scarp 2 (Fig. 2.13). Finally, due to the fact that in Figure 2.12 the valley regression-lines plot below the ridge regression-lines compared to Figure 2.11 (discussed below), we focused our further evaluation on the ridge-profile data of scarps 1 and 3 (Figs. 2.12A and 2.12C), and the ridge-crest profile data of scarp 2 (Fig. 2.13).

To approximate the age of the Rex Hills scarps, we plotted our results together with the calibrated normal fault-scarp data of Machette et al. (2001) and Friedrich et al. (2004) indicated by thin black lines in Figure 2.14. This approach was required because no such data are available for reverse fault scarps. Machette et al. (2001) collected data from scarps of known age formed in sandy gravels from across the Basin and Range Province (e.g., Bucknam and Anderson, 1979). The conglomerate comprising the Rex Hills is mostly

composed of gravel-sized clasts with a fine-grained sandy to silty fraction (e.g., Fig. 2.4D; Simon Kübler and Markus Hoffmann, 2009, pers. comm.). The similarity between the calibrated scarp and the Rex Hills scarp material suggests that it is not unreasonable to compare the Rex Hills data with the calibration curves of Machette et al. (2001) and Friedrich et al. (2004). We do recognize, however, that we ignored climatic variations and the effect of variations in internal stratigraphic and structural architectures between the scarp sets when we did this.

The maximum age obtained for the basal fault scarp by Menges et al. (2003) is 2 ka equivalent to the Fish Springs regression line (thin black line number 2 in Fig. 2.14). The slope of this regression line is steeper than that of the regression line for the basal fault scarp (scarp 1, thick black line labeled S1 in Fig. 2.14) and scarp 2 (thick black line labeled S2), but it is similar to the slope of the regression line for fault scarp 3 (thick black line labeled S3). Due to the small lithologic differences in the data set of Machette et al. (2001; e.g., sandy gravel) and the Rex Hills data (e.g., fine-grained sandy to silty gravel), and the broad overlap and scatter in the data characterizing the three Rex Hills scarps, we cannot assign a precise age to these scarps. However, our age estimate is consistent with the age derived by Menges et al. (2003) because the regression lines of the three scarps plot near or above the 2 ka Fish Springs line (Fig. 2.14). Furthermore, the Rex Hills scarp regression-lines plot clearly above the regression line of a well constrained event in Crescent Valley (3 ka; gravel deposits; Friedrich et al., 2004).

Fig. 2.11 Plots of scarp height H versus slope angle θ for the three fault scarps differentiating between ridge and valley scarps in order to reduce and explain the scatter observed in Figure 2.10. Black lines correspond to ridge regression-lines, whereas gray ones correspond to valley regression-lines. The thin error bars indicate scarp-height uncertainties. **(A)** Scarp 1: basal fault scarp with a broad overlap between ridge and valley data. **(B)** Scarp 2: between scarp 1 and 3, also with a broad overlap between ridge and valley data. **(C)** Scarp 3: uppermost scarp shows a clear difference between ridges and valleys although only a few data points had been obtained.

A

θ = 22.649 + 5.4168 log H
R² = 0.252

θ = 17.755 + 8.1276 log H
R² = 0.4223

● Ridge scarps
○ Valley scarps

Slope angle θ (°)

B

θ = 31.694 + 1.3923 log H
R² = 0.0125

θ = 25.536 + 4.426 log H
R² = 0.0896

Slope angle θ (°)

C

θ = 22.636 + 6.3756 log H
R² = 0.2085

θ = 13.571 + 6.902 log H
R² = 0.3213

Slope angle θ (°)

Scarp height H (m)
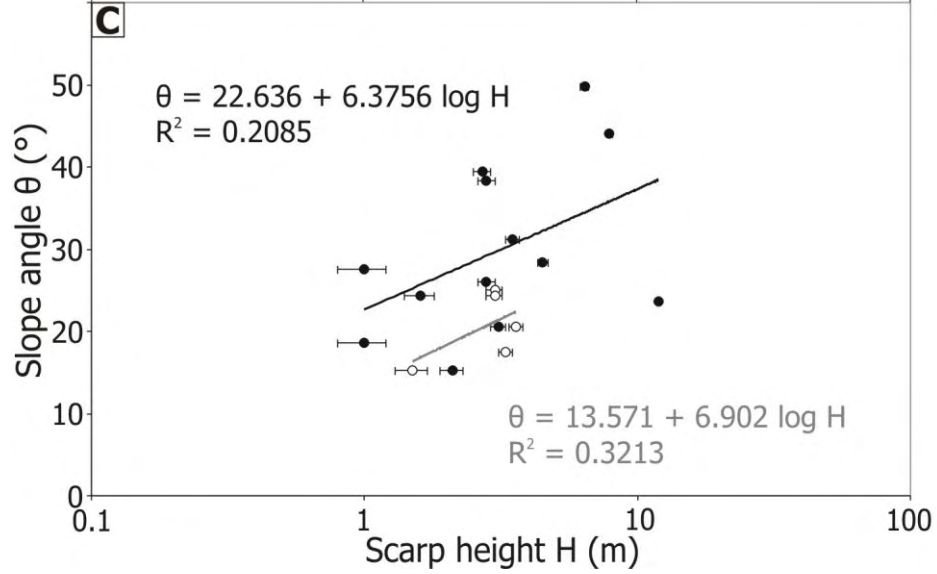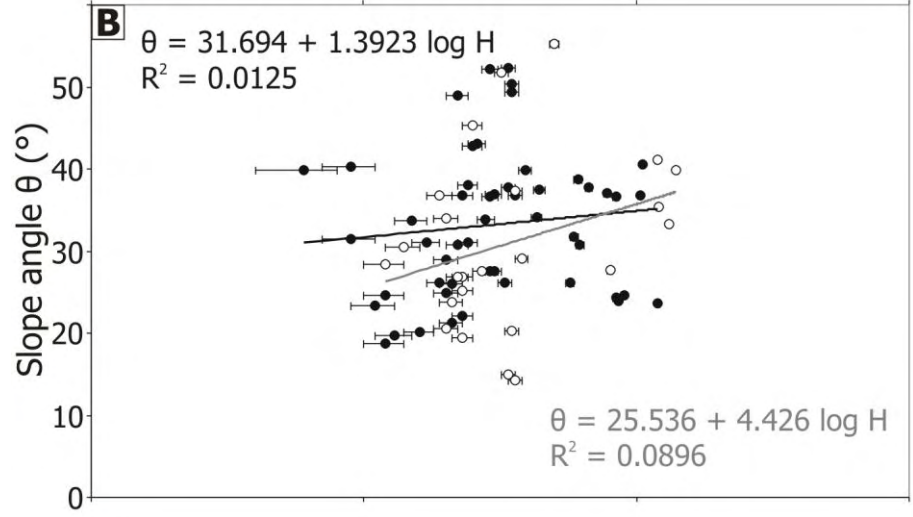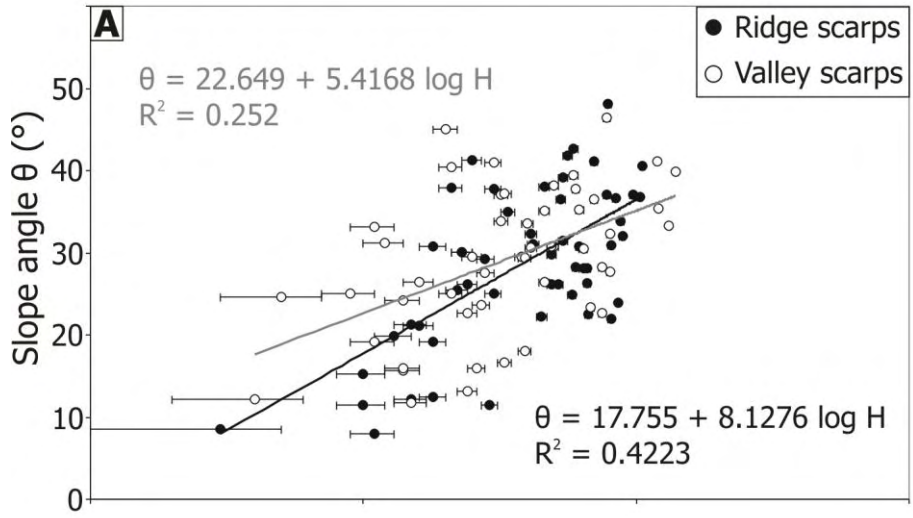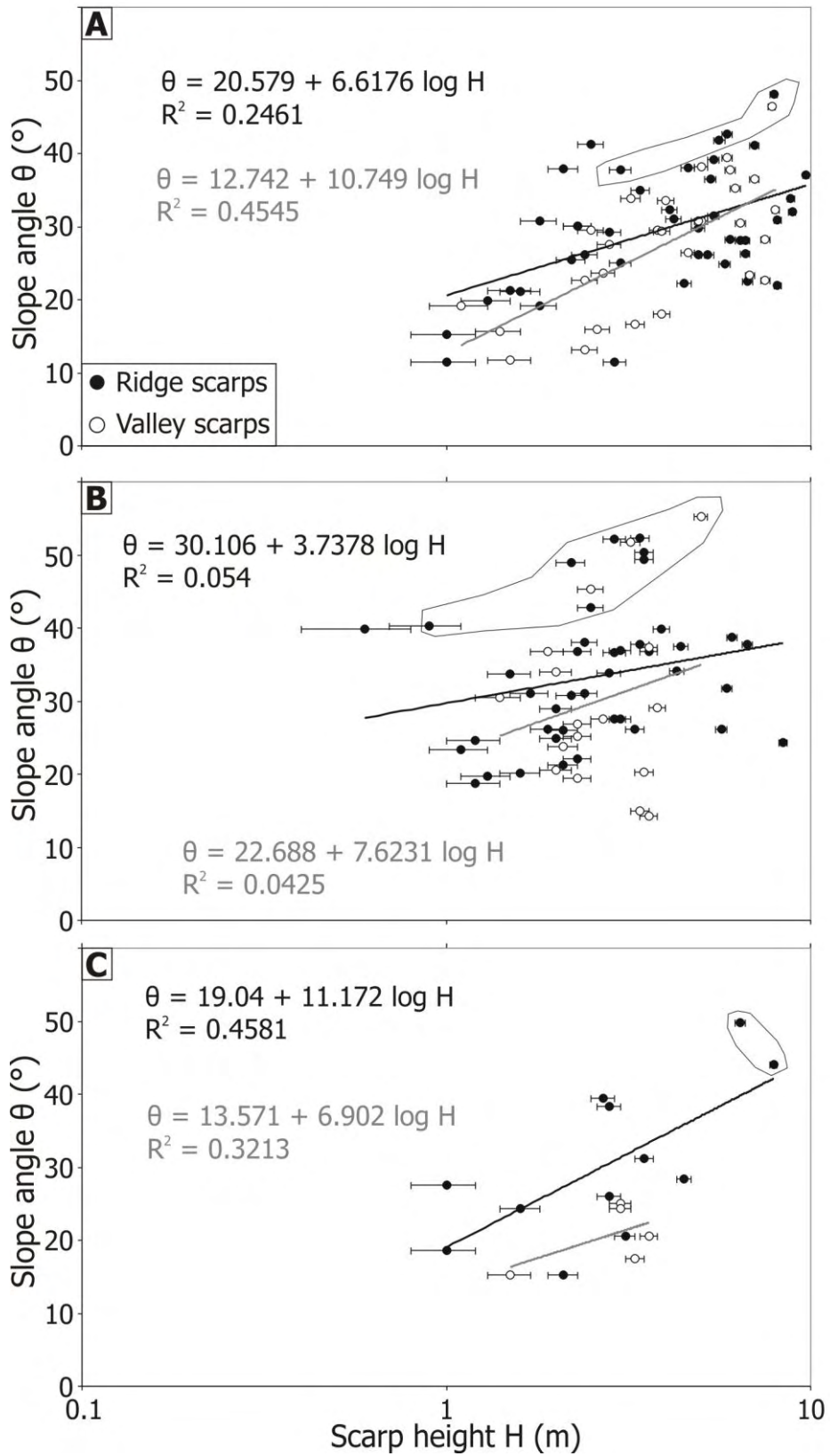
Fig. 2.12 These plots are similar to Figure 2.11. They show the results after reducing the data of the three fault scarps as described in the text. The difference between ridge and valley profiles is now obvious. The gray valley regression-lines generally plot below the black ridge regression-lines suggesting that scarp degradation is more efficient in the valleys than on the ridges. The thin error bars again indicate scarp-height uncertainties. The thin black lines outline high-angle scarp profiles (>40°) localized in the area of profile numbers 55–69 (Fig. 2.8A) plotting above the average data population (details discussed in the text). **(A)** Plot of scarp height H versus slope angle θ shows the results for scarp 1 after eliminating ambiguous scarps whose upper part was interpreted to belong to scarp 2 and its lower part to scarp 1 (e.g., profile numbers 32, 42, 53, 54, 60, 64, 64, 71, 77, and 80 in Fig. 2.8), and removed scarps located at segment tips of scarp 1 (e.g., profile numbers 1, 2, 3, 7, 8, 9, 13, 18, 23, 25, 34, 43, 44, 45, and 59 in Fig. 2.8). **(B)** Plot of scarp height H versus slope angle θ for scarp 2 after removing ambiguous scarp whose upper part was interpreted to belong to scarp 3 and its lower part to scarp 2 (e.g., profile number 22 in Fig. 2.8), and eliminating scarps located at segment tips of scarp 2 (e.g., profile numbers 24, 25, 33, and 55 in Fig. 2.8). **(C)** Plot of scarp height H versus slope angle θ for scarp 3 after the elimination of the ambiguous scarp whose upper part was interpreted to belong to scarp 3 and its lower part to scarp 2 (e.g., profile number 22 in Fig. 2.8).

$$\theta = 28.591 + 6.9218 \log H$$
$$R^2 = 0.1424$$
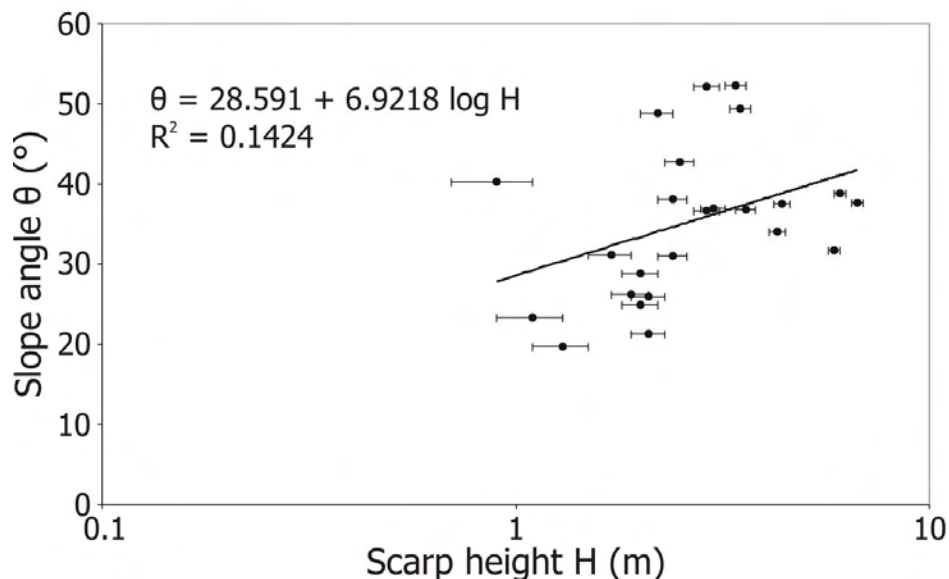
Fig. 2.13 Plot of scarp height H versus slope angle θ for scarp 2 including only data from scarps solely located on the actual ridge crests to obtain a better correlation for this scarp. Fault scarps from valley walls and floors are neglected due to erosion affecting the scarp morphology especially in valleys. Removed scarps previously indicated as ridge scarps are (compared to Fig. 2.12B), e.g., profile numbers 17, 20, 21, 32, 38, 41, 47, 51, 57, 62, 69, 72, and 74 (Fig. 2.8). These scarp profiles are actually located on the uppermost valley walls where the slope is gentle compared to the middle part of a valley wall (Fig. 2.6). The thin error bars indicate scarp-height uncertainties.

2.7. Discussion

2.7.1. Fault-Scarp Pattern

The southern Rex Hills slope is characterized by three fault scarps. The most continuous scarp lies along the toe of the slope, whereas the upper part of the slope exhibits a discontinuous, less distinct set of scarps (Fig. 2.8). We detected the basal scarp while conducting geologic mapping where we determined bedding attitudes next to the scarp, and inferred the fault dip in several places (Figs. 2.3B and 2.4D). The two remaining scarps were identified during the topographic profile analysis.

The scarp slope-angle pattern of the southern Rex Hills slope is characterized by a general increase from E to W. The eastern part of the slope is dominated by lower scarp slope-angles (blue and green in Fig. 2.8A), and the western part by higher angles (red to yellow). The fault branch associated with the basal scarp 1 exhibits a near-surface dip of up to ~10–15°, whereas the fault related to scarp 2 is characterized by a steeper dip of approximately ~10–20° (Fig. 2.5C). Furthermore, the slope angle of scarp 2 is often steeper than that of scarp 1 along strike, e.g., areas of profile numbers 39–45 or 57–62 (Fig. 2.8A).

Fault dip can affect scarp morphology, and a different dip between fault branches may account for observed variations in fault-scarp steepness (e.g., Carretier et al., 2002). Moreover, internal oblique reverse faults of flower structures tend to be steeper in dip than the bounding faults (e.g., Sylvester, 1988). This suggests that the fault dip may be a factor influencing the scarp steepness along the southern Rex Hills slope due to the approximated difference in near-surface dip of the faults related to scarps 1 and 2 (Fig. 2.5C). However, the degree of the influence is difficult to evaluate given that the upper scarp 2 is less continuous than scarp 1 (Fig. 2.8), and that we do not have any direct information about the fault orientation in the subsurface.

Spatially correlated factors, e.g., lithologic heterogeneity, may also control scarp morphology. For example, the western part of the southern Rex Hills slope is characterized by a concentration of high-angle fault scarps (slope angle >40°; area of profile numbers 55–69 in Fig. 2.8A). This concentration of steep scarps may be due to lithologic contrasts; the Plio-Pleistocene conglomerate (Fig. 2.3B) may be more consolidated in this part of the Rex Hills resulting in generally steeper scarps. Scarp morphology may also be controlled by across strike lithologic contrasts within the Plio-Pleistocene conglomerate, which could account for the average slope-angle difference observed between scarps 1 and 2, although this is difficult to evaluate due to the extremely poor bedding exposures within the Rex Hills conglomerate. Also, it is worth noting that there is no obvious difference in the conglomerate in terms of grain size, clast composition, or consolidation across the scarps, which suggests that the material is probably very similar in character across strike.

All three scarps show signs of fault segmentation, with the basal scarp exhibiting the clearest segmentation pattern (Fig. 2.8B). The basal scarp is divided into five segments, and the second scarp into four segments along strike. The highest and most degraded scarp is too discontinuous to evaluate with confidence. The basal scarp segments transferred an approximately constant, net vertical slip from one segment of the reverse fault branch to the next one, in one case via a right stepover implying dextral offset (Fig. 2.8B).

The fault-scarp segmentation pattern suggests that the faults may be characterized by a changing geometry along strike. Variations in reverse fault dip could result in decreasing scarp height towards fault-segment tips as observed in Figure 2.8B. Segmentation may be caused by variations in fault strength, geometry, and loading distribution, and may control the extent and magnitude of ruptures (e.g. Hilley et al., 2001). For example, Hilley et al. (2001) used boundary element models to study these effects on surface offsets along the Cholame and Carrizo segments of the San Andreas fault. Their results suggest that the observed offset

gradient at the segment boundary is caused by strength contrasts between the overlapping fault segments.
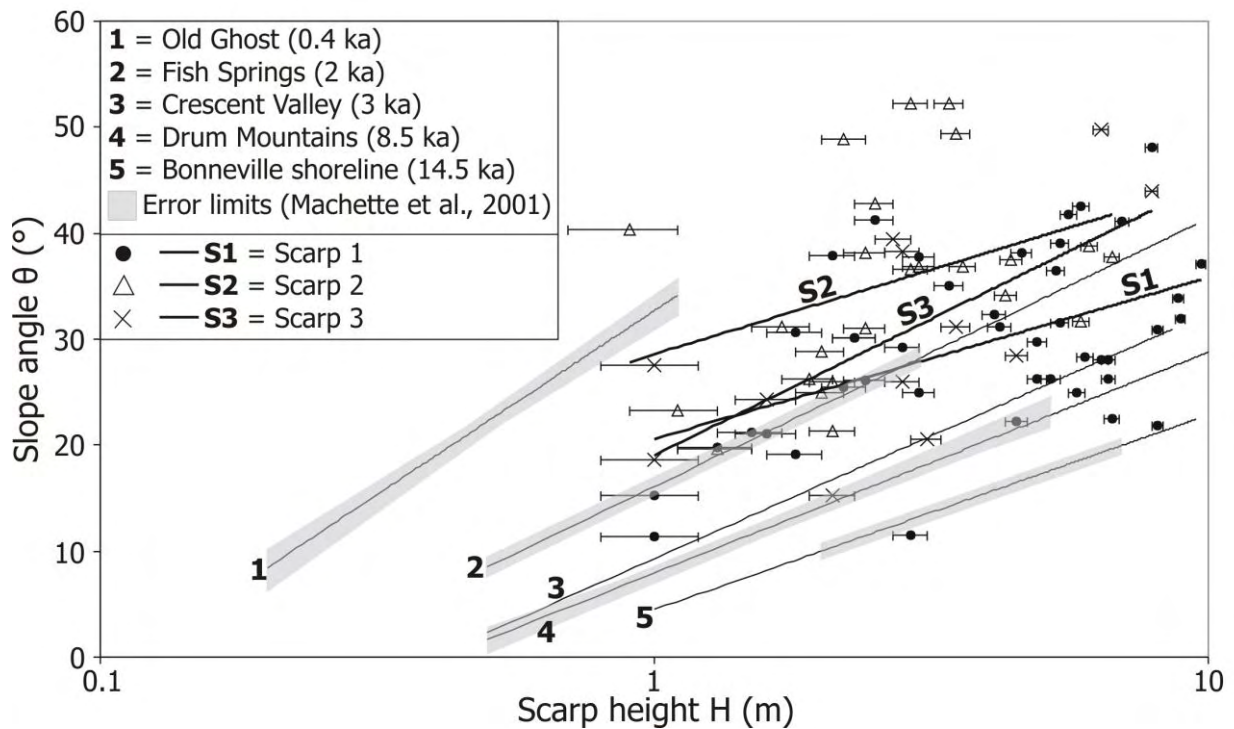
Fig. 2.14 Plot of scarp height H versus slope angle θ for the three identified fault scarps with ridge-profile data of scarps 1 and 3 from Figures 2.12A and 2.12C and ridge-crest profile data of scarp 2 from Figure 2.13 in order to determine the age of the Rex Hills scarps. The thick black lines with labels S1 for scarp 1, S2 for scarp 2, and S3 for scarp 3 are the corresponding regression lines. The thin black lines (numbered 1–5) correspond to the regression lines of previously published data (Machette et al., 2001; Friedrich et al., 2004). The error bars indicate scarp-height uncertainties.

2.7.2. Scarp Height and Slope Angle

The preservation potential of small fault scarps along a hillside cut by ridges and valleys is higher on ridge crests relative to the adjacent valleys. Our evaluation of the scarp-height versus slope-angle relationship for the three fault scarps indicates that scarps exposed in valleys are slightly more degraded than scarps exposed on ridges (Fig. 2.12). Most of the valley scarps are characterized by a lower slope angle than ridge scarps of a similar height (e.g., scarp 3, Fig. 2.12C) implying that degradation is more efficient in valleys than on ridges given that these scarps have the same age.

Carretier et al. (2002) observed that scarp morphology for cumulative reverse fault scarps along the Gurvan Bogd fault system, which is similar to the Rex Hills setting, is controlled by slope erosion and the internal structure (e.g., folding, Fig. 2.15A). The dip of faulted beds may therefore have an impact on scarp-degradation processes, although, as noted above, this is very difficult to evaluate due to the general lack of bedding exposures in the study area. The variations in scarp morphology between valleys and ridges, on the other hand, suggests that slope erosion plays an important, possibly dominant, role in controlling the scarp morphology along the southern Rex Hills slope, which consists of poorly sorted conglomerate and shows no clear evidence of internal structures such as folds (Fig. 2.3B). We observed that scarp profiles from adjacent ridge crests and valleys are markedly different. Ridge crests preserve smaller individual scarps, whereas valleys exhibit longer wavelength, low-amplitude scarps

(Fig. 2.15B). We attribute this along-strike variation to different degradation processes acting on ridges and in valleys. On ridge crests, degradation is controlled by the local slope and height of the scarp as well as local material properties. Whereas, on valley walls and valley bottoms water flows episodically, and is concentrated in channels thereby exerting a strong effect on the erosion and redistribution of material (Fig. 2.15B). This implies that ridge crests of the Rex Hills are preferable for accurate scarp-profile analyses, and explains much of the scatter observed in scarp slope-angle–height space where valley and valley-wall profiles are included (Figs. 2.11 and 2.12).

This interpretation is further supported by a linear diffusion analysis performed for the basal fault scarp. We examined the spatial variability of the diffusivity parameter (κ) and the degradation coefficient (τ) by assuming a known age of 2 ka for this scarp (Menges et al., 2003). Both parameters are twice as much for valleys than for ridge crests implying that for the past 2 ka scarp degradation occurred at twice the rate in valleys than occurred on ridges.

Lithologic differences and slumping also induce scatter in scarp slope-angle–height space. The western part of the southern Rex Hills slope exhibits a concentration of high-angle fault scarps (slope angle >40°; area of profile numbers 55–69 in Fig. 2.8A) that plot above the average population (outlined with black thin lines in Fig. 2.12). This concentration of steep scarps may not only be due to lithology contrasts as discussed previously, the steep slope of these scarps may alternatively be inherited from a steeper paleotopography, localized slumping, or subsidence.

After we reduced the initial data set by removing points which may not represent purely diffusive degradation processes, we attempted to provide an independent estimate of the scarp ages by comparing our fault-scarp data with data compiled from other scarps formed in poorly consolidated gravel elsewhere in the Basin and Range by Machette et al. (2001) and Friedrich et al. (2004) (Fig. 2.14). In this comparison, our data plot between the 0.4 ka Old Ghost curve and the 8.5 ka Drum Mountains curve, and overlap the 2 ka Fish spring curve of Machette et al. (2001). More specifically, the scarp 1 data points generally lie on or below the 2 ka curve suggesting that it is slightly older than 2 ka, whereas the scarp 2 points plot well above the 2 ka curve suggesting a slightly younger age for this scarp. If we assume that the scarps are from the same event, then it is likely that this event has occurred around 2 ka consistent with the estimate of Menges et al. (2003). The alternative that the scarps represent different events that occurred a few hundred years apart is impossible to evaluate due to a lack of offset stratigraphic markers. However, if this was the case, it would be a possible example of earthquake clustering (e.g., Doser, 1986; Wallace, 1987).

The general evolution of the Rex Hills flower structure is consistent with the results of analogue models of restraining stepovers in strike-slip fault systems. This interpretation is mainly supported by the pronounced surface expression of the basal reverse fault related to scarp 1, and the less distinct expression of faults related to scarps 2 and 3 (Fig. 2.8). This is similar to the observed evolution of the experimental pop-up structures, which are characterized by a widening of the structure and the outward propagation of the bounding basal faults (McClay and Bonora, 2001).

2.7.3. Dextral Offsets and Displacement Rate

Cumulative dextral offsets are caused by repeated, individual seismic events, for example, along the San Andreas fault (Sieh, 1978), where numerous late Holocene dextral offsets are observed along the rupture of the 1857 earthquake. The youngest offsets reach up to 9.5 m between Cholame and Wrightwood in central and southern California, and are related to the 1857 event (Sieh, 1978), whereas older offsets represent multiple ruptures as documented by e.g., the 120 m and 380 m offset channels at Wallace Creek (Sieh and Jahns, 1984; their Fig. 1b). The drainage-offset magnitudes observed at the Rex Hills site suggest a similar scenario,

where large offsets represent multiple events while smaller offsets of a few meters or less represent the most recent event.

The surface displacement of a single earthquake recorded along multiple fault branches is often characterized by a wide range of values, e.g., along the San Andreas fault (Sieh, 1978; Hilley et al., 2001). Hence, individual measured surface displacements cannot be easily transferred into average displacement rates, and we calculated first the average displacement of a single rupture event along the Rex Hills fault segment. Dextral offset magnitudes identified in the Rex Hills LDEM vary from 7.77 m to 56.5 m (Fig. 2.9; Fig. DR3 and Table DR2). The smallest, individual dextral gully offsets of 0.75–1.5 m were measured in the field. Menges et al. (2003) observed that dextral drainage offsets range from 0.5 to ~5 m along the SFS. They related these offsets to an earthquake with an expected M_w of 7.1–7.3 and a latest Holocene age (≤2 ka) based on the surface displacement–magnitude relationship derived by Wells and Coppersmith (1994). This suggests that for a single earthquake along the SFS displacement is greater than 0.75– 1.5 m. For a 7.1–7.3 magnitude earthquake along the SFS, we calculated an average displacement of 1.5–3 m using the same approach (Wells and Coppersmith, 1994; additional detail below). We suggest that the offsets determined in the LDEM represent cumulative offsets of several earthquakes recorded by gullies older than ~2 ka.

We focused displacement-rate determinations on the four most obvious dextral offsets from the LDEM (Figs. 2.9B–2.9E). Cumulative offsets of 8.5–19 m would be the result of ~3–12 earthquakes with an average offset of 1.5–3 m for each earthquake, respectively. Due to poorly constrained evidence for an older rupture event along the SFS, Menges et al. (2003) approximated a preliminary earthquake recurrence-interval of 10 ka. Based on their data, we estimated here a recurrence-interval range of 5–15 ka containing an uncertainty bound of 50% (equal to 1 σ). Using this recurrence-interval range, the ~3–12 earthquakes correspond to a time span of ~15–180 ka. These results suggest an average displacement rate for the Rex Hills fault segment of ~0.05–1.3 mm/a during the past 15–180 ka spanning two orders of magnitude. This rate is in the same range as slip-rate estimates of 0.04 ± 0.03 mm/a for the central part of the SFS and 0.03 ± 0.02 mm/a for the northern part (Stepp et al., 2001) as well as the geodetic rate of 0.7–1.2 mm/a inferred by Wernicke et al. (2004). Furthermore, the upper bound of our displacement-rate estimate (1.3 mm/a) is roughly half of the long-term minimum, time-averaged, geologic rate determined for the Mesquite segment of the SFS (~2.3 mm/a; Guest et al., 2007). It is unclear whether our tentative displacement-rate determination is representative of the displacement rate for the entire Pahrump segment of the SFS without any additional data from this segment, and so it is difficult to evaluate its significance in context of the entire fault system.
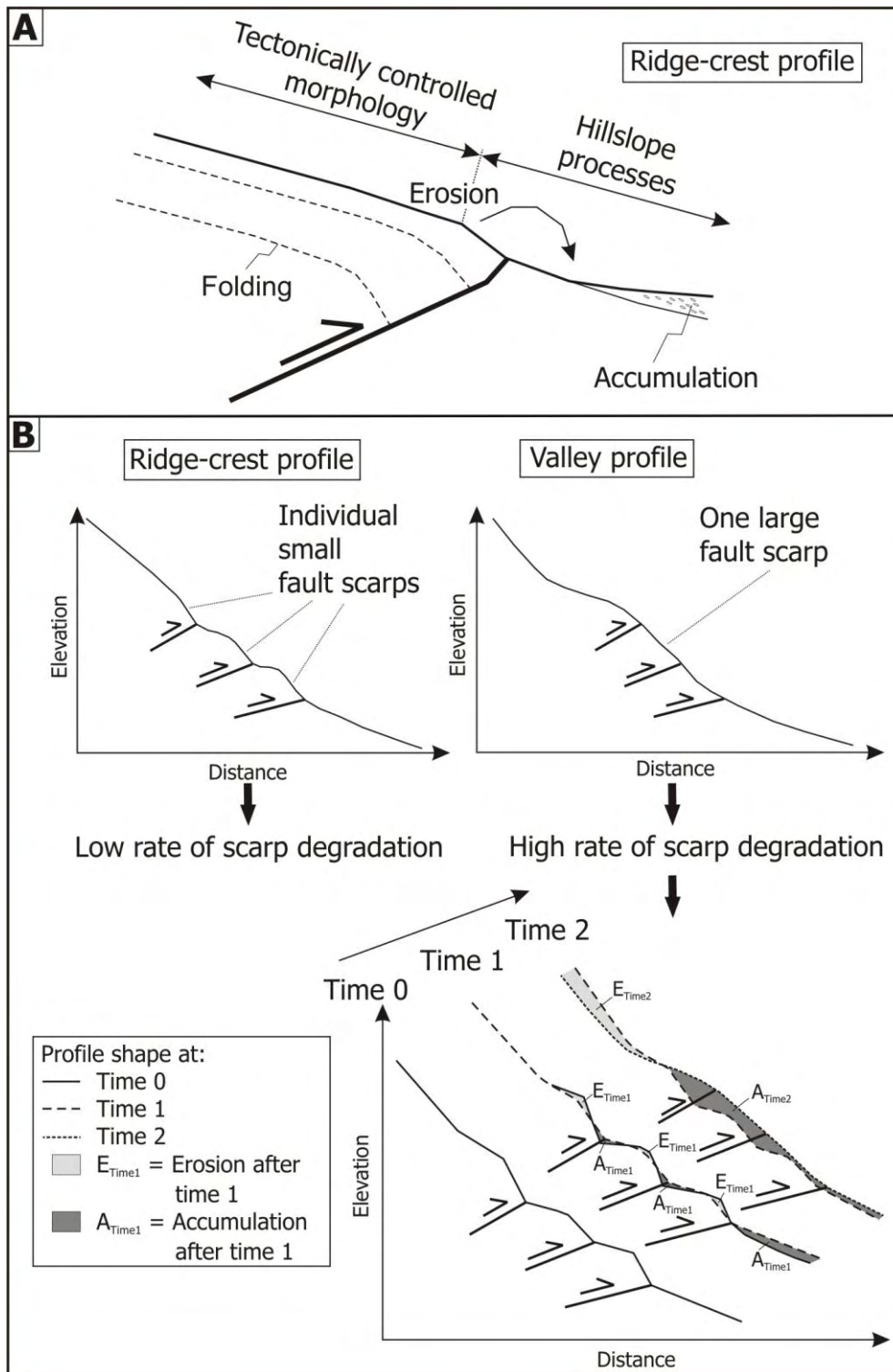
Fig. 2.15 Schematic diagrams showing degradation behaviour of closely-spaced reverse fault scarps developed on poorly consolidated conglomerate. (**A**) Scarp morphology of a reverse fault scarp is controlled by slope erosion and internal structure in terms of folding (structural setting modified after Carretier et al., 2002). (**B**) The sketch shows schematic profiles and preservation potential of individual fault scarps on ridge crests and in valleys. Degradation processes are concentrated within a valley, and therefore individual, small fault scarps merge to one large scarp with time.

2.8. Conclusions

We quantified the morphology and structure of the kilometer-scale Rex Hills flower structure by combining field mapping and high-resolution DEM analysis. The use of very high-resolution DEM data derived from a terrestrial laser-scanning campaign allowed us to conduct a detailed study of fault-scarp patterns exposed on the southern Rex Hills slope, and to ultimately attempt to distinguish different scarps in terms of apparent age.

The southern Rex Hills slope is characterized by a complex pattern of three fault scarps which are related to three individual reverse fault branches (Fig. 2.8). Two scarps show signs of segmentation (Fig. 2.8B), and we suggest that the faults may be characterized by laterally variable fault dips resulting in rupture segmentation and offset gradients as observed at the tips of the basal fault-scarp segments (Fig. 2.8B). Furthermore, fault dip, lithologic contrasts, and degradation processes appear to significantly influence the scarp morphology along the southern Rex Hills slope resulting in broad scatter and overlap in scarp-height–slope-angle space (Figs. 2.10–2.14). A key aspect of this study was to identify the source of scatter in our slope-angle–scarp-height data. With this goal in mind, we noted that the southern slope is characterized by the alternation of small-scale ridges and valleys (Fig. 2.5), and that scarp-degradation processes are likely to be higher in these valleys than on the ridges (Fig. 2.15B). By removing data obtained from the valley bottoms and valley walls, we were able to realize a significant improvement in the data distributions, and from this we suggest that the preservation potential of small, individual fault scarps is greater on ridge crests than on hillslopes and valley floors, and that ridge-crest profiles provide more accurate information about closely-spaced fault branches.

The most promising aspect of high-resolution topographic data for neotectonics is that it has the potential to allow for fault-scarp population studies. This would be possible where scarps could be assigned well constrained ages and then be grouped into event populations that represent the group of scarps associated with a particular earthquake. Based on the Rex Hills fault-scarp analysis, we can distinguish clear statistical differences between the scarps, but the implied difference in absolute age is difficult to evaluate without making fairly radical assumptions. It is clear, therefore, that for this type of analysis to be truly compelling tight geochronological constraints are required. The Rex Hills site, though well suited to the laser-scanning survey, is unfortunately not very well suited to a geochronological study (absence of well datable material), and is therefore probably not the best site for additional work on this important problem.

Lastly, and most importantly, our study reveals that high-resolution topographic analysis has the potential to significantly improve our understanding of the geometry and evolution of small-scale tectonic topography in general, and when combined with subsurface data and geochronological data, it provides a comprehensive data scheme for neotectonic studies.

2.9. References

Arrowsmith, J.R., Rhodes, D.D., and Pollard, D.D.; 1998; Morphologic dating of scarps formed by repeated slip events along the San Andreas Fault, Carrizo Plain, California; Journal of Geophysical Research, vol. 103, p. 10141–10160.

Avouac, J.-P.; 1993; Analysis of scarp profiles: Evaluation of errors in morphologic dating; Journal of Geophysical Research, vol. 98, p. 6745–6754.

Buckley, S.J., Howell, J.A., Enge, H.D., and Kurz, T.H.; 2008; Terrestrial laser scanning in geology: Data acquisition, processing and accuracy considerations; Journal of the Geological Society, London, vol. 165, p. 625–638.

Bucknam, R.C., and Anderson, R.E.; 1979; Estimation of fault-scarp ages from a scarp-height-slope-angle relationship; Geology, vol. 7, p. 11–14.

Burchfiel, B.C., Hamill, G.S., and Wilhelms, D.E.; 1983; Structural geology of the Montgomery Mountains and the northern half of the Nopah and Resting Spring ranges, Nevada and California; Geological Society of America Bulletin, vol. 94, p. 1359–1376.

Carretier, S., Ritz, J.-F., Jackson, J., and Bayasgalan, A.; 2002; Morphological dating of cumulative reverse fault scarps: examples from the Gurvan Bogd fault system, Mongolia; Geophysical Journal International, vol. 148, p. 256–277.

Cooper, J.D., Miller, R.H., and Sundberg, F.A.; 1982; Environmental stratigraphy of the lower part of the Nopah Formation (Upper Cambrian), southwestern Great Basin; *in:* Cooper, J.D., et al. (eds.); Geology of selected areas in the San Bernadino Mountains, western Mojave Desert, and southern Great Basin, California (Guidebook); Anaheim, Geological Society of America, p. 97–116.

Cowgill, E., Yin, A., Arrowsmith, J.R., Feng, W.X., and Shuanhong, Z.; 2004a; The Akato Tagh bend along the Altyn Tagh fault, northwest Tibet 1: Smoothing by vertical-axis rotation and the effect of topographic stresses on bend-flanking faults; Geological Society of America Bulletin, vol. 116, p. 1423–1442.

Cowgill, E., Arrowsmith, J.R., Yin, A., Feng, W.X., and Shuanhong, Z.; 2004b; The Akato Tagh bend along the Altyn Tagh fault, northwest Tibet 2: Active deformation and the importance of transpression and strain hardening within the Altyn Tagh system; Geological Society of America Bulletin, vol. 116, p. 1443–1464.

Crowell, J.C.; 1974; Sedimentation along the San Andreas Fault, California; *in:* Dott, R.H., and Shaver, R.H. (eds.); Modern and ancient geosynclinal sedimentation; Special Publication, Society of Economic Paleontologists and Mineralogists, vol. 19, p. 292–303.

Cunningham, W.D., and Mann, P.; 2007; Tectonics of strike-slip restraining and releasing bends; *in:* Cunningham, W.D., and Mann, P. (eds.); Tectonics of strike-slip restraining and releasing bends; Geological Society, London, Special Publications, vol. 290, p. 1–12.

Dokka, R.K., and Travis, C.J.; 1990; Role of the eastern California shear zone in accommodating Pacific-North American plate motion; Geophysical Research Letters, vol. 17, p. 1323–1326.

Dooley, T.P., and McClay, K.R.; 1996; Strike-slip deformation in the Confidence Hills, southern Death Valley fault zone, eastern California, USA; Journal of the Geological Society, London, vol. 153, p. 375–387.

Doser, D.; 1986; Earthquake processes in the Rainbow Mountain–Fairview Peak–Dixie Valley, Nevada region 1954–1959; Journal of Geophysical Research, vol. 91, p.12572–12586.

Friedrich, A.M., Wernicke, B., Niemi, N.A., Bennett, R.A., and Davis, J.L.; 2003; Comparison of geodetic and geologic data from the Wasatch region, Utah, and implications for the spectral character of earth deformation at periods of 10 to 10 million years; Journal of Geophysical Research, vol. 108, doi: 10.1029/2001JB000682.

Friedrich, A.M., Lee, J., Wernicke, B.P., and Sieh, K.; 2004; Geologic context of geodetic data across a Basin and Range normal fault, Crescent Valley, Nevada; Tectonics, vol. 23, TC2015, doi: 10.1029/2003TC001528.

Guest, B., Niemi, N.A., and Wernicke, B.P.; 2007; Stateline fault system: A new component of the Miocene-Quaternary Eastern California shear zone; Geological Society of America Bulletin, vol. 119, p. 1337–1347.

Hanks, T.C., Bucknam, R.C., Lajoie, K.R., and Wallace, R.E.; 1984; Modification of wave-cut and faulting-controlled landforms; Journal of Geophysical Research, vol. 89, p. 5771–5790.

Harding, T.P.; 1985; Seismic characteristics and identification of negative flower structures, positive flower structures, and positive structural inversion; American Association of Petroleum Geologists Bulletin, vol. 69, p. 582–600.

Hill, E.M., and Blewitt, G.; 2006; Testing for fault activity at Yucca Mountain, Nevada, using independent GPS results from the BARGEN network; Geophysical Research Letters, vol. 33, L14302, doi: 10.1029/2006GL026140.

Hilley, G.E., Arrowsmith, J.R., and Stone, E.; 2001; Inferring segment strength contrasts and boundaries along low-friction faults using surface offset data, with an example from the Cholame-Carrizo segment boundary along the San Andreas Fault, Southern California; Bulletin of the Seismological Society of America, vol. 91, p. 427–440.

Landgraf, A., Ballato, P., Strecker, M.R. Friedrich, A., Tabatabaeiand, S.H., and Shahpasandzadeh, M.; 2009; Fault-kinematic and geomorphic observations along the North Tehran Thrust and Mosha Fasham Fault, Alborz mountains Iran: implications for fault-system evolution and interaction in a changing tectonic regime; Geophysical Journal International, vol. 177, doi: 10.1111/j.1365-246X.2009.04089.x.

Machette, M.N., Menges, C., Slate, J., Crone, A.J., Klinger, R.E., Piety, L.A., Sarna-Wojcicki, A.M., and Thompson, R.A.; 2001; Field trip guide for day B, Furnace Creek area; *in:* Machette, M.N., Johnson, M.L., and Slate, J.L. (eds.); Quaternary and Late Pliocene geology of the Death Valley region: Recent observations on tectonics, stratigraphy, and lake cycles, Pacific cell – Friends of the Pleistocene field trip, February 17-19, 2001; U.S. Geological Survey, Open file report 01-51.

McClay, K.R., and Dooley, T.P.; 1995; Analogue models of pull-apart basins; Geology, vol. 23, p. 711–714.

McClay, K.R., and Bonora, M.; 2001; Analog models of restraining stepovers in strike-slip fault systems; American Association of Petroleum Geologists Bulletin, vol. 85, p. 233–260.

Menges, C.M., Fridrich, C., Blakely, R.J., and Thompson, R.; 2003; Late Quaternary surface rupture and associated transpressive uplift on a section of the State Line Fault in the south-central Amargosa Desert

basin, southwestern Nevada; Eos, Transactions of the American Geophysical Union, vol. 84, Fall Meeting Supplement, Abstract S11D-0327.

Nash, D.B.; 1980; Morphologic dating of degraded normal fault scarps; Journal of Geology, vol. 88; p. 353–360.

Naylor, M.A., Mandl, G., and Sijpesteijn, C.H.K.; 1986; Fault geometries in basement-induced wrench faulting under different initial stress states; Journal of Structural Geology, vol. 8, p. 737–752.

Nivière, B., Marquis, G., and Maurin, J.-C.; 1998; Morphologic dating of slowly evolving scarps using a diffusive analogue; Geophysical Research Letters, vol. 25, p. 2325–2328.

Poole, F.G., and Sandberg, C.A.; 1977; Mississippian paleogeography and tectonics of the western United States; *in:* Stewart, J.H., et al. (eds.); Pacific Coast Paleogeography Symposium 1, Paleozoic paleogeography of the western United States; Bakersfield, California, p. 67–85.

Schweickert, R.A., and Lahren, M.M.; 1997; Strike-slip fault system in Amargosa Valley and Yucca Mountain, Nevada; Tectonophysics, vol. 272, p. 25–41.

Sieh, K.E.; 1978; Slip along the San Andreas fault associated with the great 1857 earthquake; Bulletin of the Seismological Society of America, vol. 68, p. 1421–1448.

Sieh, K.E., and Jahns R.H.; 1984; Holocene activity of the San Andreas fault at Wallace Creek, California; Geological Society of America Bulletin, vol. 95, p. 883–896.

Stepp, J.C., Wong, I., Whitney, J., Quittmeyer, R., Abrahamson, N., Toro, G., Youngs, R., Coppersmith, K. Savy, J., Sullivan, T., and Yucca mountain PSHA Project Members; 2001; Probabilisitic seismic hazard analyses for ground motions and fault displacement at Yucca Mountain, Nevada; Earthquake Spectra, vol. 17, p. 113–151.

Stevens, C.H.; 1991; Paleogeographic and structural significance of an upper Mississippian facies boundary in southern Nevada and east-central California; Geological Society of America Bulletin, vol. 103, p. 876–885.

Stewart, J.H.; 1980; Geology of Nevada; Nevada Bureau of Mines and Geology Special Publication, vol. 4, p. 1–136.

Sylvester, A.G., and Smith, R.R.; 1976; Tectonic transpression and basement-controlled deformation in San Andreas fault zone, Salton Trough, California; American Association of Petroleum Geologists Bulletin, vol. 60, p. 2081–2102.

Sylvester, A.G.; 1988; Strike-slip faults; Geological Society of America Bulletin, vol. 100, p. 1666–1703.

van der Pluijm, B.A., and Marshak, S.; 2004; Earth structure – An introduction to structural geology and tectonics; W.W. Norton & Company, 656 pp.

Wakabayashi, J., Hengesh, J.V., and Sawyer, T.L.; 2004; Four-dimensional transform fault processes: Progressive evolution of step-overs and bends; Tectonophysics, vol. 392, p. 279–301.

Walker, J.D., Burchfiel, B.C., and Davis, G.A.; 1995; New age controls on initiation and timing of foreland belt thrusting in the Clark Mountains; Geological Society of America Bulletin, vol. 107, p. 742–750.

Wallace, R.E.; 1977; Profiles and ages of young fault scarps, north-central Nevada; Geological Society of America Bulletin, vol. 88, p. 1267–1281.

Wallace, R.E.; 1987; Grouping and migration of surface faulting and variations in slip rates on faults in the Great Basin province; Bulletin of the Seismological Society of America, vol. 77, p. 868–876.

Wells, D.L., and Coppersmith, K.J.; 1994; New empirical relationships among magnitude, rupture length, rupture width, rupture area, and surface displacement; Bulletin of the Seismological Society of America, vol. 84, p. 974–1002.

Wernicke, B.P., Davis, J.L., Bennett, R.A., Normandeau, J.E., Friedrich, A.M., and Niemi, N. A.; 2004; Tectonic implications of a dense continuous GPS velocity field at Yucca Mountain, Nevada; Journal of Geophysical Research, vol. 109, B12404, doi: 10.1029/2003JB002832.

Wesnousky, S.G.; 2005; Active faulting in the Walker Lane; Tectonics, vol. 24, TC3009, doi: 10.1029/2004TC001645.

Wilcox, R.E., Harding, T.P., and Seely, D.R.; 1973; Basic wrench tectonics: American Association of Petroleum Geologists Bulletin, vol. 57, p. 74–96.

Yeats, R.S., Sieh, K.E., and Allen, C.R.; 1997; The geology of earthquakes; Oxford University Press, New York, 576 pp.

3. Chapter II

Short-Term Sediment Transport in Context of Post-Glacial Landscape Evolution: Insights from Field Mapping and High-Resolution LiDAR Measurements, Alp Valley, Switzerland

3.1. Abstract

A mountain belt is a topographic composite of erosional and depositional landforms. Such landforms contain detailed information about a particular process that can be used to decode the evolution of a mountainous landscape. In the Alps, geomorphic mapping based on recently available high-resolution topographic data allowed to evaluate the long-term landscape response to deglaciation following the last glacial maximum (LGM), when the Alpine land surface was exposed to the atmosphere for thousands of years. In contrast, even small mountainous streams are capable to transport substantial amounts of material within a short time, e.g., during heavy thunderstorms. Morphologic changes that occurred during large, rare floods and their long-term effects on a landscape are often documented and discussed, but changes due to more frequent, smaller floods are rarely considered. This is mainly due to the great variability of short-term sediment transport, and a lack of appropriate topographic data from which such changes can be quantified. Repeated terrestrial laser-scanning surveys provide the unique opportunity to monitor even shortest-term (days to years) fluctuations in sediment transport, erosion and storage, and to quantify its variability. The new challenge is to derive information that can be related to the long-term evolution of a mountainous landscape. In this study, we evaluated the context between short-term sediment transport and the post-glacial evolution of the Alp Valley in central Switzerland. We combined detailed mapping of erosion and sedimentation patterns in this valley to place constraints on its Holocene evolution using a high-resolution (2 m) digital elevation model, and repeated high-resolution (<1 cm locally) laser-scanning campaigns conducted along two tributaries, the Erlenbach and Vogelbach, to monitor channel-morphology changes and the nature of shortest-term sediment transport. Our results revealed that short-term sediment transport is enhanced when a channel bed, such as that of the Erlenbach, formed on a dip-slope, in contrast to a channel, such as that of the Vogelbach, which is cut into a non-dip-slope mountainous flank. The sediment flux through the former type of channel is transport-limited, because dip-slopes often promote massive landsliding. This explains the transport-limited flux of material in the Erlenbach, which is indeed incised into an unconsolidated landslide deposit. In contrast, the sediment flux through the latter type of channel is supply-limited, because such landslides usually do not occur on non-dip-slopes. This explains the supply-limited sediment flux in the Vogelbach which incises into bedrock. Moreover, the increased short-term sediment transport in the Erlenbach compared to the Vogelbach confirms the hypothesis that bedrock channels are more stable than gravel-bed channels. The latter may effectively prevent bedrock erosion up to a few thousand years, e.g., ~2 ka in case of the Erlenbach. This approximation is based on the transport length of single decimeter- to meter-sized boulders and the recurrence interval of floods with varying magnitude, as well as our observations that a ~5-m-sized boulder exhibited no transport during those floods obvious from a dense vegetation cover on top of the boulder and that the landslide deposit is up to several tens of meters thick. Hence, we suggest that the buffering effect has prevailed throughout the Holocene equal to a time-scale of ten thousand years. Finally, the change from glacially influenced erosion and deposition in the

Alp Valley to the recent pattern dominated by mass wasting and fluvial processes occurred progressively after the LGM. It started in the north and propagated to the south in direction of glacier retreat based on two facts: (i) fluvial gravel cover a ground-moraine deposit in the north, and late-Würmian lateral and terminal moraines occur only in the south; and (ii) these moraines – located at the base of the Mythen rock cliffs – form an effective sediment trap for rock-fall debris derived from these cliffs.

3.2. Introduction

Mountain belts are composite landscapes with inherited topographic signatures (e.g., Alborz mountains; Landgraf et al., 2009) that can be used to decipher their evolution. In mountainous terrain, erosional and depositional landforms, such as head scarps of landslides or glacial moraines, are the type of geomorphic signal from which very detailed information about a specific process can be extracted to reconstruct spatiotemporal erosion and sedimentation patterns (e.g., Schlunegger et al., 2002; Allen, 2008). In the Alps, for example, repeated glaciations during the Pleistocene and glacial advances of the younger past – e.g., Little Ice Age, 16th–19th century – had been identified based on the occurrence of terminal moraines (e.g., Penck and Brückner, 1909). However, recently available high-resolution topographic data sets provide the unique opportunity to derive such detailed information, and had been efficiently utilized, e.g., to investigate the post-glacial sedimentation pattern in a central Alpine valley (Otto et al., 2009).

During the last (Würmian) glaciation, most areas of the Alpine land surface had been covered with ice for several thousand years (e.g., Kelly et al., 2004). During glacial retreat, this land surface was exposed quite rapidly to atmospheric conditions within thousands of years. According to Ballantyne (2002), the Alpine landscape was prone to a rapid change, which also incorporated a change of the dominating erosion processes – from glacial- to fluvial-dominated (e.g., Church and Ryder, 1972). In the Alps, the response to this change had often been investigated on a long-term scale of thousands of years based on Alpine and local sediment-budget studies, the analysis of topographic data etc. (e.g., Müller, 1999; Hinderer, 2001; Schlunegger et al., 2002; Norton et al., 2008).

In mountainous areas, however, even small streams are capable to transport large amounts of material during a short time, e.g., following heavy precipitation (e.g., Wolman and Miller, 1960). The cumulative effect of several of such short-term erosion events for the long-term sediment flux from a drainage basin is only rarely considered because there seems to be a limit due to the high variability in sediment transport on short time-scales (days – years – centuries). In contrast, from previous comparisons of short- and long-term erosion measurements (e.g., Kirchner et al., 2001) as well as from the evaluation of magnitude-frequency flood distributions (e.g., Molnar, 2001; Molnar et al., 2006) it became obvious that the size and frequency of large events is particularly relevant in this context. However, landscape changes that occurred during such large floods are most frequently documented, e.g., changes along longitudinal river profiles (Molnar et al., 2008), but there is a lack of data from which morphologic changes in channel beds can be quantified when more frequent floods had occurred.

Terrestrial laser scanning has recently developed into an effective tool in geomorphology to monitor even shortest-term fluctuations in sediment transport and storage (e.g., Heritage and Hetherington, 2007; Entwistle and Fuller, 2009). The new challenge is to quantify the variability of short-term erosion, transport, and sedimentation, and to extract information that can be compared to longer-term measurements. For this purpose, repeated measurements can be used for precise monitoring of episodic sediment transport, because a laser-scanner survey can rapidly (within minutes) acquire large amounts of topographic data with both a high resolution (up to a few cm) and high accuracy (of only a few mm; e.g., Buckley et al., 2008).

By comparing such topographic data of the same area but from different acquisition dates, it should be possible to constrain vertical surface changes, which can be the type of parameter that can be compared to longer-term measurements.

One of the best study sites in the Alps to evaluate the context between short-term sediment transport and post-glacial landscape evolution is the Alp Valley in central Switzerland (Fig. 3.1A). This is because the valley was covered by glaciers during the Würmian glaciation (e.g., Hantke, 1967 and 1970), and recent monitoring of hydrology and sediment transport is carried out by the Swiss Federal Institute for Forest, Snow and Landscape Research (WSL) that established several monitoring sites since the late 1960s (e.g., Burch, 1994). Here, we first present results of a detailed geomorphic-geologic mapping campaign to constrain post-glacial landscape evolution and current erosion and sedimentation patterns in the Alp Valley (Plate I [see footnote 2]). Our mapping is based on a LiDAR (Light Detection And Ranging) derived digital elevation model (DEM; horizontal resolution 2 m, vertical resolution 1 m). Next, we present results of repeated photographic and ground-based LiDAR surveys that we conducted along two mountainous gravel-bed dominated channel beds – the Erlenbach and Vogelbach (Fig. 3.1B; Plate I). Our approach is supplemented by the independent monitoring of the WSL. Lastly, we compared historical documents and combined it with a literature search focused on the historic development of this area to investigate landscape evolution over a few hundred years.

Fig. 3.1 (A) Shaded relief map of the Western Alps showing the location of the Alp Valley (Fig. 3.1B; modified after Willett et al.; 2006). Abbreviations: PF – Periadriatic fault, JF – Jura front, HF – Helvetic front, and PT – Penninic thrust.. **(B)** Geologic map and profile of the Alp Valley area modified after Winkler et al. (1985). We outlined the mapping areas of the Alp Valley (Plate I), Erlenbach basin (Fig. 3.2), and Vogelbach basin (Fig. 3.8) accordingly. Black tick marks with annotated numbers depict Swiss coordinates in km, and gray tick marks with annotated numbers depict northern latitude and eastern longitude.

Plate I New detailed geomorphic map of the Alp Valley. The location of the Vogelbach and Erlenbach basins is indicated with according text boxes. Tick marks with thick annotated numbers depict Swiss coordinates in km, and tick marks with thin annotated numbers depict northern latitude and eastern longitude. The map is contained in the envelope attached at the inside of the back-cover [see footnote 2].

---

[2] Plate I is contained in the envelope attached at the inside of the back-cover.

A

JF

N

Jura Mountains

Molasse

Fig. 3.1B

basin

HF

PT

PF

Po basin

Marseille

Major Alpine faults

Alpine crystalline massifs

100 km

48°N

46°N

44°N

4°E   6°E   8°E   10°E

B

695   700

N

2 km

Einsiedeln

Lake Sihl

220

Plate I

Alp river

a

Fig. 3.8

A

215

Alpthal

Fig. 3.2

a'

b

KM

GM

R

210

MG

S

b'

47°06'

47°04'

47°02'

47°00'

8°42'   8°46'

Legend

Subalpine Molasse

Habkern melange (Wild Flysch)

Schlieren Flysch

Wägital Flysch (Tertiary)

Wägital Flysch (Cretaceous)

Wild Flysch of the Rothenflue

Sub-Helvetic imbrications

Helvetic nappes

Penninic cliffs

Upper Austroalpine and Iberg ophiolite nappe

Thrust fault

Abbreviations

A - Amselspitz
GM - Grosser Mythen
KM - Kleiner Mythen
MG - Mördergruebli
R - Rotenflue
S - Schijen

a   a' b   b'

A   S   1500 m

?   ?   ?   ?   500 m

67

3.3. Study Area – Background

The Alp Valley is located in the northern Swiss Prealps, south of the town of Einsiedeln (Fig. 3.1). The Alp River drains the valley northward. Our two study sites are the small tributary basins of the Erlenbach and Vogelbach. The former is located on the eastern flank of the upper Alp Valley, and the latter on the western flank of the central valley (Fig. 3.1B). We first describe the general geologic-geomorphic setting of the Alp Valley, and continue with detailed descriptions of the Erlenbach and Vogelbach basins including known aspects about geology, channel morphology, sediment transport, hydrology, and vegetation.

3.3.1. Alp Valley

Geological Setting

The Alp Valley is cut into Alpine thrust sheets that are composed of sedimentary rocks (Fig. 3.1B). On one hand, these rocks comprise resistant rocks such as massive conglomerate and limestone, and on the other hand less resistant rocks such as sandstone, marl and shale. According to Kühni and Pfiffner (2001), the Alp Valley is located at the border between rocks of high erodibility to the north and medium erodibility to the south.

In the north, the Helvetic frontal thrust forms the contact between the subalpine Molasse to the north and the Cretaceous Wägital Flysch to the south (Fig. 3.1). The Oligocene to Miocene Molasse consists of massive conglomerate, the Nagelfluh, and sandstone (Plate I [see footnote 2]; e.g., Ringholz, 1904). The Wägital Flysch belongs to the Ultrahelvetic-Penninic Flysch series exposed in the central and southern Alp Valley, which further comprise the Habkern and Schlieren Flysch (Fig. 3.1B; Hantke, 1967). These Flysch series are distinguished by their tectonic position where the Schlieren Flysch represents the eastern-most appearance and the Wägital Flysch the western-most (Stammbach, 1988). Both, the Ultrahelvetic-Penninic Flysch series and Molasse units are characterized by a high erodibility (Kühni and Pfiffner, 2001).

The Habkern Flysch consists of beige limestone, green shale and gray marl (Stammbach, 1988), and is only locally exposed in the southeastern Alp Valley and east of Amselspitz (Fig. 3.1B; Plate I). The Schlieren Flysch mainly consists of brownish marl, green shale, calcareous sandstone, and calcarenite (Hantke, 1967), and is exposed over a wide area of the southeastern-most Alp Valley (Fig. 3.1B; Plate I). The Wägital Flysch is exposed in the central Alp Valley (Fig. 3.1B; Plate I). It is composed of two fractions: the Cretaceous fraction comprising irregular bedded brecciated sandstone and silty marl, as well as irregularly bedded calcarenite with silty marly shale; and the Eocene fraction consisting of marl and marly shale, silty to sandy shale, and calcareous sandstone (Winkler et al., 1985).

The southern Alp Valley is marked by the prominent Penninic cliffs of the Grosser and Kleiner Mythen (Fig. 3.1B; Plate I). These rocky cliffs mainly consist of massive dolostone and red limestone of Triassic to Cretaceous age (Ringholz, 1904). They are characterized by a medium erodibility, the resistance of a lithology against incision by rivers/glaciers and mass wasting by slope processes (Kühni and Pfiffner, 2001; erodibility map based on geotechnical map of Switzerland), and were thrust over Helvetic and Ultrahelvetic-Penninic Flysch units (Fig. 3.1B). The Helvetic units are part of the so-called Einsiedler Schuppenzone (e.g., Kuhn, 1972), and comprise Nummulite beds, which consist of sandstone and limestone, and the Amdener beds, which consist of marl (Plate I; e.g., Ringholz, 1904; Stammbach, 1988).

Quaternary Deposits

Lateral and terminal as well as ground moraines formed below the base of the Mythen mountain peaks in the south (Plate I). These moraines formed during late stages of the Würmian glaciation – the Chindli and Nasen stages (Hantke, 1967 and 1970). Furthermore, a Würmian-aged terrace deposit formed in the north (Plate I; Hantke, 1967). Two post-glacial landslide deposits occur along the eastern flank of the Alp Valley: one of them is located in the area of the Erlenbach in the south, and another one is located ~2 km farther north (Plate I).

Valley Morphology

The geomorphology of the Alp Valley floor varies markedly between the north and south. While the appearance of the northern valley floor is dominated by the flat surface of the Würmian-aged gravel terrace that is bounded by a steep and up to more than 10 m high escarpment, several alluvial fans occur in the southern valley (Plate I).

Wide areas of the Alp Valley flanks, especially in the central and southern area, are subject to sliding processes and exhibit a typical hummocky topography (Plate I; e.g., Hantke, 1967). Most of the small tributary streams incise unconsolidated sliding material – e.g., Erlenbach, one of our sub-study sites – whereas bedrock is mainly exposed along channel beds – e.g., Vogelbach, the other sub-study site – and at local rock cliffs (Plate I). However, rock cliffs such as the Mythen mountain peaks are characterized by steep slopes (angles up to more than 85°), whereas the post-glacial landslide deposits or alluvial fans exhibit much gentler slopes with angles that typically range between 5° and 25° (Fig. 6.2-1).

3.3.2. Erlenbach

The Erlenbach is a small tributary located on the eastern Alp Valley flank in the south (Figs. 3.1 and 3.2; Plate I). The catchment covers an area of 0.74 km² with a mean channel slope of 18% (~10°), and a catchment altitude of 1110–1655 m (Table 3.1; e.g., Burch, 1994; Schuerch et al., 2006). The lower two-thirds of the Erlenbach basin are developed on a large landslide that mainly consists of late Cretaceous to middle Eocene Wägital Flysch (Fig. 3.2; Plate I; e.g., Rickenmann & McArdell, 2007). The Flysch is composed of mudstone and calcareous sandstone (Winkler et al., 1985), and covered by a gleyic soil of very low permeability (Rickenmann and Dupasquier, 1994; Yager, 2006). Weathering of this material results in silty sand with clay, gravel, and sparse boulders of up to 2 m in diameter (Schuerch, 2005).

Intact Eocene Flysch bedrock consists mainly of mudstone, and is exposed only along the upper Erlenbach channel (Fig. 3.2; Schuerch et al. 2006). Furthermore, the Helvetic Amdener beds are exposed in the uppermost catchment, where a thrust fault defines the contact to the Eocene Wägital Flysch (Fig. 3.2; Plate I; e.g., Hantke 1967; Stammbach, 1988).

The Erlenbach channel bed, especially the well studied lowermost ~530 m of the channel, is characterized by a step-pool to cascade morphology (Hegg and Rickenmann, 1998) where steps are formed by woody debris and boulders of 0.5–2.5 m in diameter with a highly variable horizontal step-spacing of 10–50 m (e.g., Rickenmann and Dupasquier, 1995; Schuerch et al., 2006). Apart from these large, relatively immobile boulders, mostly sandstone, the channel bed is further composed of intervening finer and more mobile sediment patches (Yager, 2006). The average grain-size distribution of the surface-bed material is characterized by d_{90} = 350 mm, d_{50} = 75 mm, and d_{30} = 18 mm (Hegg and Rickenmann, 1998). The characteristic grain sizes of transported material range from 125–140 mm for d_{90} to 20–40 mm for d_{50} (Ziltener, 2007).

Small slides occur on the hill-slopes adjacent to the Erlenbach channel (Fig. 3.2), and deliver episodically large amounts of poorly sorted sediment to the channel (Schuerch et al., 2006). Along the lowermost ~530 m of the channel, the southern channel bank exhibits a series of active slides, whereas slides are far less frequent on the northern bank (Schuerch, 2005). The head scarps of these slides are usually 1–2 m high, and they do not affect bedrock. Furthermore, the slides frequently appear to move as multiple blocks with different velocities, and vegetation patches on the slide masses are separated by bare sub-soil (Schuerch et al., 2006).

The Erlenbach basin is characterized by a mean annual precipitation of 2300 mm (Table 3.1; e.g., Rickenmann, 1997). High intensity storms occur frequently in the summer, whereas from November to April the precipitation usually consists of snow summing up to 30–40% of the annual precipitation (e.g., Hegg and Rickenmann, 1998). The Erlenbach exhibits a mean annual stream flow of 1850 mm (Table 3.1; Rickenmann, 1997). Increased water discharge in winter and spring is either due to snow-melt, or rain-on-snow events (Schuerch et al., 2006). High water discharges in summer are caused by frequent, high-intensity storms resulting in sharp rises to peaks of short duration (e.g., Rickenmann and McArdell, 2007). This rapid runoff response to rainfall with extreme flood peaks is mainly due to the low infiltration capacity of the shallow loamy soils (Rickenmann, 1997; Molnar et al., 2008).

On average more than 20 bed-load transport events occur each year in the Erlenbach (Rickenmann and Fritschi, 2010), and between 1986 and 1989 the average annual suspended sediment yield was 1225 t/km² a (Table 3.1; Keller and Weibel, 1991). During the largest recorded flood (20th June 2007) with a peak water-discharge of 16 m³/s, a bulk sediment volume of 1650 m³ had been transported (e.g., Turowski et al., 2009). Grains of step-forming size (>0.5 m in diameter) and woody debris had been deposited in the sediment retention basin (Molnar et al., 2008). For comparison, the second largest flood (25th July 1984) with a maximum water-discharge of 12 m³/s transported a total sediment volume of 2000 m³ with boulders of 1 m in diameter (Rickenmann, 1997). However, the June 2007 event yielded a complex reorganization of the channel bed and its step-pool morphology (Molnar et al., 2010). Prior to this flood, from 1993 to 2004, aggradation of up to ~2.5 m occurred in two broad zones along the lowermost ~530 m of the channel bed that coincide with the location of major landslides and high channel slopes (Schuerch et al., 2006). In contrast, during the flood in 2007, erosion of up to ~3 m and the formation of new steps mainly occurred in these broad zones where the major landslides are located (Molnar et al., 2010).

Lastly, the Erlenbach basin is covered by 40% coniferous forest and 60% wetlands with grass and shrubs (Table 3.1; Hegg and Rickenmann, 1998). Where toppled coniferous trees lie on the ground, newly growing vegetation consists of alder and shrubs (Schuerch, 2005). During the 20th century, systematic logging took place within the catchment, but was stopped within the last 20 years.

3.3.3. Vogelbach

The Vogelbach is a small tributary located on the western flank of the central Alp Valley with a catchment elevation of 1000–1500m, a drainage area of 1.56 km², and a channel slope of 10–30% (~6–17°; Milzow et al., 2006; Figs. 3.1 and 3.8; Plate I). It incises into calcareous sandstone, argillite and bentonite schist – Cretaceous Wägital Flysch (Fig. 3.8). Following Hantke (1967), the trunk channel of the Vogelbach trends parallel to a thrust fault that deformed the Wägital Flysch internally (Plate I).

The Vogelbach channel bed is dominated by a step-pool morphology, and a heterogeneous sediment mixture ranging in grain size from gravel to boulders, including a few small and discontinuously-weathered bedrock outcrops (e.g., Fig. 3.9; Milzow et al., 2006). The hill-

slopes of the Vogelbach basin are covered by a clay-rich soil with low infiltration rate (Milzow et al., 2006).

The Vogelbach catchment exhibits a mean annual precipitation of 2050 mm, 30–40% as snow, which is similar to that of the Erlenbach basin (Table 3.1; e.g., Keller and Weibel, 1991). The Vogelbach shows a fast runoff response to precipitation due to low infiltration, steep slopes and a well-developed channel network (Milzow et al., 2006). Furthermore, large floods occur after high intensity storms especially when precipitation coincides with the snow melt. In general, the Vogelbach is characterized by a low flow stage in winter and a higher flow stage during snow-melt season and in the summer. The highest water discharge had been recorded during the summers of 1995 and 1998 (6.4 m³/s; Milzow et al., 2006). For comparison, the peak water-discharge during the flood from 20th June 2007 was ~4.3 m³/s (J. Turowski, pers. comm., 2008). The mean annual suspended-sediment yield between 1986 and 1989 was 725 t/km² a (Table 3.1; Keller and Weibel, 1991). Lastly, the Vogelbach basin is covered by 65% forest as well as 35% meadows and pastures (Table 3.1).

Table 3.1: Characteristics of the Erlenbach and Vogelbach basins.

Catchment parameter	Erlenbach	Vogelbach
Area (km²)	0.74	1.56
Mean elevation (m)	1350	1365
Mean slope (°)	~10°	6–17°
Forest cover (%)	40	65
Wetland & grassland (%)	60	35
Mean annual precipitation (mm)	2300	2050
Mean annual stream flow (mm)	1850	1460
Mean suspended-load 1986–1989 (t/km² a)	1225	725

Compiled from Keller and Weibel (1991), Milzow et al. (2006), and Rickenmann and McArdell (2007).

3.4. Methods and Data

We combined detailed geomorphic mapping in the Alp Valley with the analysis of high-resolution laser-scanner measurements from the Erlenbach and Vogelbach channels to better integrate observations on sediment transport of a few days to a few years in length into the post-glacial evolution of the valley over the last couple of thousand years. We supplemented this approach by considering the historical record of the Alp Valley area that allowed us to qualitatively examine its landscape evolution over a few hundred years.

3.4.1. Mapping and Photo Documentation

We carried out detailed geomorphological and geological field mapping in the Alp Valley and the two tributary basins of the Erlenbach and Vogelbach at a scale of 1:10.000 (Figs. 3.2 and 3.8; Plate I). Our mapping is based on a LiDAR derived DEM with a horizontal resolution of 2 m and vertical resolution of 1 m (provided by WSL, 2006). Previously derived, published maps of the Alp Valley lack either structural and geomorphic detail (Fig. 3.1B; e.g., Hantke, 1967; Winkler et al., 1985), or cover only parts of the Alp Valley (e.g., Stammbach, 1988). However, the high resolution of the DEM allows to bridge this gap, because it enabled us to map the entire valley at a consistent level of detail, and we combined geomorphic and geologic structures in one map (Plate I). Thus, we mapped the morphology of the Alp Valley floor and its hill-slopes in coherent, unprecedented detail, previously only available for the Erlenbach area in the south (Fig. Plate I; Stammbach, 1988). We also added structural detail, such as bedding orientation, and reconstructed the orientation of local fold axes (Figs. 3.2 and

3.8; Plate I) in order to better evaluate potential causes of differences in erosion and deposition patterns across the Alp Valley. Furthermore, we conducted photographic surveys along the trunk streams of the Erlenbach and Vogelbach to better document the nature of short-term sediment transport (e.g., grain-sizes of transported material), and to evaluate channel-morphology changes (Figs. 3.3 and 3.9).

3.4.2. Historical Record

To describe the landscape evolution in the Alp Valley region over a scale of a few hundred years, we analyzed a number of historical documents, including paintings, photographs, and other illustrations (Figs. 3.14, 6.2-6 and 6.2-7) as well as literature on the historic development of this area (e.g., Saurer, 2002). These historical documents, largely from the area of the Benedictine monastery of Einsiedeln founded in 934 AD (Eberle, 1984), provide a long-term basis to evaluate landscape evolution over the last ~500 a. So far, this approach is rarely considered in geomorphologic studies as pointed out by Rees (1973).

3.4.3. Laser-Scanner Surveys

We conducted several laser-scanning campaigns along the lowermost reaches of the Erlenbach and Vogelbach to determine short-term channel-bed changes and sediment transport (Figs. 3.2 and 3.8; Plate I). We used two terrestrial medium-range scanners: the *Leica ScanStation*® in 2008, and *TOPCON GLS-1000*® in 2009. Both scanners measure across distances of a few hundred meters. We scanned with a resolution of 3 cm (*Leica ScanStation*®) and 1 cm (*TOPCON GLS-1000*®) at a distance of 30 m to gain a high point density across the focus site. A calibration of the two scanners yielded no significant differences.

Field work with both laser scanners followed the same principle (e.g., Heritage and Hetherington, 2007; Buckley et al., 2008; Baran et al., 2010). The scanner is mounted on a tripod at successive positions, and the area of interest is mapped by scans with variable overlap. Along the Erlenbach and Vogelbach channel beds, the scanner was set up at four different positions to cover ~40 meter-long sections of the lowermost channel beds (Figs. 3.2 and 3.8). We captured transient sediment transport by choosing three different scan-interval lengths (Table 3.2): (i) daily scans in the Erlenbach to evaluate the effect of an increased water discharge following precipitation; (ii) an interval length of several months (seasonal) in the Erlenbach and Vogelbach to investigate the time-averaged response probably due to several bed-load transport events; and (iii) monthly scans in both channel beds bridging the gap between (i) and (ii).

Lastly, we defined a set of fixed reference points distributed along each channel-bed section. When several reference points were visible from the different scan positions, it was more accurate to merge the individual scans into a common point cloud of a channel-bed section. Later, we also used these fixed reference points to convert the point-cloud data from local project into Swiss coordinates. For this, we combined kinematic GPS measurements and surveying by a total station (*Leica TCRP1203+*®) to determine the Swiss coordinates of our reference points.

Table 3.2: Laser scanning Erlenbach and Vogelbach – 2008 and 2009.

Erlenbach				Vogelbach		Year
Retention basin		Channel bed		Channel bed		
4 June	●	5 June	●			2008
21 October	●	21 October	●			
17 May	●/●●	16 May	●/●●	17 May	●/●●	
17 June	●●	17 June	●●	16 June	●●	
16 July	●●	15 July	●●	14 July	●●	
13 August	●●	13 August	●●	12 August	●●	2009
7 September	●●	6 September	●●	8 September	●●	
28 October	●/●●	29 October	●/●●/●●●	30 October	●/●●	
		31 October	●●●			
		1 November	●●●			
		3 November	●●●			
		6 November	●●●			

Scan interval: ● Seasonal   ●● Monthly   ●●● Daily

3.4.4. Data Processing and Error Analysis

We utilized various software packages for our data processing – *ScanMaster*[©], *Cyclone*[©], *Pointools*[©], *Octave*[©], *Perl*[©], and *Generic Mapping Tools*[©] – because it allowed us to customize the processing for our purpose. To generate a single high-resolution point cloud of a channel bed for a certain time, we first registered each scan of a particular laser-scanner survey in the same coordinate system by using the fixed reference points defined in the field, or by using alternative points that we selected manually from overlapping areas of individual scans.

Next, it was necessary to geo-reference each point cloud to quantify the difference between two point clouds covering the same area, but which were acquired at different times. For this purpose, we used the fixed reference points from which we knew the coordinates. In some cases, we also used alternative reference points that we selected manually from the point cloud, which yielded the smallest geo-referencing error, by using our fixed reference points (error $\leq \pm 1$ cm, 1 σ). We used this latter approach to reduce the geo-referencing error that we derived when using only the fixed reference points.

We transformed the Erlenbach data into the Swiss coordinate system, and the Vogelbach data into a local project coordinate system. Each choice is due to the resulting total error from both, the scan registration and the geo-referencing process (further detail below). For the Erlenbach, the transformation into Swiss coordinates yielded a smaller error (maximum of ± 3.1 cm, 1 σ) than into local coordinates (maximum error ± 5.2 cm, 1 σ). In contrast, for the Vogelbach the transformation into local coordinates yielded a smaller error (maximum ± 4.6 cm, 1 σ) than into Swiss coordinates (maximum error ± 5.7 cm, 1 σ). Thus, the total error of the Erlenbach data is in the range of ± 4 cm (1 σ) based on the maximum error of ± 3.1 cm, which resulted from the transformation of the Erlenbach data into Swiss coordinates. The total error (1 σ) of the Vogelbach data is on the order of ± 5 cm approximated from the maximum error of ± 4.6 cm (1 σ), that occurred during the transformation of the Vogelbach data into local coordinates.

To quantify channel-bed changes that may have occurred between two laser-scanner surveys, we constructed interferograms of data sets acquired at different times. Based on the point clouds for the Erlenbach and Vogelbach, we generated regular grids with a horizontal resolution of 5 cm for each data set, and by subtracting one grid from another we quantified the vertical difference between them. Schaefer et al. (2004) introduced this approach to determine surface deformation of several cm at the lock gates of a hydropower station during the filling and draining process. We then visualized the results of this subtraction for the

Erlenbach in Figure 3.4, and the Vogelbach in Figure 3.10. We often observed changes concentrated along the grid margins, which we ascribed to the fact that the Erlenbach and Vogelbach channel banks are more or less vertical in those areas (e.g., Figs. 3.4B and 3.10A). The grid subtraction is not appropriate to quantify vertical changes along vertical planes.

We validated the choice of transforming the Erlenbach data into Swiss coordinates and the Vogelbach data into local ones. We therefore compared the results of the grid subtraction when the data had been transformed into local coordinates with the results after their conversion into Swiss coordinates. In particular, the grid-subtraction results for the Vogelbach based on the Swiss coordinates sometimes yielded local differences that we did not observe for the results with the local coordinates (Fig. 3.10). In these cases, our field observations during laser scanning in the Vogelbach agree with the results of the grid subtraction based on the local coordinates.

To allow for an appropriate interpretation of the grid-subtraction results (Figs. 3.4 and 3.10) we carried out a manual inspection of each point cloud. For this, we used the point clouds derived from measurements with the *TOPCON GLS-1000*® scanner. With the integrated camera of this scanner, we acquired photos of the scanned area. With the color information contained in the images, it was possible to color those point clouds using the software *ScanMaster*©. After the coloring, each point in a cloud bears information on space (xyz coordinates) and color (RGB values). By a visual inspection of two point clouds from different times, we had been able to characterize the nature of short-term sediment transport in the Erlenbach and Vogelbach (Figs. 3.5 and 3.11). This approach is similar to the comparison of photographs taken along both channels at different times (Figs. 3.3 and 3.9).

3.4.5. Erlenbach: Retention Basin and Event Data

For two reasons the Erlenbach provides a unique opportunity to evaluate our laser-scanning based observations on channel-bed changes and sediment transport in context of accompanying environmental conditions. First, a sediment-retention basin, that was constructed in 1982 and designed to trap sediment for research purposes (e.g., Rickenmann and McArdell, 2007), enabled us to monitor the total sedimentation of the Erlenbach quasi simultaneously to our scanning surveys along the channel (Fig. 3.6). The basin was slowly drained prior to each survey to avoid disturbing sedimentary deposits. We scanned the basin deposit several times in 2008 and 2009 (Table 3.2) based on the approach described above, and utilized a scan resolution of 3 cm at a distance of 30 m. The data processing comprised similar steps. Both, the registration of individual scans into a common point cloud and the transformation of point clouds into Swiss coordinates are based on the usage of fixed reference points. Here, the reference points and their Swiss coordinates had been determined and provided by the WSL (2008). The total error associated with the scan registration and geo-referencing process is in the range of ±1 cm (1 σ). We generated regular grids with a horizontal resolution of 5 cm for each data set, and by subtracting one grid from another we determined the sedimentation in the basin (Fig. 3.6). Second, independently obtained continuous data on bed-load discharge, water discharge and precipitation in the Erlenbach catchment were available from the WSL covering the time interval of our laser scanning (Fig. 3.6, Tables 6.2-1 and 6.2-2). We refer to the appendix of this chapter for details about these data, e.g., including information about associated errors.

3.5. Results

3.5.1. Alp Valley

Based on our field mapping, the Alp Valley can be divided into four characteristic lithological units (Plate I [see footnote 2]): (i) the Molasse; (ii) the Flysch series and Amdener beds; (iii) the Helvetic units (limestone) and Penninic cliffs; and (iv) the Quaternary deposits of the Alp Valley floor. These four units are in agreement with Hantke (1967), Winkler et al. (1985), and Stammbach (1988).

The subalpine Molasse exposed in the northern Alp Valley exhibits a uniform structural pattern. The Molasse dips to the S-SSE with angles of 35–55°. The conglomerate (Nagelfluh) forms elongated rocky cliffs with a steep north slope and a gentle southern dip-slope (Plate I). Rock-fall occurs on the north slopes, where we found conglomerate boulders deposited at the cliff bases. The southern dip-slopes exhibit a hummocky topography typical for sliding areas. Moreover, streams are often parallel to the strike of the conglomerate beds particularly on the western flank of the Alp Valley (Plate I). These small streams incise the Molasse bedrock in some places. Moreover, the conglomerate is composed of rounded clasts with a manifold origin (e.g., sedimentary and granitic rock types), and a calcareous, fine-grained matrix. As weathering of the matrix proceeds the rounded clasts preferentially drop out, and they also compose the alluvial channel-bed cover.

Our mapping revealed in agreement with Hantke (1967) and Stammbach (1988) that large parts of the central and southern Alp Valley flanks are subject to sliding processes and exhibit a typical hummocky topography (Plate I). This is the area in which the Ultrahelvetic-Penninic Flysch series and Amdener beds are exposed. Where the marl of the Amdener beds is exposed in the south, it exhibits badland-style erosion with deep and steep gullies (Plate I). However, sliding areas were often found along S to SE directed dip-slopes, but they are not restricted to this condition (Plate I). Furthermore, the orientation of ridges and valleys is in some places along the central Alp Valley flanks parallel to the approximate ENE-WSW to NE-SW strike of fold axes and thrust faults (Plate I).

The Penninic cliffs of the Mythen mountain peaks form steep, rocky cliffs that dominate the landscape of the southern Alp Valley (Plate I). Debris cones, composed of angular limestone clasts ranging in size from less than 1 cm to several m, formed at the base of the Mythen cliffs (Plate I). Similarly to the Molasse conglomerate, the Helvetic limestone forms steep, rocky cliffs with rock-fall debris at their base on one hand, and a dip-slope with a hummocky topography due to sliding processes on the other hand – e.g., top of the eastern Alp Valley flank in the north (Plate I).

Quaternary deposits of the Alp Valley floor are markedly different between the north and south. In the south, lateral and terminal as well as ground moraines formed below the base of the Mythen mountain peaks (Plate I). These Würmian-aged moraines (Hantke, 1970) are composed of poorly sorted massive limestone clasts with boulders up to several m in size. The northern Alp Valley floor is dominated by a flat terrace plain that is bounded by an up to 15 m high escarpment (Plate I). In the upper ~10–15 m, the Würmian-aged terrace deposit (Hantke, 1967) consists of well sorted and rounded fluvial gravels containing local lithologies mentioned earlier. The fluvial gravels are underlain by discontinuous, ~0.2–0.3 m thick, varved clay deposits which are again underlain by a ~0.75–1 m thick ground moraine. The latter one is poorly sorted, contains local lithologies, and is composed of a fine-grained matrix and scratched boulders up to ~0.5 m in diameter.

To evaluate the efficiency of fluvial and rock-fall processes, we mapped the corresponding deposition and erosion areas (Fig. 6.2-5). An alluvial fan is the deposit derived from fluvial transport of material, and a drainage basin located upstream of a fan apex defines the corresponding erosion area (Fig. 6.2-5A, Table 6.2-3). Similarly, a debris cone is the deposit

that is due to rock-fall on steep rock cliffs, where the cliff walls represent the erosion area (Fig. 6.2-5B, Table 6.2-4). Hence, we used the deposition area – i.e., area of alluvial fans or debris cones – and erosion area – i.e., area of drainage basins or rock cliffs – as proxies for the spatial scale affected by a particular process (Fig. 3.14). This approach is appropriate because the erosion and deposition areas do not overlap (Fig. 6.2-5). In contrast, we did not consider the post-glacial landslides because the degree of overlap between erosion and deposition area is uncertain. For example, the surface area of the Erlenbach landslide is ~1.4 km² (Plate I), but we were not able to map the corresponding erosion area appropriately because the landslide deposit covers most parts of the basal slip-plane.

Lastly, to approximate temporal variations of erosion in the Alp Valley we considered the sedimentary record of the neighbouring Sihl Valley, east of the Alp Valley (Fig. 3.1B). Lüdi (1939) evaluated a series of drill cores from the Sihl Valley that had been derived prior to the establishment of the reservoir lake in the 1930s (Saurer, 2002). He observed fine laminated marls resulting from sedimentation in a stagnant water body, and suggested that a post-glacial lake existed in the valley. The lake had been progressively filled with sediment from the south towards the north within 10 ka (Lüdi, 1939). The siltation of this lake was further promoted by a base-level drop of the Sihl River, which progressively incised into a terminal moraine that bounded the lake in the north thereby inducing a decrease of the water table. However, based on a profile through the sediment body derived by Lüdi (1939), we approximated the maximal horizontal delta growth in the Sihl Valley during the Holocene (Fig. 3.13). We observed a slow progradation from 10–6 ka (650 m/ka), a rapid increase from 6–5 ka (3400 m/ka), and a slower progradation 5–3 ka ago (1950 m/ka).

3.5.2. Erlenbach

Geomorphic-Geologic Setting

Our detailed field mapping in the Erlenbach basin revealed that small slides occur almost along the entire trunk channel-banks (Fig. 3.2). Along the lowermost ~1.2 km, the trunk stream is cut into a post-glacial landslide deposit, and locally it is even incised down to the bedrock, that consists of Eocene Wägital Flysch (Fig. 3.2; Plate I). The landslide deposit is generally characterized by a gentle, hummocky toporaphy (Fig. 3.2). In contrast, the Amdener beds exposed upstream of the landslide deposit in the uppermost part of the Erlenbach basin exhibit a badland-style erosion with deeply incised gullies (Fig. 3.2).

The Erlenbach channel trends nearly parallel to the bedding-strike orientation along the rare Wägital Flysch bedrock outcrops, whereas it crosscuts the bedding of the Amdener beds in the uppermost catchment (Fig. 3.2). The bedrock in the upper Erlenbach basin generally dips to the SSE-SE. However, since a substantial part of the eastern Alp Valley flank is covered by the landslide with a surface area of ~1.4 km² further structural information on bedrock geology is lacking.

Short-Term Channel-Bed Changes and Sediment Transport

Along the Erlenbach channel bed, we derived similar results from both, the comparison of photographic surveys (Fig. 3.3) and the evaluation of our laser-scanning data (Figs. 3.4 and 3.5). The comparison of photographs indicated that the small slides along the stream delivered lots of material to the channel bed (Fig. 3.3), and we observed sliding vegetation on top of the slide masses (Fig. 3.3B). We further observed that large boulders of several m in diameter exhibited no transport (Fig. 3.3A). The grain size of transported material ranges from silt and sand (Fig. 3.3B) to boulders of several dm in diameter (Fig. 3.3A) and m-sized boulders (Fig. 3.3B).

The quantitative comparison of the Erlenbach laser-scanner data, the grid-substraction results, revealed that channel-bed changes generally occurred in localized areas with a stained or punctual shape (Fig. 3.4). For example, in 2008 we observed a point-shaped negative change in channel-bed elevation of roughly 1 m (Fig. 3.4A left) that was due to the transport of a ~1-m-sized boulder. The stained shape of the observed changes can also be due to the transport of loose tree branches. Furthermore, the qualitative evaluation of the laser-scanner data revealed that the transport length of dm-sized boulders is in the range of several m (Fig. 3.5A), and that the grain size of transported sediment ranges from boulders of several dm in diameter (Fig. 3.5B) to silt and sand (Fig. 3.5C). In contrast, buried boulders in the channel bed exhibited no transport (Fig. 3.5D). In summary, current sediment transport in the Erlenbach from 2008–2010 appears to be active, and only very large or buried boulders are 'immobile' according to Schuerch et al. (2006) and Yager (2006).

Retention Basin and Event Data

We quantified the total sedimentation in the Erlenbach retention basin based on repeated laser scanning of the basin deposit (Table 3.2). We observed the complete excavation of the deposit in 2008, because it was required to excavate the basin due to ongoing construction work (Fig. 3.6A). In this case, the empty basin represents a planar reference frame to monitor the growth of the deposit in 2009 (Fig. 3.6). We observed no sedimentation during the winter term from October 2008 to May 2009 (Fig. 3.6A), whereas episodic sedimentation occurred during the summer term which was greatest from May to August 2009 (Fig. 3.6B). For example, we observed localized sedimentation of up to ~4 m from June to July, of up to ~2 m from July to August, and less than ~1m from August to September (Fig. 3.6B).

Bed-load discharge, water discharge and precipitation had been independently monitored by the WSL. We summarized the data of the bed-load transport events that occurred during our laser scanning in Figure 3.7. In both years, 2008 and 2009, we observed that most of the events occurred during the summer term, and that the greatest bed-load discharge was recorded during events from June to August, whereas the smallest events occurred in the winter term (Fig. 3.7A). Similarly, water discharge and precipitation during these events were greatest and more frequent in the summer, whereas they were lowest and less frequent in the winter (Figs. 3.7B and 3.7C).
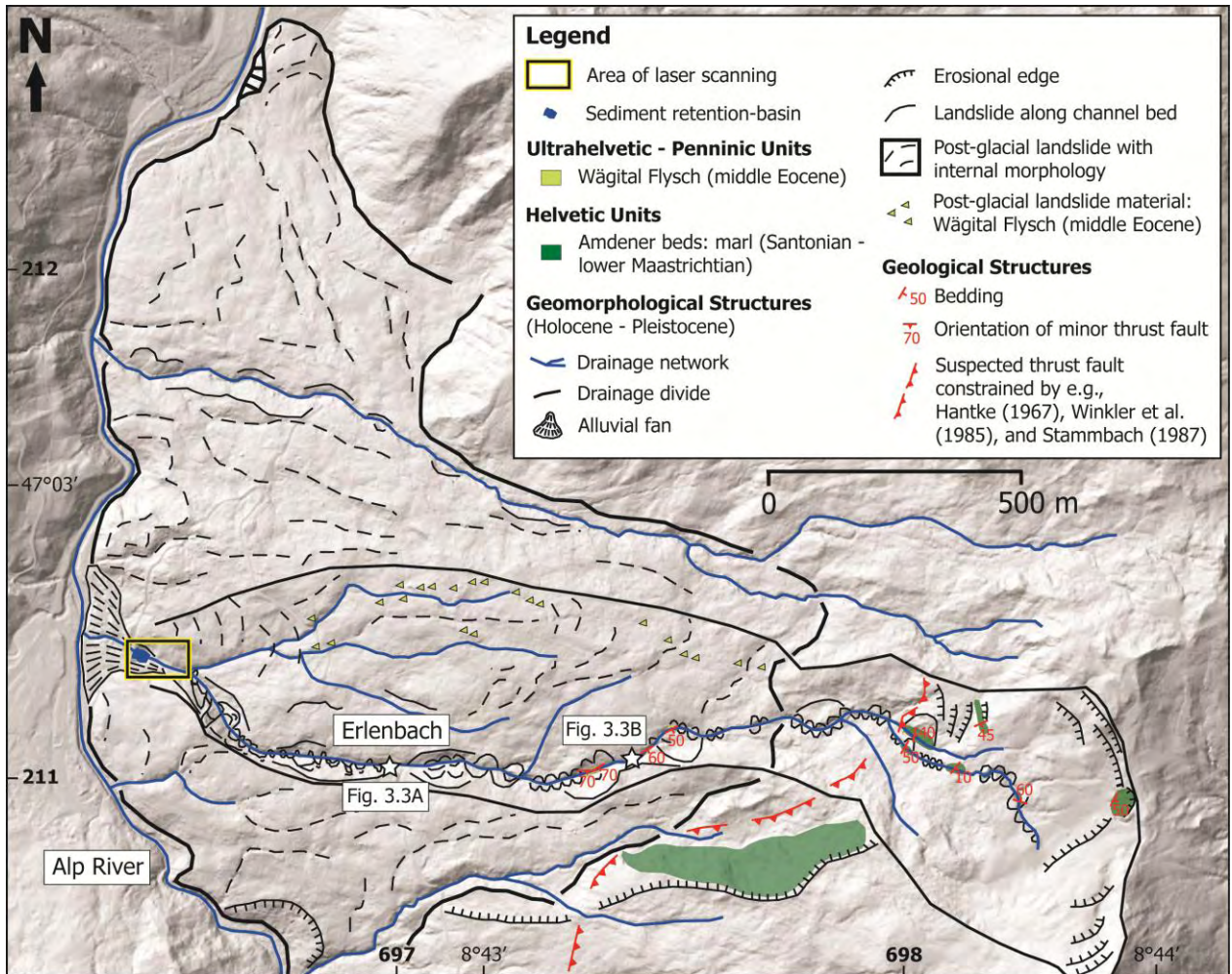
Fig. 3.2 Detailed geomorphic map of the Erlenbach. The location of the photographs shown in Figure 3.3 is indicated with white stars. Tick marks with thick annotated numbers depict Swiss coordinates in km, and tick marks with thin annotated numbers depict northern latitude and eastern longitude.

Fig. 3.3 Photographs along the Erlenbach channel bed where ellipses indicate changes between 2009 and 2010. Note that photos have a slightly different scale resulting from different camera angles when pictures had been acquired. The location of the examples is indicated in Figure 3.2. **(A)** ~5 m sized boulder exhibited no change in position. In contrast, smaller boulders of ~0.4 m or less in size and vegetation such as small trees had been transported. Slides delivered material to the channel bed. Line of sight is upstream. **(B)** Slide on the southern channel bank where boulders up to ~2 m in size had been transported. Especially the base of the slide delivered material to the channel bed. We observed no changes in the uppermost part of the slide. The arrow in the upper right corner indicates downstream direction is to the west.   **→ NEXT PAGE**

A

31 August 2009

18 August 2010

B

→ W

18 May 2009

14 August 2009

7 September 2009

28 October 2009

10 August 2010

79
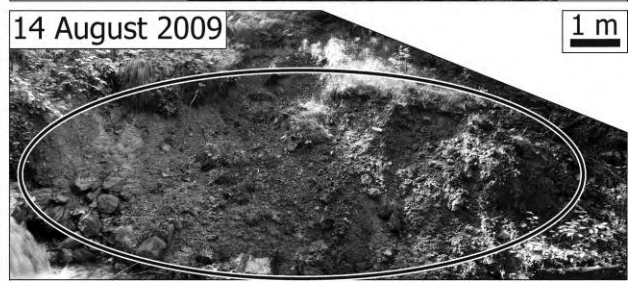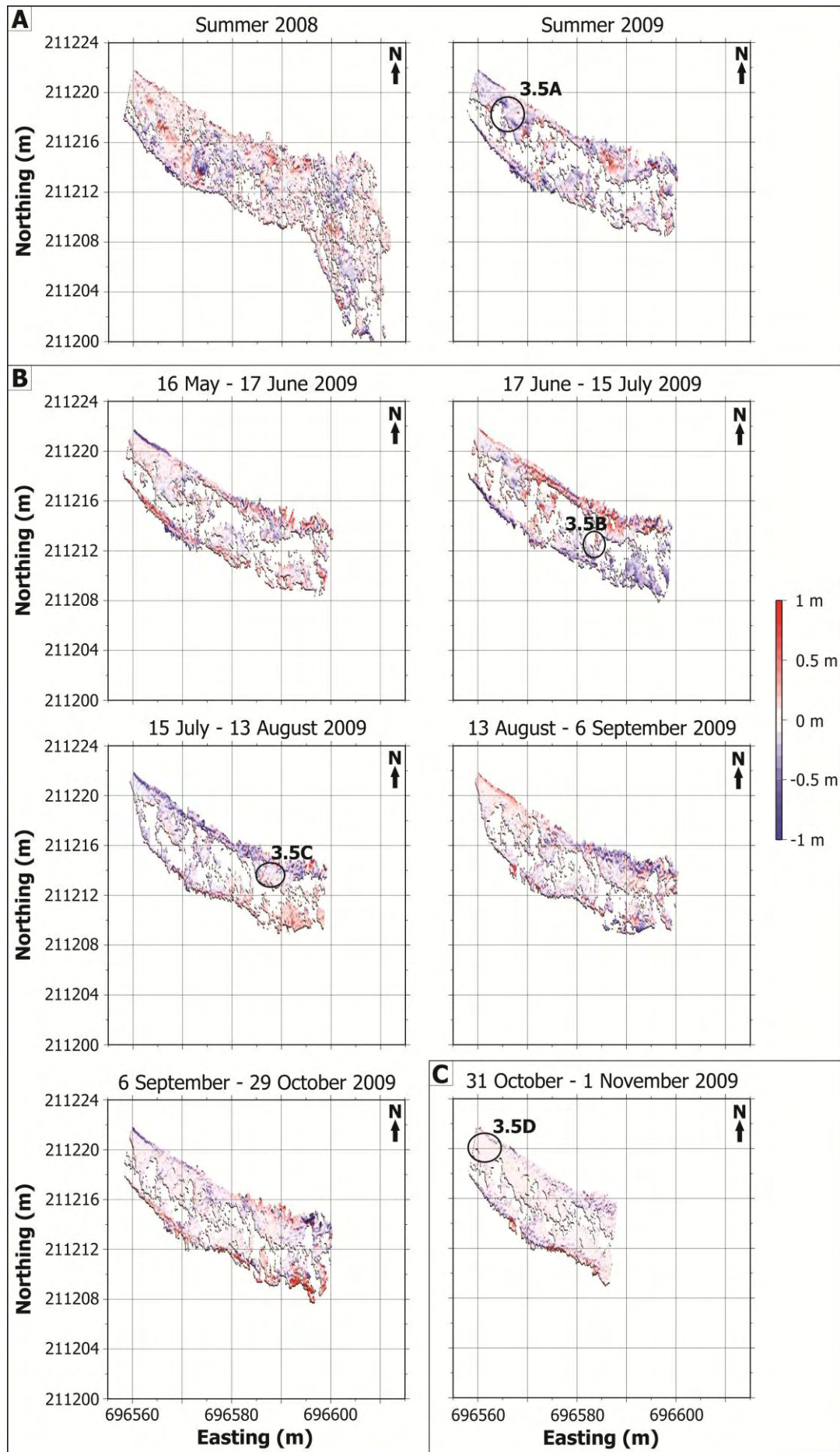
Fig. 3.4 Quantitative results of channel-bed changes for the Erlenbach that are related to the grid subtraction described in the text, and based on the point clouds of the Erlenbach channel bed. An enlarged version of this figure is contained in the appendix (Fig. 6.2-2). Note that the vertical and horizontal axes are of different scale to facilitate the visualization of channel-bed changes because the channel section is much longer than the channel bed is wide. Tick marks with annotated numbers depict Swiss coordinates in m. We indicate the location of examples compiled in Figure 3.5 accordingly. Channel-bed changes generally occurred in localized areas, and have a blurry or punctual shape. **(A)** Seasonal intervals, 2008 and 2009. **(B)** Monthly intervals, 2009. **(C)** Daily interval, 2009. Additionally, Figure 6.2-2 in the appendix contains the remaining results for the daily intervals.

Fig. 3.5 Examples related to our visual comparison of point clouds derived for the Erlenbach channel bed. Their location is indicated in Figure 3.4, and ellipses indicate channel-bed changes in 2009. **(A)** One ~0.6 m sized boulder had been transported by ~3.4 m. White arrows in the left and middle image represent the tips of the arrow in the right image, in which the left and middle image are shown simultaneously. **(B)** Boulders up to ~0.5 m in size and **(C)** fine-grained material had been transported. **(D)** Buried boulders exhibited no change in position.
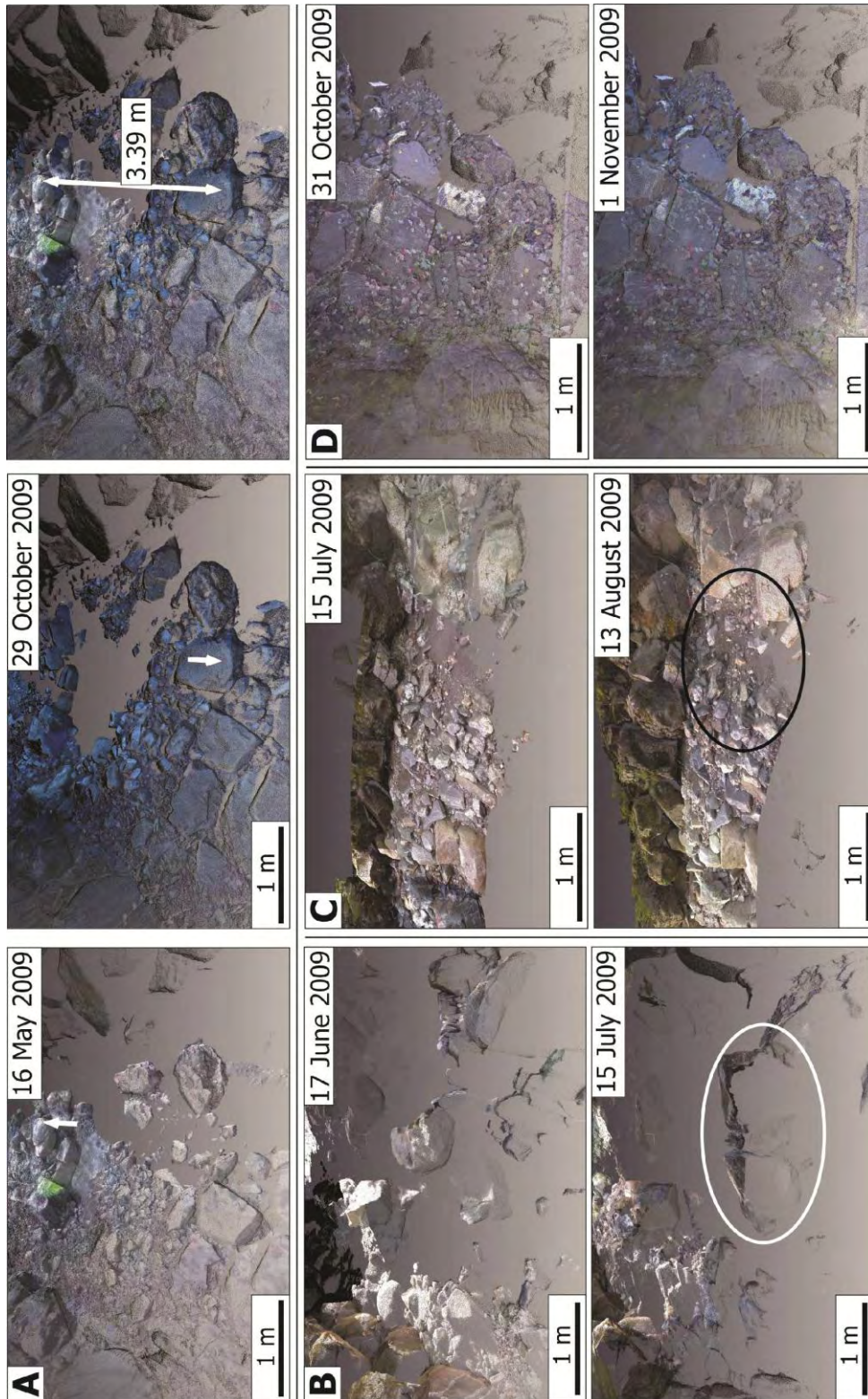
Fig. 3.6 Quantitative results of the sedimentation in the Erlenbach retention-basin that are based on the grid subtraction mentioned in the text and on the point clouds of the basin deposit. An enlarged version of this figure is contained in the appendix (Fig. 6.2-3). Tick marks with annotated numbers depict Swiss coordinates in m. We observed the excavation of the basin deposit that was necessary due to ongoing construction work in 2008, and the growth of the deposit in 2009. **(A)** Seasonal intervals, 2008 and 2009. **(B)** Monthly intervals, 2009.

→ **NEXT PAGE**

82
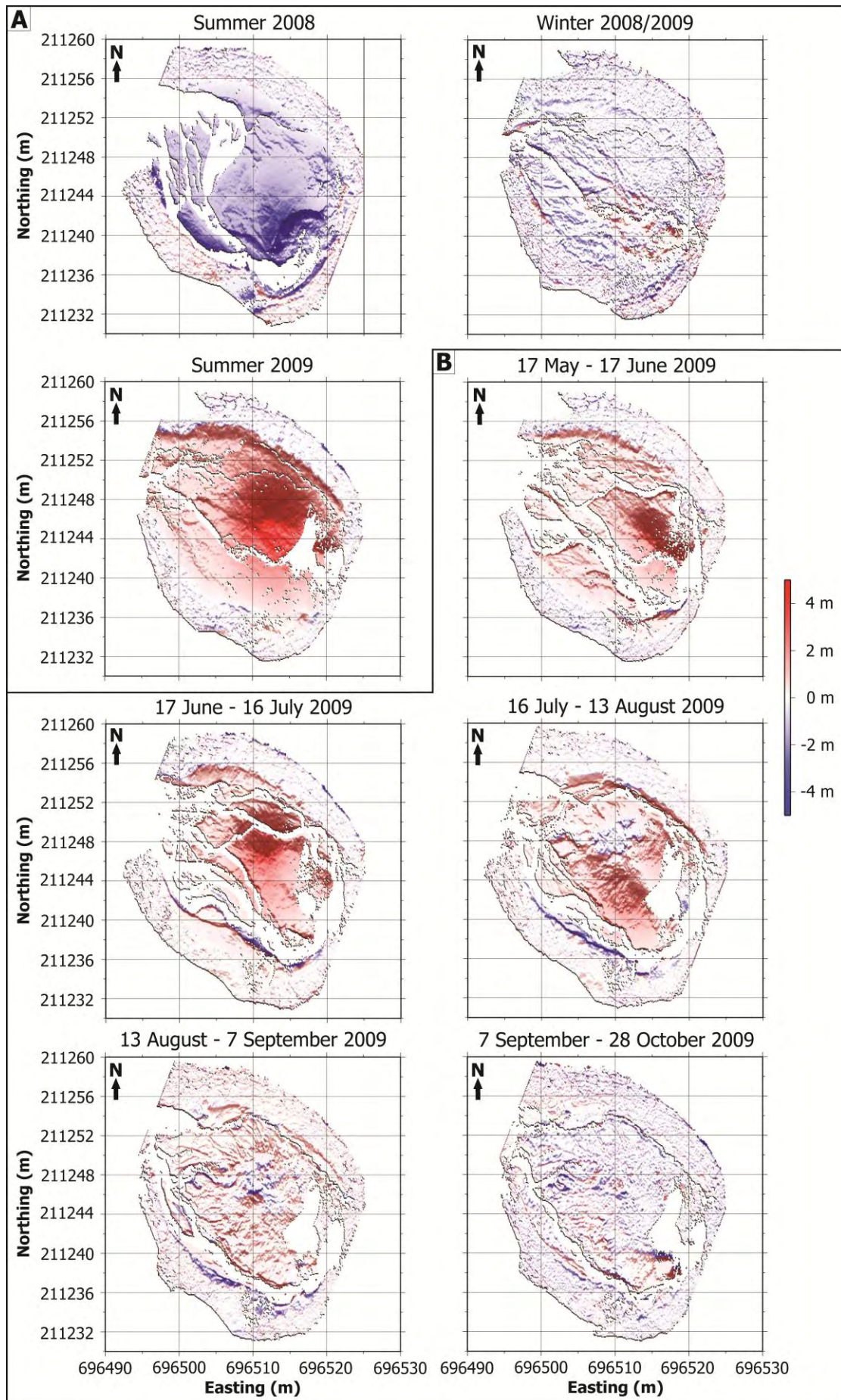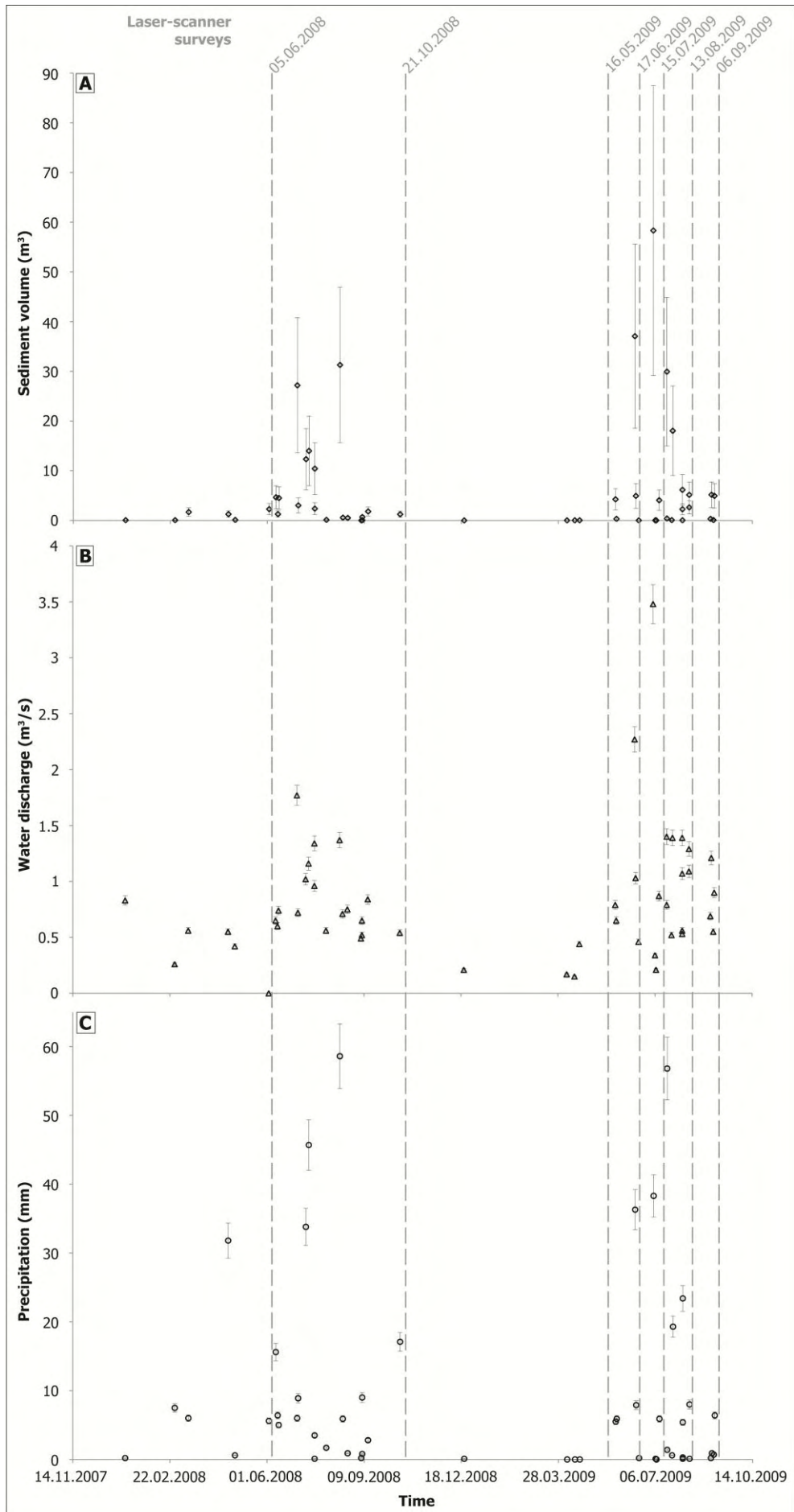
Fig. 3.7 Erlenbach event data on sediment discharge (**A**), water discharge (**B**), and precipitation (**C**) for 2008 and 2009. We additionally compiled these data in Tables 6.2-1 and 6.2-2 in the appendix, and marked the timing of our laser-scanner campaigns in gray.

3.5.3. Vogelbach

Geomorphic-Geologic Setting

Our detailed field mapping in the Vogelbach basin (Fig. 3.8; Plate I) revealed that the Wägital Flysch exposed along the trunk channel is intensively deformed. The Flysch exhibits folds of varying wavelength (up to ~10 m) and style (narrow to open). In many cases, the channel trends nearly parallel to the local bedding-strike and fold-axis orientation, whereas in other cases, the trunk stream crosscuts fold cores as well as bedding (Fig. 3.8). Dip-slopes occur often on the northern trunk channel-bank facilitating sliding. Slides also appear at fold-core locations, e.g., along the southern bank of the lowermost trunk channel (Fig. 3.8). Furthermore, wide areas of the upper Vogelbach basin exhibit a hummocky topography characteristic for active sliding (Fig. 3.8).

Short-Term Channel-Bed Changes and Sediment Transport

Along the Vogelbach channel bed, both the comparison of photographic surveys (Fig. 3.9) and the evaluation of the laser-scanning data (Figs. 3.10 and 3.11) yielded similar results. The comparison of photographs revealed that bedrock exposures along the trunk channel exhibited no change (Fig. 3.9), and that only boulders of up to ~0.3 m in diameter (Fig. 3.9A) as well as loosely deposited limbs (Fig. 3.9B) had been transported. The quantitative comparison of our laser-scanner data, the grid-substraction results, indicated that the Vogelbach channel-bed morphology remained mainly unmodified for most of the time (Fig. 3.10). If a change occurred it was often localized at spots (e.g., circle labelled with 3.11C in Fig. 3.10B). The qualitative evaluation of the laser-scanner data revealed that large m-sized boulders did not move (e.g., Figs. 3.11A and 3.11B). We also observed that mainly loose limbs (Fig. 3.11A) and boulders of ~0.4 m or less in size (Fig. 3.11C) had been transported. In summary, current sediment transport in the Vogelbach from 2009–2010 appears to be restricted to particles of less than ~0.5 m in diameter, and woody debris.

3.5.4. Historical Record

During the last ~200 a, the morphology of the Alp Valley did not change based on a comparison of canvas, post cards and our own field photos (Figs. 3.14, 6.2-5 and 6.2-6). We mainly observed an increase in forest respectively vegetation cover (Fig. 3.14), and residential areas, e.g., the growth of Alpthal village in the central Alp Valley (Fig. 3.1B). The drainage network of the Alp River and its tributaries had been modified during the last decades (Peter Steiner, pers. comm., 2011). The main course of the Alp River had been channelized, and check dams had been constructed along the lower channel beds of several tributaries and the Alp River bed to stabilize them. Many of these constructions had been destroyed or seriously damaged during a large flood on 25th July 1984, and had been rebuilt afterwards (Peter Steiner, pers. comm., 2011). Lastly, the landscape morphology around the monastery of Einsiedeln exhibited no change during the last ~500 a (Fig. 6.2-7). Instead, we observed drastic changes in the forest cover, and the growth of Einsiedeln city around the monastery.
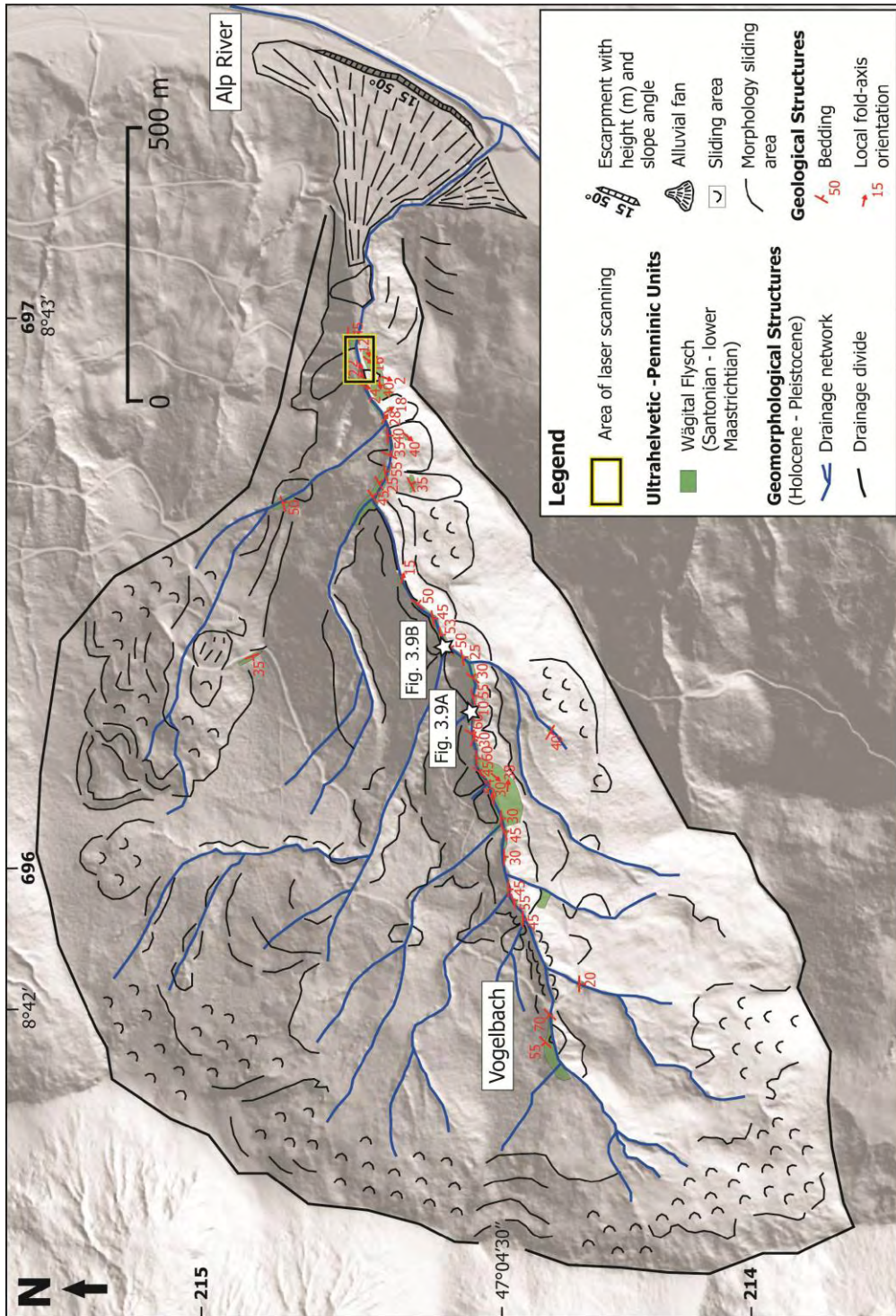
Fig. 3.8 Detailed geomorphic map of the Vogelbach. The location of the photographs shown in Figure 3.9 is indicated with white stars. Tick marks with thick annotated numbers depict Swiss coordinates in km, and tick marks with thin annotated numbers depict northern latitude and eastern longitude.

86

Fig. 3.9 Photographs along the Vogelbach channel bed where ellipses indicate changes between 2009 and 2010. The location of the examples is indicated in Figure 3.8. Line of sight is upstream. **(A)** Only boulders of ~0.3 m or less in size had been transported, whereas bedrock exposures and large m-sized boulders exhibited no change in position. **(B)** Loosely deposited limbs in the channel bed had been transported.
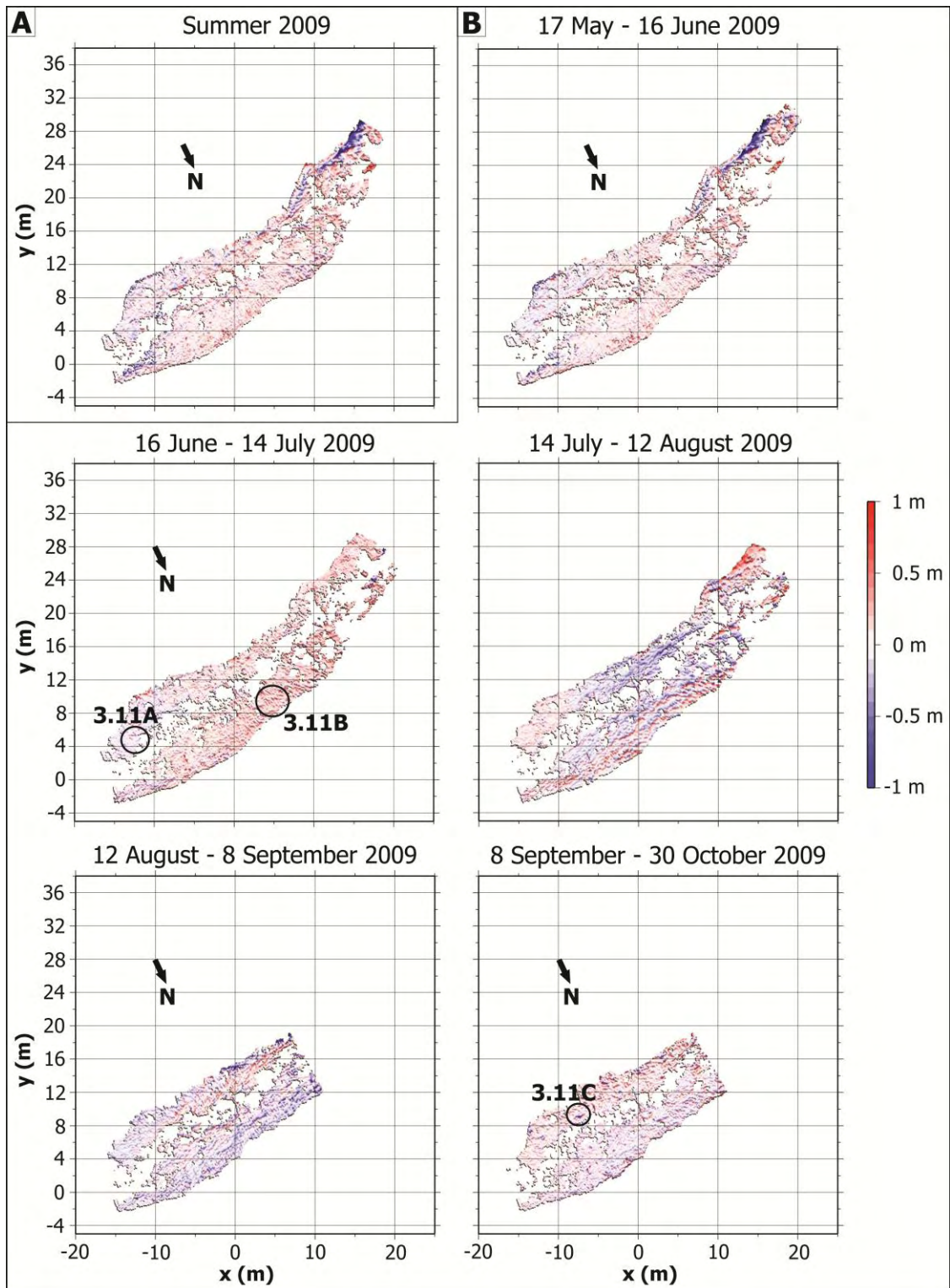
Fig. 3.10 Quantitative results of channel-bed changes for the Vogelbach that are related to the grid subtraction mentioned in the text, and based on the point clouds of the Vogelbach channel bed. An enlarged version of this figure is contained in the appendix (Fig. 6.2-4). Note that the vertical and horizontal axes are of different scale to facilitate the visualization of channel-bed changes because the channel section is longer than the channel bed is wide. Tick marks with annotated numbers depict local project coordinates in m. We indicate the location of examples shown in Figure 3.11 accordingly. Channel-bed morphology generally exhibited no change most of the time, and if a change occurred it had been localized at spots, e.g., 12C in (B). **(A)** Seasonal interval, 2009. **(B)** Monthly intervals, 2009.
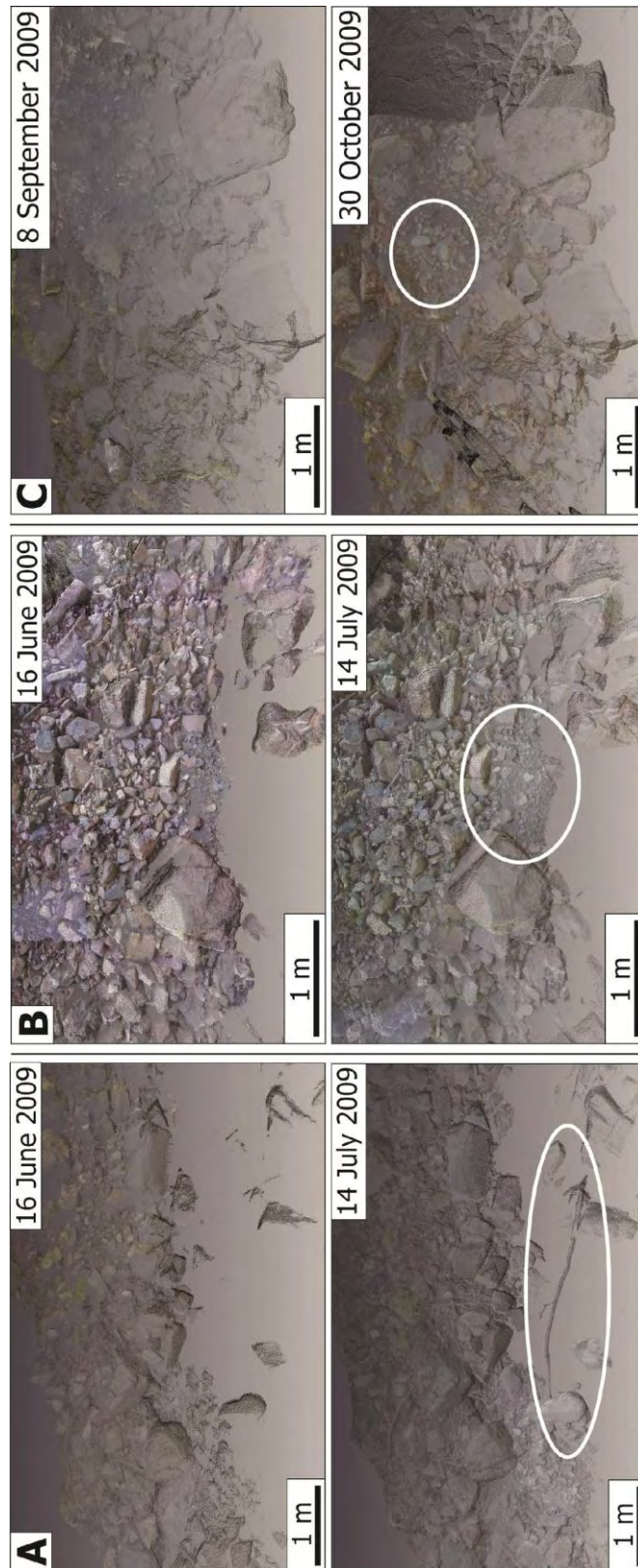
Fig. 3.11 Examples related to our visual comparison of point clouds derived for the Vogelbach channel bed. Their location is indicated in Figure 3.10, and ellipses indicate channel-bed changes in 2009. We observed that boulders up to ~0.4 m and finer grained material, as wells as loosely deposited limbs had been transported. **(A)** Transported limb. **(B)** Transport of gravels and finer grained material. **(C)** Transport of ~0.4 m sized boulder.

89

3.6. Interpretation

3.6.1. Erlenbach and Vogelbach

Short-Term Sediment Transport

Sediment transport along the Erlenbach channel is currently much more active than along the Vogelbach based on our short-term monitoring (Figs. 3.3–3.5 compared with Figs. 3.9–3.11). Our results indicate that: (i) the maximum grain size of transported sediment is greater in the Erlenbach than in the Vogelbach; (ii) decimeter to meter-sized boulders are transported more frequently in the Erlenbach than in the Vogelbach; (iii) numerous small slides deliver large amounts of fine-grained sediment to the Erlenbach channel in contrast to the Vogelbach; and (iv) channel-bed changes occur more often in the Erlenbach than in the Vogelbach over the time interval of our monitoring. The sediment flux in the Vogelbach appears to be controlled by the availability of material for transport (supply-limited), whereas the sediment flux in the Erlenbach appears to be controlled by the ability of the stream to transport material (transport-limited).

We suggest that these differences originate from the morphologic differences between the Vogelbach and Erlenbach basins. The morphology of the former possesses a clear non-dip-slope situation (Fig. 3.8), whereas the morphology of the latter bears great resemblance to a dip-slope situation (Fig. 3.2). The similarity with a dip-slope situation is well documented along the middle reach of the Erlenbach, and the regional dip of stratigraphic units is consistent with such a situation (Fig. 3.2; Plate I). But bedding in the upper Erlenbach basin exhibits a contrary dip to the SE, and the bedrock is buried beneath the post-glacial landslide deposit across wide areas so that structural information is lacking, and we cannot entirely preclude a non-dip-slope situation for the Erlenbach (Fig. 3.2; Plate I).

Short-term sediment transport in the Erlenbach is marked by clear seasonal differences as revealed by our laser scanning, and the WSL monitoring. Sedimentation in the retention basin and the occurrence of changes along the Erlenbach channel were most significant from May to August 2009 when the greatest bed-load transport events and most intense precipitation were recorded (Figs. 3.4B and 3.6B compared with Fig. 3.7). In contrast, we observed no sedimentation in the basin and channel-bed changes during the late autumn 2009 when we also carried out daily laser scanning (Figs. 3.4B, 3.4C and 3.6B).

Short-term sediment transport in the Erlenbach appears to exhibit temporal differences. In the late spring and summer 2009, we observed that several landslides along the lowermost ~530 m of the channel delivered large amounts of sediment to the channel bed (e.g., Fig. 3.3B). Simultaneously, we observed the growth of the basin deposit (Fig. 3.6B), and channel-bed changes that were often due to the transport of boulders ranging in size from several dm in diameter up to m-sized boulders (e.g., Figs. 3.3B, 3.5A and 3.5C). From 2003–2004, however, Schuerch et al. (2006) observed that landslide derived sediment discharge to the channel was greatest during the winter and spring months, while most of the fluvial sediment transport occurred during short, intense summer storms. We suggest that the current pattern of sediment transport that we observed may have prevailed since the occurrence of a large flood on 20th June 2007, and that erosion of the channel bed during this flood may have resulted in a longer-term destabilization of the landslides and increased sediment input as we observed (Fig. 3.3B).

We further suggest that the spatial extent of potential channel-bed changes correlates with the magnitude of a sediment transport event. Our monitoring in the Erlenbach (Figs. 3.3–3.5) and the WSL monitoring (Fig. 3.7) revealed that particularly the more frequent and smaller events yielded only localized changes along the channel often due to the transport of single

90

boulders. In contrast, infrequent large floods, such as in June 2007, yielded a complete reorganization of the step-pool morphology along the stream (Molnar et al., 2010).

Short-Term Scale and Post-Glacial Landscape Evolution

The marked differences in sediment-transport activity between the Erlenbach and Vogelbach may also originate from the fact that the former incises unconsolidated landslide material whereas the latter incises bedrock (Plate I; e.g., Keller and Weibel, 1991). At short-term scales, such behavior may indicate that bedrock channels might be more stable than gravel bed channels, and that the latter type buffers bedrock erosion. This behavior may have prevailed over thousands of years since the termination of the last glaciation because lateral moraines of late-Würmian age occur only in the upper Alp Valley (Plate I).

The Erlenbach channel may effectively buffer bedrock erosion on time-scales of at least a few hundred years based on an exemplary and simplified approximation of ours. A single ~0.6-m-sized boulder had been transported across a distance of ~3.4 m between June and July 2009 (Fig. 3.5A). Here, we illustrated the difference between May and October to indicate that the boulder exhibited no further transport. However, it was most likely transported during the greatest event 2009 with a peak water discharge of 3.48 m³/s (Fig. 3.7A; Table 6.2-2). If we simply assume an annual recurrence of such an event during which the boulder is transported for ~3.4 m, and that the boulder was initially located ~1 km upstream at the upper limit of the landslide complex (Plate I), it requires ~300 a until the boulder passes the basin outlet. In contrast, we observed that boulders of more than 1 m in diameter exhibited no transport during our monitoring (e.g., Fig. 3.3A), but such boulders exhibited transport during the large flood in June 2007 with a peak water discharge of 16 m³/s (e.g., Turowski et al., 2009). Turowski et al. (2009) observed a minimum transport length of ~22 m for one m-sized boulder during this flood. It requires ~2100 a to transport such a boulder across a distance of ~1 km from the upper limit of the landslide complex towards the basin outlet assuming an estimated recurrence interval of 47 a (Turowski et al., 2009). Hence, it is more likely that the buffering of bedrock erosion is effective on even longer time-scales of a few thousand years.

We investigated the context between short-term sedimentation based on laser scanning of the Erlenbach retention basin (Fig. 3.6) and long-term delta growth in the Sihl Valley (Fig. 3.13) to better understand how short-term measurements compare with long-term ones. In 2009, maximum sedimentation rates in the Erlenbach basin range between ~1 m/a in the lower and 4 m/a in the upper part of the basin (Fig. 3.6A) equal to ~1000–4000 m/ka. Holocene delta-growth rates in the Sihl Valley were on the same order of magnitude, and range from ~650–3400 m/ka (Fig. 3.13). Hence, short- and longer-term measurements of sedimentation appear to be compatible at least on the local scale defined by the Alp and Sihl Valleys.

3.6.2. General Mode – Alp Valley

The erosion and sedimentation pattern of the Alp Valley is likely lithologically and structurally influenced. Wide areas of the hill-slopes are subject to sliding processes, especially where the Wägital and Schlieren Flysch composed of marl, shale, and sandstone are exposed (Plate I). Most tributaries of the Alp River incise sliding material, e.g., the Erlenbach, whereas bedrock is mainly exposed along channel beds, e.g., the Vogelbach, or at rock cliffs, e.g., the Mythen mountain peaks (Plate I). Such rocky cliffs are mainly composed of massive conglomerate or limestone, and debris cones and slopes at the cliff bases consist of angular clasts and boulders characteristic for rock-fall deposits (Plate I). Furthermore, valleys and ridges on the eastern flank of the central Alp Valley and to the west of the valley exhibit the same orientation as fold axes in the Wägital Flysch (Plate I). We also observed that

tributary channels are parallel to thrust faults, e.g., the Vogelbach in the central Alp Valley (Plate I). Lastly, we often observed hummocky topography due to sliding along hill-slopes that are dip-slopes, e.g., in areas underlain by Molasse conglomerate in the north, or Wägital Flysch on the western valley flank in agreement with Stammbach (1988; Plate I).

We suggest that the current landscape of the Alp Valley is due to a change from glacially influenced erosion and sedimentation to a pattern dominated by mass movements and fluvial processes (Plate I). This change occurred progressively since the LGM, starting in the north and propagated to the south in direction of glacier retreat. This is because we observed fluvial gravels overlying a ground-moraine deposit in the north, and lateral and terminal moraines of late-Würmian age occur only in the south (Plate I). Moreover, a series of debris cones developed at the base of the Mythen cliffs, and at their base the late-Würmian lateral and terminal moraines form a sediment trap for the rock-fall material (Plate I). Hence, we propose that the processes currently shaping the Alp Valley have been active since the termination of the Würmian glaciation at the beginning of the Holocene. Prior to this change, glacial processes affected the entire Alp Valley at least during the Würmian glaciation in the late Pleistocene.

Currently active erosion and sedimentation processes affect different spatial scales in the Alp Valley. We compared the efficiency of fluvial processes and rock-fall. Clearly, alluvial fans cover a larger area than debris cones, and the area affected by fluvial processes is larger than the area affected by rock-fall (Plate I; Figs. 3.12 and 6.2-4). Hence, fluvial processes appear to be much more efficient than rock-fall during the Holocene (Fig. 3.12). We further suggest that landsliding is a common process shaping the Alp Valley based on the surface area of ~1.4 km² of the post-glacial landslide deposit in the Erlenbach area (Plate I).

Erosion in the Alp Valley may have undergone changes during the Holocene based on our approximation of Holocene delta-growth rates in the Sihl Valley, east of the Alp Valley (Fig. 3.13). Here, sedimentation was slow from 10–6 ka (650 m/ka), followed by a rapid increase from 6–5 ka (3400 m/ka), and a slower sedimentation from 5–3 ka (1950 m/ka; Fig. 3.13). Furthermore, by using the delta-growth rates as a proxy for erosion, we also suggest that Holocene climate variations may have influenced erosion in the Sihl Valley. Küchler (2002) summarized the results of the pollen analysis of the lake Sihl sediments: a cool climate with tundra vegetation prevailed since the LGM, followed by a warming period (birchs and pines), and a warm period with deciduous forests. When considering these findings in context of the delta-growth rates in Figure 3.13, we suggest that erosion was low during the time of the prevailing cooler climate, and increased during the time of the prevailing warmer climate.

On shorter time-scales of a few hundred years, the landscape of the Alp Valley area appears to be stable based on our evaluation of the historical record (e.g., Fig. 3.14). Although we observed anthropogenic changes on the hydrologic system, e.g., the main course of the Alp River had been channelized and stabilized with check dams (Peter Steiner, pers. comm., 2011), drastic changes in the vegetation and forest cover due to de- and reforestations, e.g., around the monastery of Einsiedeln (Fig. 6.2-7), as well as the growth of villages and cities (e.g., Figs. 6.2-6 and 6.2-7), the general morphology exhibited no major change. In contrast, we suggest that these changes had mainly localized effects, and sliding processes affecting the Alp Valley slopes might be either very slow or even inactive on such short time-scales.
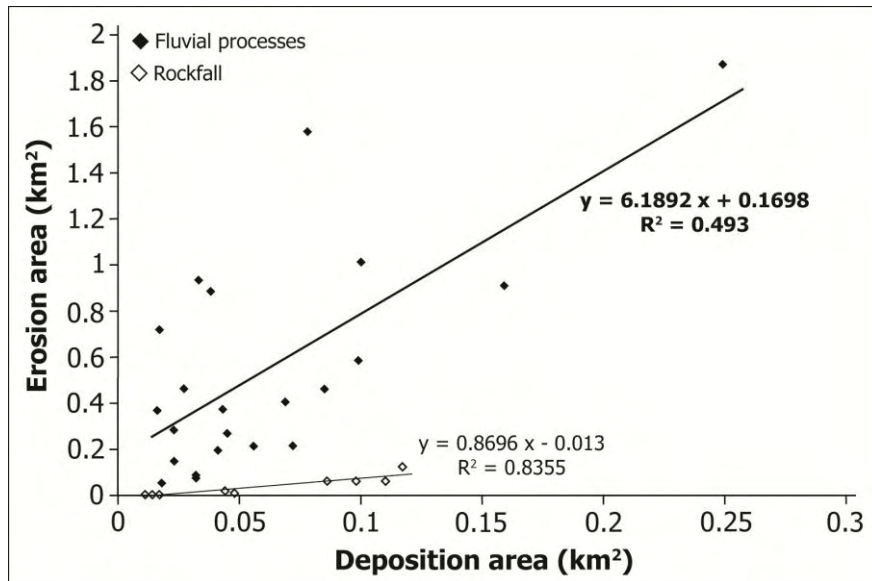
Fig. 3.12 Plot of deposition area versus erosion area to compare the efficiency of rock-fall and fluvial processes during the Holocene. Fluvial processes appear to be more efficient than rock-fall. We used the deposition area – i.e. area of alluvial fans and debris cones – and erosion area – i.e. area of drainage basins and rock cliffs – as proxies for the spatial scale affected by fluvial processes and rock-fall. This approach is satisfied because the erosion and deposition areas do not overlap (Fig. 6.2-5). Based on the 2 m LiDAR-DEM, we mapped the erosion and deposition areas accordingly (Fig. 6.2-5), and compiled these data in Tables 6.2-3 and 6.2-4 in the appendix.
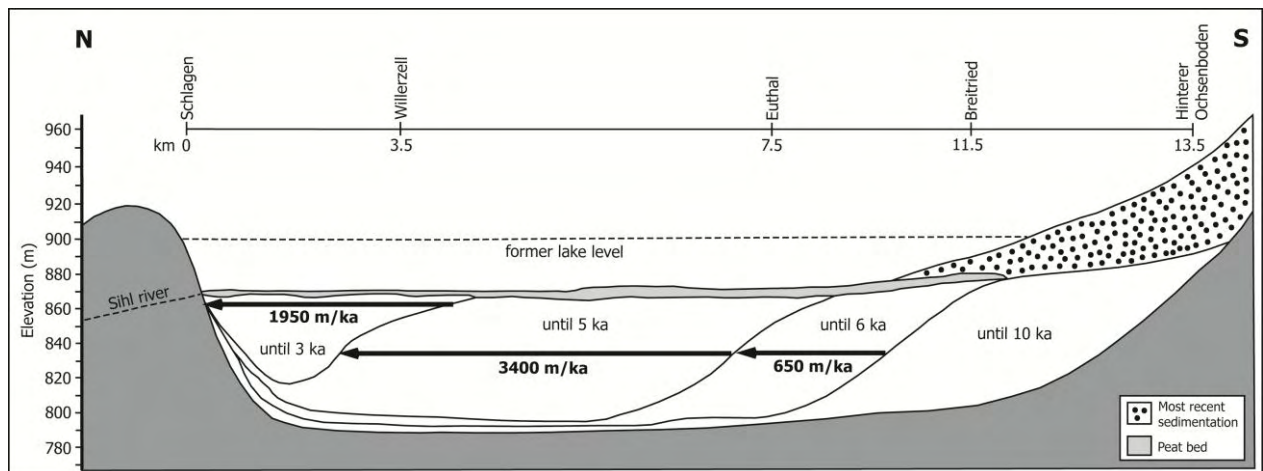
Fig. 3.13 Maximal horizontal delta growth rates in the Sihl Valley during the Holocene. We modified the profile through the sediment body of the post-glacial Sihl lake after Lüdi (1939) and Küchler (2002). The original profile of Lüdi (1939) was reconstructed based on a series of drill cores from the Sihl Valley that cover the area of the recent reservoir lake and the post-glacial lake. Please note the varying length scale of the horizontal distance axis along the profile. The peat bed appears to be a few thousand years old (Küchler, 2002). However, we suggest that its age is at least 3 ka because the peat bed covers the youngest post-glacial lake filling.
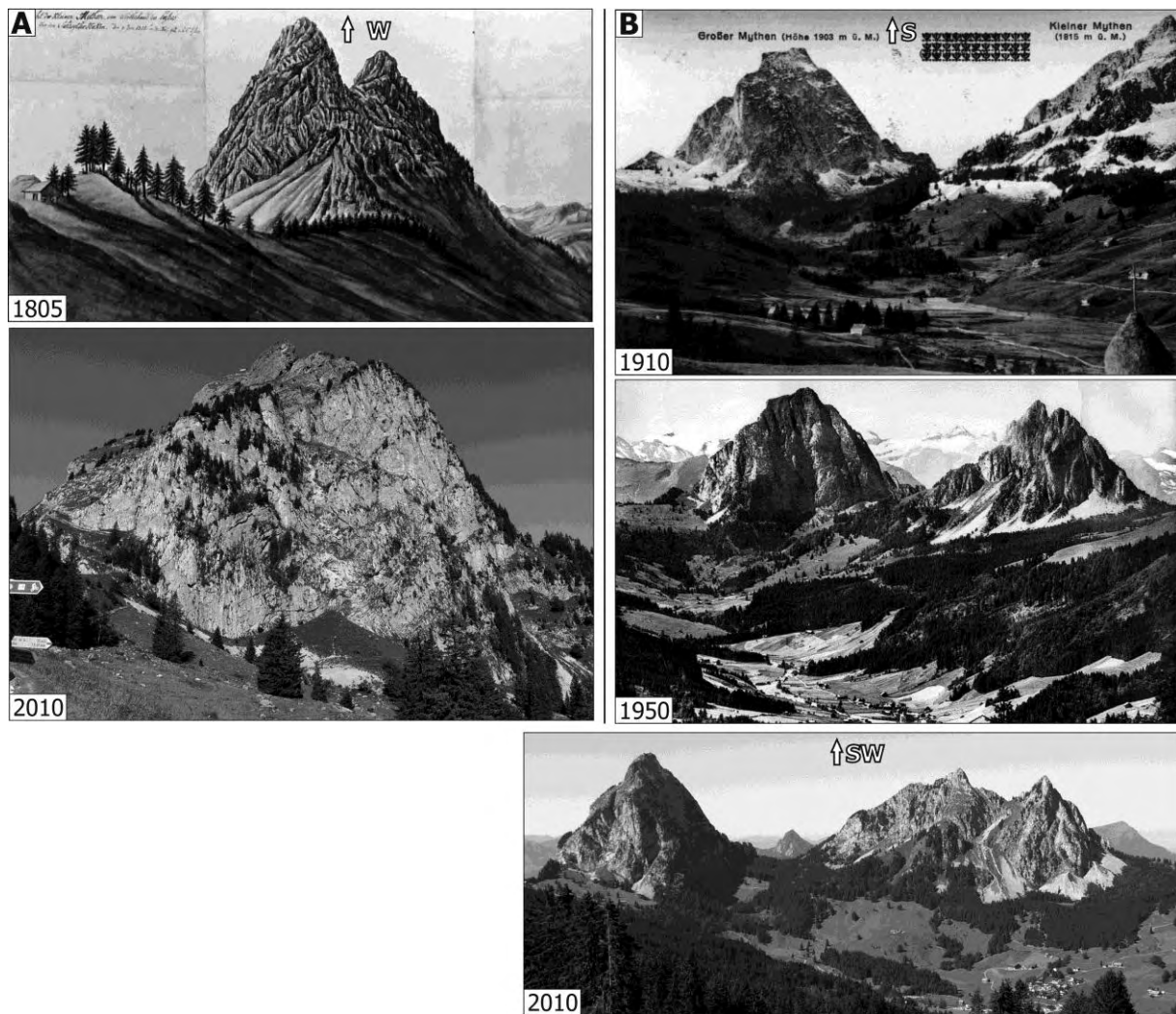
Fig. 3.14 Historical record of the upper Alp Valley and area of the Mythen mountain peaks (location in Fig. 3.1B). Line of sight is indicated on top of the figure. We observed an increase in forest cover, and an increase in vegetation cover on top of the Grosser Mythen debris cones. **(A)** Grosser Mythen. 1805: Mythen mountain peaks, painting by H.C. Escher von der Linth. 2010: Photograph of the Grosser Mythen by R. Baran. **(B)** Upper Alp Valley. 1910: Post card of the upper Alp Valley provided by A. Fassler (pers. comm., 2010). 1950: Post card of the upper Alp Valley provided by A. Fassler (pers. comm., 2010). 2010: Photograph upper Alp Valley by R. Baran.

3.7. Discussion

3.7.1. Erlenbach and Vogelbach

Short-Term Sediment Transport

Our short-term monitoring on sediment-transport activity in the Erlenbach and Vogelbach revealed that transport in the former (Figs. 3.3–3.5) differs considerably from that in the latter (Figs. 3.9–3.11). Our results point to an increased activity in the Erlenbach compared to the Vogelbach, and coincide with observations on suspended-load in both streams from 1986–1989, which was ~40% higher in the Erlenbach (Table 3.1; Keller and Weibel, 1991). Apparently, sediment flux in the Erlenbach is transport-limited and that in the Vogelbach supply-limited, and we suggest that this difference is due to the morphologic differences

between both basins, a dip-slope setting for the Erlenbach and non-dip-slope for the Vogelbach.

Such a difference had also been reported for E-facing and W-facing valley flanks of drainages in the eastern Swiss Alps (Schneider et al., 2008). There, lithological series dip sub-parallel to the E-facing flanks promoting landsliding, and providing an explanation for the transport-limited sediment flux on these slopes. In contrast, this structural setting stabilizes hill-slopes of the W-facing valley flanks, and can explain the supply-limited sediment flux from these slopes. Furthermore, our detailed mapping in the Erlenbach (Fig. 3.2) and Vogelbach (Fig. 3.8) revealed a great similarity with the geomorphic setting of the E- and W-facing valley flanks described by Schneider et al. (2008). Similar to the Erlenbach (Fig. 3.2), the E-facing flanks are characterized by gentle slopes, a low channel density and a low degree of channel branching, and they are affected by large landslides that are important sediment sources. Similar to the Vogelbach (Fig. 3.8), no such slides had been observed on the W-facing valley flanks, and they are characterized by a highly branched channel network along which bedrock is exposed.

These observations exemplify theoretical concepts indicating that the ratio between sediment discharge on hill-slopes and that in channels has a significant impact on mountainous landscapes (e.g., Simpson and Schlunegger, 2003). In summary, these models predict that a high dependence of sediment discharge on hill-slope processes leads to the formation of landscapes with smooth topographies, low hill-slope relief, and non-branched valleys, whereas the predominance of channelized processes leads to the formation of hill-slopes dissected by a stable and highly branched channel network (Schlunegger et al., in press). A high sediment discharge on transport-limited hill-slopes such as the Erlenbach (Fig. 3.2) thererfore prevents the formation of a stable channel network (e.g., Schlunegger et al., in press). So far, the theoretical models lack quantitative data that could resemble their predictions, but the detailed results of our short-term monitoring on sediment transport in the Erlenbach and Vogelbach by using laser scanning and photo documentation support the model predictions and provide quantitative insight (Figs. 3.3–3.5 compared to Figs. 3.9–3.11).

Sediment transport in both streams, the Erlenbach and the Vogelbach, exhibits a pronounced event character and clear seasonal differences (e.g., Figs. 3.4 and 3.6). Although detailed observations on the boundary conditions in our study were limited to the Erlenbach (Fig. 3.7), both basins are characterized by similar climatic conditions (e.g., Keller and Weibel, 1991; Table 3.1). Most of the sediment transport events occurred during short, intense summer thunderstorms in agreement with e.g., Rickenmann (1997). Furthermore, our results agree well with observations on the Erlenbach and Vogelbach suspended-load, where the mean monthly load of both streams was greatest during the summer term and much smaller in the winter term (Keller and Weibel, 1991).

Rare large floods in the Erlenbach, such as the June 2007 event, do not only change the mode of the short-term sediment-transport pattern, they also have a longer-term impact on this pattern. Prior to this flood, slides along the lower channel delivered material to the channel bed mostly in winter and spring, and fluvial transport occurred during thunderstorms in summer (Schuerch et al., 2006). After this flood, we recognized the simultaneous fluvial transport and sediment delivery from the slides to the channel in late spring and summer (e.g., Figs. 3.3B, 3.5A and 3.6B). Our observations are consistent with the results of Turowski et al. (2009) who detected an increased sediment discharge in the aftermath of the June 2007 event lasting for about a year or longer. In agreement with Turowski et al. (2009), we attributed the increased sediment-delivery activity of the landslides to be due to the destabilization of the channel bed and its banks that originated from this exceptional flood.

Observations from numerous rivers, including magnitude-frequency flood distributions, indicate that annual recurring floods transport most of the suspended-load and in some regions much of the bed-load (e.g., Wolman and Miller, 1960; Molnar, 2001; Molnar et al., 2006).

Such floods appear to have only small effects on a landscape compared to infrequent large floods that not only transport bed-load but also expose the bedrock (Molnar et al., 2006). This behavior is confirmed by observations in the Erlenbach suggesting that the magnitude of sediment-transport events has an impact on the spatial extent of potential channel-bed changes. However, we quantified the small effects just mentioned that were due to the occurrence of more frequent floods (Fig. 3.7). We observed only localized changes along the channel that were mostly due to the transport of single boulders (Figs. 3.3 and 3.5). In contrast, a complete reorganization of the step-pool geometry occurred along the Erlenbach during the June 2007 flood accompanied by local erosion of up to ~3 m (Molnar et al., 2010).

Short-Term Scale and Post-Glacial Landscape Evolution

The interpretation, that the distinct differences in short-term sediment transport between the Erlenbach and Vogelbach result from the fact that the former incises unconsolidated landslide material and the latter bedrock (e.g., Keller and Weibel, 1991), is an aspect that relates to the contrasting settings of both basins, the dip-slope vs. non-dip-slope situation discussed in the previous chapter. However, this behavior implies that bedrock channels are more stable than gravel-bed channels at short-term scales, and that gravel-bed channels buffer bedrock erosion. For the Erlenbach, we approximated the time-scales at which it can effectively buffer bedrock erosion. It prevents actual bedrock erosion on time-scales of up to a few thousand years based on simplified calculations using the transport length of single boulders and the recurrence interval of different floods. Turowski et al. (2008) and Stark et al. (2009) noted that alluvial cover overlying bedrock can buffer bedrock erosion over similar time-scales that also appear to depend on the cover thickness.

The short-term differences in sediment transport between the Erlenbach and Vogelbach most likely have prevailed over thousands of years since the termination of the last glaciation because late-Würmian aged moraines occur only in the upper Alp Valley (Plate I). Similarly, our comparison of short-term sedimentation rates in the Erlenbach retention basin (Fig. 3.6) and long-term delta-growth rates in the Sihl Valley (Fig. 3.13) revealed that such short- and longer-term measurements seem to be compatible on the local scale of the Alp and Sihl Valleys. Our suggestion contrasts the findings of Kirchner et al. (2001). They found that conventional sediment-yield measurements can significantly underestimate long-term average rates of sediment delivery. These contrasting implications highlight the need for a careful analysis when comparing erosion and sedimentation measurements from different temporal scales. This appears to be easier at the local scale of the Alp and Sihl Valleys, because geomorphic-geologic and environmental conditions usually do not change that drastically across such small scales which otherwise might explain differences. In contrast, these conditions can change significantly at larger spatial scales thereby complicating the interpretation of measurements from different time-scales.

3.7.2. General Mode – Alp Valley

The erosion and sedimentation pattern in the Alp Valley is likely lithologically controlled (Plate I). For example, we observed active sliding in areas where the Wägital Flysch is exposed, or rock-fall at rock cliffs that are often composed of massive limestone (Plate I). According to the erodibility map of Kühni and Pfiffner (2001), the Alp Valley is located at the border between rocks of medium erodibility to the south and high erodibility to the north. The Ultrahelvetic-Penninic Flysch series and Molasse units are characterized by a high erodibility, whereas Mesocoic carbonates of the Penninic units exhibit a medium erodibility (Kühni and Pfiffner, 2001). We also mapped two post-glacial landslides in an area underlain by Wägital

Flysch (Plate I). Similarly, the largest landslides in the eastern Swiss Alps cluster in the region underlain by Bündner schists and Flysch (Korup and Schlunegger, 2009).

Furthermore, the erosion and sedimentation pattern in the Alp Valley is likely structurally influenced (Plate I). We observed that valleys and ridges are parallel to thrust faults and fold axes (Plate I). Similarly, even the major Rhone and Rhine River courses in the central Western Alps are trapped by faults and thrusts (Schlunegger and Hinderer, 2001; e.g., Fig. 3.1A), or the Inn, Salzach, and Enns Valleys in the Eastern Alps are trapped by strike-slip faults (e.g., Robl et al., 2008).

Dip-slopes form natural slip surfaces facilitating active sliding. In the Alp Valley, we often observed a hummocky topography on such slopes that is a characteristic indicator for active sliding (Fig. 3.8; Plate I). The most prominent local example in this context is the Goldau landslide from 1806, ~10 km west of the Alp Valley (e.g., Zehnder 1988). It occurred on a dip-slope flank of the Rossberg mountain in an area underlain by Molasse conglomerate (Thuro et al., 2005; Thuro and Hatem, 2010). However, further examples in this context had been reported from the southern Rocky Mountains and Mackenzie Mountains in western Canada (Trenhaile, 2007), or southern New Zealand (Pearce and O'Loughlin, 1985).

Based on Alpine and local sediment-budget studies, Hinderer (2001) and Müller (1999) invoked a major change of the Alpine erosion pattern due to deglaciation. They found that post-LGM denudation rates were significantly higher than during Holocene and modern times reflecting the accelerated denudation and sediment supply during deglaciation. This is in agreement with the paraglacial model of Church and Ryder (1972), in which the increased sediment supply is due to the availability of large amounts of unconsolidated ice-marginal sediments. Also, drainage-basin scale studies of Schlunegger et al. (2002), Schlunegger and Schneider (2005) and Norton et al. (2008) in the northern Swiss Prealps revealed that the current erosion pattern initiated after the termination of the last glaciation. These findings are in line with our detailed geomorphic-geologic mapping in the Alp Valley (Plate I). Our results indicate that the change from glacial influenced erosion and sedimentation to a pattern controlled by mass wasting and fluvial processes occurred progressively from north to south in direction of glacier retreat since the LGM. For example, the late-Würmian lateral and terminal moraines at the base of the Mythen rock cliffs form a sediment trap for rock-fall debris derived from these cliffs (Plate I).

We next recognized the areal difference between the area affected by rock-fall and the area influenced by fluvial processes (Plate I; Fig. 6.2-5). We quantified this difference by comparing the corresponding erosion and deposition areas. Fluvial processes were much more efficient than rock-fall throughout the Holocene, because both erosion and deposition area related to fluvial processes are larger than those for rock-fall (Fig. 3.12). We further identified landsliding as a common process shaping the Alp Valley based on the surface area of the landslide deposit in the Erlenbach area (~1.4 km²; Plate I). This is in agreement with the dense clustering of landslides (>1 km²) in the eastern Swiss Alps (Korup and Schlunegger, 2009). In summary, our analysis indicates that simultaneously active erosion processes affect different spatial scales, and can be differentiated by their relative contribution on sculpting the modern Alp Valley landscape; fluvial processes and landsliding prevail over rock-fall processes.

We approximated Holocene delta-growth rates in the Sihl Valley, and found that sedimentation rates varied by a factor of three to five throughout the Holocene (Fig. 3.13). Furthermore, we considered these rates as a suitable erosion proxy, and propose that Holocene climate variations may have an impact on erosion in the Sihl Valley based on the pollen analysis of the post-glacial lake Sihl sediments (Küchler, 2002). Our suggestion is in agreement with e.g., Leemann and Niessen (1994) or McDonald et al. (2003). Leemann and Niessen (1994) interpreted that the sedimentary record of the Lake Silvaplana in the southeastern Swiss Alps reflects relative changes of summer air temperature during the Holocene. Also, McDonald et al. (2003) demonstrated that a period of increased alluvial fan

deposition in the Mojave Desert, California, coincided with a more humid climate during the Pleisto-Holocene transition.

Lastly, the Alp Valley landscape appears to be stable throughout the last centuries although numerous anthropogenic changes on the hydrologic system or forest cover occurred in this area (e.g., Fig. 3.14). These changes had only localized effects that had been reported so far. For example, mountain slopes and stream banks became unstable due to massive deforestation carried out by the first settlers during the 13th–15th century (Saurer, 2002; e.g., Fig. 6.2-7). Furthermore, in some places sliding processes on the Alp Valley hill-slopes are inactive at short-term scales of few hundred years in length, e.g., the western valley flank in the south appears to be inactive in contrast to the eastern flank (Stammbach, 1988; Plate I).

3.8. Conclusions

We evaluated short-term sediment transport in two pre-Alpine channel beds, the Erlenbach and Vogelbach, in context of the Alp Valley evolution throughout the Holocene. The use of a high-resolution (2 m horizontally, 1 m vertically) DEM allowed us to map erosion and sedimentation patterns in the Alp Valley in great detail, and to attempt to reconstruct the post-glacial landscape evolution on a long-term scale of thousands of years (Figs. 3.2 and 3.8; Plate I). We further attempted to supplement this reconstruction by comparing historical documents to investigate the landscape evolution over several decades to hundreds of years (e.g., Fig. 3.14). Finally, we carried out repeated photographic and high-resolution (<1 cm locally) laser-scanning campaigns to monitor channel-morphology changes and the nature of shortest-term sediment transport, on a seasonal, monthly, and daily scale (Table 3.1; Figs. 3.3–3.5 and 3.9–3.11).

At short-term scales, our results indicate that sediment transport is enhanced when a channel bed is formed on a dip-slope valley flank, e.g. Erlenbach (Figs. 3.2–3.5), in contrast to a channel cut into a non-dip-slope flank, e.g., Vogelbach (Figs. 3.8–3.11). The sediment flux through dip-slope channels is transport-limited, and that through non-dip-slope channels is supply-limited. Dip-slopes promote landsliding, which explains the transport-limited flux in the Erlenbach channel. This channel is mostly incised into an unconsolidated landslide deposit (Fig. 3.2; Plate I). In contrast, such landslides usually do not occur on non-dip-slopes explaining the supply-limited sediment flux in the Vogelbach, which incises into bedrock (Fig. 3.8; Plate I). Insofar, the interpretation of Keller and Weibel (1991), that the differences in sediment-transport activity between both streams originate from the fact that the Erlenbach incises unconsolidated landslide material and the Vogelbach bedrock, is a consequence of the contrasting geomorhic settings between both basins.

The increased short-term sediment transport in the Erlenbach compared to the Vogelbach confirms the hypothesis, that bedrock channels are more stable than gravel-bed channels (Figs. 3.3–3.5 and 3.9–3.11). The latter type of channel appears to effectively prevent bedrock erosion up to a few thousand years, e.g., ~2 ka for the Erlenbach. Taking into account that this approximation is based on the transport length of single dm- to m-sized boulders and the recurrence interval of floods with different magnitude, as well as that a ~5 m sized boulder appears to exhibit no transport during those floods deduced from a dense vegetation cover on top of the boulder (Fig. 3.3A), and that the landslide deposit is up to several tens of m thick, we conclude that the buffering effect has prevailed throughout the Holocene equal to a time-scale of ten thousand years.

On top of this, morphologic changes along a channel bed correlate with the size and frequency of an event as revealed by observations along the Erlenbach. We quantified the localized changes in the channel bed that occurred during smaller, more frequent floods (Fig. 3.4), whereas a complete reorganization of the step-pool structure occurred during exceptional floods (Turowski et al., 2009). Furthermore, there exists a temporal alternation of aggradation

and erosion along the Erlenbach stream profile. Schuerch et al. (2006) observed decadal scale aggradation of up to ~2.5 m along the lowermost ~530 m of the profile between 1993 and 2004, where Molnar et al. (2010) detected up to 3 m erosion during the June 2007 flood event. Such complex temporal alternations of aggradation and erosion along gravel-bed channels further contribute to the buffering effect discussed above.

A comparison of sedimentation rates in the Erlenbach retention basin (Fig. 3.6) with Holocene delta-growth rates in the Sihl Valley (Fig. 3.13) revealed that short- and long-term measurements of sedimentation appear to be compatible at least on the local scale of the Alp and Sihl Valleys. However, due to the differences in sediment transport along bedrock (Vogelbach) and gravel-bed (Erlenbach) channels, it requires longer monitoring of sediment transport in bedrock than in gravel-bed channels until short-term erosion rates match long-term rates. Based on our short-term sedimentation rates from the Erlenbach (Fig. 3.6), monitoring periods along gravel-bed channels can be as short as one year to match long-term rates. In contrast, during the exceptional June 2007 event increased bed-load transport had also been observed in the Vogelbach (e.g., J. Turowski, pers. comm., 2008), while we observed only minor sediment-transport activity during our monitoring (Figs. 3.9–3.11). With an estimated return period of 47 a for the June 2007 flood (Turowski et al., 2009), it becomes obvious that monitoring periods along bedrock channels on the order of tens of years are required until short-term rates would match long-term ones.

Lastly, the change from glacial influenced erosion and deposition in the Alp Valley to the current pattern dominated by mass wasting and fluvial processes occurred progressively, starting in the north and propagated to the south in direction of glacier retreat (Plate I). This is for two reasons: (i) we found fluvial gravels overlying a ground-moraine deposit in the north, and lateral and terminal moraines of late-Würmian age occur only in the south (Plate I); and (ii) these moraines located at the base of the Mythen rock cliffs form a sediment trap for rock-fall debris derived from these cliffs (Plate I). Finally, the erosion pattern of the Alp Valley also appears to be lithologically and structurally controlled, e.g., rock-fall at limestone cliffs, or sliding along dip-slopes (Plate I).

3.9. References

Allen, P.A.; 2008; From landscapes into geological history; Nature, vol. 451, p. 274–276.

Ballantyne, C.K.; 2002; Paraglacial geomorphology; Quaternary Science Reviews, vol. 21, p. 1935–2017.

Baran, R., Guest, B., and Friedrich, A.M.; 2010; High-resolution spatial rupture pattern of a multiphase flower structure, Rex Hills, Nevada: New insights on scarp evolution in complex topography based on 3-D laser scanning; Geological Society of America Bulletin, vol. 122, p. 897–914.

Buckley, S.J., Howell, J.A., Enge, H.D., and Kurz, T.H.; 2008; Terrestrial laser scanning in geology: data acquisition, processing and accuracy considerations; Journal of the Geological Society, London, vol. 165, p. 625–638.

Burch, H.; 1994; Rückblick auf die hydrologische Forschung der WSL im Alptal; Beiträge zur Geologie der Schweiz-Hydrologie, vol. 35, p. 18–33.

Church, M., and Ryder, J.M.; 1972; Paraglacial sedimentation: a consideration of fluvial processes conditioned by glaciations; Geological Society of America Bulletin, vol. 83, p.3059–3072.

Eberle, J.; 1984; Das alte Einsiedeln in Wort und Bild; Kunst- und kartenverlag Josef Eberle, Einsiedeln, Switzerland, 108 pp.

Entwistle, N.S., and Fuller, I.C.; 2009; Terrestrial laser scanning to derive the surface grain size facies character of gravel bars; *in:* Heritage, G., and Large, A.R.G. (eds.); Laser scanning for the environmental sciences; Wiley-Blackwell; p. 102–114.

Hantke, R.; 1967; Geologische Karte des Kantons Zürich und seiner Nachbargebiete; Kommissionsverlag Leemann, Zürich, Switzerland.

Hantke, R.; 1970; Die spätwürmeiszeitlichen Stadien auf der schweizerischen Alpennordseite; Eiszeitalter und Gegenwart, vol. 21, p. 71–80.

Hegg, C., and Rickenmann, D.; 1998; Short-time relations between runoff and bed load transport in a steep mountain torrent; *in:* Modelling Soil Erosion, Sediment Transport and Closely Related Hydrological Processes (Proceedings of a symposium held at Vienna, July 1998), IAHS Publication no. 249, p. 317–324.

Heritage, G., and Hetherington, D.; 2007; Towards a protocol for laser scanning in fluvial geomorphology; Earth Surface Processes and Landforms, vol. 32, p. 66–74.

Hinderer, M.; 2001; Late Quaternary denudation of the Alps, valley and lake fillings and modern river loads; Geodinamica Acta, vol. 14, p. 231–263.

Keller, H.M., and Weibel, P.; 1991; Suspended sediments in streamwater – indicators of erosion and bed load transport in mountainous basins; *in:* Sediment and Stream Water Quality in a Changing Environment: Trends and Explanation, Proceedings of the Vienna Symposium, August 1991, IAHS Publication no. 203, p. 53–61.

Kelly, M.A., Buoncristiani, J.-F., and Schlüchter, C.; 2004; A reconstruction of the last glacial maximum (LGM) ice-surface geometry in the western Swiss Alps and contiguous Alpine regions in Italy and France; Eclogae Geologicae Helvetiae, vol. 97, p. 57–75.

Kirchner, J.W., Finkel, R.C., Riebe, C.S., Granger, D.E., Clayton, J.L., King, J.G., and Megahan, W.F.; 2001; Mountain erosion over 10 yr, 10 k.y., and 10 m.y. time scales; Geology, vol. 29, p. 591–594.

Korup, O., and Schlunegger, F.; 2009; Rock-type control on erosion-induced uplift, eastern Swiss Alps; Earth and Planetary Science Letters, vol. 278, p. 278–285.

Küchler, M.; 2002; Die Moore des Sihltales; *in:* Der Sihlsee – Eine Landschaft verändert ihr Gesicht; Saurer, K.; Offizin Verlag, Zurich, Switzerland, 176 pp.

Kuhn, J.A.; 1972; Stratigraphisch-mikropaläontologische Untersuchungen in der Äusseren Einsiedler Schuppenzone und im Wägital Flysch E und W des Sihlsees (Kt. Schwyz); Eclogae Geologicae Helvetiae, vol. 65, p. 485–553.

Kühni, A., and Pfiffner, O.A.; 2001; The relief of the Swiss Alps and adjacent areas and its relation to lithology and structure: topographic analysis from a 250-m DEM; Geomorphology, vol. 41, p. 285–307.

Landgraf, A., Ballato, P., Strecker, M.R., Friedrich, A., Tabatabaeiand, S.H., and Shahpasandzadeh, M.; 2009; Fault-kinematic and geomorphic observations along the North Tehran Thrust and Mosha Fasham Fault, Alborz mountains Iran: Implications for fault-system evolution and interaction in a changing tectonic regime; Geophysical Journal International, vol. 177, p. 676–690, doi: 10.1111/j.1365-246X.2009.04089.x.

Leemann, A., and Niessen, F.; 1994; Holocene glacial activity and climatic variations in the Swiss Alps: reconstructing a continuous record from proglacial lake sediments; The Holocene, vol. 4, p. 259–268, doi: 10.1177/095968369400400305.

Lüdi, W.; 1939; Die Geschichte der Moore des Sihltales bei Einsiedeln; Veröffentlichungen des Geobotanischen Institutes Rübel in Zürich, vol. 15, 95 pp.

McDonald, E.V., McFadden, L.D., and Wells, S.G.; 2003; Regional response of alluvial fans to the Pleistocene-Holocene climatic transition, Mojave Desert, California; *in:* Enzel, Y., Wells, S.G., and Lancaster, N. (eds.); Paleoenvironments and paleohydrology of the Mojave and southern Great Basin Deserts; Geological Society of America Special Paper 368, p. 189–205.

Milzow, C., Molnar, P., McArdell, B.W., and Burlando, P.; 2006; Spatial organization in the step-pool structure of a steep mountain stream (Vogelbach, Switzerland); Water Ressources Research, vol. 42: 11 pp., doi: 10.1029/2004WR003870.

Molnar, P.; 2001; Climate change, flooding in arid environments, and erosion rates; Geology, vol. 29, p. 1071–1074.

Molnar, P., Anderson, R.S., Kier, G., and Rose, J.; 2006; Relationships among probability distributions of stream discharges in floods, climate, bed load transport, and river incision; Journal of Geophysical Research, vol. 111, 10 pp., doi: 10.1029/2005JF000310.

Molnar, P., Densmore, A.L., McArdell, B.W., and Burlando, P.; 2008; Scaling and variability in the channel morphology of steep mountain streams; *in:* Sediment Dynamics in Changing Environments (Proceedings of a symposium held in Christchurch, New Zealand, December 2008), IAHS Publication no. 325, p. 1–7.

Molnar, P., Densmore, A.L., McArdell, B.W., Turowski, J.M., and Burlando, P.; 2010; Analysis of changes in the step-pool morphology and channel profile of a steep mountain stream following a large flood; Geomorphology, vol. 124, p. 85–94.

Müller, B.U.; 1999; Paraglacial sedimentation and denudation processes in an Alpine valley of Switzerland. An approach to the quantification of sediment budgets; Geodinamica Acta, vol. 12, p. 291–301.

Norton, K.P., von Blanckenburg, F., Schlunegger, F., Schwab, M., and Kubik, P.W.; 2008; Cosmogenic nuclide-based investigation of spatial erosion and hillslope channel coupling in the transient foreland of the Swiss Alps; Geomorphology, vol. 95, p. 474–486.

Otto, J.-C., Schrott, L., Jaboyedoff, M., and Dikau, R.; 2009; Quantifying sediment storage in a high alpine valley (Turtmanntal, Switzerland); Earth Surface Processes and Landforms, vol. 34, p. 1726–1742.

Pearce, A.J., and O'Loughlin, C.L.; 1985; Landsliding during a M 7.7 earthquake: Influence of geology and topography; Geology, vol. 13, p. 855–858.

Penck, A., and Brückner, E.; 1909; Die Alpen im Eiszeitalter; Tauchnitz, Leipzig, Germany, 1199 pp.

Rees, R.; 1973; Geography and landscape painting: An introduction to a neglected field; Scottish Geographical Magazine, vol. 89, p. 147–157.

Rickenmann, D. and Dupasquier, P. 1994; Messung des Feststofftransportes im Erlenbach; Beiträge zur Geologie der Schweiz-Hydrologie, vol. 35, p. 134–144.

Rickenmann, D., and Dupasquier, P.; 1995; EROSLOPE Project EV5V-0179: Final Scientific Report; Swiss Federal Institute for Forest, Snow, and Landscape Research, Birmensdorf, Switzerland, 57 pp.

Rickenmann, D.; 1997; Sediment transport in Swiss torrents; Earth Surface Processes and Landforms, vol. 22, p. 937–951.

Rickenmann, D., and McArdell, B.W.; 2007; Continuous measurement of sediment transport in the Erlenbach stream using piezoelectric bedload impact sensors; Earth Surface Processes and Landforms, vol. 32, p. 1362–1378.

Rickenmann, D., and Fritschi, B.; 2010; Bedload transport measurements using piezoelectric impact sensors and geophones; *in:* Gray, J.R., Laronne, J.B., and Marr, J.D.G. (eds.); Bedload-surrogate monitoring technologies; U.S. Geological Survey Scientific Investigations Report 2010–5091.

Ringholz, P.O.; 1904; Einleitung - Das Gebiet des Stiftes Einsiedeln; *in:* Ringholz, P.O.; Geschichte des fürstlichen Benediktiner Stiftes U.L.F. von Einsiedeln; 1. Band; Verlagsanstalt Benziger & Co. A.-G., p. 1–24.

Robl, J., Hergarten, S., and Stüwe, K.; 2008; Morphological analysis of the drainage system in the Eastern Alps; Tectonophysics, vol. 460, p. 263–277.

Saurer, K.; 2002; Der Sihlsee – Eine Landschaft verändert ihr Gesicht; Offizin Verlag, Zurich, Switzerland, 176 pp.

Schaefer, Th., Weber, Th., Kyrinovič, P., and Zámečniková, M.; 2004; Deformation measurement using terrestrial laser scanning at the hydropower station of Gabčíkovo; INGEO 2004 and FIG Regional Central and Eastern European Conference on Engineering Surveying; Bratislava, Slovakia; 11-13November 2004; 10 pp.

Schlunegger, F., and Hinderer, M.; 2001; Crustal uplift in the Alps: why the drainage pattern matters; Terra Nova, vol. 13, p. 425–432.

Schlunegger, F., Detzner, K., and Olsson, D.; 2002; The evolution towards steady state erosion in a soil-mantled drainage basin: semi-quantitative data from a transient landscape in the Swiss Alps; Geomorphology, vol. 43; p. 55–76.

Schlunegger, F., and Schneider, H.; 2005; Relief-rejuvenation and topographic length scales in a fluvial drainage basin, Napf area, Central Switzerland; Geomorphology, vol. 69, p. 102–117.

Schlunegger, F., Norton, K., and Caduff, R.; in press; Hillslope processes in temperate environments; *in:* Shroder, J., Jr., Marston, R., and Stoffel, M. (eds.); Treatise on Geomorphology; vol. 7, Academic Press, San Diego, California, 18 pp.

Schneider, H., Schwab, M., and Schlunegger, F.; 2008; Channelized and hillslope sediment transport and the geomorphology of mountain belts; International Journal of Earth Sciences, vol. 97, p. 179–192.

Schuerch, P.; 2005; Sediment Budget of a Mountain Stream; Geological Institute, ETH Zurich, Switzerland, unpubl. diploma thesis, 83 pp.

Schuerch, P., Densmore, A.L., McArdell, B.W., and Molnar, P.; 2006; The influence of landsliding on sediment supply and channel change in a steep mountain catchment; Geomorphology, vol. 78, p. 222–235.

Simpson, G., and Schlunegger, F.; 2003; Topographic evolution and morphology of surfaces evolving in response to coupled fluvial and hillslope sediment transport; Journal of Geophysical Research, vol. 108, 16 pp., doi: 10.1029/2002JB002162.

Stammbach, M.; 1988; Rutschungen im hinteren Alptal (Kt. Schwyz); University Zurich, Switzerland, unpubl. diploma thesis, 96 pp.

Stark, C.P., Foufoula-Georgiou, E., and Ganti, V.; 2009); A nonlocal theory of sediment buffering and bedrock channel evolution; Journal of Geophysical Research, vol. 114, 14 pp., doi: 10.1029/2008JF000981.

Thuro, K., Berner, C., and Eberhardt, E.; 2005; The 1806 Goldau rock slide: failure mechanisms in interbedded conglomerates and marls; *in:* Veröffentlichungen von der 15. Tagung Ingenieurgeologie, 6.–9. April 2005, Erlangen (Friedrich-Alexander-Universität), p. 303–308.

Thuro, K., and Hatem, M.; 2010; The 1806 Goldau landslide event – analysis of a large rock slide; *in:* Williams, A.L., Pinches, G.M., Chin, C.Y., McMorran, T.J., and Massey, C.I.; Geologically active; 11th IAEG Congress, Auckland, New Zealand, 5.-10. Sept. 2010, vol. 443, p. 3693–3700.

Trenhaile, A.S.; 2007; Geomorphology – A Canadian perspective; Oxford University Press, Canada, 498 pp.

Turowski, J.M., Hovius, N., Wilson, A., and Horng, M.-J.; 2008; Hydraulic geometry, river sediment and the definition of bedrock channels; Geomorphology, vol. 99, p. 26–38.

Turowski, J.M., Yager, E.M., Badoux, A., Rickenmann, D., and Molnar, P.; 2009; The impact of exceptional events on erosion, bedload transport and channel stability in a step-pool channel; Earth Surface Processes and Landforms, vol. 34, p. 1661–1673.

Willett, S.D., Schlunegger, F., and Picotti, V.; 2006; Messinian climate change and erosional destruction of the central European Alps; Geology, vol. 34, p. 613–616.

Winkler, P.W., Wildi, W., van Stuijvenberg, J., and Caron, C.; 1985; Wägital-Flysch et autres flyschs penniques en Suisse Centrale - Stratigraphie, sédimentlogie et comparaisons; Eclogae Geologicae Helvetiae, vol. 78; p. 1–22.

Wolman, M.G., and Miller, J.P.; 1960; Magnitude and frequency of forces in geomorphic processes; Journal of Geology, vol. 68, p. 54–74.

Yager, E.M.; 2006; Prediction of sediment transport in steep, rough streams; PhD thesis, University of California, Berkeley, USA, 232 pp.

Zehnder, J.N.; 1988; Der Goldauer Bergsturz – Seine Zeit und sein Niederschlag; Stiftung Bergsturzmuseum Goldau, 272 pp.

Ziltener, L.; 2007; Sediment dynamics in a small mountain catchment from field observations and high resolution time series; Department of Earth Sciences, Swiss Federal Institute of Technology Zurich, Switzerland, unpubl. diploma thesis, 88 pp.

4. Chapter III

Sediment Transport and Erosion Rates in the Alps on Scales Ranging from Years to Millions of Years – Implications for the Variability of Mountainous Erosion

4.1. Abstract

Erosion, sediment transport, and deposition are episodic. This is due to changes in factors that relate to the magnitude of forces capable to transport material, such as flash floods, and that are endemic to sediment supply, such as the availability of material for transport. However, there is a contradiction between this actual episodicity and an apparent continuity originating from the extrapolation of short-term, basin-averaged erosion rates to longer-term scales, and the fact that longer-term measurements of erosion were similarly given as averaged rates. Since profound comparisons of erosion rates covering a variety of these scales are lacking to a certain extent in the geologic literature, we carried out such a comparison based on an approach utilized to study the spectral character of tectonic deformation. The cumulative-displacement-with-time approach allowed to directly evaluate the significance of geologic and geodetic measurements along intra-continental faults on time-scales of 10 to 10 millions years. We considered cumulative erosion with time to evaluate the long- (millions of years), medium- (thousands to ten thousand years), and short-term (years to decades) variability of erosion. Due to the availability of abundant data sets, we collected published data from the Alps to quantitatively compare erosion rates. Moreover, short-term data on bed-load transport from the small Erlenbach basin in central Switzerland enabled us to investigate the short-term characteristics of mountainous erosion. Long-term erosion in the Alps is presumably dominated by tectonic processes in accordance with results revealed by a thorough re-evaluation of the Alpine sediment budget (chapter IV). For the Western Alps, this suggestion is supported by a comparison of our cumulative erosion estimates for the last ~35 Ma with estimates derived from other data sets. For example, our estimates of up to ~32 km coincide with an approximation of ~30 km based on a restored geological 'eroded cross-section'. Medium- and short-term erosion in the Alps is mainly influenced by climatic and weather variations, respectively. Pleistocene climatic changes appear to result in changes of the prevailing erosional mode at glacial-interglacial transitions. We infer from our linear compilation that Alpine erosion rates rapidly declined during the Holocene, and associated the increased sediment transport during deglaciation immediately after the last glacial maximum to the availability of large amounts of unconsolidated sediments and high transport capacities similar to previous findings. The Erlenbach data revealed that seasonal differences in precipitation explain differences in water discharge during bed-load transport events, which in turn affect the magnitude of an event. In conclusion, our approach to evaluate cumulative erosion across a variety of spatiotemporal scales provides an efficient approach to directly compare different erosion measurements as well as to evaluate the variability of medium- and short-term mountainous erosion appropriately, but additional data covering the intermediate time-scale between our medium- and long-term scale need to be considered to allow for a better comparison between these scales.

4.2. Introduction

Erosion of mountainous regions, sediment transport, and deposition in sedimentary basins are intermittent across a variety of spatiotemporal scales (e.g., Wolman and Miller, 1960). This is due to changes in factors that affect the magnitude of forces capable to transport sediment, e.g., flash floods, and changes in factors that are endemic to sediment supply, e.g., the availability of sediment for transport (Frostick and Jones, 2002; Dühnforth et al., 2007), and the availability of water or wind as transport agent (e.g., Hugenholtz and Wolfe, 2010). Fluctuations in sediment supply can be decoded from sedimentary deposits. Large floods, for example, flush sediment into coastal areas where they are recorded in the form of noticeable packages in the deposits, or repeated incision and aggradation along a river bed can be due to the passage of sediment waves through a reach (Frostick and Jones, 2002).

The sporadic nature of fluvial processes had often been recognized during the short-term monitoring of sediment yields in mountainous rivers (e.g., Wolman and Miller, 1960; Keller and Weibel, 1991; Loizeau and Dominik, 2000). The length of these monitoring periods commonly ranges from a few years up to tens of years as, for example, in the Alps (Schlunegger and Hinderer, 2001). In the past, erosion rates based on such short-term observations were reported as basin-averaged rates (e.g., Hinderer, 2001; Vezzoli, 2004), and had often been extrapolated to longer time-scales implying continuity without temporal variations (Richards, 2002). Similarly, longer-term erosion measurements over thousands to millions of years were given as average values without considering the event character of erosion. Wittmann et al. (2007), for example, determined post-LGM (last glacial maximum) basin-averaged denudation rates in the central Western Alps using cosmogenic nuclide dating of river sediments.

The contradiction between the apparent continuity and obvious episodicity of erosion as well as the restrictive consideration of individual spatial and temporal scales hampers a comprehensive process understanding (e.g., Frostick and Jones, 2002). It therefore requires an integrated view of erosion across all scales (e.g., Jones and Frostick, 2002). A comprehensive comparison of erosion estimates from different temporal scales that also cover broader spatial scales are rarely found and discussed in the literature (e.g., Kirchner et al., 2001; Frostick and Jones, 2002). Furthermore, various methods have been established to quantify erosion at different scales and various terms are utilized to refer to erosion thereby challenging a comparison of different erosion estimates. We, therefore, compiled basic definitions of relevant terms in Table 4.1, and evaluated their significance in terms of representing rather a minimum or maximum approximation of erosion.

To conduct a comprehensive comparison of erosion estimates, we selected an approach that has been originally established to investigate the spectral character of tectonic deformation. Friedrich et al. (2003) utilized the cumulative displacement with time approach to evaluate the significance of geologic, thermochronologic, geomorphic, and geodetic measurements along intra-continental faults on time-scales from 10 to 10 million years (Fig. 4.1). This allowed the direct comparison of displacement rates from different temporal scales (Fig. 4.1). We adopted this approach and considered cumulative erosion with time to evaluate the variability of erosion at three time-scales: the long- (millions of years), medium- (thousands to ten thousand years), and short-term (years to decades) scales. We compiled published data from the Alps to compare erosion rates quantitatively. Lastly, we selected the highest-resolution temporal and spatial data based on continuity and high sampling rate of erosion measurements. One example of a well-monitored study site on the local and short-term scale is the small Erlenbach basin in the northern Swiss Prealps, which allowed us to evaluate the short-term characteristics of mountainous bed-load erosion (Fig. 4.2A). This data set is unique in the Alps because of its continuity and a generally high sampling rate of every 10 minutes since 1986 (e.g., Turowski et al., 2009). However, we recognized that in principle

at least eight of such local-scale study sites need to be evaluated to allow for a statistically representative value.

Table 4.1: Erosion terms.

Term	Definition
Weathering	In-situ process: no transport of material – destruction of rocks, minerals, and soils exposed at the Earth's surface: a) Mechanical: destruction of rocks, minerals, and soils under atmospheric conditions, e.g., heat – subsequent material transport as bed- and suspended-load b) Chemical: effect of atmospheric or biologically produced chemicals on destruction of rocks, minerals, and soils, e.g., solution – subsequent material transport as dissolved-load.
Sediment yield of rivers	Transport of material as: a) Bed-load: particle transport due to sliding, rolling, or saltation – **minimum approximation of erosion** b) Suspended-load: particle transport within flowing water detached from river bed – **minimum approximation of erosion** c) Dissolved-load: chemical dissolved material transported by flowing water – **minimum approximation of erosion.**
Sediment transport	Mass of material transported respectively exported from a certain area during a certain time – **maximum approximation of erosion.**
Sediment budget	Sediment budget as direct monitoring of erosion: mass of sediments deposited in basins to determine average erosion rates of the source terrain (Kuhlemann et al., 2001). Unknown dissolved- and suspended-load (silt to clay), and unknown effects due to re-erosion of basin deposits – **minimum approximation of erosion.**
Denudation	Loss of mass from both surface and subsurface by mechanical and chemical weathering (Corcoran & Doré, 2005) – **maximum approximation of erosion.**
Exhumation	Removal of overburden material such that previously buried rocks are exposed (Corcoran & Doré, 2005). Displacement of rocks with respect to the surface: rate of exhumation is simply rate of erosion, or rate of removal of overburden by tectonics (England & Molnar, 1990). Exhumation as erosion rate – **maximum approximation of erosion.**
Erosion	Local subaerial or submarine removal of material by mechanical and chemical processes (Corcoran & Doré, 2005). Erosional flux of a mountain belt – mass of material removed from an orogen (e.g. Willett & Brandon, 2002).

4.3. Alpine Orogeny

The Alpine orogeny is often described as a series of episodes of tectonic, metamorphic, and erosional activity from Cretaceous to Quaternary times (e.g., Kempf and Pfiffner, 2004; Schlunegger et al., 2007; Bernet et al., 2009; Handy et al., 2010). The convergence between the European and Adriatic plates started in the late Cretaceous, and resulted in the collision of both plates during the late Eocene (Schmid et al., 1996). Slab break-off occurred presumably at about 34–29 Ma (von Blanckenburg and Davies, 1995), during which the dense oceanic part of the subducting European plate was detached from its upper buoyant part (Davies and von Blanckenburg, 1995; Regard et al., 2008). However, convergence continued after the collision obvious from thrusting along the Periadriatic fault and propagation of the Helvetic nappes from 32–19 Ma, as well as foreland propagation in the Southern Alps since 19 Ma (Fig. 4.2; Schmid et al., 1996). Foreland basins formed north and south of the Alps due to continental collision and convergence since the Eocene that led to crustal thickening and loading of the subducting European plate (Fig. 4.2; e.g., Schmid et al., 1996; Andeweg and Cloetingh, 1998; Cederbom et al., 2004).

Sedimentation in the north-Alpine foreland basin, the area of the Molasse basin located north of the Alps (Fig. 4.2A; e.g., Kuhlemann and Kempf, 2002), during the Oligocene was characterized by deep marine conditions with deposition of turbidites, locally referred to as Flysch deposits (e.g., Hesse, 1975; Sinclair, 1997). In contrast, the so-called Molasse sedimentation was characterized by shallow marine conditions during the early Miocene and more continental conditions during the late Miocene (e.g., Doppler, 1989; Schlunegger et al., 2001; Kuhlemann et al., 2001). Deposition of sediments in the Molasse basin ceased between 8.5 and 4.5 Ma (Fig. 4.2A; e.g., Lemcke, 1974; Bernet et al., 2009). Parts of the basin deposits were affected by the propagating thrust front and consequently exhumed to the surface, where they are reworked since the late Miocene (e.g., Kuhlemann et al., 2001).

Sedimentation in the south-Alpine foreland basin, in principle the area of the Po basin located south of the Alps, during the early Oligocene occurred under deep marine conditions due to turbidity currents, and from late Oligocene to middle Miocene under submarine conditions along submarine fans and canyons (Fig. 4.2A; e.g., Schlunegger, 1999). Following the desiccation of the Mediterranean from 5.6–5.5 Ma, renewed sedimentation occurred under fluvial-deltaic and lagoonal conditions obvious from the stratigraphic record of the Lago Mare deposits of the Messinian salinity crisis (Willett et al., 2006).

The Mediterranean was separated from the global oceanic system during this crisis and dried out imposing a drastic base-level drop (Hsü et al. 1977). Consequently, the southern margin of the Alps exhibited massive erosion. The Alpine rivers cut deep valleys across the recent Po basin far back into the Alps due to the base-level drop of hundreds or even thousands of meters (e.g., Fig. 4.2A; Willett et al., 2006). Recently, these over-deepened valleys are filled with up to ~1 km of sediment (e.g., Hinderer, 2001), and confine the Alpine lakes of northern Italy (e.g., Bini et al., 1978). However, the Messinian base-level drop at 5.6 Ma affected only the southern flanks of the Alps, but in early Pliocene times the Danube river draining the north-Alpine foreland basin to the east until the late Miocene was captured by the Rhone river obvious from recycled Molasse and Bresse graben deposits (e.g., Cederbom et al., 2011). This in turn might have been triggered by the Messinian base-level drop affecting the Rhone river (e.g., Mocochain et al., 2009).

Exhumation in the Alps is due to a combination of normal faulting and erosion at the surface (e.g., Bernet et al., 2009) similar to other convergent orogens (e.g., Ring et al., 1999). Large extensional structures, such as the Tauern window in the Eastern Alps (Fig. 4.2A), are treated as indicators of tectonic exhumation (e.g., Schlunegger and Willett, 1999). Zircon fission-track ages of exposed bedrock show clear differences in Alpine cooling ages between the Western and Eastern Alps (Bernet et al., 2001). Cooling ages in large parts of the Western Alps are relatively young (less than 36 Ma), and older in most areas of the Eastern Alps (more than 50 Ma). However, such thermochronologic constraints often provide the basis to evaluate whether erosion, tectonics, or to which degree both are responsible for exhuming rocks from depths (e.g., Vernon et al., 2008, 2009).
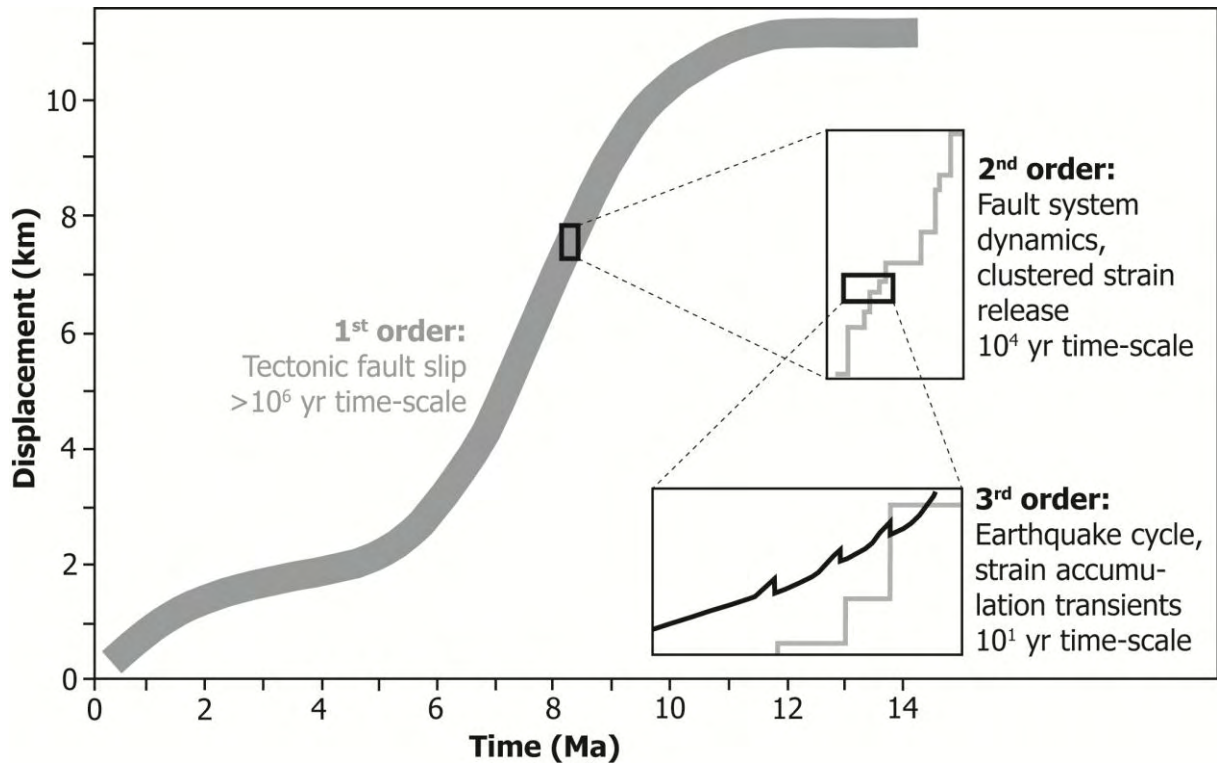
Fig. 4.1 Schematic diagram indicating the significance of tectonic, fault dynamic and transient processes on three different temporal scales (modified after Friedrich et al., 2003).
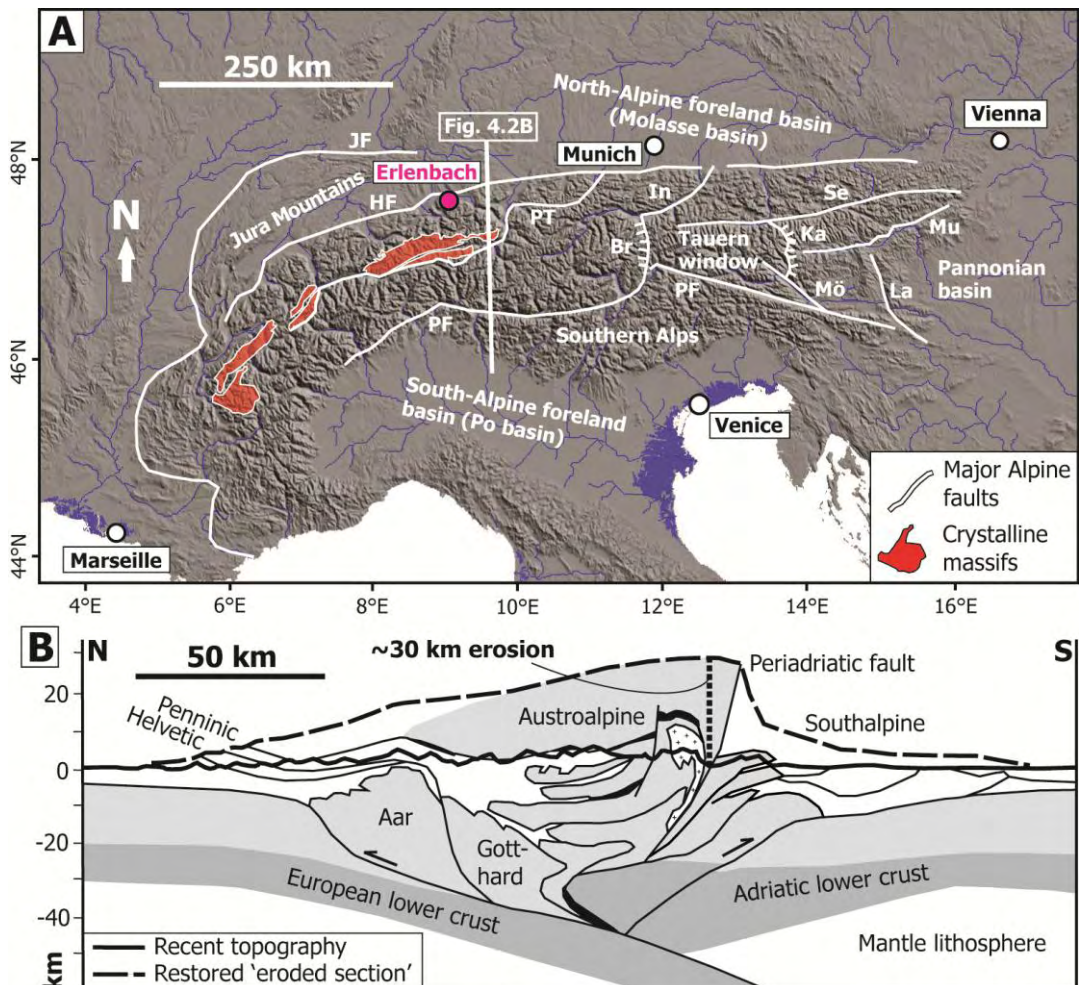
Fig. 4.2 (A) Shaded relief map of the Alps showing major geologic units and fault systems, and the location of the Erlenbach (compiled from Willett et al., 2006; Robl et al., 2008). Abbreviations: Br – Brenner fault, In – Inntal fault, Ka – Katschberg fault, La – Lavanttal fault, Mö – Mölltal fault, Mu – Mur-Mürz fault, PF – Periadriatic fault, Se – Salzachtal-Ennstal fault, JF – Jura front, HF – Helvetic front, and PT – Penninic thrust. The solid white line denotes the location of the geological transect in Figure 4.2B. **(B)** Crustal-scale geological cross-section through the Western Alps based on seismic and structural data (modified after Pfiffner et al., 2000). We highlighted the difference between recent topography (bold solid line) and the restored 'eroded section' of Pfiffner et al. (2000; bold dashed line): approximately up to 30 km had been eroded (bold dotted line) during the collision phase of the Alpine orogeny from late Eocene to present time.

4.4. Quantification of Erosion over Time

Suitable data are required to evaluate the variability of mountainous erosion. For the Alps, as one of the most extensively studied mountain belts in the world, published data covering various scales are available. We compiled data for three time-scales: the long-term scale in Table 6.3-4 (millions of years), the medium-term scale in Table 6.3-5 (thousands to ten thousand of years), and the short-term scale in Table 6.3-6 (years to decades). We found it suitable to introduce the structure of our data base first in general and add then more detail to facilitate the understanding of the outcome (Plates II–IV [see footnote 3]).

The left-hand columns in Tables 6.3-4–6.3-6 contain the original data and relevant information about location, methodology, uncertainties etc. The columns on the right-hand side contain the erosion rates that we derived by converting the original data. To follow this conversion, we provided information on the drainage area of considered basins (Table 6.3-1), erosion area (Table 6.3-2), and unit conversions (Table 6.3-3). Based on the converted erosion rates, the right-hand columns in Tables 6.3-4–6.3-6, we determined long-, medium- and short-term cumulative erosion as shown in Plates II–IV ([see footnote 3]). This is simply done by summation of erosion rates over the considered time period. For example, an erosion rate of 5 mm/a prevailing over 10 years equals 50 mm of cumulative erosion after 10 years, or a rate of 2 m/ka over the last 18 ka equals 36 m of cumulative erosion after 18 ka. When the uncertainties of erosion measurements had been published (left-hand columns in Tables 6.3-4–6.3-6), we considered them in our conversion to erosion rates (right-hand columns in Tables 6.3-4–6.3-6) and our calculation of the cumulative erosion (Plates II–IV [see footnote 3]). In Figure 4.3 we indicated the location of each data set, e.g., the location of drainage basins (Figs. 4.3B and 4.3C), and we divided the drainage basins into four classes to easily distinguish their size (inset Fig. 4.3; Table 6.3-1). Lastly, we further separated the Alpine data sets according to their location in order to better identify spatial differences in erosion (upper left corner of Fig. 4.3).

4.4.1. Long-Term and Alpine Scale

Erosion is per definition considered to be one of the processes to exhume rocks from depth to the surface of the Earth (Table 4.1; England and Molnar, 1990). Deep-seated rocks are often exposed at the surface in the central part of a mountain belt. For example, rocks from ca. 25 km depth are exposed in the Tauern window within the Eastern Alps (Fig. 4.2A; e.g., von Blanckenburg et al., 1989). We thus considered the long-term scale over millions of years for a comprehensive comparison of erosion rates across spatiotemporal scales. In the Alps, two approaches are utilized to estimate long-term rates, at which erosional and/or tectonic processes contribute to the exhumation of rocks (Plate II [see footnote 3]; Table 6.3-4).

For the first approach, thermochronological data are used to determine exhumation rates (details in e.g., von Blanckenburg et al., 1989; Fügenschuh et al., 1997; Schlunegger and

Willett, 1999; Bogdanoff et al., 2000; Bernet et al., 2001, 2009; Cederbom et al., 2004; left-hand columns in Table 6.3-4). If exhumation of deep-seated rocks occurred only due to erosion, then these exhumation rates provide a maximum approximation of long-term erosion (Table 4.1). The second approach is the sediment budget, for which the volume of sediments deposited in circum-Alpine sedimentary basins is related to the area of the Alps to derive erosion rates (e.g., Schlunegger, 1999; Kuhlemann et al., 2001; Schlunegger et al., 2001, 2007; left-hand columns in Table 6.3-4). Although these data provide a direct measure of erosion (e.g., Ring et al., 1999), they represent a minimum approximation of long-term erosion (Table 4.1). This is because material transport as dissolved- and suspended-load from the Alps toward the basins, and the effect of the erosion of already deposited material are often poorly known (Table 4.1; e.g., Kuhlemann et al., 2001). Furthermore, sediments are dispersed over hundreds to thousands of km away from an orogen, so that a comparison between the volume of eroded material and exhumation depth is rather difficult (Ring et al., 1999). Eroded material from the Alps is indeed dispersed over such distances towards the North or Black Sea (e.g., Kuhlemann et al., 2002).

We identified one source of uncertainty related to the conversion of long-term original data. The data of Kuhlemann et al. (2001) were given in km³/Ma (left-hand columns in Table 6.3-4). Our conversion to erosion rates, the right-hand columns in Table 6.3-4, is based on the current erosion area of the Alps given by Kuhlemann et al. (2001; Table 6.3-2). We do not exactly know how the erosion area changed with time, hence our converted erosion rates may either under- or overestimate actual rates by an unknown degree. However, converted erosion rates would change in response to a change of the erosion area, i.e., an increase of the erosion area by 10% would yield a decrease of the converted erosion rate by 10%. Given that we considered the typical error of 50% derived by Kuhlemann et al. (2001) when converting the sediment-budget data to erosion rates and for simplify matters, we discard this potential error in the following (Plate II; Table 6.3-4). Instead, we refer specifically to chapter IV of this thesis in which we address this issue.

4.4.2. Medium-Term and Regional Scale

We considered the medium-term scale over thousand to ten thousand years for our analysis of Alpine erosion due to the availability of various data covering this time-scale. Moreover, it represents the specific time-scale that allows to bridge the gap between the long- and short-term scale (Plate III [see footnote 3]; Table 6.3-5). We generally compiled erosion measurements from individual drainage basins, where rates are given as basin-average values, e.g., data from Hinderer (2001), Wittmann et al. (2007), and Norton et al. (2011; left-hand columns in Table 6.3-5). In contrast, the data of Valla et al. (2010) provide a localized incision rate (Plate III; left-hand columns in Table 6.3-5). Medium-term erosion rates in the Alps were either derived by approximating the sediment yield from a drainage basin based on sediment volumes trapped in valleys and Alpine lakes (e.g., Müller, 1999; Hinderer, 2001; Schlunegger et al., 2002; Korup and Schlunegger, 2009), or by approximating the denudation using cosmogenic nuclide dating of river sediments (details in e.g., Wittmann et al., 2007; Norton et al., 2008, 2011; Delunel et al., 2010; left-hand columns in Table 6.3-5). According to Table 4.1, the former approach yielded minimum and the latter one maximum approximations of medium-term erosion.

4.4.3. Short-Term and Local Scale: Alpine and Erlenbach Data

Short-term measurements of Alpine river sediment-loads over a few years up to tens of years revealed the episodic character of mountainous erosion (e.g., Keller and Weibel, 1991; Loizeau and Dominik, 2000). Hence, such data need to be considered when evaluating this

event character (Plate IV [see footnote 3]; Table 6.3-6). Nevertheless, short-term observations in the Alps are usually reported as basin- and time-averaged rates, and are based on either suspended- or bed-load data (left-hand columns in Table 6.3-6). Such rates represent minimum approximations of short-term erosion according to Table 4.1, and they are not particularly well suited to investigate the episodic nature of erosion. Local erosion measurements carried out by Descroix and Mathys (2003) using e.g., measurement sticks, over a few years are similarly not suited for this purpose, and they did not allow to calculate a meaningful basin-averaged erosion rate (Plate IV; Table 6.3-6). We further noted that the uncertainties of short-term erosion measurements are rarely constrained (Table 6.3-6). The data of Mathys et al. (2003; Plate IV; Table 6.3-6) suggest that potential uncertainties are in the range of up to 50%, and we report this approximate error in the text below in squared brackets, although we did not considered this error when converting original data to erosion rates (Table 6.3-6) and calculating the cumulative erosion (Plate IV).

Among the available data on short-term sediment transport in the Alps, the Erlenbach basin in the northern Swiss Prealps provides the unique opportunity to evaluate the short-term variability of mountainous erosion (Fig. 4.2A). From 1986–2007, continuous time series on bed-load discharge, water discharge, and precipitation are available from the Swiss Federal Institute for Forest, Snow and Landscape Research (WSL; Table 6.3-7). From 1986–1999, the intensity of bed-load transport had been recorded with piezoelectric bed-load impact sensors (PBIS; Rickenmann and McArdell, 2007). In 2000, these sensors had been replaced with geophones. This indirect monitoring of sediment transport required a calibration following Rickenmann and McArdell (2007) for the PBIS data from 1986–1999, and D. Rickenmann (pers. comm., 2008) for the geophone data from 2000–2007. We refer to the supplementing material of this chapter for details about the calibration.

The former piezoelectric bed-load impact sensors and recently running geophone systems of the Erlenbach allow to monitor indirectly and continuously bed-load discharge and its intensity. Continuous monitoring is of great advantage compared to other methods, e.g., assessing the movement of tracer particles or collecting moving particles (Rickenmann and McArdell, 2007). These methods are often limited in their temporal and spatial resolution mainly due to extensive field work and operating instrumentation (e.g., Reid et al., 1980; Habersack et al., 2001). However, we summarized the major concerns such as the need for calibration on measuring bed-load transport with piezoelectric bed-load impact sensors and geophones in the appendix (compiled from Rickenmann and McArdell, 2007; Turowski and Rickenmann, 2011).

We used linear calibration relationships, i.e., equations (A2) and (A3), to determine the bed-load discharge of individual events (Table 6.3-7). Hence, we consider a single bed-load discharge event as the shortest possible time-scale. Based on the observation of Rickenmann and McArdell (2007) that impulses recorded by bed-load impact sensor no. 3 account for 56.5% of the total number of impulses recorded by all piezoelectric bed-load impact sensors between 1986 and 1999 (details given in the appendix), we set the uncertainty related to the calculation of sediment volumes to 50% (Table 6.3-7).

The actual water level of the Erlenbach is determined with a float system adjusted to a trapezoidal channel cross-section (Burch, 1994). These gauging measurements are transferred into water discharges by using calibration curves and tables based on hydraulic laboratory experiments. The associated standard deviation is lower than 5%, and the main source of uncertainty is represented by temporarily deposited sediment changing the initial trapezoidal shape of the channel cross-section (Burch, 1994; Table 6.3-7).

Precipitation in the Erlenbach basin is recorded with totalizers collecting the precipitation volume over time, as well as compensators and/or balances measuring the precipitation rate with a resolution of 0.1 mm over time based on volume and weight of the precipitation quantity (e.g., Burch, 1994). The accuracy of conventional rain-gauge measurements is

mainly influenced by the deflection of hydrometers in the wind field above the gauge orifice, wetting of the gauge walls, evaporation from the container, and snow drift into the gauge (e.g., Frei and Schär, 1998). In Switzerland, however, the annual mean of rain gauges shows a systematic under-catch of 7% at lower elevations or protected sites, and up to 25% for wind exposed sites at higher elevations (Sevruk, 1985). On average, the annual mean under-catch for Switzerland was approximated to 8% (Sevruk, 1985; Table 6.3-7).
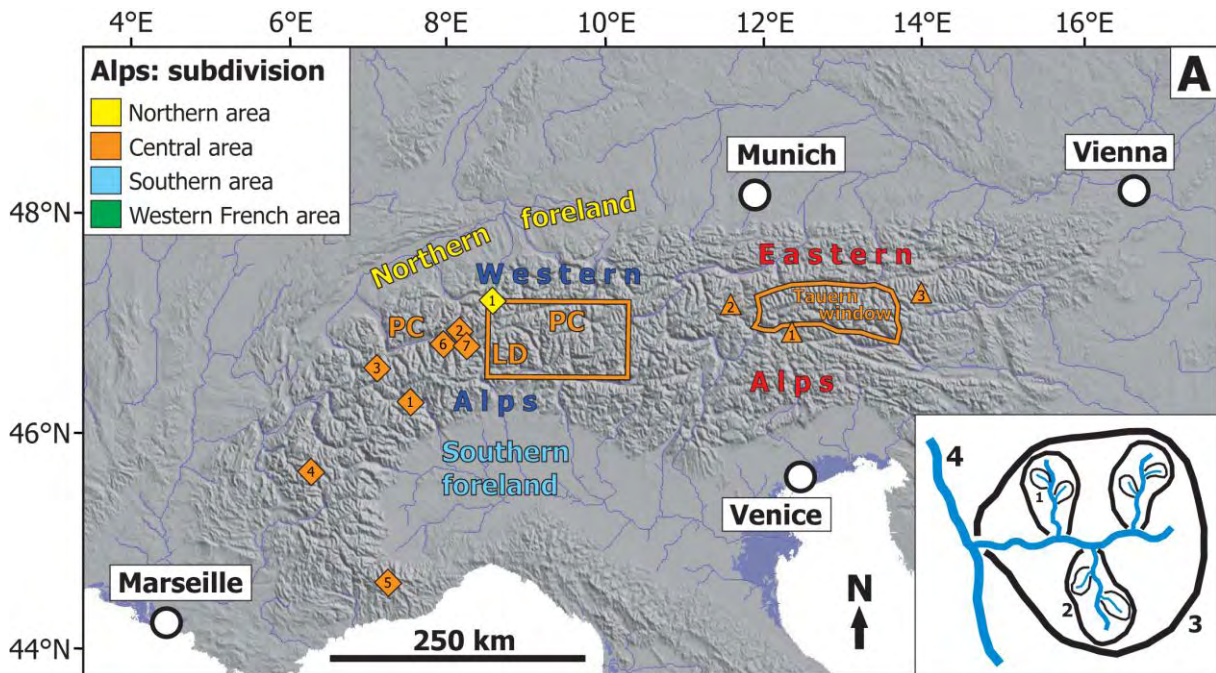
Western Alps

Kuhlemnann et al. (2001), Bernet et al. (2001 & 2009)

Northern foreland Schlunegger (1999), Schlunegger et al. (2001 & 2007), Cederbom et al. (2004), Haeuselmann et al. (2007)

◇ Aare (3)

◇ 1 Aosta Valley: Malusà & Vezzoli (2006)
◇ 2 Aar massif: Schlunegger & Willett (1999), Bogdanoff et al. (2000)
◇ 3 Mt. Blanc massif: Bogdanoff et al. (2000)
◇ 4 Pelvoux massif: Bogdanoff et al. (2000)
◇ 5 Argentera massif: Bogdanoff et al. (2000)
◇ 6 Simplon area: Clark & Jäger (1969)
◇ 7 Gotthard area: Clark & Jäger (1969)

PC Penninic crystalline: Schlunegger & Willett (1999)
LD Lepontine dome: Schlunegger (1999)
☐ Bernet et al. (2009)

Southern foreland Willett et al. (2006)

Eastern Alps

Kuhlemnann et al. (2001)

Tauern window Clark & Jäger (1969), Frisch et al. (2000), Most (2003)
western Tauern window von Blanckenburg et al. (1989), Christensen et al. (1994), Hejl (1997), Fügen-schuh et al. (1997)
south-eastern Tauern window Cliff et al. (1985), Hejl (1997)

⚠ Riesenferner pluton (Steenken et al., 2002)
⚠ West and ⚠ East of Tauern window (Frisch et al., 2000)

Drainage-basin classes

1 Small tributaries, e.g., Erlenbach (0.74 km²)

2 Moderate tributaries, e.g., Alp Valley (~ 30 km²)

3 Larger basins, e.g., Linth (~ 530 km²)

4 Major basins, e.g., Rhone (~ 5200 km²)

Alps: subdivision
- Northern area
- Central area
- Southern area
- Western French area

48°N

46°N

44°N

4°E 6°E 8°E 10°E 12°E 14°E 16°E

B

Munich

Vienna

Venice

Marseille

250 km

N

4
1
2
3
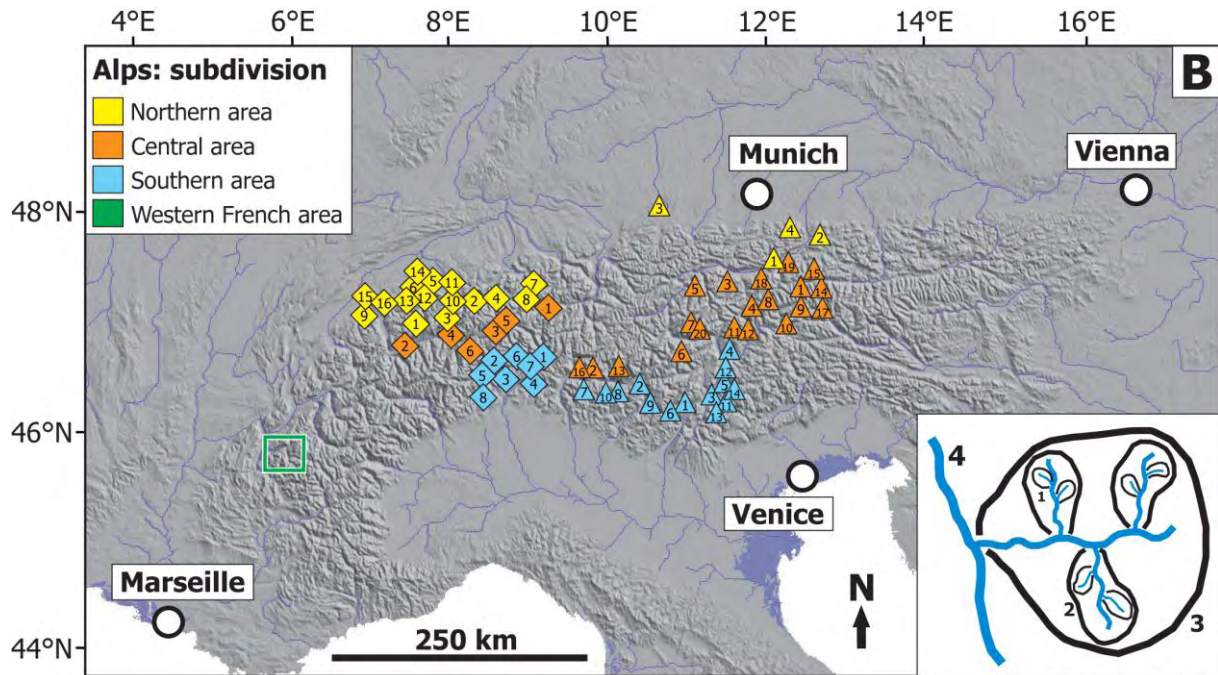
Western Alps

1 Lütschine (3)	1 Rhine (4)
2 Reuss (3)	2 Rhone (4)
3 Aare (3)	3 Chie (3)
4 Linth (3)	4 Lonza (2)
5 Klem (3)	5 Furka (2)
6 Emme (3)	6 Gren (1)
7 Walen lake Valley (3)	
8 Seez (3)	1 Ticino (3)
9 Sense (3)	2 Toce (3)
10 Melchaa (2)	3 Mela (3)
11 Fischenbach (2)	4 Adda (3)
12 Fontanne (2)	5 Anza (3)
13 Trub (2)	6 Maggia (3)
14 Wasen (2)	7 Verz (3)
15 Taf (2)	8 Sesia (3)
16 Buetsch (2)	

Delunel et al. (2010) and Valla et al. (2010)

Eastern Alps

1 Inn (4)	1 Krimmler (3)
2 Tiroler Ache (3)	2 Masino (3)
3 Iller (3)	3 Melach (3)
4 Weissach (2)	4 Pfitsch (3)
	5 Pitze (3)
1 Sarca (3)	6 Plima (3)
2 Oglio (3)	7 Schnalz (3)
3 Nero (3)	8 Zemm (3)
4 Talfer (3)	9 Ahrn (2)
5 Avisio (3)	10 Antholzer (2)
6 Arno (2)	11 Bergler (2)
7 Bitto (2)	12 Flagger (2)
8 Castello (2)	13 Fusino (2)
9 di Adame (2)	14 Hoeller (2)
10 di Venina (2)	15 Mhl (2)
11 Fersina (2)	16 Novate (2)
12 Lagorai (2)	17 Tauern (2)
13 Silla (2)	18 Watten (2)
14 val Moena (2)	19 Widshoenau (2)
	20 Ziel (2)

Drainage-basin classes

1 Small tributaries, e.g., Erlenbach (0.74 km²)

2 Moderate tributaries, e.g., Alp Valley (~ 30 km²)

3 Larger basins, e.g., Linth (~ 530 km²)

4 Major basins, e.g., Rhone (~ 5200 km²)

Alps: subdivision
- Northern area
- Central area
- Southern area
- Western French area

Western Alps

1 Lütschine (3)	1 Rhine (4)	
2 Linth (3)	2 Rhone (4)	
3 Glatt (3)	3 Hinterrhine (3)	
4 Thur (3)	4 Albula (3)	
5 Emme (3)	5 Dora Baltea (3)	
6 Reuss (3)	6 Visp (3)	
7 Simme (3)	7 Landquart (3)	
8 Broye (3)	8 Lonza (2)	
9 Kander (3)		
10 Sarine (3)	1 Maggia (3)	
11 Aare (3)	2 Ticino (3)	
12 Melchaa (2)	3 Moesa (3)	
✦ Erlenbach (1)	4 Cassarate (2)	

Descroix & Mathys (2003) and Mathys et al. (2003)

1 Arve (3)

Eastern Alps

1 Inn (4)
2 Tiroler Ache (3)
3 Iller (3)
4 Ammer (3)
5 Weissach (2)

Drainage-basin classes

1 Small tributaries, e.g., Erlenbach (0.74 km²)

2 Moderate tributaries, e.g., Alp Valley (~ 30 km²)

3 Larger basins, e.g., Linth (~ 530 km²)

4 Major basins, e.g., Rhone (~ 5200 km²)

Fig. 4.3 Shaded relief map of the Alps showing the location of reviewed data for the three different time-scales: (**A**) long-term, (**B**) medium-term, and (**C**) short-term scale. The inset in the lower right corner shows a simplified sketch to illustrate our classification of the drainage-basin size.

---

[3] Plates II, III, and IV are contained in the envelope attached at the inside of the back-cover.

4.5. Results

4.5.1. Long-Term and Alpine Scale Erosion

Plate II contains the results of our approximation of long-term cumulative erosion in the Western and Eastern Alps. We first converted the original sediment-budget and exhumation data contained in the left-hand columns of Table 6.3-4 to erosion rates given in km/Ma contained in the right-hand columns of Table 6.3-4. We then calculated the long-term cumulative erosion over time as described above (km over millions of years; Plate II).

Sediment-budget based erosion estimates for the Western Alps are significantly higher than for the Eastern Alps. Estimates based on the data of Kuhlemann et al. (2001) range between ~15–50 km in the Western Alps after 34 Ma (dark blue curve in Plate IIA) and ~1–5 km in the Eastern Alps after ~33 Ma (red curve in Plate IIB). We observed a broad overlap between exhumation and sediment-budget based erosion estimates in the Western Alps (Plate IIA). In particular, exhumation based estimates for the central Western Alps (orange data points in Plate IIA) overlap with sediment-budget based estimates for the entire and northern area of the Western Alps (dark blue and yellow curves in Plate IIA). In some cases, however, the sediment-budget based estimates are even greater than the exhumation ones (Plate IIA). Exhumation and sediment-budget based erosion estimates in the Eastern Alps are in the same range during the last 15 Ma (overlap between orange data points and red curve in Plate IIB), and show a simultaneous increase at 15–20 Ma (Plate IIB). From 20–35 Ma, exhumation based estimates are greater than the sediment-budget based ones (Plate IIB).

4.5.2. Medium-Term and Regional Scale Erosion

To estimate the cumulative medium-term erosion in the Western and Eastern Alps illustrated in Plates IIIA respectively IIIB, we converted published data on sediment yield and denudation, left-hand columns in Table 6.3-5, to erosion rates in m/ka, right-hand columns in Table 6.3-5. Based on these rates, we then determined the medium-term cumulative erosion over time as mentioned previously (m over thousands of years; Plates IIIA and IIIB).

Medium-term erosion rates increase with drainage-basin size, e.g., the large Inn basin exhibited a higher rate with 0.57±0.29 m/ka than the small Weissach basin with 0.42±0.21 m/ka throughout the last 17 ka (Fig. 4.3B and Plate IIIB). Furthermore, erosion rates in the central Western Alps are generally greater than in the northern and southern Western Alps (orange data points compared to yellow and light blue ones in Plate IIIA). Similarly in the Eastern Alps, erosion rates in the central area are slightly higher than in the southern area; rates range between 0.3±0.06 to 1.47±0.34 m/ka in the central area, and between 0.17±0.05 to 1.04±0.23 m/ka in the southern area (orange data points compared to light blue ones in Plate IIIB). Medium-term rates for Bündner schists and Flysch exposed in the Rhine basin are four times as much as for crystalline rocks during the last 9.5–12 ka; 4±2 m/ka for the former compared to 0.7±0.35 m/ka for the latter (Plate IIIA; Korup and Schlunegger, 2009).

Finally, the high erosion estimate for the Gorge du Diable in the western French Alps represents a localized incision rate (green data points with number 1 in Plate IIIA). In contrast, since medium-term erosion estimates based on sediment yield and cosmogenic nuclide data provide basin-averaged values and cover similar ranges (Plates IIIA and IIIB), we compiled those results again in Plate IIIC. We indicated a decreasing trend that we observed for cumulative medium-term erosion estimates with a gray arrow (Plate IIIC).

4.5.3. Short-Term and Local Scale Erosion

Plate IV (without inset) contains the results of our calculation of short-term cumulative erosion in the Alps. For this, we converted the published data on sediment transport, left-hand columns in Table 6.3-6, to erosion rates in mm/a, right-hand columns in Table 6.3-6. These rates in turn provide the base to determine the short-term cumulative erosion over time as outlined above (mm over years; Plate IV). We similarly estimated the cumulative erosion for the Erlenbach basin using the data of the bed-load transport events that occurred in this basin (red curve in Plate IV; Table 6.3-7). We further evaluated cumulative frequency distributions for these events by separating the data for bed-load discharge, water discharge, and precipitation into seasons, and comparing the seasonal frequency distributions with the total one (Fig. 4.4).

Short-term cumulative erosion in the Alps can be separated into two fields (Plate IV without inset). First, erosion in the western French Alps is high with rates between ~2.1±0.9 mm/a (Moulin, 1988–2000) and 33±[17] mm/a (Izon la B., 1990–1995; green data points in Plate IV). Second, erosion in the remaining Alps occurs with rates of less than 1±[0.5] mm/a (Plate IV). Erosion rates generally increase with drainage-basin size (Plate IV). In the Eastern Alps, for example, the large Inn basin exhibits a higher rate of 0.1±[0.05] mm/a (1953–1979) than the small Weissach basin with 0.04±[0.02] mm/a (1955–1965). Furthermore, short-term rates are approximately twice as much in the central (orange data points in Plate IV) than in the northern and southern area of the Western Alps (yellow and light blue data points in Plate IV).

Short-term monitoring periods of erosion are on average much longer in the Western and Eastern Alps than in the western French Alps spanning several decades (Plate IV). The highest erosion rates observed in the western French Alps were based on localized measurements, e.g., measurement sticks and slope profiles. In contrast, basin-outlet measurements of bed- and suspended-load in the remaining Alps yielded lower erosion rates that represent basin-averaged values (Plate IV). Moreover, erosion estimates based on suspended- and bed-load measurements yielded both similar values (Plate IV). For the Ticino and Maggia basins in the southern Western Alps, however, we observed that delta-growth data yielded lower erosion rates based on a longer monitoring period (Ticino: 0.1±[0.05] mm/a, 1932–1986; Maggia: 0.17±[0.85] mm/a, 1926–1984) than suspended-load data that yielded higher rates based on a shorter monitoring period (Ticino: 0.22±[0.11] mm/a; 1979–1995; Maggia: 0.27±[0.14] mm/a, 1985–1993; Plate IV).

Short-term erosion in the Erlenbach from 1986–2007 is characterized by periods of increased erosion that alternate with periods of less erosion (red curve in Plate IV). To better understand this temporal variation, we compared the seasonal frequency distributions with the total one (Fig. 4.4). We observed that: (i) summer distributions show the greatest similarity with the total distribution; and (ii) spring and autumn distributions are quite similar, and plot between the summer and winter distributions. In summary, events with the greatest bed-load and water discharge as well as precipitation amount occur in summer, whereas events with the lowest values occur in winter.

4.6. Interpretation and Significance of Individual Scales

4.6.1. Long-Term and Alpine Scale Erosion

We expected that exhumation based cumulative erosion estimates for the Alps would be in the range of sediment-budget based estimates according to the definition, that exhumation is the rate of erosion plus the rate of removal of overburden by tectonics (Table 4.1; England and Molnar, 1990). Or, that exhumation based erosion estimates would be greater than the

sediment-budget based estimates. However, based on our long-term erosion estimates we found major differences between the Western and Eastern Alps (Plate II). For the Western Alps, we observed both an overlap between exhumation and sediment-budget based erosion estimates, and that the latter estimates are even greater than the exhumation based estimates (Plate IIA). This latter observation contradicts our expectation, and suggests that the definition of England and Molnar (1990) cannot easily be applied to the Western Alps (Table 4.1). For the Eastern Alps, we observed an overlap between exhumation and sediment-budget based erosion estimates over the last 15 Ma, whereas from 20–35 Ma exhumation based erosion estimates are greater than sediment-budget based estimates (Plate IIB). These observations agree with our expectation, and thus the definition of England and Molnar (1990; Table 4.1) can be applied to the Eastern Alps.

We extracted three cumulative erosion estimates derived for the Eastern Alps from Plate IIB to illustrate the implications, if the definition of England and Molnar (1990; Table 4.1) can be applied or not (Fig. 4.5). Erosion estimates are either based on sediment budget (red in Fig. 4.5) or exhumation (orange in Fig. 4.5) data. In this example, exhumation based estimates are greater than the sediment-budget based estimate from 13–30 Ma (Fig. 4.5). Thus, the definition of England and Molnar (1990; Table 4.1) can be applied here. Since sediment-budget data, as those of the Alps (Kuhlemann et al., 2001), are a direct measure of erosional exhumation (e.g., Ring et al., 1999), we highlighted the term erosion in red (Fig. 4.5). From the difference between exhumation and sediment-budget based estimates, we approximated the tectonic signal contributing to exhumation (blue in Fig. 4.5). In the other case, when the definition of England and Molnar (1990; Table 4.1) cannot be applied, exhumation based estimates simply represent tectonic measurements, and sediment-budget based estimates are measurements of erosion (Fig. 4.5). However, we interpret that tectonic processes are the major process in the Eastern Alps to exhume rocks from depth whether the definition of England and Molnar (1990; Table 4.1) can be applied or not.

In the Western Alps, exhumation based estimates are sometimes lower than sediment-budget based erosion estimates contradicting our expectation based on the definition of England and Molnar (1990; Table 4.1; Plate IIA). Hence, our suggestion that the definition cannot be applied in this case implies, that exhumation based estimates are tectonic measurements, and sediment-budget based estimates are erosion measurements as indicated in Figure 4.5. However, we interpret that erosion and tectonic processes occurred at similar rates in the Western Alps based on the overlap between exhumation and sediment-budget based estimates that we also observed (Plate IIA).

4.6.2. Medium-Term and Regional Scale Erosion

Medium-term cumulative erosion in the Alps decreased throughout the Holocene (Plate IIIC). Our observation coincides with a decrease of sedimentation rates determined in the Walen lake Valley (Müller, 1999) as well as a decrease of the Alpine sediment yield (Hinderer, 2001) during the Holocene. We interpret that this decrease is due to a change from glacially-dominated erosional processes to a fluvially-dominated erosion pattern during deglaciation after the LGM according to the paraglacial model of Church and Ryder (1972).

Repeated glaciations of the Alps occurred due to Pleistocene climate changes (e.g., Muttoni et al., 2003). However, during glaciations glacial erosion processes prevail, while fluvial processes dominate during interglacials. A change of the erosional mode thus occurs at the transition between glacials and interglacials, and appears to culminate in increased erosion at this time as suggested by the Alpine data (Plate IIIC). The paraglacial model of Church and Ryder (1972) explains increased sediment transport at the end of a glacial and beginning of an interglacial. It implies low transport rates prior and after deglaciation, and high rates during

deglaciation mainly due to the availability of large amounts of unconsolidated sediments and high transport capacities (Hinderer, 2001).

Based on these considerations and in agreement with the definition given in Table 4.1, we deduced a theoretical model characterized by decreasing sediment-transport rates during the time of glacials and interglacials, and increased rates at the transitions between both (dashed gray line in Fig. 4.6A). This would yield a step function of cumulative erosion during the late Pleistocene as shown by the dashed gray line in Figure 4.6B. Alpine medium-term erosion estimates compiled in Plate IIIC agree with our suggestion (Fig. 4.6B). Furthermore, sediment-transport data determined by Hinderer (2001) for the last 140 ka from Quaternary and post-LGM sediment volumes are similarly in agreement with the model (black, solid thin line in Fig. 4.6). These data show considerable increases of sediment transport at the transition between glacials and interglacials. Nevertheless, we note that further data are required to validate the theoretical model.

4.6.3. Short-Term and Local Scale Erosion

We found significant differences in short-term erosion throughout the Alps with much higher erosion rates of up to 33±[17] mm/a in the western French Alps (e.g., Descroix and Mathys, 2003), and lower rates of less than 1±[0.5] mm/a in the remaining Alps (e.g., Hinderer, 2001; Plate IV). Two aspects can be related to this difference, the monitoring length and the type of measurement. First, the short-term erosion estimates in the western French Alps are based on very short observation periods of only a few years in length (e.g., Descroix and Mathys, 2003), but the longer this period is the smaller is the erosion rate (green data points in Plate IV). Accordingly, the lower rates detected elsewhere in the Alps are usually based on much longer monitoring periods of up to several decades in length (Plate IV; Table 6.3-5). Second, erosion estimates from the western French Alps are based on very localized measurements, e.g., point measurements with sticks or slope profiles (Descroix and Mathys, 2003). These estimates are thus not representative for an entire drainage basin, whereas short-term erosion estimates from elsewhere in the Alps based on basin-outlet measurements can be considered as basin-average values.

That the length of monitoring and the type of measurement affect the approximation of short-term erosion rates is further supported by observations for the Ticino and Maggia basins in the southern Western Alps. Delta-growth data from Hinderer (2001) revealed lower erosion rates for a longer monitoring period (Ticino: 0.1±[0.05] mm/a, 1932–1986; Maggia: 0.17±[0.85] mm/a, 1926–1984) than suspended-load data from Schlunegger and Hinderer (2003) that yielded higher rates for much shorter periods (Ticino: 0.22±[0.11] mm/a; 1979–1995; Maggia: 0.27±[0.14] mm/a, 1985–1993; Plate IV). These results suggest that long monitoring periods are required to determine a short-term erosion rate that would be comparable to a medium-term one. However, Kirchner et al. (2001) noted that even conventional sediment-yield measurements made over several decades can greatly underestimate longer-term average rates of sediment delivery based on a comparison of short- and long-term erosion measurements in the Idaho Mountains.

According to the definitions given in Table 4.1, delta-growth measurements do not consider suspended- and dissolved-load, and suspended-load measurements do not consider bed- and dissolved-load. Hence, both measurements considered alone represent minimum approximations of erosion. The suspended-load of Alpine rivers appears to be greater than the bed-load, since delta growth based erosion rates of the Ticino and Maggia basins are lower than suspended-load based rates (Plate IV). Simultaneously, however, the available short-term data for the Alps indicate that low rates whether based one suspended- or bed-load are in the same range (Plate IV). Even if bed- and suspended-load data for a single basin are available and added, the resulting erosion rate most likely will not exceed 1±[0.5] mm/a, e.g., the

Ticino basin with 0.1±[0.05] mm/a from bed-load data (1932–1986) and 0.22±[0.11] mm/a from suspended-load data (1979–1995; Plate IV).

Finally and most importantly, the Erlenbach data clearly indicate that short-term erosion is characterized by alternating periods of increased and decreased activity (Plate IV). In this context, the episodic character of short-term erosion can be approximated with a step function (inset Plate IV). Furthermore, the shape of this function is influenced by seasonal weather differences. Events with the greatest bed-load discharge occur in summer, whereas the smallest events occur in winter as revealed by seasonal frequency distributions (Fig. 4.4). Accordingly, steps with the greatest height are produced by events that occurred during summer (inset Plate IV).

Plate II Cumulative long-term erosion based on published Alpine data: **(A)** Western Alps, and **(B)** Eastern Alps. Associated errors are marked by colored boxes. When original data were reported as a range of values, we also determined a range of erosion rates. To visualize such a range, we connected data points of the lower cumulative erosion curve and points of the upper curve by thin lines. The actual cumulative curve should then vary between the lower and upper limit indicated by the colored area. The location of the studied areas is shown in Figure 4.3A. The figure is contained in the envelop attached at the inside of the back-cover.

Plate III Cumulative medium-term erosion based on published Alpine data: **(A)** Western Alps, and **(B)** Eastern Alps. Associated errors are marked by colored boxes. The location of the drainage basins is shown in Figure 4.3B. **(C)** Cumulative medium-term erosion of Western and Eastern Alps derived from sediment yield and cosmogenic nuclide data only, compiled from Plates IIIA and IIIB. The decreasing trend of erosion estimates is highlighted with the gray arrow. The figure is contained in the envelop attached at the inside of the back-cover.

Plate IV Cumulative short-term erosion based on published Alpine data. We also included the cumulative erosion based on event data of the Erlenbach from 1986–2007 (inset diagram). The location of the drainage basins is shown in Figure 4.3C. The figure is contained in the envelop attached at the inside of the back-cover.
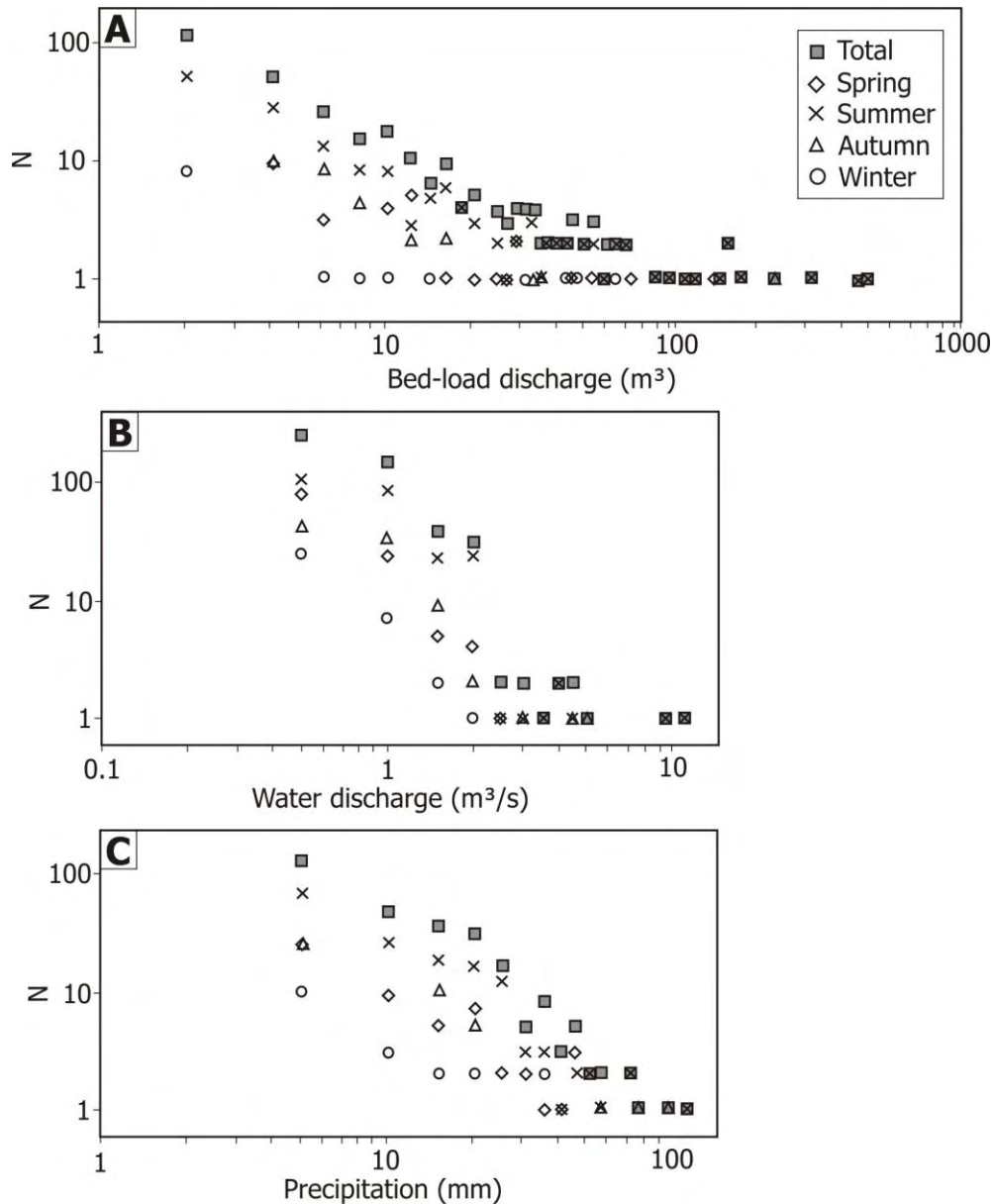
Fig. 4.4 Seasonal and total cumulative frequency plots for bed-load discharge **(A)**, peak-water discharge **(B)**, and precipitation **(C)** of the Erlenbach event data to characterize the temporal variability of erosion from 1986–2007. Data provided by the Swiss WSL.

4.7. Erosion Across Scales

For a comparison of erosion rates across spatiotemporal scales, we reviewed the significance of erosion rates that we calculated for the different scales considered in this study. The majority of Alpine short- and medium-term erosion rates can be compared with each other (right-hand columns of Tables 6.3-5 and 6.3-6). This is because most of the short-term erosion rates are derived from suspended- and bed-load data (Plate IV, Table 6.3-6), and most of the medium-term erosion rates are based on sediment yield and cosmogenic nuclide data (Plate IIIC, Table 6.3-5). As outlined previously, all these measurements yielded basin- and time-averaged erosion rates. The bed-load transport data of the Erlenbach compiled in Table 6.3-7 represent basin-outlet measurements. At the same time, these data allow for evaluating the episodic nature of erosion (inset Plate IV and Fig. 4.4) as well as for determining basin-averaged erosion rates (red curve in Plate IV). Moreover, the short- and

medium-term erosion rates derived from sediment-yield data can in principle also be compared to long-term erosion rates derived from sediment-budget data, because in all three cases a volume of transported material is related to a specific erosion area. However, since different processes dominate the signal on the long-term scale, we did not compared the short- and medium-term rates with the long-term ones.

Long-term Alpine erosion estimates derived from sediment-budget data (Plate II; e.g., Kuhlemann et al., 2001) are in principle similar to the tectonic fault slip in Figure 4.1. These cumulative erosion estimates define the erosional flux from an orogen according to the orogenic wedge model (Fig. 4.7; e.g., Willett et al., 1993). In the Western Alps, Pfiffner et al. (2000) evaluated the linkage between the accretionary and erosional flux using numerical forward modelling. Their results indicate that long-term erosion in the Alps depends on the convergence between the European and Adriatic plates. Average denudation rates of 1.5 mm/a are equal to 15 km of denudation per 100 km convergence, and maximum rates of 3 mm/a translate into 30 km of denudation per 100 km convergence (Pfiffner et al., 2000). Their results agree reasonably well with our long-term erosion estimates for the Western Alps (Plate IIA). An approximation of erosion derived from a restored 'eroded' geological cross-section through the Western Alps yielded a similar value of ~30 km (Fig. 4.2B; Pfiffner et al., 2000). From our evaluation of the applicability of the definition of exhumation to the Alps (Table 4.1; Molnar and England, 1990), we interpreted that tectonic processes control the long-term erosion in the Alps (e.g., Fig. 4.5).

Our interpretation is further supported by results based on a renewed analysis of the Alpine sediment budget (Kuhlemann et al., 2001; chapter IV). Sediment-budget based erosion estimates in the Western Alps document increased erosion over the last 5 Ma (yellow and dark blue curves in Plate IIA). This increase is presumably due to a tectonically induced uplift of the Alpine foreland basins that caused a lowering of the regional base-level. Subsequent head-ward erosion by rivers draining the Alpine foreland occurred across the basins thereby removing substantial amounts of Alpine derived material deposited in the foreland basins prior to 5 Ma (further details in chapter IV).

Medium-term erosion rates in the Alps are generally greater than the short-term ones (Plate IIIC compared to Plate IV). This suggests a decreasing trend of erosion rates throughout the Holocene, which is already obvious when only the relevant medium-term erosion estimates are considered (Plate IIIC). Drainage basins in the Eastern Alps, for example, exhibit two to ten times greater medium-term rates (Plate IIIB compared to Plate IV). Here, the medium-term rate for the Inn basin is approximately six times greater than the short-term one (0.57±0.29 m/ka for the last 17 ka compared to 0.1±[0.05] mm/a from 1953–1979), or the medium-term rate for the Weissach basin is ten times greater than the short-term one (0.42±0.21 m/ka for the last 17 ka compared to 0.04±[0.02] m/ka from 1955–1965). The declining trend appears to be independent of the size of the drainage basin, because the sizes of the Inn and Weissach basins differ by two orders of magnitude according to our drainage-basin classification (Figs. 4.3B and 4.3C; Table 6.3-1).

However, medium-term cumulative erosion can be approximated with a step-like function (e.g., Fig. 4.6B). This function is analogous to the cumulative displacement characterizing fault-system dynamics (Fig. 4.7 compared to Fig. 4.1). The shape of the step function appears to be influenced by the change of the dominating erosional mode at glacial-interglacial transitions due to Pleistocene climate changes (Fig. 4.6B; e.g., Muttoni et al., 2003), because variations in temperature and precipitation affect the extent of glaciers. We ascribed the increased sediment transport during deglaciation to the availability of large amounts of unconsolidated sediments and high transport capacities (Plate IIIC and Fig. 4.6; e.g., Müller, 1999; Hinderer, 2001).

Based on the Erlenbach data (inset Plate IV), we determined a step function of cumulative erosion at the short-term scale. This function is basically similar to that derived for the

earthquake cycle except that the time-scale of an 'erosion cycle' is shorter than for an earthquake cycle (Fig. 4.1 compared to Fig. 4.7). The shape of the erosional step function depends on seasonal weather differences as revealed by the Erlenbach data (e.g., inset Plate IV). These differences are due to differences in temperature and precipitation (Fig. 4.4). The amount of precipitation in turn influences water discharge, and the magnitude of an erosional event depends on water discharge (e.g., Turowski et al., 2011) as well as the availability of material for transport (e.g., Keller and Weibel, 1991).

In summary, our rigorous analysis of the applicability of the exhumation definition to the Alps implies, that tectonic processes play a dominant role to exhume rocks from depth (Fig. 4.5; Table 4.1). This is supported by a comparison of our long-term erosion estimates with estimates derived from numerical modeling and crustal-scale structural data (Plate II compared to Fig. 4.2B; Pfiffner et al., 2000). Moreover, our review of Alpine erosion rates indicates that not all of the data can be explained with linear, averaged rates of erosion. At the medium- and short-term scale, erosion can be approximated with a step function to constrain the actual magnitude of the process (inset Plate IV and Fig. 4.6B). Alpine medium-term erosion data are characterized by a great variability that results from repeated changes of the prevailing erosional mode due to Pleistocene climate changes (Plate IIIC and 4.6). Short-term erosion rates exhibit a pronounced variability mainly due to seasonal weather differences as revealed by the Erlenbach data (inset Plate IV and Fig 4.4). We further determined a basin- and time-averaged erosion rate for the Erlenbach basin (red curve in Plate IV), and compared it with the un-averaged curve (inset Plate IV), and Alpine short-term erosion rates estimated with linear trends (Plate IV without inset). The averaged Erlenbach curve has the same shape as the un-averaged one except that it is smoother (Plate IV). Thus, the short-term variability of mountainous erosion can still be detected when using averaged erosion rates, but it cannot when these rates are approximated with linear trends (Plate IV). Lastly, it is rather difficult to infer longer-term erosion rates from short-term erosion data judging from our previous evaluation of the significance of Alpine short-term erosion measurements. Long monitoring periods of several tens of years are most likely required to measure an erosion rate that can approximate a longer-term one. Even then, this rate can greatly underestimate the longer-term rate (e.g., Kirchner et al., 2001).
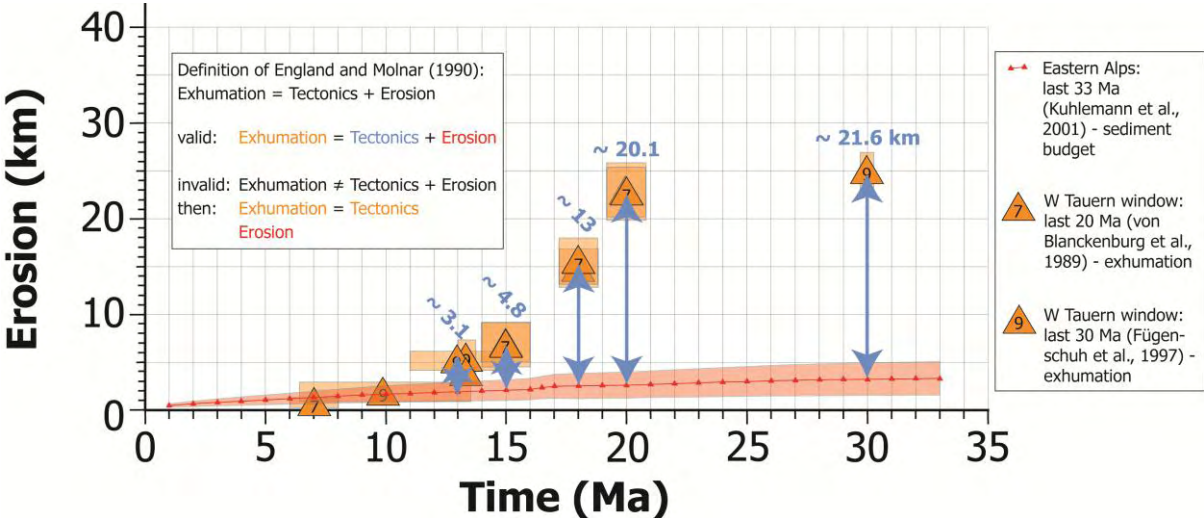
Fig. 4.5 Selected cumulative erosion estimates of the Eastern Alps from Plate IIB based on sediment budget (in red) and exhumation (in orange) data to clarify the difference between validity and invalidity of the definition for exhumation given by England and Molnar (1990; Table 4.1). Sediment-budget data represent a direct measure of erosional exhumation following e.g., Ring et al. (1999). Hence, the term erosion is highlighted in red in both cases of validity and invalidity of the definition. If the definition can be applied, then the tectonic signal can be reconstructed indicated in blue. If the definition cannot be applied, then exhumation based estimates represent a measure of tectonic deformation.
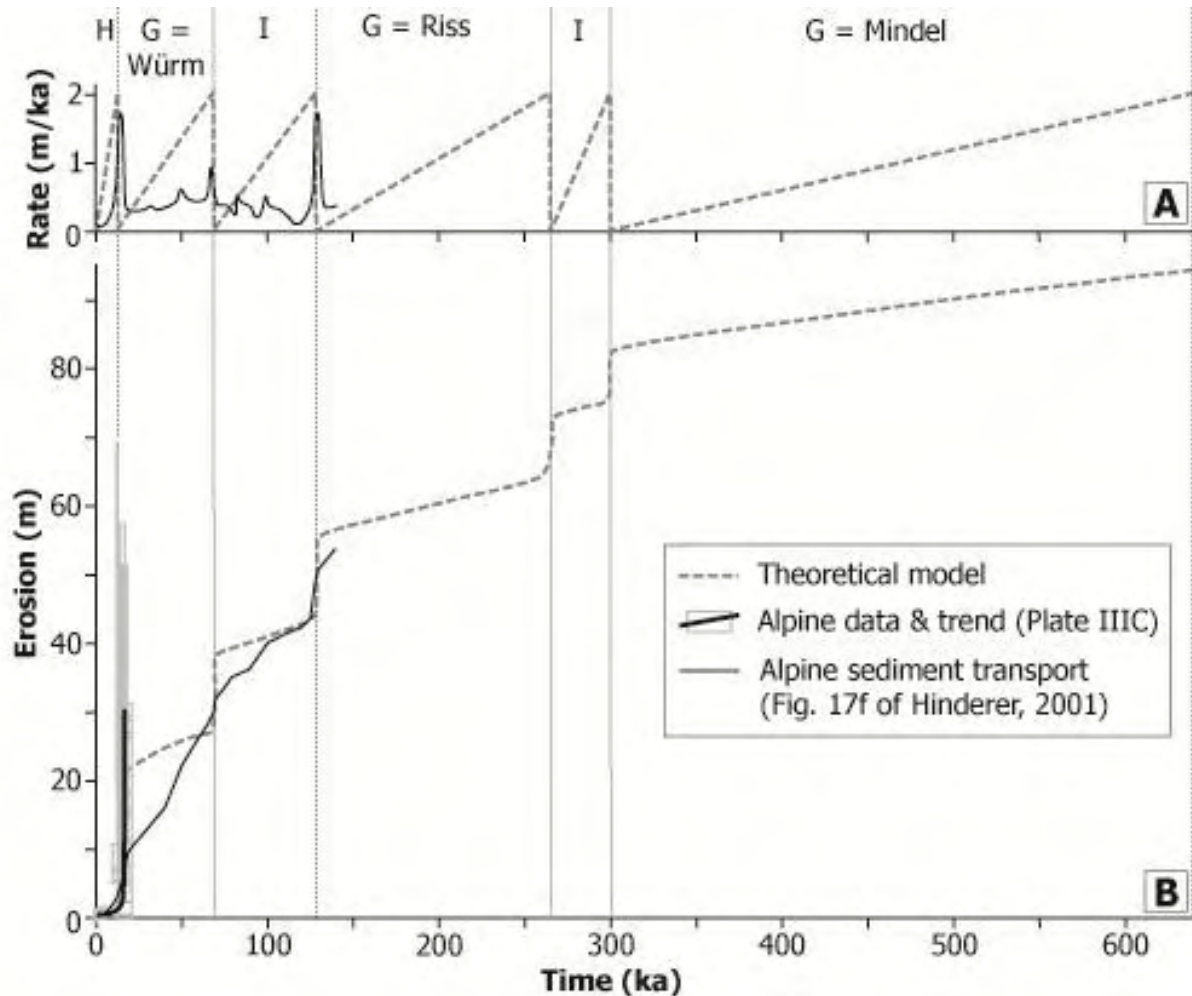
Fig. 4.6 Sediment-transport rate **(A)** and resulting cumulative erosion **(B)** during repeated Alpine glaciations in the Pleistocene. Following the paraglacial model of Church and Ryder (1972), the dashed dark gray line, sediment-transport rates decrease to low values during glacials and interglacials, and increase at the transitions between glacials and interglacials. The Alpine data from Plate IIIC, the light gray rectangles and bold solid black line, and Alpine sediment-transport rates for the last 140 ka derived by Hinderer (2001) based on Quaternary and post-LGM sediment volumes, the thin solid black line, are in agreement with the model. Prior to 140 ka, data are required to further validate the model. Abbreviations: H – Holocene, G – Glacial, and I – Interglacial. Timing of glacials Mindel 640-300 ka, Riss 265-130 ka, and Würm 70-12 ka taken from Hinderer (2001) and Bernet et al. (2004). Thus, timing of interglacials is 300-265 ka, 130-70 ka, and 12-0 ka (Holocene).

4.8. Conclusions

In this study, we compiled cumulative erosion estimates for the Alps from three different time-scales, the long- (millions of years), medium- (thousands to ten thousand years), and short-term (years to decades) scales, to evaluate the variability of mountainous erosion. Our comparison is based on an approach that was established to investigate the significance of geologic and geodetic measurements along intra-continental faults on time-scales of millions to tens of years (Fig. 4.1; Friedrich et al., 2003). Our results indicate that this approach is well suited to examine the variability of erosion at the medium- and short-term scale (inset Plate IV and Fig. 4.6). However, further data on erosion need to be evaluated covering the intermediate time-scale over ten thousands to hundred thousands of years between our medium- and long-term scale to finally bridge the gap to the long-term scale, and allow for an appropriate comparison of erosion rates from different scales. Lastly, we found similarities between the cumulative displacement with time and cumulative erosion with time (Fig. 4.1 compared to Fig. 4.7). Long-term erosion in the Alps is presumably controlled by tectonic processes in agreement with a re-evalution of the Alpine sediment budget carried out in chapter IV (e.g., Fig. 4.5). In contrast, medium-term erosion rates decline during the Holcene until recently throughout the Alps based on a comparison of medium- and short-term erosion rates (Plate IIIC compared to Plate IV). Medium-term erosion rates are thus influenced by climate changes that yielded major changes in the prevailing erosional mode of the Alps (Plate IIIC; Figs. 4.6 and 4.7), and short-term erosion is strongly affected by seasonal weather differences (inset Plate IV, Figs. 4.4 and 4.7).
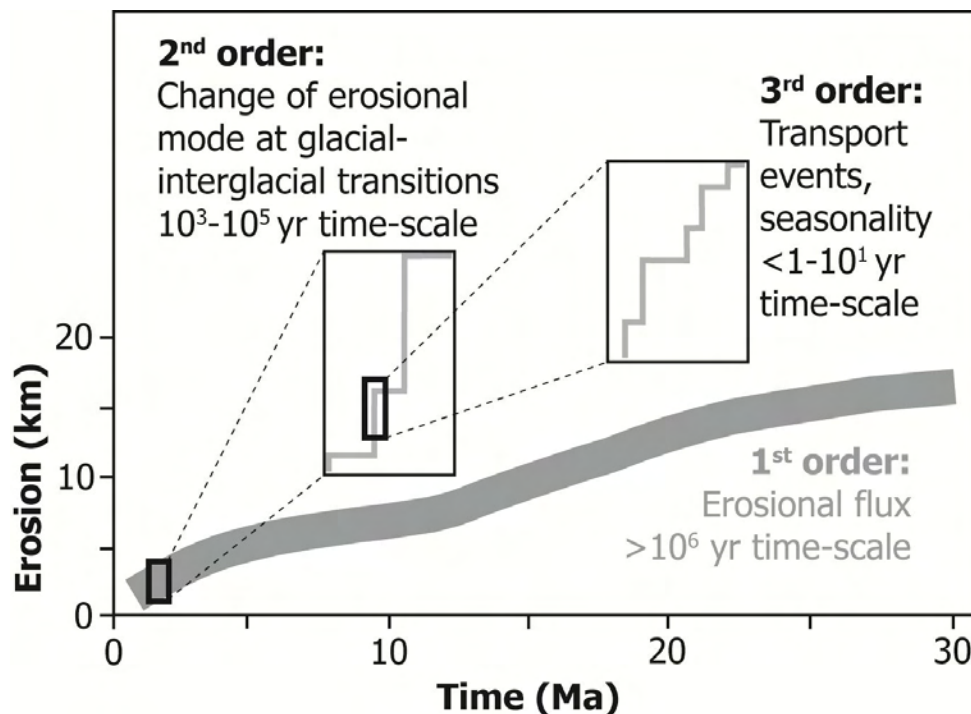
Fig. 4.7 Schematic diagram indicating the significance of erosion and sediment-transport processes on three different temporal scales.

4.9. References

Andeweg, B., and Cloetingh, S.; 1998; Flexure and 'unflexure' of the North Alpine German-Austrian Molasse Basin: constraints from forward tectonic modeling; *in:* Mascle, A., Puigdefàbregas, C., Luterbacher, H.P., and Fernandez, M. (eds); Cenozoic Foreland Basins of Western Europe; Geological Society, London, Special Publications, vol. 134, p. 403–422.

Bernet, M., Zattin, M., Garver, J.I., Brandon, M.T., and Vance, J.A.; 2001; Steady-state exhumation of the European Alps; Geology, vol. 29, p. 35–38.

Bernet, M., Brandon, M.T., Garver, J.I., and Molitor, B.; 2004; Downstream Changes of Alpine Zircon Fission Track Ages in the Rhône and Rhine Rivers; Journal of Sedimentary Research, vol. 74, p. 82–94.

Bernet, M., Brandon, M., Garver, J., Balestieri, M.L., Ventura, B., and Zattin, M.; 2009; Exhuming the Alps through time: clues from detrital zircon fission-track thermochronology; Basin Research; vol. 21, p. 781–798.

Bini, A., Cita, M.B., and Gaetani, M.; 1978; Southern Alpine lakes – Hypothesis of an erosional origin related to the Messinian entrenchment; Marine Geology, vol. 27, p. 271–288.

Bogdanoff, S., Michard, A., Mansour, M. and Poupeau, G.; 2000; Apatite fission track analysis in the Argentera massif: evidence of contrasting denudation rates in the external massifs of the western Alps; Terra Nova, vol. 12, p. 117–125.

Burch, H.; 1994; Ein Rückblick auf die hydrologische Forschung der WSL im Alptal; Beiträge zur Geologie der Schweiz-Hydrologie, vol. 35, p. 18–33.

Cederbom, C.E., Sinclair, H.D., Schlunegger, F., and Rahn, M.K.; 2004; Climate-induced rebound and exhumation of the European Alps; Geology, vol. 32, p. 709–712.

Cederbom, C.E., van der Beek, P., Schlunegger, F., Sinclair, H.D., and Oncken, O.; 2011; Rapid extensive erosion of the North Alpine foreland basin at 5–4Ma; Basin Research, vol. 23, p. 528–550, doi: 10.1111/j.1365-2117.2011.00501.x.

Champagnac, J.D., Schlunegger, F., Norton, K., von Blanckenburg, F., Abbühl, L.M., and Schwab, M.; 2009; Erosion-driven uplift of the modern Central Alps; Tectonophysics, vol. 474 , p. 236–249.

Christensen, J.N., Selverstone, J., Rosenfeld, J.L., and DePaolo, D.J.; 1994; Correlation by Rb-Sr geochronology of garnet growth histories from different structural levels within the Tauern Window, Eastern Alps; Contributions to Mineralogy and Petrology, vol. 118, p. 1–12.

Church, M., and Ryder, J.M.; 1972; Paraglacial sedimentation: a consideration of fluvial processes conditioned by glaciations; Geological Society of America Bulletin, vol. 83, p. 3059–3072.

Clark jr., S.P., and Jäger, E.; 1969; Denudation rate in the Alps from geochronologic and heat flow data; American Journal of Science, vol. 267, p. 1143–1160.

Cliff, R.A., Droop, G.T., and Rex, D.C.; 1985; Alpine metamorphism in the south-east Tauern Window, Austria: 2. Rates of heating, cooling and uplift; Journal of Metamorphic Geology, vol. 3, p. 403–415.

Corcoran, D.V., and Doré, A.G.; 2005; A review of techniques for the estimation of magnitude and timing of exhumation in offshore basins; Earth Science Reviews, vol. 72, p. 129–168.

Davies, J.H., and von Blanckenburg, F.; 1995; Slab breakoff: A model of lithosphere detachment and its test in the magmatism and deformation of collisional orogens; Earth and Planetary Science Letters, vol. 129, p. 85–102.

Delunel, R., van der Beek, P.A., Carcaillet, J., Bourlès, D.L., and Valla, P.G.; 2010; Frost-cracking control on catchment denudation rates: Insights from in situ produced [10]Be concentrations in stream sediments (Ecrins–Pelvoux massif, French Western Alps); Earth and Planetary Science Letters, vol. 293, p. 72–83.

Descroix, L., and Mathys, N.; 2003; Processes, Spatio-temporal factors and measurements of current erosion in the French southern Alps: a review; Earth Surface Processes and Landforms, vol. 28, p. 993–1011.

Doppler, G.; 1989; Zur Stratigraphie der nördlichen Vorlandmolasse in Bayrisch-Schwaben; Geologica Bavarica vol. 94, p. 83–133.

Dühnforth, M., Densmore, A.L., Ivy-Ochs, S., Allen, P.A., and Kubik, P.W.; 2007; Timing and patterns of debris flow deposition on Shepherd and Symmes creek fans, Owens Valley, California, deduced from cosmogenic [10]Be; Journal of Geophysical Research, vol. 112, 11 pp., doi. 10.1029/2006JF000562.

England, P., and Molnar, P.; 1990; Surface uplift, uplift of rocks, and exhumation of rocks; Geology, vol. 18, p. 1173–1177.

Frei, C., and Schär, C.; 1998; A precipitation climatology of the Alps from high-resolution rain-gauge observations; International Journal of Climatology, vol. 18, p. 873–900.

Friedrich, A.M., Wernicke, B.P., and Niemi, N.A.; 2003; Comparison of geodetic and geologic data from the Wasatch region, Utah, and implications for the spectral character of Earth deformation at periods of 10 to 10 million years; Journal of Geophysical Research, vol. 108, doi: 10.1029/2001JB000682.

Frisch, W., Dunkl, I., and Kuhlemann, J.; 2000; Post-collisional orogen-parallel large-scale extension in the Eastern Alps; Tectonophysics, vol. 327, p. 239–265.

Frostick, L.E., and Jones, S.J.; 2002; Impact of periodicity on sediment flux in alluvial systems: grain to basin scale; Geological Society; London; Special Publications; v. 191; p. 81–95; doi: 10.1144/GSL.SP.2002.191.01.06.

Fügenschuh, B., Seward, D., and Mancktelow, N.; 1997; Exhumation in a convergent orogen: the western Tauern window; Terra Nova, vol. 9, p. 213–217.

Habersack, H.M., Nachtnebel, H.P., and Laronne, J.B.; 2001; The continuous measurement of bedload discharge in a large alpine gravel bed river; Journal of Hydraulic Research, vol. 39, p. 125–133.

Handy, M.R., Schmid, S.M., Bousquet, R., Kissling, E., and Bernoulli, D.; 2010; Reconciling plate-tectonic reconstructions of Alpine Tethys with the geological–geophysical record of spreading and subduction in the Alps; Earth Science Reviews, vol. 102, p. 102–158, doi: 10.1016/j.earscirev.2010.06.002.

Haeuselmann, P., Granger, D.E., Jeannin, P.-Y., and Lauritzen, S.E.; 2007; Abrupt glacial valley incision at 0.8 Ma dated from cave deposits in Switzerland; Geology, vol. 35, p. 143–146.

Hejl, E.; 1997; 'Cold spots' during the Cenozoic evolution of the Eastern Alps: thermochronological interpretation of apatite fission-track data; Tectonophysics, vol. 272, p. 159–173.

Hesse, R.; 1975; Turbiditic and non-turbiditic mudstone of Cretaceous flysch sections of the East Alps and other basins; Sedimentology, vol. 22, p. 387-416.

Hinderer, M.; 2001; Late Quaternary denudation of the Alps, valley and lake fillings and modern river loads; Geodinamica Acta, vol. 14, p. 231–263.

Hsü, K.J., Montadert, L., Bernoulli, D., Cita, M.B., Erickson, A., Garrison, R.E., Kidd, R.B., Melieres, F., Muller, C., and Wright, R.;1977; History of Mediterranean salinity crisis; Nature, vol. 267, p. 399–403, doi: 10.1038/267399a0.

Hugenholtz, C.H., and Wolfe, S.A.; 2010; Rates and environmental controls of aeolian dust accumulation, Athabasca River Valley, Canadian Rocky Mountains; Geomorphology, vol. 121, p. 274–282, doi: 10.1016/j.geomorph.2010.04.024.

Jones, S.J., and Frostick, L.E.; 2002; Introduction; Geological Society; London; Special Publications; v. 191; p. 1–4; doi: 10.1144/GSL.SP.2002.191.01.01.

Keller, H.M., and Weibel, P.; 1991; Suspended sediments in streamwater – indicators of erosion and bed load transport in mountainous basins; *in:* Sediment and Stream Water Quality in a Changing Environment: Trends and Explanation, Proceedings of the Vienna Symposium, August 1991, IAHS Publication no. 203, p. 53–61.

Kempf, O., and Pfiffner, O.A.; 2004; EarlyTertiary evolution of the North Alpine Foreland Basin of the Swiss Alps and adjoining areas; Basin Research, vol. 16, p. 549–567, doi: 10.1111/j.1365-2117.2004.00246.x.

Kirchner, J.W., Finkel, R.C., Riebe, C.S., Granger, D.E., Clayton, J.L., King, J.G., and Megahan, W.F.; 2001; Mountain erosion over 10 yr, 10 k.y., and 10 m.y. time scales; Geology; v. 29; p. 591–594.

Korup, O., and Schlunegger, F.; 2009; Rock-type control on erosion-induced uplift, eastern Swiss Alps; Earth and Planetary Science Letters, vol. 278, p. 278–285.

Kuhlemann, J., Frisch, W., Dunkl, I., and Székely, B.; 2001; Quantifying tectonic versus erosive denudation by the sediment budget: the Miocene core complexes of the Alps; Tectonophysics, vol. 330, p. 1–23.

Kuhlemann, J., Frisch, W., Székely, B., I. Dunkl, I., and Kázmér, M.; 2002; Post-collisional sediment budget history of the Alps: tectonic versus climatic control; International Journal of Earth Sciences, vol. 91, p. 818–837, doi: 10.1007/s00531-002-0266-y.

Kuhlemann, J., and Kempf, O.; 2002; Post-Eocene evolution of the North Alpine Foreland Basin and its response to Alpine tectonics; Sedimentary Geology, vol.152, p. 45–78.

Kühni, A., and Pfiffner, O.A.; 2001; The relief of the Swiss Alps and adjacent areas and its relation to lithology and structure: topographic analysis from a 250-m DEM; Geomorphology, vol. 41, p. 285–307.

Lemcke, K.; 1974; Vertikalbewegungen des vormesozioschen Sockels im nördlichen Alpenvorland Perm bis zur Gegenwart?; Eclogae Geologicae Helvetiae, vol. 67, p. 121–133.

Loizeau, J.-L. and Dominik, J.; 2000; Evolution of the Upper Rhone River discharge and suspended sediment load during the last 80 years and some implications for Lake Geneva; Aquatic Sciences, vol. 62, p. 54–67.

Malusà, M., and Vezzoli,G.; 2006 Interplay between erosion and tectonics in the Western Alps; Terra Nova, vol. 18, p. 104–108.

Mathys, N., Brochot, S., Meunier, M., and Richard, D.; 2003; Erosion quantification in the small marly experimental catchments of Draix (Alpes de Haute Provence, France). Calibration of the ETC rainfall–runoff–erosion model; Catena; vol. 50, p. 527–548.

Mocochain, L., Audra, P., Clauzon, G., Bellier, O., Bigot, J.-Y., Parize, O., and Monteil, P.; 2009; The effect of river dynamics induced by the Messinian Salinity Crisis on karst landscape and caves: Example of the Lower Ardèche river (mid Rhône valley); Geomorphology, vol. 106, p. 46–61, doi: 10.1016/j.geomorph.2008.09.021.

Most, P.; 2003; Late Alpine cooling histories of tectonic blocks along the central part of the Transalp-Traverse (Inntal – Gadertal): constraints from geochronology; PhD thesis, Eberhardt-Karls-University Tübingen, Germany, pp. 151.

Müller, B.U.; 1999; Paraglacial sedimentation and denudation processes in an Alpine valley of Switzerland. An approach to the quantification of sediment budgets; Geodinamica Acta, vol. 12, p. 291–301.

Muttoni, G., Carcano, C., Garzanti, E., Ghielmi, M., Piccin, A., Pini, R., Rogledi, S., and Sciunnach, D.; 2003; Onset of major Pleistocene glaciations in the Alps; Geology, vol. 31, p. 989–992.

Norton, K.P., von Blanckenburg, F., Schlunegger, F., Schwab, M., and Kubik, P.W.; 2008; Cosmogenic nuclide-based investigation of spatial erosion and hillslope channel coupling in the transient foreland of the Swiss Alps; Geomorphology, vol. 95, p. 474–486.

Norton, K.P., von Blanckenburg, F., DiBiase, R., Schlunegger, F., and Kubik, P.W.; 2011; Cosmogenic [10]Be-derived denudation rates of the Eastern and Southern European Alps; International Journal of Earth Sciences, vol. 100, p. 1163–1179, doi: 10.1007/s00531-010-0626-y. Reid, I., Layman, J.T., and Frostick, L.E.; 1980; The continuous measurement of bedload discharge; Journal of Hydraulic Research, vol. 18, p. 243–249.

Pfiffner, O.A., Ellis, S., and Beaumont, C.; 2000; Collision tectonics in the Swiss Alps: Insight from geodynamic modeling; Tectonics, vol. 19, p. 1065–1094.

Reid, I., Layman, J.T., and Frostick, L.E.; 1980; The continuous measurement of bedload discharge; Journal of Hydraulic Research, vol. 18, p. 243–249.

Richards, K.; 2002; Drainage basin structure, sediment delivery and the response to environmental change; Geological Society; London; Special Publications; v. 191; p. 149–160; doi: 10.1144/GSL.SP.2002.191.01.10.

Rickenmann, D., and McArdell, B.W.; 2007; Continuous measurement of sediment transport in the Erlenbach stream using piezoelectric bedload impact sensors; Earth Surface Processes and Landforms, vol. 32, p. 1362–1378.

Ring, U., Brandon, M.T., Willett, S.D., and Lister, G.S.; 1999; Exhumation Processes; Geological Society; London; Special Publications; vol. 154; p. 1–27; doi: 10.1144/GSL.SP.1999.154.01.01.

Robl, J., Hergarten, S., and Stüwe, K.; 2008; Morphological analysis of the drainage system in the Eastern Alps; Tectonophysics, vol. 460, p. 263–277.

Schlunegger, F.; 1999; Controls of surface erosion on the evolution of the Alps: constraints from the stratigraphies of the adjacent foreland basins; International Journal of Earth Sciences, vol. 88, p. 285–304.

Schlunegger, F., and Willett, S.; 1999; Spatial and temporal variations in exhumation of the central Swiss Alps and implications for exhumation mechanisms; *in:* Ring, U., Brandon, M.T., Lister, G.S., and Willett, S.D. (eds); Exhumation Processes: Normal Faulting, Ductile Flow and Erosion; Geological Society, London, Special Publications, vol. 154, p. 157–179.

Schlunegger, F., and Hinderer, M.; 2001; Crustal uplift in the Alps: why the drainage pattern matters; Terra Nova, vol. 13, p. 425–432.

Schlunegger, F., Melzer, J., and Tucker, G.E.; 2001; Climate, exposed source-rock lithologies, crustal uplift and surface erosion: a theoretical analysis calibrated with data from the Alps/North Alpine Foreland Basin system; International Journal of Earth Sciences, vol. 90, p. 484–499.

Schlunegger, F., Detzner, K., and Olsson, D.; 2002; The evolution towards steady state erosion in a soil-mantled drainage basin: semi-quantitative data from a transient landscape in the Swiss Alps; Geomorphology, vol. 43; p. 55–76.

Schlunegger, F., and Hinderer, M.; 2003; Pleistocene/Holocene climate change, re-establishment of fluvial drainage network and increase in relief in the Swiss Alps; Terra Nova, vol. 15, p. 88–95.

Schlunegger, F., Rieke-Zapp, D., and Ramseyer, K.; 2007; Possible environmental effects on the evolution of the Alps-Molasse Basin system; Swiss Journal of Geosciences, vol. 100, p. 383–405.

Schmid, S.M., Pfiffner, O.A., Froitzheim, N., Schönborn, G., and Kissling, E.; 1996; Geophysical-geological transect and tectonic evolution of the Swiss-Italian Alps; Tectonics; v. 15; p. 1036–1064.

Sevruk, B.; 1985; Systematischer Niederschlagmessfehler in der Schweiz; *in:* Sevruk, B. (ed.), Der Niederschlag in der Schweiz, Beiträge Geologie Schweiz – Hydrologie, vol. 31, p. 65–75.

Sinclair, H.D.; 1997; Flysch to molasse transition in peripheral foreland basins: The role of the passive margin versus slab breakoff; Geology, vol. 25, p. 1123–1126.

Steenken, A., Siegesmund, S., Heinrichs, T., and Fügenschuh, B.; 2002; Cooling and exhumation of the Rieserferner Pluton (Eastern Alps, Italy/Austria); International Journal of Earth Sciences, vol. 91, p. 799–817, doi: 10.1007/s00531-002-0260-4.

Turowski, J.M., Yager, E.M., Badoux, A., Rickenmann, D., and Molnar, P.; 2009; The impact of exceptional events on erosion, bedload transport and channel stability in a step-pool channel; Earth Surface Processes and Landforms, vol. 34, p. 1661–1673.

Turowski, J.M., and Rickenmann, D.; 2011; Measuring the statistics of bedload transport using indirect sensors; Journal of Hydraulic Engineering, vol. 137, p. 116–121.

Valla, P.G., van der Beek, P.A., and Carcaillet, J.; 2010; Dating bedrock gorge incision in the French Western Alps (Ecrins-Pelvoux massif) using cosmogenic [10]Be; Terra Nova, vol. 22, p. 18–25.

Vernon, A.J., van der Beek, P., Sinclair, H.D., and Rahn, M.K.; 2008; Increase in late Neogene denudation of the European Alps confirmed by analysis of a fission-track thermochronology database; Earth and Planetary Science Letters, vol. 270, p. 316–329, doi: 10.1016/j.epsl.2008.03.053.

Vernon, A.J., van der Beek, P., Sinclair, H.D., Persano, C., Foeken, J., and Stuart, F.M.; 2009; Variable late Neogene exhumation of the central European Alps: Low-temperature thermochronology from the Aar Massif, Switzerland, and the Lepontine Dome, Italy; Tectonics, vol. 28, 21 pp., doi:10.1029/2008TC002387.

Vezzoli, G.; 2004; Erosion in the Western Alps (Dora Baltea Basin): 2. Quantifying sediment yield; Sedimentary Geology, vol. 171, p. 247–259.

von Blanckenburg, F., Villa, I.M., Baur, H., Morteani, G., and Steiger, R.H.; 1989; Time calibration of a PT-path from the Western Tauern Window, Eastern Alps: the problem of closure temperatures; Contributions to Mineralogy and Petrology, vol. 101, p. 1–11.

von Blanckenburg, F., and Davies, J.H.; 1995; Slab breakoff: A model for syncollisional magmatism and tectonics in the Alps; Tectonics, vol. 14, p. 120–131.

Willett, S.D., Beaumont, C., and Fullsack, P.; 1993; Mechanical model for the tectonics of doubly vergent compressional orogens; Geology, vol. 21, p. 371–374.

Willett, S.D., and Brandon, M.T.; 2002; On steady states in mountain belts; Geology, vol. 30, p. 175–178.

Willett, S.D., Schlunegger, F., and Picotti, V.; 2006; Messinian climate change and erosional destruction of the central European Alps; Geology, vol. 34, p. 613–616.

Wittmann, H., von Blanckenburg, F., Kruesmann, T., Norton, K.P., and Kubik, P.; 2007; The relation between rock uplift and denudation from cosmogenic nuclides in river sediment in the Central Alps of Switzerland; Journal of Geophysical Research-Earth Surface, vol. 112; doi:10.1029/2006JF000729.

Wolman, M.G., and Miller, J.P.; 1960; Magnitude and frequency of forces in geomorphic processes; Journal of Geology, vol. 68, p. 54–74.

5. Chapter IV

Erosion of Dying Foreland Basins: Did the Sediment Discharge of the Alps Really Accelerate Five Million Years Ago?

5.1. Abstract

The fundamental discussion of whether or not climate change triggered a global acceleration of erosion at 5 Ma is widely based on the usage of the sediment-budget concept. The sediment yield of the Alps is one of the most striking data sets in the world apparently recording a substantial increase in sediment accumulation over the past ~5 Ma. Recently, however, this increase has been challenged by the argument that it may be an artefact due to observation and measurement biases. We therefore reassessed the basic assumption of the sediment-budget concept – namely, the volume of debris eroded from a source terrain and deposited in sedimentary basins allows to constrain erosion rates of the source terrain – by re-evaluating the Alpine sediment budget. We found that from ~34–5 Ma eroded Alpine material was deposited in proximal basins such as the north-Alpine foreland basin, whereas from ~5–0 Ma most of the sediments were deposited in distal basins such as the Black Sea, while stratigraphic evidence documents erosion of the proximal foreland basins. Therefore, the sediment-budget concept holds in the first stage because material deposited in the foreland basins is solely derived from the Alps. It does not hold in the second stage when erosion of Alpine-derived sediments deposited in the foreland basins prior to ~5 Ma and their re-deposition in the distal basins occurred. This implies an approximately threefold increase of the potential erosion area. We re-calculated the Alpine sediment yield for the past 5 Ma based on previously published observations that the north-Alpine foreland basin was inverted around 5 Ma. Our analysis yields much lower values than previously published, and we conclude that the Alpine sediment discharge since 5 Ma remained more or less constant, while sediment discharge since 5 Ma also affected the large areas of the proximal foreland basins. The discharge of Alpine-derived material deposited in the foreland basins prior to ~5 Ma presumably increases throughout the Plio-Pleistocene in agreement with an erosional unconformity observed between Miocene and Quaternary rocks in the Swiss and German Molasse basin. The substantial erosion of the foreland basins appears to be due to their tectonically induced inversion about 5 Ma ago indicated by subsidence curves derived from the stratigraphic record of the north-Alpine foreland basin. Our findings challenge currently dominating views that climate change accelerated erosion of high mountain areas since 5 Ma. Models that invoke climatically-triggered isostatic rebound of the Alps since 5 Ma must be reconsidered in light of our results.

5.2. Introduction

There is a fundamental debate of whether or not climate-triggered erosion has significantly increased globally around 5 Ma (e.g., Hay et al., 1988; Molnar and England, 1990; Zhang et al., 2001; Willett, 2010). The sediment-budget approach has been the dominant mode to address this question (e.g., Molnar, 2004). However, this increase has recently been challenged by Willenbring and von Blanckenburg (2010), although global isotopic data point to changes in climatic conditions at around 5 Ma (e.g., Raymo and Ruddiman, 1992; Zachos et al., 2001). Willenbring and von Blanckenburg (2010) suggested that the globally synchronous increase in sediment accumulation may simply be an artefact due to observation

and measurement biases. One reason for their argumentation is that, given sufficient time, sedimentary basins might be inverted, and hence the erosion of sediment is observed resulting in progressively decreasing strata volumes.

Central to this debate are the data of Kuhlemann et al. (2001 and 2002), that record a substantial increase in the sediment yield of the Alps over the past ca. 5 Ma (Fig. 5.1). Their interpretation of the Alpine sediment budget is based on the assumption that debris derived from the Alps and deposited in circum-Alpine sedimentary basins (dark gray in inset maps of Europe in Fig. 5.1) allows to place constraints on erosion rates of the Alpine source area (light gray in inset maps of Europe in Fig. 5.1). According to the argumentation of Willenbring and von Blanckenburg (2010), however, they also recognized that the erosion of sediment and its re-deposition is a major problem in the subalpine Molasse. The restoration of imbricated Molasse thrust sheets is a critical source of error that potentially affects the Oligo- to early Miocene sediment budget of the north-Alpine foreland basin, and the middle to latest Miocene budget of the southern foreland basin. In contrast, the increased Plio-Pleistocene sediment budget is not affected by this error according to Kuhlemann et al. (2001 and 2002). Here, we therefore reassess their basic assumption by re-evaluating the Alpine sediment budget. Our re-interpretation teased a re-calculation of the Alpine sediment yield for the past 5 Ma. We conclude that the substantial increase discussed above is only apparent, and that actual Alpine sediment-discharge rates throughout the last 5 Ma might have been much lower than previously thought. Simultaneously, the discharge of Alpine-derived debris deposited in the foreland basins prior to ca. 5 Ma presumably increases throughout the Plio-Pleistocene.
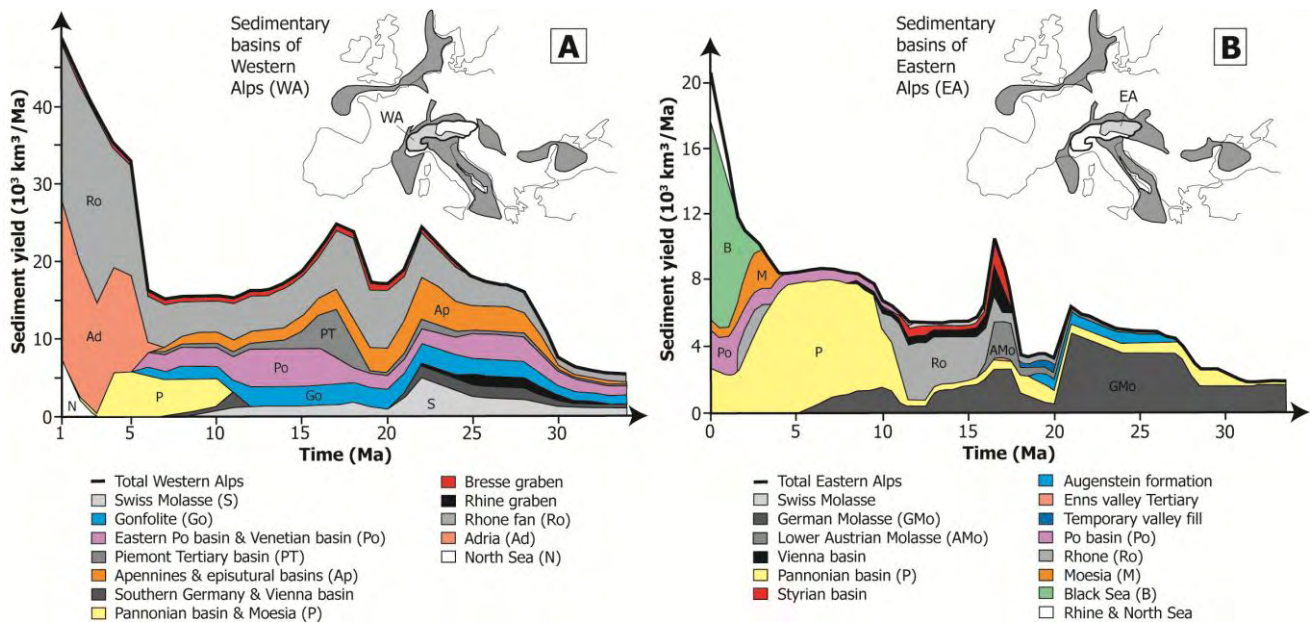
Fig. 5.1 Cumulative sediment-discharge rates for the Western Alps **(A)** and Eastern Alps **(B)** since the Oligocene separated for major sediment sinks (redrawn from Kuhlemann et al., 2001 and 2002). The inset maps of Europe show the location of the sedimentary basins supplied by the Alps.

5.3. Alpine Orogeny and Foreland Basins

The Alpine orogeny is often described as a series of episodes of tectonic, metamorphic, and erosional activity from Cretaceous to Quaternary times (e.g., Kempf and Pfiffner, 2004; Schlunegger et al., 2007; Bernet et al., 2009; Handy et al., 2010). The convergence between the European and Adriatic plates started in the late Cretaceous, and resulted in the collision of both plates during the late Eocene (Schmid et al., 1996). Slab break-off occurred presumably at about 34–29 Ma (von Blanckenburg and Davies, 1995), during which the dense oceanic part of the subducting European plate was detached from its upper buoyant part (Regard et al., 2008). However, convergence continued after the collision obvious from thrusting along the Periadriatic fault and propagation of the Helvetic nappes from 32–19 Ma, as well as foreland propagation in the Southern Alps since 19 Ma (Fig. 5.2; Schmid et al., 1996). Foreland basins formed north and south of the Alps due to continental collision and convergence since the Eocene that led to crustal thickening and loading of the subducting European plate (Fig. 5.2; e.g., Schmid et al., 1996; Andeweg and Cloetingh, 1998; Cederbom et al., 2004). Subsidence curves derived by Lemcke (1974) for 13 wells distributed over the north-Alpine foreland basin area indicate, that subsidence occurred during the Oligo- and Miocene, whereas a substantial uplift of several hundred meters occurred since the Pliocene (Figs. 5.2 and 5.3).

Sedimentation in the north-Alpine foreland basin, the area of the Molasse basin located north of the Alps between Lake Geneva in the west and Lower Austria in the east (Figs. 5.2A and 5.3; e.g., Andeweg and Cloetingh, 1998; Kuhlemann and Kempf, 2002), during the Oligocene was characterized by deep marine conditions commonly referred as Flysch sedimentation (e.g., Hesse, 1975; Sinclair, 1997). In contrast, the so-called Molasse sedimentation was characterized by shallow marine conditions during the early Miocene and more continental conditions during the late Miocene (e.g., Doppler, 1989; Schlunegger et al., 2001; Kuhlemann et al., 2001). Deposition of sediments in the Molasse basin ceased between 8.5 and 4.5 Ma (Fig. 5.2A; e.g., Lemcke, 1974; Bernet et al., 2009). Parts of the basin deposits were affected by the propagating thrust front and consequently exhumed to the surface, where they are reworked since the late Miocene (e.g., Kuhlemann et al., 2001). However, sedimentation in the south-Alpine foreland basin, in principle the area of the Po basin located south of the Alps analogous to the north, during the early Oligocene occurred under deep marine conditions due to turbidity currents, and from late Oligocene to middle Miocene under submarine conditions along submarine fans and canyons (Fig. 5.2A; e.g., Schlunegger, 1999). Following the desiccation of the Mediterranean from 5.6–5.5 Ma, renewed sedimentation occurred under fluvial-deltaic and lagoonal conditions obvious from the stratigraphic record of the Lago Mare deposits of the Messinian salinity crisis (Willett et al., 2006).

Fig. 5.2 (A) Shaded relief map of the Alps showing major units and fault systems (compiled from Willett et al., 2006; Robl et al., 2008). Abbreviations: Br – Brenner fault, In – Inntal fault, Ka – Katschberg fault, La – Lavanttal fault, Mö – Mölltal fault, Mu – Mur-Mürz fault, PF – Periadriatic fault, Se – Salzachtal-Ennstal fault, JF – Jura front, HF – Helvetic front, and PT – Penninic thrust. The solid white line denotes the location of the geological transect in Figure 5.2B. **(B)** Crustal-scale geological cross-section through the Western Alps based on seismic and structural data (modified after Pfiffner et al., 2000). We highlighted the difference between recent topography (bold solid line) and the restored 'eroded section' of Pfiffner et al. (2000; bold dashed line) that is based on the estimated volume of eroded material.   → **NEXT PAGE, UPPERMOST FIGURE**

Figure showing (A) regional map of the Alps with major Alpine faults and crystalline massifs, (B) cross-section from north to south through the Alps, and subsidence diagrams for various boreholes.
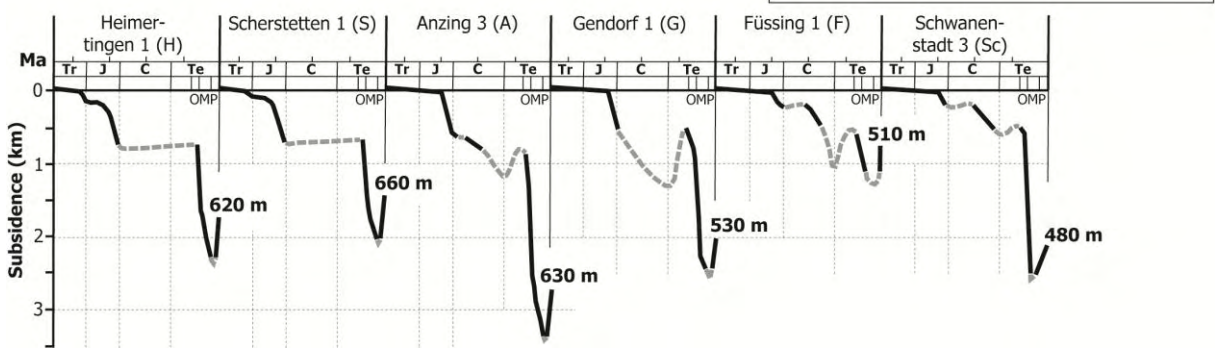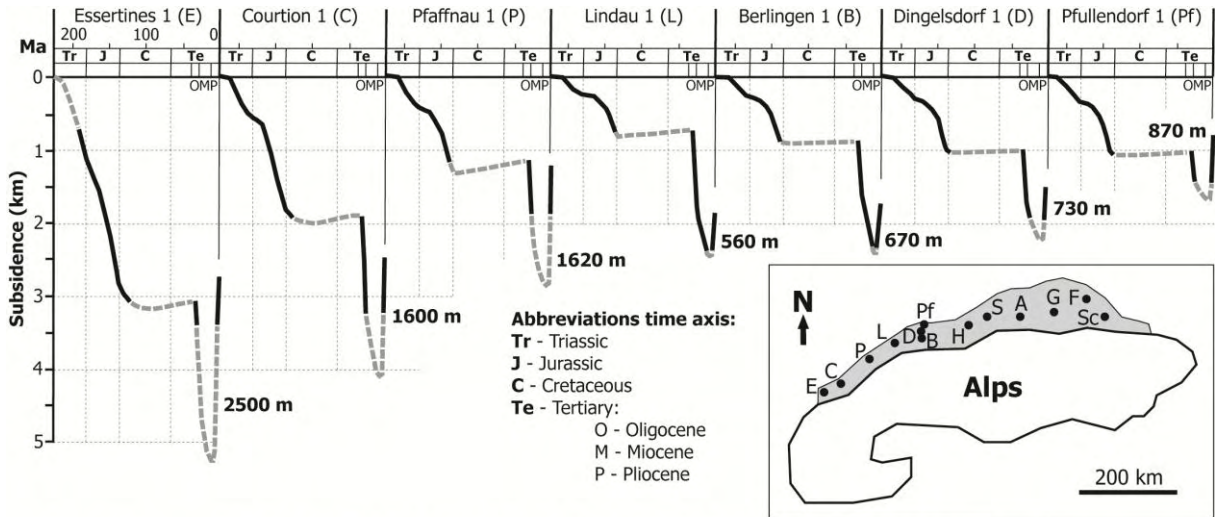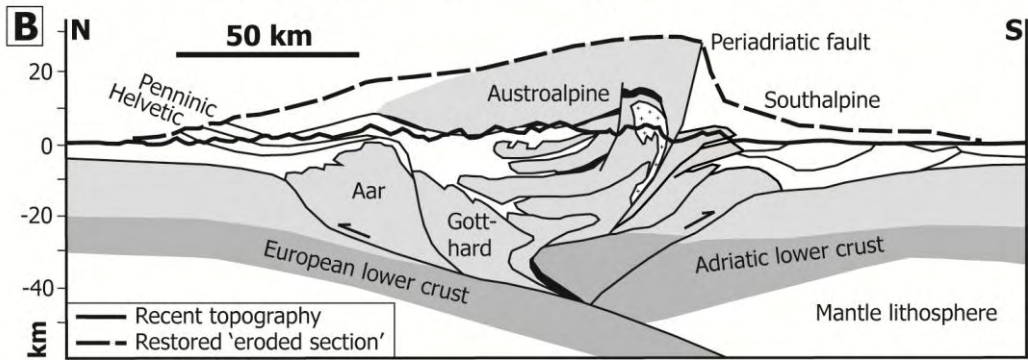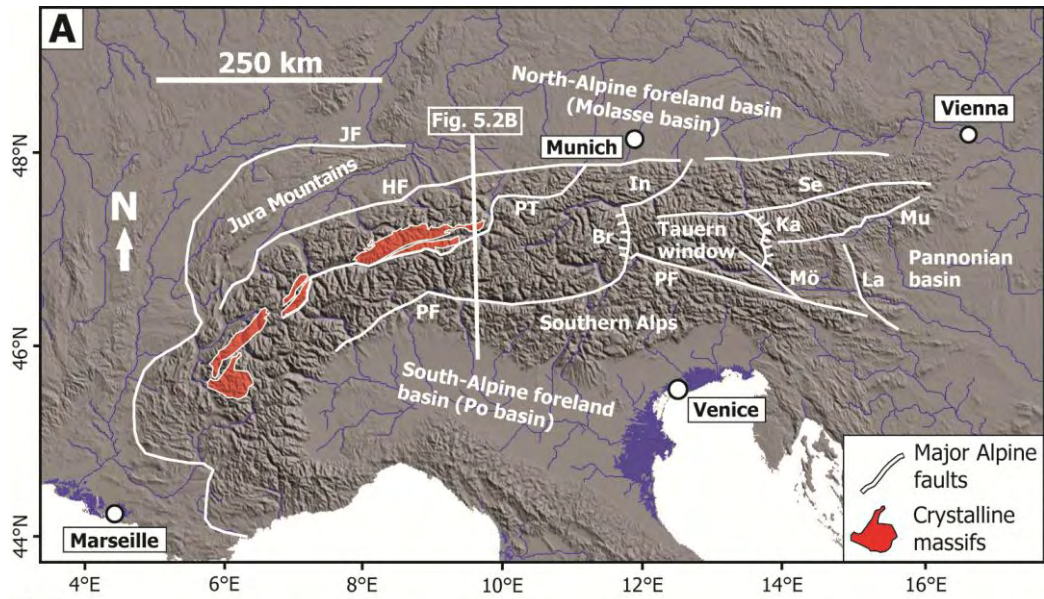
Fig. 5.3 Subsidence curves derived for several wells located in the north-Alpine foreland basin, whose position is shown in the inset (modified after Lemcke, 1974). Significant late Cenozoic uplift generally decreases from west to east, and is indicated by bold numbers attached to the lower end of the curves. Gray dashed lines are extrapolated, and denote eroded parts of the stratigraphy.

5.4. Alpine Sediment Budget: Original Data

The sediment budgets of the Western and Eastern Alps derived by Kuhlemann et al. (2001 and 2002) are shown in Figure 5.1. They determined only the volumes of Alpine-derived material deposited in all circum-Alpine basins based on a literature compilation. These data include, for example, digitized thickness maps of strata or base contour-lines of sedimentary basins. Subsequently, the calculated volumes of sediment were re-compacted to a porosity, which is equivalent to the solid rock of the source terrain (details in Kuhlemann et al., 2001 and 2002). However, their main assumption is that the volume of Alpine-derived sediments deposited in all circum-Alpine basins (dark gray in inset maps of Europe in Fig. 5.1) allows to calculate average erosion rates of the source terrain, the Western respectively Eastern Alps (light gray in inset maps of Europe in Fig. 5.1). This assumption holds, although Kuhlemann et al. (2002) noted that Alpine-derived sediments were deposited in basins of generally increasing distance to the Alps.

There are three factors behind this latter observation that represent severe sources of error associated with the Alpine sediment budget. First, sedimentary basins might be inverted given sufficient time, and hence the erosion of sediment is observed yielding progressively declining sediment volumes (Willenbring and von Blanckenburg, 2010). Kuhlemann et al. (2001 and 2002) recognized that the erosion of sediment and its re-deposition is a major problem in the subalpine Molasse, because the restoration of imbricated Molasse thrust sheets represents a critical source of error. This error potentially affects the Oligocene to early Miocene sediment budget of the north-Alpine foreland basin, and the middle to latest Miocene budget of the southern foreland basin, whereas the increased Plio-Pleistocene sediment budget is not affected by this error. Second, most of the circum-Alpine basins are not supplied solely from the Alps but also from further source terrains, which is relevant for the late Miocene to recent sediment budget (Kuhlemann et al., 2001). For example, the Pannonian basin receives sediments from the Alps as well as the Carpathians located northeast of the basin. This is a minor issue as long as a basin is located close to the Alps, so that the Alps define the major source terrain, and available provenance data in the form of heavy mineral compositions etc. allow for the distinction among various source terrains (potential error in the range of ±20%). However, this error may increase substantially for basins located far away from the Alps, e.g., the Black Sea. In such cases, mixing of fine grained debris occurs often under shallow marine conditions challenging the separation of various source terrains based on e.g., heavy mineral compositions (Kuhlemann et al., 2001). Third, as the drainage area of a basin increases with distance to the Alps, the relative contribution of material derived from the Alps to the basin fill will decrease yielding an estimated potential error on the order of ±30% in case of the Pleistocene Rhine and Plio-Pleistocene Danube catchments (Kuhlemann et al., 2001).

5.5. New Aspects of the Alpine Sediment Budget

The calculated cumulative sediment-yield rates of the Alps had additionally been differentiated for major sediment sinks (Fig. 5.1). We used this specific information provided by Kuhlemann et al. (2001 and 2002) to re-evaluate the sediment budget of the Western and Eastern Alps (Fig. 5.5). Surprisingly, we noted that the Rhone fan and Pannonian basin,

although situated at opposite sides of the Alps received sediments from both the Eastern and Western Alps (Fig. 5.1). In contrast, we expected that the Rhone fan would receive sediments only from the Western Alps and the Pannonian basin soley from the Eastern Alps based on the spatial separation between the Eastern and Western Alps defined by the meridian of the Alpine Rhine river and Lake Como (Kuhlemann et al., 2002). A potential explanation, however, is that the dominating direction of material transport in the north-Alpine foreland basin exhibited temporal changes (e.g., Schlunegger, 1999; Kuhlemann et al., 2006; Schlunegger et al., 2007). For example, the Rhone fan received east-Alpine debris during periods when the Pannonian basin received less east-Alpine sediments (Fig. 5.1B). This is most likely due to the fact that material was transported mainly to the west in times when the Rhone fan received east-Alpine debris, and to the east when the Pannonian basin received this kind of debris (Fig. 5.4). However, due to this ambiguity we did not consider the Pannonian basin data for the Western Alps (Fig. 5.1A) and the Rhone fan data for the Eastern Alps (Fig. 5.1B) in our re-evaluation of the Alpine sediment budget (Fig. 5.5). This is of course a simplification, but in the Western Alps, for example, the amount of material eroded in the Western Alps and deposited in the Pannonian basin over time is much smaller than the amount of material deposited in the Rhone fan (Fig. 5.1A). Instead, we considered the Rhone fan data only for the Western Alps and the Pannonian basin data only for the Eastern Alps according to our expectation.

The cumulative sediment-discharge rates of the Western and Eastern Alps show the significant increase starting about 5 Ma ago (bold black lines in Figs. 5.1 and 5.5). During the Oligocene and Miocene sediments had been deposited mainly in proximal basins, such as the northern Molasse basin (blue areas in Fig. 5.5). In contrast, during the past ~5 Ma the majority of sediments derived from the Alps were deposited in distal basins, such as the Black Sea, Adria, and North Sea (red areas in Fig. 5.5). The Rhone delta is an exception from this pattern because Alpine sediments had been deposited throughout the last 34 Ma (Fig. 5.5A). This delta is a distal basin because Alpine material is not transported any further from there. However, the Rhone delta is the distal basin among the distal ones that is located closest to the Alps (compare inset maps of Europe in Fig. 5.5) rising the potential to receive Alpine debris.

The Alpine sediment yield calculated by Kuhlemann et al. (2001 and 2002) is based on the assumption that all Alpine sediments, whether they had been deposited in proximal or distal basins, are derived exclusively from the Alps. During the Oligocene and Miocene, most of the Alpine sediments were derived from the Alps and deposited in the proximal basins in agreement with their assumption (emphasized by the right-hand sketches at the bottom of Figs. 5.5A and 5.5B). However, Kuhlemann et al. (2001 and 2002) further recognized that the erosion of sediment and its re-deposition occurred during the Oligocene to early Miocene in the north-Alpine foreland basin, and during the middle to latest Miocene in the southern foreland basin, but they did not consider that this effect might have occurred during the Plio-Pleistocene, the time of the calculated increase in the Alpine sediment yield. In contrast, our re-interpretation that most of the Alpine sediments had been deposited in distal basins during the last ~5 Ma implies that these sediments had not only been derived from the Alps but also from the proximal basins (emphasized by the left-hand sketches at the bottom of Figs. 5.5A and 5.5B). This is in agreement with observations from the Swiss and German Molasse basin. An unconformity between lower or middle Miocene and Quaternary rocks in the Swiss Molasse basin had been interpreted to be due to approximately 2 km of erosion near Geneva in the southwest declining to ca. 0.3 km in the northeast around Zurich (Cederbom et al., 2004). Lemcke (1974) suggested that up to 0.1 km of erosion occurred in the area of Anzing, east of Munich, in the German Molasse basin (Fig. 5.3), because the Anzing well is located in the area where the youngest earliest Pliocene Upper Freshwater Molasse is exposed.

Hence, we rather suggest that a major increase of the potential erosion area occurred at ca. 5 Ma. During the Oligo-Miocene (~34–5 Ma), the proximal basins had been supplied from the Alps, where the Western Alps cover an area of 20000 km² , and the Eastern Alps an area of 67000 km² (bottom part and inset of Fig. 5.5). During the Plio-Pleistocene (~5–0 Ma), the distal basins were supplied from the area of the Alps and the proximal basins. This is equivalent to a more than threefold increase of the potential erosion area for the Western Alps from 20000 km² to ca. 74000 km² , and an approximately threefold increase for the Eastern Alps from 67000 km² to ca. 199000 km² (bottom part and inset of Fig. 5.5). We note that these latter approximations of the potential erosion area represent an upper limit, because to simplify matters we considered the entire area of the proximal basins. Most of these basins, however, were not only supplied by the Alps but also from other source terrains (Kuhlemann et al., 2001). It is therefore most likely that Alpine sediments had not been deposited across the entire area of the proximal basins prior to their erosion and re-deposition in the distal basins. However, in some cases our approximation of the potential erosion area is appropriate. For example, in the German portion of the north-Alpine foreland basin Molasse deposits are exposed across the entire basin area up to its northern margin (e.g., Bachmann and Müller, 1992; Geological map of Bavaria).
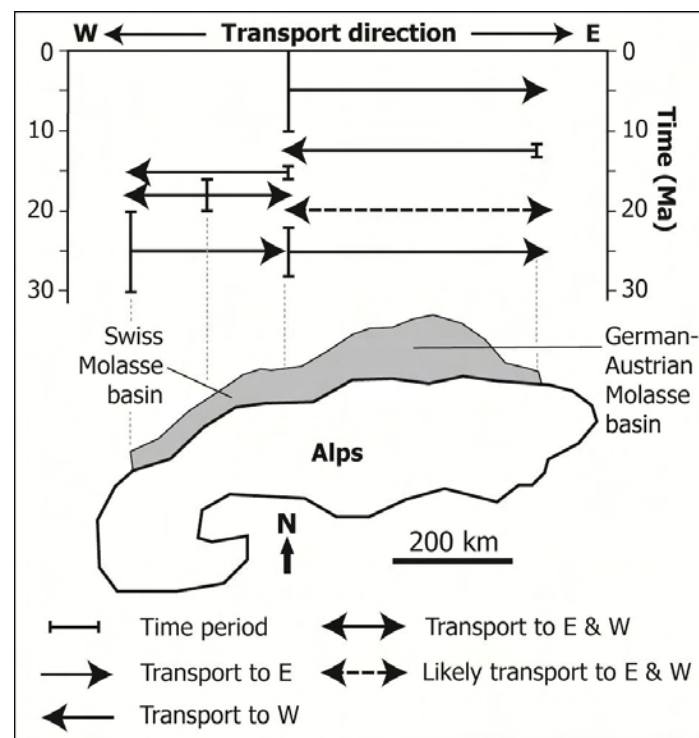
Fig. 5.4 Major basin-axial transport direction of sediment in the north-Alpine foreland basin through time. Data of the Swiss Molasse basin compiled from Schlunegger (1999) and Schlunegger et al. (2007), and those of the German-Austrian Molasse basin taken from Lemcke (1984) and Kuhlemann et al. (2006).

Fig. 5.5 Re-evaluation of the cumulative sediment-discharge rates for the Western Alps **(A)** and Eastern Alps **(B)** by Kuhlemann et al. (2001 and 2002) differentiated for major sediment transport directions (inset maps of Europe modified after Kuhlemann et al., 2002). Bluish colors indicate that sediments had been deposited mainly in proximal Alpine basins during the Oligocene and Miocene. In contrast, most of the sediments had been deposited in distal basins during the last ca. 5 Ma indicated by reddish colors. Based on these observations, we suggest that a substantial increase in the potential erosion area occurred approximately 5 Ma ago highlighted by diagrams and sketches at the bottom of the figure. In the inset, we provide estimates of the surface area for the Western and Eastern Alps and major proximal basins.
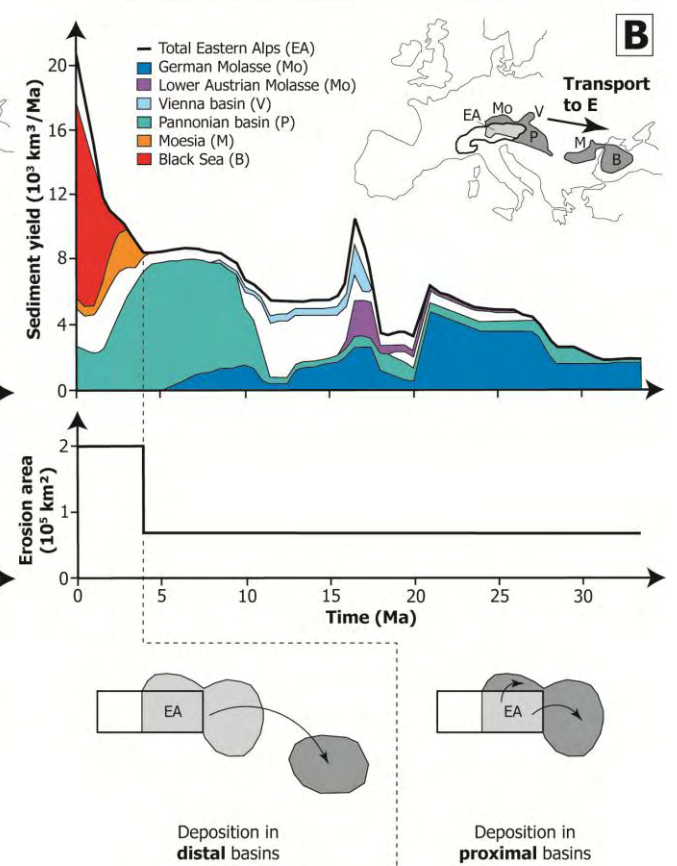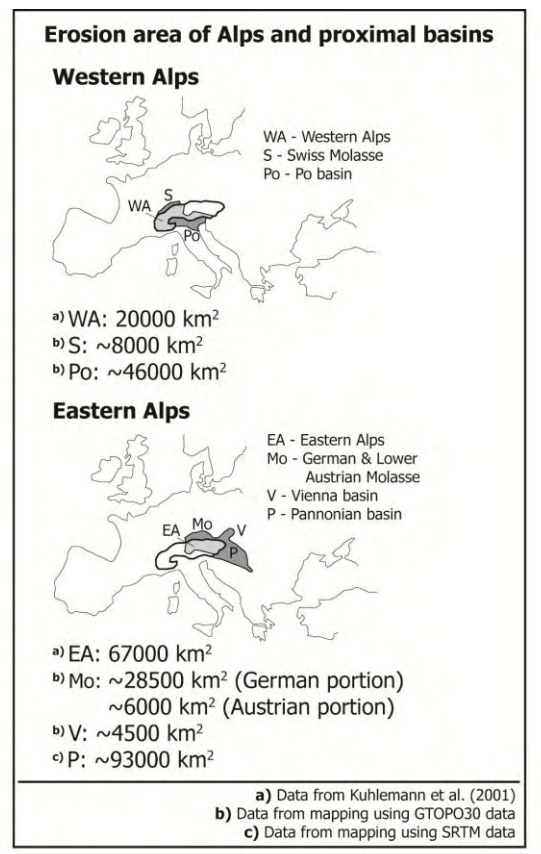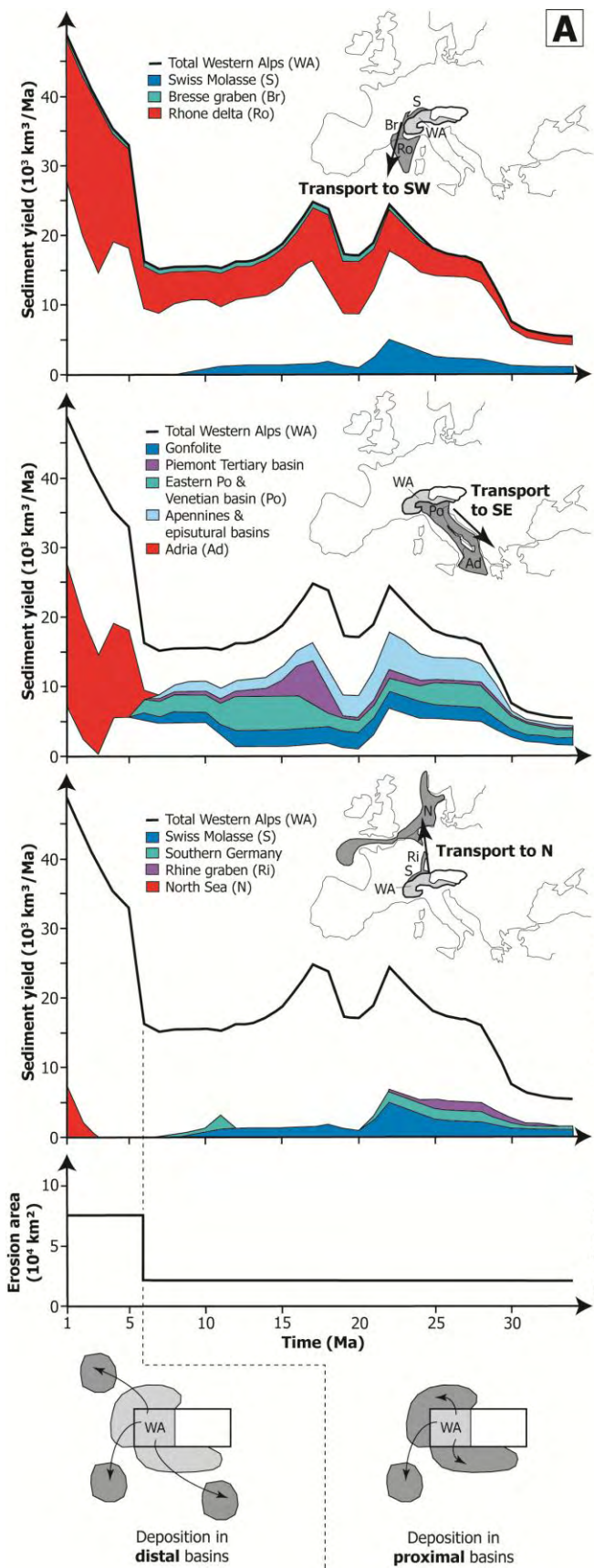
5.6. Recalculation of Sediment Budgets and Erosion Rates

If the potential erosion area increased ~5 Ma ago as we suggested, the actual sediment yield derived from the Alps alone should be lower than calculated by Kuhlemann et al. (2001 and 2002). Simultaneously, the sediment yield derived from the area of the proximal basins should increase at ca. 5 Ma. We therefore first recalculated the Alpine sediment yield for the past ~5 Ma in four steps (Fig. 5.6; Table 5.1), and based on this we then constrained the potential sediment yield derived from the proximal basins over the past ~5 Ma (Fig. 5.7; Table 5.2). However, we note that both of our sediment-yield calculations exhibit an error of ±50% which is the typical error of the Kuhlemann et al. (2001 and 2002) data. This is simply because our calculations are based on these data.

5.6.1. Alps

Step 1)

In the first step of our recalculation of the Alpine sediment yield, we separated the sediment-yield data of Kuhlemann et al. (2001 and 2002) into two time windows. We distinguished the data that cover the past 5 Ma from the data that cover the time prior to ~5 Ma. In Figure 5.6, the former data are highlighted by the black solid lines and the latter by the black dashed lines. In the second column of Table 5.1, we listed the sediment-yield data that cover the last 5 Ma according to our separation. These data define the starting point of the actual recalculation.

Step 2)

In the second step, we calculated the erosion rates for the past 5 Ma following the basic assumption of Kuhlemann et al. (2001 and 2002). According to their assumption, the high sediment yields during this time as given in the second column of Table 5.1 have to be related to the area of the Western and Eastern Alps only. We therefore divided the sediment-yield data separated in the first step by the surface area of the Western and Eastern Alps, 20000 km² and 67000 km². This calculation is represented by step 2) according to Table 5.1. It yielded high erosion rates of up to 2.4 km/Ma for the Western Alps and much lower rates of up to 0.31 km/Ma for the Eastern Alps (third column of Table 5.1).

Step 3)

In the third step, we determined the erosion rates for the same time window by also including the regions undergoing erosion in the proximal basins. Hence, we divided the sediment-yield data separated in the first step by the surface area of the Western and Eastern Alps plus the area of the proximal basins, ~74000 km² and ~199000 km². This is step 3) according to Table 5.1. The calculation yielded more than three times lower erosion rates than the calculation in the second step (compare the third with the forth column of Table 5.1).

Step 4)

In the last step, the fourth, we used the erosion rates derived in step 3) to recalculate the actual sediment yield of the Alps. We did so by multiplying these erosion rates with the surface area of the Western and Eastern Alps, 20000 km² and 67000 km² (last column of Table 5.1). We compared the recalculated Alpine sediment yields indicated by gray solid lines

in Figure 6 with the sediment yield derived by Kuhlemann et al. (2001 and 2002) represented by black solid lines in this figure. The recalculation indeed yielded lower sediment-discharge rates (Fig. 5.6). Moreover, our recalculated rates show first a decrease and then an increase towards recent times, and they are in a similar range as Oligo- to Miocene rates (black dashed line in Fig. 5.6). For the Eastern Alps, Kuhlemann et al. (2001) provided an estimate of the recent sediment yield on the order of 12000 km³/Ma (black circle in Fig. 5.6B). This value is much lower than the original approximation (black line in Fig. 5.6B) suggesting that our recalculation is reasonable (gray line in Fig. 5.6B).

5.6.2. Proximal Basins

Step 1)

Based on the results presented in Figure 5.6, we constrained the potential Alpine sediment yield derived from the proximal basins over the past 5 Ma (Fig. 5.7, Table 5.2). Since the black solid line in Figure 5.7 defines the sediment yield derived from the Alps and proximal basins together, and the dark gray solid line in the same figure represents the sediment yield derived solely from the Alps, the difference between both should be equal to the sediment yield derived solely from the proximal basins (light gray shaded area in Fig. 5.7). In the first step, we therefore calculated this difference simply by subtracting our recalculated sediment yields (third column of Table 5.2) from the total sediment yields (second column in Table 5.2). The results of this subtraction were listed in the fourth column of Table 5.2, and indicated by light gray lines in Figure 5.7. Our results imply that the sediment yield derived from the Alpine-proximal basins may have increased drastically throughout the Plio-Pleistocene (Fig. 5.7).

Step 2)

In an additional second step, we determined the erosion rates of the proximal basins over the last 5 Ma. For this, we considered the surface area of the proximal basins of the Western and Eastern Alps, ~54000 and ~132000 km², and we multiplied the potential sediment yield from the proximal basins (fourth column of Table 5.2) with this area (last column of Table 5.2). This calculation yielded much lower erosion rates of up to 0.1 km/Ma for the proximal basins of the Eastern Alps than for the proximal basins of the Western Alps with rates of up to 0.64 km/Ma.
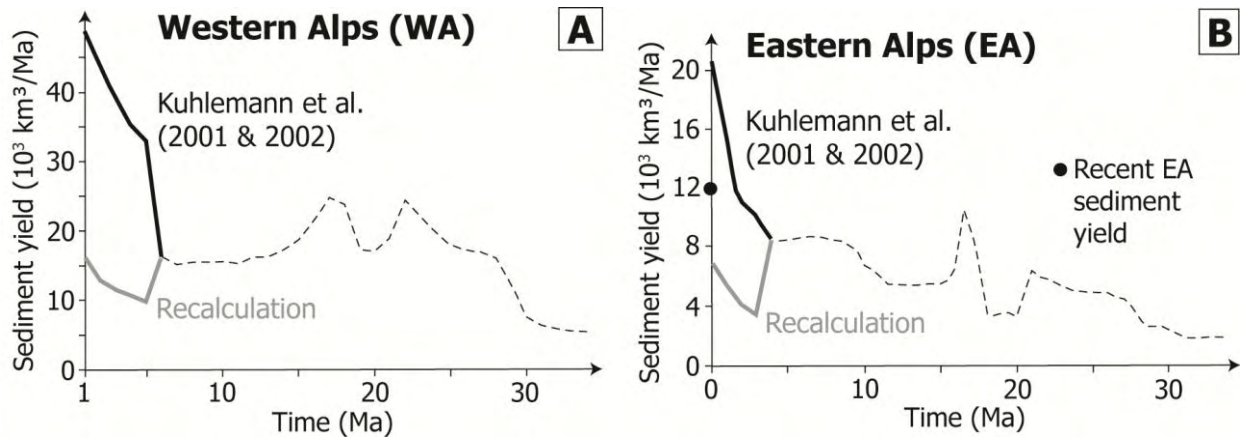
Fig. 5.6 Recalculated sediment-yield rates during the last ca. 5 Ma for the Western Alps (**A**) and Eastern Alps (**B**) indicated by gray solid lines. The recalculation is based on the four steps described in the text, and given in Table 5.1A (Western Alps) respectively Table 5.1B (Eastern Alps). The original sediment yield data derived by Kuhlemann et al. (2001 and 2002) are shown by black solid lines. For the Eastern Alps, we had been able to compare our recalculation with an estimate of the recent sediment yield given by Kuhlemann et al. (2001) and marked by a black circle in Figure 5.6B.

Table 5.1A: Recalculation of sediment yield for Western Alps (WA) – Figure 5.6A.

Time (Ma)	Sediment yield (km³/Ma) of WA [1]	Erosion rate (km/Ma) of WA [2]	Erosion rate (km/Ma) of WA & proximal basins [3]	Recalculated sediment yield (km³/Ma) of WA [4]
1	48000	2.4	0.65	13000
2	43000	2.15	0.58	11600
3	40000	2	0.54	10800
4	36000	1.8	0.49	9800
5	33000	1.65	0.45	9000

Table 5.1B: Recalculation of sediment yield for Eastern Alps (EA) – Figure 5.6B.

Time (Ma)	Sediment yield (km³/Ma) of EA [1]	Erosion rate (km/Ma) of EA [2]	Erosion rate (km/Ma) of EA & proximal basins [3]	Recalculated sediment yield (km³/Ma) of EA [4]
0	20500	0.31	0.1	6700
1	15500	0.23	0.08	5400
2	11000	0.16	0.06	4000
3	10000	0.15	0.05	3400

Step 1) Sediment-yield data of Kuhlemann et al. (2001 & 2002) shown by black solid lines in Figure 5.6.
Step 2) Erosion rates of WA and EA based on sediment-yield data of Kuhlemann et al. (2001 & 2002), and surface area of 20000 km² for WA and 67000 km² for EA taken from Kuhlemann et al. (2001).
Step 3) Erosion rates of WA & their proximal basins and EA & their proximal basins based on sediment-yield data of Kuhlemann et al. (2001 & 2002), and surface area of ~74000 km² for WA & their proximal basins and ~199000 km² for EA & their proximal basins taken from inset of Figure 5.5.
Step 4) Recalculated sediment yield of WA and EA based on erosion rates from step 3), and surface area of 20000 km² for WA and 67000 km² for EA taken from Kuhlemann et al. (2001) – gray solid line in Figure 5.6.

138
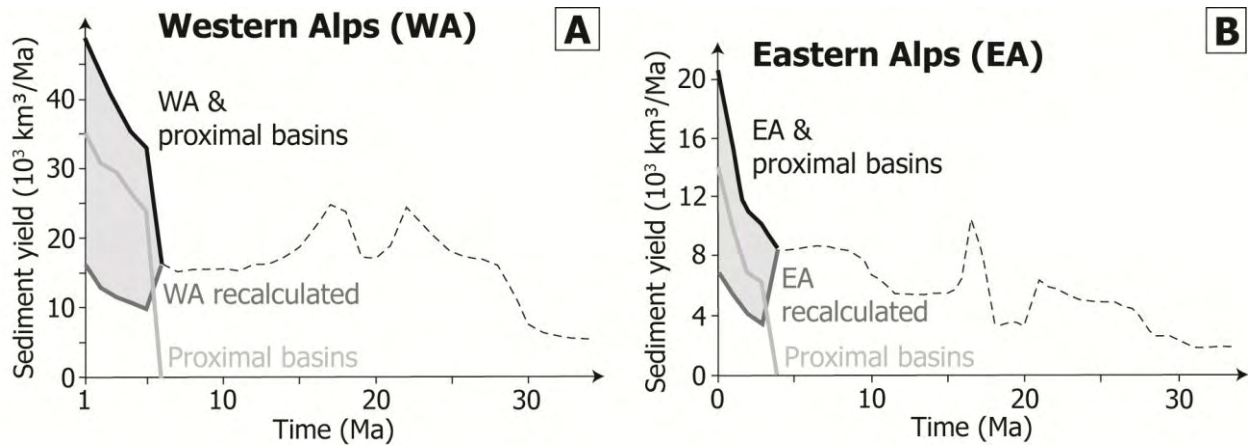
Fig. 5.7 Calculated potential sediment-yield rates during the last ca. 5 Ma for the proximal basins of the Western Alps **(A)** and Eastern Alps **(B)** indicated by light gray solid lines. The calculation is based on the description in the text, and given in Table 5.2A (Western Alps) respectively Table 5.2B (Eastern Alps). The total sediment-yield data of Kuhlemann et al. (2001 and 2002) are shown by black solid lines and the recalculated Alpine sediment yields by dark gray solid lines. The difference between the total and recalculated sediment yields is the potential sediment yield of the proximal basins highlighted by the light gray shaded areas.

Table 5.2A: Calculation of sediment yield for proximal basins of Western Alps (WA) – Figure 5.7A.

Time (Ma)	Total sediment yield (km³/Ma)	Recalculated sediment yield (km³/Ma) of WA	Sediment yield (km³/Ma) for proximal basins of WA [1]	Erosion rate (km/Ma) for proximal basins of WA [2]
1	48000	13000	35000	0.64
2	43000	11600	31400	0.58
3	40000	10800	29400	0.55
4	36000	9800	26200	0.49
5	33000	9000	24000	0.45

Table 5.2B: Calculation of sediment yield for proximal basins of Eastern Alps (EA) – Figure 5.7B.

Time (Ma)	Total sediment yield (km³/Ma)	Recalculated sediment yield (km³/Ma) of EA	Sediment yield (km³/Ma) for proximal basins of EA [1]	Erosion rate (km/Ma) for proximal basins of EA [2]
0	20500	6700	13800	0.1
1	15500	5400	10100	0.08
2	11000	4000	7000	0.05
3	10000	3400	6600	0.05

Step 1) Calculation of sediment yield for proximal basins of WA and proximal basins of EA (light gray solid lines in Fig. 5.7) based on the difference between total sediment yield (black solid lines in Fig. 5.7), and recalculated sediment yield of WA and EA (dark gray lines in Fig. 5.7). This difference is further highlighted by light gray area in Figure 5.7.

Step 2) Erosion rates for proximal basins of WA and proximal basins of EA based on sediment yield from step 1), and surface area of ~54000 km² for proximal basins of WA and ~132000 km² for proximal basins of EA taken from inset of Figure 5.5.

5.7. Discussion

We distinguished two stages in the evolution of the Alpine sediment budget. In the first stage from ca. 34–5 Ma, eroded Alpine material was deposited in proximal basins such as the north-Alpine foreland basin (illustrated by the right-hand sketches at the bottom of Figs. 5.5A and 5.5B), whereas in the second stage from ca. 5–0 Ma, most of the sediments were deposited in distal basins such as the Black Sea (illustrated by the right-hand sketches at the bottom of Figs. 5.5A and 5.5B). This two-stage evolution over the last 34 Ma is consistent with the subsidence history of the Molasse basin (Fig. 5.3). Subsidence curves determined by Lemcke (1974) for wells located within this basin indicate that it subsided during the Oligo-Miocene, and was uplifted by several hundred meters since the Pliocene representing the net en-bloc rise of the Alpine foreland (Fig. 5.3).

The origin of the uplift during the second stage had been rarely discussed in the past. Andeweg and Cloetingh (1998) modeled the deflection of the European plate underlying the Molasse basin due to overthrusting of the African plate (e.g., Fig. 5.2B) in terms of an elastic plate model loaded by the Alpine thrust belt and limited subsurface loads with the superposition of Plio-Pleistocene uplift of several hundred meters (phase of 'unflexure'). They suggested that the uplift may be due to break-up or delamination of European crust. In contrast, Schlunegger et al. (2007) proposed based on the data of Kuhlemann (2000) that the climate became wetter at the Mio-Pliocene boundary. Erosion subsequently increased relative to crustal accretion, and active deformation shifted toward the internal part of the Alpine orogen. This resulted in net unloading of the orogen and hence in flexural rebound of the foreland plate (Schlunegger et al., 2007). However, regardless of the origin of the uplift it caused the inversion of the Alpine foreland basins about 5 Ma ago, and resulted in a significant increase of the erosion area (bottom part of Fig. 5.5).

The Plio-Pleistocene erosion of the proximal basins removed Alpine-derived sediments deposited in these basins prior to 5 Ma. This is obvious from the occurrence of an erosional unconformity between Miocene and Quaternary rocks across the Swiss and German Molasse basin (e.g., Lemcke, 1974). Cederbom et al. (2004) constrained the magnitude of Plio-Pleistocene erosion in the northeastern Swiss Molasse basin using apatite fission-track data from three vertical sections. These sections are located along a transect from the undeformed Molasse in the north to the thrust-faulted subalpine Molasse in the south. Approximately 1.9–4.5 km of erosion occurred in this area of the Molasse basin over the past ~5 Ma (Cederbom et al., 2004). This is equivalent to potential erosion rates in the range of 0.4–0.8 km/Ma. Similarly, in a recent study Cederbom et al. (2011) estimated the early Pliocene erosion rate for the Swiss Molasse basin to be on the order of ~0.8 km/Ma. These rates agree well with our inferred erosion rates for the western Alpine foreland basins ranging from 0.45 up to 0.64 km/Ma (last column of Table 5.2A). The latter rates are based on our approximation of the reworked Alpine sediment yield derived from the proximal basins over the last ~5 Ma (Fig. 5.7).

The data of Cederbom et al. (2004, 2011) actually provide an independent estimate of the erosion that occurred in the Alpine foreland over the last 5 Ma. Cederbom et al. (2004) also considered the sediment budget of the Western Alps to record a doubling of erosion in the Western Alps during this time (Fig. 5.1A). Consequently, they identified a coincidence of increased erosion in the Alpine foreland and Alpine mountain chain. Since this increased erosion coincided with a decline in structural deformation in the Swiss Alps (Schmid et al., 1996), it appears likely that erosional unroofing of the Alps was greater than crustal thickening during the past ~5 Ma, and that isostatic rebound and erosion of the Alpine foreland would have been triggered by the accelerated erosion in the Swiss Alps (Cederbom et al., 2004).

A projection of the basin rebound into the interior of the mountain belt carried out by Cederbom et al. (2004) indicates, that ~6.5 km of erosion should have occurred in the central area of the Western Alps. This is equal to an erosion rate of 1.3 km/Ma throughout the past ~5 Ma for the Western Alps. This latter approximation is similar to erosion rates that we calculated for the Western Alps according to the main assumption of Kuhlemann et al. (2001 and 2002; third column of Table 5.1A), but it is twice as much as our recalculated erosion rates for the Western Alps (forth column in Table 5.1A).

However, our estimate of erosion rates of ~0.45–0.65 km/Ma over the past ~5 Ma based on the Alpine sediment budget yielded similar values for both, the Western Alps and the area of their proximal basins (compare forth column of Table 5.1A with last column of Table 5.2A). If so, it would be difficult to invoke a climatic shift toward wetter conditions throughout Europe (e.g., Willett, 2010) due to an intensification of the Atlantic Gulf Stream ~4.6 Ma ago (Cederbom et al., 2004) to explain the relatively uniform erosion in the interior of the mountain belt and its foreland. If instead, erosional unroofing of the Alps was more or less constant at a lower rate since long before 5 Ma, then erosion can be ruled out as the leading cause of isostatically induced uplift of the Alps since 5 Ma. Based on our analysis, the only documented change at around 5 Ma appears to have been the significant increase of the eroding surface area by a factor of three (bottom part of Fig. 5.5). Therefore, it appears unlikely that erosional unroofing of the Alps was greater than crustal thickening during the past ~5 Ma, or in other words that the erosional flux exceeded the accretionary flux. Instead, we suggest that regional-scale tectonic processes resulted in surface uplift and erosion of the western Alpine proximal basins.

The uplift of the Alpine foreland basins should have induced a relative lowering of the regional base-level, and subsequent retrograde erosion across the basins by rivers draining the foreland. Thus, the inner Alps would have not exhibited enhanced erosion until the enhanced rates have been propagated through the uplifted foreland, which is in agreement with our results (Fig. 5.7). In principle, the Danube river may have recorded such an evolution. Since the late Miocene, the river drains most parts of the Molasse basin to the east (Fig. 5.4; Lemcke, 1984). This is also obvious from the sediment budget of the Eastern Alps, because the sediment discharge to the German Molasse basin started to decline at ~10 Ma, and ceased at ~5 Ma (Fig. 5.1B). At about 10 Ma, however, the Danube river system presumably enters the Molasse basin from the east (Lemcke, 1984), and by subsequent head-ward expansion of the river system to the west, previously deposited Alpine material was eroded. This in turn can explain the decline and cessation of the sediment discharge from the German Molasse basin (Fig. 5.1B).

Lastly, the magnitude of the erosion-induced isostatic uplift determined by Champagnac et al. (2007) would be accordingly smaller, because their calculation relies on the validity of the sediment-budget concept. They modeled an uplift of 0.5 km since 1 Ma to have occurred in the central Western Alps in response to a removal of 1.5 km of rock over this time yielding an uplift rate of 0.5 mm/a. We calculated that only ~0.65 km of rock had been eroded in the Western Alps throughout the last 1 Ma (first cell in forth column of Table 5.1A). This is approximately one third of the estimate given by Champagnac et al. (2007). Hence, we expect that isostatically induced uplift in the Western Alps may be on the order of ~0.2 km over the last 1 Ma presuming that the parameter set used by Champagnac et al. (2007) is not changed during the calculation. Assuming a constant rate of erosion over the last 1 Ma, Champagnac et al. (2007) compared their isostatically-induced uplift rate of 0.5 mm/a with the recent vertical motion obtained by precise measurement of leveling lines in Switzerland, that yielded rates of up to 1.1 mm/a in the central Western Alps (Gubler et al., 1981; Kahle et al., 1997). Thus, half of the current vertical motion may be due to isostatically induced uplift (Champagnac et al., 2007). In contrast, if only ~0.2 km of isostatically induced uplift would have occurred in the

last 1 Ma equal to a rate of 0.2 mm/a, then most of the recent vertical motion of 1.1 mm/a in the Western Alps can be explained by tectonic processes.

5.8. Conclusions

Renewed observations made for the Alpine sediment budget shown in Figure 5.1 indicate substantial temporal and spatial differences of the Alpine erosion-deposition pattern during the time from ~34–5 and ~5–0 Ma (Fig. 5.5). The sediment-budget concept holds in the first stage, when eroded material was derived solely from the Alps and deposited in proximal basins such as the Molasse basin (bottom part Fig. 5.5). In contrast, it does not hold in the second stage, when material was eroded from the area of the Alps as well as the proximal foreland basins, and deposited in distal basins such as the Black Sea (bottom part Fig. 5.5). This suggests an approximately threefold increase of the erosion area (bottom part Fig. 5.5), that teased a re-calculation of the Alpine sediment yield for the past 5 Ma, and yielded much lower values than previously thought (Fig. 5.6).

The Alpine sediment discharge remained relatively constant during this time, while the discharge of Alpine-derived material deposited in the foreland basins prior to ~5 Ma increases throughout the Plio-Pleistocene (Fig. 5.7). This is in agreement with an erosional unconformity between Miocene and Quaternary rocks found in the Swiss and German Molasse basin. The erosion of the foreland basins is presumably due their tectonic inversion ~5 Ma ago, as suggested by subsidence curves based on the stratigraphic record of the Molasse basin (Fig. 5.3). Our results contradict recent views that a global climate change led to substantial erosion of mountainous areas since 5 Ma around the world. Instead, regional-scale tectonic processes appear to dictate mountainous erosion over this time span at least in the Alps. Despite the absence of comparable data, such as the Alpine sediment budget (Fig. 5.1), from other mountain belt-foreland basin systems, the inversion of foreland basins as observed in the Alps is a critical component during the orogenic evolution that governs erosion in the associated mountain belt on a long-term scale of millions of years.

5.9. References

Andeweg, B., and Cloetingh, S.; 1998; Flexure and 'unflexure' of the North Alpine German-Austrian Molasse Basin: constraints from forward tectonic modeling; *in:* Mascle, A., Puigdefàbregas, C., Luterbacher, H.P., and Fernandez, M. (eds); Cenozoic Foreland Basins of Western Europe; Geological Society, London, Special Publications, vol. 134, p. 403–422.

Bachmann, G.H., and Müller, M.; 1992; Sedimentary and structural evolution of the German Molasse Basin; Eclogae Geologicae Helvetiae, vol. 85, p. 519–530.

Bernet, M., Brandon, M., Garver, J., Balestieri, M.L., Ventura, B., and Zattin, M.; 2009; Exhuming the Alps through time: clues from detrital zircon fission-track thermochronology; Basin Research; vol. 21, p. 781–798.

Cederbom, C.E., Sinclair, H.D., Schlunegger, F., and Rahn, M.K.; 2004; Climate-induced rebound and exhumation of the European Alps; Geology, vol. 32, p. 709–712.

Cederbom, C.E., van der Beek, P., Schlunegger, F., Sinclair, H.D., and Oncken, O.; 2011; Rapid extensive erosion of the North Alpine foreland basin at 5–4Ma; Basin Research, vol. 23, p. 528–550, doi: 10.1111/j.1365-2117.2011.00501.x.

Champagnac, J.D., Molnar, P., Anderson, R.S., Sue, C., and Delacou, B.; 2007; Quaternary erosion-induced isostatic rebound in the western Alps; Geology, vol. 35, p. 195–198, doi: 10.1130/G23053A.1.

Doppler, G.; 1989; Zur Stratigraphie der nördlichen Vorlandmolasse in Bayrisch-Schwaben; Geologica Bavarica vol. 94, p. 83–133.

Handy, M.R., Schmid, S.M., Bousquet, R., Kissling, E., and Bernoulli, D.; 2010; Reconciling plate-tectonic reconstructions of Alpine Tethys with the geological–geophysical record of spreading and subduction in the Alps; Earth Science Reviews, vol. 102, p. 102–158, doi: 10.1016/j.earscirev.2010.06.002.

Hay, W.W., Sloan II, J.L., and Wold, C.N.; 1988; Mass/Age Distribution and Composition of Sediments on the Ocean Floor and the Global Rate of Sediment Subduction; Journal of Geophysical Research, vol. 93, p. 14933–14940.

Hesse, R.; 1975; Turbiditic and non-turbiditic mudstone of Cretaceous flysch sections of the East Alps and other basins; Sedimentology, vol. 22, p. 387-416.

Geological map of Bavaria; Bavarian Geological Survey, Germany, scale 1:500000.

Gubler, E., Kahle, H.G., Klingele, E., Mueller, S., and Olivier, R.; 1981; Recent crustal movements in Switzerland and their geophysical interpretation; Tectonophysics, vol. 71, p. 125–152, doi: 10.1016/0040-1951(81)90054-8.

Kahle, H.G., Geiger, A., Buerki, B., Gubler, E., Marti, U., Wirth, B., Rothacher, M., Gurtner, W., Beutler, G., Bauersima, I., and Pfiffner, O.A.; 1997; Recent crustal movements, geoid and density distribution: Contribution from integrated satellite and terrestrial measurements; *in:* Pfiffner, O.A., et al. (eds.); Results of NRP 20: Deep structure of the Swiss Alps; Basel, Boston, Berlin, Birkhäuser Verlag, p. 251–259.

Kempf, O., and Pfiffner, O.A.; 2004; EarlyTertiary evolution of the North Alpine Foreland Basin of the Swiss Alps and adjoining areas; Basin Research, vol. 16, p. 549–567, doi: 10.1111/j.1365-2117.2004.00246.x.

Kuhlemann, J.; 2000; Post-collisional sediment budget of circum-Alpine basins (Central Europe); Memorie degli Istituti di Geologia e Mineralogia dell' Universita di Padova, vol. 52, 91 pp.

Kuhlemann, J., Frisch, W., Dunkl, I., and Székely, B.; 2001; Quantifying tectonic versus erosive denudation by the sediment budget: the Miocene core complexes of the Alps; Tectonophysics, vol. 330, p. 1–23.

Kuhlemann, J., Frisch, W., Székely, B., I. Dunkl, I., and Kázmér, M.; 2002; Post-collisional sediment budget history of the Alps: tectonic versus climatic control; International Journal of Earth Sciences, vol. 91, p. 818–837, doi: 10.1007/s00531-002-0266-y.

Kuhlemann, J., and Kempf, O.; 2002; Post-Eocene evolution of the North Alpine Foreland Basin and its response to Alpine tectonics; Sedimentary Geology, vol.152, p. 45–78.

Kuhlemann, J., Dunkl, I., Brügel, A., Spiegel, C., and Frisch, W.; 2006; From source terrains of the Eastern Alps to the Molasse Basin: Detrital record of non-steady-state exhumation; Tectonophysics, vol. 413, p. 301–316.

Lemcke, K.; 1974; Vertikalbewegungen des vormesozioschen Sockels im nördlichen Alpenvorland Perm bis zur Gegenwart?; Eclogae Geologicae Helvetiae, vol. 67, p. 121–133.

Lemcke, K.; 1984; Geologsiche Vorgänge in den Alpen ab Obereozän im Spiegel vor allem der deutschen Molasse; Geologische Rundschau, vol. 73, p. 371–397.

Molnar, P., and England, P.; 1990; Late Cenozoic uplift of mountain ranges and global climate change: chicken or egg?; Nature, vol. 346, p. 29–34.

Molnar, P.; 2004; Late Cenozoic Increase in Accumulation Rates of Terrestrial Sediment: How Might Climate Change Have Affected Erosion Rates?; Annual Review of Earth and Planetary Sciences, vol. 32, p. 67–89.

Pfiffner, O.A., Ellis, S., and Beaumont, C.; 2000; Collision tectonics in the Swiss Alps: Insight from geodynamic modeling; Tectonics, vol. 19, p. 1065–1094.

Raymo, M.E., and Ruddiman, W.F.; 1992; Tectonic forcing of late Cenozoic Climate; Nature, vol. 359, p. 117–122.

Regard, V., Faccenna, C., Bellier, O., and Martinod, J.; 2008; Laboratory experiments of slab break-off and slab dip reversal: insight into the Alpine Oligocene reorganization; Terra Nova, vol. 20, p. 267–273, doi: 10.1111/j.1365-3121.2008.00815.x.

Robl, J., Hergarten, S., and Stüwe, K.; 2008; Morphological analysis of the drainage system in the Eastern Alps; Tectonophysics, vol. 460, p. 263–277.

Schlunegger, F.; 1999; Controls of surface erosion on the evolution of the Alps: constraints from the stratigraphies of the adjacent foreland basins; International Journal of Earth Sciences, vol. 88, p. 285–304.

Schlunegger, F., Melzer, J., and Tucker, G.E.; 2001; Climate, exposed source-rock lithologies, crustal uplift and surface erosion: a theoretical analysis calibrated with data from the Alps/North Alpine Foreland Basin system; International Journal of Earth Sciences, vol. 90, p. 484–499.

Schlunegger, F., Rieke-Zapp, D., and Ramseyer, K.; 2007; Possible environmental effects on the evolution of the Alps-Molasse Basin system; Swiss Journal of Geosciences, vol. 100, p. 383–405, doi: 10.1007/s00015-007-1238-9.

Schmid, S.M., Pfiffner, O.A., Froitzheim, N., Schönborn, G., and Kissling, E.; 1996; Geophysical-geological transect and tectonic evolution of the Swiss-Italian Alps; Tectonics; v. 15; p. 1036–1064.

Sinclair, H.D.; 1997; Flysch to molasse transition in peripheral foreland basins: The role of the passive margin versus slab breakoff; Geology, vol. 25, p. 1123–1126.

von Blanckenburg, F., and Davies, J.H.; 1995; Slab breakoff: A model for syncollisional magmatism and tectonics in the Alps; Tectonics, vol. 14, p. 120–131.

Willenbring, J.K., and von Blanckenburg, F.; 2010; Long-term stability of global erosion rates and weathering during late-Cenozoic cooling; Nature, vol. 465, p. 211–214, doi:10.1038/nature09044.

Willett, S.D., Schlunegger, F., and Picotti, V.; 2006; Messinian climate change and erosional destruction of the central European Alps; Geology, vol. 34, p. 613–616.

Willett, S.D.; 2010; Late Neogene Erosion of the Alps: A Climate Driver?; Annual Review of Earth and Planetary Sciences, vol. 38, p. 411–437.

Zachos, J., Pagani, M., Sloan, L., Thomas, E. and Billups, K.; 2001; Trends, Rhythms, and Aberrations in Global Climate 65 Ma to Present; Science, vol. 292, p. 686–693, doi: 10.1126/science.1059412.

Zhang, P., Molnar, P., and Downs, W.R.; 2001; Increased sedimentation rates and grain sizes 2±4 Myr ago due to the influence of climate change on erosion rates; Nature, vol. 410, p. 891–897.

6. Appendices

6.1. Appendix: Chapter I

6.1.1. Reprint of the Geological Society of America Bulletin

High-resolution spatial rupture pattern of a multiphase flower structure, Rex Hills, Nevada: New insights on scarp evolution in complex topography based on 3-D laser scanning

Ramona Baran[†], Bernard Guest[§], and Anke M. Friedrich[#]
Department of Earth and Environmental Sciences, Ludwig-Maximilians-University Munich, Luisenstrasse 37, 80333 Munich, Germany

ABSTRACT

Fault scarps represent the most obvious expression of tectonic activity at the Earth's surface. Studies on scarp morphology place constraints on fault kinematics and scarp-degradation processes, and were often based on geomorphic dating techniques. Fault scarps exposed in areas of simple topography facilitate data acquisition and interpretation, whereas little work had been done where fault scarps are superimposed on complex, dissected topography. Fault scarps developed in complex topography are commonly observed along flower structures and at tips of strike-slip faults. Such structures are important elements for evaluating the evolution and linking of strike-slip fault systems, and appear to be scale-independent from several meters to hundreds of kilometers. We examined the detailed meter- to hundred meter–scale structure and surface expression of a flank of one fault scarp–bounded pressure ridge (Rex Hills flower structure) by combining field mapping with high-resolution digital elevation model (DEM) analysis. Based on terrestrial laser scanning we generated a detailed DEM and extracted high-resolution topographic cross sections, which enabled us to identify fault scarps and to determine their relative ages and geometry. Our study site is located on the transpressional left-bend between the Pahrump and Amargosa segments of the dextral Stateline fault system. The topography is characterized by alternating valleys and ridges (each ~100 m long, relief of ~4 m). We observed the following: the southern Rex Hills slope exhibits three fault scarps related to three reverse fault branches; the basal scarp (scarp 1) is most continuous, and exhibits five segments, the upper two scarps (scarps 2 and 3) are less continuous. Furthermore, fault scarps exposed on ridge crests are more numerous (up to four to five scarps), and smaller (~5 m high); valleys often exhibit single large (>10 m high), smoothed scarps. To easily detect differences between the scarps, we evaluated the height and slope angle of the scarps using topographic cross sections. Our analysis indicates that scarp shape is influenced by fault dip, lithology, and degradation processes resulting in large scatter and broad overlap in scarp-height–slope-angle space. The analysis further indicates that scarp degradation is stronger in the valleys, and that the preservation potential of small, individual fault scarps is therefore greater on the ridge crests. We compared our fault-scarp data with published, calibrated data yielding an age of ~2 ka for the Rex Hills scarps consistent with an earlier finding. This suggests that the scarp shape mainly reflects progressive degradation since the most recent surface rupture. Our approach of analyzing high-resolution topographic data of closely spaced fault scarps is promising especially when combined with subsurface data as well as geochronological and paleoseismic data, and it provides a basic scheme for analyzing scarp populations in a complex topographic region. Despite the absence of subsurface data, our approach allowed the study of complex high-resolution fault-scarp morphologies across a flower structure for the first time.

INTRODUCTION

Generally, fault scarps represent the best recognizable natural surface expression of seismic activity along active fault systems (e.g., Wallace, 1977; Yeats et al., 1997). Fault-scarp morphology studies had been conducted to constrain fault kinematics and especially scarp degradation often by using geomorphic dating techniques (Fig. 1; e.g., Bucknam and Anderson, 1979; Hanks et al., 1984; Avouac, 1993; Arrowsmith et al., 1998, as examples along strike-slip and normal faults). Typically these studies are carried out where fault scarps are continuously exposed in areas of relatively simple and uniform topography, and where single isolated fault-scarp profiles can be easily acquired using labor-intensive techniques (e.g., Arrowsmith et al., 1998). These techniques are difficult to apply in areas where many small scarps are exposed, or where scarps are very subtle. Consequently, the patterns that result from fault scarps that are superimposed on a more complex and dissected topography have not been adequately explored at smaller spatial scales and compared with a larger spatial scale as considered by, e.g., Landgraf et al. (2009).

A potentially efficient solution to close this gap in our knowledge is provided by recently developed terrestrial laser-scanning technologies, which are rapidly developing into effective research tools in tectonic geomorphology. A laser-scanner survey can rapidly (within minutes) acquire large amounts of topographic data with both a high resolution (up to a few cm) and high accuracy (of only a few mm; e.g., Buckley et al., 2008). These data can then be converted into high-resolution digital elevation models from which geomorphological data sets can be extracted. Furthermore, the high resolution of these data permits the extraction of large sub-data sets, and the identification and analysis of subtle features not obvious in the field.

Fault scarps that form in complex topography are commonly observed along flower structures occurring at fault bends and tips of strike-slip faults (e.g., Sylvester and Smith, 1976; Sylvester, 1988; van der Pluijm and Marshak, 2004; Cowgill et al., 2004a, 2004b). These structures are particularly important for the evolution and linkage of separate strike-slip

[†]E-mail: ramona.baran@iaag.geo.uni-muenchen.de
[§]Current address: Department of Geoscience, University of Calgary, 2500 University Drive Northwest, Calgary, Alberta, T2N 1N4, Canada, e-mail: bguest@ucalgary.ca
[#]E-mail: friedrich@lmu.de

897
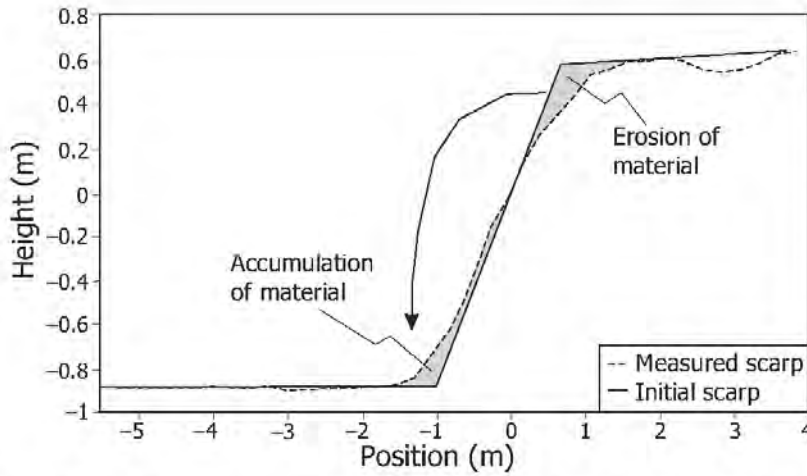
Figure 1. Vertical exaggerated topographic profile of a 100-yr-old scarp where the dotted line indicates the measured profile and the black line is the form of the initial scarp derived by using an initial slope of 41° (modified after Nivière et al., 1998). The gray shaded areas mark the location of erosion and accumulation of material along the scarp profile explaining scarp degradation.

ing geologic mapping, seismic data, and analog modeling (e.g., Wilcox et al., 1973; Harding, 1985; Naylor et al., 1986; McClay and Dooley, 1995; Dooley and McClay, 1996; McClay and Bonora, 2001). In contrast, however, few detailed studies of small-scale, flower-structure surface morphology have been documented in the geologic literature. The likely reason is that these studies require time-consuming and occasionally expensive field work, and the complexity of the data returned requires acquisition of a very large data set. Therefore, a large amount of under-utilized information about the geometry and kinematics of flower structures is contained in their surface expression, especially in surfaces exhibiting fault scarps or sets of fault scarps. For example, fault-scarp analysis can provide information about how deformation is distributed in time and space on the thousand to hundred thousand year scales (e.g., Wallace, 1987; Arrowsmith et al., 1998; Carretier et al., 2002; Friedrich et al., 2003, 2004; Wesnousky, 2005; Landgraf et al., 2009). To this end, high-resolution surface scans provide an efficient approach for extracting and analyzing the detailed surface characteristics of a given structure and quantifying its spatial and temporal evolution.

fault segments (Cunningham and Mann, 2007; Landgraf et al., 2009).

As with faults in general, flower structures are scale-independent features ranging in size from the orogen scale of hundreds of kilometers to more regional scales of tens of kilometers in extent, such as the Confidence Hills in southern Death Valley (Dooley and McClay, 1996), and down to the tens of meters scale of small sag ponds and pressure ridges (e.g., Crowell, 1974; Wakabayashi et al., 2004 for the latter two scales). As such, there have been many studies of these features where their internal geometry and evolution typically are inferred by interpret-

There are several small-scale transpressional flower structures within the eastern California shear zone; however, only a few exhibit surface fault scarps. The Rex Hills (informal name) flower structure is located near Pahrump, Nevada, on a left-bend of the Stateline fault system (Fig. 2), and it exhibits a set of subtle fault
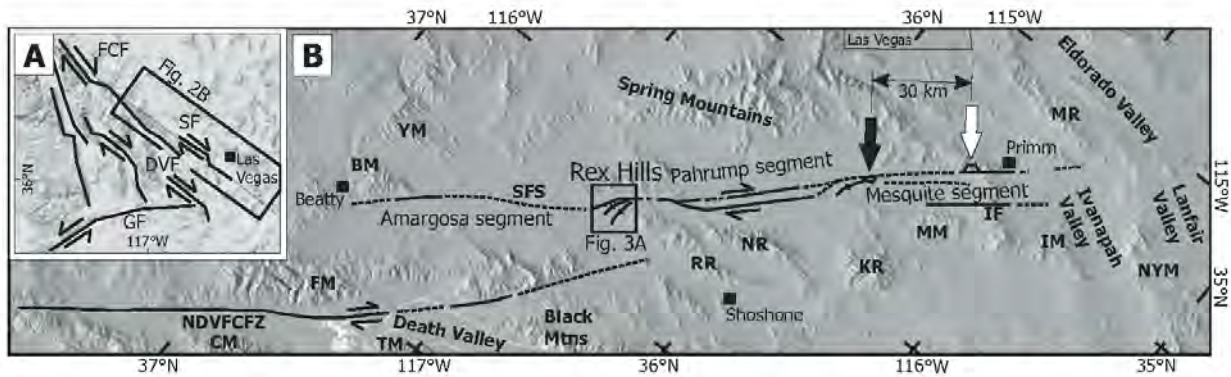
Figure 2. (A) Simplified location map of the Stateline fault and major fault zones of the eastern California shear zone. Abbreviations: GF—Garlock fault, SF—Stateline fault, FCF—Furnace Creek fault, DVF—Death Valley fault. (B) Shaded relief map showing the Stateline fault system (SFS) and nearby major active faults of the surrounding area (modified after Guest et al., 2007). The white arrow marks the position of the Devil Peak rhyolite intrusions, and the black arrow marks the offset volcanic and associated rock-avalanche deposits at Black Butte described by Guest et al. (2007). Abbreviations: IF—Ivanapah fault, NDVFCFZ—northern Death Valley Furnace Creek fault zone, SFS—Stateline fault system, BM—Bare Mountains, CM—Cottonwood Mountains, FM—Funeral Mountains, IM—Ivanapah Mountains, KR—Kingston Range, MM—Mesquite Mountains, MR—McCullough Range, NR—Nopah Range, NYM—New York Mountains, RR—Resting Spring Range, TM—Tucki Mountain, YM—Yucca Mountain.

scarps on its flanks, which are challenging to map in the field using traditional methods. Furthermore, due to their size and accessibility the Rex Hills are an excellent natural laboratory to study the surface expression of a positive flower structure in an arid environment using a terrestrial laser scanner.

In this paper we present the results of a study aimed at characterizing the shape of fault scarps exposed along the kilometer-scale Rex Hills flower structure where we combined detailed field mapping with high-resolution digital elevation model (DEM) analysis. A new feature of our approach is the use of very high-resolution DEM data derived from a ground-based laser-scanning survey. This technique allows us to identify very subtle scarps not recognized otherwise, and facilitates efficient extraction of sub-data sets. It also provides a potentially powerful tool for evaluating scarp degradation (Fig. 1) superposed on larger scale erosion patterns of hillslopes, and for morphological relative dating within scarp populations. The latter may be the critical component required to evaluate ancient scarp populations.

STATELINE FAULT SYSTEM

The Stateline fault system is a dextral strike-slip fault that, between latitudes 35°N and 37°N, probably forms the eastern limit of the eastern California shear zone–southern Walker Lane belt as defined by Dokka and Travis (1990) and Stewart (1980) (Guest et al., 2007; Fig. 2A). Geodetic data indicate an increase in the NW component of the surface velocity across the northernmost segment of the Stateline fault system (Fig. 2B) from ~0 mm/a east of the fault to 0.9–1.1 mm/a west of the fault with respect to a fixed North American reference frame (Wernicke et al., 2004). Holocene activity along portions of the Stateline fault system and Pleistocene activity along the entire fault is documented by tectono-geomorphic observations (Menges et al., 2003; Guest et al., 2007).

Offset estimates for different segments of the Stateline fault system range from ~25–45 km (Poole and Sandberg, 1977; Cooper et al., 1982; Stevens, 1991; Schweickert and Lahren, 1997) in the north to ~10 km in Stewart Valley, west of Pahrump (Burchfiel et al., 1983), and 3 km (Walker et al., 1995) in the south. These offset estimates are typically based on the offset of pre-Cenozoic markers. The most recent offset estimate of ~30 km during the past ~13.1 Ma along the southern Stateline fault system was determined by Guest et al. (2007), and is based on the dextral offset of ~13.1 Ma old proximal volcanic and associated rock-avalanche deposits (Fig. 2B). This provides a minimum long-term,

time-averaged geologic displacement rate of ~2.3 mm/a for the southern Pahrump and Mesquite segments of the Stateline fault system (Fig. 2B). The geodetic surface velocity across the northern part of the Stateline fault system alone is 0.7–1.2 mm/a with respect to a fixed North American reference frame (Wernicke et al., 2004; Hill and Blewitt, 2006).

On the earthquake-recurrence time scale (~10 ka), however, fault-scarp degradation (Fig. 1) and morphologic changes due to ruptures along the Stateline fault system are poorly documented and have therefore not been related to the evolution of fault structures and the Stateline fault system. Hence, we evaluated fault scarps and drainage offsets related to the Rex Hills flower structure using high-resolution topographic data based on 3-D laser scanning.

TECTONO-GEOMORPHIC SETTING OF THE STUDY AREA

Following Guest et al. (2007), the Stateline fault system is divided into three segments that are separated by contractional left-bends: the Amargosa segment to the north, the central Pahrump segment, and the Mesquite segment to the south (Fig. 2B).

The Rex Hills study site lies along a transpressional left-bend between the Pahrump and Amargosa segments of the Stateline fault system where the central part of the Stateline fault system crosses from Stewart Valley into southern Amargosa Valley (Fig. 2B). Late Quaternary surface deformation along this portion of the Stateline fault system is associated with a large transpressive domal uplift centered on the northern piedmont of the Resting Spring Range (Menges et al., 2003). Linear pressure ridges in this area are typically bounded by a discontinuous, 8- to 10-km-long set of aligned, en echelon fault scarps. These scarps are up to ~3 m high with slope angles of 20°–30°, and associated with dextral drainage offsets of 0.5 to ~5 m. Menges et al. (2003) determined vertical and lateral offsets yielding an average dextral-reverse net slip of ~3 m for the most recent faulting event. Furthermore, they inferred a latest Holocene age (<2 ka) for this event based on stratigraphic relationships and scarp morphology. This rupture event was a M_w 7.1–7.3 event whose rupture zone most likely continued ~35–40 km to the SE through Stewart Valley into northwestern Pahrump Valley (Menges et al., 2003). Lastly, this rupture-length estimate is based on the rupture length–displacement relationship of Wells and Coppersmith (1994) because the rupture length is poorly constrained in this area, and the displacement size indicates that the rupture length is greater than the exposed fault-scarp system.

The Rex Hills are two small connected hills: the NW hill is 40 m high and has a dome shape with a diameter of ~900 m; the SE hill is 45 m high, boat-hull shaped, and ~1500 m long by ~750 m wide (Fig. 3A). The hills consist of poorly consolidated Plio-Pleistocene conglomerate with rare bedding exposures that strike parallel to the trend of the hills (Fig. 3B). Unconsolidated and locally overturned (Fig. 4A), Plio-Pleistocene fluvio-lacustrine sediments are located at the base of the southern Rex Hills flank and on their northwestern slope (Fig. 3B). The sediments exposed at the Rex Hills site consist of quartzite and carbonate clasts, and are presumably derived from the Montgomery Mountains and Resting Spring Range, which consist of Precambrian and Paleozoic sedimentary rocks (Figs. 2B and 3B; Burchfiel et al., 1983). However, due to uncertainty about the amount of dextral offset in this region, other source regions are possible.

The Rex Hills fault pattern exhibits a reverse and a dextral strike-slip component. The dextral component is expressed as drainage offsets with a magnitude of up to ~10 m (Fig. 4C), commonly associated with zones of highly fractured clasts within the Plio-Pleistocene conglomerate that show dextral sense of shear (Fig. 4D). The thrust component is expressed as 0.3- to 2-m-high fault scarps (Fig. 4B).

The southern flank of the eastern Rex Hills is defined by a N-dipping reverse fault. The main evidence supporting this interpretation is the presence of steeply N-dipping, overturned, channelized fluvial sediments sticking out in the footwall of the fault defining the north limb of a footwall syncline (Figs. 4A and 3B). The surface expression of this fault is characterized by 1- to 2-m-high fault scarps (Fig. 4B) and dextral drainage offsets of 0.75–1.5 m.

The northern flank of the Rex Hills is also bounded by dextral oblique reverse faults. The eastern Rex Hills north flank exhibits clear dextral offsets of 2–3 m (Fig. 4C) as well as small poorly defined fault scarps (Fig. 3B). Faults exposed along the western Rex Hills north flank exhibit dextral drainage offsets of 2–3 m to ~10 m, dextrally fractured conglomerate, and 1- to 2-m-high fault scarps. Here, the fault is vertical to steeply S-dipping (Fig. 3B) based on fracture orientations in the conglomerate. The Plio-Pleistocene strata on the northern flank show no clear evidence of folding (e.g., overturned bedding), but bedding adjacent to the fault in the footwall dips steeply to the SW.

The fault pattern in the adjacent area SE of the Rex Hills is marked by a general NW-SE trend. The fault location is inferred from different characteristics: two springs are located in this area where several shrubs lie along a NW-SE

147
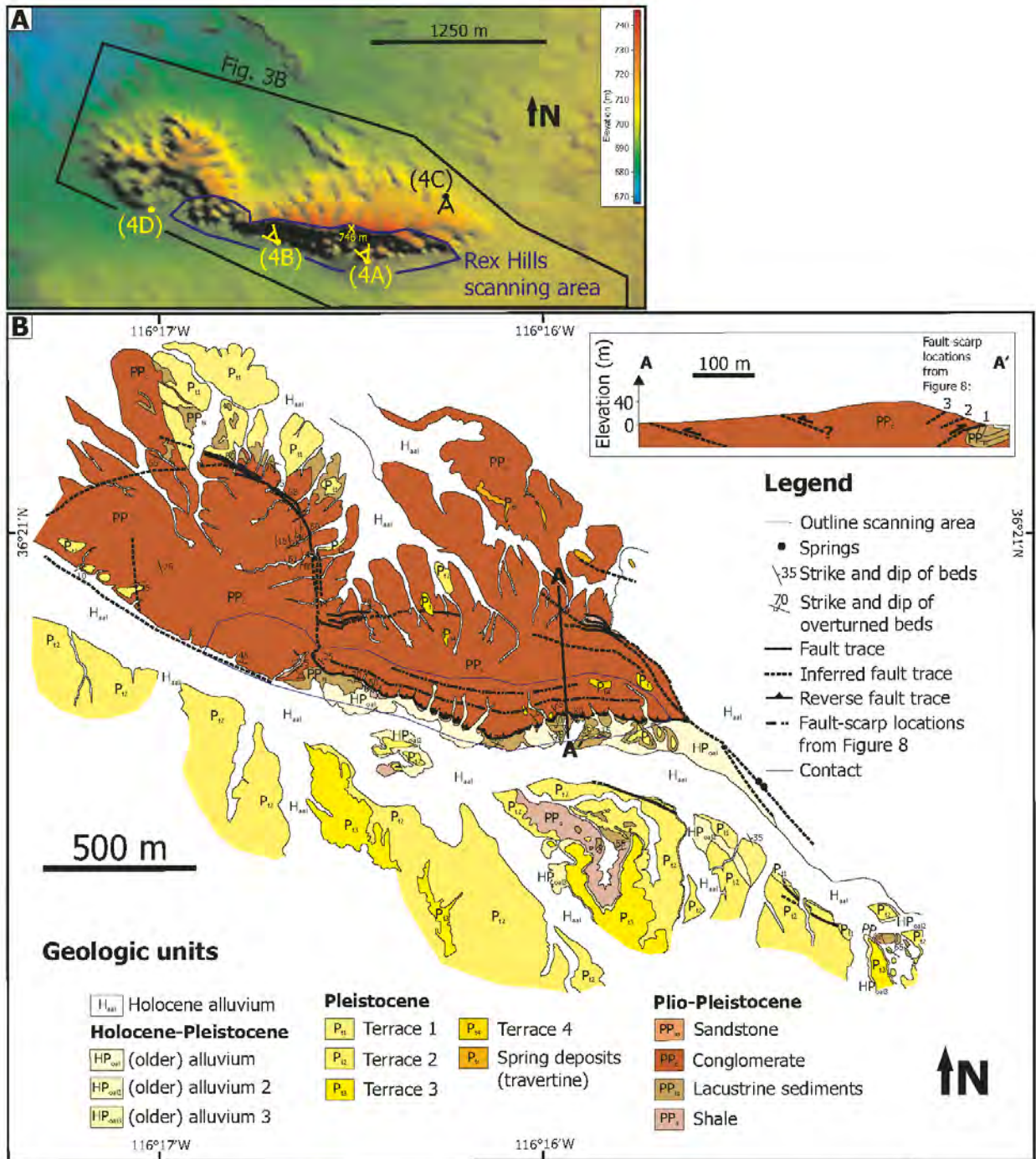
Figure 3. (A) U.S. Geological Survey digital elevation model (DEM) of the Rex Hills with 10 m resolution derived from the National Elevation Data set (NED). The mapping (Fig. 3B) and laser-scanning area are indicated with a black frame and a blue frame, respectively. Labels in brackets and points with indicated view direction (yellow and black) emphasize the locations of pictures shown in Figure 4. (B) Detailed geologic map of the Rex Hills site. The scanning area is marked with a blue frame. The inset shows a general geologic cross section.

148
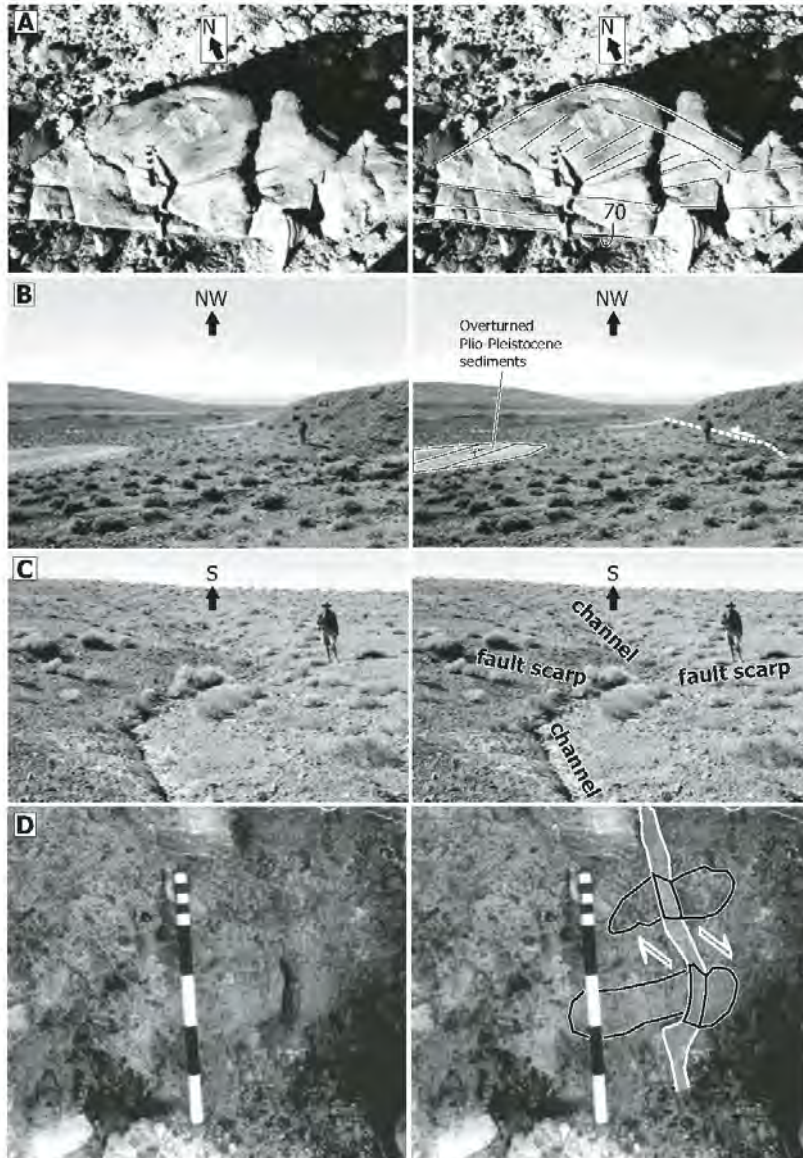
Figure 4. Locations of pictures are shown in Figure 3A. The colored version of this figure is contained in Figure DR4 [see footnote 1]. (A) Photo looking down onto overturned Plio-Pleistocene lacustrine sedimentary rock sticking out at the southern Rex Hills base. The black lines emphasize bedding, outline of the trough, and crossbedding within this small trough. The strike and dip of the bed measured at the steeply dipping bedding plane (upside down) is 110/70 NNE, and indicated by the appropriate symbol. The bedding plane appears as a line due to the map-view perspective of this photo. The arrow pointing to the north is rotated slightly relative to the strike and dip symbol in order to ensure the accuracy of the view. (B) Fault scarp exposed on the southern flank of the Rex Hills. (C) Dextral drainage offset exposed on the northern Rex Hills flank. The location of the offset channel and fault scarp are indicated by appropriate text labels. (D) Fault zone within the Plio-Pleistocene conglomerate. The vertical fault plane is indicated by transparent white, and is outlined with a solid white line. The offset clasts are outlined by a solid black line. The right-hand white arrow is supposed to indicate movement out of the rock along the fault, whereas the left-hand white arrow indicates movement into the rock.

trend, subparallel to the strike of the main fault trace (Fig. 3B). Small scarps observed on the surface of the Pleistocene terrace level P_{t2} are aligned in NW-SE direction and are probably fault related (Fig. 3B).

METHODS

To study the morphology of the Rex Hills scarps, we combined detailed geologic mapping (Fig. 3B) with the interpretation of a high-resolution DEM (Fig. 5). We focused on mapping of individual faults, fault scarps, and offsets recorded in bedrock gullies. The DEM is based on measurements made with a terrestrial laser scanner (Riegl 3-D laser scanner LMS-Z420i®) in March and April 2006, and it covers the E-W–trending southern flank of the eastern boat hull–shaped half of the Rex Hills indicated by a blue frame in Figure 3. This method is based on the emission of a laser beam and its reflection from the terrain surface. The resulting point data are used to generate a detailed DEM with cm-scale resolution. We summarized the field work and scanning procedure in the GSA Data Repository Figure DR1[1].

RESULTS

Laser Scanner–Based DEM (LDEM)

Two surface features of the Rex Hills southern slope are identified in different display formats of the LDEM; different views of the LDEM (Figs. 5A and 5B) on one hand and a contour map of the LDEM (Fig. 5C) on the other. The first feature is the alternation of small valleys and ridges (each ~100 m long, relief of ~4 m) descending from the main ridge axis along the S-dipping slope of the Rex Hills (Figs. 5A and 5C). The second is a set of triangular facets at the base of the slope related to the oblique-reverse fault scarps (Fig. 5A), which we interpreted as gravity-controlled faces due to fluvial undercutting of their base resulting in scarp retreat. Hence, they will not be considered further.

The slope angle is a critical diagnostic feature of fault scarps (e.g., Bucknam and Anderson, 1979; Nash, 1980). Young scarps should have a steep slope angle, whereas the slope angle

149

Figure 5. High-resolution topographic maps showing the results of the 3-D laser-scanner survey with cm-scale resolution. (A) 3-D view of the laser scanner–based digital elevation model (LDEM). Triangular facets described in the text and the alternation of ridges and valleys are clearly visible in this view. The location of the LDEM is marked in Figure 3 by a blue frame. The black arrow on the right side of the LDEM indicates the elevation difference of 40 m. The dashed white line at the bottom of the LDEM marks the location of the lowermost points of topographic profiles extracted from the LDEM. The profile numbering is also shown, and the topographic profiles are evenly spaced between the indicated profile location intervals traversing along the ridges and valleys. The white frame shows the outline of the LDEM contour map (Fig. 5C). (B) Both pictures show an oblique 3-D view of the LDEM looking east along the Rex Hills front. The location of the basal scarp is obvious in this view, and is indicated by a solid white line in the right-hand picture. In contrast, the mapped upper fault trace is more difficult to recognize, and indicated by a dashed white line. (C) Contour map of a LDEM section (Fig. 5A for location). The black lines indicate local fault traces.

150

decreases with age assuming a constant diffusivity, and a homogenous material (e.g., Bucknam and Anderson, 1979). We used the slope map of the LDEM to identify fault scarps and to attempt a distinction between the different fault scarps (Fig. 6B). All scarps formed in the same material because the entire southern Rex Hills slope consists of Plio-Pleistocene conglomerate (Fig. 3B). Linear features with a steep angle are assumed to be fault scarps, if there is no alternative scarp-producing process available, e.g., fluvial drainage. These linear features are evident in the LDEM at the base of the southern Rex Hills slope (Fig. 6B) and correspond to the reverse segment identified in Figure 3B. In

contrast, the eastern part of the southern slope is characterized by the alternation of small valleys and ridges with steep slopes (Fig. 6A), which makes fault-scarp mapping using the slope map in this area more difficult. We marked the traces mapped along the eastern Rex Hills slope (Fig. 6B) in an oblique view of the LDEM for comparison (Fig. 5B). Furthermore, the set of gravity-controlled and fault-related triangular facets observed in Figure 5A are characterized by a steep angle, and marked with a dotted line as retreating scarp (Fig. 6B).

In order to detect fault scarps that cannot be identified in the LDEM at first sight, and to image especially their spatial distribution and

continuation, 83 detailed topographic profiles mainly perpendicular to the E-W trend of the eastern half of the Rex Hills were extracted. These profiles are spaced unevenly based on the width of the valleys and ridges, and include profiles that traverse along small valleys and ridge crests (Fig. 5A). The profiles were used to extract the scarp height and slope angle for each identified scarp (Table DR1 [see footnote 1]; Fig. 7A). Frequently more than one scarp can be observed in a profile (Fig. DR2 [see footnote 1]). In these cases, the fault-scarp labeling listed in Table DR1 starts with the lowermost scarp.

The uncertainty associated with the scarp-height determinations amounts to ±20 cm (1 σ).

Figure 6. Slope-angle map of the laser scanner–based digital elevation model (LDEM): the very light-gray color fits to a minimum slope angle of 0°, and the dark-gray color correlates with slope angles of 45°. The colored version of this figure is further contained in Figure DR5 [see footnote 1]. (A) Slope map showing the alternation of gullies and ridges. (B) Slope map showing location of mapped fault scarps, inferred fault traces, and gravity-controlled scarps.

151
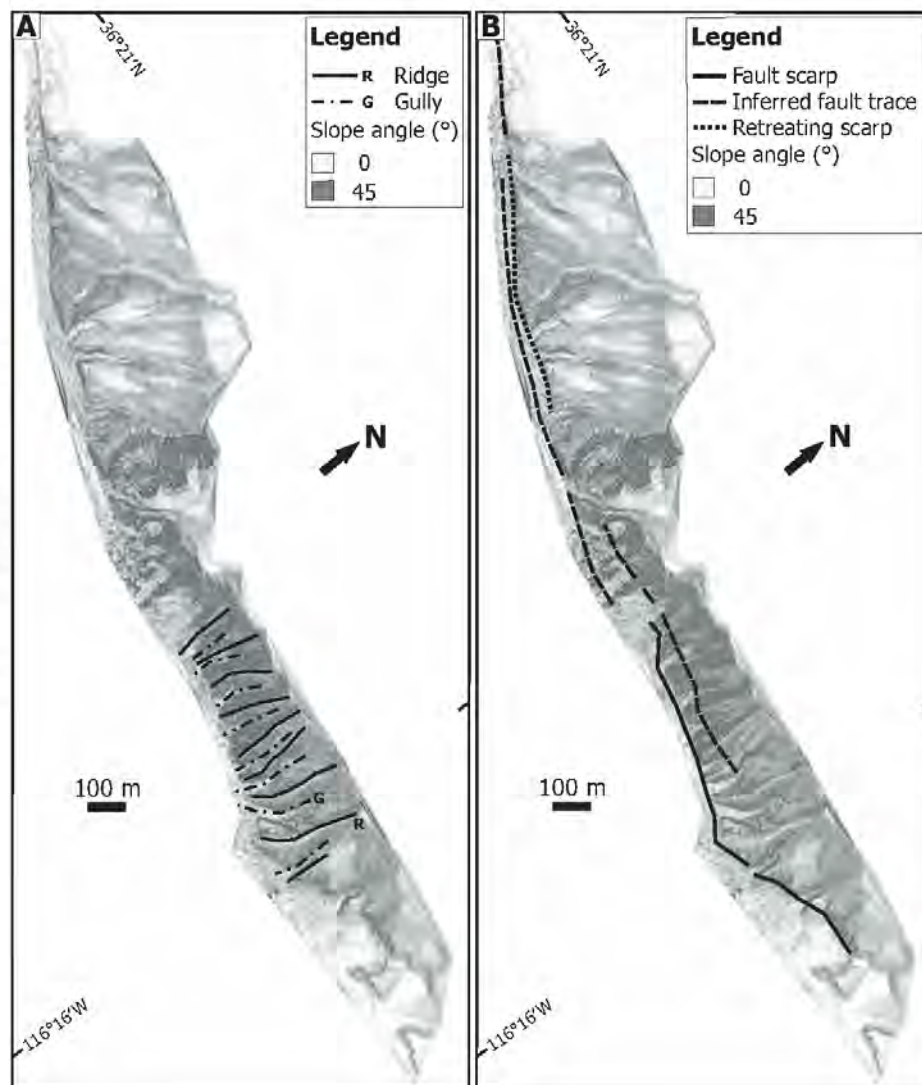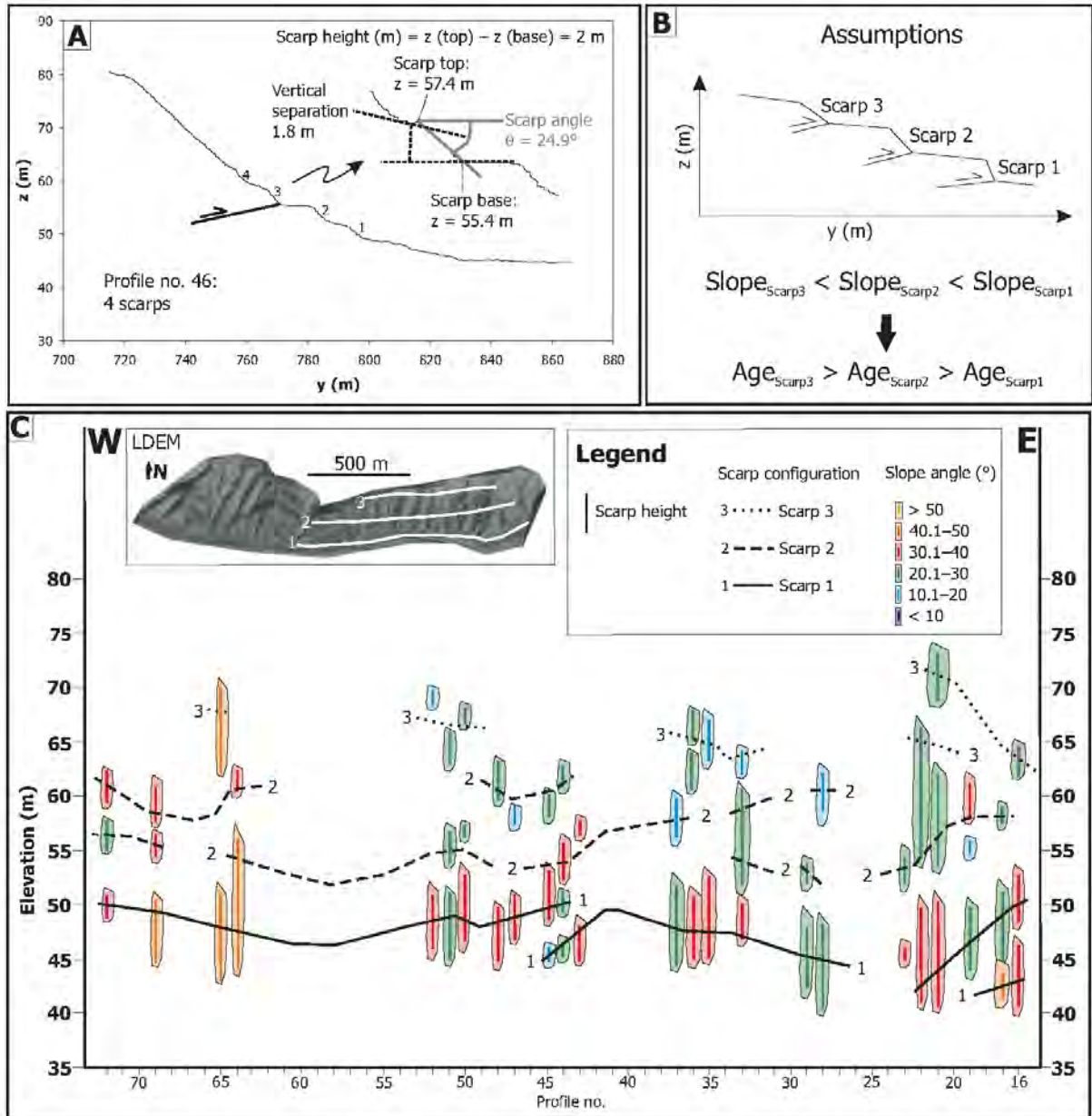
Figure 7. (A) Topographic profile number 46 and definition of scarp height, slope angle θ, and vertical separation used for the profile analysis in Figure 8. The profile location is shown in Figure 5A. (B) The sketch shows the expected fault-scarp profile according to the assumption that the scarp-slope angle decreases with age (Bucknam and Anderson, 1979). (C) Scarp profiles extracted from the laser scanner–based digital elevation model (LDEM) fitting the expected profile shape shown in Figure 7B. We inferred the scarp configuration based on these selected profiles and adopted this pattern in Figure 8. The location of the three fault scarps is also shown in the LDEM, and the profile locations can be obtained from Figure 5A.

152

Individual point locations have a measurement uncertainty of ±5 cm (1 σ) representing an error induced by the laser scanner. The scarp height, as indicated in Figure 7A, is defined by the difference in the z-coordinate between two points resulting in a total measurement uncertainty of ±10 cm (1 σ). The remaining uncertainty of ±10 cm (1 σ) is subjectively introduced by selecting the base and top points of each scarp profile manually (Fig. 7A). Due to the large point-cloud density, repeated selection of single top and base points yielded similar scarp-height values for each scarp differing by ~20 cm. Thus, the total uncertainty adds up to ±20 cm (Figs. 10–14).

To establish a fault-branch configuration that explains the observed fault-scarp pattern, we followed the assumptions first stated by Bucknam and Anderson (1979) that the slope angle of fault scarps decreases with time and therefore with age (Fig. 7B). Next, we isolated a set of fault-scarp profiles fitting this assumption (Fig. 7C), and based on this evaluation we assigned a possible configuration of reverse fault branches and segmentation patterns to the entire fault-scarp set (Fig. 8). The scarp lines 1–3 in Figure 8 are intended to give the general configuration of the scarps and associated fault branches. We used these lines to approximate fault locations based on scarp symmetry, although the exact fault locations cannot be determined without subsurface data.

Based on the topographic profile analysis, we identified three fault scarps (Fig. 8): scarp 1 is continuous, extends along the base of the slope, and exhibits five segments; scarps 2 and 3 are less distinct and extend along the upper part of the slope where scarp 2 exhibits four segments. In an oblique 3-D view of the LDEM, scarp 1 is most obvious due to its continuous surface expression in contrast to scarp 2 which is less clearly defined (Fig. 5B). Scarp 3 cannot be detected using such a perspective.

Generally, the steeper, smaller, individual fault scarps are better preserved along profiles that lie parallel to a ridge crest (e.g., profile numbers 20, 39, 46, and 61; Fig. 8A), whereas profiles located in valleys commonly exhibit a higher, single fault scarp (e.g., profile numbers 42, 53, 64, and 77; Fig. 8A). The scarp height for all scarps ranges from 0.3 m up to 13.2 m over two orders of magnitude. The slope angles generally increase from E to W (Fig. 8A).

To evaluate the influence of fault dip on scarp morphology along the Rex Hills slope, we approximated the local near-surface dip angle of the two fault branches related to the more continuous scarps 1 and 2 (Fig. 5C). Where possible we mapped the fault trace on a topographic map of the LDEM (1 m contour-line interval; Fig. 5C) by assuming that the base of scarps 1 and 2 are

equivalent to the fault trace (Fig. 8). Based on the intersection of the local fault trace with topography, we inferred that the fault associated with scarp 1 exhibits a shallow near-surface dip of 10°–15°. In contrast, the scarp 2 fault is characterized by a steeper dip of ~10°–20° (Fig. 5C).

Dextral offsets in the drainage network were identified in the field as a common morphological feature of the Rex Hills structure (Fig. 4C). Within the LDEM, magnitudes for nine dextral offset features were measured along straight lines, taken from one termination of the offset feature to the other (Fig. 9; Fig. DR3 [see footnote 1]). All of these features were formed in poorly consolidated Plio-Pleistocene conglomerate (Fig. 3B). The offset magnitude ranges from 7.77 m to 56.5 m (Fig. 9; Table DR2 and Fig. DR3 [see footnote 1]). We estimated the uncertainty bound for each measurement to be 30% (equal to 3 σ) of the derived offset value given that some of the offset features are curvilinear and intersect the fault at low angles (Fig. 9B; Table DR2 [see footnote 1]). Moreover, erosion focused in the drainage valleys led to the deposition of younger sediments, which may have masked parts of the older offset channel bed. The 30% bound further accounts for subjectively introduced uncertainties mainly due to the fact that some offset features are not as obvious as the examples shown in Figures 9B–9E. In some cases, the offset evaluation is further hampered by the LDEM resolution. Where the LDEM grid next to the offset feature is coarser, e.g., triangles increase in size, the low point-cloud density is due to shielding effects during the scanning induced by the Rex Hills valley-ridge morphology (e.g., Fig. DR3E [see footnote 1]).

Scarp-Height versus Slope-Angle Plots

The height and slope angle of fault scarps are two diagnostic features required to characterize the evolution of normal fault scarps in cohesionless material (Bucknam and Anderson, 1979; Nash, 1980; Hanks et al., 1984; Fig. 1 for comparison). Profile studies on late Quaternary normal fault scarps revealed that the slope angle is related to the logarithm of scarp height for a given age, and that for fault scarps of a given height the slope angle decreases with age (Bucknam and Anderson, 1979). Here, the approach described by Bucknam and Anderson (1979) is sufficient although more sophisticated models are available. We evaluated the relationship between scarp height and slope angle for the scarps identified in the 83 topographic profiles extracted along the southern slope of the Rex Hills (Fig. 8). Using this basic approach enabled us to easily detect differences between several fault scarps in detail without any modeling efforts.

Considering slope angle and scarp height of all scarps extracted from the 83 profiles yields a scatter plot with a near circular data distribution (Fig. 10) resulting in poor correlation for the three fault scarps. In an effort to reduce the scatter, we plotted the profile results from ridges (black dots) and valleys (white dots) separately for each scarp (Fig. 11). The resultant scatter plots show an improvement in the ridge-profile correlation coefficients for scarps 1 and 3, and minimal improvement for scarp 2 (black regression lines in Fig. 11). The valley-profile data (gray regression lines in Fig. 11) generally exhibit less correlation except for scarp 3 (Fig. 11C).

To further improve the correlations and obtain insights into the surface processes controlling the scarp geometries, we reduced the data in several steps until better correlation coefficients were obtained compared to Figure 11. This procedure is justified because we extracted the topographic profiles manually from the LDEM. First, we removed ambiguous scarp profiles from the fault-scarp data. These are possible compound fault scarps where the upper and lower portions may belong to separate scarps that have merged (e.g., profile numbers 22, 42, 53, 64, 77, and 80 in Fig. 8). Secondly, we eliminated scarp profiles located at the tips of fault-scarp segments (e.g., profile numbers 43, 44, and 45 for the basal fault scarp in Fig. 8B), which are characterized by smaller offsets than the central portion of the segments. After completing this operation, we were able to obtain a slight improvement in the overall correlation (Fig. 12), and noted that we obtained better correlation for the ridge-profile data (black regression lines) than for the valley-profile data (gray regression lines) except in the case of scarp 2 (Fig. 12B), which exhibits less correlation than scarps 1 and 3 (Figs. 12A and 12C). To further improve the correlation for scarp 2, we isolated profiles that are located solely on the ridge crests and neglected profiles from the entire valley walls and floors where erosion would affect scarp morphology. Some of the scarp profiles previously indicated as ridge profiles (Figs. 11B and 12B) are not located on ridge crests. They are actually located on the uppermost valley walls (e.g., profile number 21 in Fig. 8), where the slope is rather gentle compared to the middle part of a valley wall (also Fig. 6). Considering only ridge-crest profiles yields an improved correlation coefficient for scarp 2 (Fig. 13). Finally, due to the fact that in Figure 12 the valley regression lines plot below the ridge regression lines compared to Figure 11 (discussed below), we focused our further evaluation on the ridge-profile data of scarps 1 and 3 (Figs. 12A and 12C), and the ridge-crest profile data of scarp 2 (Fig. 13).

153
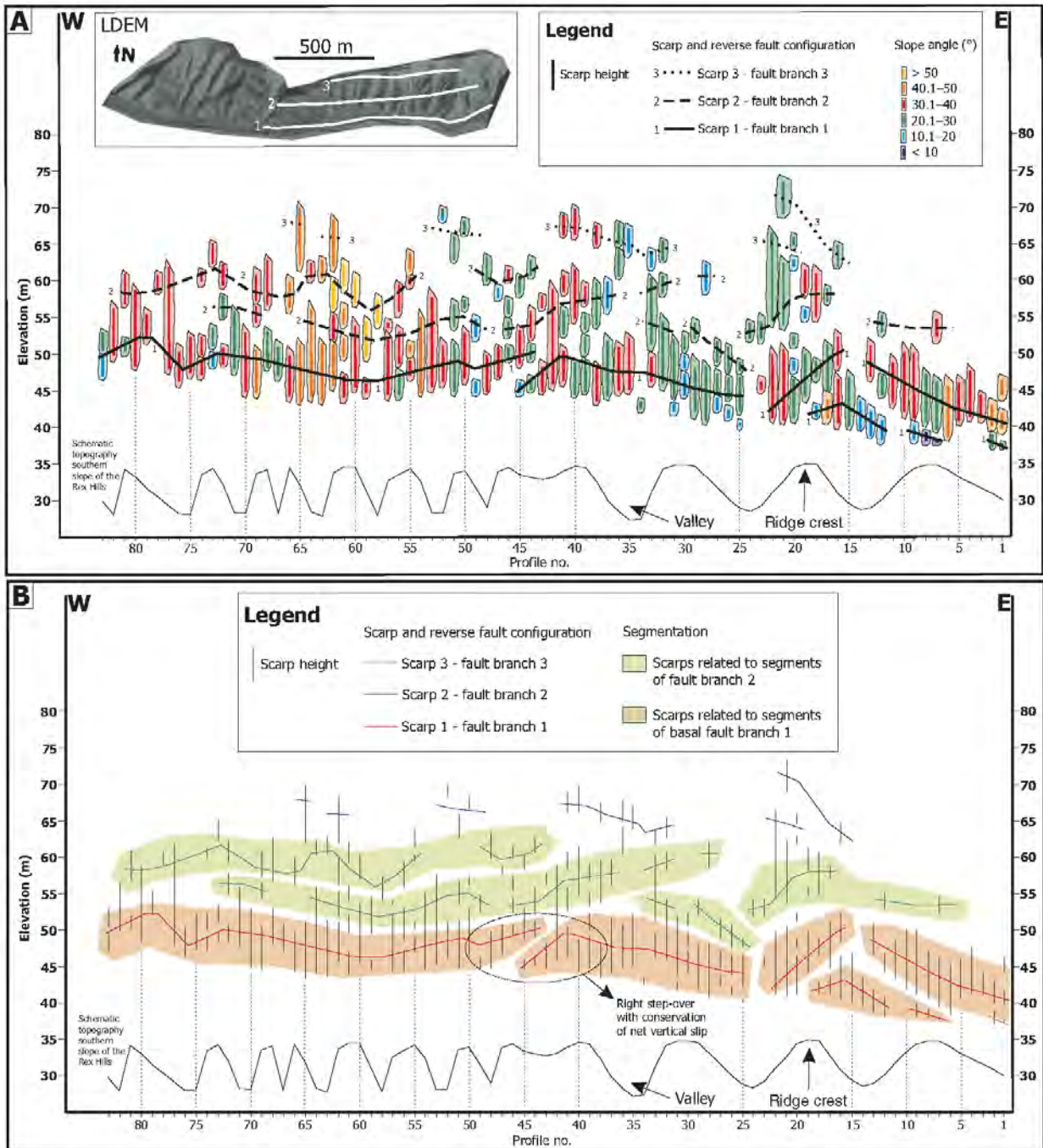
Figure 8. Summary of the topographic profile analysis. (A) The scarp-slope map shows scarp heights and maximum slope angles of the individual fault scarps identified in the 83 topographic profiles extracted from the laser scanner–based digital elevation model (LDEM). The location of the topographic profiles is sketched at the bottom of the plot, and can be alternatively inferred from Figure 5A. The location of the three fault scarps is shown in the LDEM. (B) This plot is similar to Figure 8A but without the scarp slope angle. Instead, it shows only the scarp heights of the individual fault scarps. The possible configuration of reverse fault branches and their segmentation are colored in order to explain the observed fault-scarp pattern.

Figure 9. (A) The location of nine measured dextral offsets is marked in the laser scanner–based digital elevation model (LDEM), and summarized in Table DR2 [see footnote 1]. The offsets marked with a continuous rectangle are shown in detail in Figures 9B–9E. In contrast, no detail is shown for offsets marked with a dashed rectangle. The legend is valid for the offsets shown in Figures 9B–9E. (B) Details of dextral offset number 1. (C) Details of offset number 2. (D) Details of offset number 5. (E) Details of offset number 9.
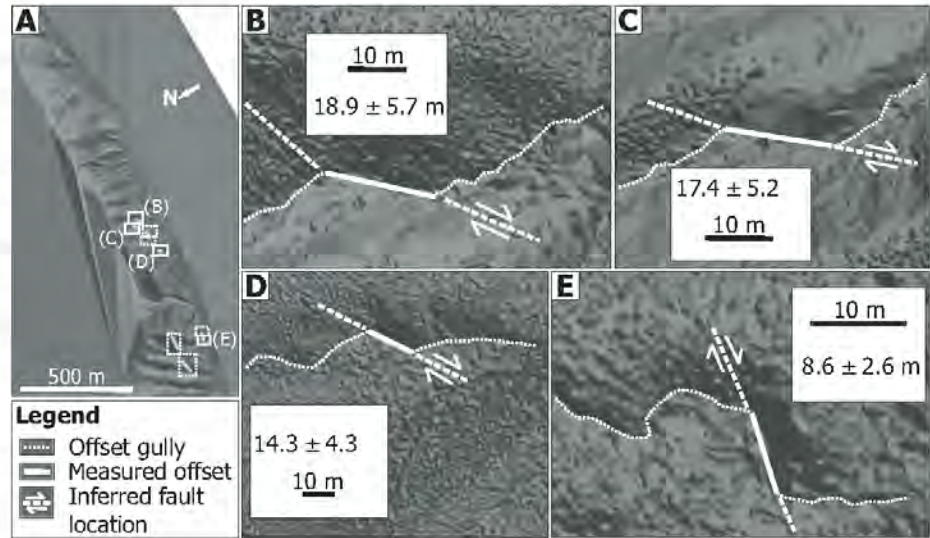
To approximate the age of the Rex Hills scarps, we plotted our results together with the calibrated normal fault-scarp data of Machette et al. (2001) and Friedrich et al. (2004) indicated by thin black lines in Figure 14. This approach was required because no such data are available for reverse fault scarps. Machette et al. (2001) collected data from scarps of known age formed in sandy gravels from across the Basin and Range Province (e.g., Bucknam and Anderson, 1979). The conglomerate comprising the Rex Hills is mostly composed of gravel-sized clasts with a fine-grained sandy to silty fraction (e.g., Fig. 4D; Simon Kübler and Markus Hoffmann, 2009, personal commun.). The similarity between the calibrated scarp and the Rex Hills scarp material suggests that it is not unreasonable to compare the Rex Hills data with the calibration curves of Machette et al. (2001) and Friedrich et al. (2004). We do recognize, however, that we ignored climatic variations and the effect of variations in internal stratigraphic and structural architectures between the scarp sets when we did this.

The maximum age obtained for the basal fault scarp by Menges et al. (2003) is 2 ka equivalent to the Fish Springs regression line (thin black line number 2 in Fig. 14). The slope of this regression line is steeper than that of the regression line for the basal fault scarp (scarp 1, thick black line labeled S1 in Fig. 14) and scarp 2 (thick black line labeled S2), but it is similar to the slope of the regression line for fault scarp 3 (thick black line labeled S3). Due to the small lithologic differences in the data set of Machette et al. (2001; e.g., sandy gravel) and the Rex Hills data (e.g., fine-grained sandy to silty
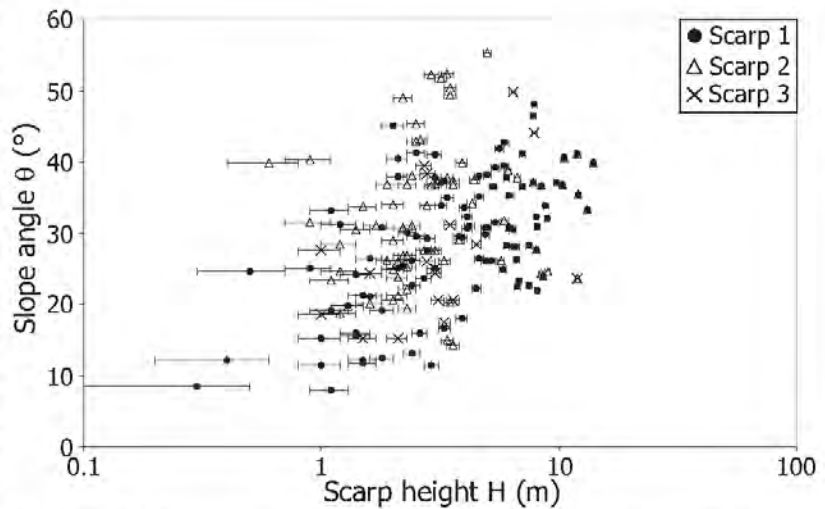
Figure 10. Plot of scarp height H versus slope angle θ for the three identified fault scarps showing broad scatter. The thin error bars indicate scarp-height uncertainties.

gravel), and the broad overlap and scatter in the data characterizing the three Rex Hills scarps, we cannot assign a precise age to these scarps. However, our age estimate is consistent with the age derived by Menges et al. (2003) because the regression lines of the three scarps plot near or above the 2 ka Fish Springs line (Fig. 14). Furthermore, the Rex Hills scarp regression lines plot clearly above the regression line of a well-constrained event in Crescent Valley (3 ka; gravel deposits; Friedrich et al., 2004).

DISCUSSION

Fault-Scarp Pattern

The southern Rex Hills slope is characterized by three fault scarps. The most continuous scarp lies along the toe of the slope, whereas the upper part of the slope exhibits a discontinuous, less distinct set of scarps (Fig. 8). We detected the basal scarp while conducting geologic mapping where we determined bedding attitudes next to

155
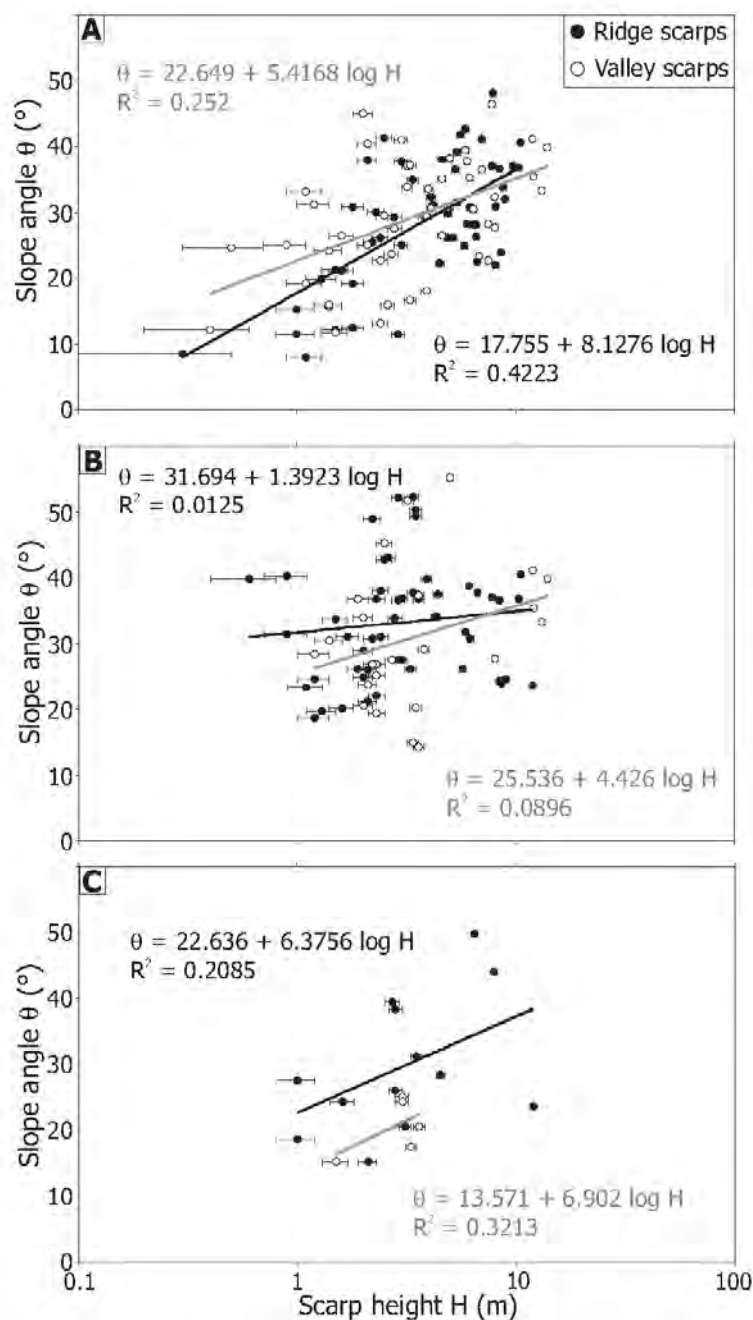
Figure 11. Plots of scarp height H versus slope angle θ for the three fault scarps differentiating between ridge and valley scarps in order to reduce and explain the scatter observed in Figure 10. Black lines correspond to ridge regression lines, whereas gray ones correspond to valley regression lines. The thin error bars indicate scarp-height uncertainties. (A) Scarp 1: basal fault scarp with a broad overlap between ridge and valley data. (B) Scarp 2: between scarp 1 and 3, also with a broad overlap between ridge and valley data. (C) Scarp 3: uppermost scarp shows a clear difference between ridges and valleys although only a few data points had been obtained.

the scarp, and inferred the fault dip in several places (Figs. 3B and 4D). The two remaining scarps were identified during the topographic profile analysis.

The scarp slope-angle pattern of the southern Rex Hills slope is characterized by a general increase from E to W. The eastern part of the slope is dominated by lower scarp slope angles (blue and green in Fig. 8A), and the western part by higher angles (red to yellow). The fault branch associated with the basal scarp 1 exhibits a near-surface dip of up to ~10°–15°, whereas the fault related to scarp 2 is characterized by a steeper dip of approximately ~10°–20° (Fig. 5C). Furthermore, the slope angle of scarp 2 is often steeper than that of scarp 1 along strike, e.g., areas of profile numbers 39–45 or 57–62 (Fig. 8A).

Fault dip can affect scarp morphology, and a different dip between fault branches may account for observed variations in fault-scarp steepness (e.g., Carretier et al., 2002). Moreover, internal oblique reverse faults of flower structures tend to be steeper in dip than the bounding faults (e.g., Sylvester, 1988). This suggests that the fault dip may be a factor influencing the scarp steepness along the southern Rex Hills slope due to the approximated difference in near-surface dip of the faults related to scarps 1 and 2 (Fig. 5C). However, the degree of the influence is difficult to evaluate given that the upper scarp 2 is less continuous than scarp 1 (Fig. 8), and that we do not have any direct information about the fault orientation in the subsurface.

Spatially correlated factors, e.g., lithologic heterogeneity, may also control scarp morphology. For example, the western part of the southern Rex Hills slope is characterized by a concentration of high-angle fault scarps (slope angle >40°; area of profile numbers 55–69 in Fig. 8A). This concentration of steep scarps may be due to lithologic contrasts; the Plio-Pleistocene conglomerate (Fig. 3B) may be more consolidated in this part of the Rex Hills resulting in generally steeper scarps. Scarp morphology may also be controlled by across-strike lithologic contrasts within the Plio-Pleistocene conglomerate, which could account for the average slope-angle difference observed between scarps 1 and 2, although this is difficult to evaluate due to the extremely poor bedding exposures within the Rex Hills conglomerate. Also, it is worth noting that there is no obvious difference in the conglomerate in terms of grain size, clast composition, or consolidation across the scarps, which suggests that the material is probably very similar in character across strike.

All three scarps show signs of fault segmentation, with the basal scarp exhibiting the clearest

156

segmentation pattern (Fig. 8B). The basal scarp is divided into five segments, and the second scarp into four segments along strike. The highest and most degraded scarp is too discontinuous to evaluate with confidence. The basal scarp segments transferred an approximately constant, net vertical slip from one segment of the reverse fault branch to the next one, in one case via a right stepover implying dextral offset (Fig. 8B).

The fault-scarp segmentation pattern suggests that the faults may be characterized by a changing geometry along strike. Variations in reverse fault dip could result in decreasing scarp height toward fault-segment tips as observed in Figure 8B. Segmentation may be caused by variations in fault strength, geometry, and loading distribution, and may control the extent and magnitude of ruptures (e.g., Hilley et al., 2001).

Figure 12. These plots are similar to Figure 11. They show the results after reducing the data of the three fault scarps as described in the text. The difference between ridge and valley profiles is now obvious. The gray valley regression lines generally plot below the black ridge regression lines suggesting that scarp degradation is more efficient in the valleys than on the ridges. The thin error bars again indicate scarp-height uncertainties. The thin black lines outline high-angle scarp profiles (>40°) localized in the area of profile numbers 55–69 (Fig. 8A) plotting above the average data population (details discussed in the text). (A) Plot of scarp height H versus slope angle θ shows the results for scarp 1 after eliminating ambiguous scarps whose upper part was interpreted to belong to scarp 2 and its lower part to scarp 1 (e.g., profile numbers 32, 42, 53, 54, 60, 64, 71, 77, and 80 in Fig. 8), and removed scarps located at segment tips of scarp 1 (e.g., profile numbers 1, 2, 3, 7, 8, 9, 13, 18, 23, 25, 34, 43, 44, 45, and 59 in Fig. 8). (B) Plot of scarp height H versus slope angle θ for scarp 2 after removing ambiguous scarp whose upper part was interpreted to belong to scarp 3 and its lower part to scarp 2 (e.g., profile number 22 in Fig. 8), and eliminating scarps located at segment tips of scarp 2 (e.g., profile numbers 24, 25, 33, and 55 in Fig. 8). (C) Plot of scarp height H versus slope angle θ for scarp 3 after the elimination of the ambiguous scarp whose upper part was interpreted to belong to scarp 3 and its lower part to scarp 2 (e.g., profile number 22 in Fig. 8).

A. $\theta = 20.579 + 6.6176 \log H$
$R^2 = 0.2461$

$\theta = 12.742 + 10.749 \log H$
$R^2 = 0.4545$

● Ridge scarps
○ Valley scarps

B. $\theta = 30.106 + 3.7378 \log H$
$R^2 = 0.054$

$\theta = 22.688 + 7.6231 \log H$
$R^2 = 0.0425$

C. $\theta = 19.04 + 11.172 \log H$
$R^2 = 0.4581$

$\theta = 13.571 + 6.902 \log H$
$R^2 = 0.3213$

Scarp height H (m)

157
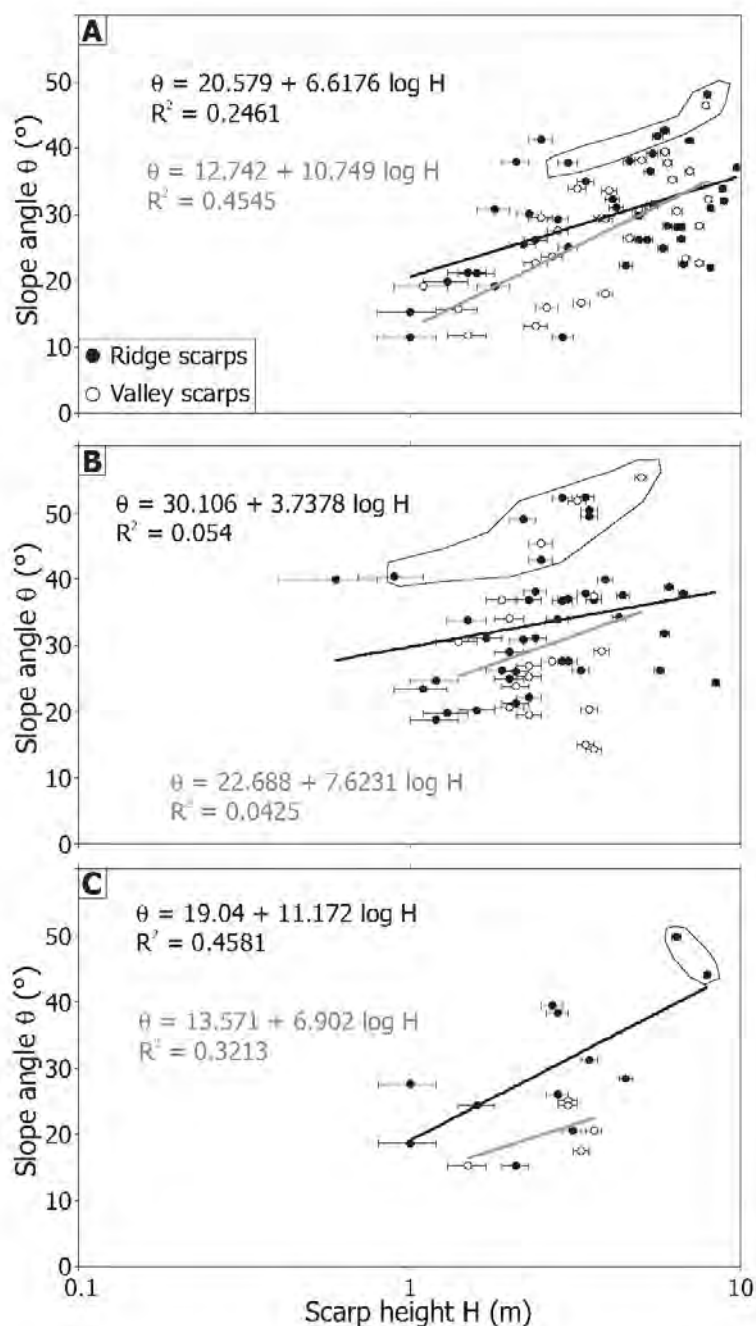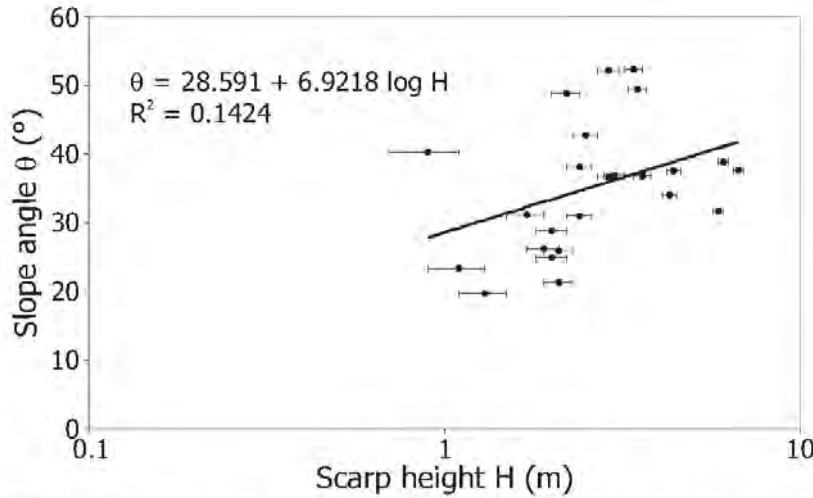
Figure 13. Plot of scarp height H versus slope angle θ for scarp 2 including only data from scarps solely located on the actual ridge crests to obtain a better correlation for this scarp. Fault scarps from valley walls and floors are neglected due to erosion affecting the scarp morphology especially in valleys. Removed scarps previously indicated as ridge scarps are (compared to Fig. 12B), e.g., profile numbers 17, 20, 21, 32, 38, 41, 47, 51, 57, 62, 69, 72, and 74 (Fig. 8). These scarp profiles are actually located on the uppermost valley walls where the slope is gentle compared to the middle part of a valley wall (Fig. 6). The thin error bars indicate scarp-height uncertainties.

For example, Hilley et al. (2001) used boundary element models to study these effects on surface offsets along the Cholame and Carrizo segments of the San Andreas fault. Their results suggest that the observed offset gradient at the segment boundary is caused by strength contrasts between the overlapping fault segments.

Scarp Height and Slope Angle

The preservation potential of small fault scarps along a hillside cut by ridges and valleys is higher on ridge crests relative to the adjacent valleys. Our evaluation of the scarp-height versus slope-angle relationship for the three fault scarps indicates that scarps exposed in valleys are slightly more degraded than scarps exposed on ridges (Fig. 12). Most of the valley scarps are characterized by a lower slope angle than ridge scarps of a similar height (e.g., scarp 3, Fig. 12C) implying that degradation is more efficient in valleys than on ridges given that these scarps have the same age.

Carretier et al. (2002) observed that scarp morphology for cumulative reverse fault scarps along the Gurvan Bogd fault system, which is similar to the Rex Hills setting, is controlled by slope erosion and the internal structure (e.g.,
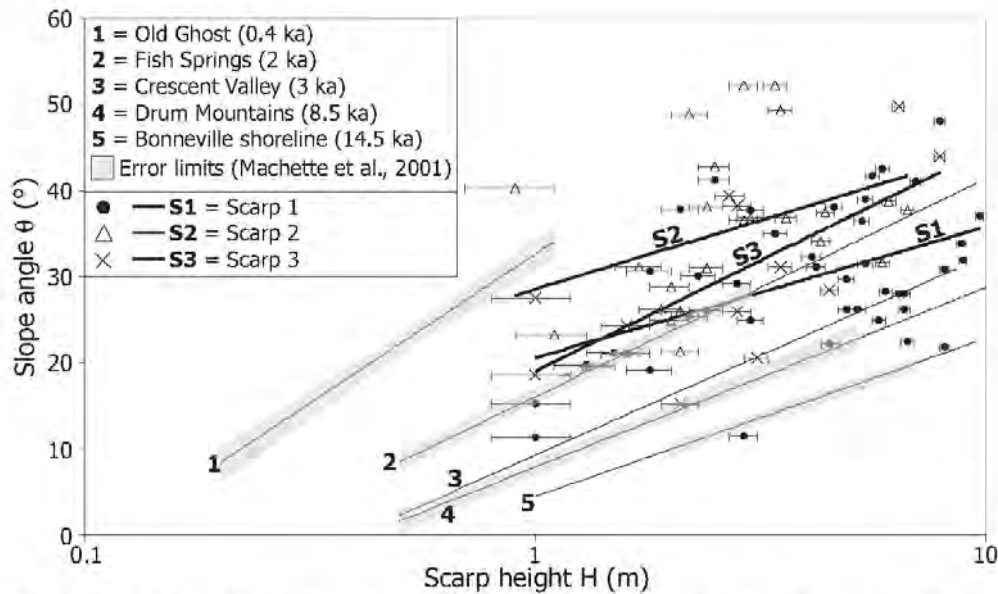
Figure 14. Plot of scarp height H versus slope angle θ for the three identified fault scarps with ridge-profile data of scarps 1 and 3 from Figures 12A and 12C, and ridge-crest profile data of scarp 2 from Figure 13 in order to determine the age of the Rex Hills scarps. The thick black lines with labels S1 for scarp 1, S2 for scarp 2, and S3 for scarp 3 are the corresponding regression lines. The thin black lines (numbered 1–5) correspond to the regression lines of previously published data (Machette et al., 2001; Friedrich et al., 2004). The error bars indicate scarp-height uncertainties.

158

folding, Fig. 15A). The dip of faulted beds may therefore have an impact on scarp-degradation processes, although, as noted above, this is very difficult to evaluate due to the general lack of bedding exposures in the study area. The variations in scarp morphology between valleys and ridges, on the other hand, suggest that slope erosion plays an important, possibly dominant, role in controlling the scarp morphology along the southern Rex Hills slope, which consists of poorly sorted conglomerate and shows no clear evidence of internal structures such as folds (Fig. 3B). We observed that scarp profiles from adjacent ridge crests and valleys are markedly different. Ridge crests preserve smaller individual scarps, whereas valleys exhibit longer wavelength, low-amplitude scarps (Fig. 15B). We attribute this along-strike variation to different degradation processes acting on ridges and in valleys. On ridge crests, degradation is controlled by the local slope and height of the scarp as well as local material properties. Whereas, on valley walls and valley bottoms water flows episodically, and is concentrated in channels thereby exerting a strong effect on the erosion and redistribution of material (Fig. 15B). This implies that ridge crests of the Rex Hills are preferable for accurate scarp-profile analyses, and explains much of the scatter observed in scarp slope angle–height space where valley and valley-wall profiles are included (Figs. 11 and 12).

This interpretation is further supported by a linear diffusion analysis performed for the basal fault scarp. We examined the spatial variability of the diffusivity parameter (κ) and the degradation coefficient (τ) by assuming a known age of 2 ka for this scarp (Menges et al., 2003). Both parameters are twice as much for valleys than for ridge crests implying that for the past 2 ka scarp degradation occurred at twice the rate in valleys than occurred on ridges.

Lithologic differences and slumping also induce scatter in scarp slope angle–height space. The western part of the southern Rex Hills slope exhibits a concentration of high-angle fault scarps (slope angle >40°; area of profile numbers 55–69 in Fig. 8A) that plot above the average population (outlined with black thin lines in Fig. 12). This concentration of steep scarps may not only be due to lithology contrasts as discussed previously, the steep slope of these scarps may alternatively be inherited from a steeper paleotopography, localized slumping, or subsidence.

After we reduced the initial data set by removing points that may not represent purely diffusive degradation processes, we attempted to provide an independent estimate of the scarp ages by comparing our fault-scarp data with data
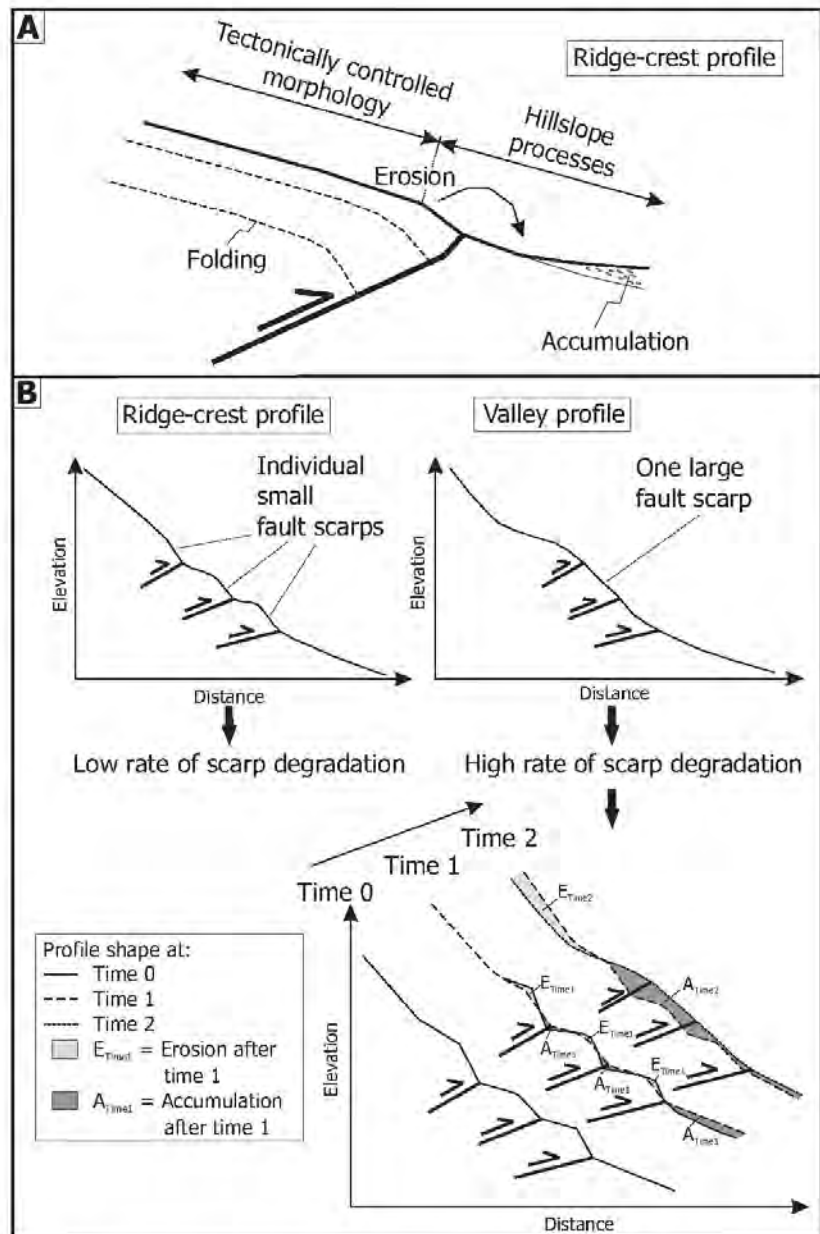
Figure 15. Schematic diagrams showing degradation behavior of closely spaced reverse fault scarps developed on poorly consolidated conglomerate. (A) Scarp morphology of a reverse fault scarp is controlled by slope erosion and internal structure in terms of folding (structural setting modified after Carretier et al., 2002). (B) The sketch shows schematic profiles and preservation potential of individual fault scarps on ridge crests and in valleys. Degradation processes are concentrated within a valley, and therefore individual, small fault scarps merge to one large scarp with time.

compiled from other scarps formed in poorly consolidated gravel elsewhere in the Basin and Range by Machette et al. (2001) and Friedrich et al. (2004) (Fig. 14). In this comparison, our data plot between the 0.4 ka Old Ghost curve and the 8.5 ka Drum Mountains curve, and overlaps the 2 ka Fish Spring curve of Machette et al. (2001). More specifically, the scarp 1 data points generally lie on or below the 2 ka curve suggesting that it is slightly older than 2 ka, whereas the scarp 2 points plot well above the 2 ka curve suggesting a slightly younger age for this scarp. If we assume that the scarps are from the same event, then it is likely that this event has occurred ~2 ka consistent with the estimate of Menges et al. (2003). The alternative that the scarps represent different events that occurred a few hundred years apart is impossible to evaluate due to a lack of offset stratigraphic markers. However, if this was the case, it would be a possible example of earthquake clustering (e.g., Doser, 1986; Wallace, 1987).

The general evolution of the Rex Hills flower structure is consistent with the results of analog models of restraining stepovers in strike-slip fault systems. This interpretation is mainly supported by the pronounced surface expression of the basal reverse fault related to scarp 1, and the less distinct expression of faults related to scarps 2 and 3 (Fig. 8). This is similar to the observed evolution of the experimental pop-up structures, which are characterized by a widening of the structure and the outward propagation of the bounding basal faults (McClay and Bonora, 2001).

Dextral Offsets and Displacement Rate

Cumulative dextral offsets are caused by repeated, individual seismic events, for example, along the San Andreas fault (Sieh, 1978), where numerous late Holocene dextral offsets are observed along the rupture of the 1857 earthquake. The youngest offsets reach up to 9.5 m between Cholame and Wrightwood in central and southern California, and are related to the 1857 event (Sieh, 1978), whereas older offsets represent multiple ruptures as documented by, e.g., the 120 m and 380 m offset channels at Wallace Creek (Sieh and Jahns, 1984, their fig. 1b). The drainage-offset magnitudes observed at the Rex Hills site suggest a similar scenario, where large offsets represent multiple events while smaller offsets of a few meters or less represent the most recent event.

The surface displacement of a single earthquake recorded along multiple fault branches is often characterized by a wide range of values, e.g., along the San Andreas fault (Sieh, 1978; Hilley et al., 2001). Hence, individual

measured surface displacements cannot be easily transferred into average displacement rates, and we calculated first the average displacement of a single rupture event along the Rex Hills fault segment. Dextral offset magnitudes identified in the Rex Hills LDEM vary from 7.77 m to 56.5 m (Fig. 9; Fig. DR3 and Table DR2 [footnote 1]). The smallest, individual dextral gully offsets of 0.75–1.5 m were measured in the field. Menges et al. (2003) observed that dextral drainage offsets range from 0.5 to ~5 m along the Stateline fault system. They related these offsets to an earthquake with an expected M_w of 7.1–7.3 and a latest Holocene age (≤2 ka) based on the surface displacement–magnitude relationship derived by Wells and Coppersmith (1994). This suggests that for a single earthquake along the Stateline fault system displacement is greater than 0.75–1.5 m. For a 7.1–7.3 magnitude earthquake along the Stateline fault system, we calculated an average displacement of 1.5–3 m using the same approach (Wells and Coppersmith, 1994; additional detail below). We suggest that the offsets determined in the LDEM represent cumulative offsets of several earthquakes recorded by gullies older than ~2 ka.

We focused displacement-rate determinations on the four most obvious dextral offsets from the LDEM (Figs. 9B–9E). Cumulative offsets of 8.5–19 m would be the result of ~3–12 earthquakes with an average offset of 1.5–3 m for each earthquake, respectively. Due to poorly constrained evidence for an older rupture event along the Stateline fault system, Menges et al. (2003) approximated a preliminary earthquake recurrence interval of 10 ka. Based on their data, we estimated here a recurrence-interval range of 5–15 ka containing an uncertainty bound of 50% (equal to 1 σ). Using this recurrence-interval range, the ~3–12 earthquakes correspond to a time span of ~15–180 ka. These results suggest an average displacement rate for the Rex Hills fault segment of ~0.05–1.3 mm/a during the past 15–180 ka spanning two orders of magnitude. This rate is in the same range as slip-rate estimates of 0.04 ± 0.03 mm/a for the central part of the Stateline fault system and 0.03 ± 0.02 mm/a for the northern part (Stepp et al., 2001) as well as the geodetic rate of 0.7–1.2 mm/a inferred by Wernicke et al. (2004). Furthermore, the upper bound of our displacement-rate estimate (1.3 mm/a) is roughly half of the long-term minimum, time-averaged, geologic rate determined for the Mesquite segment of the Stateline fault system (~2.3 mm/a; Guest et al., 2007). It is unclear whether our tentative displacement-rate determination is representative of the displacement rate for the entire Pahrump segment of the Stateline fault system

without any additional data from this segment, and so it is difficult to evaluate its significance in context of the entire fault system.

CONCLUSIONS

We quantified the morphology and structure of the kilometer-scale Rex Hills flower structure by combining field mapping and high-resolution DEM analysis. The use of very high-resolution DEM data derived from a terrestrial laser-scanning campaign allowed us to conduct a detailed study of fault-scarp patterns exposed on the southern Rex Hills slope, and to ultimately attempt to distinguish different scarps in terms of apparent age.

The southern Rex Hills slope is characterized by a complex pattern of three fault scarps which are related to three individual reverse fault branches (Fig. 8). Two scarps show signs of segmentation (Fig. 8B), and we suggest that the faults may be characterized by laterally variable fault dips resulting in rupture segmentation and offset gradients as observed at the tips of the basal fault-scarp segments (Fig. 8B). Furthermore, fault dip, lithologic contrasts, and degradation processes appear to significantly influence the scarp morphology along the southern Rex Hills slope resulting in broad scatter and overlap in scarp-height–slope-angle space (Figs. 10–14). A key aspect of this study was to identify the source of scatter in our slope-angle–scarp-height data. With this goal in mind, we noted that the southern slope is characterized by the alternation of small-scale ridges and valleys (Fig. 5), and that scarp-degradation processes are likely to be higher in these valleys than on the ridges (Fig. 15B). By removing data obtained from the valley bottoms and valley walls, we were able to realize a significant improvement in the data distributions, and from this we suggest that the preservation potential of small, individual fault scarps is greater on ridge crests than on hillslopes and valley floors, and that ridge-crest profiles provide more accurate information about closely spaced fault branches.

The most promising aspect of high-resolution topographic data for neotectonics is that it has the potential to allow for fault-scarp population studies. This would be possible where scarps could be assigned well-constrained ages and then be grouped into event populations that represent the group of scarps associated with a particular earthquake. Based on the Rex Hills fault-scarp analysis, we can distinguish clear statistical differences between the scarps, but the implied difference in absolute age is difficult to evaluate without making fairly radical assumptions. It is clear, therefore, that for this type of analysis to be truly compelling, tight

geochronological constraints are required. The Rex Hills site, though well suited to the laser-scanning survey, is unfortunately not very well suited to a geochronological study (absence of well-datable material), and is therefore probably not the best site for additional work on this important problem.

Lastly, and most importantly, our study reveals that high-resolution topographic analysis has the potential to significantly improve our understanding of the geometry and evolution of small-scale tectonic topography in general, and when combined with subsurface data and geochronological data, it provides a comprehensive data scheme for neotectonic studies.

REFERENCES CITED

Arrowsmith, J.R., Rhodes, D.D., and Pollard, D.D., 1998, Morphologic dating of scarps formed by repeated slip events along the San Andreas Fault, Carrizo Plain, California: Journal of Geophysical Research, v. 103, p. 10,141–10,160, doi: 10.1029/98JB00505.

Avouac, J.-P., 1993, Analysis of scarp profiles: Evaluation of errors in morphologic dating: Journal of Geophysical Research, v. 98, p. 6745–6754, doi: 10.1029/92JB01962.

Buckley, S.J., Howell, J.A., Enge, H.D., and Kurz, T.H., 2008, Terrestrial laser scanning in geology: Data acquisition, processing and accuracy considerations: Journal of the Geological Society, v. 165, p. 625–638, doi: 10.1144/0016-76492007-100.

Bucknam, R.C., and Anderson, R.E., 1979, Estimation of fault-scarp ages from a scarp-height–slope-angle relationship: Geology, v. 7, p. 11–14, doi: 10.1130/0091-7613(1979)7<11:EOFAFA>2.0.CO;2.

Burchfiel, B.C., Hamill, G.S., and Wilhelms, D.E., 1983, Structural geology of the Montgomery Mountains and the northern half of the Nopah and Resting Spring ranges, Nevada and California: Geological Society of America Bulletin, v. 94, p. 1359–1376, doi: 10.1130/0016-7606(1983)94<1359:SGOTMM>2.0.CO;2.

Carretier, S., Ritz, J.-F., Jackson, J., and Bayasgalan, A., 2002, Morphological dating of cumulative reverse fault scarps: Examples from the Gurvan Bogd fault system, Mongolia: Geophysical Journal International, v. 148, p. 256–277, doi: 10.1046/j.1365-246X.2002.01599.x.

Cooper, J.D., Miller, R.H., and Sundberg, F.A., 1982, Environmental stratigraphy of the lower part of the Nopah Formation (Upper Cambrian), in Cooper, J.D., Troxel, B.W., and Wright, L.A., eds., Guidebook to Selected Areas in the San Bernardino Mountains, Mojave Desert, and Southwestern Great Basin: Geological Society of America Cordilleran Section Annual Meeting Field Trip, no. 9, p. 97–116.

Cowgill, E., Yin, A., Arrowsmith, J.R., Feng, W.X., and Shuanhong, Z., 2004a, The Altyn Tagh bend along the Altyn Tagh fault, northwest Tibet 1: Smoothing by vertical-axis rotation and the effect of topographic stresses on bend flanking faults: Geological Society of America Bulletin, v. 116, p. 1423–1442, doi: 10.1130/B25359.1.

Cowgill, E., Arrowsmith, J.R., Yin, A., Feng, W.X., and Shuanhong, Z., 2004b, The Akato Tagh bend along the Altyn Tagh fault, northwest Tibet 2: Active deformation and the importance of transpression and strain hardening within the Altyn Tagh system: Geological Society of America Bulletin, v. 116, p. 1443–1464, doi: 10.1130/B25360.1.

Crowell, J.C., 1974, Sedimentation along the San Andreas Fault, California, in Dott, R.H., and Shaver, R.H., eds., Modern and Ancient Geosynclinal Sedimentation: Society of Economic Paleontologists and Mineralogists, Special Publication, v. 19, p. 292–303.

Cunningham, W.D., and Mann, P., 2007, Tectonics of strike-slip restraining and releasing bends, in Cunningham, W.D., and Mann, P., eds., Tectonics of strike-slip restraining and releasing bends: The Geological Society of London, Special Publications, v. 290, p. 1–12.

Dokka, R.K., and Travis, C.J., 1990, Role of the eastern California shear zone in accommodating Pacific-North American plate motion: Geophysical Research Letters, v. 17, p. 1323–1326, doi: 10.1029/GL017i009p01323.

Dooley, T.P., and McClay, K.R., 1996, Strike-slip deformation in the Confidence Hills, southern Death Valley fault zone, eastern California, USA: Journal of the Geological Society of London, v. 153, p. 375–387, doi: 10.1144/gsjgs.153.3.0375.

Doser, D., 1986, Earthquake processes in the Rainbow Mountain–Fairview Peak–Dixie Valley, Nevada region 1954–1959: Journal of Geophysical Research, v. 91, p. 12,572–12,586, doi: 10.1029/JB091iB12p12572.

Friedrich, A.M., Wernicke, B., Niemi, N.A., Bennett, R.A., and Davis, J.L., 2003, Comparison of geodetic and geologic data from the Wasatch region, Utah, and implications for the spectral character of earth deformation at periods of 10 to 10 million years: Journal of Geophysical Research, v. 108, doi: 10.1029/2001JB000682.

Friedrich, A.M., Lee, J., Wernicke, B.P., and Sieh, K., 2004, Geologic context of geodetic data across a Basin and Range normal fault, Crescent Valley, Nevada: Tectonics, v. 23, p. TC2015, doi: 10.1029/2003TC001528.

Guest, B., Niemi, N.A., and Wernicke, B.P., 2007, Stateline fault system: A new component of the Miocene Quaternary Eastern California shear zone: Geological Society of America Bulletin, v. 119, p. 1337–1347, doi: 10.1130/0016-7606(2007)119[1337:SFSANC]2.0.CO;2.

Hanks, T.C., Bucknam, R.C., Lajoie, K.R., and Wallace, R.E., 1984, Modification of wave-cut and faulting-controlled landforms: Journal of Geophysical Research, v. 89, p. 5771–5790, doi: 10.1029/JB089iB07p05771.

Harding, T.P., 1985, Seismic characteristics and identification of negative flower structures, positive flower structures, and positive structural inversion: American Association of Petroleum Geologists Bulletin, v. 69, p. 582–600.

Hill, E.M., and Blewitt, G., 2006, Testing for fault activity at Yucca Mountain, Nevada, using independent GPS results from the BARGEN network: Geophysical Research Letters, v. 33, p. L14302, doi: 10.1029/2006GL026140.

Hilley, G.E., Arrowsmith, J.R., and Stone, E., 2001, Inferring segment strength contrasts and boundaries along low-friction faults using surface offset data, with an example from the Cholame-Carrizo segment boundary along the San Andreas Fault, southern California: Bulletin of the Seismological Society of America, v. 91, p. 427–440, doi: 10.1785/0120000248.

Landgraf, A., Ballato, P., Strecker, M.R., Friedrich, A., Tabatabaeiand, S.H., and Shahpasandzadeh, M., 2009, Fault-kinematic and geomorphic observations along the North Tehran Thrust and Mosha Fasham Fault, Alborz mountains Iran: Implications for fault-system evolution and interaction in a changing tectonic regime: Geophysical Journal International, v. 177, doi: 10.1111/j.1365-246X.2009.04089.x.

Machette, M.N., Menges, C., Slate, J., Crone, A.J., Klinger, R.E., Piety, L.A., Sarna-Wojcicki, A.M., and Thompson, R.A., 2001, Field trip guide for day B, Furnace Creek area, in Machette, M.N., Johnson, M.L., and Slate, J.L., eds., Quaternary and Late Pliocene geology of the Death Valley region: Recent observations on tectonics, stratigraphy, and lake cycles, Pacific cell—Friends of the Pleistocene field trip, February 17–19, 2001: U.S. Geological Survey Open-File Report 01-51.

McClay, K.R., and Dooley, T.P., 1995, Analogue models of pull-apart basins: Geology, v. 23, p. 711–714, doi: 10.1130/0091-7613(1995)023<0711:AMOPAB>2.3.CO;2.

McClay, K.R., and Bonora, M., 2001, Analog models of restraining stepovers in strike-slip fault systems: American Association of Petroleum Geologists Bulletin, v. 85, p. 233–260.

Menges, C.M., Fridrich, C., Blakely, R.J., and Thompson, R., 2003, Late Quaternary surface rupture and associated transpressive uplift on a section of the State Line Fault in the south-central Amargosa Desert basin, southwestern Nevada: Eos (Transactions, American Geophysical Union), v. 84, Fall Meeting Supplement, Abstract S11D-0327.

Nash, D.B., 1980, Morphologic dating of degraded normal fault scarps: The Journal of Geology, v. 88, p. 353–360, doi: 10.1086/628513.

Naylor, M.A., Mandl, G., and Sijpesteijn, C.H.K., 1986, Fault geometries in basement-induced wrench faulting under different initial stress states: Journal of Structural Geology, v. 8, p. 737–752, doi: 10.1016/0191-8141(86)90022-2.

Nivière, B., Marquis, G., and Maurin, J.-C., 1998, Morphologic dating of slowly evolving scarps using a diffusive analogue: Geophysical Research Letters, v. 25, p. 2325–2328, doi: 10.1029/98GL01845.

Poole, F.G., and Sandberg, C.A., 1977, Mississippian paleogeography and tectonics of the western United States, in Stewart, J.H., Stevens, C.H., and Fritsche, A.E., eds., Paleozoic paleogeography of the western United States: Pacific Section, Society for Sedimentary Geology (SEPM) Symposium 1, p. 67–85.

Schweickert, R.A., and Lahren, M.M., 1997, Strike-slip fault system in Amargosa Valley and Yucca Mountain, Nevada: Tectonophysics, v. 272, p. 25–41, doi: 10.1016/S0040-1951(96)00274-0.

Sieh, K.E., 1978, Slip along the San Andreas fault associated with the great 1857 earthquake: Bulletin of the Seismological Society of America, v. 68, p. 1421–1448.

Sieh, K.E., and Jahns, R.H., 1984, Holocene activity of the San Andreas fault at Wallace Creek, California: Geological Society of America Bulletin, v. 95, p. 883–896, doi: 10.1130/0016-7606(1984)95<883:HAOTSA>2.0.CO;2.

Stepp, J.C., Wong, I., Whitney, J., Quittmeyer, R., Abrahamson, N., Toro, G., Youngs, R., Coppersmith, K., Savy, J., Sullivan, T., and Yucca Mountain Probabilistic Seismic Hazard Analysis Project Members, 2001, Probabilistic seismic hazard analyses for ground motions and fault displacement at Yucca Mountain, Nevada: Earthquake Spectra, v. 17, p. 113–151.

Stevens, C.H., 1991, Paleogeographic and structural significance of an upper Mississippian facies boundary in southern Nevada and east central California: Geological Society of America Bulletin, v. 103, p. 876–885, doi: 10.1130/0016-7606(1991)103<0876:PASSOA>2.3.CO;2.

Stewart, J.H., 1980, Geology of Nevada: Nevada Bureau of Mines and Geology Special Publication, v. 4, p. 1–136.

Sylvester, A.G., 1988, Strike-slip faults: Geological Society of America Bulletin, v. 100, p. 1666–1703, doi: 10.1130/0016-7606(1988)100<1666:SSF>2.3.CO;2.

Sylvester, A.G., and Smith, R.R., 1976, Tectonic transpression and basement-controlled deformation in San Andreas fault zone, Salton Trough, California: American Association of Petroleum Geologists Bulletin, v. 60, p. 2081–2102.

van der Pluijm, B.A., and Marshak, S., 2004, Earth structure—An introduction to structural geology and tectonics: W.W. Norton and Company, 656 p.

Wakabayashi, J., Hengesh, J.V., and Sawyer, T.L., 2004, Four-dimensional transform fault processes: Progressive

161

evolution of step-overs and bends: Tectonophysics, v. 392, p. 279–301, doi: 10.1016/j.tecto.2004.04.013.

Walker, J.D., Burchfiel, B.C., and Davis, G.A., 1995, New age controls on initiation and timing of foreland belt thrusting in the Clark Mountains: Geological Society of America Bulletin, v. 107, p. 742–750, doi: 10.1130/0016-7606(1995)107<0742:NACOIA>2.3.CO;2.

Wallace, R.E., 1977, Profiles and ages of young fault scarps, north-central Nevada: Geological Society of America Bulletin, v. 88, p. 1267–1281, doi: 10.1130/0016-7606(1977)88<1267:PAAOYF>2.0.CO;2.

Wallace, R.E., 1987, Grouping and migration of surface faulting and variations in slip rates on faults in the Great Basin province: Bulletin of the Seismological Society of America, v. 77, p. 868–876.

Wells, D.L., and Coppersmith, K.J., 1994, New empirical relationships among magnitude, rupture length, rupture width, rupture area, and surface displacement: Bulletin of the Seismological Society of America, v. 84, p. 974–1002.

Wernicke, B.P., Davis, J.L., Bennett, R.A., Normandeau, J.E., Friedrich, A.M., and Niemi, N.A., 2004, Tectonic implications of a dense continuous GPS velocity field at Yucca Mountain, Nevada: Journal of Geophysical Research, v. 109, p. B12404, doi: 10.1029/2003JB002832.

Wesnousky, S.G., 2005, Active faulting in the Walker Lane: Tectonics, v. 24, p. TC3009, doi: 10.1029/2004TC001645.

Wilcox, R.E., Harding, T.P., and Seely, D.R., 1973, Basic wrench tectonics: American Association of Petroleum Geologists Bulletin, v. 57, p. 74–96.

Yeats, R.S., Sieh, K.E., and Allen, C.R., 1997, The Geology of Earthquakes: New York, Oxford University Press, 576 p.

162

6.1.2. Data Repository Item

Data Repository Item 2010050

Laser-scanning method and LDEM data from 83 topographic profiles

To accompany High-resolution spatial rupture pattern of a multiphase flower structure, Rex Hills, Nevada: New insights on scarp evolution in complex topography based on 3-D laser scanning

Ramona Baran[*][†]
Bernard Guest[*][‡]
Anke M. Friedrich[*][††]
[*] *Department of Earth and Environmental Sciences, Ludwig-Maximilians-University Munich, Luisenstr. 37, 80333 Munich, Germany*
[†] *e-mail : ramona.baran@iaag.geo.uni-muenchen.de*
[††] *e-mail: friedrich@lmu.de*
[‡] *now at: Department of Geoscience, University of Calgary, 2500 University Drive Northwest, Calgary, Alberta, T2N 1N4, Canada, e-mail: bguest@ucalgary.ca*

LASER-SCANNING METHOD

The field work with the scanner (Riegl 3-D laser scanner *LMS-Z420i*[®]) follows a relatively simple principle. The scanner was set up on a tripod at the first scan position at an appropriate distance (~ 100 m) from the object of interest (Fig. DR1). The scanner power was taken from a car battery. The scanning procedure was easily controlled with a laptop (Riegl software *RiSCAN PRO*[®]). Both a wireless and a default wire-lead data transmission between scanner and laptop were possible. A digital camera was mounted on top of the scanner which allows the later combination of scans and photographs (Fig. DR1a). During each scan, the scanner rotated 360° around a vertical axis. While the scanner was set up at its position, several tripod-mounted reflectors were distributed as marker points in the region of interest (eight reflectors in this example, Fig. DR1b) to avoid distortions during subsequent DEM generation. Following a calibration process for the camera and scanner (scan resolution of 0.066° etc.), the first scan was performed at position P1 (Fig. DR1b) while the camera took pictures of the scanned area. The scanner was then moved to the next position (P2) together with some of the reflectors (open circles in Fig. DR1b). At least three reflectors remained at their original (P1) positions (black circles in Fig. DR1b) and should also be located in the overlapping region of scans P1 and P2 (white area in Fig. DR1b). Using the scanner software, it was possible to search for these overlapping marker points within individual scans and thereby link these scans to form a merged data set covering a larger area. This procedure was repeated until the area of interest was completely covered. In the case presented here, eleven scan positions were required to scan the southern Rex Hills flank.

The result of the laser-scanner measurements was a large point cloud. We removed 35 % of the points from the cloud by defining this threshold in the filter options of the scanner software. The reduced point cloud represents the basis for the DEM. The DEM was generated by triangulation, where the DEM surface is defined by a triangular network, in which the points represent the triangle corners. Finally, we created a very detailed DEM (Fig. 5) and a set of cross sections with a cm-scale resolution (accuracy of around ± 5 cm). For the purpose of this study to examine the surface expression of the Rex Hills structure, geo-referencing of this DEM was not necessary. Therefore, all coordinates shown in Figures 5, 7, 8, and DR2 are relative. The high-resolution cross sections allow the very detailed analysis of different of fault scarps.

1
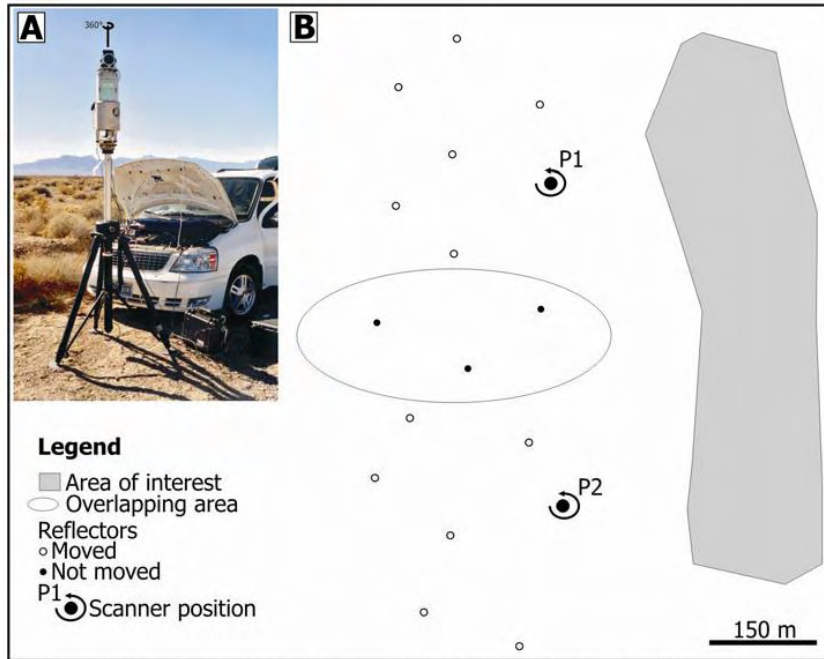
Fig. DR1 (A) Picture of the laser scanner *LMS-Z420i*[®] set-up for field work. The vertical rotation axis of the scanner is additionally shown. (B) The sketch emphasizes the scanning procedure. The scanner is shifted from position P1 to P2 after the first scan. The second scan is performed at P2. An overlap (white area) exists between both positions where reflectors (black circles) are used to link the individual scans.

Profile 1
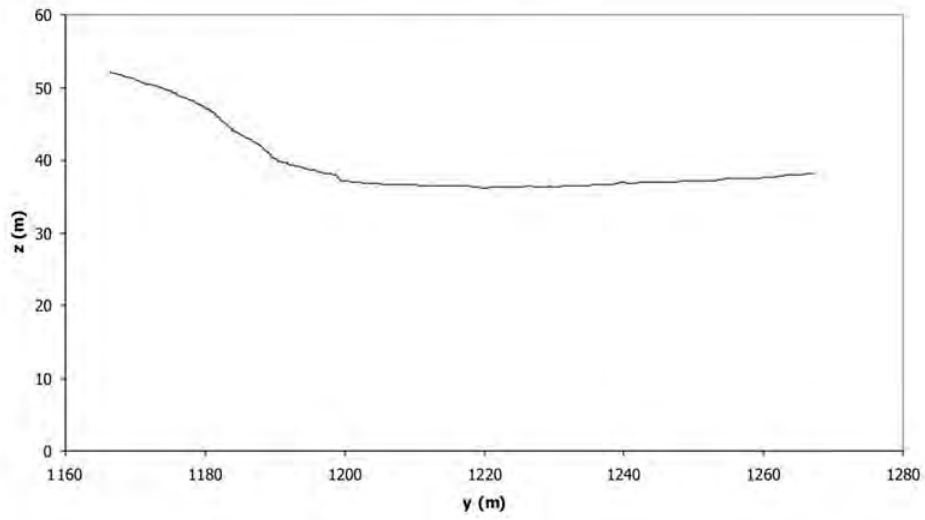
Profile 2
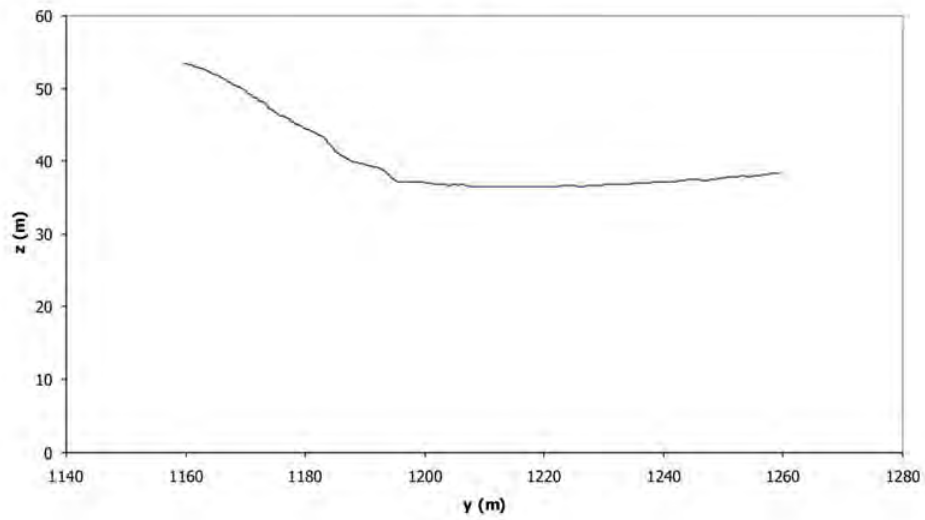
Profile 3

3
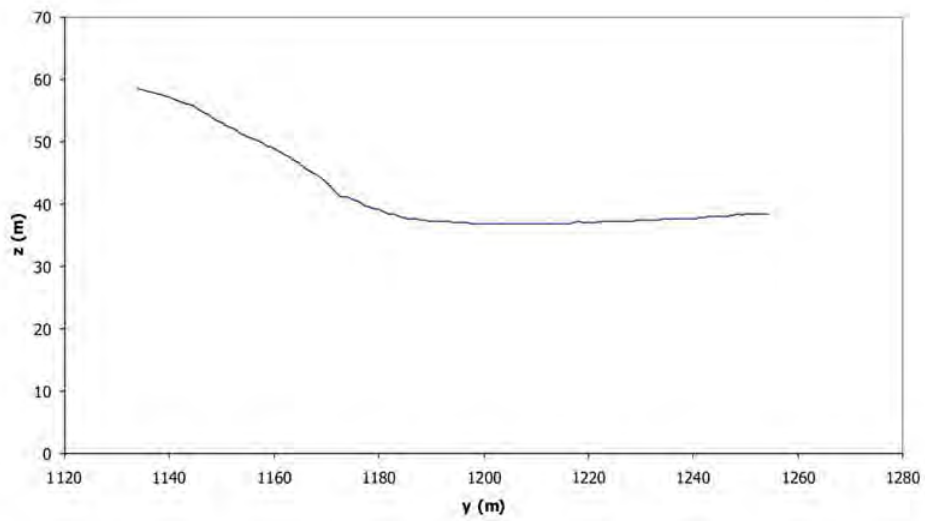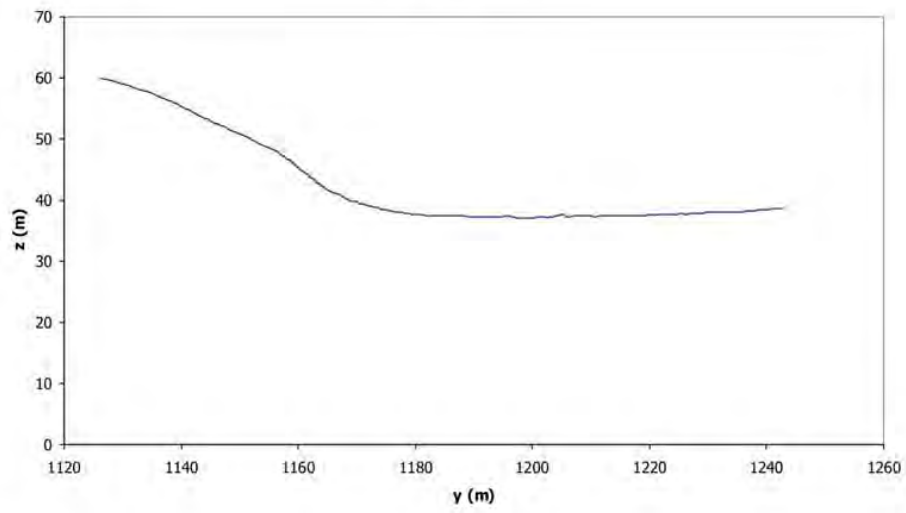
Profile 4

Profile 5

Profile 6

4
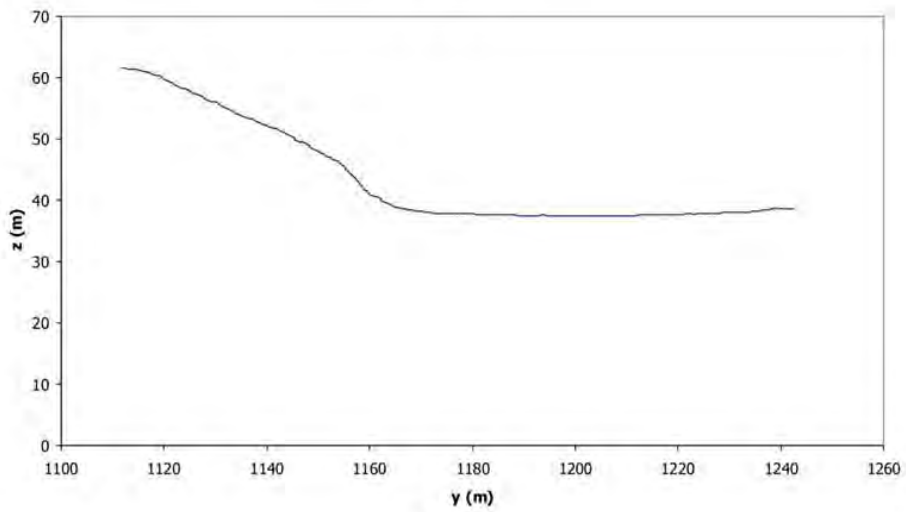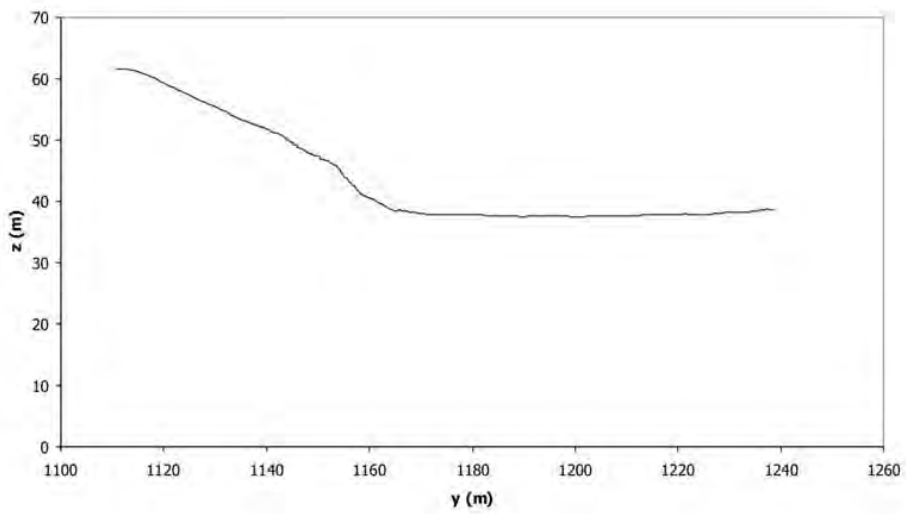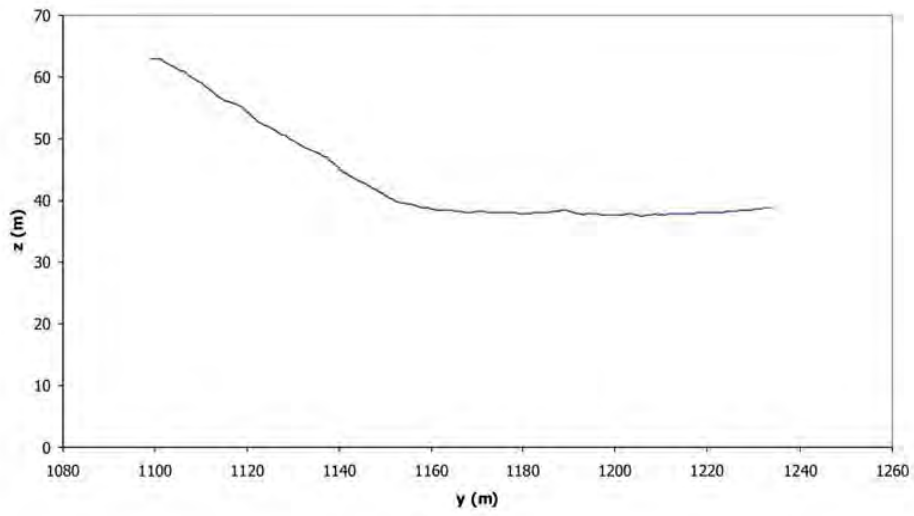
Profile 7

Profile 8

Profile 9

5
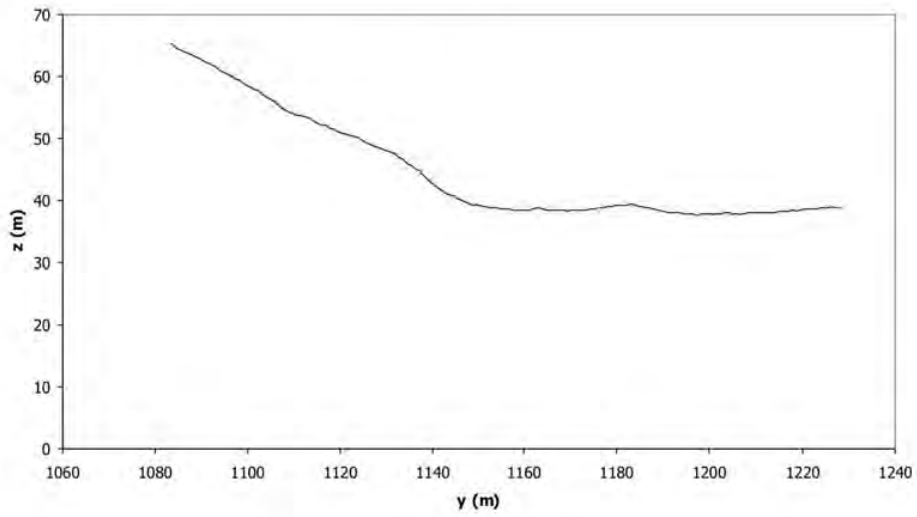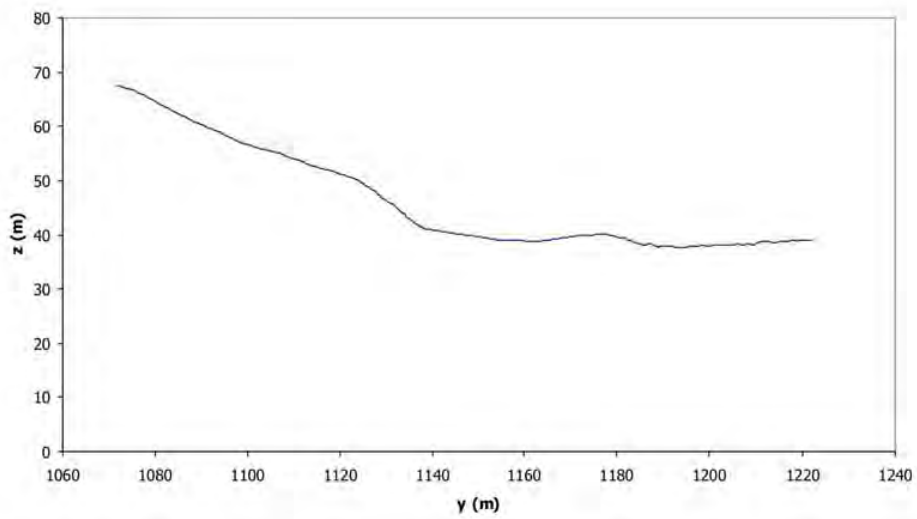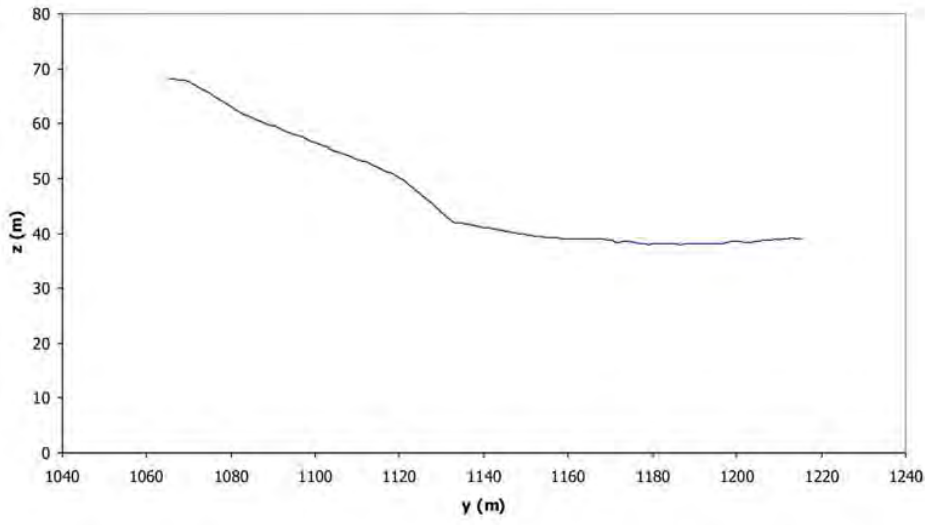
Profile 10

Profile 11
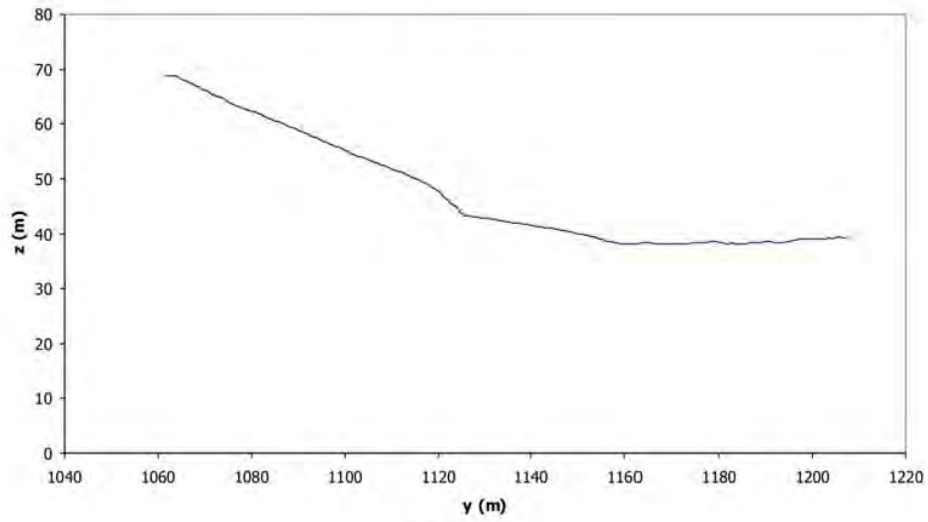
Profile 12
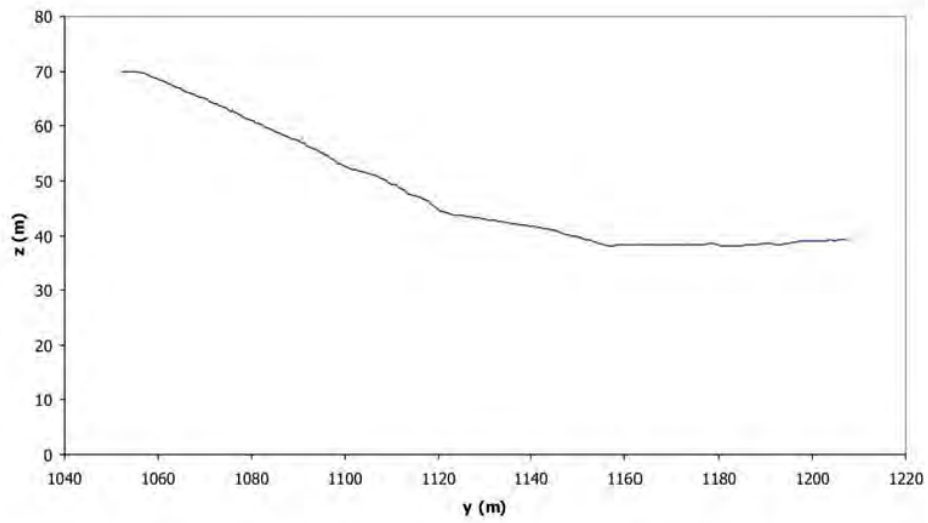
Profile 13
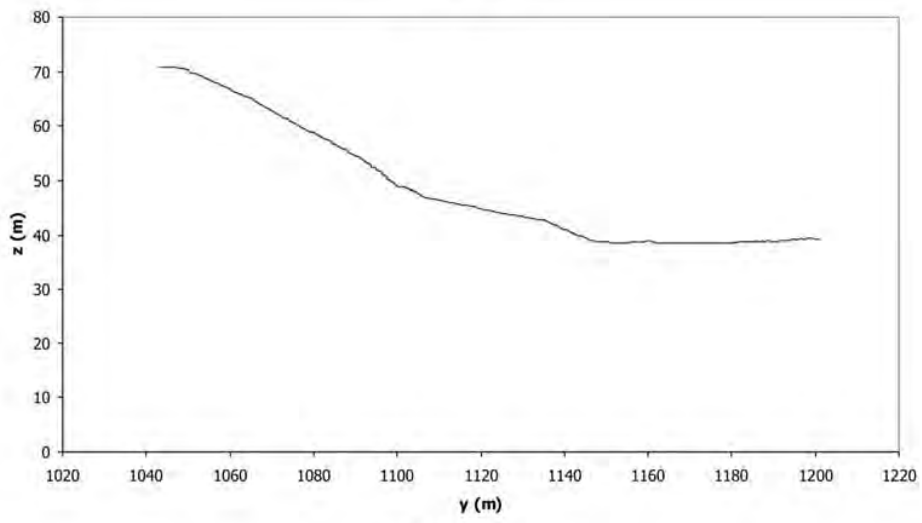
Profile 14

Profile 15

7
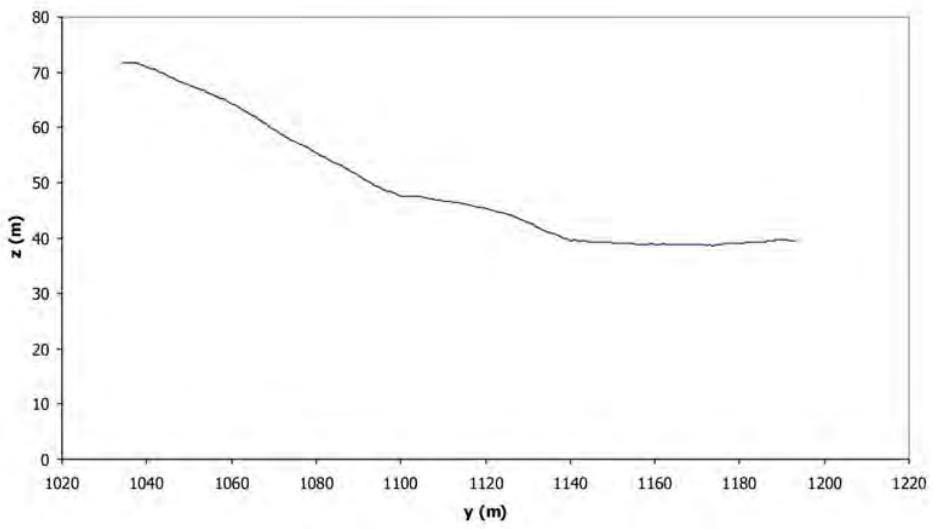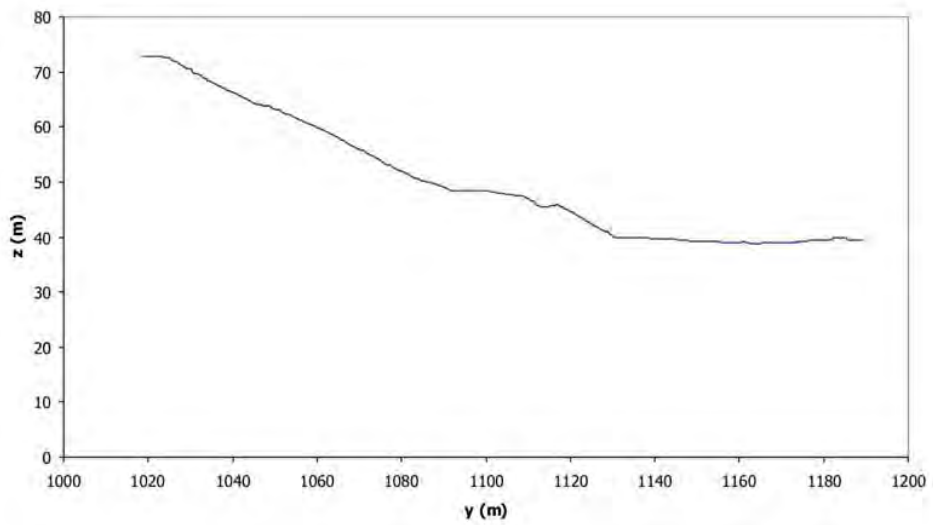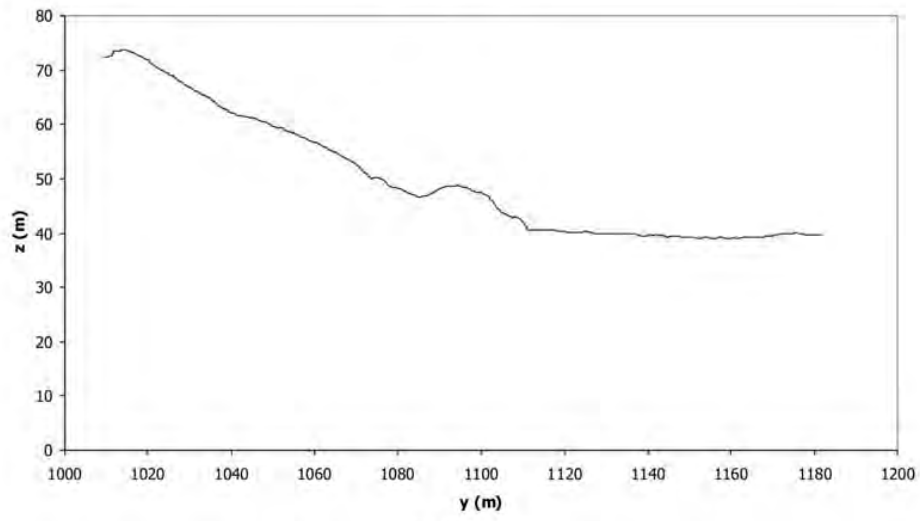
Profile 16

Profile 17
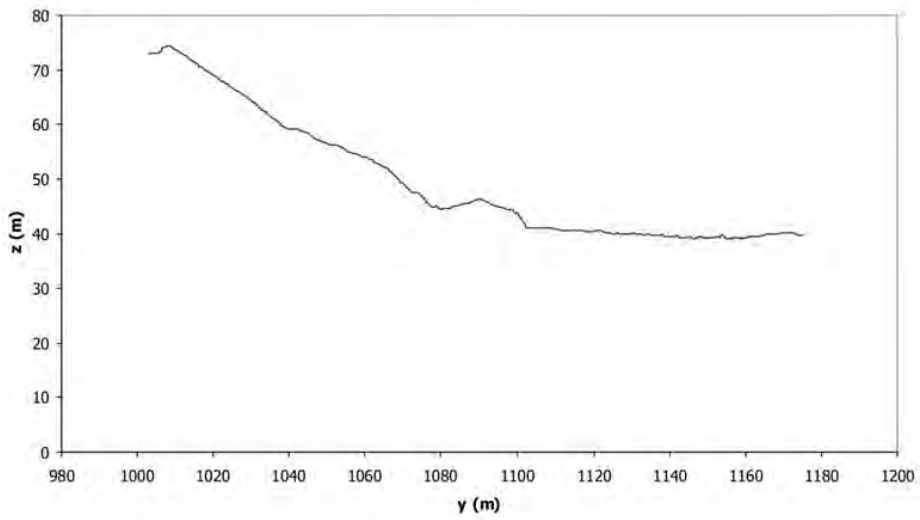
Profile 18

8
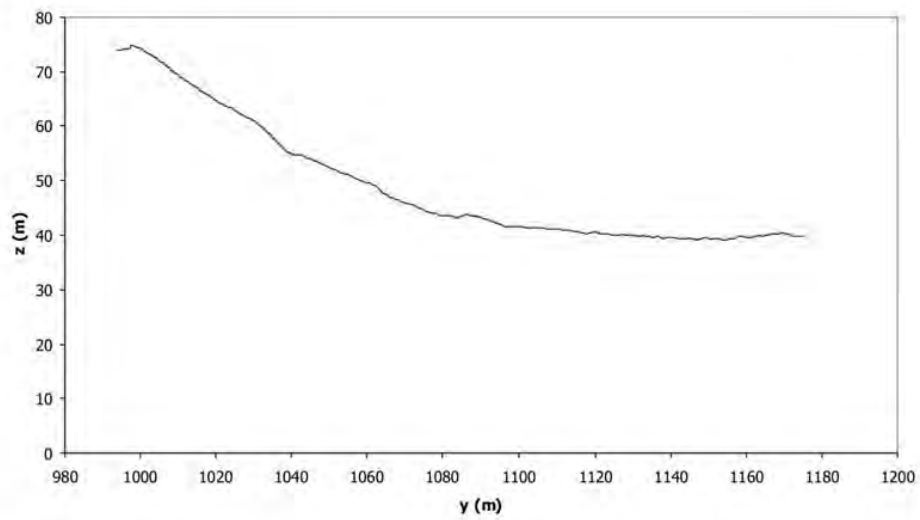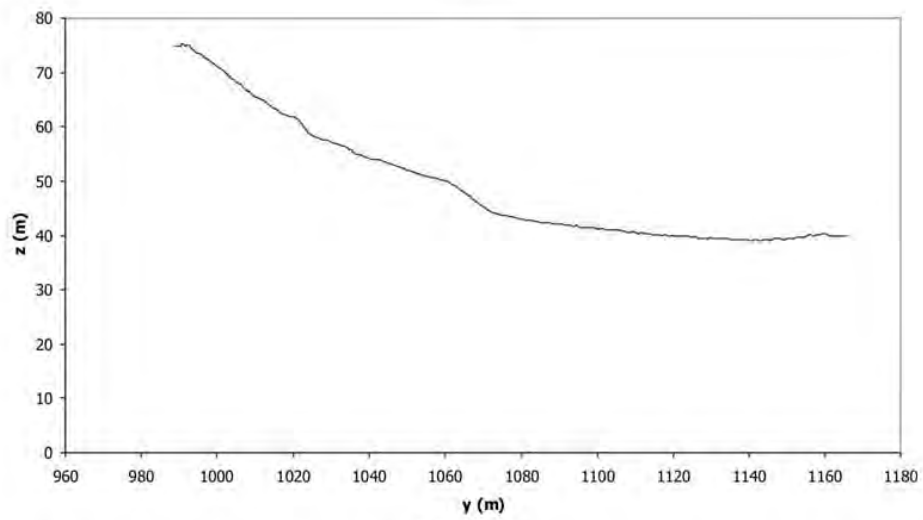
Profile 19

Profile 20

Profile 21

9
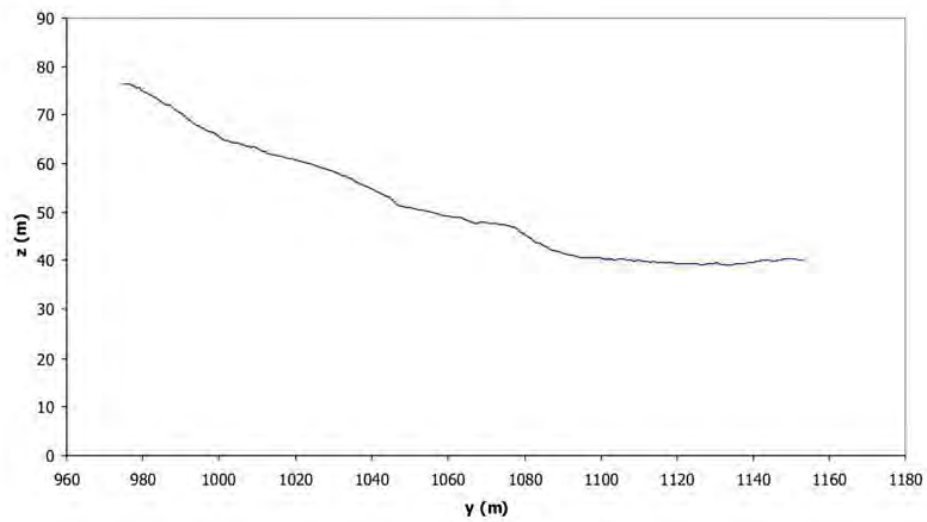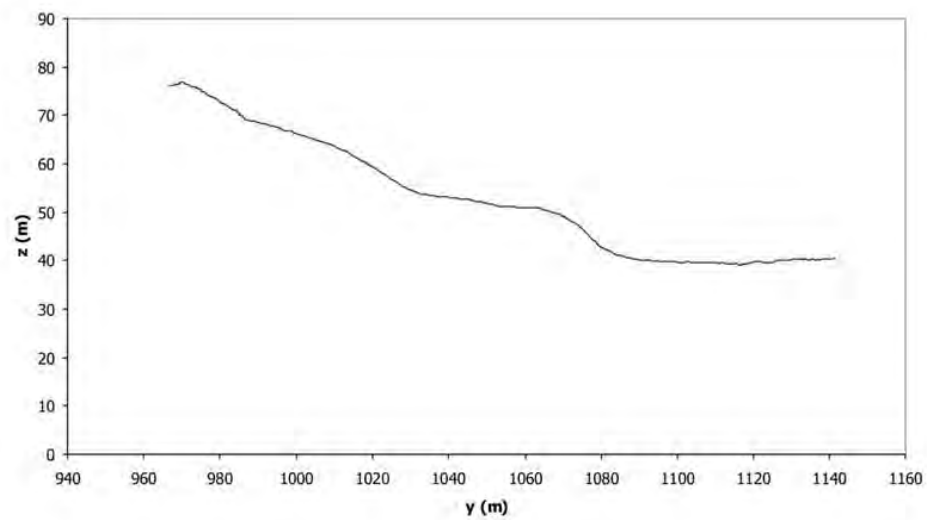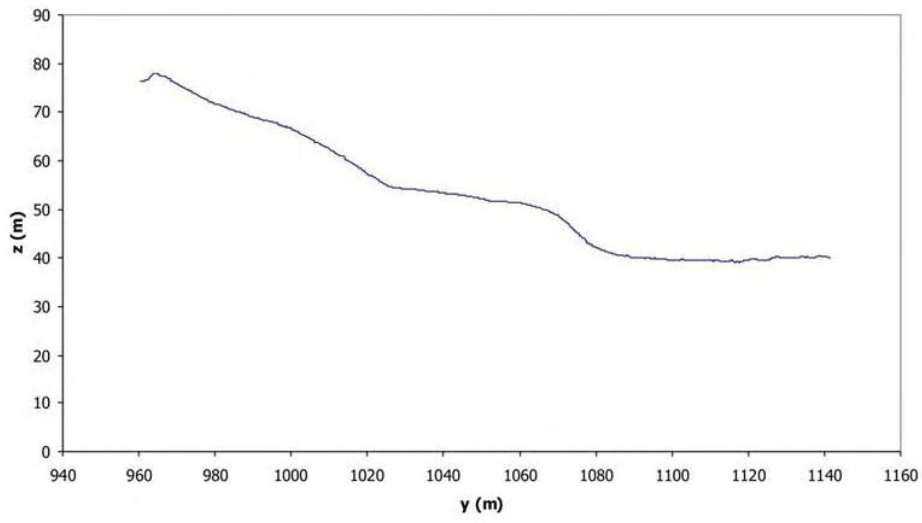
Profile 22

Profile 23

Profile 24

10
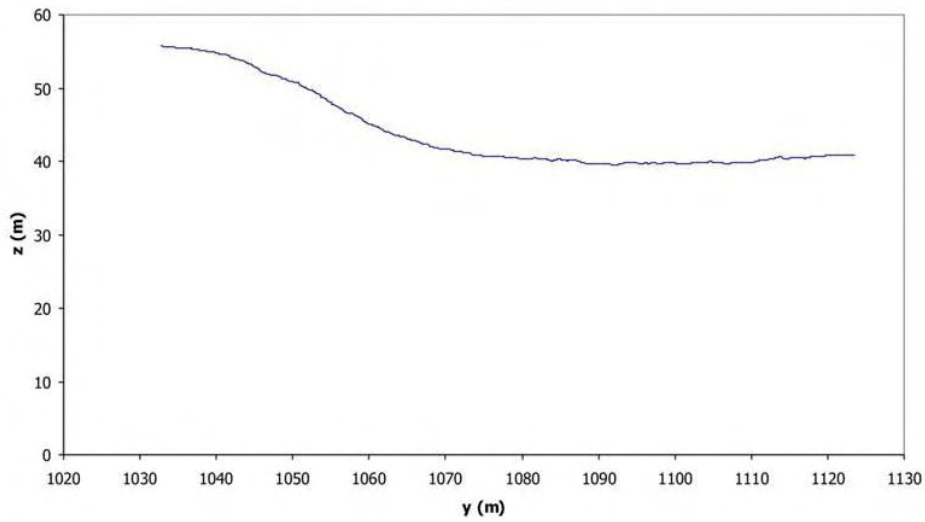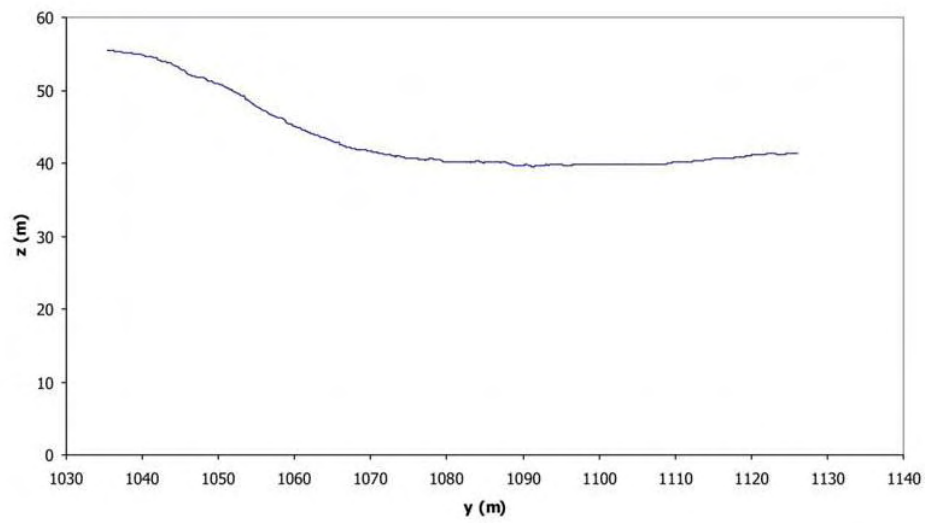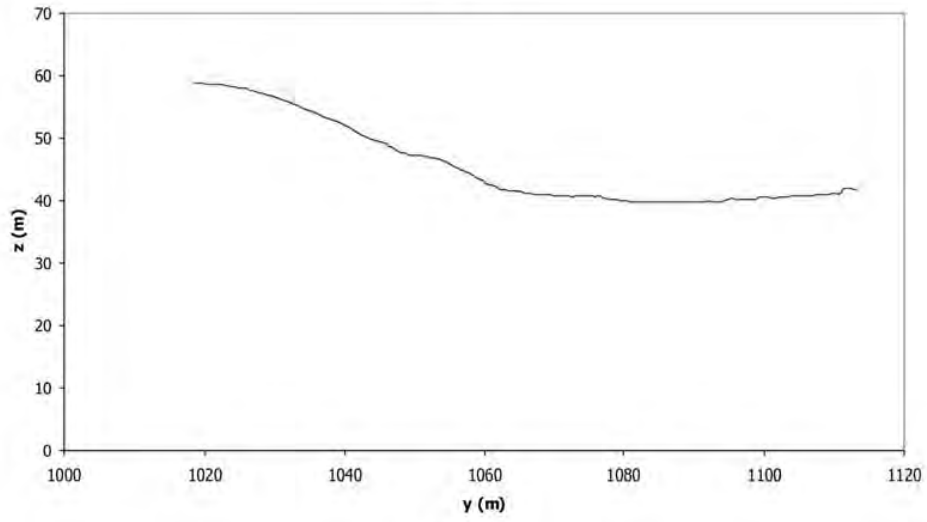
Profile 25

Profile 26

Profile 27

11
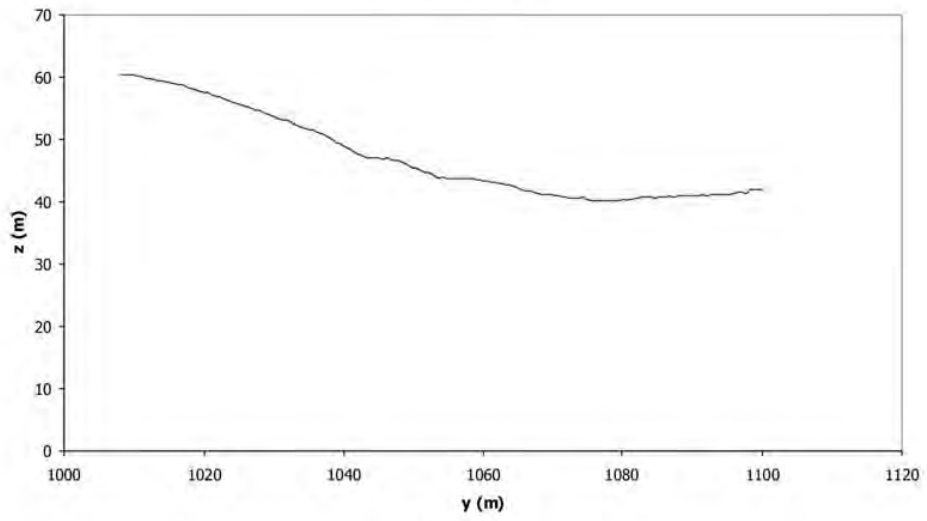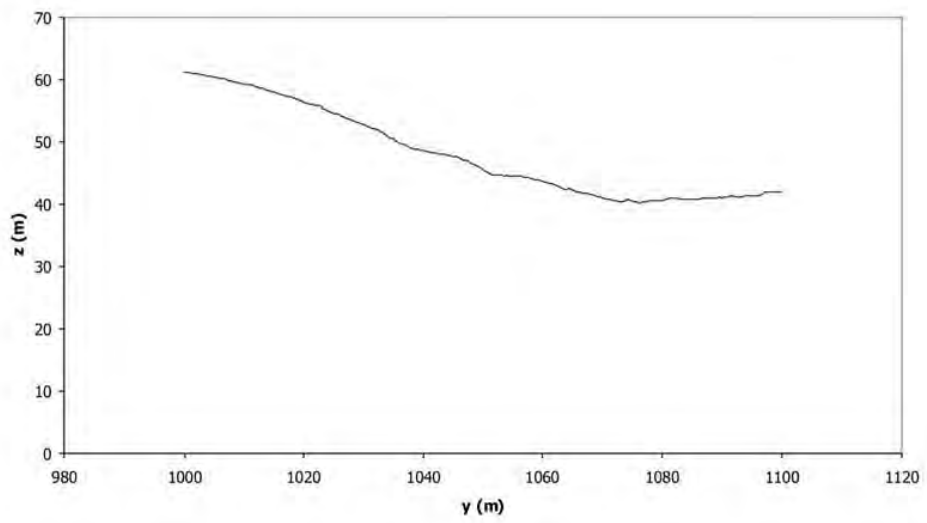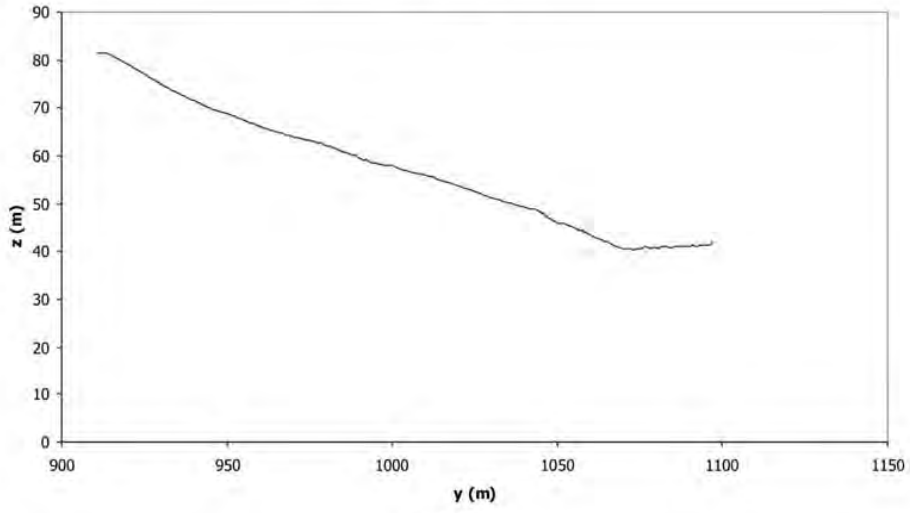
Profile 28

Profile 29
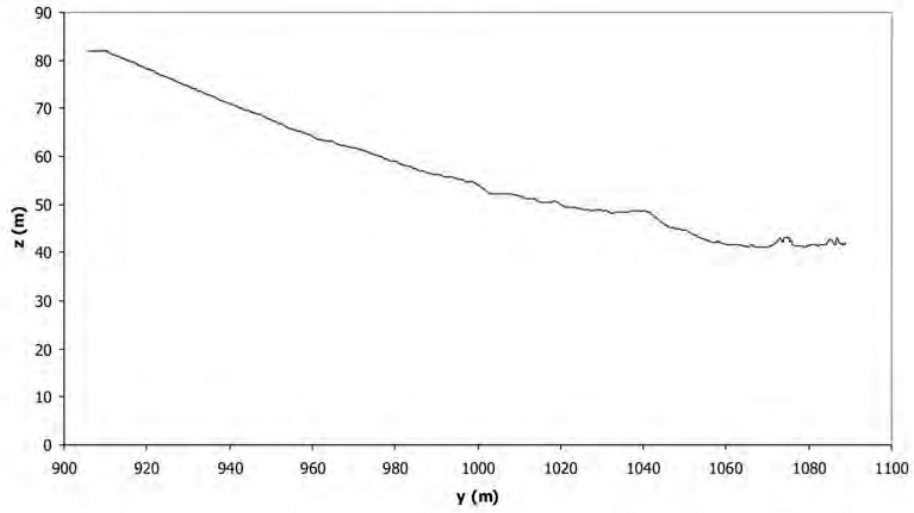
Profile 30
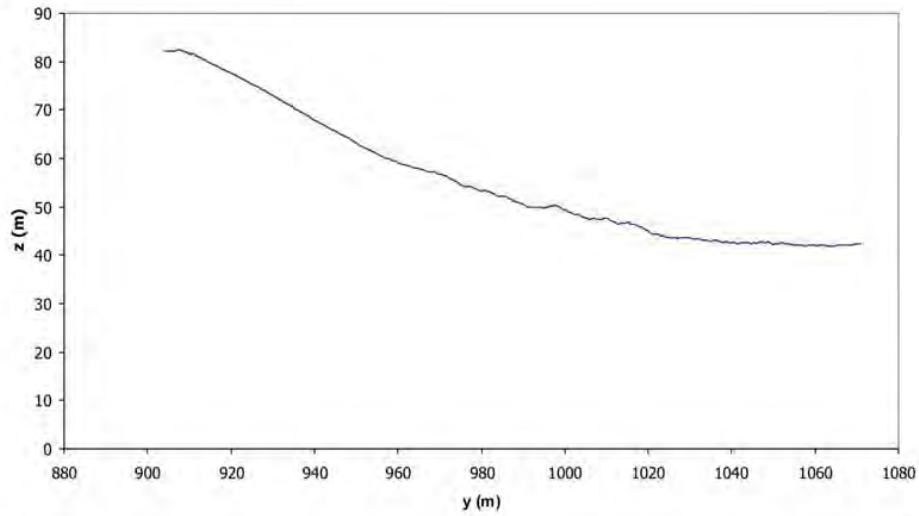
Profile 31
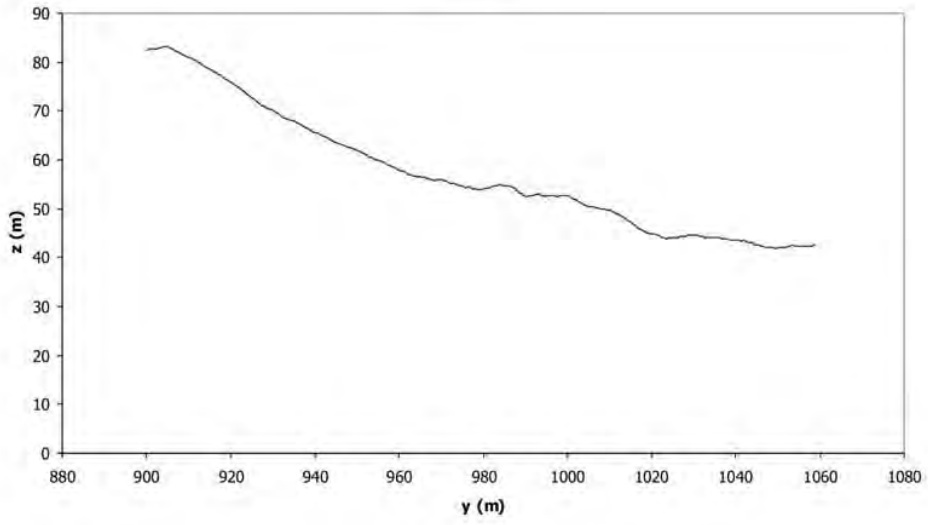
Profile 32
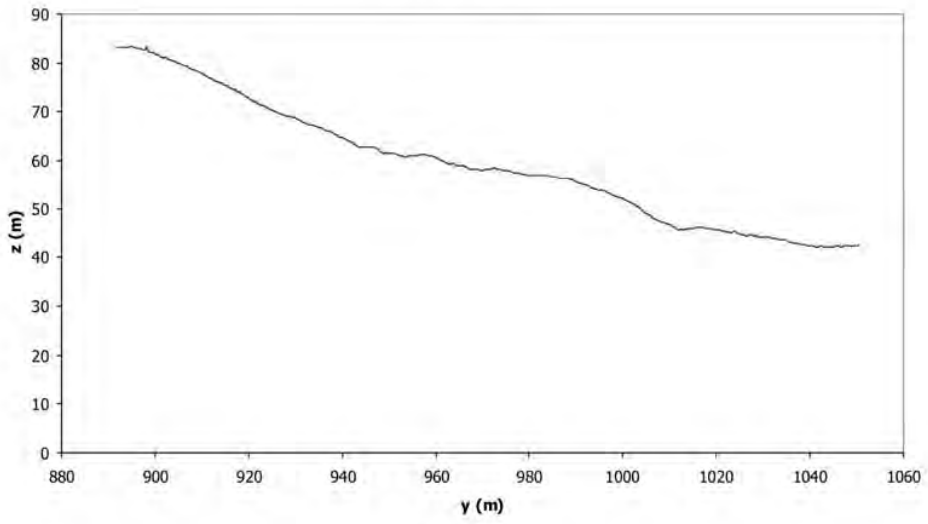
Profile 33

13
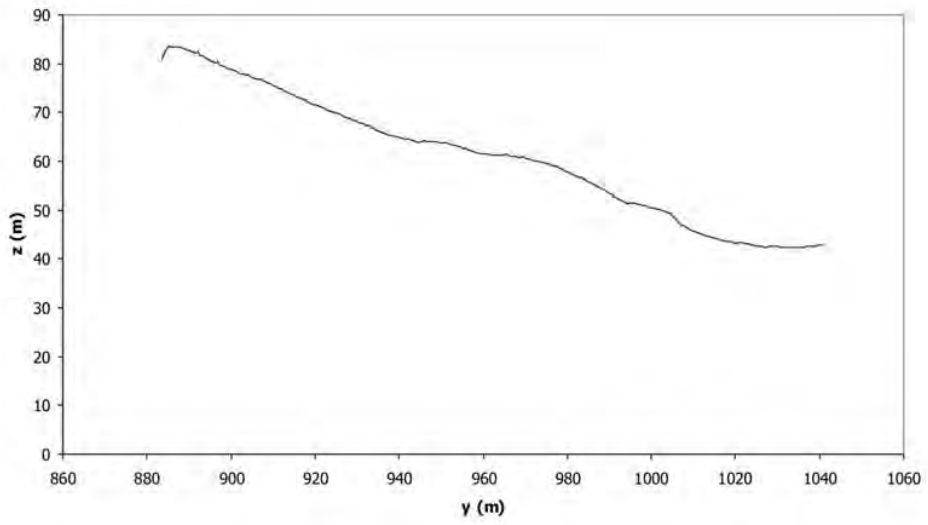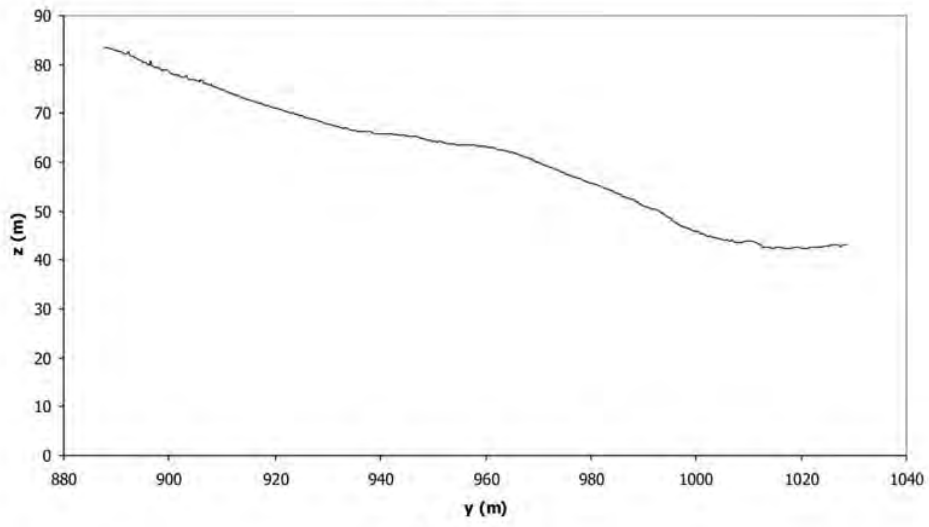
Profile 34

Profile 35

Profile 36

14
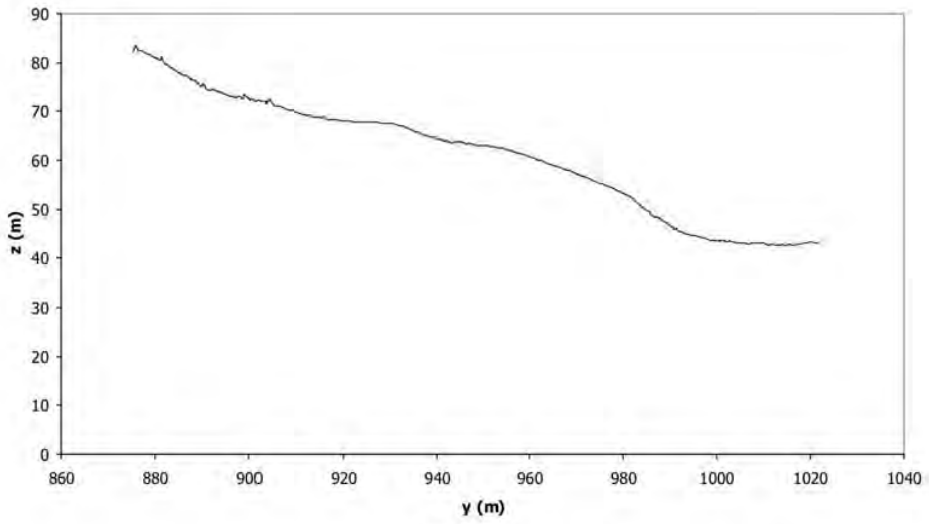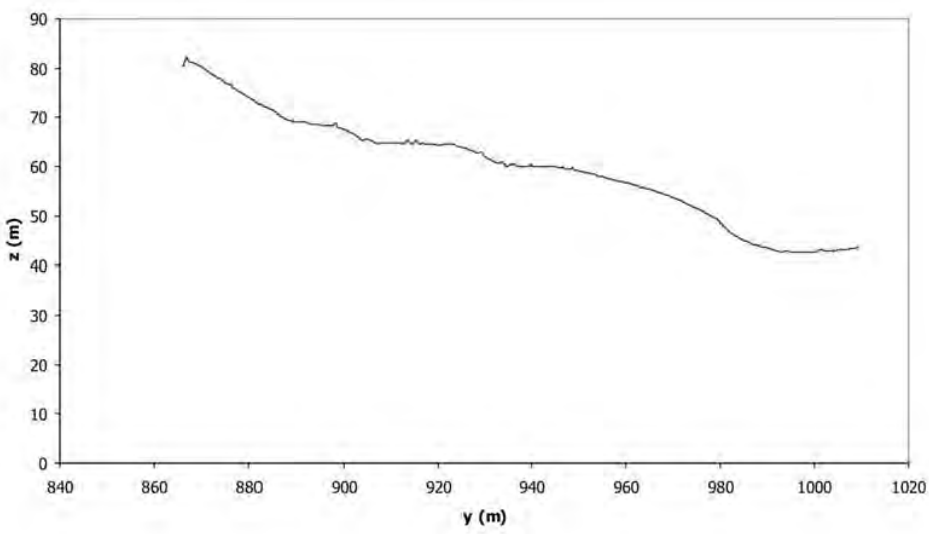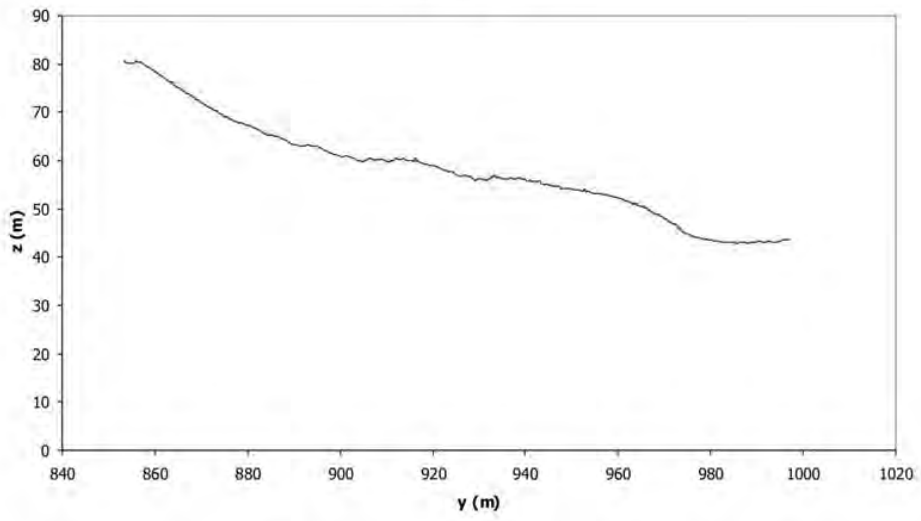
Profile 37

Profile 38
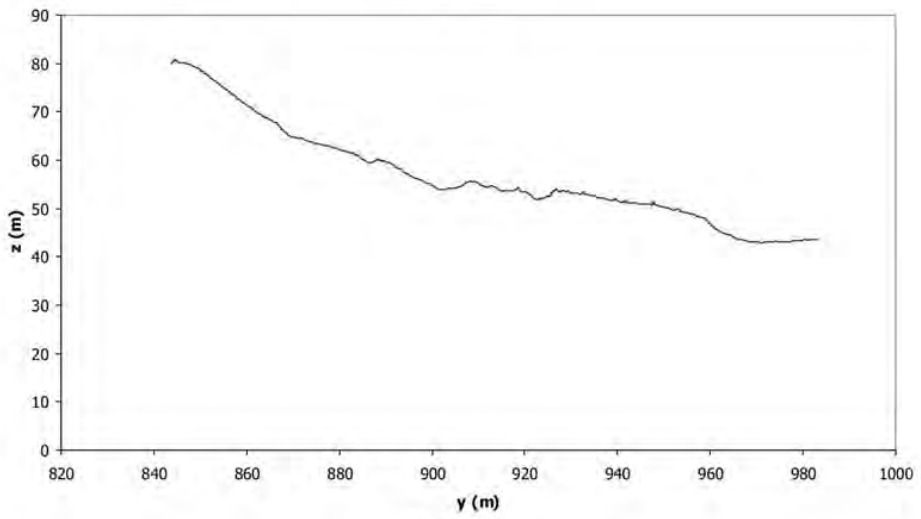
Profile 39
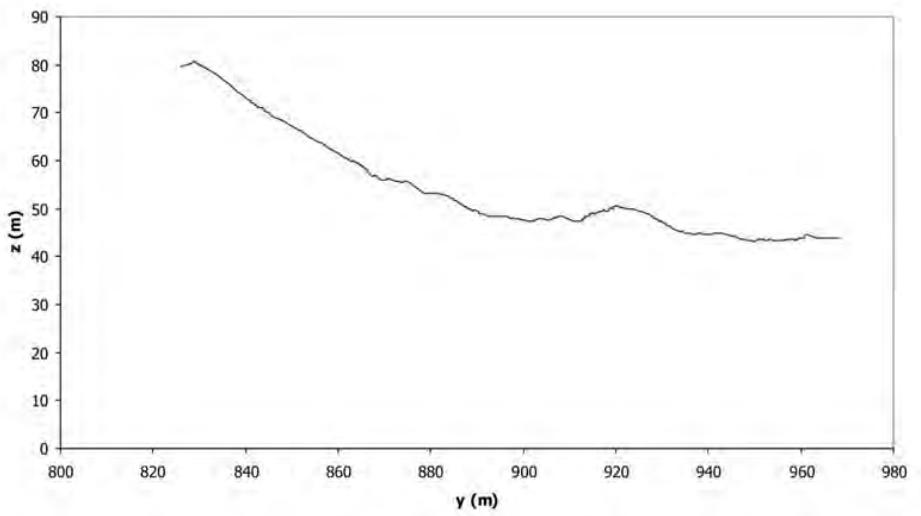
Profile 40
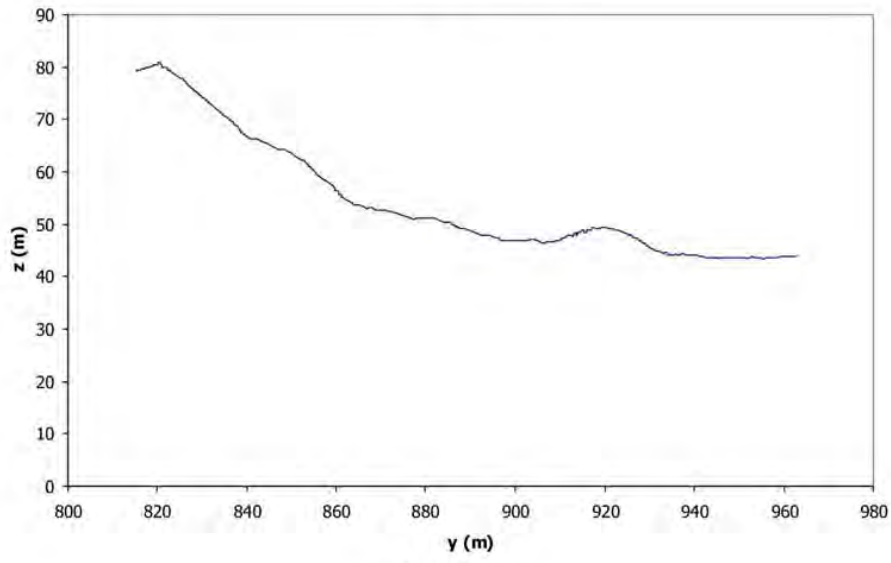
Profile 41
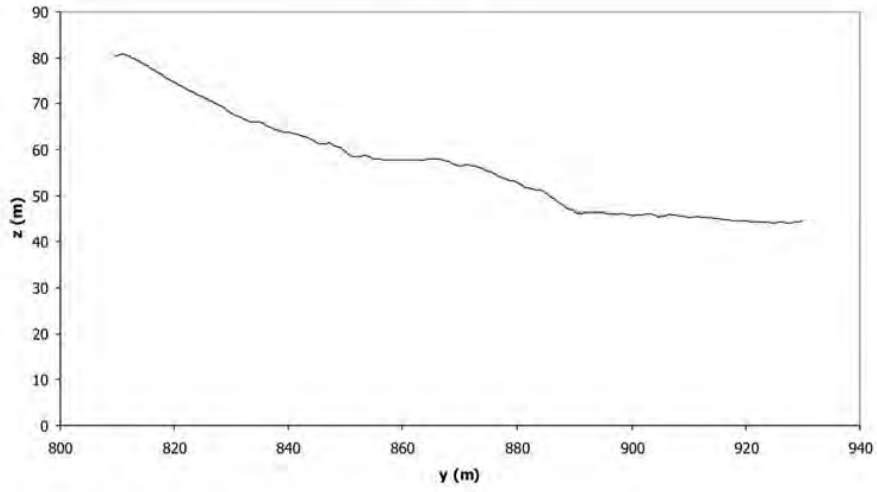
Profile 42
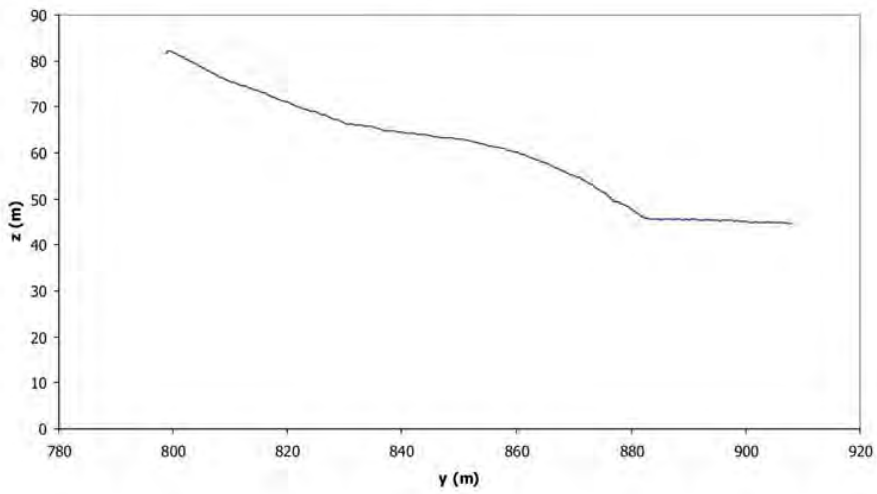
Profile 43
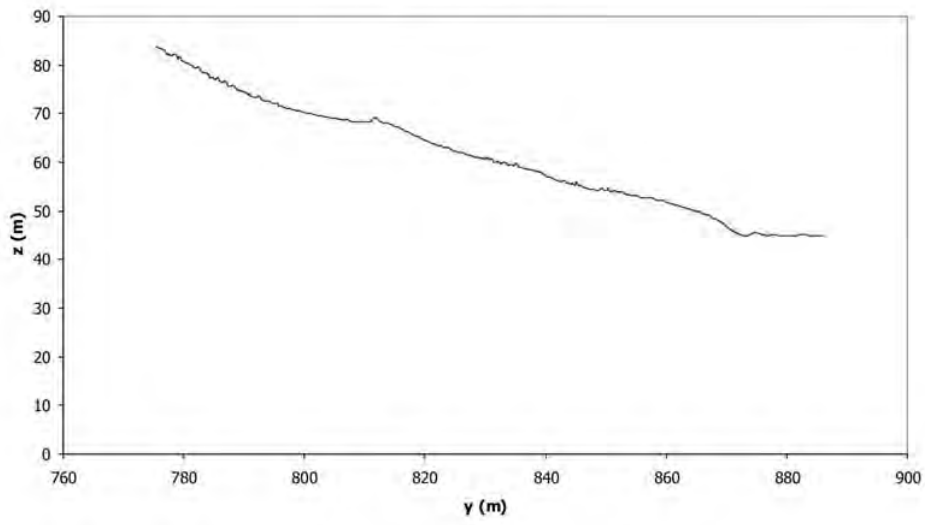
Profile 44

Profile 45

17
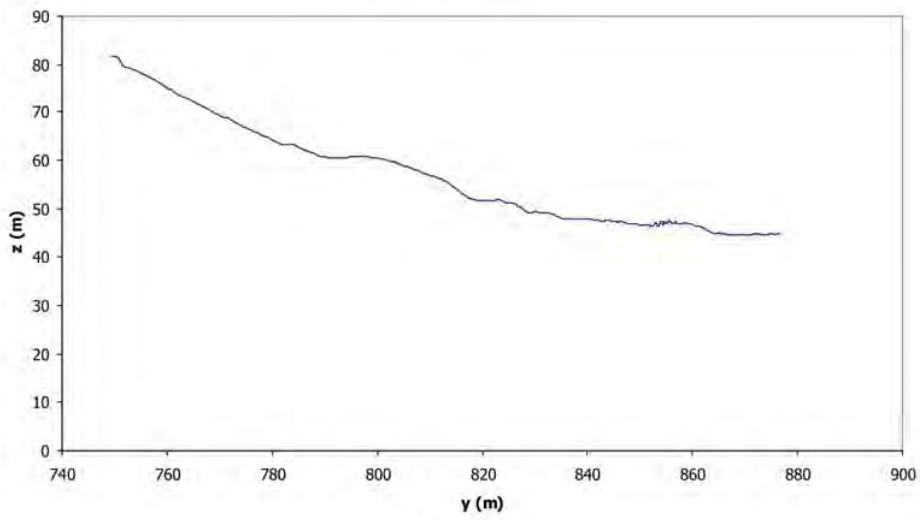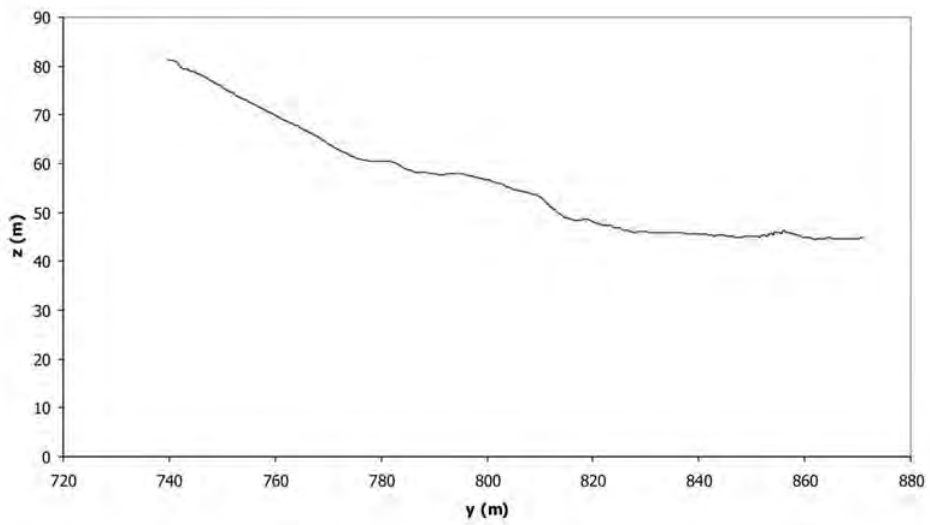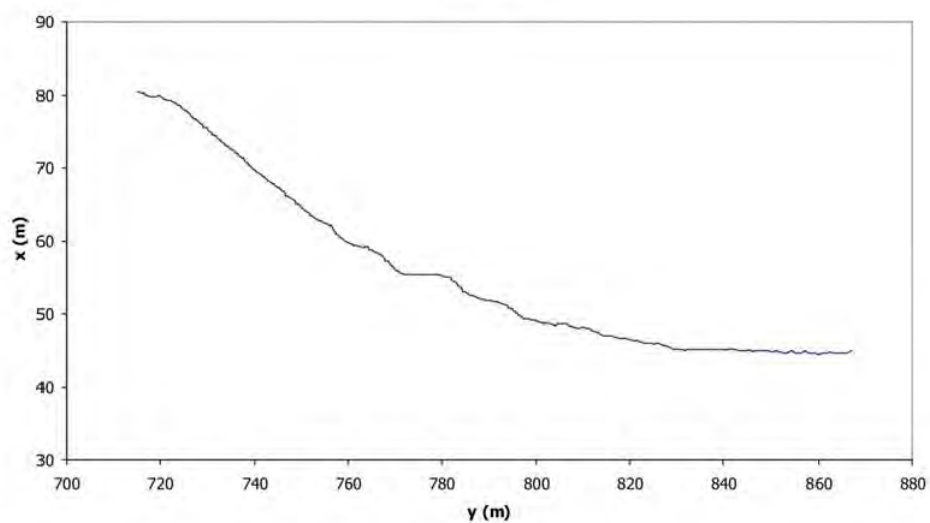
Profile 46

Profile 47
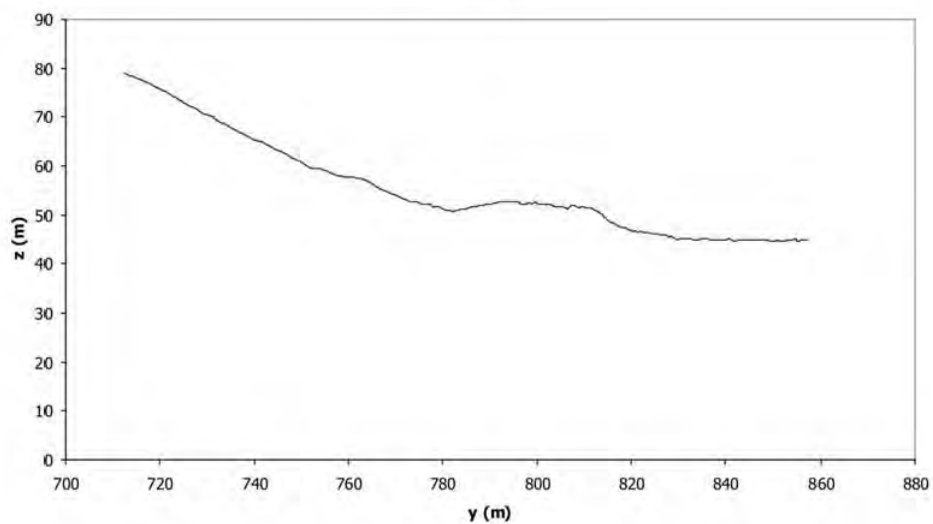
Profile 48
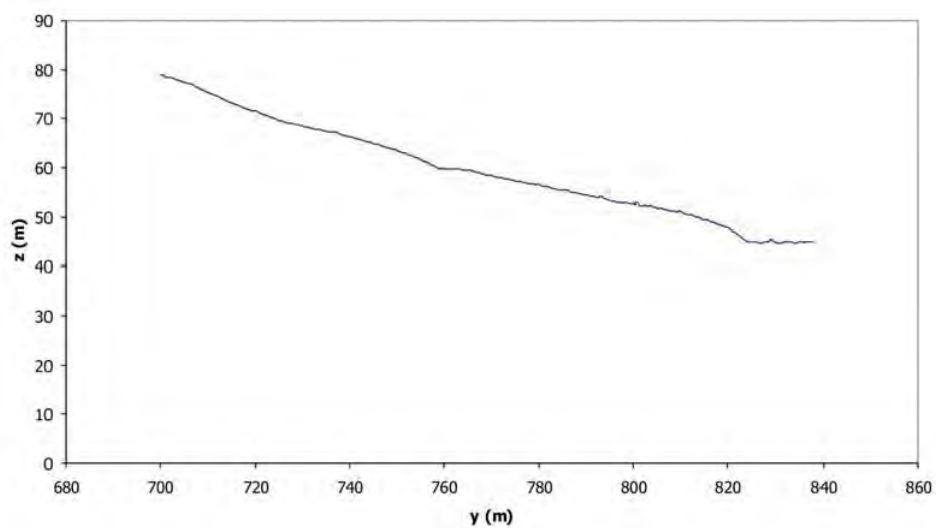
Profile 49
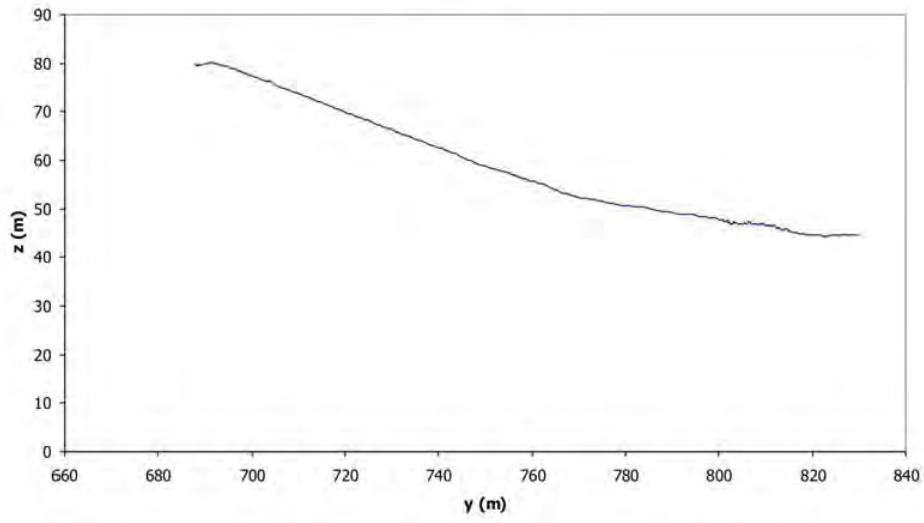
Profile 50

Profile 51

19
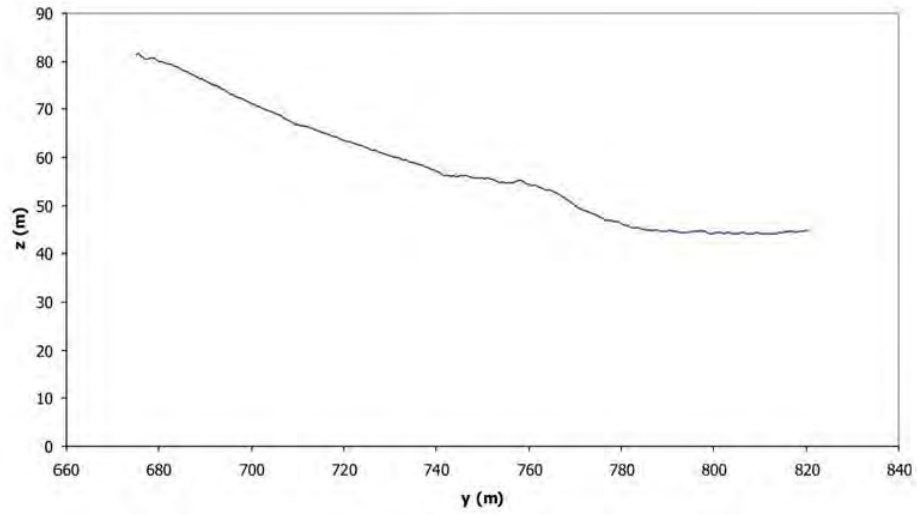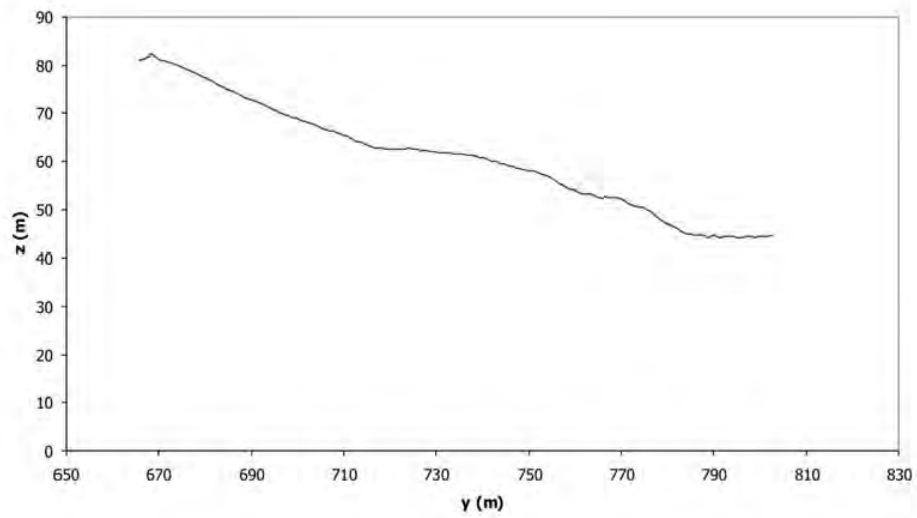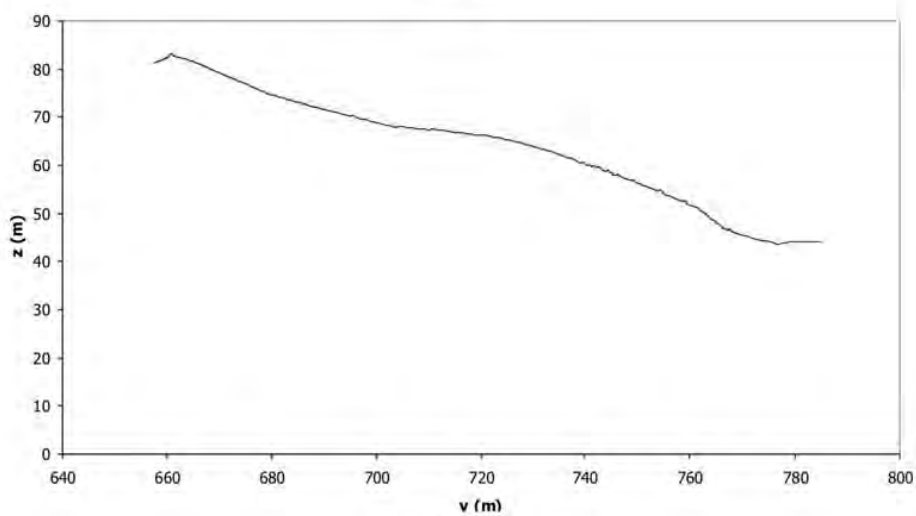
Profile 52

Profile 53

Profile 54

20
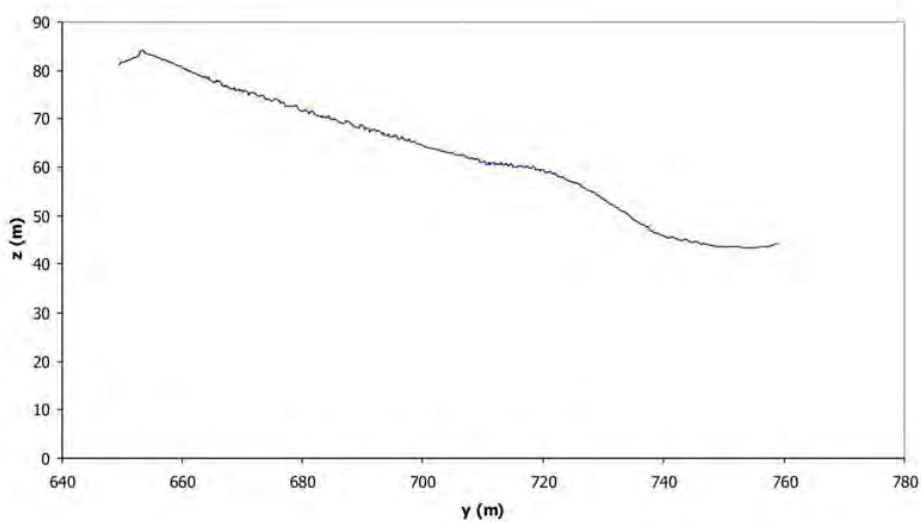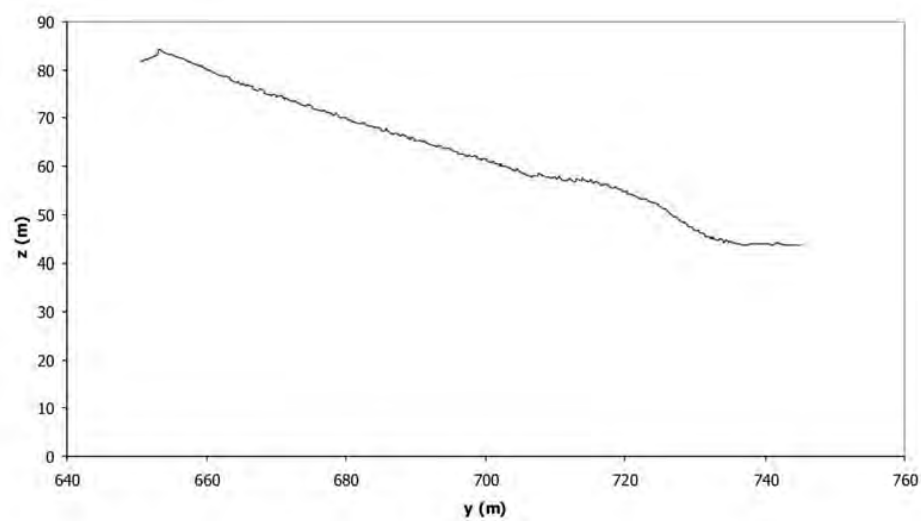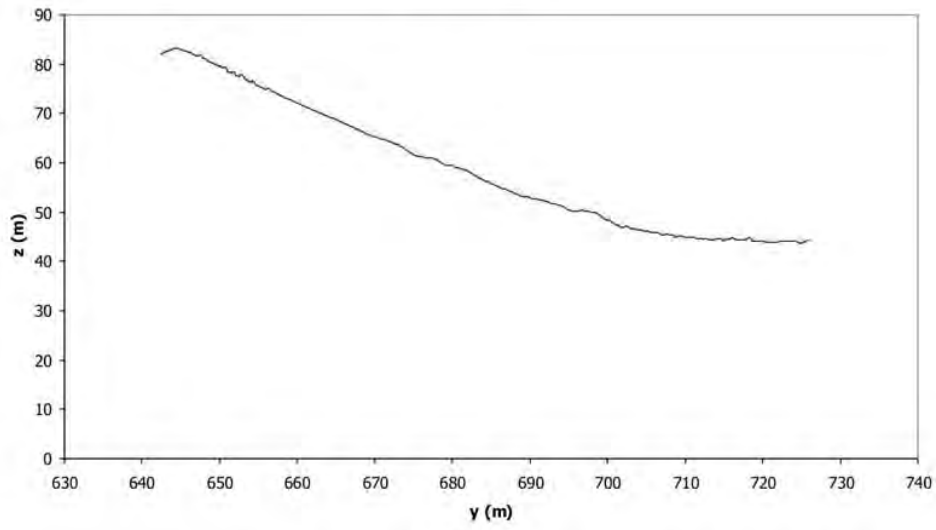
Profile 55

Profile 56

Profile 57

21
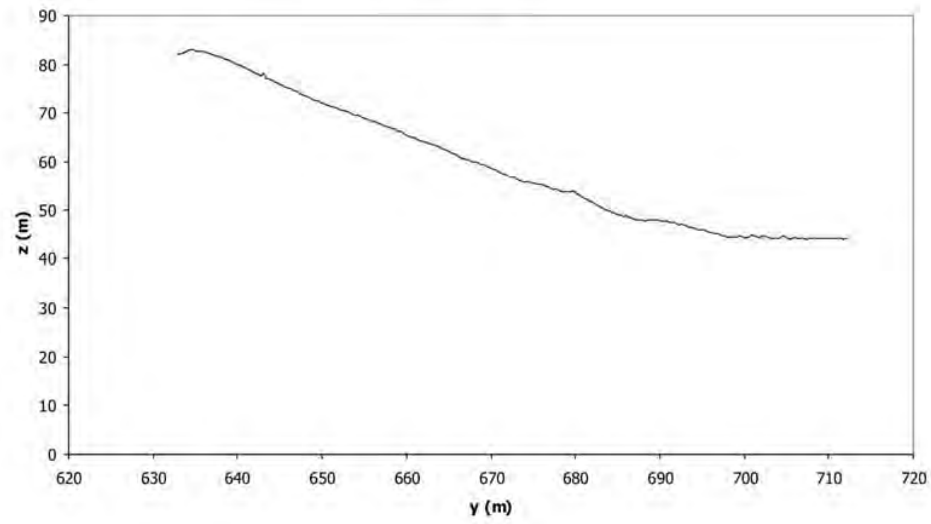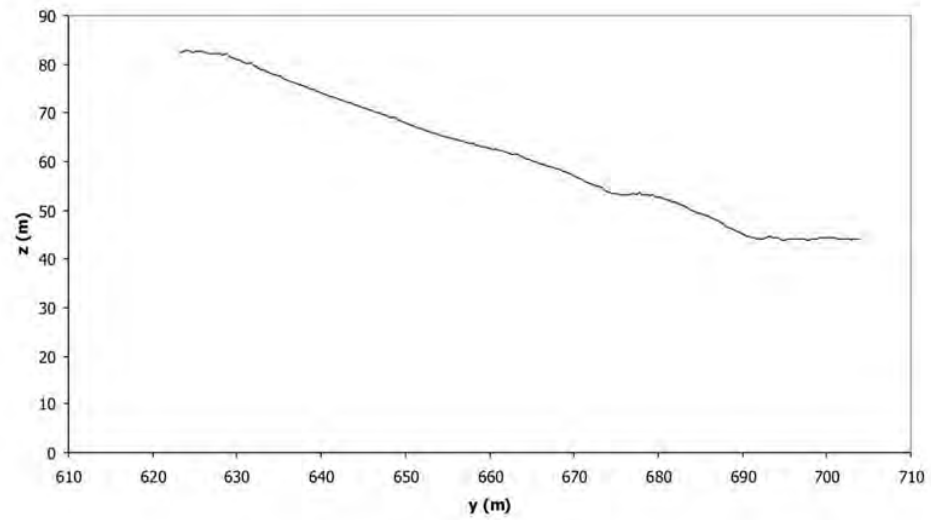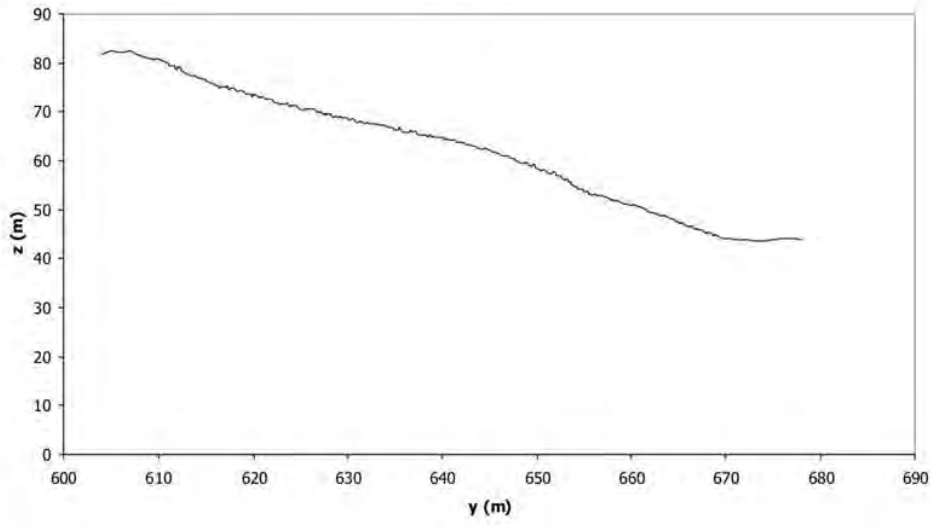
Profile 58

Profile 59

Profile 60

22
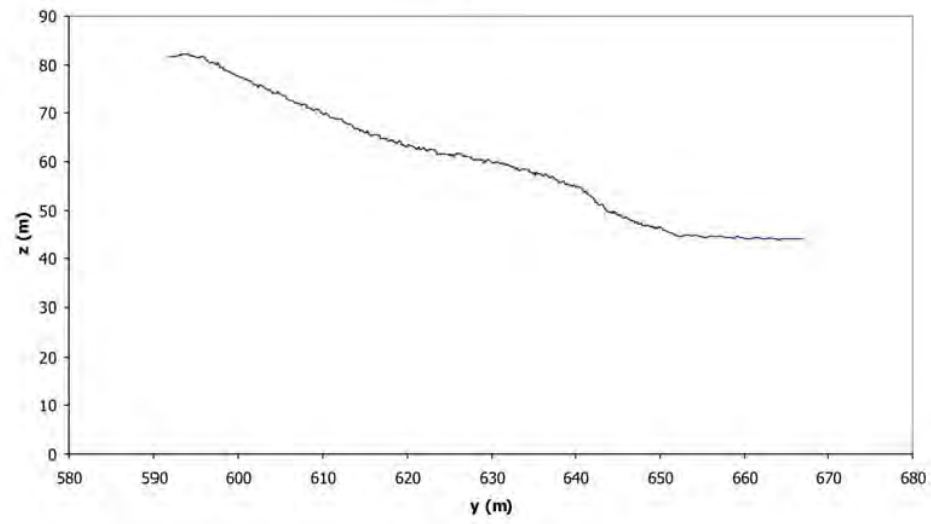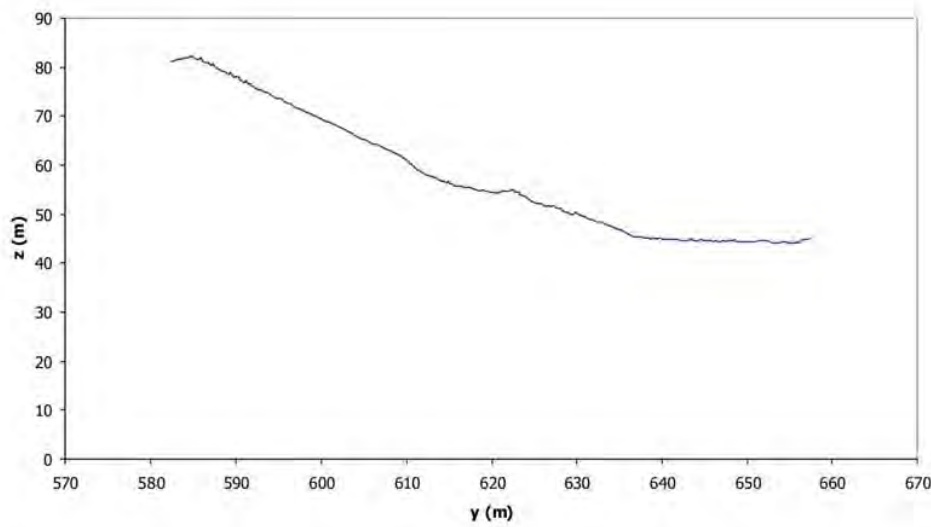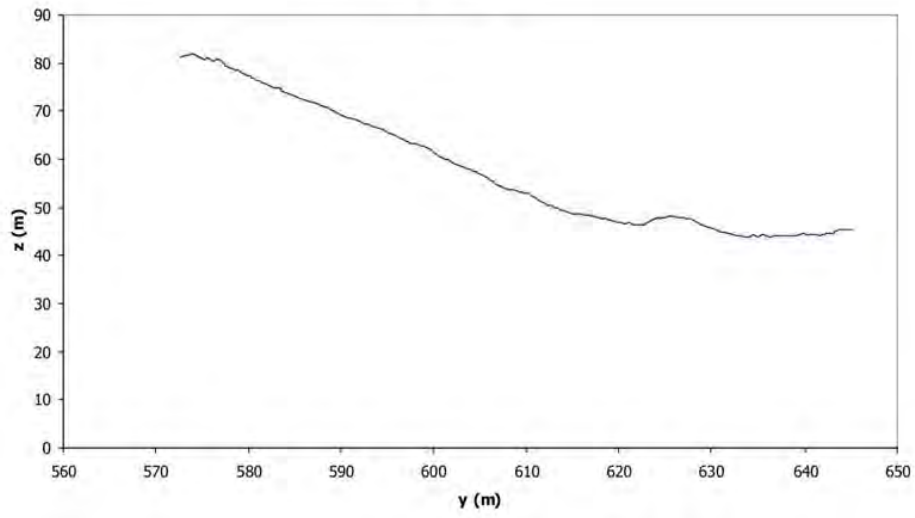
Profile 61

Profile 62
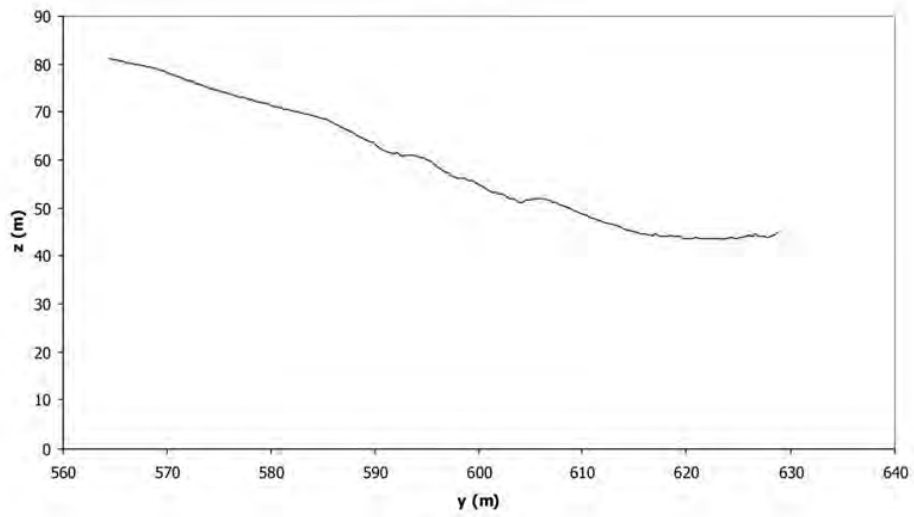
Profile 63

23
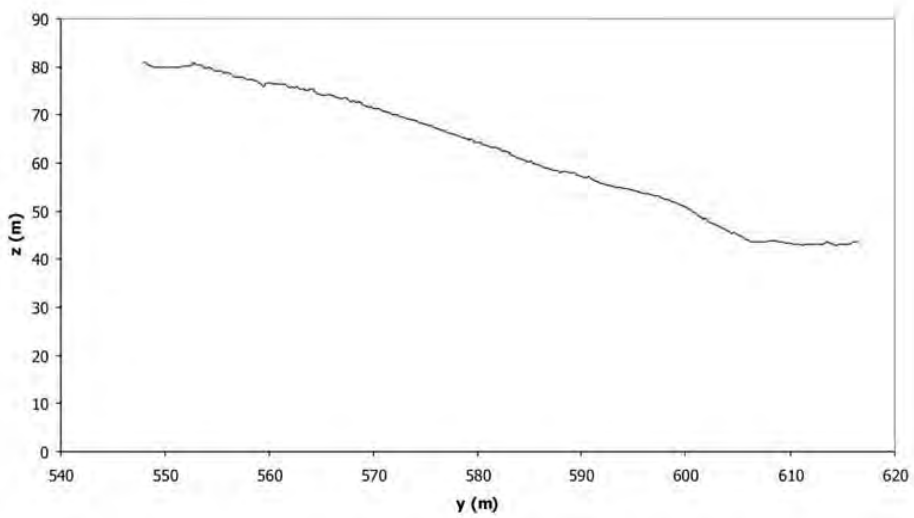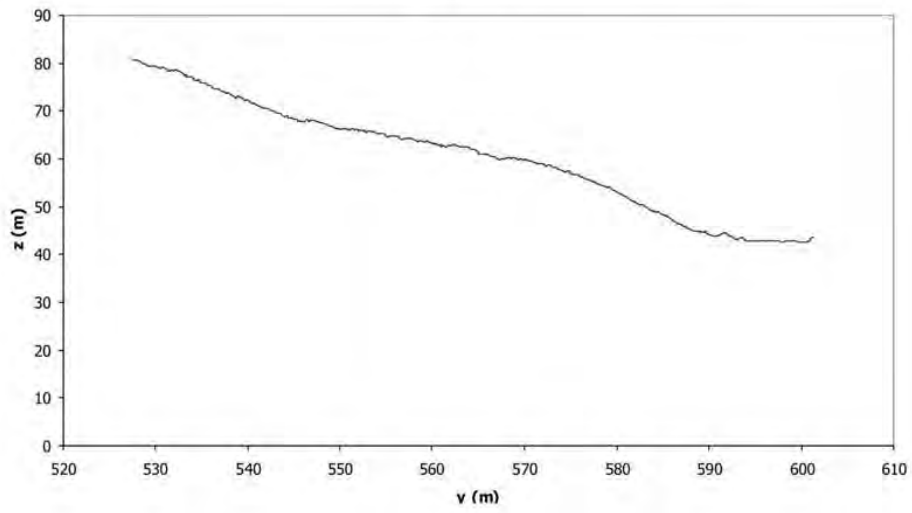
Profile 64

Profile 65

Profile 66

24
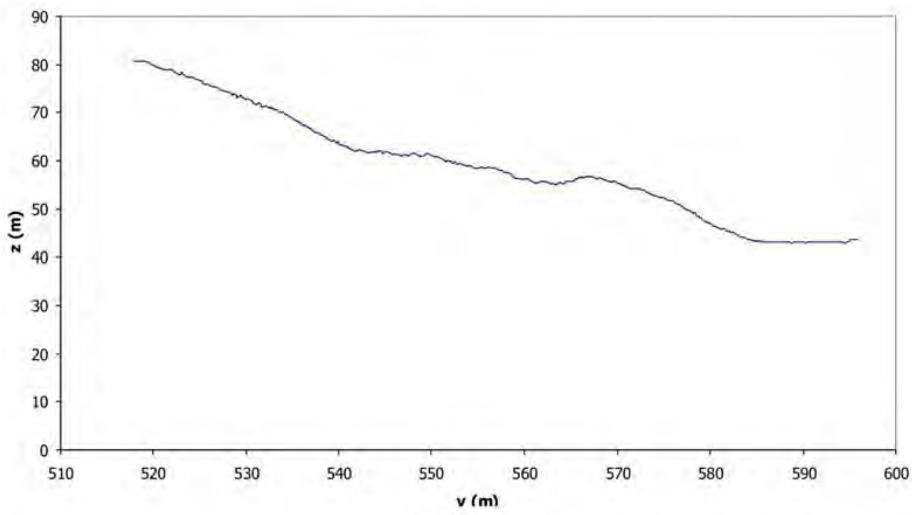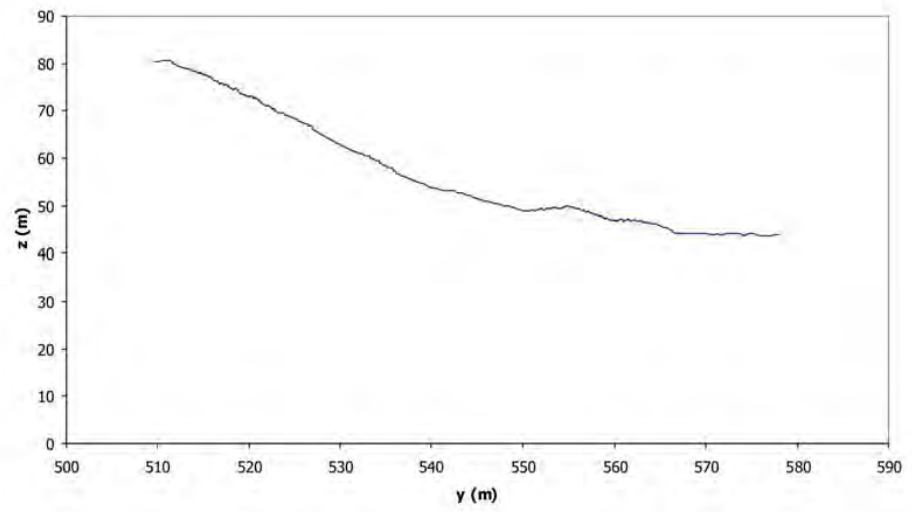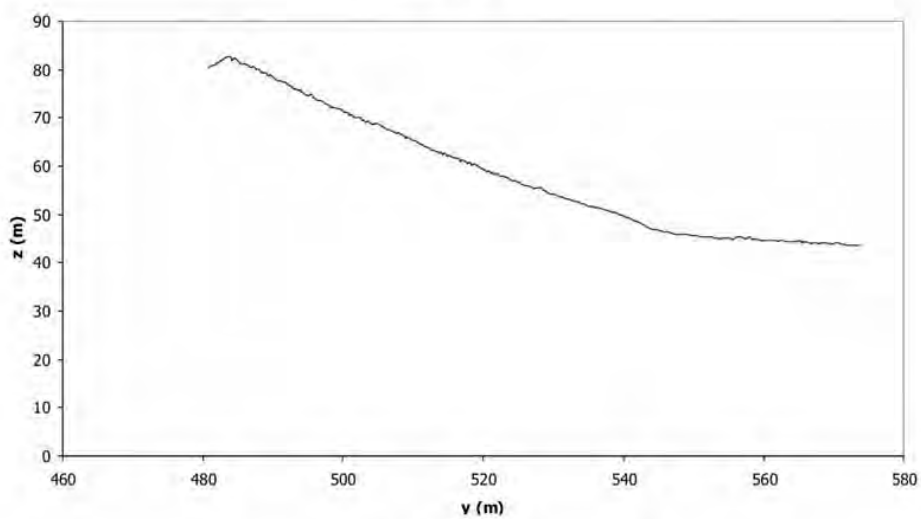
Profile 67

Profile 68

Profile 69

25
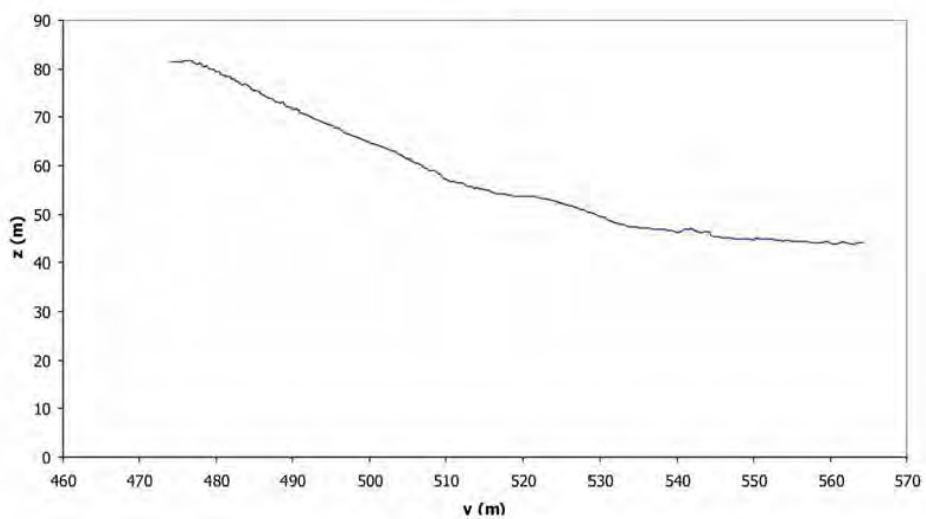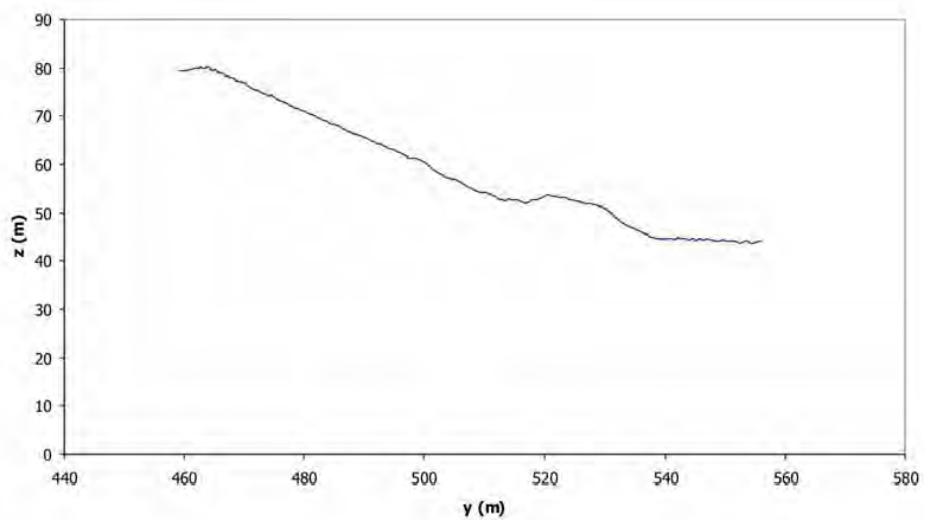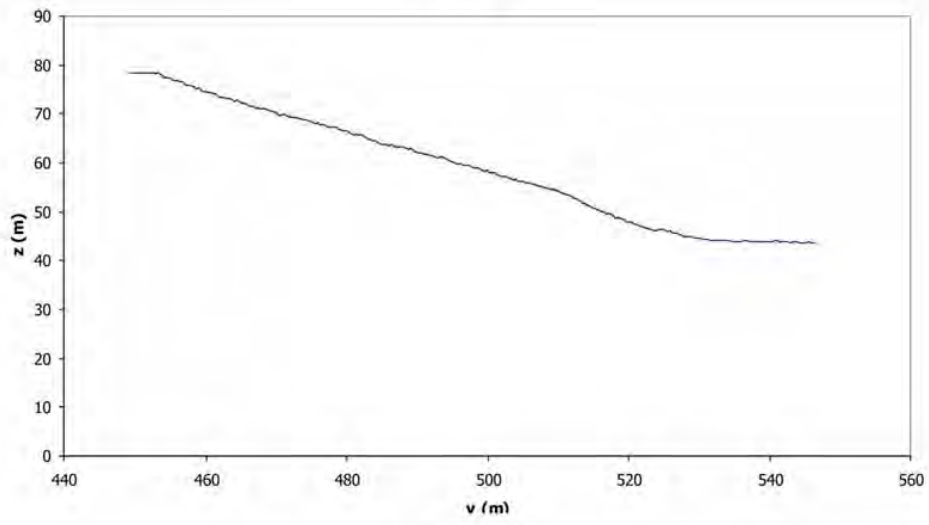
Profile 70

Profile 71

Profile 72

26
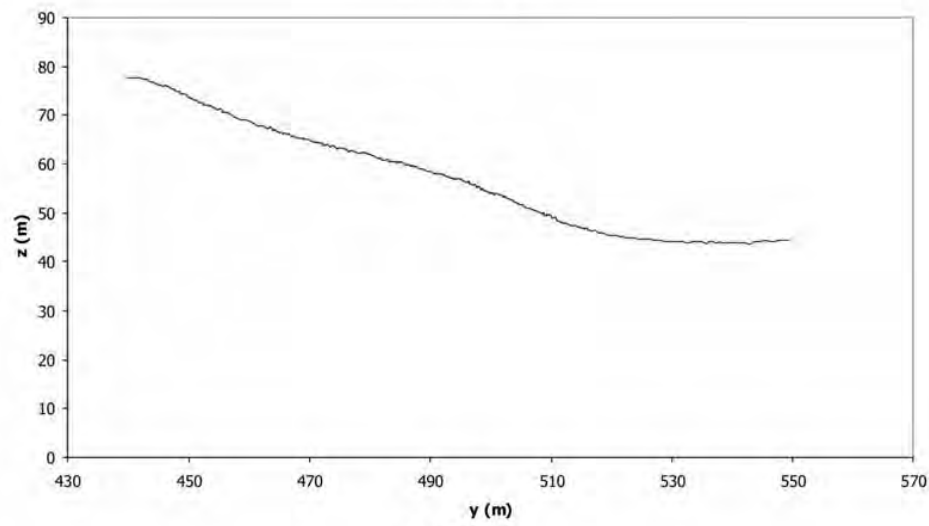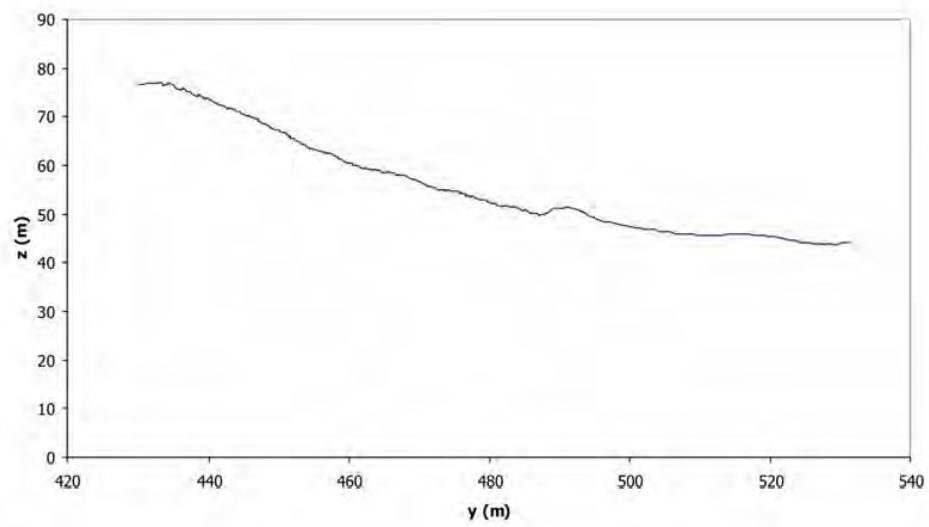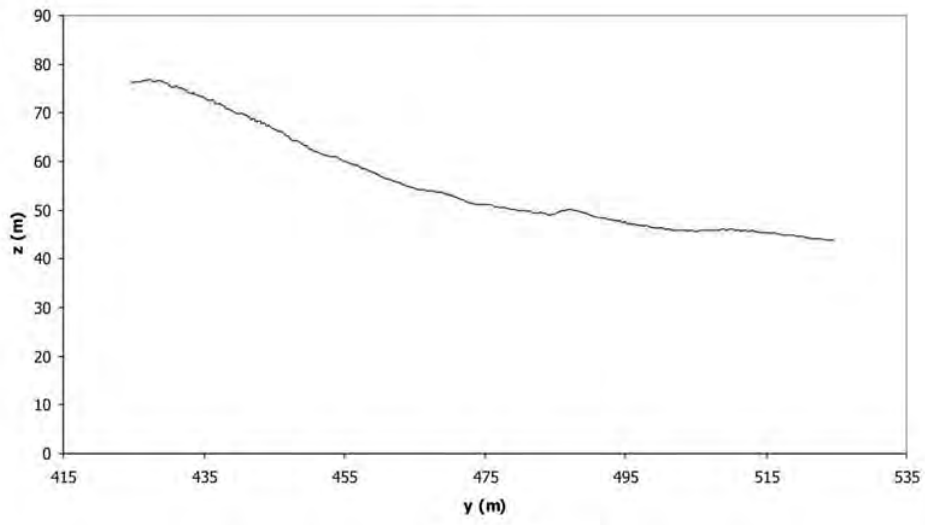
Profile 73

Profile 74

Profile 75

27
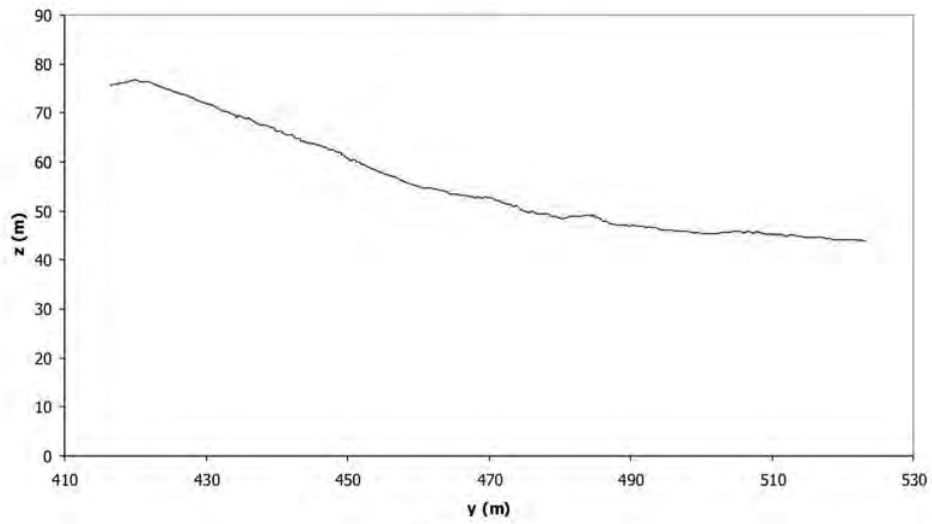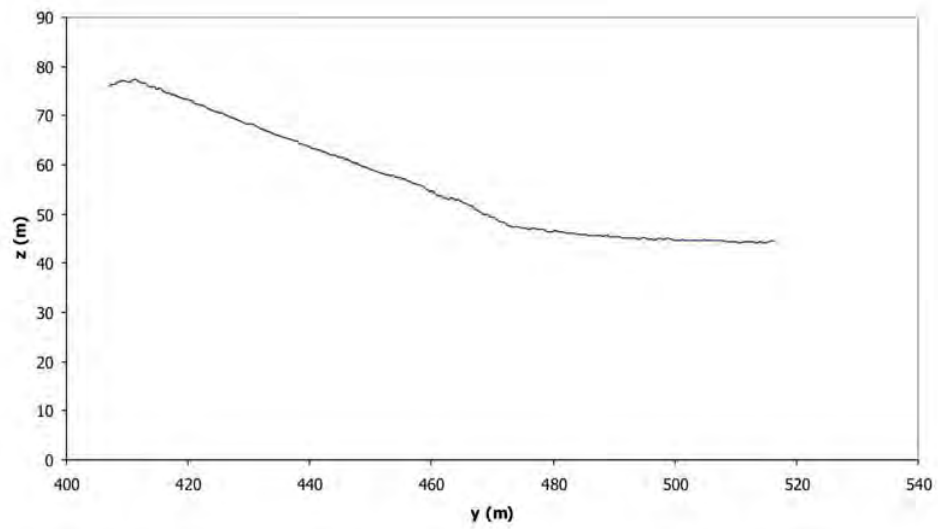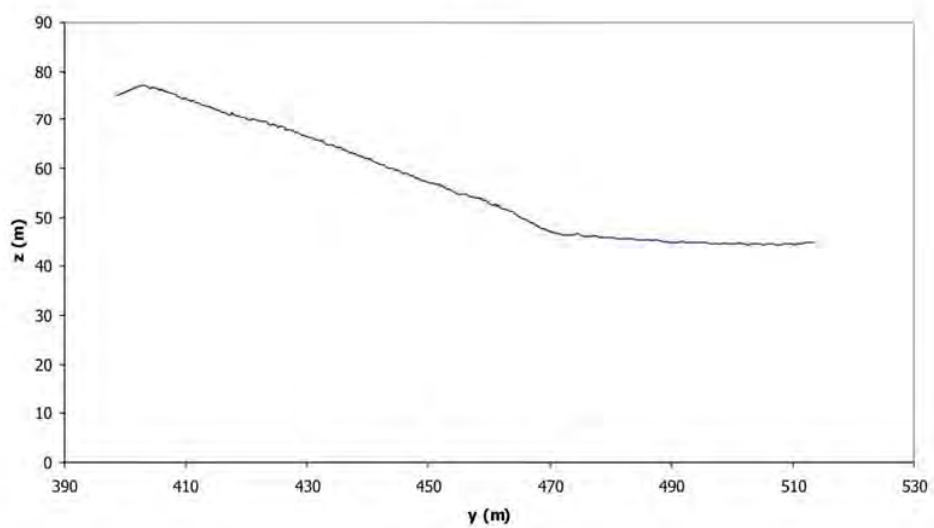
Profile 76

Profile 77

Profile 78

28

190
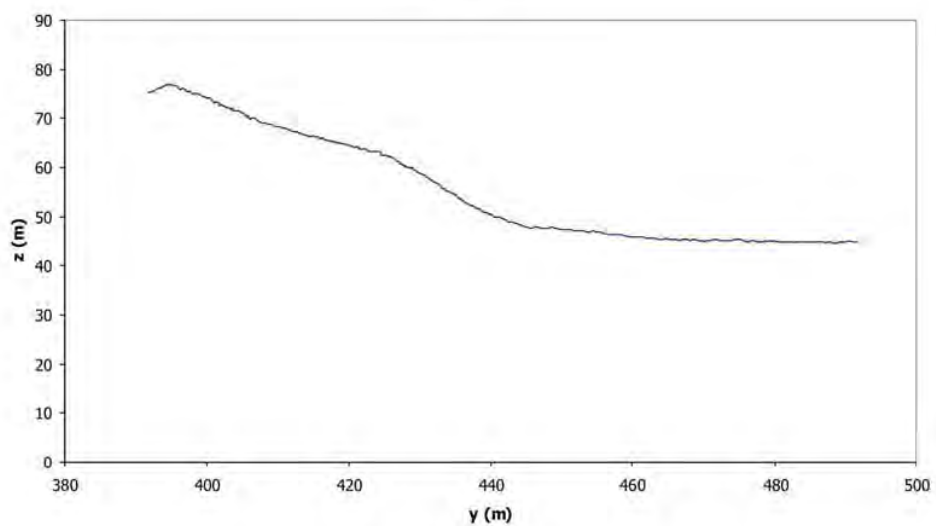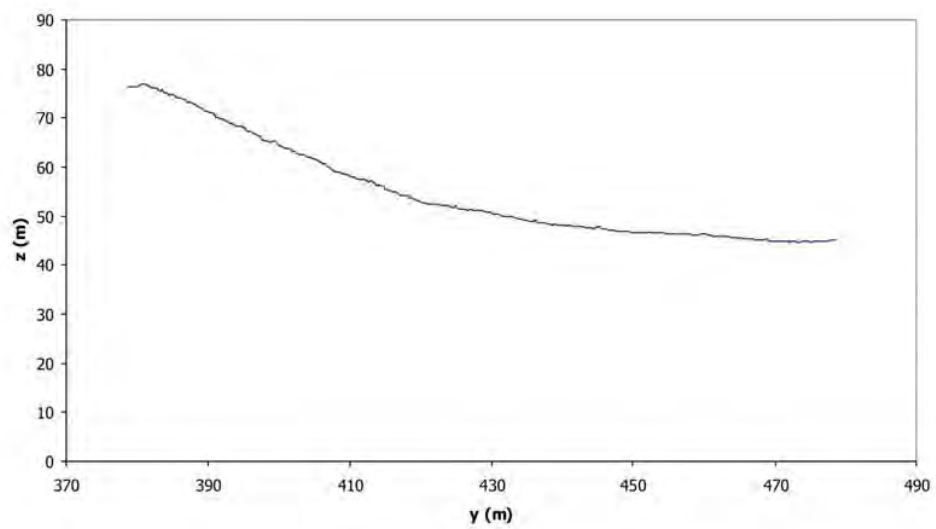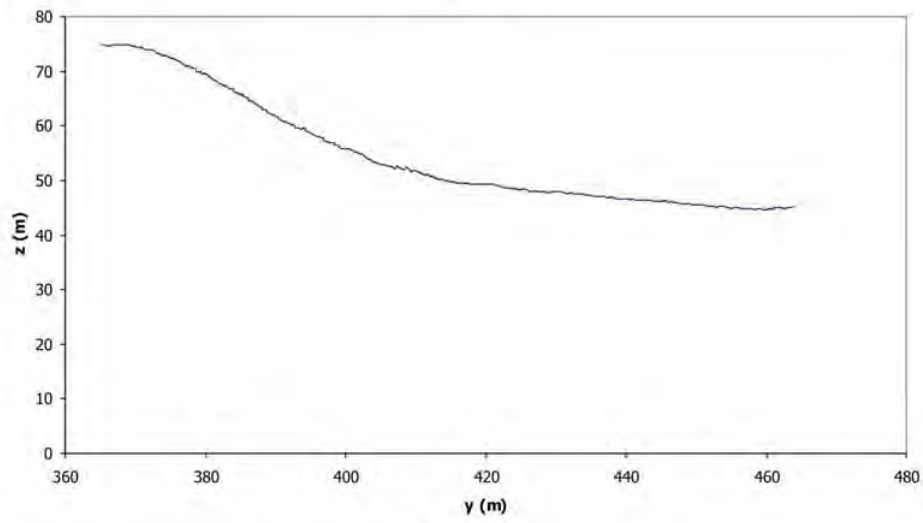
Profile 79

Profile 80

Profile 81

29
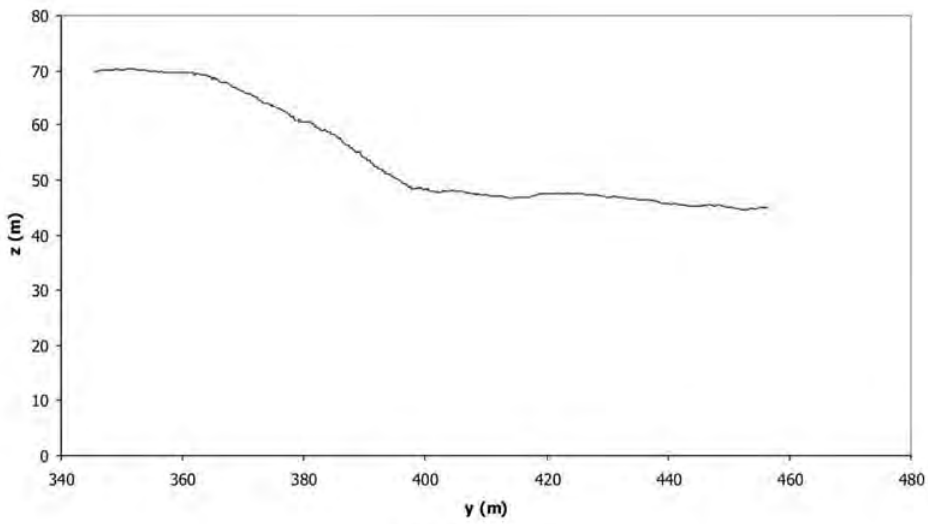
Profile 82
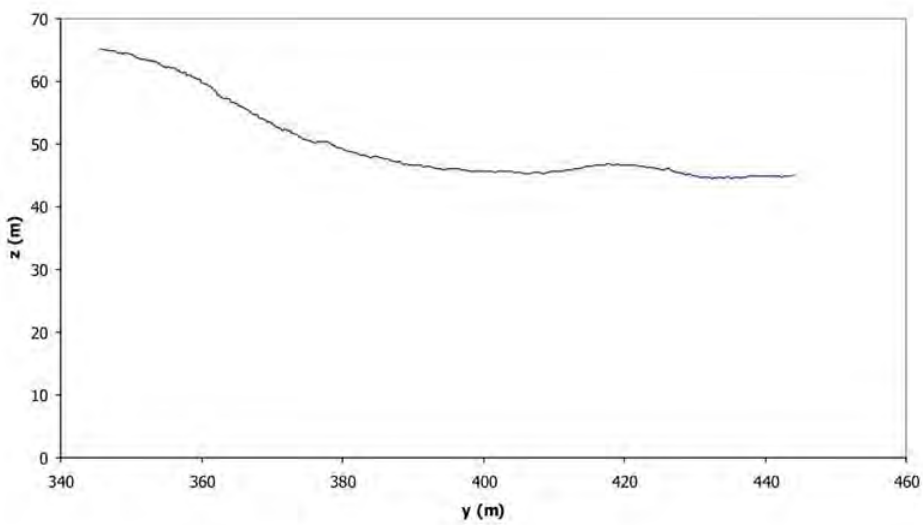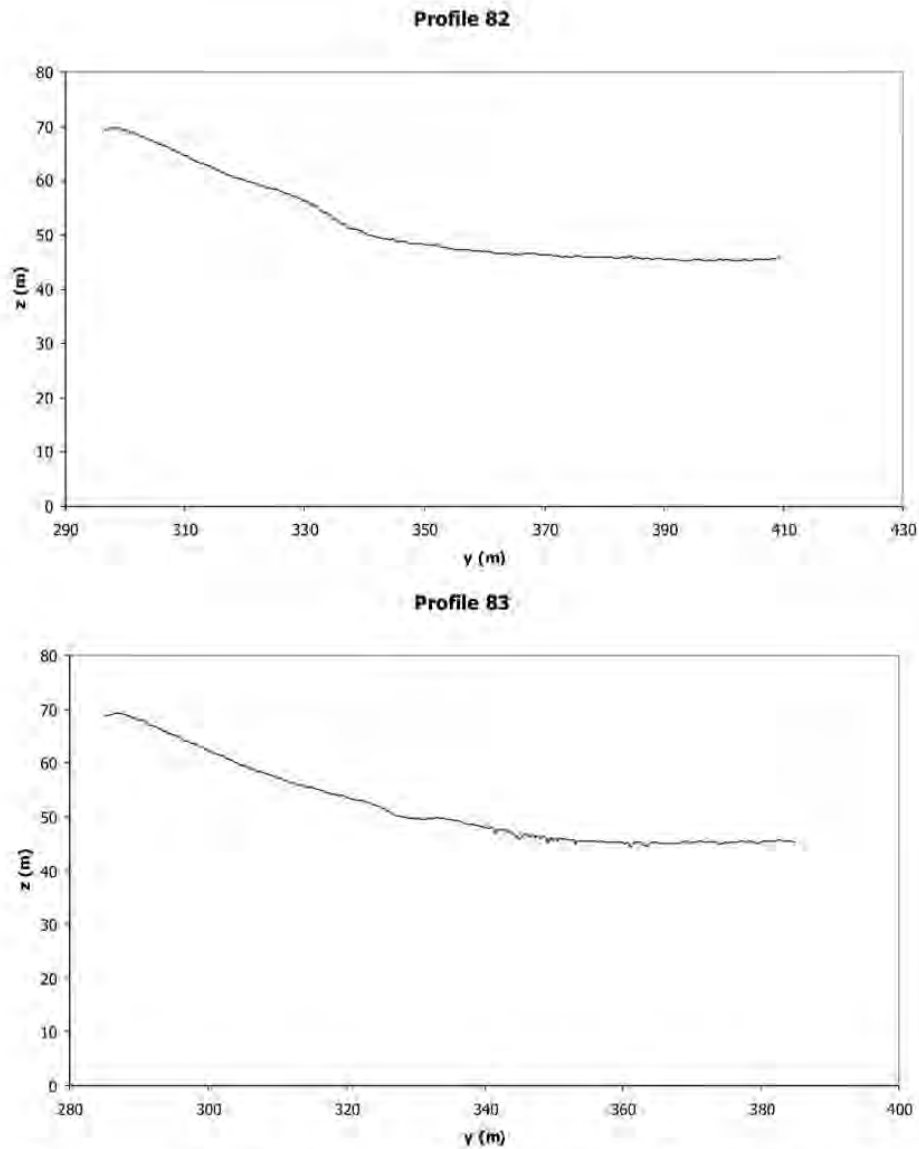
Profile 83

Fig. DR2 Topographic profiles extracted from the LDEM are shown. The location of the profiles is already shown on Figure 5a respectively at the bottom of Figure 8.

TABLE DR1. LIST OF 83 TOPOGRAPHIC PROFILES EXTRACTED FROM THE LDEM AND RELATED FAULT SCARPS WITH VALUES FOR FAULT-SCARP HEIGHT, SLOPE ANGLE, AND VERTICAL SEPARATION.

Profile no.	z-coordinate (m) base of scarp	z-coordinate (m) top of scarp	Scarp height (m) = difference between base and top	Max. slope angle θ (°)	Vertical separation (m)
1	37.1	37.6	0.5	24.6	0.3
	39.7	41.7	2	45	1.7
	44.2	46.3	2.1	40.4	1.6
2	37.1	38.7	1.6	26.4	1.1
	40	43	3	41	2.1
3	41.1	44.3	3.2	37	1.7
4	41.4	47.6	6.2	35.2	2.8
5	40.6	46	5.4	39.1	3.2
6	38.5	45.5	7	41.1	4.1
7	37.7	38	0.3	8.6	0.2
	39.5	46.2	6.7	22.5	3.5

30

192

	52.3	54.7	2.4	31	1.9

	Col1	Col2	Col3	Col4	Col5
	52.3	54.7	2.4	31	1.9
8	38	39.1	1.1	8	0.9
	40.6	47.2	6.6	28.1	3.2
9	38.2	40	1.8	12.5	1.5
	41.1	50	8.9	32	4.8
10	42	50.1	8.1	30.9	4.3
11	43.3	48.6	5.3	36.5	2.7
12	38.3	40.7	2.4	13.1	1.4
	44.3	46.8	2.5	29.5	2
	52.8	55.1	2.3	26.8	1.8
13	38.7	42	3.3	16.7	2.1
	46.9	51	4.1	30.6	2
14	39.6	43.5	3.9	18	2.7
15	40	46.8	6.8	23.4	5.6
16	40.5	46.5	6	37.8	4
	48.4	52.2	3.8	29.5	2.5
	61.7	64.7	3	25.1	1.6
17	41.1	43.6	2.5	41.2	2
	44.8	51.2	6.4	28.1	4
	57.1	58.7	1.6	20.1	0.9
18	41.4	42.9	1.5	12.2	1.1
	46.6	48.8	2.2	25.5	1
	55	60.9	5.9	31.7	2.7
19	44.1	49.9	5.8	24.9	3.2
	54.7	56	1.3	19.7	0.7
	58.3	61.3	3	36.9	1.5
20	41.3	46.5	5.2	26.2	4.1
	47.7	48.7	1	15.2	0.8
	51.1	52.3	1.2	24.6	0.8
	61.9	62.9	1	18.6	0.6
	64.8	65.8	1	27.5	0.5
21	40.8	50.5	9.7	37.1	7.7
	53.9	62.3	8.4	24.3	4.7
	69	73.5	4.5	28.4	2.4
22	41.1	49.9	8.8	33.9	7.2
	54.5	66.5	12	23.7	7.5
23	45.1	46.2	1.1	33.2	0.9
	52	54.3	2.3	25.2	1.8
24	52	54.2	2.2	26.8	1.9
25	40.1	40.5	0.4	12.2	0.3
	42.1	46.7	4.6	26.4	3.4
	47.6	48.8	1.2	28.4	1
26	41.2	42.3	1.1	19.1	0.8
	43.9	46.6	2.7	23.7	1.9
	47.1	50.9	3.8	29.1	1.8
27	42.4	43.8	1.4	15.6	1.1
	44.8	47.2	2.4	22.6	1.7
	48.9	51.6	2.7	27.5	1.6
28	40.7	48.2	7.5	22.6	3.5
	58.5	62.1	3.6	14.2	1.8
29	42	48	6	28.3	4.5
	52.1	54.2	2.1	26	1.4
30	44.3	47.2	2.9	11.5	2.6
	47.8	49.6	1.8	19.1	1.6
	49.8	51.9	2.1	21.3	1.6
31	42	43	1	11.4	0.8
	43.9	52	8.1	21.9	5.9
32	45.7	54.3	8.6	23.9	7.3
	58.3	60.6	2.3	22.1	1.7
	62.7	65.5	2.8	26	1.9
33	46.1	49.5	3.4	35	2.4
	51.3	60.3	9	24.6	6.6
	61.7	63.8	2.1	15.3	1.6
34	42.5	43.4	0.9	25	0.8
35	45.1	52.1	7	36.5	3.3
	63.7	67	3.3	17.5	2.8
36	45	50.9	5.9	39.5	3.4
	60.5	64.1	3.6	20.6	3.1
	64.7	67.7	3	24.4	2.3
37	44.1	51.6	7.5	28.3	4.7
	56.2	59.6	3.4	15	3.1
38	43.5	48.1	4.6	38.1	2.8
	53.9	59.6	5.7	26.1	3.3
	64.8	67.5	2.7	39.5	1.4
39	44.8	49.7	4.9	26.2	3.3
	49.5	52.3	2.8	29.2	2.1
	53.2	55.2	2	28.9	1.4

	56.8	59.2	2.4	38.1	1.2
40	44.3	48.8	4.5	22.3	3.7
	54.8	61.5	6.7	37.7	4.5
	66.3	69.8	3.5	31.2	0.9
41	46.3	50.4	4.1	32.3	3.2
	52.6	55.9	3.3	26.2	2.7
	58.4	60.7	2.3	36.8	1.7
	66.2	69	2.8	38.3	1.2
42	45.7	58.9	13.2	33.3	7.5
43	44.9	48.2	3.3	37.2	2.1
	56.3	57.7	1.4	30.5	0.6
44	45.1	46.5	1.4	24.2	1
	49.2	51.3	2.1	25.1	1.9
	52.2	55.8	3.6	37.3	1.9
	60.7	62.7	2	20.5	1.8
45	44.6	46	1.4	16	1
	48.6	53.2	4.6	35.1	2.9
	58.2	60.3	2.1	23.8	1.4
46	49.3	50.8	1.5	21.2	1.1
	52.5	54.4	1.9	26.2	1.5
	55.4	57.4	2	24.9	1.8
	59.8	61.5	1.7	31.1	1.3
47	46.7	50.9	4.2	31.1	2.6
	57.7	58.9	1.2	18.7	0.9
48	44.8	49.8	5	30.8	3.6
	59.8	63.3	3.5	20.3	2.2
49	44.6	46.1	1.5	11.7	0.6
	52.4	54.7	2.3	19.4	2.1
50	46.6	52.8	6.2	30.8	4.3
	56.2	57.3	1.1	23.3	0.9
	66.6	68.2	1.6	24.3	1
51	44.8	51.4	6.6	26.3	6.2
	53.6	56.6	3	27.6	2.1
	62.8	65.9	3.1	20.5	1.3
52	46.1	51.1	5	38.2	2.1
	68.3	69.8	1.5	15.3	0.8
53	45.5	57.6	12.1	35.4	8.8
54	44.6	55.1	10.5	40.6	6.2
55	47	49.1	2.1	37.9	2
	50.2	51.1	0.9	40.3	0.8
	59.5	60.4	0.9	31.5	0.7
	61.3	63.9	2.6	43.1	1.1
56	44.4	47.4	3	25	2.6
	48.6	53	4.4	37.5	3
	55.8	59.4	3.6	36.8	2.9
57	44.4	52.2	7.8	37	6.8
	53.5	54.1	0.6	39.8	0.3
58	54.1	57.3	3.2	51.7	1.8
59	44.6	45.8	1.2	31.2	1
	49.5	54.5	5	55.3	3.2
60	45.5	53.9	8.4	36.7	5.6
	57	60.4	3.4	52.3	1.9
61	44	47	3	37.7	2.2
	49.6	52.1	2.5	42.8	1.9
	54	56.2	2.2	48.9	2
	59.3	62.2	2.9	52.2	1.6
62	45.6	51.2	5.6	41.8	4.9
	51.4	55.3	3.9	39.9	3
	56.3	59.8	3.5	50.4	3.2
	61.9	68.3	6.4	49.8	3.7
63	43.6	51.4	7.8	46.4	3.9
	60.4	62.9	2.5	45.3	1.2
64	44.1	56	11.9	41.1	9.8
	60.4	62.4	2	34	1.1
65	43.3	51.2	7.9	48.1	4.9
	62.1	70	7.9	44	3.7
66	44.3	49.7	5.4	31.5	4.7
	56.4	59.9	3.5	49.4	1.6
67	47	50.9	3.9	29.4	2
68	48.1	53	4.9	29.8	3.8
	56.7	62.8	6.1	38.8	3.8
69	44.6	50.5	5.9	42.6	4
	54.3	56.5	2.2	30.7	2.1
	57.3	60.7	3.4	37.8	1.5
70	44.9	52.9	8	32.3	3
71	47.9	55.9	8	27.7	4.2
72	48.5	50.8	2.3	30.1	1.9

	55	57.9	2.9	27.6	2.2
	59.4	62.2	2.8	33.9	1.6
73	48.4	49.7	1.3	19.8	1.1
	51.1	53.5	2.4	26.1	1.9
	62.3	65.2	2.9	36.6	1.9
74	47.2	49	1.8	30.7	1.5
	50	52.3	2.3	30.1	2.2
	59.8	61.3	1.5	33.7	0.9
75	47.4	52.3	4.9	30.7	2.7
76	46.3	50.3	4	33.5	2.7
77	47.9	61.9	14	39.8	8.3
78	59	60.9	1.9	36.8	1.2
79	52.2	55.4	3.2	33.8	1.5
80	48.4	58.7	10.3	36.8	4.5
81	50.4	52	1.6	21.1	0.7
	56.7	61	4.3	34.1	2.9
82	49.9	56.3	6.4	30.5	4.8
83	47	49.6	2.6	16	1.9
	50.1	52.9	2.8	27.5	1.3
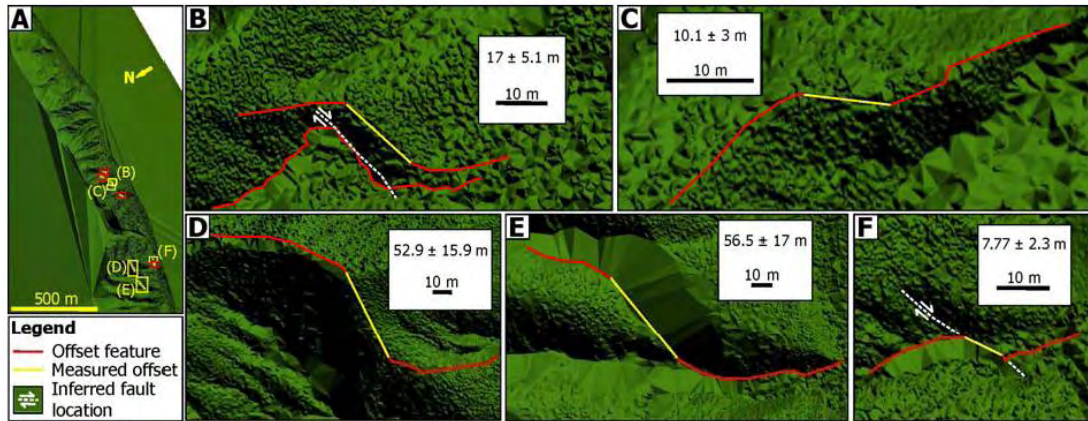
Fig. DR3 (A) The location of nine measured dextral offsets is shown in the LDEM (also Table DR2). The offsets marked in yellow are shown in detail in Figures b to f. In contrast, no detail is shown for offsets marked in red as those are shown in Figure 9b to e. The legend is valid for the offsets shown in Figures b to f. (B) Details of offset no. 3 (ridge crest). (C) Details of offset no. 4 (ridge crest). (D) Details of offset no. 6 (ridge crest). (E) Details of offset no. 7 (gully). (F) Details of offset no. 8 (gully).

TABLE DR2. LIST OF NINE DEXTRAL OFFSETS MEASURED IN THE LDEM.

Offset no.	Measured offset (m)	Uncertainty 30% bound (m)
1	18.9	±5.7
2	17.4	±5.2
3	17	±5.1
4	10.1	±3
5	14.3	±4.3
6	52.9	±15.9
7	56.5	±17
8	7.77	±2.3
9	8.6	±2.6
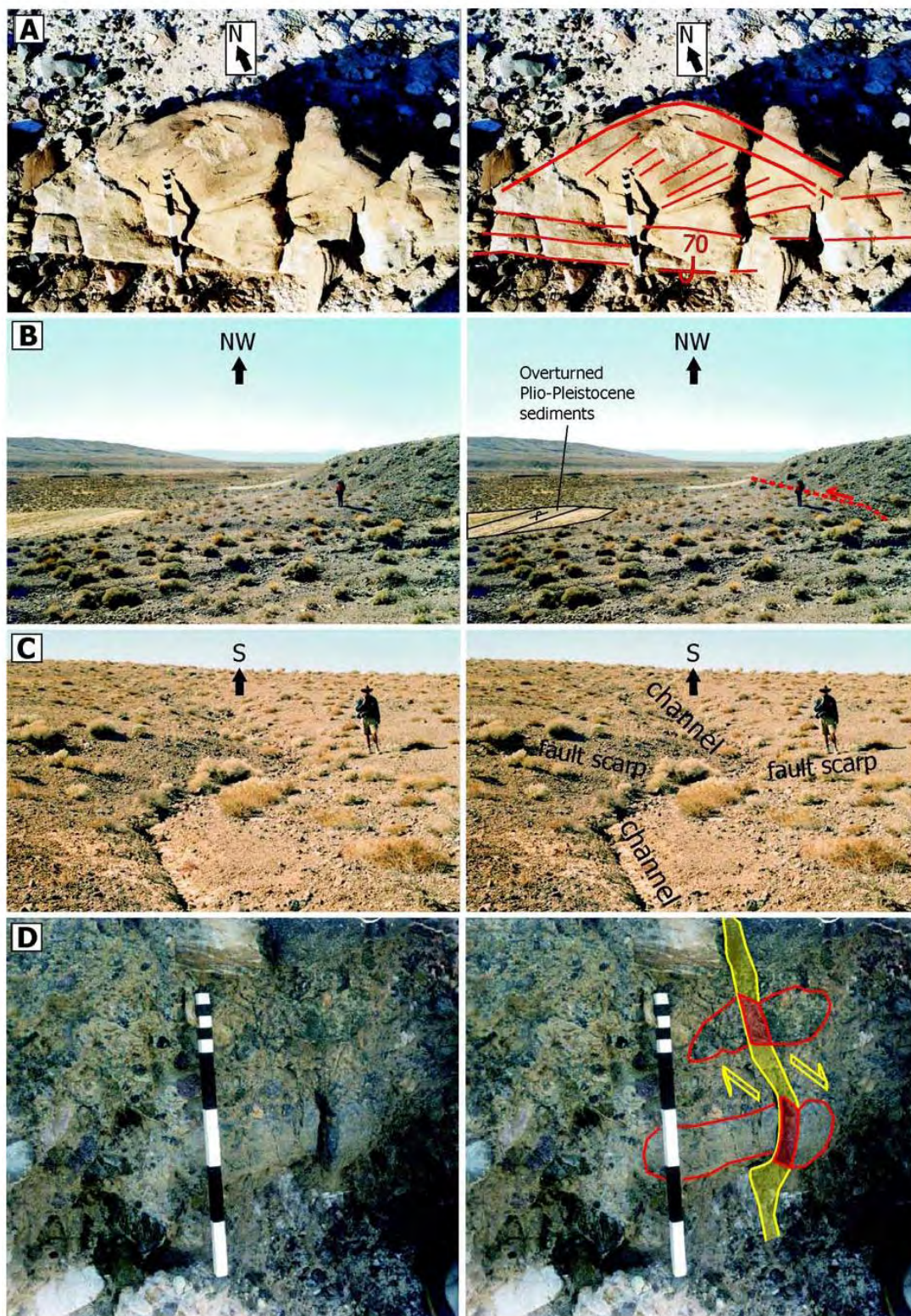
Fig. DR4 Colored version of Figure 4.
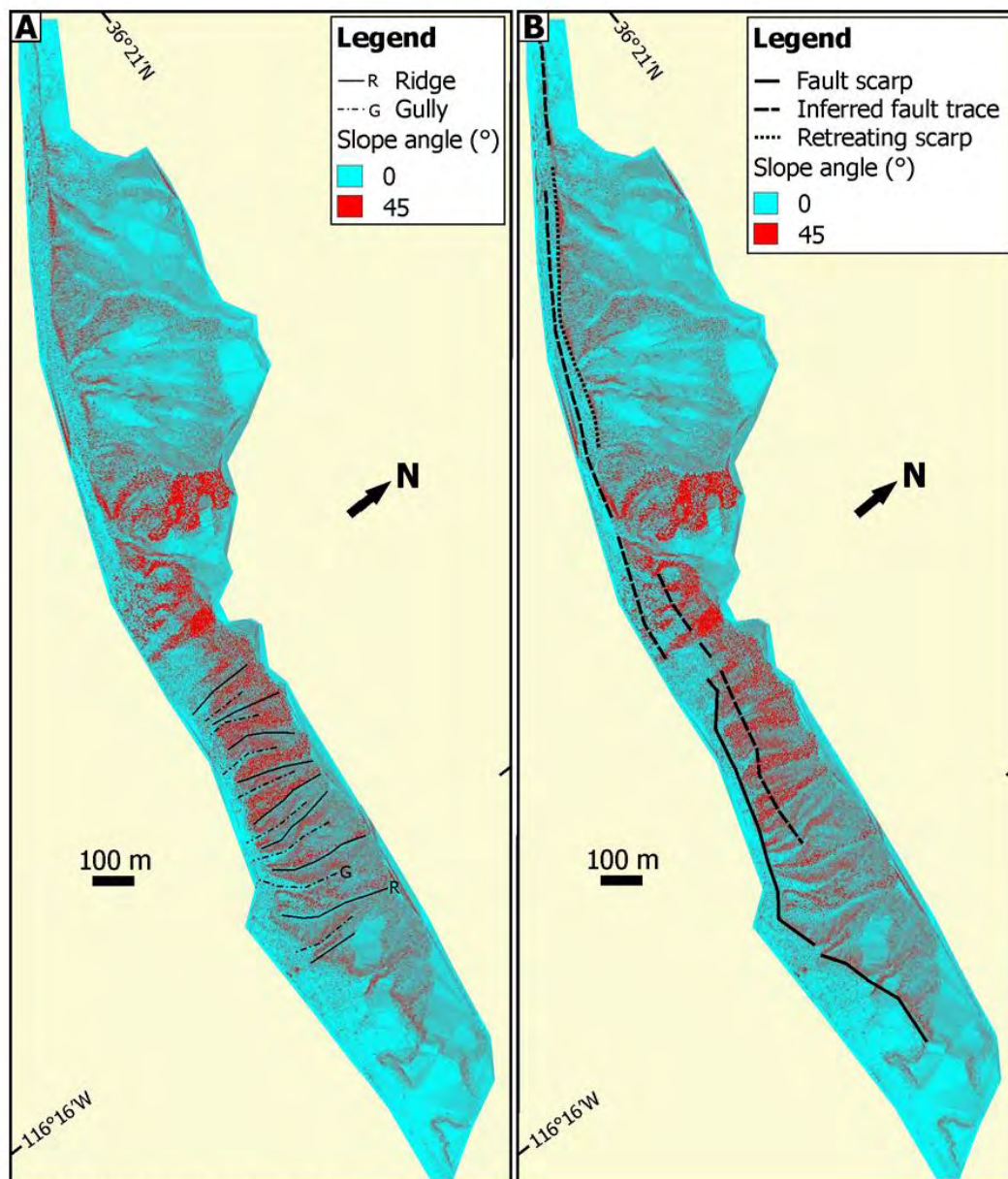
Fig. DR5 Colored version of Figure 6.

35

6.2. Appendix: Chapter II

6.2.1. Erlenbach Event Data of 2008 and 2009

Bed-Load Discharge

The intensity of bed-load transport in the Erlenbach has been recorded continuously with piezoelectric bed-load impact sensors (PBIS) from 1986–1999 (Rickenmann and McArdell, 2007). In 2000, the sensors had been replaced by geophones. This indirect monitoring required a calibration following an equation derived by D. Rickenmann (pers. comm., 2008) to convert the 2008 and 2009 geophone data into sediment volumes of individual transport events:

$$F = 0.4484 \, SP \tag{A1}$$

where 0.4484 is the calibration factor, and the correlation coefficient R^2 is 0.965. The sum of impulses recorded by geophone no. 8 (*SP8*) is defined as the number of recorded impulses divided by 1000.

The impulses recorded by the former PBI sensor no. 3 accounted for 56.5% of the total number of impulses recorded by all sensors between 1986 and 1999 (Rickenmann and McArdell, 2007). This was due to the mounting position next to the center-line of the channel-bed cross-section, and to slightly asymmetric flow conditions upstream of the sensor array, that resulted in dominant bed-load transport along the orographic right side of the cross-section (Rickenmann and McArdell, 2007). Therefore, sensor no. 3 provided most reliable and representative data on bed-load transport. Due to the fact that geophone no. 8 is mounted in the former position of the PBI sensor no. 3, we considered the impulses recorded by this geophone in 2008 and 2009 as most representative, and finally, we set the uncertainty related to the calculation of sediment volumes to 50% (Tables 6.2-1 and 6.2-2).

The Erlenbach impulse data have been evaluated in terms of plausibility (J. Turowski, pers. comm., 2008). Evenly distributed impuls counts among the sensors are unlikely, and had been removed from the time series. This includes, for example, data resulting from intense precipitation. However, the definition of an bed-load transport event is solely based on sensor activity. If a short break in sensor activity occurred at high or increasing water discharge, no new event was defined (J. Turowski, pers. comm., 2008).

Limitations

The geophone and former PBIS systems record impulses during bed-load transport that are due to sliding, rolling and saltating sediment particles across the sensors (Rickenmann and McArdell, 2007). The impulse data are converted into sediment volumes using a linear calibration equation (D. Rickenmann, pers. comm., 2008). This approach is based on Rickenmann and McArdell (2007) who related the PBIS impulse data to the volume of sediment trapped within the Erlenbach sediment-retention basin. To evaluate the conversion from impulse to sediment volume data, we address some uncertainties and limitations influencing PBIS respectively geophone measurements and their interpretation (compiled from Rickenmann and McArdell, 2007).

The grain size of the sediment is a crucial factor controlling these measurements. The critical grain size required to produce an impulse on the PBIS is a diameter of 10 mm as revealed by laboratory experiments using the Erlenbach sensors and sediment (Etter, 1996). Hence, moving particles with a grain diameter less than 10 mm are not detected directly by the sensors during bed-load transport. But field data of floods occurring in the Erlenbach

showed that 50% of the deposited sediment volume comprises grains that are coarse enough to cause a sensor impulse (Rickenmann, 1997; Rickenmann and McArdell, 2007).

The Erlenbach grain-size distributions of transported material deposited in the retention basin and surface-bed material upstream of the basin are markedly different. The characteristic grain sizes of the transported sediment are much smaller than those of the surface-bed material, e.g. d_m of 11.3 mm for the first and d_m of 51.2 mm for the latter. The deposits in the retention basin are coarser in the upper part of the basin and finer (grain size smaller than fine sand; <0.25 mm) in the lower part as well as along its sides. Furthermore, a detailed analysis of the basin deposits revealed that during typical flood conditions probably almost no sediment coarser than fine sand is transported off the basin (Rickenmann and McArdell, 2007). In contrast, during larger floods a substantial transport of silt- and clay-sized grains through the basin may be possible. However, Rickenmann and McArdell (2007) approximated that the proportion of bed-load and suspended load is constant during different flood events, and expected that part of the scatter in their calibration relationship is due to a changing grain-size distribution of the transported sediment with flood size. In summary, we suggest that the calibration relationship used to convert sensor impulses into sediment volumes account at least partly for suspended load.

Water Discharge and Precipitation

The actual water level of the Erlenbach is determined with a float system adjusted to a trapezoidal channel cross-section (Burch, 1994). These gauging measurements are transferred into water discharges by using calibration curves and tables which are based on hydraulic laboratory experiments. The associated standard deviation is lower than 5%, and the main source of uncertainty is represented by temporary deposited sediment changing the initial trapezoidal shape of the channel cross-section (Burch, 1994; Tables 6.2-1 and 6.2-2).

Precipitation in the Erlenbach basin is recorded with totalizers collecting the precipitation volume over time, as well as compensators and/or balances measuring the precipitation rate with a resolution of 0.1 mm over time based on volume and weight of the precipitation quantity (e.g. Burch, 1994). The accuracy of conventional rain-gauge measurements is mainly influenced by deflection of hydrometers in the wind field above the gauge orifice, wetting of the gauge walls, evaporation from the container, and snow drift into the gauge (e.g. Frei and Schär, 1998). In Switzerland, the annual mean of rain gauges shows a systematic under-catch of 7% at lower elevations or protected sites, and up to 25% for wind exposed sites at higher elevations (Sevruk, 1985). This under-catch is characterized by an annual cycle which is lowest in summer, 5% for protected a 10% for exposed sites, and highest in winter, 8% respectively 30%. However, on average the annual mean under-catch for Switzerland was approximated to 8% (Sevruk, 1985; Tables 6.2-1 and 6.2-2).

6.2.2. References

Burch, H.; 1994; Ein Rückblick auf die hydrologische Forschung der WSL im Alptal; Beiträge zur Geologie der Schweiz-Hydrologie, vol. 35, p. 18-33.

Etter, M.; 1996; Zur Erfassung des Geschiebetransportes mit Hydrophonen; Diploma thesis, Institute of Geography, University of Bern, and WSL, Switzerland, 110 pp.

Frei, C., and Schär, C.; 1998; A precipitation climatology of the Alps from high-resolution rain-gauge observations; International Journal of Climatology, vol. 18, p. 873-900.

Rickenmann, D.; 1997; Sediment transport in Swiss torrents; Earth Surface Processes and Landforms, vol. 22, p. 937-951.

Rickenmann, D., and McArdell, B.W.; 2007; Continuous measurement of sediment transport in the Erlenbach stream using piezoelectric bedload impact sensors; Earth Surface Processes and Landforms, vol. 32, p. 1362-1378.

Sevruk, B.; 1985; Systematischer Niederschlagsmessfehler in der Schweiz; *in:* Sevruk, B. (ed.), Der Niederschlag in der Schweiz, Beiträge Geologie Schweiz – Hydrologie, vol. 31, p. 65-75.

Table 6.2-1: Erlenbach data – events 2008.

Date	Sediment discharge m³	Uncertainty 50%	Peak water discharge m³/s	Uncertainty 5%	Precipitation mm	Uncertainty 8%
07.01.2008	0.06	0.03	0.83	0.04	0.2	0.02
27.02.2008	0.06	0.03	0.26	0.01	7.5	0.60
12.03.2008	1.69	0.85	0.56	0.03	6	0.48
22.04.2008	1.27	0.63	0.55	0.03	31.8	2.54
29.04.2008	0.11	0.06	0.42	0.02	0.6	0.05
03.06.2008	2.28	1.14	0.00	0.00	5.6	0.45
10.06.2008	4.66	2.33	0.65	0.03	15.6	1.25
12.06.2008	1.28	0.64	0.60	0.03	6.4	0.51
13.06.2008	4.52	2.26	0.74	0.04	5	0.40
02.07.2008	27.18	13.59	1.77	0.09	6	0.48
03.07.2008	3.03	1.52	0.72	0.04	8.9	0.71
11.07.2008	12.33	6.17	1.02	0.05	33.8	2.70
14.07.2008	13.99	6.99	1.16	0.06	45.7	3.66
20.07.2008	2.38	1.19	0.96	0.05	0.1	0.01
20.07.2008	10.43	5.21	1.34	0.07	3.5	0.28
01.08.2008	0.12	0.06	0.56	0.03	1.7	0.14
15.08.2008	31.29	15.64	1.37	0.07	58.6	4.69
18.08.2008	0.57	0.29	0.71	0.04	5.9	0.47
23.08.2008	0.51	0.26	0.75	0.04	0.9	0.07
06.09.2008	0.01	0.01	0.49	0.02	0.2	0.02
07.09.2008	0.05	0.03	0.52	0.03	0.8	0.06
07.09.2008	0.69	0.35	0.65	0.03	9	0.72
13.09.2008	1.81	0.90	0.84	0.04	2.8	0.22
16.10.2008	1.25	0.62	0.54	0.03	17.1	1.37
21.12.2008	0.01	0.01	0.21	0.01	0.1	0.01

Table 6.2-2: Erlenbach data – events 2009.

Date	Sediment discharge m³	Uncertainty 50%	Peak water discharge m³/s	Uncertainty 5%	Precipitation mm	Uncertainty 8%
06.04.2009	0.02	0.01	0.17	0.01	0	0
14.04.2009	0.03	0.01	0.15	0.01	0	0
19.04.2009	0.03	0.01	0.44	0.02	0	0
26.05.2009	4.26	2.13	0.79	0.04	5.5	0.44
27.05.2009	0.33	0.16	0.65	0.03	5.9	0.47
15.06.2009	37.07	18.54	2.27	0.11	36.3	2.90
16.06.2009	4.94	2.47	1.03	0.05	7.9	0.63
19.06.2009	0.02	0.01	0.46	0.02	0.2	0.02
04.07.2009	58.33	29.17	3.48	0.17	38.3	3.06
06.07.2009	0.03	0.02	0.34	0.02	0.1	0.01
07.07.2009	0.02	0.01	0.21	0.01	0	0
10.07.2009	4.07	2.04	0.87	0.04	5.9	0.47
18.07.2009	29.93	14.96	1.40	0.07	56.8	4.54
18.07.2009	0.40	0.20	0.79	0.04	1.4	0.11
23.07.2009	0.07	0.04	0.52	0.03	0.6	0.05
24.07.2009	18.04	9.02	1.39	0.07	19.3	1.54
03.08.2009	0.04	0.02	0.53	0.03	0.1	0.01
03.08.2009	0.04	0.02	0.56	0.03	0.3	0.02
03.08.2009	2.26	1.13	1.07	0.05	5.4	0.43
03.08.2009	6.16	3.08	1.39	0.07	23.4	1.87
10.08.2009	2.62	1.31	1.29	0.06	0.1	0.01
10.08.2009	5.15	2.57	1.09	0.05	8	0.64
01.09.2009	0.32	0.16	0.69	0.03	0.2	0.02
02.09.2009	5.17	2.58	1.21	0.06	0.9	0.07
04.09.2009	0.08	0.04	0.55	0.03	0.7	0.06
05.09.2009	4.95	2.48	0.90	0.05	6.4	0.51

Table 6.2-3: Alp Valley – deposition and erosion area of alluvial fans.

No.	Name	Deposition area (km²)	Erosion area (km²)
1	Erlenbach	0.017	0.720
2	Etterenbach	0.100	1.013
3	Butzibach	0.249	1.871
4	Gämschbach	0.159	0.909
5	Chösterliwald 1	0.032	0.088
6	Chlösterliwald 2	0.056	0.213
7	Geissbuebenrietli	0.072	0.215
8	Farenfeld	0.018	0.055
9	Rüti 1	0.043	0.375
10	Rüti 2	0.099	0.586
11	Stöcken	0.033	0.935
12	Malosenbach	0.085	0.462
13	Hirzenstock	0.069	0.407
14	Vogelbach	0.078	1.579
15	Sunnenberg	0.016	0.368
16	Pfauenbach	0.038	0.885
17	Eigenbach	0.027	0.464
18	Trachslau 1	0.032	0.077
19	Trachslau 2	0.045	0.268
20	Trachslau 3	0.041	0.196
21	Trachslau 4	0.023	0.150
22	Trachslau 5	0.023	0.285

Table 6.2-4: Alp Valley – deposition and erosion area of debris cones.

No.	Name	Deposition area (km²)	Erosion area (km²)
1	Grosser Mythen N-slope 1	0.086	0.061
2	Grosser Mythen N-slope 2	0.117	0.124
3	Kleiner Mythen N-slope 1	0.110	0.062
4	Kleiner Mythen E-slope 2	0.098	0.062
5	Butziflue 1	0.017	0.007
6	Butziflue 2	0.044	0.019
7	Butziflue 3	0.011	0.004
8	Ufem Tritt 1	0.014	0.005
9	Ufem Tritt 2	0.048	0.013

Fig. 6.2-1 Slope map of the Alp Valley. Tick marks with annotated numbers depict Swiss coordinates in km.

Slope (°)
88
80
72
64
56
48
40
32
24
16
8
0

1.000 m

203

A

5 June - 21 October 2008
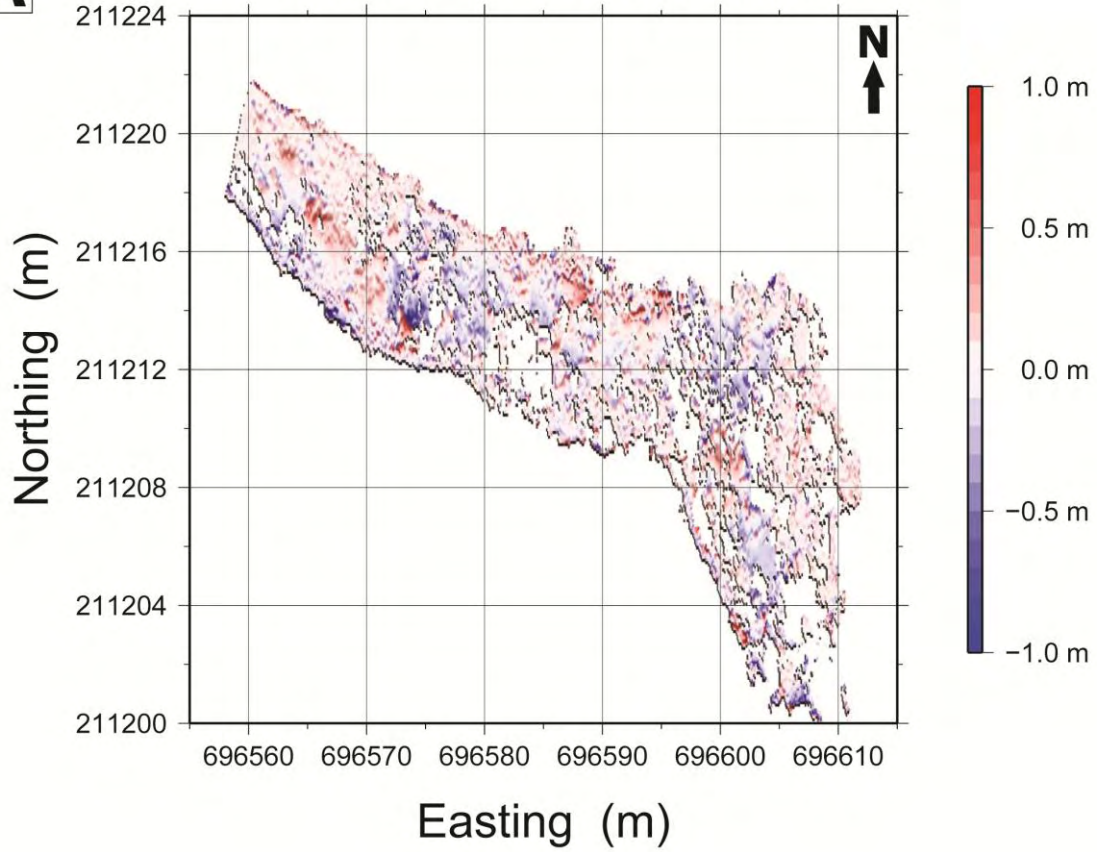
16 May - 29 October 2009
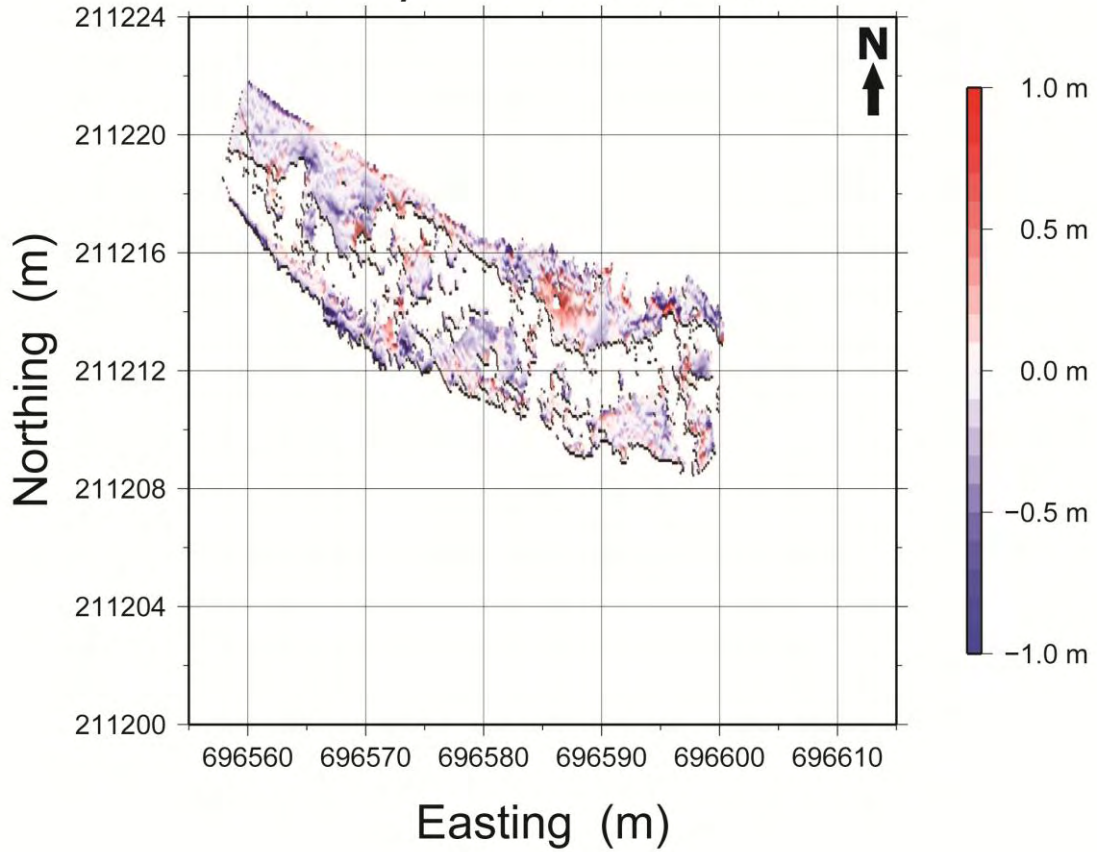
B

16 May - 17 June 2009
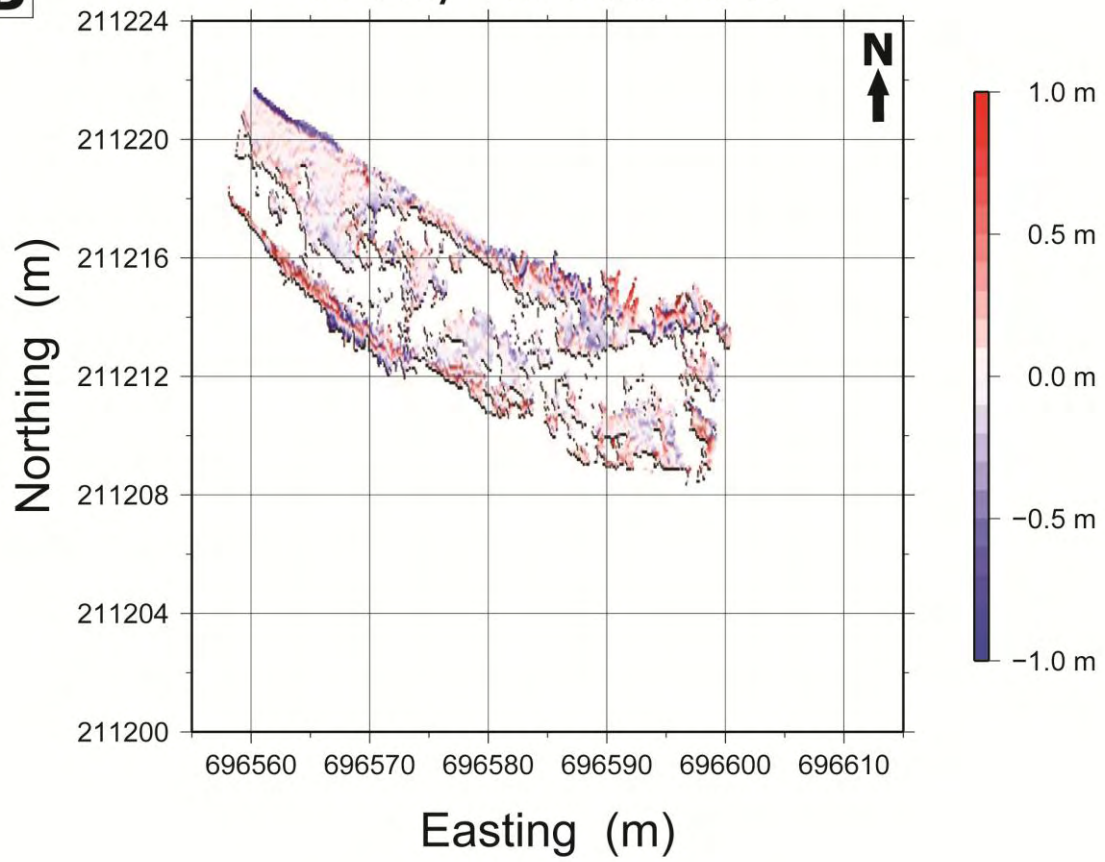
17 June - 15 July 2009
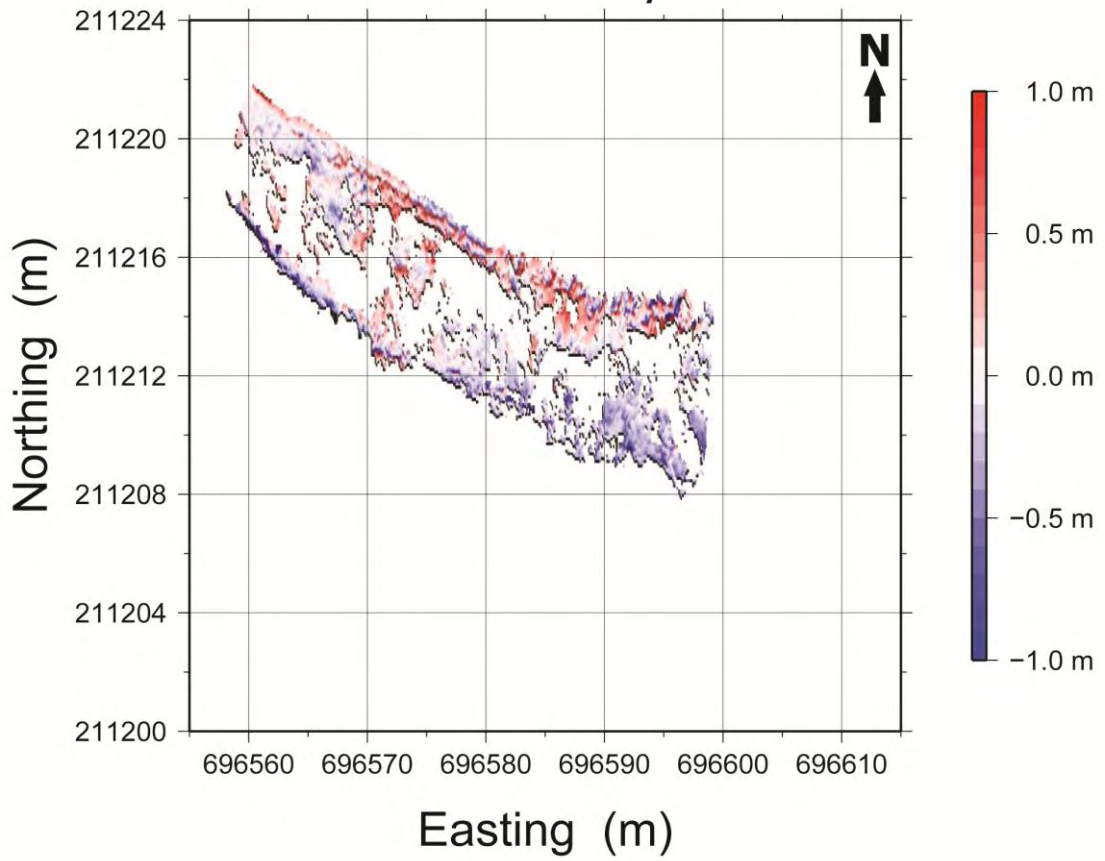
15 July - 13 August 2009
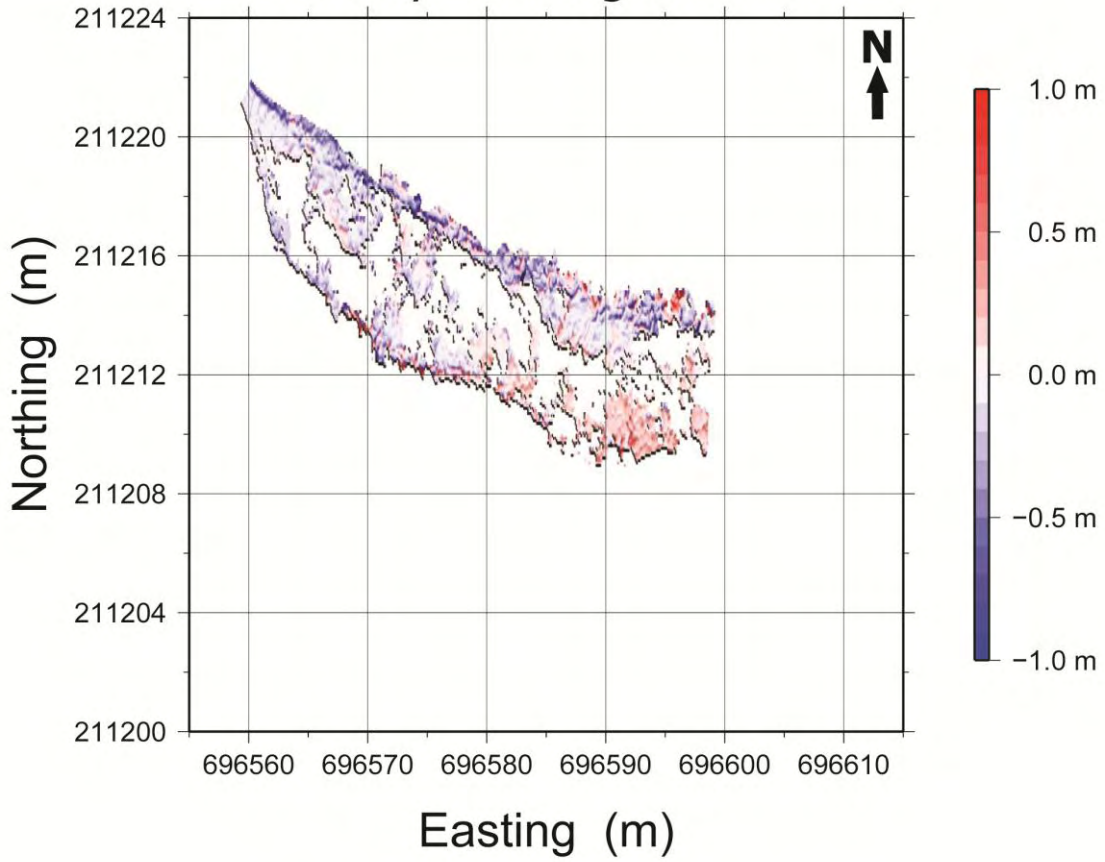
13 August - 6 September 2009
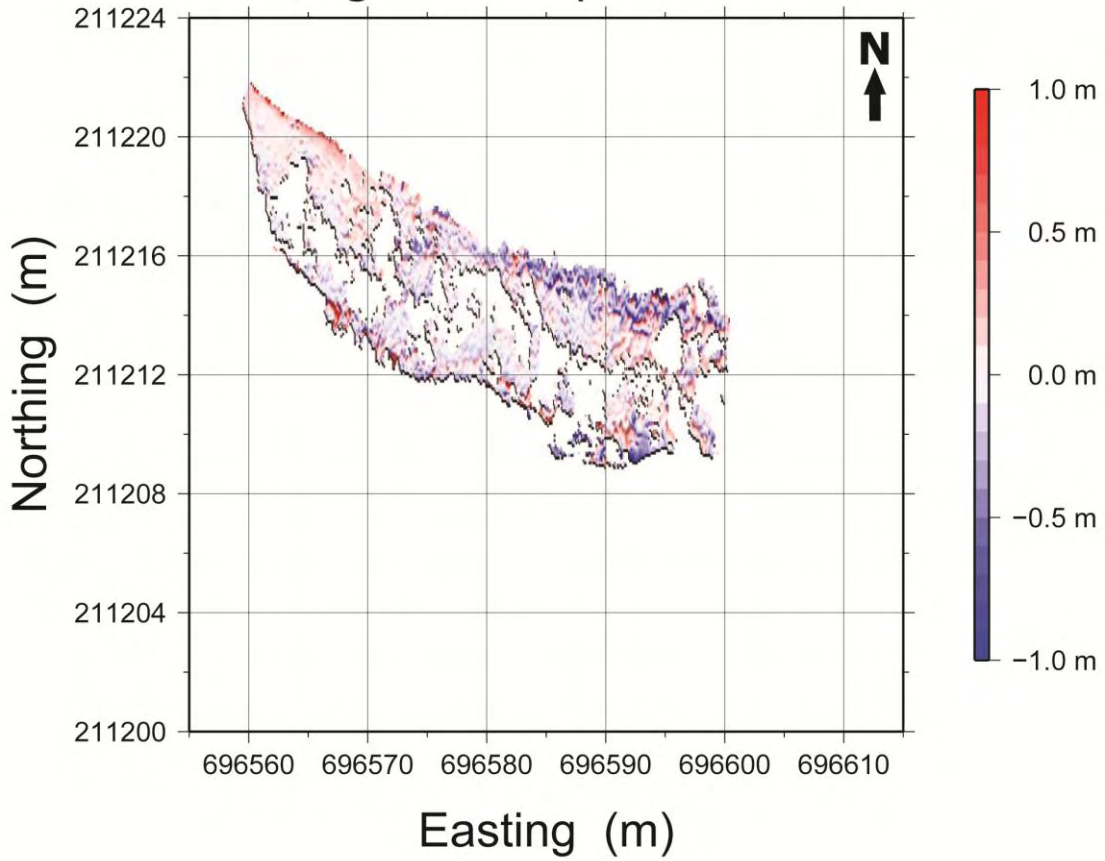
6 September - 29 October 2009
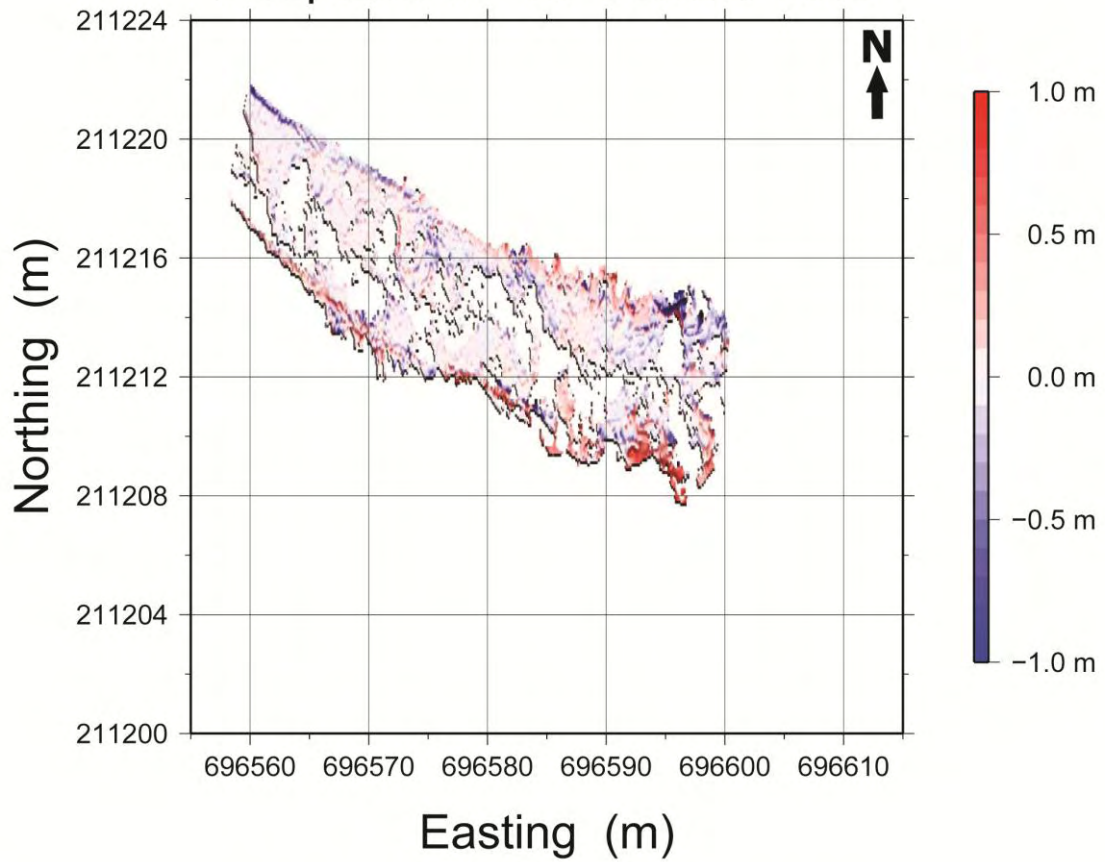
C

29 October - 31 October 2009
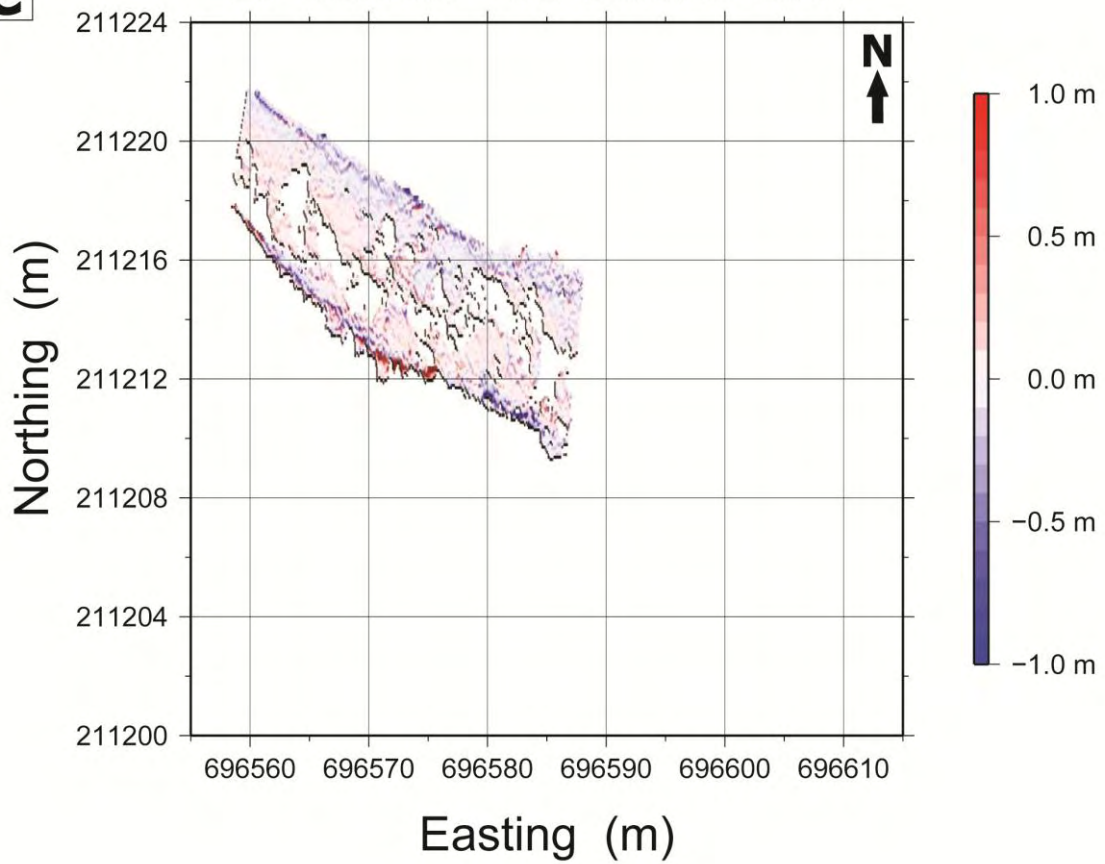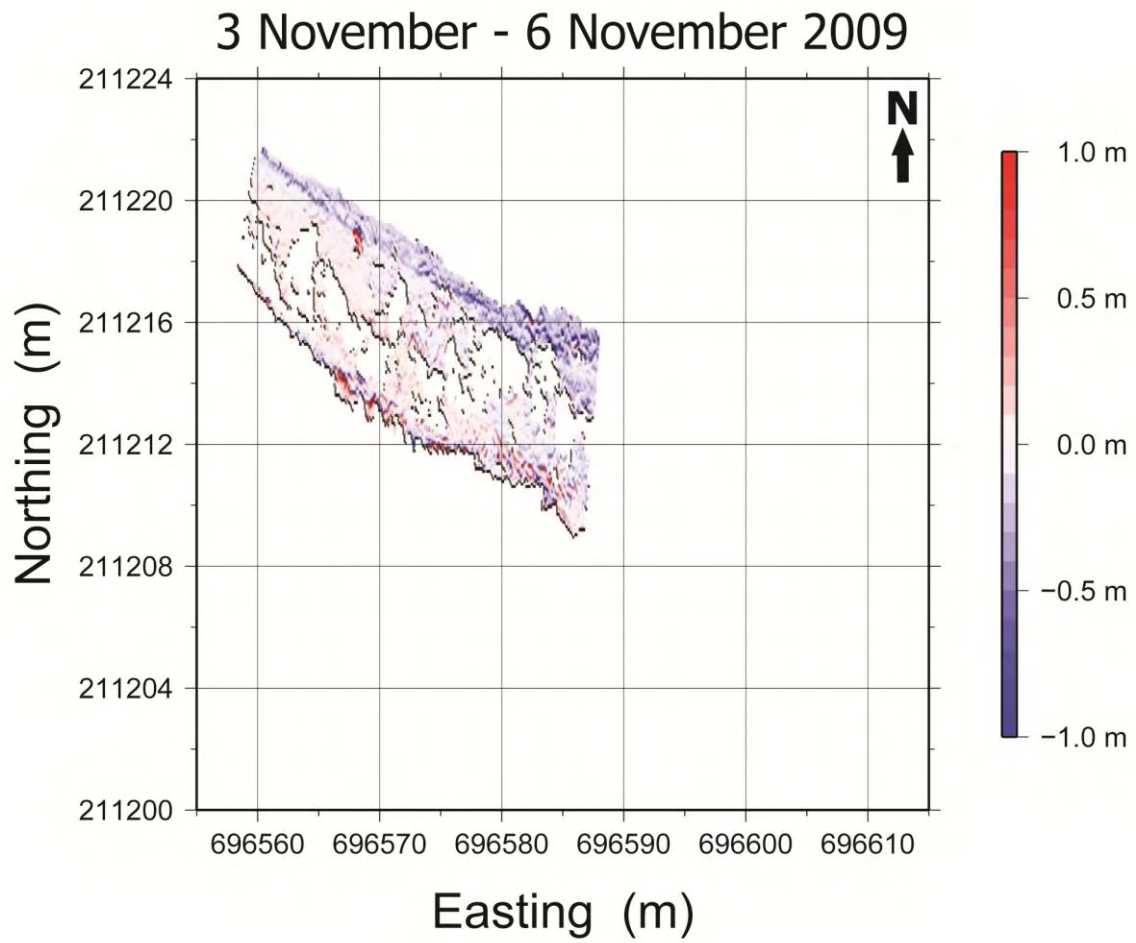
Fig. 6.2-2 Enlarged version of Figure 3.4. (**C**) Here, we also included our remaining quantitative results for the Erlenbach – daily intervals, 2009.

Fig. 6.2-3 Enlarged version of Figure 3.6.

A

4 June - 21 October 2008
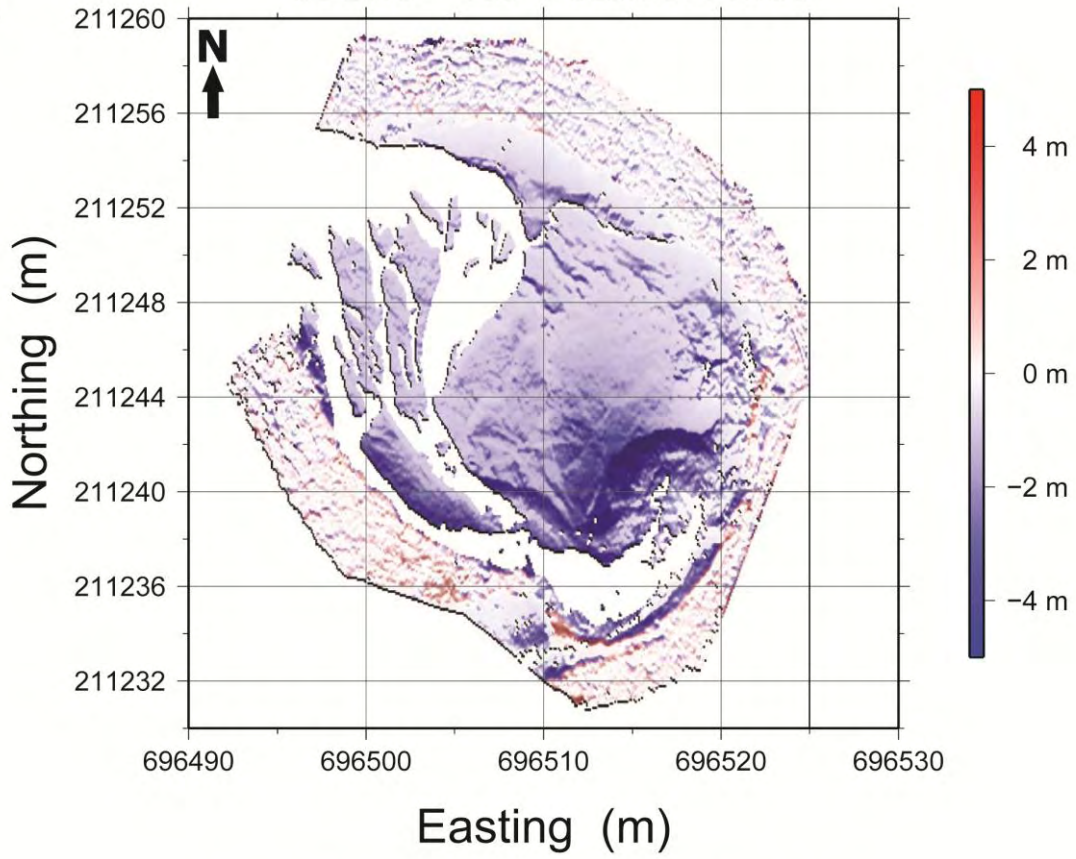
21 October 2008 - 17 May 2009

17 May - 28 October 2009
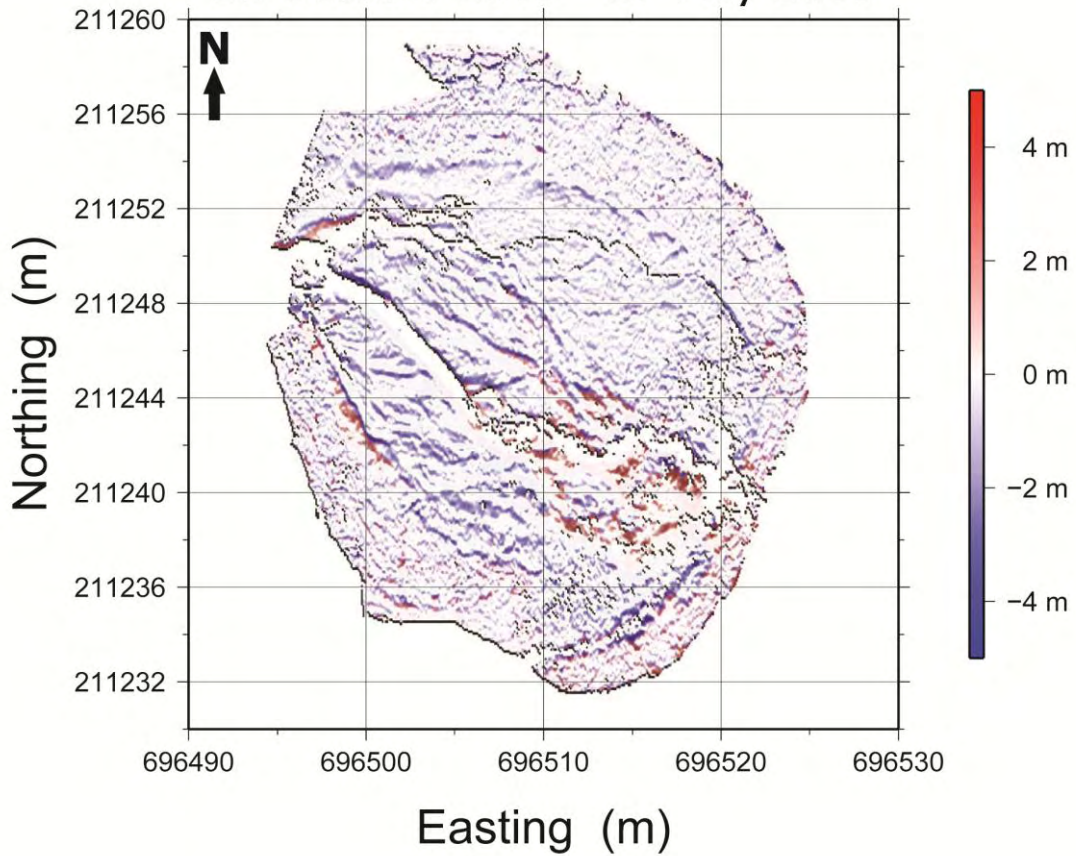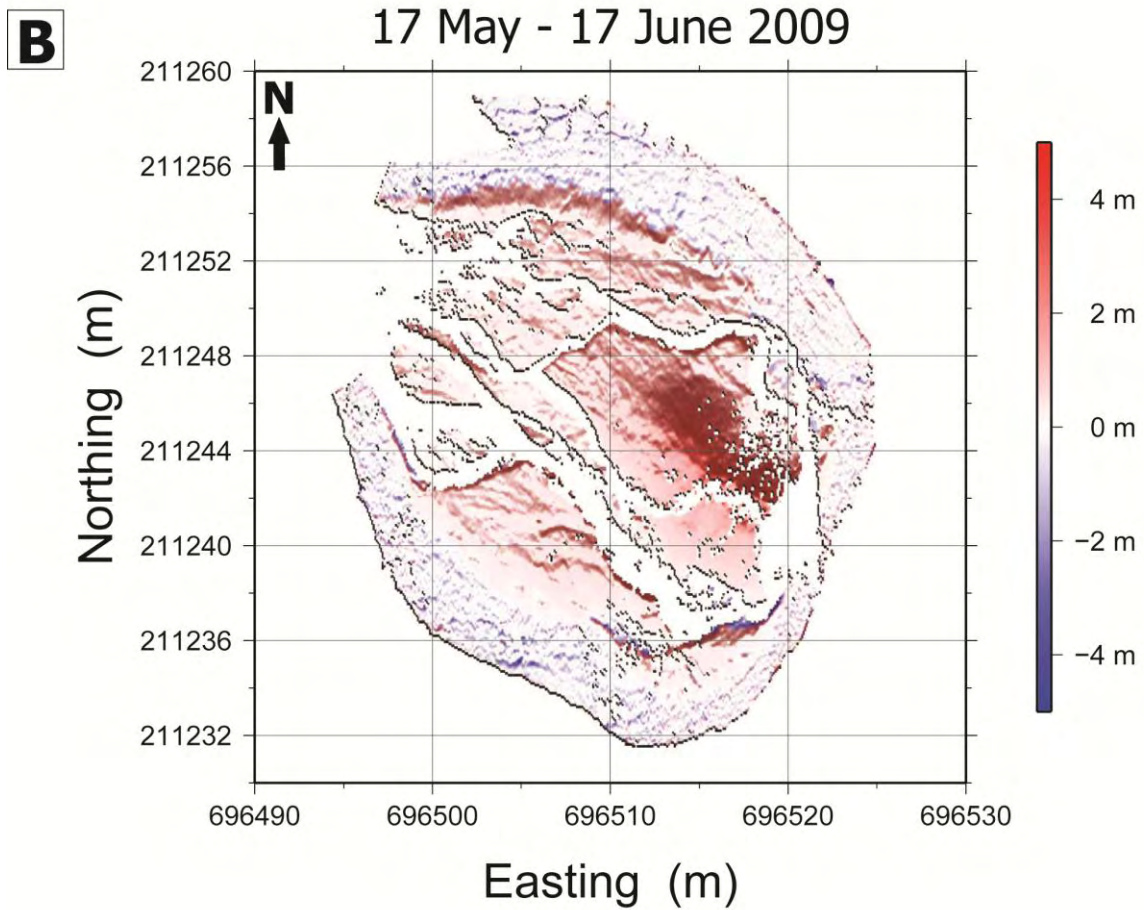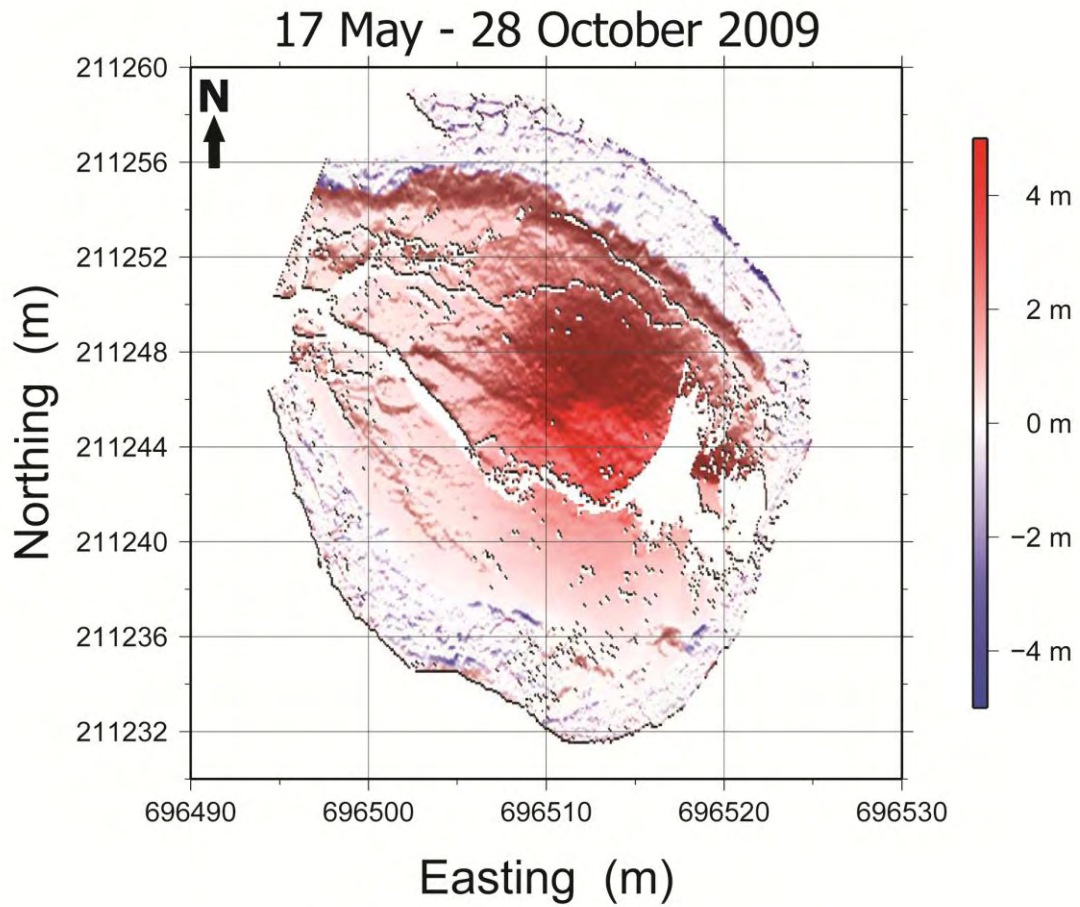
17 May - 17 June 2009
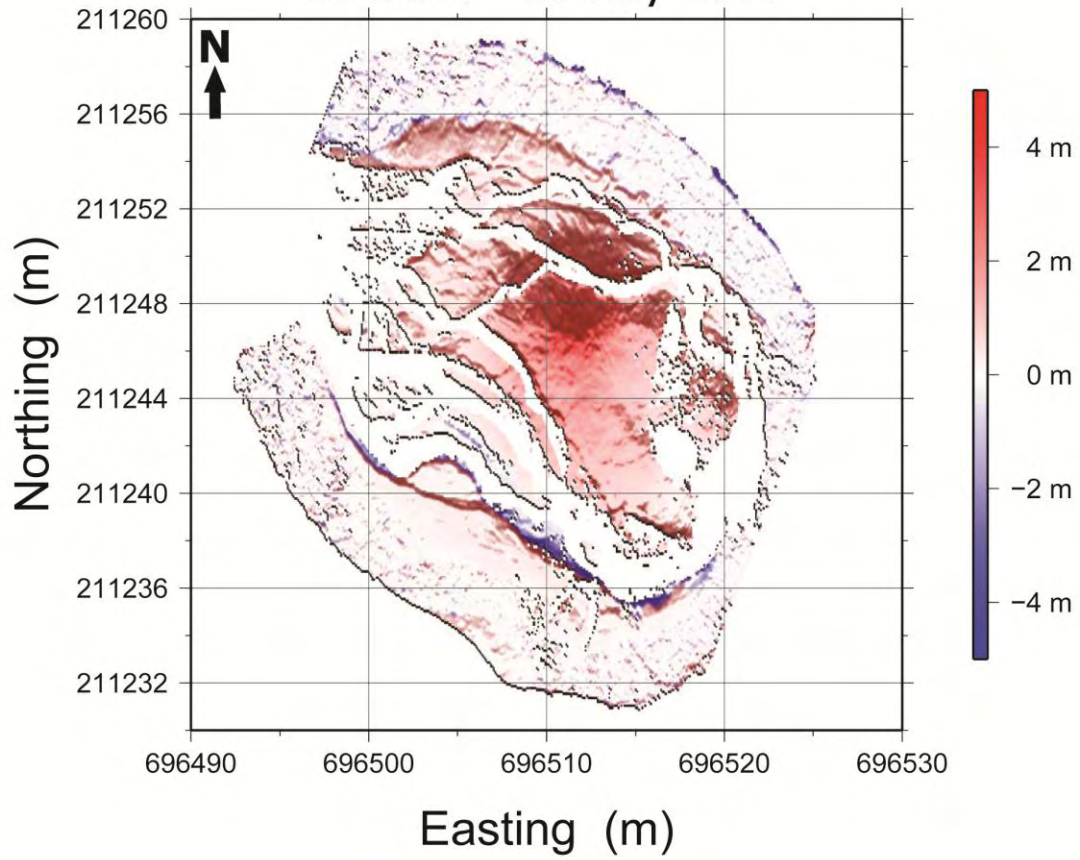
17 June - 16 July 2009

16 July - 13 August 2009
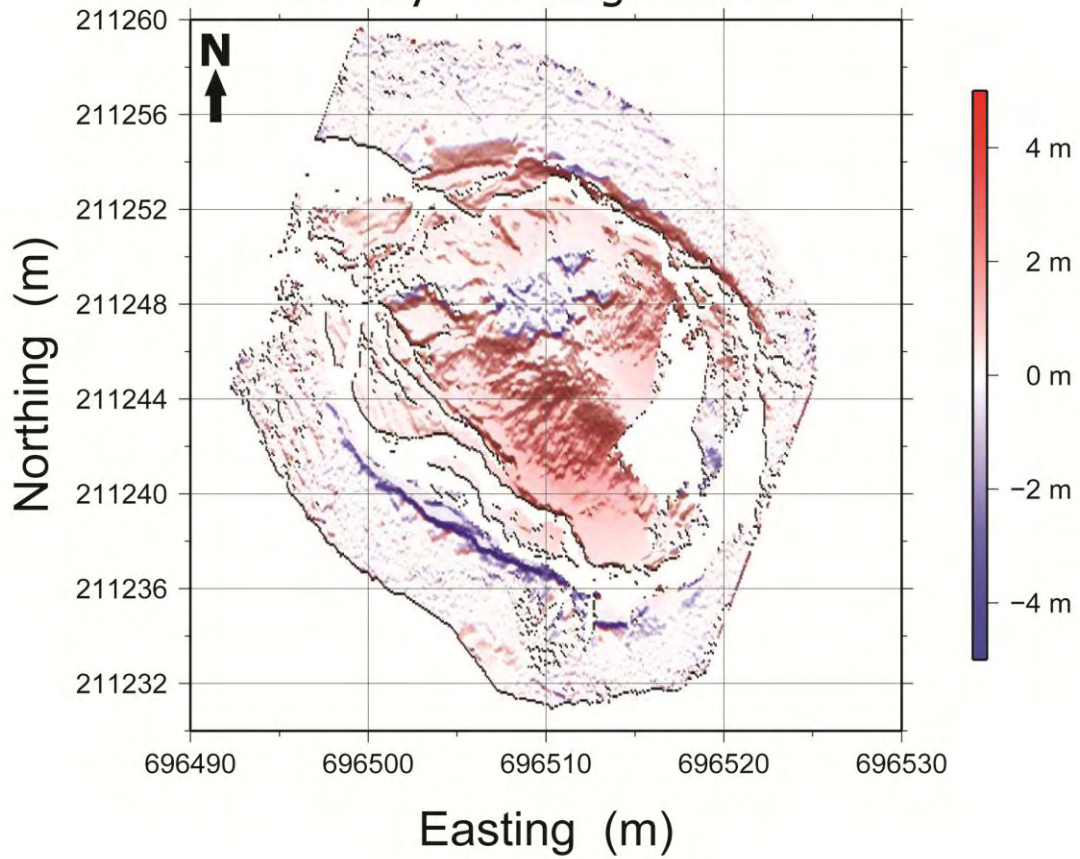
13 August - 7 September 2009
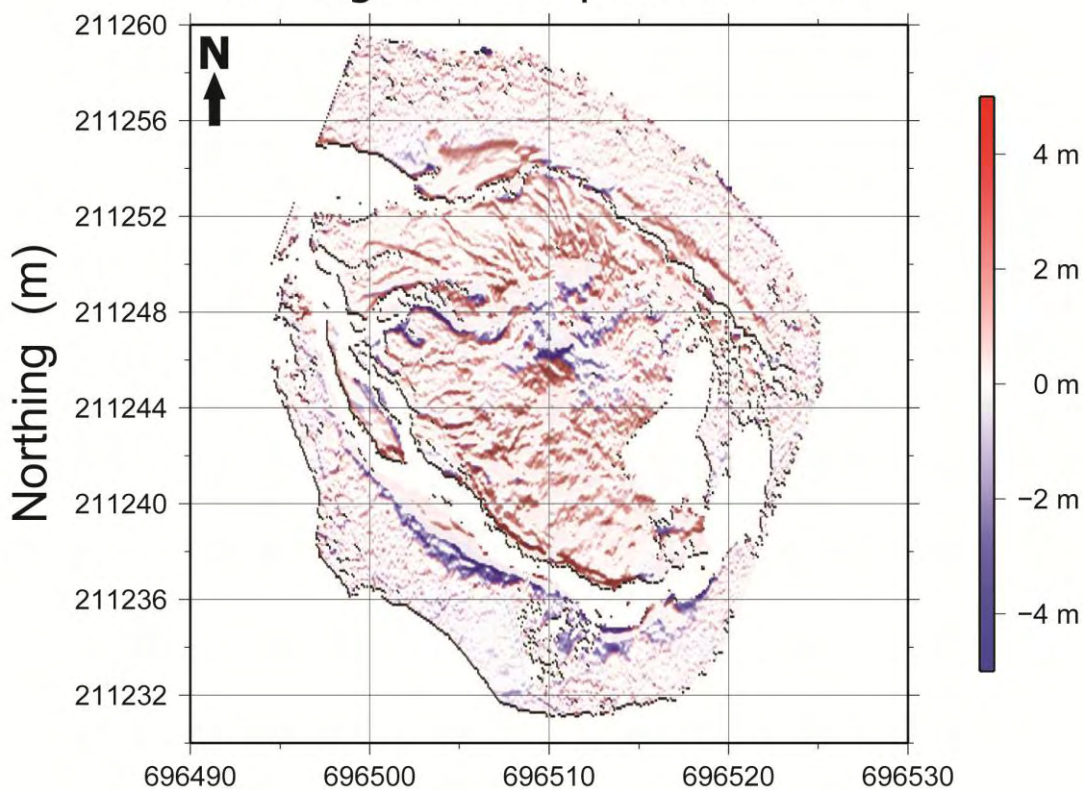
7 September - 28 October 2009
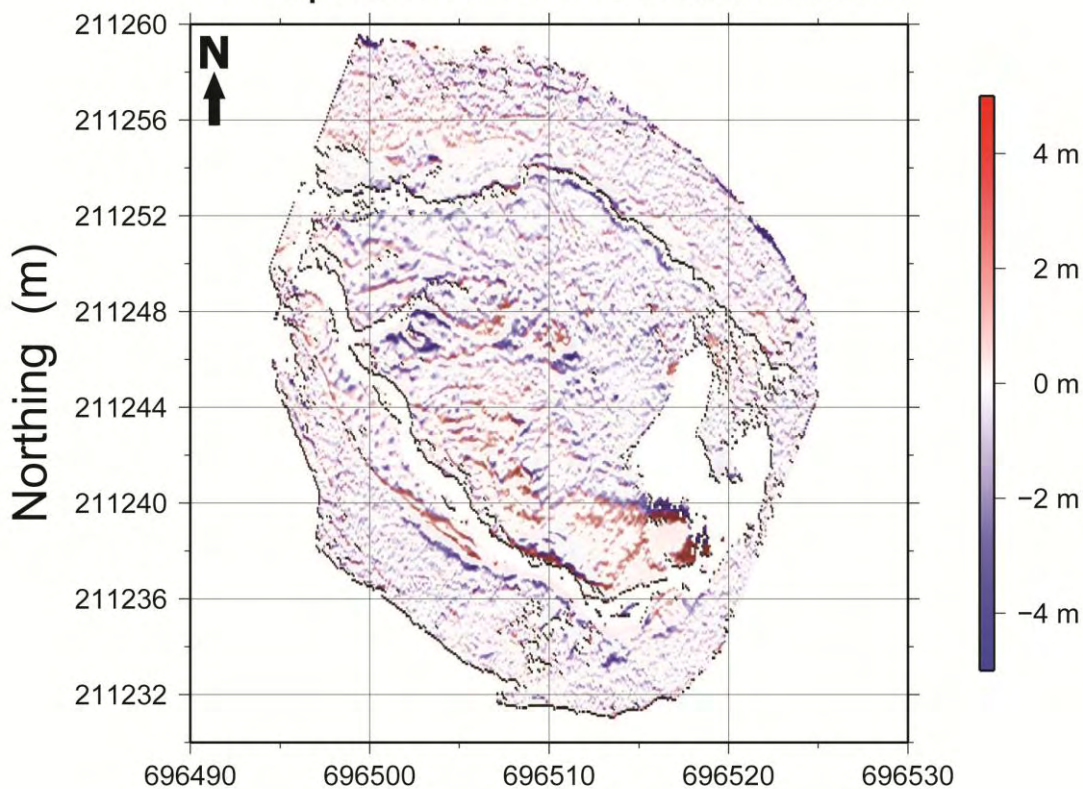
A 17 May - 30 October 2009
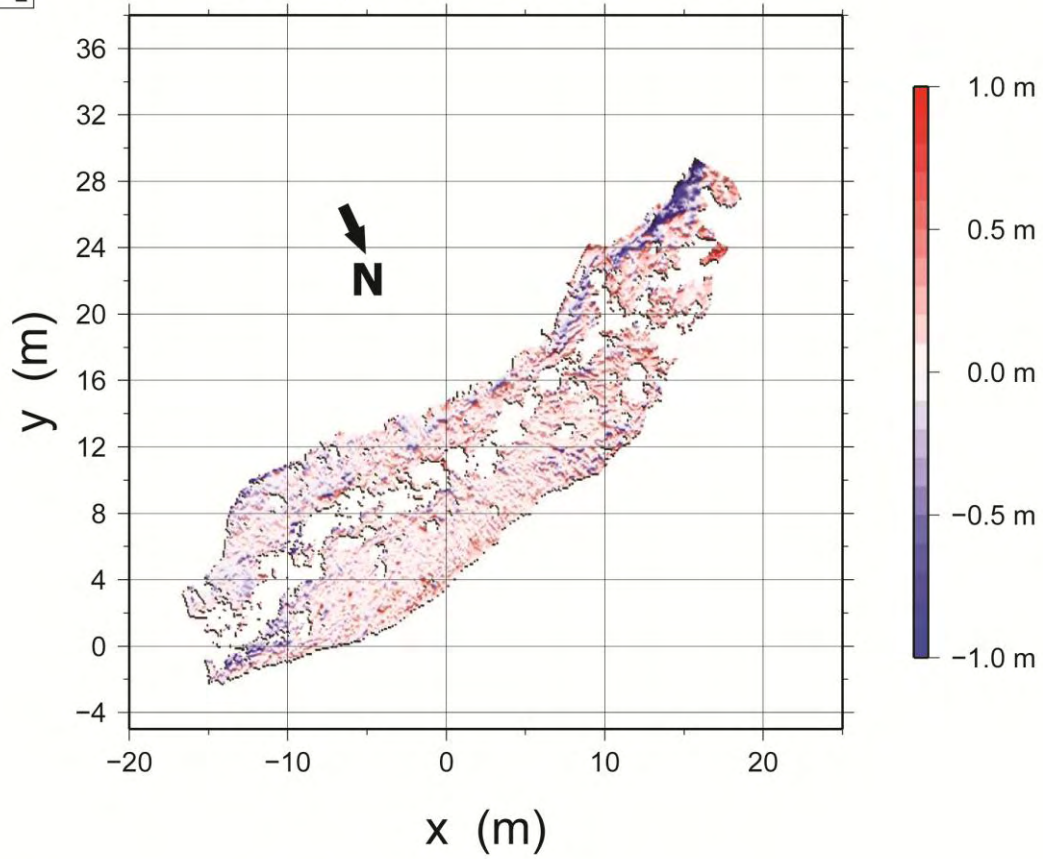
B 17 May - 16 June 2009
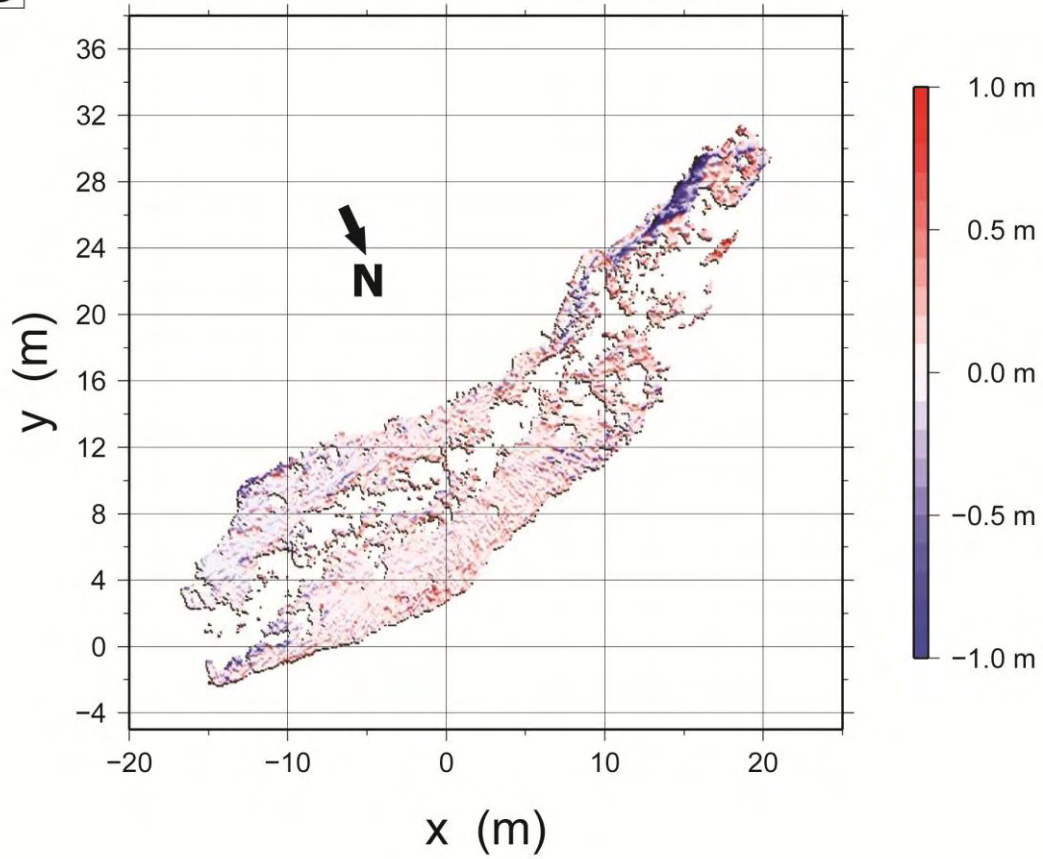
16 June - 14 July 2009
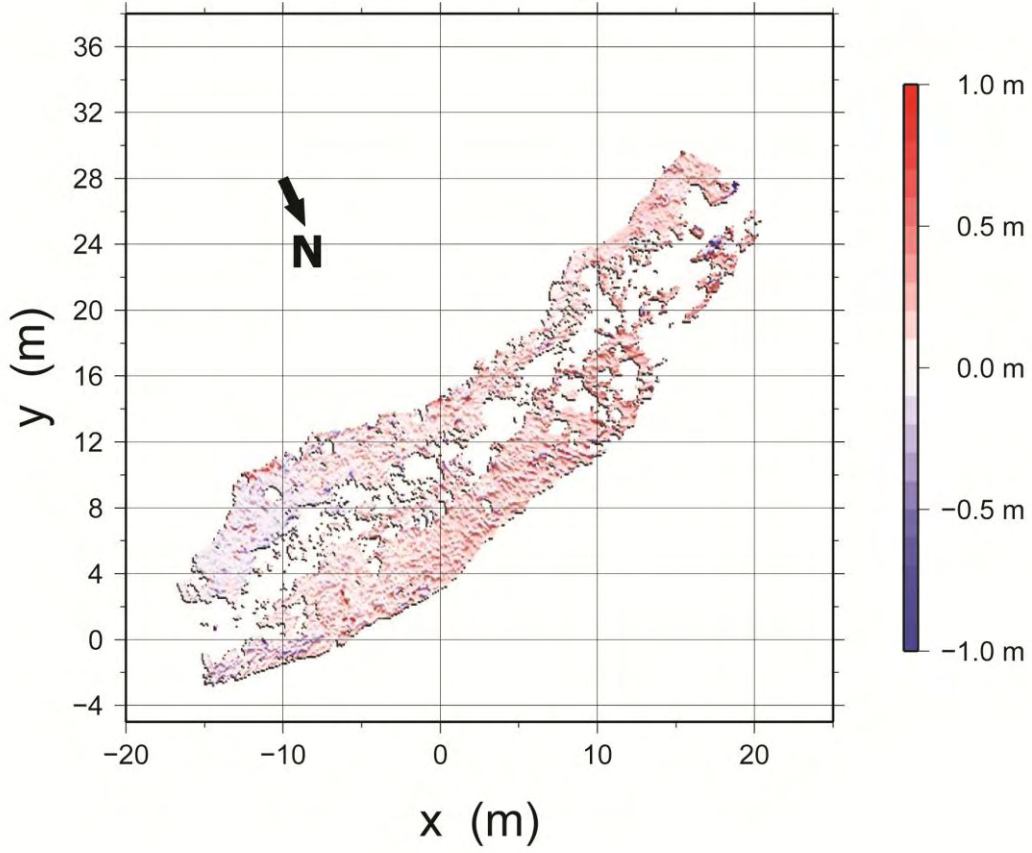
14 July - 12 August 2009
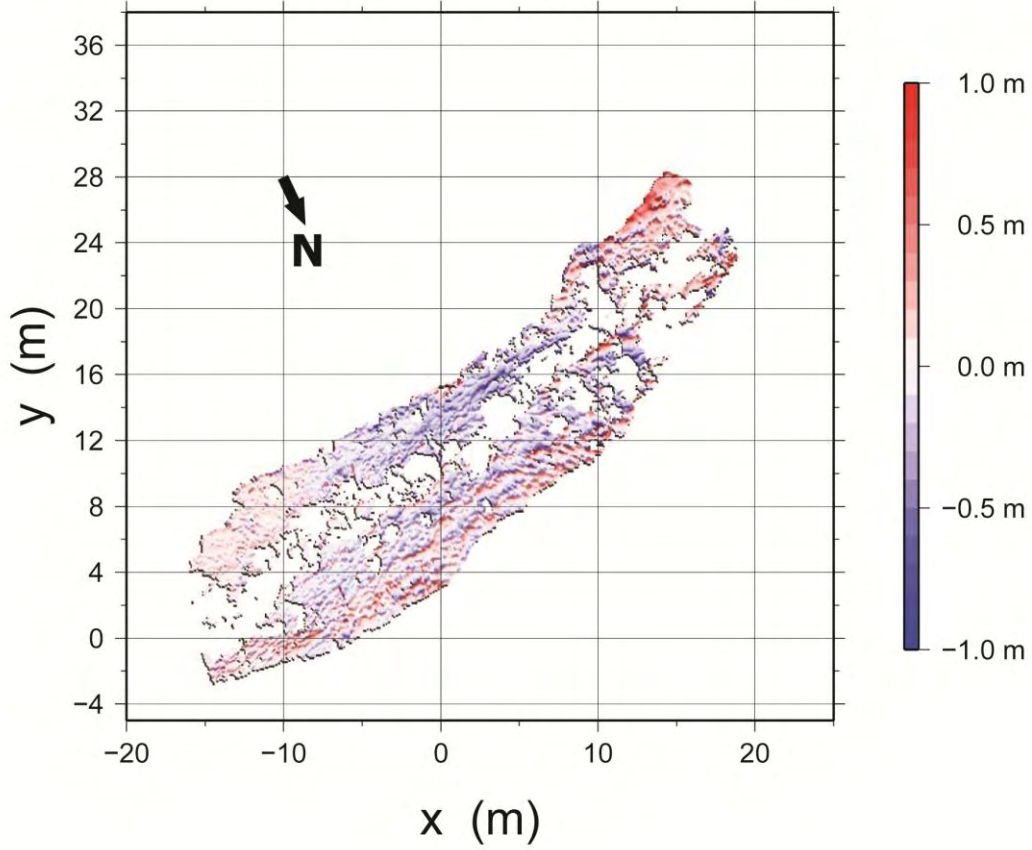
12 August - 8 September 2009
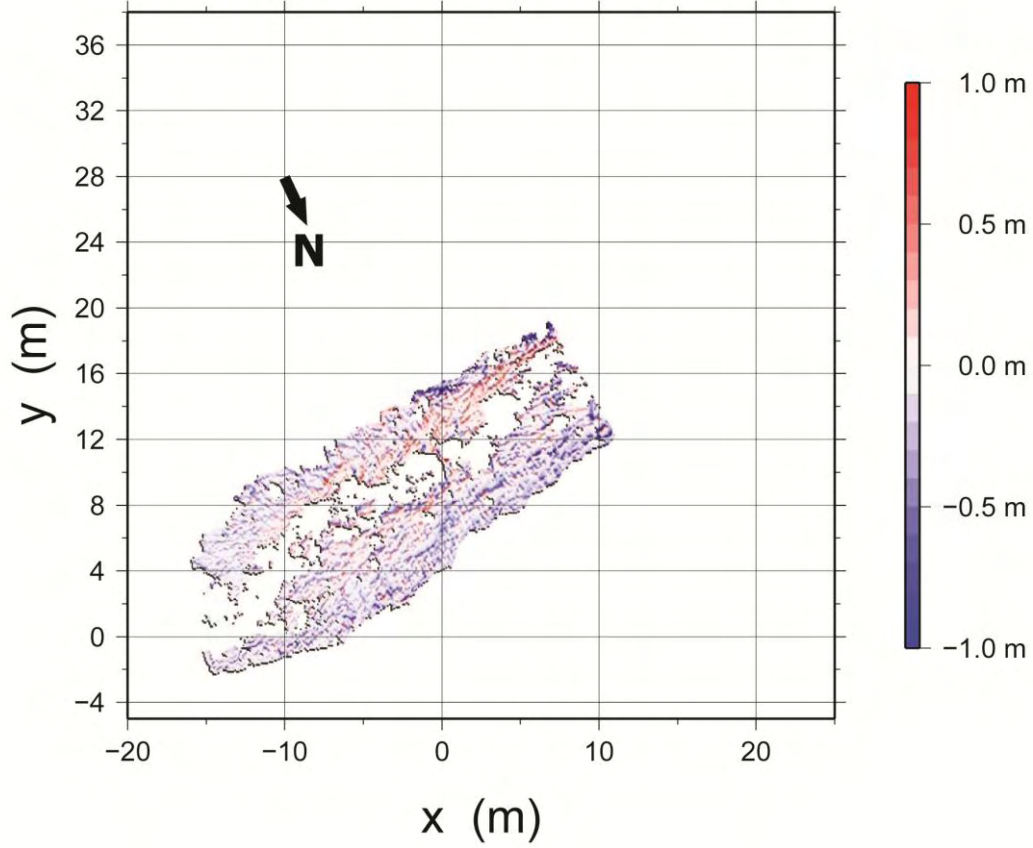
8 September - 30 October 2009
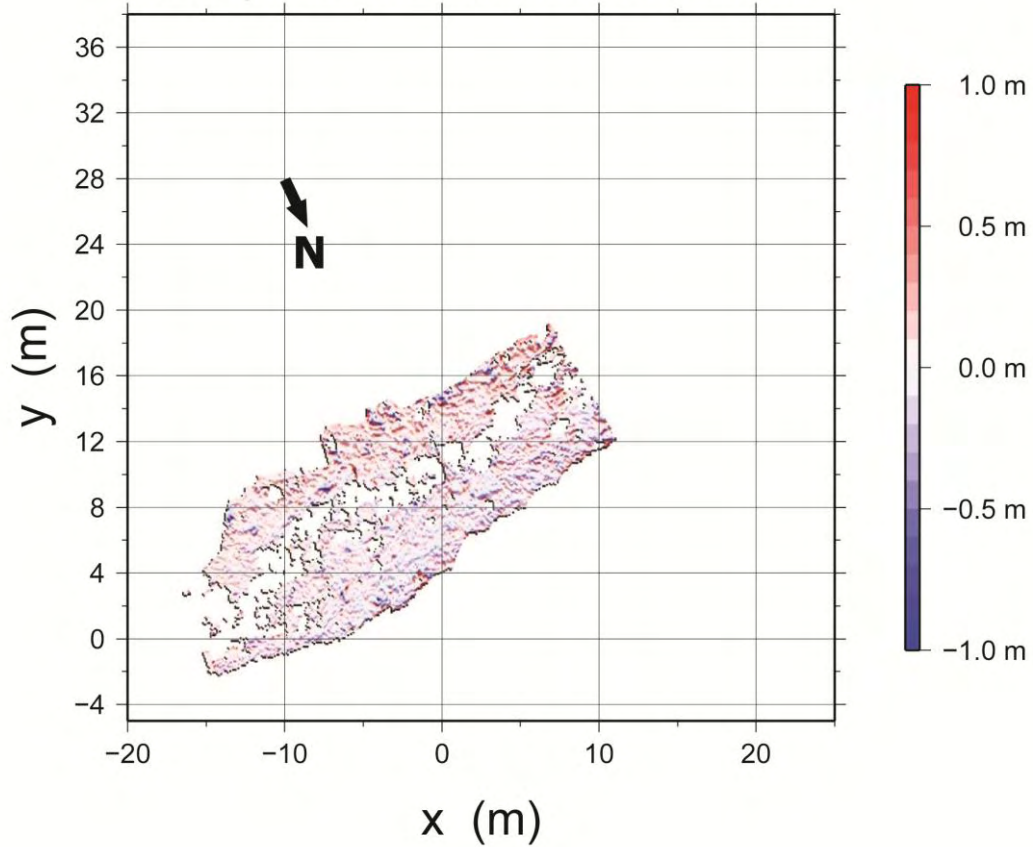
Fig. 6.2-4 Enlarged version of Figure 3.10.

Fig. 6.2-5 Location of deposition and erosion area compiled in Table 6.2-3 for alluvial fans and Table 6.2-4 for debris cones. Numbers are the same as in both tables. **(A)** Location alluvial fans. **(B)** Location debris cones.
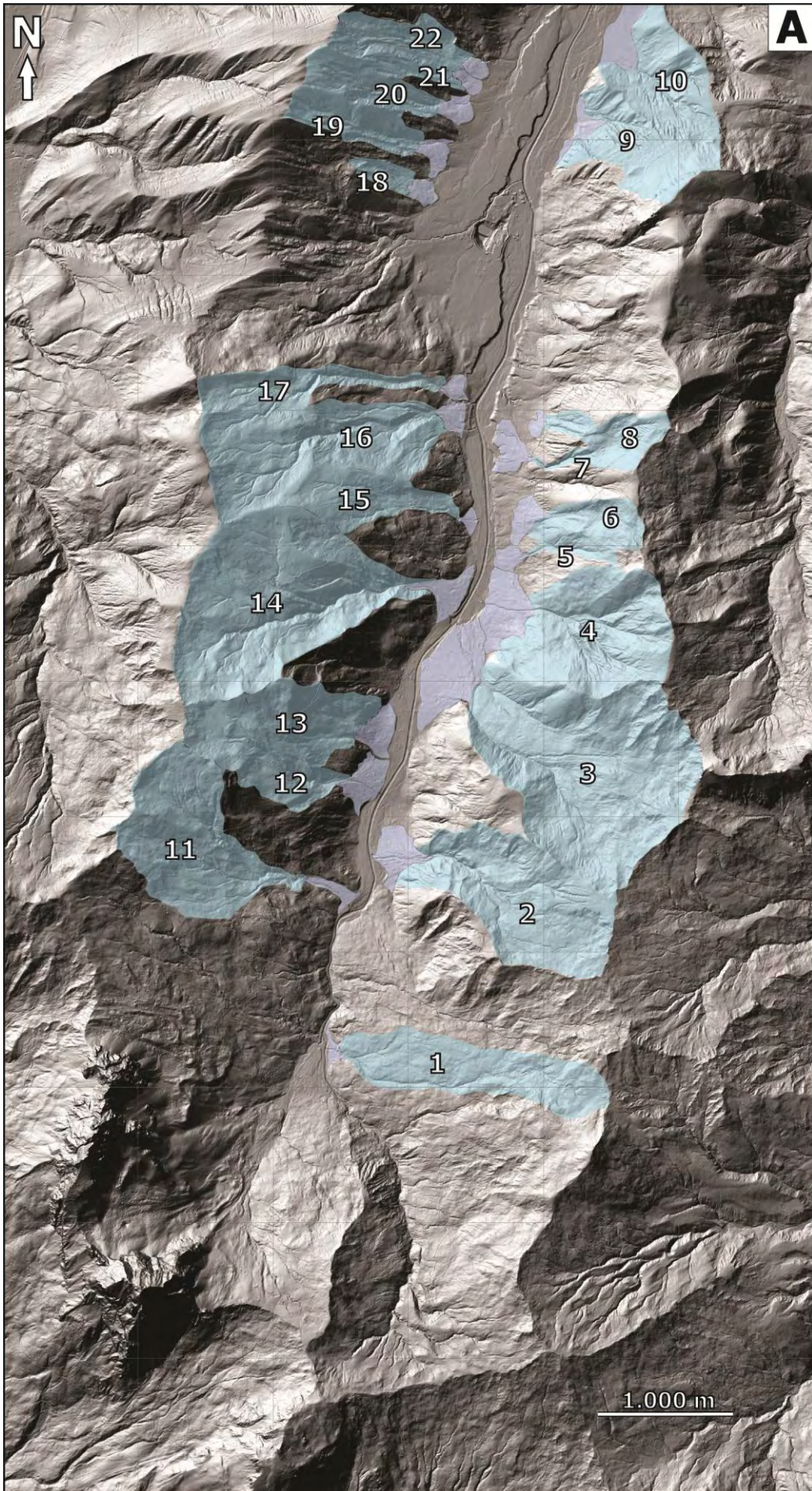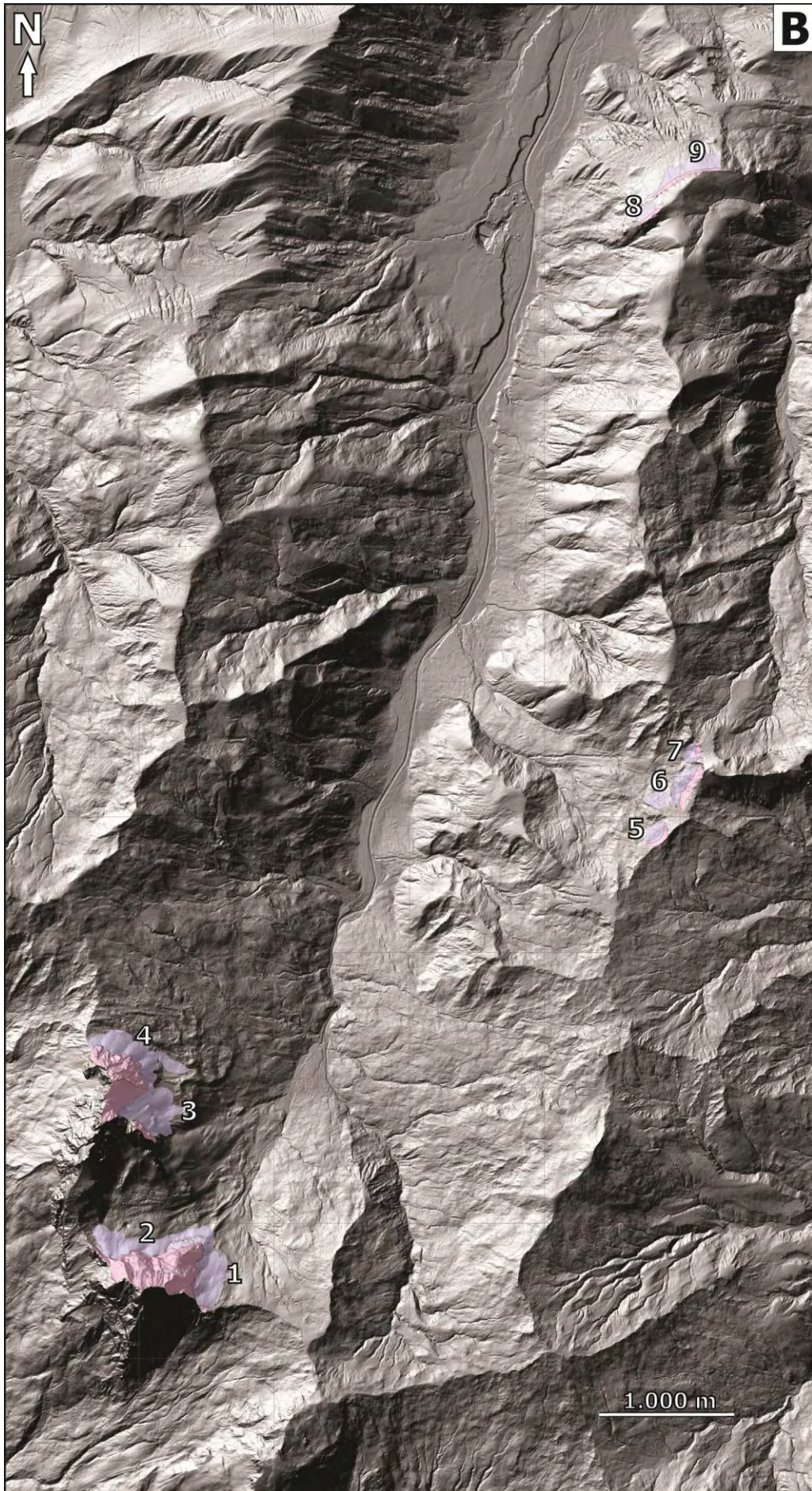
Fig. 6.2-6 Historical record of Alpthal village in the central Alp Valley (location in Fig. 3.1B). Line of sight is indicated on top of the figure. We observed an increase in forest cover especially between 1820 and 1900, and the growth of the village. 1820: Chapel of Alpthal, painting by M. Kälin (1792-1834). 1900: Photograph of Alpthal village taken from a brochure of the local authority from October 1993. 2010: Photograph in Alpthal village by R. Baran.
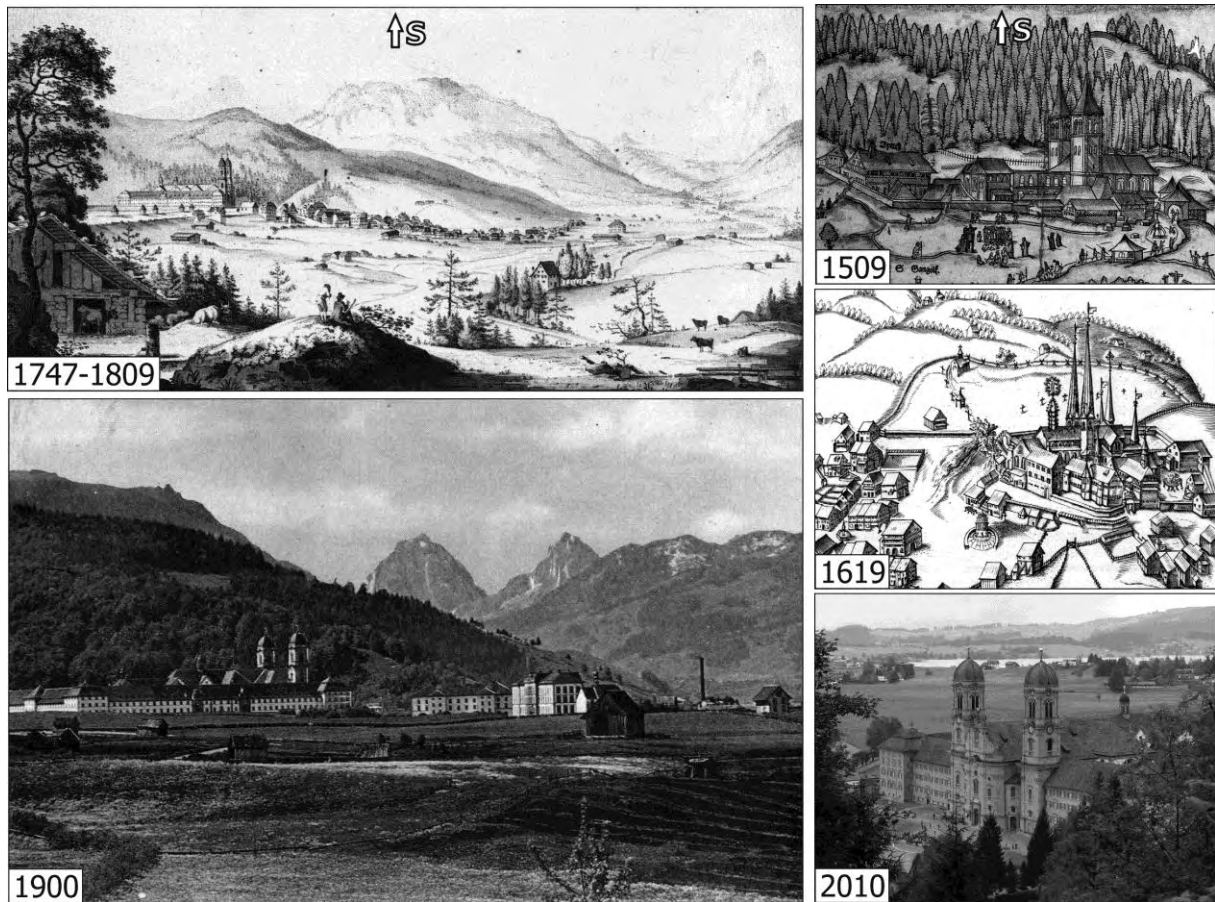
Fig. 6.2-7 Historical record of Einsiedeln (location in Fig. 3.1B). Line of sight is indicated on top of the figure. We observed drastic changes of the forest cover mainly due to chopping and reforestation activity during the last centuries. 1509: The oldest illustration of the monastery of Einsiedeln is a xylograph, and recently available as official post card. 1619: Etching "Einsidlen" taken from Eberle (1984). 1747-1809: Monastery of Einsiedeln, painting by J.J. Aschmann. 1900: Post card of the monastery of Einsiedeln, taken from Eberle (1984). 2010: Photograph of the monastery of Einsiedeln by R. Baran.

6.3. Appendix: Chapter III

6.3.1. Erlenbach Bed-Load Discharge

Calibration

The indirect monitoring of sediment transport in the Erlenbach using piezoelectric bed-load impact sensors (PBIS) and geophones required a data calibration. For any continuative details on this approach we refer to e.g. Rickenmann and McArdell (2007). However, to convert the PBIS data (1986–1999) into sediment volumes we used the equation of Rickenmann and McArdell (2007):

$$F = 0.934 \, SP3 \tag{A2}$$

with F as sediment volume in m³. The sum of impulses recorded by bed-load impact sensor no. 3 (*SP3*) is defined as the number of recorded impulses divided by 1000. The number 0.934 is the mean individual calibration factor k of Rickenmann and McArdell (2007), and the correlation coefficient R^2 is 0.872. To convert the geophone data (2000–2007) into sediment volumes we used the equation provided by D. Rickenmann (pers. comm., 2008):

$$F = 0.4484 \, SP8 \tag{A3}$$

where 0.4484 is the calibration factor, and the correlation coefficient R^2 is 0.965. The sum of impulses recorded by geophone no. 8 (*SP8*) is defined as the number of recorded impulses divided by 1000.

The impulses recorded by bed-load impact sensor no. 3 account for 56.5% of the total number of impulses recorded by all sensors between 1986 and 1999 (Rickenmann and McArdell, 2007). This is due to the mounting position next to the center-line of the channel-bed cross-section, and to slightly asymmetric flow conditions upstream of the sensor array resulting in dominant bed-load transport along the orographic right side of the cross-section (Rickenmann and McArdell, 2007). Hence, sensor no. 3 provided most reliable and representative impulse data on bed-load transport, and we therefore focused our analysis on data recorded by sensor no. 3. Furthermore, we treated the data recorded by geophone no. 8 (2000 and 2007) similarly because it is mounted in the former position of bed-load impact sensor no. 3.

The Erlenbach impulse data have been evaluated in terms of plausibility (J. Turowski, pers. comm., 2008). Evenly distributed impuls counts among the sensors are unlikely, and had been removed from the time series. This includes, for example, data resulting from intense precipitation. However, the definition of an bed-load transport event is solely based on sensor activity. If a short break in sensor activity occurred at high or increasing water discharge, no new event was defined (J. Turowski, pers. comm., 2008).

Uncertainties and Limitations

The PBIS and geophone systems record impulses during bed-load transport which are due to sliding, rolling and saltating sediment particles across the sensors. The impulse data are converted into sediment volumes using the linear calibration equations (A2) and (A3). The impulse data are thereby related to the volume of sediment trapped within the Erlenbach sediment-retention basin (Rickenmann and McArdell, 2007). To evaluate the conversion from impulse to sediment volume data, we address some uncertainties and limitations influencing

PBIS and geophone measurements and their interpretation (compiled from Rickenmann and McArdell, 2007; Turowski and Rickenmann, 2011).

The grain size of the sediment is a crucial factor controlling these measurements. The critical grain size required to produce an impulse on the PBIS is a diameter of 10 mm as revealed by laboratory experiments using the Erlenbach sensors and sediment (Etter, 1996). Hence, moving particles with a grain diameter less than 10 mm are not detected directly by the sensors during bed-load transport. But field data of floods occurring in the Erlenbach showed that 50% of the deposited sediment volume comprises grains that are coarse enough to cause a sensor impulse (Rickenmann, 1997; Rickenmann and McArdell, 2007).

The Erlenbach grain-size distributions of transported material deposited in the retention basin and surface-bed material upstream of the basin are markedly different. The characteristic grain sizes of the transported sediment are much smaller than those of the surface-bed material, e.g., d_m of 11.3 mm for the first and d_m of 51.2 mm for the latter. The deposits in the retention basin are coarser in the upper part of the basin and finer (grain size smaller than fine sand; <0.25 mm) in the lower part as well as along its sides. Furthermore, a detailed analysis of the basin deposits revealed that during typical flood conditions probably almost no sediment coarser than fine sand is transported off the basin (Rickenmann and McArdell, 2007). In contrast, during larger floods a substantial transport of silt- and clay-sized grains through the basin may be possible. However, Rickenmann and McArdell (2007) approximated that the proportion of bed-load and suspended load is constant during different flood events, and expected that part of the scatter in their calibration relationship, equation (A2), is due to a changing grain-size distribution of the transported sediment with flood size. In summary, we suggest that the calibration relationships, equations (A2) and (A3), used to convert sensor impulses into sediment volumes account at least partly for suspended load.

Our approach of using a linear relationships, i.e. equations (A2) and (A3), to calibrate the PBIS and geophone impulses is well suited to determine the bed-load discharge of individual events but it is unsuitable to constrain the bed-load discharge at a very high temporal resolution of minutes (Turowski and Rickenmann, 2011). At such short time scales, bed-load discharge can vary drastically even for the same water discharge. Simultaneously, impulse vs. bed-load discharge plots exhibit broad spread, and impulse counts can fluctuate strongly for a given water and bed-load discharge (Turowski and Rickenmann, 2011). This spread is set by two distribution functions: the spread of bed-load discharge at equal water discharge, and the spread of the sensor response at a given water and bed-load discharge. However, the bed-load function and sensor-response function need to be known to allow for an appropriate conversion of impulse data into high temporal resolution bed-load discharge rates. Unfortunately, the sensor-response function is unknown, and it probably depends on site-specific conditions requiring further research (Turowski and Rickenmann, 2011).

6.3.2. References

Etter, M.; 1996; Zur Erfassung des Geschiebetransportes mit Hydrophonen; Diploma thesis, Institute of Geography, University of Bern, and WSL, Switzerland, 110 pp.

Rickenmann, D.; 1997; Sediment transport in Swiss torrents; Earth Surface Processes and Landforms, vol. 22, p. 937–951.

Rickenmann, D., and McArdell, B.W.; 2007; Continuous measurement of sediment transport in the Erlenbach stream using piezoelectric bedload impact sensors; Earth Surface Processes and Landforms, vol. 32, p. 1362–1378.

Turowski, J.M., and Rickenmann, D.; 2011; Measuring the statistics of bedload transport using indirect sensors; Journal of Hydraulic Engineering, vol. 137, p. 116–121.

Table 6.3-1: Drainage area – short- and medium-term scales.

Drainage basin	Area (km²)	Class	Reference
Aare	554	3	Hinderer (2001)
Kander	1120	3	Schlunegger & Hinderer (2001)
Linth	530	3	
Lütschine	380	3	
Melchaa	72	2	
Reuss	832	3	
Rhine	6119	4	
Rhone	5220	4	
Adda	906	3	
Cassarate	73	2	
Maggia	926	3	
Ticino	1515	3	
Ammer	600	3	
Iller	953	3	
Tiroler Ache	945	3	
Weissach	95	2	
Inn	9756	4	
Sarca	575	3	
Albula	529	3	Schlunegger & Hinderer (2003)
Broye	392	3	
Emme	940	3	
Glatt	416	3	
Hinterrhine	1575	3	
Landquart	616	3	
Lonza	77.8	2	
Moesa	471	3	
Sarine	639	3	
Simme	344	3	
Thur	1515	3	
Visp	778	3	
Klem	434	3	Wittmann et al. (2007)
Wasen	12	2	
Taf	25	2	
Sense	162	3	
Gren	6	1	
Chie	156	3	
Furka	29	2	
Verz	186	3	
Mela	333	3	
Anza	259	3	
Sesia	626	3	
Toce	361	3	
Fontanne	63	2	Norton et al. (2008)
Trub	57	2	
Ahrn	36	2	Norton et al. (2011)
Antholzer	79	2	
Arno	47	2	
Avisio	565	3	
Bergler	14	2	
Bitto	86	2	
Castello	26	2	
di Adame	98	2	
di Venina	60	2	

Fersina	71	2	
Flagger	18	2	
Fusino	53	2	
Hoeller	64	2	
Krimmler	100	3	
Lagorai	15	2	
Masino	133	3	
Melach	220	3	
Muehl	29	2	
Nero	841	3	
Novate	54	2	
Oglio	411	3	
Pfitsch	119	3	
Pitze	225	3	
Plima	143	3	
Schnalz	199	3	
Silla	25	2	
Talfer	375	3	
Tauern	77	2	
val Moena	22	2	
Watten	63	2	
Widshoenau	76	2	
Zemm	210	3	
Ziel	30	2	
Fischenbach	10	2	Schlunegger et al. (2002)
Walen lake	269	3	Müller (1999)
Dora baltea at Avise	543	3	Vezzoli (2004)
Dora Baltea at Sarre	1303	3	
Dora Baltea at Verres	2483	3	
Dora Baltea	3264	3	
Roubine	0.00133	1	Mathys et al. (2003)
Laval	0.08	1	
Moulin	0.86	1	
Brusquet	1.08	1	
Romanche	1072	3	Delunel et al. (2010)
Veneon	303	3	
Tabuc	23	2	
Saint Pierre	48	2	
Celse Nierre	27	2	
Gyr	113	3	
Roizonne	75	2	
Bonne	246	3	
Severaisse	197	3	
Gorge du Diable	20	1	Valla et al. (2010)

Table 6.3-2: Erosion area – long-term scale (Kuhlemann et al., 2001).

Western Alps:
6500 km² + 3500 km² + 3500 km² + 1000 km² + 3500 km² + 2000 km² = 20000 km²

Eastern Alps:
7500 km² + 5000 km² + 4000 km² + 19000 km² + 13000 km² + 15000 km² + 3500 km² = 67000 km²

Area supplying northern foreland basin:

6500 km²	Prealps
3500 km²	Aar massif
3500 km²	W Austroalpine nappes
1000 km²	E Penninic nappes
14500 km²	total

Area supplying southern foreland basin:

3500 km²	Lepontine dome
2000 km²	Southalpine (Western Alps)
15000 km²	Southalpine (Eastern Alps)
20500 km²	total

Table 6.3-3: Conversion of units.

1 mm/a = 1 m/ka = 1km/Ma
Density: 2.7 g/cm³ = 2700 kg/m³ = 2.7 t/m³ = 2700000000 t/km³

Short-term scale:

t/a = t/km² a	dividing with km² (drainage-basin area)
t/ha a = t/km² a	multiplying with 100
t/km² a = km/a	dividing with 2700000000 t/km³
km/a = mm/a	multiplying with 1000000
m³/a = m/a	dividing with m² (drainage-basin area)
m/a = mm/a	multiplying with 1000
mm/ka = m/ka	dividing with 1000

Medium-term scale:

m³/km² a = kg/km² a	multiplying with 2700 kg/m³
kg/km² a = t/km² a	dividing with 1000
km³ = km³/km²	dividing with km² (drainage-basin area)
km³/km² = km	
km = m	multiplying with 1000
m = m/ka	dividing with ka (time period)

Long-term scale:

km = km/Ma	dividing with Ma (time period)
km³ = km³/km²	dividing with km² (drainage-basin area)
km³/km² = km	
km³/Ma = km/Ma	dividing with km² (area)

225

Table 6.3-4: Data – long-term scale.

Value	Unit	Uncertainty	Time period (Ma)	Type of rate?	Location	Reference	Time Period (Ma)	km/Ma	Uncertainty
20500	km³/Ma	10250	0	sediment volume	**Eastern Alps**	Kuhlemann	0	0.31	0.16
15500	km³/Ma	7750	1	sediment-budget,		et al. (2001)	1	0.23	0.12
11000	km³/Ma	5500	2	circum-Alpine			2	0.16	0.08
10000	km³/Ma	5000	3	sedimentary basins			3	0.15	0.08
8500	km³/Ma	4250	4				4	0.13	0.07
8500	km³/Ma	4250	5	typical error 50%			5	0.13	0.07
8500	km³/Ma	4250	6				6	0.13	0.07
8500	km³/Ma	4250	7	temporal error:			7	0.13	0.07
8500	km³/Ma	4250	8	intervals of 0.5 & 1 Ma			8	0.13	0.07
8000	km³/Ma	4000	9	erroneous stratigraphic			9	0.12	0.06
7000	km³/Ma	3500	10	age of formations			10	0.10	0.05
6000	km³/Ma	3000	11	Pre-Pleistocene: ±20%			11	0.09	0.05
5500	km³/Ma	2750	12	Pleistocene: ±40%			12	0.08	0.04
5500	km³/Ma	2750	13				13	0.08	0.04
5500	km³/Ma	2750	14				14	0.08	0.04
5500	km³/Ma	2750	15				15	0.08	0.04
6500	km³/Ma	3250	16				16	0.10	0.05
10500	km³/Ma	5250	16.5				16.5	0.16	0.08
9000	km³/Ma	4500	17				17	0.13	0.07
3000	km³/Ma	1500	18				18	0.04	0.02
3500	km³/Ma	1750	19				19	0.05	0.03
3000	km³/Ma	1500	20				20	0.04	0.02
6000	km³/Ma	3000	21				21	0.09	0.05
5500	km³/Ma	2750	22				22	0.08	0.04
5000	km³/Ma	2500	23				23	0.07	0.04
4500	km³/Ma	2250	24				24	0.07	0.04
4500	km³/Ma	2250	25				25	0.07	0.04
4500	km³/Ma	2250	26				26	0.07	0.04
4000	km³/Ma	2000	27				27	0.06	0.03
3000	km³/Ma	1500	28				28	0.04	0.02
2500	km³/Ma	1250	29				29	0.04	0.02
2000	km³/Ma	1000	30				30	0.03	0.02

1500	km³/Ma	750	31		31	0.02	0.01
2000	km³/Ma	1000	32		32	0.03	0.02
2000	km³/Ma	1000	33		33	0.03	0.02
48000	km³/Ma	24000	1	**Western Alps**	1	2.4	1.20
43000	km³/Ma	21500	2		2	2.15	1.08
40000	km³/Ma	20000	3		3	2	1.00
36000	km³/Ma	18000	4		4	1.8	0.90
33000	km³/Ma	16500	5		5	1.65	0.83
16000	km³/Ma	8000	6		6	0.8	0.40
15000	km³/Ma	7500	7		7	0.75	0.38
16000	km³/Ma	8000	8		8	0.8	0.40
16000	km³/Ma	8000	9		9	0.8	0.40
16000	km³/Ma	8000	10		10	0.8	0.40
15000	km³/Ma	7500	11		11	0.75	0.38
16000	km³/Ma	8000	12		12	0.8	0.40
16000	km³/Ma	8000	13		13	0.8	0.40
17000	km³/Ma	8500	14		14	0.85	0.43
19000	km³/Ma	9500	15		15	0.95	0.48
22000	km³/Ma	11000	16		16	1.1	0.55
25000	km³/Ma	12500	17		17	1.25	0.63
19000	km³/Ma	9500	18		18	0.95	0.48
17000	km³/Ma	8500	19		19	0.85	0.43
17000	km³/Ma	8500	20		20	0.85	0.43
19000	km³/Ma	9500	21		21	0.95	0.48
24000	km³/Ma	12000	22		22	1.2	0.60
22000	km³/Ma	11000	23		23	1.1	0.55
20000	km³/Ma	10000	24		24	1	0.50
18000	km³/Ma	9000	25		25	0.9	0.45
17000	km³/Ma	8500	26		26	0.85	0.43
17000	km³/Ma	8500	27		27	0.85	0.43
16000	km³/Ma	8000	28		28	0.8	0.40
12000	km³/Ma	6000	29		29	0.6	0.30
8000	km³/Ma	4000	30		30	0.4	0.20
7000	km³/Ma	3500	31		31	0.35	0.18
6000	km³/Ma	3000	32		32	0.3	0.15

5000	km³/Ma	2500	33				33	0.25	0.13
5000	km³/Ma	2500	34				34	0.25	0.13
0.4-0.7	km/Ma		last 15	exhumation rate detrital zircon fission-track temporal error: 1 Ma of stratigraphic age	**Alps**	Bernet et al. (2001)	last 15	0.4-0.7	
0.4-0.7	km/Ma		last 30	exhumation rate	**Alps**	Bernet	last 30	0.4-0.7	
0.2-0.3	km/Ma		last 30	detrital zircon fission-track temporal error: 1 Ma of stratigraphic age		et al. (2009)	last 30	0.2-0.3	
					Swiss Alps	Schlunegger (1999)			
				Foreland basins	Molasse basin - N foreland				
2300	km³	1200	16.5-20	sediment volume	total		16.5-20	0.04	0.02
2500	km³	1200	20-25		Lake Geneva paleo river				
7500	km³	3750	20-25		Rigi-Höhronen & Honegg-Napf paleo rivers				
10000	km³	5000	20-25		total		20-25	0.13	0.07
1500	km³	750	25-30		Lake Geneva paleo river				
8500	km³	4250	25-30		Rigi-Höhronen & Honegg-Napf paleo rivers				
10000	km³	5000	25-30		total		25-30	0.13	0.07
650	km³/Ma	325	16.5-20	Min sediment supply rate	Molasse basin - N foreland		16.5-20	0.05	0.02
1500	km³/Ma	750	20-25	Max sediment supply rate			20-25	0.1	0.05
1500	km³/Ma	750	25-30				25-30	0.1	0.05
500	m/Ma	---	16-18	sediment supply rate	S foreland basin		16-18	0.5	---
150	m/Ma	---	20-22				20-22	0.15	---
250	m/Ma	---	30-24/22				30-24/22	0.25	---
300	m/Ma	---	0-20	erosion rate	Lepontine dome		0-20	0.3	---
400	m/Ma	---	0-20	apatite fission-track			0-20	0.4	---
500	m/Ma	---	0-20	zircon fission-track			0-20	0.5	---
1000	m/Ma	---	20-40	biotite Rb-Sr. K-Ar			20-40	1	---

1000	m/Ma	---	20-40	K-white muscovite Rb-Sr			20-40	1	---
200	m/Ma	---	0-20	max. temporal error:			0-20	0.2	---
400	m/Ma	---	0-20	6 Ma (from Fig. 10)			0-20	0.4	---
5000	m/Ma	---	20-22				20-22	5	---
400	m/Ma	---	22-40				22-40	0.4	---
600	m/Ma	---	22-40				22-40	0.6	---
3300	km³		13.5-16.5	sediment volume	**North-Alpine**	Schlunegger			
3500	km³		16.5-20		**foreland basin**	et al. (2001)			
15000	km³		20-25		**Switzerland**				
13000	km³		25-30						
90	m/Ma	45	13.5-16.5	average erosion rate			13.5-16.5	0.09	0.05
85	m/Ma	40	16.5-20				16.5-20	0.09	0.04
250	m/Ma	125	20-25				20-25	0.25	0.13
200	m/Ma	100	25-30				25-30	0.2	0.1
9500	km³		13.5-16.5	sediment volume	**North-Alpine**				
9500	km³		16.5-20		**foreland basin**				
20000	km³		20-25		**Switzerland &**				
6000	km³		25-30		**Germany**				
2000	km³		30-34						
260	m/Ma	130	13.5-16.5	average erosion rate			13.5-16.5	0.26	0.13
220	m/Ma	110	16.5-20				16.5-20	0.22	0.11
330	m/Ma	165	20-25				20-25	0.33	0.17
100	m/Ma	50	25-30				25-30	0.1	0.05
40	m/Ma	20	30-34				30-34	0.04	0.02
20000-56000	km³/Ma		0-1	sediment volume	**North-Alpine**	Schlunegger	0-1	1.38-3.86	
14000-38000	km³/Ma		1-3		**foreland basin**	et al. (2007)	1-3	0.97-2.62	
8000-22000	km³/Ma		3-5				3-5	0.55-1.52	
3000-9000	km³/Ma		5-10				5-10	0.21-0.62	
6000-18000	km³/Ma		10-17				10-17	0.41-1.24	
3000-16000	km³/Ma		17-20				17-20	0.21-1.1	
8000-18000	km³/Ma		20-22				20-22	0.55-1.24	
4000-10000	km³/Ma		22-23.5				22-23.5	0.28-0.69	
1000-4000	km³/Ma		23.5-28.5				23.5-28.5	0.07-0.28	
300	m/Ma	---	last 25	erosion rate	**Aar massif,**	Schlunegger &	last 25	0.3	---
400	m/Ma	---	last 25	apatite fission-track,	**central Swiss Alps**	Willett (1999)	last 25	0.4	---

500	m/Ma	---	last 25	zircon fission-track			last 25	0.5	---
600	m/Ma	---	last 25				last 25	0.6	---
200	m/Ma	---	last 40	erosion rate	**Penninic crystalline,**		last 40	0.2	---
300	m/Ma	---	last 40	apatite fission-track,	**eastern Swiss Alps**		last 40	0.3	---
400	m/Ma	---	last 40	zircon fission-track			last 40	0.4	---
				biotite Rb-Sr. K-Ar					
				max. temporal error:					
				5 Ma (from Fig. 8)					
				sediment volume	**Central Alps**	Willett			
20000-57000	km³/Ma		0-1	Alpine foreland	North foreland	et al. (2006)	0-1	1.38-3.93	
15000-36000	km³/Ma		1-3	basins			1-3	1.03-2.48	
8000-22000	km³/Ma		3-5				3-5	0.55-1.52	
3000-10000	km³/Ma		5-10				5-10	0.21-0.69	
6000-17000	km³/Ma		10-17				10-17	0.41-1.17	
8000-26000	km³/Ma		0-1.5		South foreland		0-1.5	0.39-1.27	
7000-18000	km³/Ma		1.5-5				1.5-5	0.34-0.88	
49000-58000	km³/Ma		5-5.5				5-5.5	2.39-2.83	
0-3000	km³/Ma		7-11.5				7-11.5	0-0.15	
0-6000	km³/Ma		11.5 16				11.5 16	0-0.29	
				erosion estimate	**Swiss North-Alpine**	Cederbom			
				apatite fission-track	**Foreland transect**	et al. (2004)			
1.7-3.5	km		last 5		Boswil		last 5	0.34-0.7	
1.4-3.3	km		last 5	max. temporal error	Hünenberg		last 5	0.28-0.66	
3.8-6.1	km		last 5	2.2 Ma	Rigi-Weggis		last 5	0.76-1.22	
				incision rate	**Aare Valley,**	Haueselmann			
1.2	km/Ma	0.1	0-0.8	cave sediments	**Swiss Alps**	et al. (2007)	0-0.8	1.2	0.1
0.12	km/Ma	0.1	0.8-4	cosmogenic 10Be & 26Al			0.8-4	0.12	0.1
				max. temporal error: 0.6 Ma					
0.4-1.5	mm/a		last 2-7.5	western block	**Aosta Valley**	Malusà &	last 2-7.5	0.4-1.5	
0.1-0.3	mm/a		last 2-7.5	eastern block	cross-section	Vezzoli (2006)	last 2-7.5	0.1-0.3	
				exhumation rate	Western Alps				
				bedrock-fission track					
				2-7.5 Ma: min. period –					
				exhumation from 3 km					
				depth with rates of western					

Value	Unit		Time	Method / Description	Location	Reference	Time	Value	
				mean denudation rate	**Western Alps**	Bogdanoff			
0.8-1.5	mm/a		0-3	apatite fission-track	Argentera massif	et al. (2000)	0-3	0.8-1.5	
0.2-0.34	mm/a		3-8		Argentera massif		3-8	0.2-0.34	
0.2-0.3	mm/a		4-9	max. temporal	Pelvoux massif		4-9	0.2-0.3	
0.8-1	mm/a		3-5	error: 1 Ma	Mont Blanc massif		3-5	0.8-1	
0.8-1	mm/a		3-5		Aar massif		3-5	0.8-1	
				denudation rate	**Alps**	Clark &			
0.4-0.5	mm/a		last 11.5	biotite Rb-Sr & K-Ar	Simplon tunnel. Min	Jäger (1969)	last 11.5	0.4-0.5	
1-1.1	mm/a		last 11.5	heat-flow data	Simplon tunnel. Max		last 11.5	1-1.1	
0.4-0.5	mm/a		last 16.5		Gotthard tunnel. Min		last 16.5	0.4-0.5	
0.7	mm/a		last 16.5		Gotthard tunnel. Max		last 16.5	0.7	
0.4-0.5	mm/a		last 20		Tauern tunnel. Min		last 20	0.4-0.5	
0.7	mm/a		last 20		Tauern tunnel. Max		last 20	0.7	
				erosion rate	**Tauern window.**	Frisch			
				mass balance in	**Eastern Alps**	et al. (2000)			
27000	km³		13-23	sedimentary basins,	W of Tauern window				
15000	km³		13-23	zircon & apatite	Tauern window				
12000	km³		13-23	fission-track	E of Tauern window				
0.15	mm/a	---	13-23		W of Tauern window		13-23 Ma	0.15	---
0.3	mm/a	---	13-23		Tauern window		13-23 Ma	0.3	---
0.06	mm/a	---	13-23		E of Tauern window		13-23 Ma	0.06	---
				exhumation rate	**W Tauern window,**	Christensen			
				Garnet Rb-Sr	**Eastern Alps**	et al. (1994)			
4	mm/a	pos.3/neg.2	30±0.8-35.4±0.6		Upper Schieferhülle		30±0.8-35.4±0.6	4	pos.3/neg.2
2	mm/a	1	30.2±1.5-32.7±1		Lower Schieferhülle		30.2±1.5-32.7±1	2	1
				exhumation rate	**SE Tauern window,**	Cliff et al. (1985)			
				Rb-Sr, K-Ar & Ar-Ar	**Eastern Alps**				
≤ 1	mm/a	---	0-16.5	33 mica samples	Gneiss dome		0-16.5	≤ 1	---
≥ 5	mm/a	---	16.5-17	20 km N-S tunnel section			16.5-17	≥ 5	---
≤ 1	mm/a	---	17-24	temporal error: 0.5 Ma			17-24	≤ 1	---
0.1	mm/a	0.4 km	0-7±1	exhumation rate	**W Tauern window,**	von Blanckenburg	0-7±1	0.1	0.4 km

0.5	mm/a	0.7 km	7±1-13.3±0.3	hornblende K-Ar, Ar-Ar	**Eastern Alps**	et al. (1989)	7±1-13.3±0.3	0.5	0.7 km
1.8	mm/a	2.3 km	13.3±0.3-15±1	mica Rb-Sr, K-Ar			13.3±0.3-15±1	1.8	2.3 km
2.9	mm/a	2.4 km	15±1-18±0.8				15±1-18±0.8	2.9	2.4 km
3.6	mm/a	2.6 km	18±0.8-20±0.8	error from Fig. 5			18±0.8-20±0.8	3.6	2.6 km
0.2	mm/a	1 km	0-9.9±3.6	exhumation rate	**W Tauern window,**	Fügenschuh	0-9.9±3.6	0.2	1 km
1	mm/a	1 km	9.9±3.6-13±2	zircon & apatite	**Eastern Alps**	et al. (1997)	9.9±3.6-13±2	1	1 km
1	mm/a	2 km	13±2-13.3±0.3	fission-track + data of			13±2-13.3±0.3	1	2 km
1	mm/a	2 km	13.3±0.3-15±1	von Blanckenburg			13.3±0.3-15±1	1	2 km
2.6	mm/a	2 km	15±1-18±0.8	et al. (1989)			15±1-18±0.8	2.6	2 km
4	mm/a	3 km	18±0.8-20±0.8				18±0.8-20±0.8	4	3 km
0.2	mm/a	2 km	20±0.8-30	error from Fig. 2			20±0.8-30	0.2	2 km
				exhumation rate	**W & SE Tauern window,**	Hejl (1997)			
				zircon & apatite	**Eastern Alps**				
3000	m	---	last 5	fission-track	Zillertal Alps (W)		last 5 Ma	0.6	---
1000	m	---	last 5		Reisseck (SE)		last 5 Ma	0.2	---
				exhumation rate	**Tauern window,**	Most (2003)			
				zircon & apatite	**Eastern Alps**				
0.6	mm/a		5-9	fission-track	Ahornspitze and		5-9 Ma	0.6	
1.1-1.2	mm/a		12-14	temporal error: 0.5 Ma	Grinbergspitze		12-14 Ma	1.1-1.2	
				(from Fig. 6.5)					
0.2	mm/a		0-13±2	exhumation rate	**Riesenferner pluton,**	Steenken	0-13±2	0.2	
0.4-0.6	mm/a		13±2-31±3	Rb-Sr & K-Ar	**Eastern Alps**	et al. (2002)	13±2-31±3	0.4-0.6	
0.2	mm/a		0-16±2	zircon & apatite	S of Tauern window		0-16±2	0.2	
0.4-0.6	mm/a		16±2-31±3	fission-track			16±2-31±3	0.4-0.6	
				temporal error from Fig. 13					

Table 6.3-5: Data – medium-term scale.

Value	Unit	Uncertainty	Time period (ka)	Type of rate?	Location	Reference	Time period (ka)	m/ka	Uncertainty
				mean denudation rate	**Swiss Alps**	Wittmann			
0.48	mm/a	0.14	last 18	in-situ produced	Klem basin	et al. (2007)	last 18	0.48	0.14
0.26	mm/a	0.14	last 18	cosmogenic 10Be	Wasen basin		last 18	0.26	0.14
0.26	mm/a	0.14	last 18	in river-borne quartz	Emme basin		last 18	0.26	0.14
0.11	mm/a	0.14	last 18		Buetsch basin		last 18	0.11	0.14
0.16	mm/a	0.14	last 18	temporal error: 3 ka	Taf basin		last 18	0.16	0.14
0.25	mm/a	0.14	last 18	moraine sample from	Sense basin		last 18	0.25	0.14
1.28	mm/a	0.3	last 18	Aare basin – LGM	Lonza basin		last 18	1.28	0.3
1.32	mm/a	0.3	last 18	18±3 ka	Gren basin		last 18	1.32	0.3
0.69	mm/a	0.3	last 18		Chie basin		last 18	0.69	0.3
1.14	mm/a	0.3	last 18		Furka basin		last 18	1.14	0.3
1.58	mm/a	0.3	last 18		Reuss basin		last 18	1.58	0.3
0.7	mm/a	0.3	last 18		Maggia basin		last 18	0.7	0.3
1.18	mm/a	0.3	last 18		Toce basin		last 18	1.18	0.3
0.59	mm/a	0.3	last 18		Verz basin		last 18	0.59	0.3
0.89	mm/a	0.3	last 18		Mela basin		last 18	0.89	0.3
0.83	mm/a	0.3	last 18		Anza basin		last 18	0.83	0.3
0.5	mm/a	0.3	last 18		Sesia basin		last 18	0.5	0.3
				basin averaged	**northern Swiss Alps**	Norton			
350	mm/ka	50	last 17	denudation rate	Trub basin	et al. (2008)	last 17	0.35	0.05
				cosmogenic 10Be	Fontanne basin,				
380	mm/ka	50	last 16		upstream knickzone		last 16	0.38	0.05
				temporal error: 3 ka	Fontanne basin,				
540	mm/ka	100	last 16		downstream knickzone		last 16	0.54	0.1
1.24-1.69	mm/a		last 15	denudation rate,	Walensee Valley,	Müller (1999)	last 15	1.24-1.69	
				sediment budget -	**eastern Swiss Alps**				
				lithological model &					
				radiocarbon dating					
				max. temporal error: 0.2 ka					
				denudation rate	**Western Alps**	Hinderer			
380	mm/ka	190	last 17	sediment fluxes	Aare basin	(2001)	last 17	0.38	0.19
730	mm/ka	365	last 17	from Alpine catchments	Linth basin		last 17	0.73	0.37

820	mm/ka	410	last 17	by sediment volume	Lütschine basin		last 17	0.82	0.41
370	mm/ka	185	last 17	trapped valleys	Melchaa basin		last 17	0.37	0.19
560	mm/ka	280	last 17	and lake basins	Reuss basin		last 17	0.56	0.28
960	mm/ka	480	last 17		Seez basin		last 17	0.96	0.48
1060	mm/ka	530	last 17	general error 50%	Rhine basin		last 17	1.06	0.53
950	mm/ka	475	last 17		Rhone basin		last 17	0.95	0.48
850	mm/ka	425	last 17	max. temporal error	Adda basin		last 17	0.85	0.43
510	mm/ka	255	last 17	<10%; 1 ka	Maggia basin		last 17	0.51	0.26
790	mm/ka	395	last 17		Ticcino basin		last 17	0.79	0.4
					Eastern Alps				
250	mm/ka	125	last 17		Iller basin		last 17	0.25	0.13
530	mm/ka	265	last 17		Tiroler Ache basin		last 17	0.53	0.27
420	mm/ka	210	last 17		Weissach basin		last 17	0.42	0.21
570	mm/ka	285	last 17		Inn basin		last 17	0.57	0.29
490	mm/ka	245	last 17		Sarca basin		last 17	0.49	0.25
					Western Alps				
950	t/km² a		last 17	sediment yields	Aare basin				
1810	t/km² a		last 17		Linth basin				
2050	t/km² a		last 17		Lütschine basin				
940	t/km² a		last 17		Melchaa basin				
1390	t/km² a		last 17		Reuss basin				
2400	t/km² a		last 17		Seez basin				
2650	t/km² a		last 17		Rhine basin				
2370	t/km² a		last 17		Rhone basin				
2120	t/km² a		last 17		Adda basin				
1280	t/km² a		last 17		Maggia basin				
1980	t/km² a		last 17		Ticcino basin				
					Eastern Alps				
620	t/km² a		last 17		Iller basin				
1330	t/km² a		last 17		Tiroler Ache basin				
1060	t/km² a		last 17		Weissach basin				
1410	t/km² a		last 17		Inn basin				
1220	t/km² a		last 17		Sarca basin				
				total mechanical denudation	**Swiss Alps**	Schlunegger &			
208	km³		last 17	volume of excavated rock	Rhine basin	Hinderer (2001)			

196	km³		last 17		Rhone basin				
4	km³		last 17		Linth basin				
21.4	km³		last 17		Reuss basin				
10	km³		last 17		Aare basin				
13	km³		last 17		Lütschine basin				
33	km³		last 17		Ticino basin				
0.034	km³/km²	0.017	last 17	sediment yield per area	Rhine basin		last 17	2.00	1.00
0.038	km³/km²	0.019	last 17		Rhone basin		last 17	2.24	1.12
0.006	km³/km²	0.003	last 17	general error 50%	Linth basin		last 17	0.35	0.18
0.026	km³/km²	0.013	last 17	(from Hinderer. 2001)	Reuss basin		last 17	1.53	0.77
0.018	km³/km²	0.009	last 17		Aare basin		last 17	1.06	0.53
0.034	km³/km²	0.017	last 17	max. temporal error	Lütschine basin		last 17	2.00	1.00
0.022	km³/km²	0.011	last 17	<10%; 1 ka	Ticino basin		last 17	1.29	0.65
				(from Hinderer. 2001)					
1.6	m/ka	---	last 15	sediment yield related	Fischenbach basin	Schlunegger	last 15	1.6	---
				to drainage basin-size	**northern Swiss**	et al. (2002)			
4.6	m/ka	---	last 15	effective sediment yield	**Prealps**		last 15	4.6	---
				related to area of					
				active surface erosion					
				15 ka: tentative age of					
				glacial deposits and surface					
				basin averaged	central & southern	Norton			
				denudation rate	**Eastern Alps**	et al. (2011)			
1230	mm/ka	290	0.57 ± 0.13	cosmogenic 10Be	Ahrn		0.57 ± 0.13	1.23	0.29
302	mm/ka	50	2.38 ± 0.39		Antholzer		2.38 ± 0.39	0.3	0.05
469	mm/ka	74	1.54 ± 0.24		Arno		1.54 ± 0.24	0.47	0.07
359	mm/ka	75	2.04 ± 0.43		Avisio		2.04 ± 0.43	0.36	0.08
246	mm/ka	42	2.92 ± 0.5	Minimum	Bergler		2.92 ± 0.5	0.25	0.04
376	mm/ka	70	1.91 ± 0.36	Maximum	Bergler		1.91 ± 0.36	0.38	0.07
436	mm/ka	76	1.71 ± 0.3		Bitto		1.71 ± 0.3	0.44	0.08
1036	mm/ka	230	0.69 ± 0.15		Castello		0.69 ± 0.15	1.04	0.23
480	mm/ka	82	1.51 ± 0.26		di Adame		1.51 ± 0.26	0.48	0.08
760	mm/ka	210	0.97 ± 0.27		di Venina		0.97 ± 0.27	0.76	0.21
325	mm/ka	66	2.31 ± 0.47		Fersina		2.31 ± 0.47	0.33	0.07
1470	mm/ka	340	0.49 ± 0.11		Flagger		0.49 ± 0.11	1.47	0.34

356	mm/ka	57	1.97 ± 0.32		Fusino		1.97 ± 0.32	0.36	0.06
350	mm/ka	110	1.11 ± 0.19	Minimum	Hoeller		1.11 ± 0.19	0.35	0.11
1090	mm/ka	470	0.66 ± 0.28	Maximum	Hoeller		0.66 ± 0.28	1.09	0.47
537	mm/ka	95	1.31 ± 0.23		Krimmler		1.31 ± 0.23	0.54	0.1
214	mm/ka	36	3.36 ± 0.57		Lagorai		3.36 ± 0.57	0.21	0.04
301	mm/ka	63	2.38 ± 0.5		Masino		2.38 ± 0.5	0.3	0.06
548	mm/ka	87	1.3 ± 0.21		Melach		1.3 ± 0.21	0.55	0.09
850	mm/ka	170	0.86 ± 0.17		Muehl		0.86 ± 0.17	0.85	0.17
287	mm/ka	50	2.62 ± 0.45		Nero		2.62 ± 0.45	0.29	0.05
710	mm/ka	130	1.03 ± 0.19		Novate		1.03 ± 0.19	0.71	0.13
660	mm/ka	110	1.09 ± 0.19		Oglio		1.09 ± 0.19	0.66	0.11
530	mm/ka	100	1.35 ± 0.26		Pfitsch		1.35 ± 0.26	0.53	0.1
680	mm/ka	140	1.04 ± 0.21		Pitze		1.04 ± 0.21	0.68	0.14
1100	mm/ka	300	0.65 ± 0.18		Plima		0.65 ± 0.18	1.1	0.3
580	mm/ka	110	1.21 ± 0.22		Schnalz		1.21 ± 0.22	0.58	0.11
240	mm/ka	47	3.31 ± 0.65		Silla		3.31 ± 0.65	0.24	0.05
324	mm/ka	57	2.26 ± 0.4		Talfer		2.26 ± 0.4	0.32	0.06
1240	mm/ka	240	0.57 ± 0.11		Tauern		0.57 ± 0.11	1.24	0.24
168	mm/ka	26	4.3 ± 0.66		val Moena		4.3 ± 0.66	0.17	0.03
519	mm/ka	90	1.39 ± 0.24		Wattem		1.39 ± 0.24	0.52	0.09
730	mm/ka	170	1.04 ± 0.24		Widshoenau		1.04 ± 0.24	0.73	0.17
710	mm/ka	130	1 ± 0.19		Zemm		1 ± 0.19	0.71	0.13
750	mm/ka	150	0.93 ± 0.19		Ziel		0.93 ± 0.19	0.75	0.15
6.5-13	mm/a		last 5	incision rate in-situ produced cosmogenic 10Be max. temporal error: 0.84 ka	Gorge du Diable, **French Western Alps**	Valla et al. (2010)	last 5	6.5-13	
				denudation rate in-situ produced cosmogenic 10Be in stream sediments	**Ecrins-Pelvoux massif. French Western Alps**	Delunel et al. (2010)			
0.38	mm/a	0.07	1.977		Romanche		1.977	0.38	0.07
0.61	mm/a	0.11	1.233		Veneon		1.233	0.61	0.11
0.89	mm/a	0.16	0.846		Upper Romanche		0.846	0.89	0.16
0.99	mm/a	0.21	0.761		Tabuc		0.761	0.99	0.21
0.67	mm/a	0.13	1.131		Saint Pierre		1.131	0.67	0.13
0.8	mm/a	0.14	0.939		Celse Nierre		0.939	0.8	0.14

1.07	mm/a	0.2	0.707			Gyr	0.707	1.07	0.2
0.35	mm/a	0.07	2.142			Roizonne	2.142	0.35	0.07
0.27	mm/a	0.05	2.735			Bonne	2.735	0.27	0.05
0.37	mm/a	0.08	2.045			Upper Bonne	2.045	0.37	0.08
0.63	mm/a	0.13	1.192			Drac	1.192	0.63	0.13
0.57	mm/a	0.11	1.308			Severaisse	1.308	0.57	0.11
4	mm/a	2	last 9-12.5	Bündner schists, flysch		Rhine basin,	Korup &	last 9-12.5	4	2
0.7	mm/a	0.35	last 9-12.5	crystalline rock		**Western Alps**	Schlunegger (2009)	last 9-12.5	0.7	0.35
				mean erosion rate					
				post-glacial sediment					
				volume of valley deposits					
				Time period constrained from					
				late-glacial lake until 12.5 ka					
				and Flims landslide 9.5 ka –					
				valley deposits mostly younger					
				than 9 ka					

Table 6.3-6: Data – short-term scale.

Value	Unit	Uncertainty	Time period	Type of rate?	Location	Reference	Time period	mm/a	Uncertainty
				sediment yield	**Western Alps**	Hinderer (2001)			
480	t/km² a	---	1898-1933	from river-load &	Aare basin		1898-1933	0.18	---
270	t/km² a	---	1964-1993	delta-growth data	Aare basin		1964-1993	0.10	---
890	t/km² a	---	1981-1993		Kander basin		1981-1993	0.33	---
410	t/km² a	---	1911-1979		Linth basin		1911-1979	0.15	---
500	t/km² a	---	1964-1993		Lütschine basin		1964-1993	0.19	---
160	t/km² a	---	1911-1987		Melchaa basin		1911-1987	0.06	---
70	t/km² a	---	1979-1993		Reuss basin		1979-1993	0.03	---
660	t/km² a	---	1911-1989		Rhine basin		1911-1989	0.24	---
380	t/km² a	---	1965-1993		Rhone basin		1965-1993	0.14	---
410	t/km² a	---	1930-1951		Cassarate basin		1930-1951	0.15	---
450	t/km² a	---	1926-1984		Maggia basin		1926-1984	0.17	---
280	t/km² a	---	1932-1986		Ticino basin		1932-1986	0.10	---
					Eastern Alps				
180	t/km² a	---	1931-1979		Ammer basin		1931-1979	0.07	---
190	t/km² a	---	1966-1970		Iller basin		1966-1970	0.07	---
280	t/km² a	---	1926-1979		Tiroler Ache basin		1926-1979	0.10	---
120	t/km² a	---	1955-1965		Weissach basin		1955-1965	0.04	---
280	t/km² a	---	1953-1979		Inn basin		1953-1979	0.10	---
				average	**Swiss Alps**	Schlunegger &			
0.206	mm/a	---	1964-1995	denudation	Aare basin	Hinderer	1964-1995	0.206	---
0.097	mm/a	---	1926-1993	rate from	Albula basin	(2003)	1926-1993	0.097	---
0.141	mm/a	---	1920-1993	suspended-load	Broye basin		1920-1993	0.141	---
0.122	mm/a	---	1984-1995	data	Emme basin		1984-1995	0.122	---
0.129	mm/a	---	1976-1993		Glatt basin		1976-1993	0.129	---
0.103	mm/a	---	1974-1993		Hinterrhein basin		1974-1993	0.103	---
0.091	mm/a	---	1970-1993		Inn basin		1970-1993	0.091	---
0.403	mm/a	---	1981-1993		Kander basin		1981-1993	0.403	---
0.59	mm/a	---	1979-1995		Landquart basin		1979-1995	0.59	---
0.189	mm/a	---	1964-1995		Linth basin		1964-1995	0.189	---
0.176	mm/a	---	1966-1995		Lonza basin		1966-1995	0.176	---
0.294	mm/a	---	1964-1995		Lütschine basin		1964-1995	0.294	---
0.272	mm/a	---	1985-1993		Maggia basin		1985-1993	0.272	---

0.115	mm/a	---	1981-1993		Moesa basin		1981-1993	0.115	---
0.113	mm/a	---	1979-1995		Reuss basin		1979-1995	0.113	---
0.242	mm/a	---	1964-1990		Rhine basin		1964-1990	0.242	---
0.239	mm/a	---	1965-1995		Rhone basin		1965-1995	0.239	---
0.134	mm/a	---	1923-1993		Sarine basin		1923-1993	0.134	---
0.153	mm/a	---	1921-1993		Simme basin		1921-1993	0.153	---
0.201	mm/a	---	1975-1995		Thur basin		1975-1995	0.201	---
0.217	mm/a	---	1979-1995		Ticino basin		1979-1995	0.217	---
0.8	mm/a	---	1965-1993		Visp basin		1965-1993	0.801	---
0.15	mm/a	---	1965-1995		Rhone basin		1965-1995	0.15	---
				denudation	**Western Alps**	Champagnac			
0.056	mm/a	---	1964-1995	rate from	Thur basin	et al. (2009)	1964-1995	0.056	---
0.097	mm/a	---	1964-1995	suspended-load	Linth basin		1964-1995	0.097	---
0.041	mm/a	---	1964-1995	data	Reuss basin		1964-1995	0.041	---
0.02	mm/a	---	1964-1995		Reuss basin		1964-1995	0.02	---
0.098	mm/a	---	1964-1995		Aare basin		1964-1995	0.098	---
0.137	mm/a	---	1964-1995		Lütschine basin		1964-1995	0.137	---
0.022	mm/a	---	1964-1995		Emme basin		1964-1995	0.022	---
0.134	mm/a	---	1964-1995		Lonza basin		1964-1995	0.134	---
0.165	mm/a	---	1964-1995		Arve basin		1964-1995	0.165	---
0.147	mm/a	---	1964-1995		Rhone basin		1964-1995	0.147	---
0.184	mm/a	---	1964-1995		Rhine basin		1964-1995	0.184	---
0.607	mm/a	---	1964-1995		Landquart basin		1964-1995	0.607	---
0.064	mm/a	---	1964-1995		Ticino basin		1964-1995	0.064	---
2000000-5000000	t/a		1915-1960	suspended sediment load	**Swiss Alps** Rhone basin	Loizeau & Dominik (2000)	1915-1960	0.14-0.35	
1000000-2500000	t/a		1960-1994				1960-1994	0.07 0.18	
				bed-load sediment yield	**Dora Baltea basin** **Aosta Valley, Western Alps**	Vezzoli (2004)			
0.21	mm/a	---	1999-2002	denudation rate	Dora baltea at Avise		1999-2002	0.21	---
0.1	mm/a	---	1999-2002		Dora Baltea at Sarre		1999-2002	0.1	---
0.07	mm/a	---	1999-2002		Dora Baltea at Verres		1999-2002	0.07	---
0.07	mm/a	---	1999-2002		Dora Baltea basin		1999-2002	0.07	---
				average	**French Southern Alps,**	Descroix &			

					"terres noires"	Mathys			
9	mm/a	---	1985-1991	soil-loss rate from rugosimeter,	Savournon	(2003)	1985-1991	9	---
8.2	mm/a	---	1987-1990	electronic	Savournon		1987-1990	8.2	---
7	mm/a	---	1985-1991	samplers,	Saint Genis		1985-1991	7	---
6.7	mm/a	---	1987-1990	bottle-siphons,	Saint Genis		1987-1990	6.7	---
5.9	mm/a	---	1983-1993	sediment traps &	Orpierre		1983-1993	5.9	---
3.8	mm/a	---	1989-1992	measurement	Orpierre		1989-1992	3.8	---
16.2	mm/a	---	1990-1991	sticks	Gallands		1990-1991	16.2	---
18.9	mm/a	---	1990-1991		Gallands		1990-1991	18.9	---
8.5	mm/a	---	1989-1992		Etoile		1989-1992	8.5	---
8.7	mm/a	---	1988-1993		Etoile		1988-1993	8.7	---
10.3	mm/a	---	1990-1991		La Vière		1990-1991	10.3	---
1.4	mm/a	---	1988-1990		Thoard		1988-1990	1.4	---
16.5	mm/a	---	1991-1993		Claret		1991-1993	16.5	---
30	mm/a	---	1990-1991		Bonneval		1990-1991	30	---
11	mm/a	---	1986-1990		Laval		1986-1990	11	---
12.1	mm/a	---	1985-1990		Roubine		1985-1990	12.1	---
11.5	mm/a	---	1985-1988		Saint Genis		1985-1988	11.5	---
6.8	mm/a	---	1962-1979		Seignon		1962-1979	6.8	---
30	mm/a	---	1990-1995		Séderon		1990-1995	30	---
7	mm/a	---	1990-1995		Eygalaye		1990-1995	7	---
8	mm/a	---	1990-1995		Vers s/M.		1990-1995	8	---
33	mm/a	---	1990-1995		Izon la B.		1990-1995	33	---
5	mm/a	---	1995-1997		La Motte C		1995-1997	5	---
				mean	**Draix, French Western Alps**	Mathys			
136	t/ha a	60	1985-2000	sediment	Roubine basin	et al. (2003)	1985-2000	5.04	2.2
112	t/ha a	46	1985-2000	yield	Laval basin		1985-2000	4.15	1.7
57	t/ha a	24	1988-2000		Moulin basin		1988-2000	2.11	0.89
0.8	t/ha a	0.7	1988-2000		Brusquet basin		1988-2000	0.03	0.03

Table 6.3-7: Data – Erlenbach (0.74 km²) – events 1986–2007.

Event number	Date Time	Sediment discharge m³	Erosion mm	Uncertainty 50%	Peak Water discharge m³/s	Uncertainty 5%	Precipitation mm	Uncertainty 8%
1	20.10.1986 21:46 20.10.1986 22:55	8.21	0.01	0.01	1.05	0.05	6.8	0.5
2	23.10.1986 03:16 23.10.1986 07:50	8.42	0.01	0.01	0.84	0.04	21.4	1.7
3	28.02.1987 03:58 28.02.1987 07:00	0.1	0.00	0.00	0.35	0.02	9.2	0.7
4	01.03.1987 06:05 01.03.1987 06:21	0.22	0.00	0.00	0.26	0.01	1.2	0.1
5	02.03.1987 11:32 02.03.1987 14:38	0.43	0.00	0.00	0.39	0.02	3.4	0.3
6	28.03.1987 08:04 28.03.1987 09:56	0.83	0.00	0.00	0.21	0.01	7.1	0.6
7	28.03.1987 12:01 28.03.1987 14:28	0.29	0.00	0.00	0.17	0.01	0.7	0.1
8	19.04.1987 16:02 19.04.1987 20:21	1.19	0.00	0.00	0.47	0.02	3.7	0.3
9	20.04.1987 05:11 20.04.1987 14:08	23.87	0.03	0.02	0.69	0.03	19.2	1.5
10	20.04.1987 15:30 21.04.1987 01:18	5.9	0.01	0.00	0.66	0.03	28.2	2.3
11	24.04.1987 17:13 24.04.1987 18:16	0.03	0.00	0.00	0.37	0.02	0	0.0
12	25.04.1987 16:17 25.04.1987 17:48	0.02	0.00	0.00	0.36	0.02	0	0.0
13	26.04.1987 13:50 26.04.1987 18:04	0.86	0.00	0.00	0.41	0.02	0	0.0
14	28.04.1987 15:03 28.04.1987 18:18	0.89	0.00	0.00	0.39	0.02	0	0.0
15	29.04.1987 13:57 29.04.1987 18:45	1.42	0.00	0.00	0.43	0.02	0	0.0
16	30.04.1987 15:41 30.04.1987 15:47	0.01	0.00	0.00	0.31	0.02	0	0.0
17	01.05.1987 15:33 01.05.1987 15:39	0.03	0.00	0.00	0.32	0.02	0	0.0
18	02.05.1987 14:05 02.05.1987 17:03	0.11	0.00	0.00	0.35	0.02	0.5	0.0
19	02.05.1987 19:31 02.05.1987 20:03	0.06	0.00	0.00	0.34	0.02	0.1	0.0
20	03.05.1987 12:20 03.05.1987 12:26	0.02	0.00	0.00	0.29	0.01	0.4	0.0
21	10.05.1987 22:17 11.05.1987 03:16	9.42	0.01	0.01	0.63	0.03	16.3	1.3
22	27.05.1987 14:29 27.05.1987 16:27	1.99	0.00	0.00	0.52	0.03	4.1	0.3
23	31.05.1987 17:57 31.05.1987 21:35	9.39	0.01	0.01	0.76	0.04	9.2	0.7
24	01.06.1987 00:34 01.06.1987 00:58	0.11	0.00	0.00	0.35	0.02	0.2	0.0

	03.06.1987 20:48							
25	03.06.1987 21:59	1.01	0.00	0.00	0.42	0.02	2.1	0.2
	04.06.1987 04:15							
26	04.06.1987 05:38	1.07	0.00	0.00	0.42	0.02	1.6	0.1
	04.06.1987 14:30							
27	04.06.1987 17:55	3.22	0.00	0.00	0.50	0.03	8.6	0.7
	05.06.1987 01:57							
28	05.06.1987 03:26	0.92	0.00	0.00	0.46	0.02	2.5	0.2
	08.06.1987 07:07							
29	08.06.1987 09:26	1.56	0.00	0.00	0.49	0.02	7.2	0.6
	09.06.1987 01:46							
30	09.06.1987 02:36	0.2	0.00	0.00	0.40	0.02	0.4	0.0
	15.06.1987 08:34							
31	15.06.1987 13:24	151.68	0.20	0.10	1.40	0.07	26.9	2.2
	15.06.1987 15:59							
32	15.06.1987 18:38	16.18	0.02	0.01	0.88	0.04	13.2	1.1
	15.06.1987 19:46							
33	16.06.1987 01:06	2.56	0.00	0.00	0.65	0.03	21.3	1.7
	18.06.1987 04:54							
34	18.06.1987 07:19	3.85	0.01	0.00	0.74	0.04	13.8	1.1
	18.06.1987 18:49							
35	18.06.1987 19:35	0.13	0.00	0.00	0.53	0.03	2.1	0.2
	18.06.1987 20:17							
36	18.06.1987 20:52	0.05	0.00	0.00	0.44	0.02	1.6	0.1
	24.06.1987 18:13							
37	24.06.1987 19:05	3.47	0.00	0.00	0.83	0.04	3.7	0.3
	24.06.1987 22:47							
38	25.06.1987 00:08	3.7	0.01	0.00	0.78	0.04	4	0.3
	25.06.1987 03:43							
39	25.06.1987 05:09	0.23	0.00	0.00	0.48	0.02	4.1	0.3
	02.07.1987 21:20							
40	02.07.1987 23:23	151.91	0.21	0.10	4.07	0.20	8.4	0.7
	07.07.1987 21:28							
41	07.07.1987 23:21	68.26	0.09	0.05	1.89	0.09	14.6	1.2
	09.07.1987 02:18							
42	09.07.1987 04:45	442.79	0.60	0.30	4.13	0.21	40.5	3.2
	27.07.1987 20:42							
43	28.07.1987 01:22	13.79	0.02	0.01	1.11	0.06	26.2	2.1
	31.07.1987 01:25							
44	31.07.1987 01:55	1.38	0.00	0.00	0.88	0.04	2.4	0.2
	05.08.1987 06:11							
45	05.08.1987 06:59	0.39	0.00	0.00	0.71	0.04	0.6	0.0
	24.08.1987 21:46							
46	25.08.1987 00:08	19.19	0.03	0.01	1.05	0.05	15.7	1.3
	25.08.1987 02:15							
47	25.08.1987 03:29	2.84	0.00	0.00	0.73	0.04	5.8	0.5
	25.08.1987 06:57							
48	25.08.1987 08:52	4.63	0.01	0.00	0.78	0.04	10.6	0.8
	25.08.1987 10:05							
49	25.08.1987 10:50	2.1	0.00	0.00	0.79	0.04	2.8	0.2
	05.09.1987 22:29							
50	05.09.1987 22:58	1.51	0.00	0.00	0.76	0.04	0.7	0.1
	16.11.1987 08:48							

51	16.11.1987 10:43	5.11	0.01	0.00	0.83	0.04	8.7	0.7
52	17.12.1987 19:55 17.12.1987 23:38	1.97	0.00	0.00	0.47	0.02	2.2	0.2
53	18.12.1987 03:28 18.12.1987 05:42	0.96	0.00	0.00	0.47	0.02	1.3	0.1
54	19.12.1987 00:20 19.12.1987 04:57	62.27	0.08	0.04	1.36	0.07	21.9	1.8
55	19.12.1987 07:41 19.12.1987 09:09	5.91	0.01	0.00	0.85	0.04	4.8	0.4
56	08.04.1988 06:41 08.04.1988 06:47	0.06	0.00	0.00	0.18	0.01	0.1	0.0
57	09.04.1988 23:48 10.04.1988 00:54	0.13	0.00	0.00	0.47	0.02	1.7	0.1
58	13.04.1988 17:24 13.04.1988 18:48	0.2	0.00	0.00	0.28	0.01	0.9	0.1
59	16.04.1988 16:05 16.04.1988 17:33	0.01	0.00	0.00	0.39	0.02	0	0.0
60	19.04.1988 16:35 19.04.1988 17:56	0.07	0.00	0.00	0.42	0.02	0	0.0
61	20.04.1988 15:16 20.04.1988 18:26	0.06	0.00	0.00	0.46	0.02	1.5	0.1
62	01.05.1988 15:14 01.05.1988 17:07	0.06	0.00	0.00	0.44	0.02	0	0.0
63	02.05.1988 14:38 02.05.1988 16:03	0.03	0.00	0.00	0.44	0.02	0	0.0
64	10.05.1988 22:25 11.05.1988 00:36	1.69	0.00	0.00	0.60	0.03	5.7	0.5
65	15.05.1988 19:48 15.05.1988 22:25	11.34	0.02	0.01	0.84	0.04	14.5	1.2
66	20.05.1988 12:07 20.05.1988 13:15	0.26	0.00	0.00	0.49	0.02	2.7	0.2
67	26.05.1988 13:27 26.05.1988 14:18	1.74	0.00	0.00	0.74	0.04	0.9	0.1
68	04.06.1988 15:29 04.06.1988 16:26	0.84	0.00	0.00	0.58	0.03	1.8	0.1
69	04.06.1988 20:58 04.06.1988 22:12	0.29	0.00	0.00	0.50	0.03	2.6	0.2
70	14.06.1988 18:30 14.06.1988 19:50	4.45	0.01	0.00	0.80	0.04	7.1	0.6
71	03.07.1988 07:31 03.07.1988 09:49	8.99	0.01	0.01	0.93	0.05	14.5	1.2
72	14.07.1988 02:27 14.07.1988 04:25	8.19	0.01	0.01	1.01	0.05	5.4	0.4
73	27.07.1988 15:19 27.07.1988 16:13	10.75	0.01	0.01	1.30	0.07	2.9	0.2
74	20.08.1988 07:59 20.08.1988 08:27	0.19	0.00	0.00	0.67	0.03	0	0.0
75	20.08.1988 11:11 20.08.1988 13:30	15.44	0.02	0.01	1.18	0.06	16.6	1.3
76	29.08.1988 01:47 29.08.1988 01:59	0.23	0.00	0.00	0.75	0.04	0	0.0
77	29.08.1988 02:30 29.08.1988 03:08	0.01	0.00	0.00	0.86	0.04	1.3	0.1

	05.10.1988 19:07							
78	05.10.1988 20:09	2.31	0.00	0.00	0.98	0.05	5.7	0.5
	10.10.1988 05:21							
79	10.10.1988 07:11	4.92	0.01	0.00	1.01	0.05	9.5	0.8
	10.10.1988 09:08							
80	10.10.1988 09:47	1.06	0.00	0.00	0.81	0.04	0.5	0.0
	13.11.1988 15:11							
81	13.11.1988 15:30	0.06	0.00	0.00	0.60	0.03	0.3	0.0
	05.12.1988 04:12							
82	05.12.1988 05:53	2.12	0.00	0.00	0.87	0.04	4.8	0.4
	05.12.1988 23:21							
83	06.12.1988 00:23	2.2	0.00	0.00	0.92	0.05	7.4	0.6
	10.05.1989 19:35							
84	10.05.1989 19:53	0.03	0.00	0.00	0.60	0.03	0.6	0.0
	01.06.1989 16:49							
85	01.06.1989 18:28	3.84	0.01	0.00	0.91	0.05	9.7	0.8
	02.07.1989 14:57							
86	02.07.1989 16:36	4.89	0.01	0.00	0.98	0.05	7.7	0.6
	27.07.1989 20:19							
87	27.07.1989 21:53	16.6	0.02	0.01	1.24	0.06	3.2	0.3
	31.07.1989 10:42							
88	31.07.1989 13:11	0.71	0.00	0.00	0.67	0.03	8.3	0.7
	31.07.1989 23:51							
89	01.08.1989 00:38	4.62	0.01	0.00	0.87	0.04	3.7	0.3
	01.08.1989 01:00							
90	01.08.1989 01:23	0.32	0.00	0.00	0.76	0.04	0.1	0.0
	01.08.1989 03:56							
91	01.08.1989 09:16	54.53	0.07	0.04	1.24	0.06	44.7	3.6
	01.08.1989 10:59							
92	01.08.1989 11:06	0.05	0.00	0.00	0.81	0.04	0	0.0
	08.08.1989 10:51							
93	08.08.1989 12:26	2.52	0.00	0.00	1.06	0.05	7.5	0.6
	08.08.1989 16:01							
94	08.08.1989 16:30	0.39	0.00	0.00	0.82	0.04	2.2	0.2
	14.08.1989 16:22							
95	14.08.1989 17:05	11.47	0.02	0.01	1.29	0.06	0.3	0.0
	27.08.1989 12:38							
96	27.08.1989 13:50	2.45	0.00	0.00	0.93	0.05	5.6	0.4
	27.08.1989 14:59							
97	27.08.1989 17:30	10.04	0.01	0.01	1.06	0.05	15.3	1.2
	27.08.1989 22:31							
98	27.08.1989 22:51	0.22	0.00	0.00	0.81	0.04	2.7	0.2
	28.08.1989 00:57							
99	28.08.1989 03:27	3.58	0.00	0.00	1.01	0.05	10.1	0.8
	28.08.1989 04:54							
100	28.08.1989 07:20	3.24	0.00	0.00	0.99	0.05	12.5	1.0
	14.10.1989 19:48							
101	14.10.1989 22:21	0.01	0.00	0.00	0.67	0.03	9.9	0.8
	19.12.1989 05:04							
102	19.12.1989 07:14	0.81	0.00	0.00	0.66	0.03	4.3	0.3
	14.02.1990 06:41							
103	14.02.1990 07:02	0.03	0.00	0.00	0.54	0.03	1	0.1
	15.02.1990 03:41							

104	15.02.1990 13:55	7.83	0.01	0.01	1.11	0.06	21.9	1.8
105	23.03.1990 04:49 23.03.1990 06:45	3.66	0.00	0.00	0.74	0.04	13.8	1.1
106	13.05.1990 19:26 13.05.1990 21:22	30.12	0.04	0.02	1.24	0.06	11.5	0.9
107	14.05.1990 21:02 14.05.1990 21:28	2.99	0.00	0.00	0.93	0.05	0.1	0.0
108	19.05.1990 16:34 19.05.1990 20:57	137.17	0.19	0.09	2.52	0.13	25.5	2.0
109	22.05.1990 23:49 23.05.1990 00:04	0.07	0.00	0.00	0.25	0.01	0.1	0.0
110	24.05.1990 21:53 24.05.1990 22:21	0.52	0.00	0.00	0.56	0.03	0.5	0.0
111	25.05.1990 06:54 25.05.1990 10:39	27.37	0.04	0.02	1.15	0.06	21.1	1.7
112	08.06.1990 08:00 08.06.1990 10:43	13.24	0.02	0.01	1.09	0.05	17.7	1.4
113	01.07.1990 06:11 01.07.1990 06:37	1.66	0.00	0.00	0.78	0.04	0.5	0.0
114	05.07.1990 17:24 05.07.1990 19:02	15.34	0.02	0.01	1.13	0.06	10	0.8
115	29.07.1990 21:15 29.07.1990 22:50	45.9	0.06	0.03	1.30	0.07	8	0.6
116	06.08.1990 15:37 06.08.1990 17:56	68.74	0.09	0.05	1.84	0.09	24.4	2.0
117	17.08.1990 07:32 17.08.1990 08:50	7.72	0.01	0.01	0.96	0.05	6.8	0.5
118	23.09.1990 05:07 23.09.1990 09:43	19.18	0.03	0.01	1.08	0.05	33.2	2.7
119	24.09.1990 04:00 24.09.1990 07:15	6.9	0.01	0.00	1.04	0.05	11.9	1.0
120	29.10.1990 08:07 29.10.1990 08:35	0.65	0.00	0.00	0.76	0.04	1.2	0.1
121	31.10.1990 12:30 31.10.1990 13:24	0.26	0.00	0.00	0.60	0.03	2.8	0.2
122	11.11.1990 16:47 11.11.1990 19:09	3.81	0.01	0.00	0.81	0.04	8.6	0.7
123	20.03.1991 02:25 20.03.1991 07:08	6.6	0.01	0.00	0.81	0.04	11.4	0.9
124	03.06.1991 07:17 03.06.1991 09:42	2.01	0.00	0.00	0.68	0.03	8.1	0.6
125	08.06.1991 07:58 08.06.1991 16:01	6.3	0.01	0.00	0.81	0.04	6.3	0.5
126	10.06.1991 03:56 10.06.1991 04:02	0.03	0.00	0.00	0.55	0.03	0.2	0.0
127	16.06.1991 12:55 16.06.1991 13:58	0.41	0.00	0.00	0.63	0.03	4.4	0.4
128	16.06.1991 19:51 16.06.1991 20:15	0.28	0.00	0.00	0.63	0.03	0.5	0.0
129	17.06.1991 07:20 17.06.1991 08:58	6.13	0.01	0.00	0.95	0.05	6.5	0.5
130	26.06.1991 14:55 26.06.1991 15:21	5.04	0.01	0.00	1.19	0.06	0.4	0.0

	27.06.1991 11:46						
131	27.06.1991 12:23	0.16	0.00	0.00	0.56	0.03	0.2	0.0
	28.06.1991 22:38						
132	29.06.1991 00:02	2.34	0.00	0.00	0.71	0.04	4.8	0.4
	12.07.1991 17:41						
133	12.07.1991 18:54	38.95	0.05	0.03	1.72	0.09	7.5	0.6
	14.07.1991 09:56						
134	14.07.1991 10:02	0.05	0.00	0.00	0.33	0.02	0.1	0.0
	14.07.1991 23:49						
135	14.07.1991 23:58	0.04	0.00	0.00	0.48	0.02	0.4	0.0
	24.07.1991 13:53						
136	24.07.1991 14:16	5.87	0.01	0.00	0.99	0.05	0.2	0.0
	26.07.1991 07:53						
137	26.07.1991 08:57	4.84	0.01	0.00	0.78	0.04	2.4	0.2
	11.09.1991 20:01						
138	11.09.1991 20:09	0.07	0.00	0.00	0.49	0.02	0.3	0.0
	23.09.1991 05:40						
139	23.09.1991 06:41	0.57	0.00	0.00	0.53	0.03	1.1	0.1
	27.09.1991 05:20						
140	27.09.1991 05:51	0.21	0.00	0.00	0.52	0.03	1.4	0.1
	30.09.1991 13:27						
141	30.09.1991 13:50	0.17	0.00	0.00	0.46	0.02	0.5	0.0
	22.12.1991 05:08						
142	22.12.1991 15:13	2.67	0.00	0.00	1.32	0.07	13.3	1.1
	15.03.1992 22:18						
143	15.03.1992 22:48	0.08	0.00	0.00	0.56	0.03	1.6	0.1
	23.04.1992 08:51						
144	23.04.1992 13:08	12.97	0.02	0.01	0.89	0.04	19.5	1.6
	28.04.1992 15:48						
145	28.04.1992 20:46	11.21	0.02	0.01	0.87	0.04	12.7	1.0
	26.05.1992 20:40						
146	26.05.1992 21:13	0.33	0.00	0.00	0.55	0.03	0.7	0.1
	10.06.1992 15:03						
147	10.06.1992 15:23	0.17	0.00	0.00	0.47	0.02	0.6	0.0
	11.06.1992 07:56						
148	11.06.1992 11:09	17.81	0.02	0.01	0.93	0.05	13.1	1.0
	21.08.1992 17:54						
149	21.08.1992 21:20	169.85	0.23	0.11	4.46	0.22	15.3	1.2
	30.08.1992 00:27						
150	30.08.1992 01:10	0.89	0.00	0.00	0.34	0.02	2.1	0.2
	31.08.1992 19:24						
151	31.08.1992 23:03	36.94	0.05	0.02	0.96	0.05	17.8	1.4
	04.09.1992 07:43						
152	04.09.1992 11:11	2.24	0.00	0.00	0.66	0.03	3.5	0.3
	04.09.1992 12:25						
153	04.09.1992 13:40	2.39	0.00	0.00	0.71	0.04	2.5	0.2
	18.09.1992 22:31						
154	18.09.1992 22:37	0.05	0.00	0.00	0.33	0.02	0	0.0
	25.10.1992 23:34						
155	26.10.1992 00:11	0.14	0.00	0.00	0.47	0.02	0.4	0.0
	28.10.1992 19:39						
156	28.10.1992 22:20	10.44	0.01	0.01	0.81	0.04	6.9	0.6
	12.12.1992 11:19						

157	12.12.1992 11:25	0.07	0.00	0.00	0.55	0.03	0.4	0.0
158	12.01.1993 17:05 12.01.1993 18:49	1.52	0.00	0.00	0.43	0.02	6.4	0.5
159	17.03.1993 18:40 17.03.1993 18:51	0.07	0.00	0.00	0.14	0.01	0	0.0
160	06.04.1993 08:47 06.04.1993 13:23	1.21	0.00	0.00	0.55	0.03	12	1.0
161	03.05.1993 18:08 03.05.1993 18:14	0.05	0.00	0.00	0.46	0.02	0.4	0.0
162	30.05.1993 18:38 30.05.1993 20:02	1.49	0.00	0.00	0.61	0.03	0.5	0.0
163	02.06.1993 15:55 02.06.1993 16:18	0.08	0.00	0.00	0.34	0.02	0.2	0.0
164	11.06.1993 18:03 11.06.1993 22:26	59.68	0.08	0.04	1.33	0.07	36.4	2.9
165	17.06.1993 09:48 17.06.1993 10:45	14.28	0.02	0.01	1.19	0.06	2.8	0.2
166	17.06.1993 13:57 17.06.1993 14:22	2.37	0.00	0.00	0.82	0.04	0.0	0.0
167	23.06.1993 17:58 23.06.1993 18:32	0.36	0.00	0.00	0.64	0.03	0.6	0.0
168	05.07.1993 21:20 06.07.1993 00:23	36.63	0.05	0.02	1.39	0.07	24.8	2.0
169	06.07.1993 01:47 06.07.1993 06:06	85.49	0.12	0.06	1.84	0.09	24.8	2.0
170	10.07.1993 21:59 11.07.1993 05:14	4.92	0.01	0.00	0.82	0.04	23.3	1.9
171	15.07.1993 02:40 15.07.1993 03:04	0.21	0.00	0.00	0.56	0.03	0	0.0
172	17.07.1993 17:22 17.07.1993 22:46	113.77	0.15	0.08	3.63	0.18	19.9	1.6
173	18.07.1993 04:12 18.07.1993 05:35	0.98	0.00	0.00	0.46	0.02	0	0.0
174	18.07.1993 18:08 18.07.1993 20:52	96.12	0.13	0.06	2.46	0.12	21.1	1.7
175	31.07.1993 05:03 31.07.1993 07:22	64.66	0.09	0.04	1.80	0.09	21.7	1.7
176	10.08.1993 16:02 10.08.1993 17:02	6.36	0.01	0.00	1.48	0.07	4.5	0.4
177	27.08.1993 18:04 27.08.1993 20:44	4.57	0.01	0.00	0.80	0.04	11.7	0.9
178	04.09.1993 04:55 04.09.1993 08:29	6.12	0.01	0.00	0.94	0.05	14	1.1
179	13.09.1993 22:43 13.09.1993 23:40	2.67	0.00	0.00	0.77	0.04	2.6	0.2
180	08.10.1993 16:22 08.10.1993 17:18	2.28	0.00	0.00	0.71	0.04	2.6	0.2
181	08.10.1993 21:34 09.10.1993 03:58	11.73	0.02	0.01	0.88	0.04	27.4	2.2
182	14.10.1993 08:31 14.10.1993 08:48	0.06	0.00	0.00	0.52	0.03	0.4	0.0
183	06.11.1993 18:30 06.11.1993 19:43	2.21	0.00	0.00	0.73	0.04	7.1	0.6

	09.12.1993 08:01							
184	09.12.1993 08:27	0.04	0.00	0.00	0.12	0.01	0	0.0
	19.12.1993 23:27							
185	20.12.1993 10:27	13.06	0.02	0.01	0.91	0.05	5.3	0.4
	21.12.1993 08:34							
186	21.12.1993 10:54	9.39	0.01	0.01	0.85	0.04	7.7	0.6
	25.01.1994 22:29							
187	25.01.1994 22:51	0.07	0.00	0.00	0.46	0.02	0.9	0.1
	26.03.1994 02:51							
188	26.03.1994 09:54	44.52	0.06	0.03	1.21	0.06	42.9	3.4
	25.04.1994 18:54							
189	25.04.1994 21:52	12.3	0.02	0.01	1.27	0.06	20.7	1.7
	19.05.1994 01:56							
190	19.05.1994 12:25	20.04	0.03	0.01	1.32	0.07	40.3	3.2
	24.05.1994 20:51							
191	24.05.1994 22:15	1.83	0.00	0.00	0.82	0.04	5.9	0.5
	26.05.1994 23:28							
192	27.05.1994 00:12	3.03	0.00	0.00	0.91	0.05	1.8	0.1
	29.05.1994 07:16							
193	29.05.1994 08:54	2.98	0.00	0.00	0.97	0.05	4.4	0.4
	09.06.1994 01:01							
194	09.06.1994 03:06	2.59	0.00	0.00	0.87	0.04	10.1	0.8
	09.06.1994 06:19							
195	09.06.1994 07:38	1.89	0.00	0.00	0.87	0.04	6.4	0.5
	06.07.1994 21:31							
196	06.07.1994 22:59	19.6	0.03	0.01	1.61	0.08	3.1	0.2
	08.08.1994 17:23							
197	08.08.1994 19:24	40.29	0.05	0.03	1.86	0.09	15	1.2
	10.08.1994 21:49							
198	10.08.1994 22:20	0.23	0.00	0.00	0.43	0.02	0.9	0.1
	13.08.1994 19:53							
199	13.08.1994 22:08	6.35	0.01	0.00	0.81	0.04	11.3	0.9
	17.08.1994 23:56							
200	18.08.1994 00:08	0.09	0.00	0.00	0.44	0.02	0.6	0.0
	18.08.1994 02:19							
201	18.08.1994 02:25	0.04	0.00	0.00	0.47	0.02	0.1	0.0
	18.08.1994 05:22							
202	18.08.1994 05:40	0.15	0.00	0.00	0.54	0.03	0	0.0
	02.09.1994 03:27							
203	02.09.1994 04:34	2.09	0.00	0.00	0.82	0.04	3.7	0.3
	08.09.1994 18:09							
204	08.09.1994 20:47	30.39	0.04	0.02	1.41	0.07	16.7	1.3
	14.09.1994 18:55							
205	14.09.1994 19:35	1.11	0.00	0.00	0.81	0.04	1.9	0.2
	14.09.1994 21:42							
206	14.09.1994 22:09	0.3	0.00	0.00	0.66	0.03	2.1	0.2
	15.09.1994 21:33							
207	15.09.1994 22:36	0.6	0.00	0.00	0.63	0.03	3.0	0.2
	10.12.1994 06:20							
208	10.12.1994 06:36	0.2	0.00	0.00	0.42	0.02	0.3	0.0
	28.12.1994 04:45							
209	28.12.1994 15:08	41.65	0.06	0.03	0.89	0.04	35.2	2.8
	25.01.1995 13:37							

210	25.01.1995 14:53	0.62	0.00	0.00	0.46	0.02	0.2	0.0
211	16.02.1995 04:12 16.02.1995 04:25	0.08	0.00	0.00	0.45	0.02	0	0.0
212	18.03.1995 08:17 18.03.1995 09:43	0.54	0.00	0.00	0.53	0.03	5	0.4
213	25.04.1995 17:31 25.04.1995 23:52	16.18	0.02	0.01	0.72	0.04	34.7	2.8
214	13.05.1995 04:36 13.05.1995 05:47	0.27	0.00	0.00	0.53	0.03	2.2	0.2
215	18.05.1995 20:02 18.05.1995 21:30	1.54	0.00	0.00	0.65	0.03	6.2	0.5
216	30.05.1995 17:37 30.05.1995 21:27	25.34	0.03	0.02	1.22	0.06	20.7	1.7
217	01.06.1995 13:57 01.06.1995 16:23	0.47	0.00	0.00	0.61	0.03	4	0.3
218	11.07.1995 21:57 11.07.1995 22:23	4.04	0.01	0.00	1.16	0.06	9.5	0.8
219	11.07.1995 22:38 12.07.1995 00:30	47.43	0.06	0.03	1.86	0.09	12.6	1.0
220	13.07.1995 17:59 13.07.1995 19:04	23.52	0.03	0.02	2.06	0.10	3.8	0.3
221	14.07.1995 15:21 14.07.1995 19:29	461.88	0.62	0.31	9.75	0.49	18.9	1.5
222	22.07.1995 22:19 22.07.1995 23:16	1.51	0.00	0.00	0.32	0.02	0.4	0.0
223	31.07.1995 17:18 31.07.1995 18:56	48.13	0.07	0.03	1.80	0.09	0.9	0.1
224	08.08.1995 23:04 09.08.1995 03:31	55.31	0.07	0.04	0.83	0.04	21.9	1.8
225	12.08.1995 16:18 12.08.1995 16:27	0.11	0.00	0.00	0.70	0.04	0	0.0
226	13.08.1995 10:17 13.08.1995 12:09	63.27	0.09	0.04	1.84	0.09	7.6	0.6
227	14.08.1995 04:28 14.08.1995 05:11	2.5	0.00	0.00	0.65	0.03	2.0	0.2
228	20.08.1995 09:15 20.08.1995 09:45	1.04	0.00	0.00	0.45	0.02	0	0.0
229	20.08.1995 15:04 20.08.1995 16:58	32.62	0.04	0.02	1.18	0.06	3.4	0.3
230	28.08.1995 02:15 28.08.1995 07:08	110.75	0.15	0.07	1.32	0.07	30.3	2.4
231	29.08.1995 02:46 29.08.1995 14:08	44.44	0.06	0.03	0.78	0.04	45.3	3.6
232	07.09.1995 17:33 07.09.1995 18:23	0.46	0.00	0.00	0.51	0.03	1.8	0.1
233	13.09.1995 18:22 13.09.1995 18:28	0.06	0.00	0.00	0.49	0.02	0	0.0
234	28.09.1995 00:10 28.09.1995 03:45	5.68	0.01	0.00	0.52	0.03	7.2	0.6
235	01.11.1995 23:34 02.11.1995 01:57	3.06	0.00	0.00	0.50	0.03	15.8	1.3
236	24.12.1995 22:49 25.12.1995 00:17	0.55	0.00	0.00	0.48	0.02	2	0.2

237	25.12.1995 03:28 25.12.1995 04:03	0.03	0.00	0.00	0.38	0.02	0.5	0.0
238	25.12.1995 13:29 25.12.1995 17:51	2.76	0.00	0.00	0.51	0.03	11.9	1.0
239	25.12.1995 22:13 25.12.1995 23:17	0.69	0.00	0.00	0.49	0.02	2.9	0.2
240	26.12.1995 00:58 26.12.1995 01:04	0.01	0.00	0.00	0.35	0.02	0.6	0.0
241	23.03.1996 04:26 23.03.1996 08:29	0.46	0.00	0.00	0.39	0.02	0.2	0.0
242	27.03.1996 03:11 27.03.1996 04:30	0.15	0.00	0.00	0.36	0.02	0.5	0.0
243	27.03.1996 08:36 27.03.1996 08:45	0.19	0.00	0.00	0.31	0.02	0.1	0.0
244	08.05.1996 19:14 08.05.1996 20:43	69.54	0.09	0.05	1.51	0.08	3.9	0.3
245	12.05.1996 19:31 12.05.1996 22:08	3.46	0.00	0.00	0.53	0.03	8	0.6
246	19.05.1996 20:04 20.05.1996 01:19	28.27	0.04	0.02	0.81	0.04	20.9	1.7
247	25.05.1996 19:13 25.05.1996 20:00	1.38	0.00	0.00	0.43	0.02	1.2	0.1
248	27.05.1996 08:21 27.05.1996 08:47	0.43	0.00	0.00	0.34	0.02	0.3	0.0
249	27.05.1996 17:16 27.05.1996 17:32	0.26	0.00	0.00	0.34	0.02	0.8	0.1
250	27.05.1996 21:40 28.05.1996 00:13	3.36	0.00	0.00	0.43	0.02	6.5	0.5
251	28.05.1996 02:56 28.05.1996 08:28	12.58	0.02	0.01	0.59	0.03	8.9	0.7
252	10.06.1996 20:18 10.06.1996 20:28	0.2	0.00	0.00	0.36	0.02	0.1	0.0
253	12.06.1996 20:01 12.06.1996 21:20	18.21	0.02	0.01	1.14	0.06	3	0.2
254	22.06.1996 07:05 22.06.1996 07:46	0.43	0.00	0.00	0.30	0.02	1.3	0.1
255	02.07.1996 17:34 02.07.1996 19:11	5.61	0.01	0.00	0.47	0.02	3.9	0.3
256	05.07.1996 17:10 05.07.1996 18:07	1.5	0.00	0.00	0.44	0.02	1.8	0.1
257	08.07.1996 00:55 08.07.1996 19:02	143.55	0.19	0.10	1.31	0.07	110	8.8
258	09.07.1996 03:01 09.07.1996 03:28	0.44	0.00	0.00	0.60	0.03	0.3	0.0
259	10.07.1996 19:24 10.07.1996 21:14	4.51	0.01	0.00	0.86	0.04	7.7	0.6
260	10.07.1996 22:57 11.07.1996 00:17	1.53	0.00	0.00	0.62	0.03	3.4	0.3
261	30.07.1996 06:39 30.07.1996 07:32	3.86	0.01	0.00	1.07	0.05	1.1	0.1
262	30.07.1996 08:46 30.07.1996 09:26	1.44	0.00	0.00	0.68	0.03	0.2	0.0
	03.08.1996 13:25							

263	03.08.1996 14:58	11.74	0.02	0.01	1.10	0.06	8.7	0.7
264	11.08.1996 22:17 11.08.1996 22:52	1.01	0.00	0.00	0.74	0.04	1	0.1
265	12.08.1996 02:37 12.08.1996 03:33	1.17	0.00	0.00	0.76	0.04	2.8	0.2
266	27.08.1996 20:30 27.08.1996 21:15	0.61	0.00	0.00	0.56	0.03	2.7	0.2
267	28.08.1996 02:46 28.08.1996 03:21	0.68	0.00	0.00	0.58	0.03	1.2	0.1
268	28.08.1996 04:57 28.08.1996 07:11	13.03	0.02	0.01	0.88	0.04	10.3	0.8
269	21.10.1996 18:46 21.10.1996 20:09	16.29	0.02	0.01	1.07	0.05	3.6	0.3
270	26.10.1996 06:32 26.10.1996 08:12	12.02	0.02	0.01	0.81	0.04	7	0.6
271	07.11.1996 18:41 07.11.1996 21:36	34.5	0.05	0.02	0.99	0.05	16.6	1.3
272	26.02.1997 12:12 26.02.1997 14:16	0.88	0.00	0.00	0.59	0.03	4.5	0.4
273	28.03.1997 11:35 28.03.1997 13:34	1.43	0.00	0.00	0.66	0.03	8.1	0.6
274	26.04.1997 06:58 26.04.1997 08:57	1.17	0.00	0.00	0.47	0.02	2.8	0.2
275	27.04.1997 04:10 27.04.1997 05:46	2	0.00	0.00	0.50	0.03	4.2	0.3
276	29.04.1997 01:08 29.04.1997 02:04	2.36	0.00	0.00	0.61	0.03	0.1	0.0
277	29.04.1997 03:00 29.04.1997 04:13	1.67	0.00	0.00	0.59	0.03	2.7	0.2
278	29.04.1997 18:12 29.04.1997 20:19	1.86	0.00	0.00	0.62	0.03	3.2	0.3
279	07.06.1997 23:17 08.06.1997 00:34	17.22	0.02	0.01	1.21	0.06	5.5	0.4
280	16.06.1997 17:40 16.06.1997 18:55	30.19	0.04	0.02	1.26	0.06	2.7	0.2
281	22.06.1997 06:42 22.06.1997 08:21	1.69	0.00	0.00	0.50	0.03	5.7	0.5
282	05.07.1997 17:08 05.07.1997 23:15	6.09	0.01	0.00	0.72	0.04	17.9	1.4
283	06.07.1997 02:00 06.07.1997 07:43	4.59	0.01	0.00	0.93	0.05	4.8	0.4
284	06.07.1997 21:06 06.07.1997 22:10	0.33	0.00	0.00	0.51	0.03	0.7	0.1
285	18.07.1997 01:56 18.07.1997 02:35	3.56	0.00	0.00	0.91	0.05	0.3	0.0
286	18.07.1997 08:32 18.07.1997 10:02	16.96	0.02	0.01	1.22	0.06	7	0.6
287	18.07.1997 18:26 18.07.1997 19:26	2.02	0.00	0.00	0.74	0.04	3.1	0.2
288	19.07.1997 00:27 19.07.1997 01:11	0.54	0.00	0.00	0.67	0.03	0.8	0.1
289	25.07.1997 21:46 25.07.1997 22:23	0.59	0.00	0.00	0.54	0.03	1.9	0.2

290	26.07.1997 03:38 26.07.1997 03:52	0.13	0.00	0.00	0.49	0.02	0.5	0.0
291	26.07.1997 06:24 26.07.1997 09:02	3.33	0.00	0.00	0.77	0.04	9.2	0.7
292	25.08.1997 19:37 25.08.1997 20:27	2.85	0.00	0.00	0.81	0.04	4.3	0.3
293	28.08.1997 14:49 28.08.1997 18:56	27.75	0.04	0.02	1.34	0.07	26.6	2.1
294	12.09.1997 22:42 13.09.1997 01:00	222.72	0.30	0.15	3.12	0.16	23.1	1.8
295	10.10.1997 23:34 10.10.1997 23:42	0.06	0.00	0.00	0.38	0.02	0	0.0
296	12.10.1997 03:28 12.10.1997 04:08	0.89	0.00	0.00	0.57	0.03	1.4	0.1
297	12.10.1997 05:34 12.10.1997 07:24	10.86	0.01	0.01	1.36	0.07	7.2	0.6
298	12.10.1997 15:28 12.10.1997 17:09	5.33	0.01	0.00	0.63	0.03	3.9	0.3
299	12.12.1997 01:02 12.12.1997 05:43	46.21	0.06	0.03	1.93	0.10	34.1	2.7
300	26.12.1997 03:22 26.12.1997 05:05	2.92	0.00	0.00	0.64	0.03	14.7	1.2
301	08.06.1998 00:18 08.06.1998 02:06	8	0.01	0.01	0.72	0.04	7.1	0.6
302	10.06.1998 16:04 10.06.1998 17:19	0.56	0.00	0.00	0.56	0.03	2.2	0.2
303	11.06.1998 07:42 11.06.1998 08:40	1.21	0.00	0.00	0.51	0.03	1.7	0.1
304	12.06.1998 18:12 12.06.1998 18:17	0.08	0.00	0.00	0.44	0.02	0.4	0.0
305	07.07.1998 17:24 07.07.1998 17:44	0.28	0.00	0.00	0.42	0.02	1.9	0.2
306	13.07.1998 17:52 13.07.1998 19:09	8.7	0.01	0.01	1.04	0.05	2.5	0.2
307	27.07.1998 23:18 28.07.1998 01:35	25.27	0.03	0.02	1.99	0.10	19.1	1.5
308	22.08.1998 07:23 22.08.1998 08:01	0.72	0.00	0.00	0.48	0.02	3.1	0.2
309	22.08.1998 21:13 22.08.1998 22:34	1.09	0.00	0.00	0.65	0.03	2.8	0.2
310	22.08.1998 23:20 23.08.1998 02:52	19.66	0.03	0.01	1.76	0.09	28.7	2.3
311	05.09.1998 06:38 05.09.1998 09:16	9.62	0.01	0.01	1.74	0.09	13.8	1.1
312	11.09.1998 04:00 11.09.1998 04:29	0.78	0.00	0.00	0.56	0.03	0.7	0.1
313	11.09.1998 08:30 11.09.1998 11:40	6.22	0.01	0.00	1.25	0.06	13.8	1.1
314	11.09.1998 23:15 11.09.1998 23:21	0.05	0.00	0.00	0.55	0.03	0.4	0.0
315	12.09.1998 01:52 12.09.1998 03:23	1.99	0.00	0.00	0.85	0.04	4.8	0.4
	29.09.1998 01:21							

316	29.09.1998 01:40	0.3	0.00	0.00	0.45	0.02	0.2	0.0
317	25.10.1998 05:34 25.10.1998 08:15	60.16	0.08	0.04	1.98	0.10	21.7	1.7
318	29.10.1998 12:43 29.10.1998 14:08	2.46	0.00	0.00	0.84	0.04	10.9	0.9
319	01.11.1998 11:39 01.11.1998 16:39	3.2	0.00	0.00	0.84	0.04	2.3	0.2
320	10.11.1998 12:59 10.11.1998 15:51	5.53	0.01	0.00	0.86	0.04	15.2	1.2
321	10.11.1998 22:12 10.11.1998 22:24	0.13	0.00	0.00	0.46	0.02	0.7	0.1
322	20.02.1999 07:53 20.02.1999 11:05	1.09	0.00	0.00	0.54	0.03	2.8	0.2
323	20.02.1999 13:43 20.02.1999 14:18	0.05	0.00	0.00	0.33	0.02	1.1	0.1
324	21.02.1999 09:49 21.02.1999 09:58	0.14	0.00	0.00	0.29	0.01	0.7	0.1
325	21.02.1999 11:55 21.02.1999 12:02	0.11	0.00	0.00	0.35	0.02	0.2	0.0
326	07.04.1999 08:01 07.04.1999 10:16	1.15	0.00	0.00	0.89	0.04	3.8	0.3
327	11.05.1999 21:44 11.05.1999 22:38	0.91	0.00	0.00	0.60	0.03	1.2	0.1
328	12.05.1999 03:03 12.05.1999 11:49	51.51	0.07	0.03	1.96	0.10	45.1	3.6
329	13.05.1999 02:12 13.05.1999 07:35	10.18	0.01	0.01	1.15	0.06	15.1	1.2
330	13.05.1999 20:53 13.05.1999 21:48	0.65	0.00	0.00	0.69	0.03	0	0.0
331	14.05.1999 08:37 14.05.1999 09:23	0.46	0.00	0.00	0.77	0.04	1.6	0.1
332	14.05.1999 16:43 14.05.1999 16:49	0.06	0.00	0.00	0.58	0.03	0	0.0
333	21.05.1999 05:25 21.05.1999 15:32	10.63	0.01	0.01	1.05	0.05	47	3.8
334	08.06.1999 06:58 08.06.1999 09:34	10.05	0.01	0.01	1.20	0.06	18.9	1.5
335	10.06.1999 18:07 10.06.1999 18:13	0.07	0.00	0.00	0.67	0.03	0.3	0.0
336	11.06.1999 02:55 11.06.1999 03:01	0.09	0.00	0.00	0.65	0.03	0.2	0.0
337	14.06.1999 00:13 14.06.1999 00:19	0.05	0.00	0.00	0.68	0.03	0.6	0.0
338	21.06.1999 08:46 21.06.1999 09:51	0.93	0.00	0.00	0.89	0.04	7.7	0.6
339	29.06.1999 22:08 29.06.1999 23:52	0.95	0.00	0.00	0.92	0.05	5.4	0.4
340	12.07.1999 05:05 12.07.1999 05:26	0.34	0.00	0.00	0.68	0.03	0	0.0
341	12.07.1999 07:17 12.07.1999 07:28	0.2	0.00	0.00	0.76	0.04	0	0.0
342	12.07.1999 10:04 12.07.1999 10:37	0.96	0.00	0.00	0.88	0.04	0.4	0.0

343	11.08.1999 12:51							
	11.08.1999 13:04	0.31	0.00	0.00	0.63	0.03	0.1	0.0
344	12.08.1999 21:44							
	12.08.1999 21:50	0.06	0.00	0.00	0.52	0.03	0.4	0.0
345	28.08.1999 11:42							
	28.08.1999 12:24	2.21	0.00	0.00	0.89	0.04	1.8	0.1
346	20.09.1999 15:47							
	20.09.1999 16:00	0.21	0.00	0.00	0.53	0.03	0.7	0.1
347	20.09.1999 23:16							
	21.09.1999 00:12	1.24	0.00	0.00	0.66	0.03	2.6	0.2
348	24.09.1999 02:47							
	24.09.1999 03:05	0.28	0.00	0.00	0.55	0.03	1.1	0.1
349	30.09.1999 13:37							
	30.09.1999 14:15	1.11	0.00	0.00	0.60	0.03	1.6	0.1
350	08.02.2000 22:47							
	09.02.2000 00:20	0.55	0.00	0.00	0.66	0.03	1.6	0.1
351	15.03.2000 00:54							
	15.03.2000 02:54	1.63	0.00	0.00	0.87	0.04	20.8	1.7
352	21.05.2000 23:53							
	22.05.2000 01:13	1.56	0.00	0.00	0.95	0.05	11.4	0.9
353	22.05.2000 03:26							
	22.05.2000 03:52	0.18	0.00	0.00	0.58	0.03	1.2	0.1
354	31.05.2000 05:19							
	31.05.2000 05:25	0.04	0.00	0.00	0.43	0.02	0.4	0.0
355	31.05.2000 11:25							
	31.05.2000 14:18	6.13	0.01	0.00	1.39	0.07	30.6	2.4
356	28.06.2000 12:57							
	28.06.2000 14:14	2.16	0.00	0.00	1.58	0.08	7.4	0.6
357	08.07.2000 08:28							
	08.07.2000 08:44	0.09	0.00	0.00	0.61	0.03	1.8	0.1
358	14.07.2000 17:47							
	14.07.2000 18:24	0.36	0.00	0.00	0.76	0.04	0	0.0
359	14.07.2000 22:07							
	15.07.2000 00:35	1.02	0.00	0.00	1.03	0.05	18.6	1.5
360	15.07.2000 09:20							
	15.07.2000 10:56	0.46	0.00	0.00	0.72	0.04	4	0.3
361	28.07.2000 06:19							
	28.07.2000 06:46	0.39	0.00	0.00	0.91	0.05	1	0.1
362	28.07.2000 07:50							
	28.07.2000 08:12	0.12	0.00	0.00	0.78	0.04	0	0.0
363	06.08.2000 01:54							
	06.08.2000 05:27	9	0.01	0.01	1.85	0.09	49	3.9
364	06.08.2000 13:57							
	06.08.2000 14:07	0.08	0.00	0.00	0.74	0.04	0	0.0
365	03.09.2000 15:29							
	03.09.2000 15:35	0.04	0.00	0.00	0.51	0.03	4	0.3
366	03.09.2000 21:51							
	03.09.2000 21:57	0.03	0.00	0.00	0.58	0.03	0	0.0
367	20.09.2000 18:56							
	20.09.2000 20:36	1.15	0.00	0.00	1.52	0.08	21.4	1.7
368	20.09.2000 23:04							
	21.09.2000 06:57	15.97	0.02	0.01	2.23	0.11	95.8	7.7
	21.09.2000 09:48							

369	21.09.2000 09:54	0.02	0.00	0.00	1.08	0.05	0.2	0.0
370	11.03.2001 17:01 12.03.2001 01:56	3.85	0.01	0.00	0.44	0.02	2.2	0.2
371	12.03.2001 21:44 12.03.2001 22:38	0.34	0.00	0.00	0.26	0.01	1.4	0.1
372	13.03.2001 01:14 13.03.2001 02:21	0.72	0.00	0.00	0.26	0.01	0.6	0.0
373	20.03.2001 22:36 21.03.2001 02:19	2.22	0.00	0.00	0.44	0.02	1.1	0.1
374	21.03.2001 04:02 21.03.2001 06:00	1.38	0.00	0.00	0.26	0.01		0.0
375	21.03.2001 11:08 21.03.2001 11:40	0.32	0.00	0.00	0.26	0.01	0.5	0.0
376	21.03.2001 14:53 21.03.2001 20:03	1.57	0.00	0.00	2.02	0.10	6	0.5
377	25.03.2001 03:17 25.03.2001 03:25	0.05	0.00	0.00	0.26	0.01	0	0.0
378	25.03.2001 05:07 25.03.2001 08:11	1.62	0.00	0.00	0.48	0.02	1.4	0.1
379	25.03.2001 09:37 25.03.2001 10:41	0.82	0.00	0.00	0.25	0.01	0	0.0
380	25.03.2001 16:33 25.03.2001 16:37	0.78	0.00	0.00	0.22	0.01	0	0.0
381	07.04.2001 00:00 07.04.2001 00:21	0.07	0.00	0.00	0.26	0.01	0.5	0.0
382	07.04.2001 02:11 07.04.2001 03:19	0.57	0.00	0.00	0.26	0.01	0.1	0.0
383	07.04.2001 06:16 07.04.2001 10:24	2.12	0.00	0.00	0.44	0.02	4.1	0.3
384	07.04.2001 11:32 07.04.2001 12:50	0.89	0.00	0.00	0.27	0.01	0.6	0.0
385	10.04.2001 00:01 10.04.2001 00:32	0.18	0.00	0.00	0.26	0.01	1	0.1
386	10.04.2001 02:04 10.04.2001 04:20	1.4	0.00	0.00	0.26	0.01	1.3	0.1
387	10.04.2001 05:50 10.04.2001 06:42	0.35	0.00	0.00	0.27	0.01	1.7	0.1
388	10.04.2001 08:56 10.04.2001 09:27	0.06	0.00	0.00	0.35	0.02	0.2	0.0
389	10.04.2001 11:13 10.04.2001 17:51	4.51	0.01	0.00	0.26	0.01	2.2	0.2
390	05.05.2001 18:23 05.05.2001 23:10	3.36	0.00	0.00	0.51	0.03	4.4	0.4
391	06.05.2001 00:34 06.05.2001 02:03	1.62	0.00	0.00	0.27	0.01	0.3	0.0
392	24.05.2001 04:59 24.05.2001 08:09	3.42	0.00	0.00	0.56	0.03	3	0.2
393	24.05.2001 17:54 24.05.2001 18:13	0.01	0.00	0.00	0.04	0.00	0	0.0
394	24.05.2001 22:26 24.05.2001 23:24	2.13	0.00	0.00	1.87	0.09	1.1	0.1
395	02.06.2001 22:02 02.06.2001 23:56	1.24	0.00	0.00	0.29	0.01	0.3	0.0

	03.06.2001 05:04							
396	03.06.2001 09:37	0.9	0.00	0.00	0.83	0.04	6.1	0.5
	06.06.2001 07:11							
397	06.06.2001 07:45	0.46	0.00	0.00	1.41	0.07	0.5	0.0
	06.06.2001 10:47							
398	06.06.2001 13:29	1.18	0.00	0.00	0.81	0.04	2.9	0.2
	06.06.2001 16:15							
399	06.06.2001 16:32	0.17	0.00	0.00	0.25	0.01	0.1	0.0
	08.06.2001 21:49							
400	09.06.2001 04:13	4.44	0.01	0.00	0.34	0.02	5.9	0.5
	09.06.2001 09:47							
401	09.06.2001 13:56	2.92	0.00	0.00	0.29	0.01	1.9	0.2
	10.06.2001 07:18							
402	10.06.2001 23:26	17.59	0.02	0.01	0.66	0.03	14.4	1.2
	15.06.2001 21:14							
403	16.06.2001 00:26	5.29	0.01	0.00	0.82	0.04	3.6	0.3
	16.06.2001 05:17							
404	16.06.2001 07:01	2.57	0.00	0.00	0.24	0.01	0.8	0.1
	16.06.2001 13:14							
405	16.06.2001 17:07	3.66	0.00	0.00	0.49	0.02	1.8	0.1
	16.06.2001 23:01							
406	16.06.2001 23:50	1.66	0.00	0.00	0.24	0.01	0.1	0.0
	17.06.2001 01:28							
407	17.06.2001 03:28	2.48	0.00	0.00	0.34	0.02	0.3	0.0
	17.06.2001 05:18							
408	17.06.2001 06:07	0.49	0.00	0.00	0.22	0.01	0.4	0.0
	17.06.2001 18:21							
409	17.06.2001 19:47	2.12	0.00	0.00	0.34	0.02	0.1	0.0
	18.06.2001 02:12							
410	18.06.2001 03:25	2.8	0.00	0.00	0.25	0.01	0.1	0.0
	18.06.2001 05:46							
411	19.06.2001 07:54	31.49	0.04	0.02	0.50	0.03	19.5	1.6
	27.06.2001 16:28							
412	27.06.2001 17:33	3.27	0.00	0.00	0.24	0.01	1.1	0.1
	27.06.2001 22:16							
413	27.06.2001 23:28	4.23	0.01	0.00	0.25	0.01	0	0.0
	28.06.2001 16:22							
414	28.06.2001 21:13	13.42	0.02	0.01	0.56	0.03	1.4	0.1
	15.07.2001 12:21							
415	16.07.2001 00:26	9.55	0.01	0.01	1.18	0.06	6.9	0.6
	16.07.2001 02:21							
416	16.07.2001 06:02	0.97	0.00	0.00	0.37	0.02	1.8	0.1
	18.07.2001 07:02							
417	18.07.2001 11:50	8.55	0.01	0.01	0.40	0.02	5.2	0.4
	20.07.2001 00:18							
418	20.07.2001 03:28	4.81	0.01	0.00	0.71	0.04	2	0.2
	20.07.2001 06:12							
419	20.07.2001 09:37	2.53	0.00	0.00	1.73	0.09	2.2	0.2
	20.07.2001 11:35							
420	20.07.2001 13:09	0.65	0.00	0.00	0.26	0.01	1.8	0.1
	20.07.2001 14:30							
421	20.07.2001 16:15	1.98	0.00	0.00	0.28	0.01	0.7	0.1
	04.08.2001 06:17							

422	04.08.2001 09:41	10.12	0.01	0.01	0.66	0.03	1.5	0.1
423	20.08.2001 17:48 20.08.2001 21:36	38.26	0.05	0.03	3.19	0.16		
424	31.08.2001 13:43 31.08.2001 15:24	3.09	0.00	0.00	0.41	0.02	0.8	0.1
425	31.08.2001 19:18 01.09.2001 01:04	8.87	0.01	0.01	0.45	0.02	2.4	0.2
426	04.09.2001 06:25 04.09.2001 08:26	2.2	0.00	0.00	0.31	0.02	0.9	0.1
427	04.09.2001 15:51 04.09.2001 19:22	4.26	0.01	0.00	0.33	0.02	0	0.0
428	04.09.2001 20:45 05.09.2001 23:12	26.8	0.04	0.02	0.70	0.04	3.1	0.2
429	07.09.2001 05:14 07.09.2001 11:12	5.93	0.01	0.00	0.34	0.02	3.8	0.3
430	09.09.2001 01:07 09.09.2001 01:46	3.34	0.00	0.00	1.58	0.08	1.2	0.1
431	09.09.2001 02:56 09.09.2001 07:27	3.11	0.00	0.00	1.24	0.06	17.4	1.4
432	16.09.2001 06:25 17.09.2001 03:46	10.76	0.01	0.01	1.12	0.06	16.1	1.3
433	21.09.2001 00:53 21.09.2001 13:53	7.67	0.01	0.01	0.70	0.04	7	0.6
434	30.11.2001 04:47 30.11.2001 23:31	7.61	0.01	0.01	1.03	0.05	21.8	1.7
435	30.12.2001 00:01 30.12.2001 03:03	30.34	0.04	0.02	0.35	0.02	3.1	0.2
436	30.12.2001 05:08 30.12.2001 05:36	0.09	0.00	0.00	0.21	0.01	0.7	0.1
437	30.12.2001 07:28 30.12.2001 07:34	0.04	0.00	0.00	0.13	0.01	0.2	0.0
438	28.06.2002 04:24 28.06.2002 13:13	5.63	0.01	0.00	0.70	0.04	27.5	2.2
439	06.07.2002 07:58 06.07.2002 09:08	0.52	0.00	0.00	0.39	0.02	2.5	0.2
440	06.07.2002 10:11 06.07.2002 10:38	0.34	0.00	0.00	0.20	0.01	0	0.0
441	06.07.2002 13:04 06.07.2002 13:20	0.26	0.00	0.00	0.21	0.01	0.4	0.0
442	06.07.2002 14:29 06.07.2002 15:06	0.49	0.00	0.00	0.20	0.01	1	0.1
443	06.07.2002 17:17 06.07.2002 17:19	0.23	0.00	0.00	0.17	0.01	2.9	0.2
444	15.07.2002 21:01 16.07.2002 01:12	5.44	0.01	0.00	1.06	0.05	7.6	0.6
445	16.07.2002 14:13 16.07.2002 20:28	5.84	0.01	0.00	0.73	0.04	9.7	0.8
446	17.07.2002 12:05 18.07.2002 09:47	33.86	0.05	0.02	1.53	0.08	70.8	5.7
447	05.08.2002 01:29 05.08.2002 02:37	1.2	0.00	0.00	0.22	0.01	0.4	0.0
448	06.08.2002 10:43 06.08.2002 11:21	0.52	0.00	0.00	0.15	0.01	0.3	0.0

449	10.08.2002 14:39 10.08.2002 15:33	0.83	0.00	0.00	0.29	0.01	2.9	0.2
450	10.08.2002 20:08 10.08.2002 22:56	2.83	0.00	0.00	0.30	0.02	1.3	0.1
451	11.08.2002 06:26 11.08.2002 08:07	1.51	0.00	0.00	0.29	0.01	4.3	0.3
452	11.08.2002 16:37 12.08.2002 09:27	31.54	0.04	0.02	1.79	0.09	57	4.6
453	12.08.2002 12:20 12.08.2002 15:57	3.22	0.00	0.00	0.27	0.01	6.4	0.5
454	12.08.2002 18:11 12.08.2002 19:18	1.27	0.00	0.00	0.19	0.01	1.1	0.1
455	20.08.2002 14:25 20.08.2002 14:35	0.22	0.00	0.00	0.01	0.00	3.5	0.3
456	20.08.2002 15:43 20.08.2002 16:06	0.28	0.00	0.00	0.01	0.00	7	0.6
457	20.08.2002 18:52 20.08.2002 22:17	2.61	0.00	0.00	0.25	0.01	8.2	0.7
458	31.08.2002 16:55 01.09.2002 14:07	31.64	0.04	0.02	1.56	0.08	56.9	4.6
459	03.09.2002 10:10 03.09.2002 10:50	0.48	0.00	0.00	0.15	0.01	0.6	0.0
460	10.09.2002 08:11 10.09.2002 08:24	0.5	0.00	0.00	0.13	0.01	0.1	0.0
461	17.10.2002 16:50 17.10.2002 17:33	0.11	0.00	0.00	1.10	0.06	5.4	0.4
462	02.11.2002 13:14 02.11.2002 13:43	0.14	0.00	0.00	1.07	0.05	4.5	0.4
463	09.11.2002 16:07 09.11.2002 19:00	0.89	0.00	0.00	1.43	0.07	19.4	1.6
464	11.11.2002 15:03 11.11.2002 16:15	0.39	0.00	0.00	1.09	0.05	6.1	0.5
465	16.11.2002 11:20 16.11.2002 17:08	2.22	0.00	0.00	1.55	0.08	38.7	3.1
466	26.04.2003 20:20 26.04.2003 20:42	0.26	0.00	0.00	1.04	0.05	2.6	0.2
467	03.05.2003 02:42 03.05.2003 02:54	0.1	0.00	0.00	0.81	0.04	1.7	0.1
468	19.05.2003 18:31 19.05.2003 19:21	0.61	0.00	0.00	1.43	0.07	4.9	0.4
469	07.06.2003 18:26 07.06.2003 19:39	6.47	0.01	0.00	2.17	0.11	3.4	0.3
470	12.06.2003 20:24 12.06.2003 20:45	0.73	0.00	0.00	1.12	0.06	1.1	0.1
471	17.07.2003 06:41 17.07.2003 07:23	0.41	0.00	0.00	0.82	0.04	7.2	0.6
472	24.07.2003 11:54 24.07.2003 13:32	2.32	0.00	0.00	1.94	0.10	14.2	1.1
473	31.08.2003 06:09 31.08.2003 06:52	0.45	0.00	0.00	0.87	0.04	4.9	0.4
474	09.10.2003 06:38 09.10.2003 08:47	0.64	0.00	0.00	1.12	0.06	8.2	0.7
	02.06.2004 21:23							

475	03.06.2004 05:26	9.58	0.01	0.01	2.11	0.11	69.1	5.5
476	12.06.2004 10:02 12.06.2004 10:39	0.17	0.00	0.00	1.39	0.07	2	0.2
477	06.07.2004 07:37 06.07.2004 08:01	0.29	0.00	0.00	1.36	0.07	1.6	0.1
478	26.08.2004 04:15 26.08.2004 09:26	3.15	0.00	0.00	2.02	0.10	34.1	2.7
479	24.09.2004 01:26 24.09.2004 02:12	0.69	0.00	0.00	1.36	0.07	7.2	0.6
480	07.06.2005 03:56 07.06.2005 04:23	0.43	0.00	0.00	0.96	0.05	1.9	0.2
481	24.06.2005 22:04 24.06.2005 23:14	2.43	0.00	0.00	1.91	0.10	7.1	0.6
482	26.07.2005 00:50 26.07.2005 01:29	0.62	0.00	0.00	0.93	0.05	2.1	0.2
483	21.08.2005 15:55 21.08.2005 19:09	1.23	0.00	0.00	1.40	0.07	19.9	1.6
484	21.08.2005 23:38 22.08.2005 00:16	0.32	0.00	0.00	1.23	0.06	1.8	0.1
485	22.08.2005 10:15 22.08.2005 19:08	4.2	0.01	0.00	1.84	0.09	52.2	4.2
486	22.08.2005 20:21 22.08.2005 21:53	0.66	0.00	0.00	1.68	0.08	10.4	0.8
487	22.08.2005 22:55 23.08.2005 01:04	1.01	0.00	0.00	1.81	0.09	14.6	1.2
488	28.05.2006 22:58 29.05.2006 00:09	0.45	0.00	0.00	1.11	0.06	8.4	0.7
489	29.05.2006 14:33 29.05.2006 17:59	1.83	0.00	0.00	1.77	0.09	26.3	2.1
490	13.07.2006 12:16 13.07.2006 13:16	0.44	0.00	0.00	1.29	0.06	4.3	0.3
491	05.08.2006 05:12 05.08.2006 06:35	2.52	0.00	0.00	2.18	0.11	9.4	0.8
492	28.08.2006 19:32 28.08.2006 20:09	0.5	0.00	0.00	1.07	0.05	3.6	0.3
493	28.08.2006 23:46 29.08.2006 00:30	0.19	0.00	0.00	1.05	0.05	2.9	0.2
494	07.09.2006 23:20 08.09.2006 03:21	44.85	0.06	0.03	5.23	0.26	35.8	2.9
495	17.09.2006 03:45 17.09.2006 10:42	23.56	0.03	0.02	4.52	0.23	73.7	5.9
496	01.01.2007 15:45 01.01.2007 15:57	0.02	0.00	0.00	0.26	0.01	0	0.0
497	12.01.2007 10:02 12.01.2007 10:06	0.001	0.00	0.00	0.16	0.01	0.3	0.0
498	17.05.2007 20:12 17.05.2007 20:26	0.06	0.00	0.00	0.74	0.04	1.6	0.1
499	21.05.2007 21:33 21.05.2007 23:14	4.07	0.01	0.00	1.22	0.06	4.8	0.4
500	12.06.2007 20:07 12.06.2007 22:31	9.38	0.01	0.01	1.98	0.10	22.9	1.8
501	20.06.2007 19:45 20.06.2007 23:18	298.59	0.40	0.20	11.09	0.55	22.1	1.8

502	25.06.2007 09:51 25.06.2007 09:55	0.002	0.00	0.00	0.01	0.00	0	0.0
503	25.06.2007 18:56 25.06.2007 23:01	7.51	0.01	0.01	0.45	0.02	15.8	1.3
504	01.07.2007 20:45 01.07.2007 20:54	0.02	0.00	0.00	0.27	0.01	0.1	0.0
505	03.07.2007 18:31 03.07.2007 18:57	0.08	0.00	0.00	0.24	0.01	0.1	0.0
506	03.07.2007 22:34 03.07.2007 22:51	0.1	0.00	0.00	0.22	0.01	5.4	0.4
507	04.07.2007 01:12 04.07.2007 05:50	39.7	0.05	0.03	0.64	0.03	14.4	1.2
508	04.07.2007 13:40 04.07.2007 14:20	0.25	0.00	0.00	0.25	0.01	0.4	0.0
509	05.07.2007 10:25 05.07.2007 12:06	1	0.00	0.00	0.24	0.01	2.2	0.2
510	09.07.2007 11:32 09.07.2007 16:53	12.2	0.02	0.01	0.35	0.02	17.6	1.4
511	09.07.2007 20:26 10.07.2007 00:35	24.3	0.03	0.02	0.74	0.04	15	1.2
512	18.07.2007 19:59 18.07.2007 21:38	16.99	0.02	0.01	1.17	0.06	0.3	0.0
513	21.07.2007 19:36 21.07.2007 19:59	0.003	0.00	0.00	0.01	0.00	0.9	0.1
514	21.07.2007 21:41 22.07.2007 03:10	3.37	0.00	0.00	0.36	0.02	25.9	2.1
515	22.07.2007 16:22 22.07.2007 16:24	0.05	0.00	0.00	0.03	0.00	4.1	0.3
516	23.07.2007 21:21 24.07.2007 01:00	51.02	0.07	0.03	1.35	0.07	26.8	2.1
517	24.07.2007 21:16 24.07.2007 22:36	0.96	0.00	0.00	0.43	0.02	2.7	0.2
518	30.07.2007 00:29 30.07.2007 05:13	10.79	0.01	0.01	0.54	0.03	23	1.8
519	07.08.2007 22:10 07.08.2007 22:48	0.13	0.00	0.00	0.45	0.02	0.3	0.0
520	08.08.2007 03:13 08.08.2007 06:34	51.6	0.07	0.03	2.21	0.11	31.2	2.5
521	08.08.2007 15:37 08.08.2007 21:14	28.01	0.04	0.02	1.94	0.10	36.1	2.9
522	29.08.2007 16:22 29.08.2007 18:43	2.04	0.00	0.00	0.54	0.03	13.9	1.1
523	03.09.2007 20:43 03.09.2007 23:27	4.31	0.01	0.00	0.59	0.03	9.5	0.8
524	18.09.2007 03:31 18.09.2007 04:23	0.19	0.00	0.00	0.47	0.02	2.3	0.2
525	18.09.2007 10:05 18.09.2007 13:18	2.99	0.00	0.00	0.52	0.03	15.5	1.2
526	18.09.2007 16:27 18.09.2007 16:54	0.13	0.00	0.00	0.47	0.02	8.5	0.7

7. List of Figures

7.1. Introduction

7.2. Chapter I

7.3. Chapter II

7.4. Chapter III

7.5. Chapter IV

7.6. Appendices

7.6.1. Chapter I

7.6.2. Chapter II

8. List of Tables

8.1. Chapter II

8.2. Chapter III

8.3. Chapter IV

8.4. Appendices

8.4.1. Chapter I

8.4.2. Chapter II

8.4.3. Chapter III

9. Curriculum Vitae

Name	Ramona Baran
Date of Birth	30.01.1980
Place of Birth	Brandenburg an der Havel, Germany

Present Position   Geologist at Steinbacher-Consult
Ingenieurgesellschaft mbH & Co. KG, Neusäß, Germany

Employment History

Geologist, Steinbacher-Consult Ingenieurgesellschaft mbH & Co. KG, Neusäß	since 01/2012
THESIS graduate fellowship, Ludwig-Maximilians-University Munich	04/2007–09/2011
Guest researcher at the Swiss Federal Institute for Forest, Snow and Landscape Research (WSL)	08/2009–12/2010
Research and teaching assistant in the Department of Earth and Environmental sciences, Ludwig-Maximilians-University Munich	10/2006–03/2007
Research and teaching assistant in the group of Prof. Dr. Anke Friedrich, Institute of Geology, Leibniz-University Hannover	10/2005–09/2006

University Education – Degrees

Enrolled in Geology at the University Potsdam, Germany	10/1999–09/2005
University education ended in September 2005 with the German diploma degree	

Diploma Thesis   *Multi-temporal monitoring of test-site surface
changes related to degradation processes*

School Attendances

School education ending with school leaving exam, Brandenburg an der Havel, Germany	09/1986–06/1999

Publications

Baran, R., Guest, B., and Friedrich, A.M. (2010) High-resolution spatial rupture pattern of a multiphase flower structure, Rex Hills, Nevada: New insights on scarp evolution in complex topography based on 3-D laser scanning: Geological Society of America Bulletin, Volume 122, Number 5/6, p. 897-914, doi: 10.1130/B26536.1

Baran, R., McArdell, B.W., Schlunegger, F., Wunderlich, T.A., and Friedrich, A.M. (in preparation for submission to Geomorphology) Short-term sediment transport in context of post-glacial landscape evolution: Insights from field mapping and high-resolution LiDAR measurements, Alp Valley, Switzerland

Baran, R., McArdell, B.W., Schlunegger, F., and Friedrich, A.M. (in preparation for submission to International Journal of Earth Sciences) Sediment Transport and Erosion Rates in the Alps on Scales Ranging from Years to Millions of Years – Implications for the Variability of Mountainous Erosion

Baran, R., Schlunegger, F., and Friedrich, A.M. (in preparation for submission to Geology) Erosion of Dying Foreland Basins: Did the Sediment Discharge of the Alps Really Accelerate Five Million Years Ago?

Awards

2nd prize Student Poster Award – Fragile Earth, 2011, GSA, DGG und GV conference, Munich, Germany:

Schmid, D.M., **Baran, R.**, Tsekhmistrenko, M., Sundermann, L., and Friedrich, A.M.; Reconstruction of fault displacement in alluvial fan deposits based on high-resolution satellite imagery and field work – Piute Creek, White Mountain fault zone, California

3rd prize Student Poster Award – Geo 2010, DGG and GV conference, Darmstadt, Germany:

Baran, R., McArdell, B.W., Schlunegger, F., Wunderlich, T.A., and Friedrich, A.M.; Monitoring the nature of short-term erosion and sediment transport in two pre-Alpine channel beds, Erlenbach and Vogelbach, Switzerland

Conference Contributions

Baran, R., Guest, B., and Friedrich, A.M. (2011) The use of high-resolution 3-D laser scanning to unravel the complex rupture pattern of a flower structure, Rex Hills, Nevada, USA: Fragile Earth – Geological Processes From Global to Local Scales, Associated Hazards & Resources, p. A60, GSA, DGG and GV Konferenz, 4-7 September 2011, München

Schmid, D.M., **Baran, R.**, Tsekhmistrenko, M., Sundermann, L., and Friedrich, A.M. (2011) Field mapping in the 21st century: Reconstruction of fault displacement in alluvial fan deposits, Piute Creek, White Mountain fault zone, California, based on high-resolution satellite imagery and field work: Fragile Earth – Geological Processes From Global to Local Scales, Associated Hazards & Resources, p. A67, GSA, DGG and GV conference, 4-7 September 2011, Munich, Germany

Baran, R., McArdell, B.W., Schlunegger, F., Wunderlich, T.A., and Friedrich, A.M. (2010) Monitoring the nature of short-term erosion and sediment transport in two pre-Alpine channel

beds using high-resolution laser-scanning, Erlenbach and Vogelbach, Switzerland: Schriftenreihe der Deutschen Gesellschaft für Geowissenschaften (SDGG), Vol. 68, p. 7; Geo 2010, DGG and GV conference, Darmstadt, Germany

Baran, R., McArdell, B.W., Schlunegger, F., Wunderlich, T.A., and Friedrich, A.M. (2009) Erosion and bed-load transport processes on time-scales from minutes to thousands of years – Alp Valley, Switzerland: 9th Alpine Workshop on Alpine Geological Studies, Abstract Volume; Cogne, Italy

Baran, R., McArdell, B.W., Schlunegger, F., Wunderlich, T.A., Weber, T., and Friedrich, A.M. (2009) Monitoring sediment migration in a pre-Alpine channel bed using a high-resolution laser scanner, Erlenbach drainage, Switzerland: Geophysical Research Abstracts, Vol. 11, EGU2009-0; EGU General Assembly, Vienna, Austria

Baran, R., Guest, B., and Friedrich, A.M. (2008) The surface expression of positive flower structures: Mapping and high-resolution laser scanning of the Rex Hills, Nevada: Schriftenreihe der Deutschen Gesellschaft für Geowissenschaften (SDGG), Vol. 60, p. 193; Geo 2008, DGG and GV conference, Aachen, Germany

Baran, R., Guest, B., and Friedrich, A.M. (2007) Role of Erosion on Closely-Spaced Fault Scarps: High-resolution Laser Scanning Data and Scarp Diffusion Modelling of the Rex Hills Flower Structure, Nevada: Eos Transactions, Vol. 88, T51C-0695; AGU Fall Meeting, San Francisco, USA

Baran, R., Friedrich, A.M., McArdell, B., and Schlunegger, F. (2007) Stream profile analysis in the Rhone valley region, Swiss Alps: 8th Alpine Workshop on Alpine Geological Studies, Abstract Volume, p. 5-6; Alpine Workshop, Davos, Switzerland

Baran, R., and Chabrillat, S. (2006) Monitoring erosion on a test surface using a 3D laser scanner: Terra Nostra, Schriften der GeoUnion Alfred-Wegener-Stiftung 2006/3, p. 28-29; GV conference, Potsdam, Germany

Hoffmann, M., Kübler, S., Guest, B., **Baran, R.,** Menges, C., Freund, A., and Heller, I. (2006) Quaternary transpression along the Rex Hills segment of the Stateline fault: structural style, magnitudes and rates: Terra Nostra, Schriften der GeoUnion Alfred-Wegener-Stiftung 2006/3, p. 54; GV conference, Potsdam, Germany

P.S.:   Ich habe durchgehalten!

PLATE I

Legend

22   Outcrop number

Anthropogenic Features
- Lake and sediment retention-basin
- Gravel pit
- Populated area

Subalpine Molasse (Oligocene - Miocene)
- Sandstone
- Conglomerate (Nagelfluh)

Ultrahelvetic - Penninic Units
- Habkern Flysch; also Wild Flysch (upper Eocene)

- Schlieren Flysch (middle Eocene - upper Maastrichtian)
- Wägital Flysch middle Eocene
- Campanian - Maastrichtian

Helvetic Units
- Sandstone (upper Eocene)
- Limestone mostly with nummulites (Paleocene - middle Eocene)
- Amdener beds: marl (Santonian - lower Maastrichtian)

Penninic Units
- Penninic cliffs (Triassic - Cretaceous)

Geomorphological Strcutures (Holocene - Pleistocene)
- Drainage network
- Major drainage divide
- 15 40° Escarpment with height (m) and slope angle
- Erosional edge
- Recent valley floor
- Fluvial modified valley floor, e.g. braided river pattern

- Terrace (fluvial-glacial gravels and varved clay deposits)
- Debris cone and talus material
- Alluvial fan
- Hillslope morphology
- Sliding area with internal morphology (convex form: looking downslope)
- Post-glacial landslide with internal morphology
- Ground moraine
- Lateral and terminal moraines (Würm)

Geological Structures
- 50 Bedding
- 2 Local fold-axis orientation
- Syncline
- Anticline
- Suspected syncline
- Thrust fault
- Concealed thrust fault
- Suspected thrust fault constrained by e.g. Hantke (1967), Winkler et al. (1985), and Stammbach (1987)
- 50 Orientation of minor thrust fault

Alp River

Vogelbach

Erlenbach

0   500   1.000 m

Plate II

A — Western Alps

- Western Alps: last 34 Ma (Kuhlemann et al., 2001) - sediment budget
- 1 Western Alps: 0.4-0.7 km/Ma last 15 Ma (Bernet et al., 2001) - exhumation
- 2 Western Alps: 0.2-0.3 km/Ma last 30 Ma (Bernet et al., 2009) - exhumation
- Western Alps N Min-Max I: last 28.5 Ma (Schlunegger et al., 2007) - sediment volume
- Western Alps N II (Germany & Switzerland): 13.5-34 Ma (Schlunegger et al., 2001) - sediment volume
- Western Alps N III (Switzerland): 13.5-30 Ma (Schlunegger et al., 2001) - sediment volume
- Western Alps N IV: 16.5-30 Ma (Schlunegger, 1999) - sediment volume
- Western Alps N Min-Max V: last 17 Ma (Willett et al., 2006) - sediment volume
- 1 Aare: 1.2 km/Ma 0-0.8 Ma; 0.12 km/Ma 0.8-4 Ma (Haeuselmann et al., 2007) - incision: cosmogenic nuclide data
- 2 Rigi-Weggis: 0.76-1.22 km/Ma last 5 Ma (Cederbom et al., 2004) - exhumation
- 3 Hüneneberg: 0.26-0.66 km/Ma last 5 Ma (Cederbom et al., 2004) - exhumation
- 4 Boswil: 0.34-0.7 km/Ma last 5 Ma (Cederbom et al., 2004) - exhumation
- 1E Aosta Valley E: 0.1-0.3 km/Ma last 7.5 Ma (Malusà & Vezzoli, 2006) - exhumation
- 1W Aosta Valley W: 0.4-1.5 km/Ma last 7.5 Ma (Malusà & Vezzoli, 2006) - exhumation
- 2a Aar massif a: 0.3-0.6 km/Ma last 25 Ma (Schlunegger & Willett, 1999) - exhumation
- 2b Aar massif b: 0.8-1 km/Ma 3-5 Ma (Bogdanoff et al., 2000) - exhumation
- 3 Mt. Blanc massif: 0.8-1 km/Ma 3-5 Ma (Bogdanoff et al., 2000) - exhumation
- 4 Pelvoux massif: 0.2-0.3 km/Ma 4-9 Ma (Bogdanoff et al., 2000) - exhumation
- 5 Argentera massif: 0.8-1.5 km/Ma 0-3 Ma; 0.2-0.34 km/Ma 3-8 Ma (Bogdanoff et al., 2000) - exhumation
- 6 Simplon area: 0.4-1.1 km/Ma last 11.5 Ma (Clark & Jäger, 1969) - exhumation
- 7 Gotthard area: 0.4-0.7 km/Ma last 16.5 Ma (Clark & Jäger, 1969) - exhumation
- 8 Penninic crystalline: 0.2-0.4 km/Ma last 40 Ma (Schlunegger & Willett, 1999) - exhumation
- 9a Lepontine dome a: 0.3-0.5 km/Ma 0-20 Ma; 1 km/Ma 20-40 Ma (Schlunegger, 1999) - exhumation
- 9b Lepontine dome b: 0.2-0.4 km/Ma 0-20 Ma; 5 km/Ma 20-22 Ma; 0.4-0.6 km/Ma 22-40 Ma (Schlunegger, 1999) - exhumation
- 10 Central Alps: 0.4-0.7 km/Ma last 30 Ma (Bernet et al., 2009) - exhumation
- Western Alps S: Min-Max last 5.5 Ma, Max 7-16 Ma (Willett et al., 2006) - sediment volume

B — Eastern Alps

- Eastern Alps: last 33 Ma (Kuhlemann et al., 2001) - sediment budget
- 1a Riesenferner pluton a: 0.2 km/Ma 0-13 Ma; 0.4-0.6 km/Ma 13-31 Ma (Steenken et al., 2002) - exhumation
- 1b Riesenferner pluton b: 0.2 km/Ma 0-16 Ma; 0.4-0.6 km/Ma 16-31 Ma (Steenken et al., 2002) - exhumation
- 2 W of Tauern window: 0.15 km/Ma 13-23 Ma (Frisch et al., 2000) - sediment mass balance
- 3 E of Tauern window: 0.06 km/Ma 13-23 Ma (Frisch et al., 2000) - sediment mass balance
- 4 Tauern window: 0.3 km/Ma 13-23 Ma (Frisch et al., 2000) - sediment mass balance
- 5 Tauern area: 0.4-0.7 km/Ma last 20 Ma (Clark & Jäger, 1969) - exhumation
- 6 Tauern window: 0.6 km/Ma 5-9 Ma; 1.1-1.2 km/Ma 12-14 Ma (Most, 2003) - exhumation
- 7 W Tauern window: last 20 Ma (von Blanckenburg et al., 1989) - exhumation
- 8a W Tauern window - upper Schieferhülle: 4 km/Ma 30-35.4 Ma (Christensen et al., 1994) - exhumation
- 8b W Tauern window - lower Schieferhülle: 2 km/Ma 30.2-32.7 Ma (Christensen et al., 1994) - exhumation
- 9 W Tauern window: last 30 Ma (Fügenschuh et al., 1997) - exhumation
- 10 W Tauern window - Zillertal Alps: 0.6 km/Ma last 5 Ma (Hejl, 1997) - exhumation
- 11 SE Tauern window - Reisseck: 0.2 km/Ma last 5 Ma (Hejl, 1997) - exhumation
- 12 SE Tauern window - gneiss dome: 1 km/Ma 0-16.5 Ma; 5 km/Ma 16.5-17 Ma; 1 km/Ma 17-24 Ma (Cliff et al., 1985)

A

Erosion (m) — Time (ka)

Western Alps

1a Lütschine a: 0.82 m/ka last 17 ka (Hinderer, 2001) - sediment yield
1b Lütschine b: 2 m/ka last 17 ka (Schlunegger & Hinderer, 2001) - sediment yield
2a Reuss a: 1.58 m/ka last 18 ka (Wittmann et al., 2007) - denudation: cosmogenic nuclide data
2b Reuss b: 1.53 m/ka last 17 ka (Schlunegger & Hinderer, 2001) - sediment yield
2c Reuss c: 0.56 m/ka last 17 ka (Hinderer, 2001) - sediment yield
3a Aare a: 0.38 m/ka last 17 ka (Hinderer, 2001) - sediment yield
3b Aare b: 1.06 m/ka last 17 ka (Schlunegger & Hinderer, 2001) - sediment yield
4a Linth a: 0.73 m/ka last 17 ka (Hinderer, 2001) - sediment yield
4b Linth b: 0.35 m/ka last 17 ka (Schlunegger & Hinderer, 2001) - sediment yield
5 Klem: 0.48 m/ka last 18 ka (Wittmann et al., 2007) - denudation: cosmogenic nuclide data
6 Emme: 0.26 m/ka last 18 ka (Wittmann et al., 2007) - denudation: cosmogenic nuclide data
7 Walen lake Valley: 1.24-1.69 m/ka last 15 ka (Müller, 1999) - sediment budget
8 Seez: 0.96 m/ka last 17 ka (Hinderer, 2001) - sediment yield
9 Sense: 0.25 m/ka last 18 ka (Wittmann et al., 2007) - denudation: cosmogenic nuclide data
10 Melchaa: 0.37 m/ka last 17 ka (Hinderer, 2001) - sediment yield
11 Fischenbach: 1.6-4.6 m/ka last 15 ka (Schlunegger et al., 2002) - sediment yield
12 Fontanne: 0.54 m/ka last 16 ka, 0.38 m/ka last 16 ka (Norton et al., 2008) - denudation: cosmogenic nuclide data
13 Trub: 0.35 m/ka last 17 ka (Norton et al., 2008) - denudation: cosmogenic nuclide data
14 Wasen: 0.26 m/ka last 18 ka (Wittmann et al., 2007) - denudation: cosmogenic nuclide data
15 Taf: 0.16 m/ka last 18 ka (Wittmann et al., 2007) - denudation: cosmogenic nuclide data
16 Buetsch: 0.11 m/ka last 18 ka (Wittmann et al., 2007) - denudation: cosmogenic nuclide data

1a Rhine a: 1.06 m/ka last 17 ka (Hinderer, 2001) - sediment yield
1b Rhine b: 2 m/ka last 17 ka (Schlunegger & Hinderer, 2001) - sediment yield
1c Rhine c: Flysch-Bündner schists 4 m/ka last 9-12.5 ka, crystalline rock 0.7 m/ka last 9-12.5 ka (Korup & Schlunegger, 2009) - sediment volume
2a Rhone a: 0.95 m/ka last 17 ka (Hinderer, 2001) - sediment yield

2b Rhone b: 2.24 m/ka last 17 ka (Schlunegger & Hinderer, 2001) - sediment yield
3 Chie: 0.69 m/ka last 18 ka (Wittmann et al., 2007) - denudation: cosmogenic nuclide data
4 Lonza: 1.28 m/ka last 18 ka (Wittmann et al., 2007) - denudation: cosmogenic nuclide data
5 Furka: 1.14 m/ka last 18 ka (Wittmann et al., 2007) - denudation: cosmogenic nuclide data
6 Gren: 1.32 m/ka last 18 ka (Wittmann et al., 2007) - denudation: cosmogenic nuclide data

1a Ticino a: 1.29 m/ka last 17 ka (Schlunegger & Hinderer, 2001) - sediment yield
1b Ticino b: 0.79 m/ka last 17 ka (Hinderer, 2001) - sediment yield
2 Toce: 1.18 m/ka last 18 ka (Wittmann et al., 2007) - denudation: cosmogenic nuclide data
3 Mela: 0.89 m/ka last 18 ka (Wittmann et al., 2007) - denudation: cosmogenic nuclide data
4 Adda: 0.85 m/ka last 17 ka (Hinderer, 2001) - sediment yield
5 Anza: 0.83 m/ka last 18 ka (Wittmann et al., 2007) - denudation cosmogenic nuclide data
6a Maggia a: 0.7 m/ka last 18 ka (Wittmann et al., 2007) - denudation: cosmogenic nuclide data
6b Maggia b: 0.51 m/ka last 17 ka (Hinderer, 2001) - sediment yield
7 Verz: 0.59 m/ka last 18 ka (Wittmann et al., 2007) - denudation: cosmogenic nuclide data
8 Sesia: 0.5 m/ka last 18 ka (Wittmann et al., 2007) - denudation: cosmogenic nuclide data

1 Gorge du Diable: 6.5-13 m/ka last 5 ka (Valla et al., 2010) - incision: cosmogenic nuclide data
2 Gyr: 1.07 m/ka last 0.707 ka (Delunel et al., 2010) - denudation: cosmogenic nuclide data
3 Tabuc: 0.99 m/ka last 0.761 ka (Delunel et al., 2010) - denudation: cosmogenic nuclide data
4 Romanche: 0.38 m/ka last 1.977 ka, 0.89 m/ka last 0.846 ka (Delunel et al., 2010) - denudation: cosmogenic nuclide data
5 Celse Nierre: 0.8 m/ka last 0.939 ka (Delunel et al., 2010) - denudation: cosmogenic nuclide data
6 Saint Pierre: 0.67 m/ka last 1.131 ka (Delunel et al., 2010) - denudation: cosmogenic nuclide data
7 Drac: 0.63 m/ka last 1.192 ka (Delunel et al., 2010) - denudation: cosmogenic nuclide data
8 Veneon: 0.61 m/ka last 1.233 ka (Delunel et al., 2010) - denudation: cosmogenic nuclide data
9 Severaisse: 0.57 m/ka last 1.308 ka (Delunel et al., 2010) - denudation: cosmogenic nuclide data
10 Bonne: 0.27 m/ka last 2.735 ka, 0.37 m/ka last 2.045 ka (Delunel et al., 2010) - denudation: cosmogenic nuclide data
11 Roizonne: 0.35 m/ka last 2.142 ka (Delunel et al., 2010) - denudation: cosmogenic nuclide data

B

Erosion (m) — Time (ka)

Eastern Alps

1 Inn: 0.57 m/ka last 17 ka (Hinderer, 2001) - sediment yield
2 Tiroler Ache: 0.53 m/ka last 17 ka (Hinderer, 2001) - sediment yield
3 Iller: 0.25 m/ka last 17 ka (Hinderer, 2001) - sediment yield
4 Weissach: 0.42 m/ka last 17 ka (Hinderer, 2001) - sediment yield

1 Krimmler: 0.54 m/ka last 1.31 ka (Norton et al., 2011) - denudation: cosmogenic nuclide data
2 Masino: 0.3 m/ka last 2.38 ka (Norton et al., 2011) - denudation: cosmogenic nuclide data
3 Melach: 0.55 m/ka last 1.3 ka (Norton et al., 2011) - denudation: cosmogenic nuclide data
4 Pfitsch: 0.53 m/ka last 1.35 ka (Norton et al., 2011) - denudation: cosmogenic nuclide data
5 Pitze: 0.68 m/ka last 1.04 ka (Norton et al., 2011) - denudation: cosmogenic nuclide data
6 Plima: 1.1 m/ka last 0.65 ka (Norton et al., 2011) - denudation: cosmogenic nuclide data
7 Schnalz: 0.58 m/ka last 1.21 ka (Norton et al., 2011) - denudation: cosmogenic nuclide data
8 Zemm: 0.71 m/ka last 1 ka (Norton et al., 2011) - denudation: cosmogenic nuclide data
9 Ahrn: 1.23 m/ka last 0.57 ka (Norton et al., 2011) - denudation: cosmogenic nuclide data
10 Antholzer: 0.3 m/ka last 2.38 ka (Norton et al., 2011) - denudation: cosmogenic nuclide data
11 Bergler: 0.25 m/ka last 2.92 ka, 0.38 m/ka last 1.91 ka (Norton et al., 2011) - denudation: cosmogenic nuclide data
12 Flagger: 1.47 m/ka last 0.49 ka (Norton et al., 2011) - denudation: cosmogenic nuclide data
13 Fusino: 0.36 m/ka last 1.97 ka (Norton et al., 2011) - denudation: cosmogenic nuclide data
14 Hoeller: 0.35 m/ka last 1.11 ka, 1.09 m/ka last 0.66 ka (Norton et al., 2011) - denudation: cosmogenic nuclide data

15 Muehl: 0.85 m/ka last 0.86 ka (Norton et al., 2011) - denudation: cosmogenic nuclide data
16 Novate: 0.71 m/ka last 1.03 ka (Norton et al., 2011) - denudation: cosmogenic nuclide data
17 Tauern: 1.24 m/ka last 0.57 ka (Norton et al., 2011) - denudation: cosmogenic nuclide data
18 Watten: 0.52 m/ka last 1.39 ka (Norton et al., 2011) - denudation: cosmogenic nuclide data
19 Widshoenau: 0.73 m/ka last 1.04 ka (Norton et al., 2011) - denudation: cosmogenic nuclide data
20 Ziel: 0.75 m/ka last 0.93 ka (Norton et al., 2011) - denudation: cosmogenic nuclide data

1 Sarca: 0.49 m/ka last 17 ka (Hinderer, 2001) - sediment yield
2 Oglio: 0.66 m/ka last 1.09 ka (Norton et al., 2011) - denudation: cosmogenic nuclide data
3 Nero: 0.29 m/ka last 2.62 ka (Norton et al., 2011) - denudation: cosmogenic nuclide data
4 Talfer: 0.32 m/ka last 2.26 ka (Norton et al., 2011) - denudation: cosmogenic nuclide data
5 Avisio: 0.36 m/ka last 2.04 ka (Norton et al., 2011) - denudation: cosmogenic nuclide data
6 Arno: 0.47 m/ka last 1.54 ka (Norton et al., 2011) - denudation: cosmogenic nuclide data
7 Bitto: 0.44 m/ka last 1.71 ka (Norton et al., 2011) - denudation: cosmogenic nuclide data
8 Castello: 1.04 m/ka last 0.69 ka (Norton et al., 2011) - denudation: cosmogenic nuclide data
9 di Adame: 0.48 m/ka last 1.51 ka (Norton et al., 2011) - denudation: cosmogenic nuclide data
10 di Venina: 0.76 m/ka last 0.97 ka (Norton et al., 2011) - denudation: cosmogenic nuclide data
11 Fersina: 0.33 m/ka last 2.31 ka (Norton et al., 2011) - denudation: cosmogenic nuclide data
12 Lagorai: 0.21 m/ka last 3.36 ka (Norton et al., 2011) - denudation: cosmogenic nuclide data
13 Silla: 0.24 m/ka last 3.31 ka (Norton et al., 2011) - denudation: cosmogenic nuclide data
14 val Moena: 0.17 m/ka last 4.3 ka (Norton et al., 2011) - denudation: cosmogenic nuclide data

C

Erosion (m) — Time (ka)

Plate III

Plate IV

Western Alps

1 Lütschine: 0.29 mm/a 1964-1995 (Schlunegger & Hinderer, 2003) - suspended-load
2a Linth a: 0.15 mm/a 1911-1979 (Hinderer, 2001) - delta growth
2b Linth b: 0.19 mm/a 1964-1995 (Schlunegger & Hinderer, 2003) - suspended-load
3 Glatt: 0.13 mm/a 1976-1993 (Schlunegger & Hinderer, 2003) - suspended-load
4a Thur a: 0.06 mm/a 1964-1995 (Champagnac et al., 2009) - suspended-load
4b Thur b: 0.2 mm/a 1975-1995 (Schlunegger & Hinderer, 2003) - suspended-load
5a Emme a: 0.02 mm/a 1964-1995 (Champagnac et al., 2009) - suspended-load
5b Emme b: 0.12 mm/a 1984-1995 (Schlunegger & Hinderer, 2003) - suspended-load
6a Reuss a: 0.02-0.04 mm/a 1964-1995 (Champagnac et al., 2009) - suspended-load
6b Reuss b: 0.11 mm/a 1979-1995 (Schlunegger & Hinderer, 2003) - suspended-load
7 Simme: 0.15 mm/a 1921-1993 (Schlunegger & Hinderer, 2003) - suspended-load
8 Broye: 0.14 mm/a 1920-1993 (Schlunegger & Hinderer, 2003) - suspended-load
9a Kander a: 0.33 mm/a 1981-1993 (Hinderer, 2001) - river-load
9b Kander b: 0.4 mm/a 1981-1993 (Hinderer, 2001) - suspended-load
10 Sarine: 0.13 mm/a 1923-1993 (Schlunegger & Hinderer, 2003) - suspended-load
11a Aare a: 0.1 mm/a 1964-1993 (Hinderer, 2001) - river-load
11b Aare b: 0.18 mm/a 1898-1933 (Hinderer, 2001) - delta growth
11c Aare c: 0.21 mm/a 1964-1995 (Schlunegger & Hinderer, 2003) - suspended-load
12 Melchaa: 0.06 mm/a 1911-1987 (Hinderer, 2001) - delta growth
■ Erlenbach: annual running average 1986-2007 (WSL) - bed-load

1 Rhine: 0.24 mm/a 1911-1989 (Hinderer, 2001) - delta growth
2 Rhone: 0.14-0.35 mm/a 1915-1960; 0.07-0.18 mm/a 1960-1994 (Loizeau & Dominik, 2000) - suspended-load

3 Hinterrhine: 0.1 mm/a 1974-1993 (Schlunegger & Hinderer, 2003) - suspended-load
4 Albula: 0.1 mm/a 1926-1993 (Schlunegger & Hinderer, 2003) - suspended-load
5a Dora Baltea a, at Verres: 0.07 mm/a 1999-2002 (Vezzoli, 2004) - bed-load
5b Dora Baltea b, at Pollein: 0.09 mm/a 1999-2002 (Vezzoli, 2004) - bed-load
5c Dora Baltea c, at Sarre: 0.1 mm/a 1999-2002 (Vezzoli, 2004) - bed-load
5d Dora Baltea d, at Avise: 0.21 mm/a 1999-2002 (Vezzoli, 2004) - bed-load
6 Visp: 0.8 mm/a 1965-1993 (Schlunegger & Hinderer, 2003) - suspended-load
7 Landquart: 0.61 mm/a 1964-1995 (Champagnac et al., 2009) - suspended-load
8a Lonza a: 0.18 mm/a 1966-1995 (Schlunegger & Hinderer, 2003) - suspended-load
8b Lonza b: 0.13 mm/a 1964-1995 (Champagnac et al., 2009) - suspended-load

1a Maggia a: 0.17 mm/a 1926-1984 (Hinderer, 2001) - delta growth
1b Maggia b: 0.27 mm/a 1985-1993 (Schlunegger & Hinderer, 2003) - suspended-load
2a Ticino a: 0.1 mm/a 1932-1986 (Hinderer, 2001) - delta growth
2b Ticino b: 0.22 mm/a 1979-1995 (Schlunegger & Hinderer, 2003) - suspended-load
3 Moesa: 0.12 mm/a 1981-1993 (Schlunegger & Hinderer, 2003) - suspended-load
4 Cassarate: 0.15 mm/a 1930-1951 (Hinderer, 2001) - delta growth

1 Arve: 0.17 mm/a 1964-1995 (Champagnac et al., 2009) - suspended-load
2 Izon la B.: 33 mm/a 1990-1995 (Descroix & Mathys, 2003) - measurement stick
3 Séderon: 30 mm/a 1990-1995 (Descroix & Mathys, 2003) - measurement stick
4 Savournon: 9 mm/a 1985-1991 (Descroix & Mathys, 2003) - rugosimeter: slope profile
5 Etoile: 8.7 mm/a 1988-1993 (Descroix & Mathys, 2003) - sediment trap
6 Vers s/M: 8 mm/a 1990-1995 (Descroix & Mathys, 2003) - measurement stick
7 Saint Genis: 7 mm/a 1985-1991 (Descroix & Mathys, 2003) - rugosimeter: slope profile

8 Eygalaye: 7 mm/a 1990-1995 (Descroix & Mathys, 2003) - measurement stick
9 Seignon: 6.8 mm/a 1962-1979 (Descroix & Mathys, 2003) - sediment trap
10 Orpierre: 5.9 mm/a 1983-1993 (Descroix & Mathys, 2003) - sediment trap
11 Roubine: 5.04 mm/a 1985-2000 (Mathys et al., 2003) - sediment yield
12 Laval: 4.15 mm/a 1985-2000 (Mathys et al., 2003) - sediment yield
13 Moulin: 2.11 mm/a 1988-2000 (Mathys et al., 2003) - sediment yield
14 Brusquet: 0.03 mm/a 1988-2000 (Mathys et al., 2003) - sediment yield

Eastern Alps

1a Inn a: 0.1 mm/a 1953-1979 (Hinderer, 2001) - river-load
1b Inn b: 0.09 mm/a 1970-1993 (Schlunegger & Hinderer, 2003) - suspended-load
2 Tiroler Ache: 0.1 mm/a 1926-1979 (Hinderer, 2001) - river-load
3 Iller: 0.07 mm/a 1966-1970 (Hinderer, 2001) - river-load
4 Ammer: 0.07 mm/a 1931-1979 (Hinderer, 2001) - river-load
5 Weissach: 0.04 mm/a 1955-1965 (Hinderer, 2001) - delta growth

Erlenbach
events 1986 - 2007 (WSL)
bed-load

Summer 1987
Summer 1993
Summer 1995